Advanced Technology for Predicting the Fluid Flow Attributes of Naturally Fractured Reservoirs from Quantitative Geologic Data and Modeling

Second Year Annual Report for the Period

September 29, 2001 to September 28, 2002

Authors: Jon E. Olson, Larry W. Lake and Steve E. Laubach

Issued: May 2003

Work Performed under Contract No. DE-FC26-00BC15308
Prepared for the U.S. Department of Energy

Daniel J. Ferguson, Project Manager

U. S. Department of Energy
National Energy Technology Laboratory
One West Third Street
Tulsa, Oklahoma 74103

Prepared by

The Center for Petroleum and Geosystems Engineering
The University of Texas at Austin
1 University Station Box C0300
Austin, TX 78712

QAe7160

Abstract:

This report summarizes the work carried out during the period of September 29, 2001 to September 28, 2002 under DOE Research Contract No. DE-FC26-00BC15308. Our goal is to establish an integrated methodology of fractured reservoir characterization and show how that can be incorporated into fluid flow simulation. We have made progress in all of our proposed tasks this year. We have continued to study the microstructures associated with fractures to document the interaction between fracture growth and diagenetic mineral growth in subsurface reservoir rocks. We have developed a model to simulate the geochemical controls on fracture mineralization. Under certain geologic conditions, the process can be classified as convection- or reaction-dominated using Peclet number and Damkohler number. The model shows that to have a relatively uniform deposition of calcite within a fracture, the velocity of supersaturated solution must be very high or the solution must be only slightly supersaturated with respect to calcite. We have postulated a preliminary model to explain the dependence of subcritical crack index on lithologic and diagenetic parameters. Grain size, cement content, and porosity dominate the subcritical index value, given the same chemical environment. Finally, using subcritical crack growth measurements from a West Texas dolomite reservoir and our fracture propagation model, we generated natural fracture networks that were imported into a reservoir simulator. We found that reservoir block permeability depended not only on the intensity of fracturing (as measured by the cumulative length of fractures per area) but also the degree of clustering and the average length of the individual fracture segments in a population. This type of modeling at the outcrop scale will be a stepping stone to determining effective simulation block permeability for field scale modeling.
Finally, we have developed a technique for a direct analysis of well rate fluctuations that allows determination of the connectivity between well pairs in injection processes. The results of this analysis appear to agree with independently-determined geological features and should be useful in determining fracture patterns flow characteristics at the field scale.

Table of Contents

Abstract: iii
List of Figures v
List of Tables viii
Executive Summary: ix
1. Introduction 1
2. Geochemical Modeling of Mineral Precipitation in Fractures 1
2.1. Influence of saturation states and flow velocity 1
2.2. Convection, diffusion and surface reaction in a fracture 7
2.3. Development of mathematical model 10
2.4. Results and discussion 15
2.5. Conclusions 25
2.6. References 26
3. Fracture Mechanics Attributes of Sandstones – An Example from the Travis Peak Formation 29
3.1. Introduction 29
3.2. Subcritical fracture model 29
3.3. Experimental measurements 34
3.4. Discussion: Controls on subcritical index 39
3.5. Micro-fractures as proxies for macro-fractures 39
3.6. Conclusions 41
3.7. References 41
4. Permeability Estimation for Geomechanically Generated Fracture Patterns 44
4.1. Introduction 44
4.2. Geomechanical Simulation 44
4.3. Flow Modeling 47
4.4. Verification 50
4.5. Chirlin Solution 52
4.6. Flow Modeling of Simulated Fracture Patterns 58
4.7. Other Factors Affecting Fracture Permeability 63
4.8. Conclusions 68
4.9. References 69
5. Technology Transfer 71
6. Plans for Next Research Steps 71
7. Appendix 1: Publications and Presentations 72
8. Appendix 2: FRAC Technology Transfer Meeting 74

List of Figures

Figure 2.1. Photomicrographs of a channel surface near the inlets of experiments showing different amounts of calcite precipitate with respect to changes in fluid velocity and saturation state. Scale bars are 150 micron. Here white spots are calcite precipitation. 3
Figure 2.2. (a) The relationship between solution saturation index with respect to calcite, and the flow velocity required to produce a 10 % change in precipitation rate in 10 and 100 cm fractures under the experiment condition. (b) The relationship between the aperture size and the flow velocity required to produce a 10\% change in precipitation rate at different supersaturations (numbers next to curves) with respect to calcite. 5
Figure 2.3. Relationship between solution/calcite volume ratio and saturation state with respect to calcite at 6.7 cm/h 6
Figure 2.4. Schematic picture of precipitation/dissolution reaction in a single fracture . 11
Figure 2.5. Fracture shape with precipitation 13
Figure 2.6. Concentration history with $N_{Pe} = 100$, $N_{Sh} = 0$ 16
Figure 2.7. Concentration profile with various N_{Sh} at $t_D = 1$ pore volume of supersaturated fluid injected. 17
Figure 2.8. Concentration profile with various N_{Pe} at $t_D = 1$ pore volume of supersaturated fluid injected 18
Figure 2.9. Dimensionless pressure difference profile with $N_{Pe} = 100$, $N_{Sh} = 2$ 20
Figure 2.10. Dimensionless aperture profile with $N_{Pe} = 100$, $N_{Sh} = 2$ 20
Figure 2.11. Dimensionless aperture profile with $N_{Pe} = 100$, $N_{Sh} = 0.2$ 21
Figure 2.12. Dimensionless aperture profile with $N_{Pe} = 1000$, $N_{Sh} = 0.2$ 21
Figure 2.13. Dimensionless aperture profile with $N_{Pe} = 567.83$, $N_{Sh} = 3.38\times10\text{-}5$ 23
Figure 2.14. Largest aperture difference history with $N_{Pe} = 567.83$, $N_{Sh} = 3.38\times10\text{-}5$ ... 23
Figure 2.15. Boundary of convection dominant vs. reaction dominant process 24
Figure 3.1: Fracture trace maps for numerical subcritical crack propagation simulations for different subcritical crack indices, using 400 initial flaws. Each case used an identical crack-perpendicular extensional strain rate. Note increasing fracture density with decreasing n, and fracture clustering for n=40 and n=80. From Olson et al. (2001). 31
Figure 3.2: Log of stress intensity vs. log of fracture velocity. The slope of this line (n = subcritical index value) is hypothesized to decrease with increase in grain size and water content and increase with a decrease in surface energy. 33
Figure 3.3: Grain size (mm) vs. subcritical index plot. The curve fit shows that the results follow the predictions based on polycrystalline materials, where subcritical index is inversely proportional to grain size (d). 34
Figure 3.4. Variation in subcritical index with carbonate cement (vol%). For carbonate values below 8 vol% samples follow the predictions as specified for polycrystalline materials (Gesing and Bradt, 1983). For values larger than 8 vol%, samples behave in the opposite sense. 36
Figure 3.5. Subcritical fracture velocity vs. stress intensity. Four tests were carried out on one sample from a depth of 9817 ft. First the sample was tested in air after a standard preparation procedure (black curves). After these tests were completed the sample was soaked in Salol and dried. The sample was tested again (light grey

curves) and a marked reduction in subcritical index was observed. The thin black and grey lines are trend lines fitted through the data. The thicker part on the curve corresponds to the data collected. 37
Figure 3.6. Difference between dry subcritical index value and submerged subcricital index value (Δ) vs. grain size. According to the literature this value should be positive since subcritical index decreases with increase in water content. However, we find this not to be true for large grain size values. 38
Figure 3.7. A) Degradation vs. depth below formation top. Large degradation values correspond to sealed micro-fractures indicating that macro-fractures will be largely non conductive. Values below 50% indicate mostly open fractures (Degradation analysis by Stephen Laubach). B) Subcritical index vs. depth below formation top. Combination of the two methods allows for subsurface fracture pattern prediction. 40
Figure 4.1. SWCF simulated fracture pattern (Realization 3) with a bed height of 10 m and SCC index of 40. 46
Figure 4.2. SWCF simulated fracture pattern (Realization 3) with a bed height of 10 m and SCC index of 80. 46
Figure 4.3. SWCF simulated fracture pattern (Realization 3) with a bed height of 5 m and SCC index of 40. 46
Figure 4.4. SWCF simulated fracture pattern (Realization 3) with a bed height of 5 m and SCC index of 80. 46
Figure 4.5. Grid cell representation of a fracture patch, showing the cell dimension and fracture aperture. 47
Figure 4.6. Schematic of grid, depicting cell dimensions and x direction permeability. 48
Figure 4.7. Schematic of grid, depicting the location of, and x direction permeability due to, a fracture. 48
Figure 4.8. Schematic of grid, depicting non-neighbor connections between cells, to model flow due to a fracture. 49
Figure 4.9. Plot showing an embedded fracture extending from end to end in a simulation grid. 51
Figure 4.10. Periodic staggered array of fractures depicting parameters used in the Chirlin solution 52
Figure 4.11. The Chirlin solution for Effective Permeability Ratio, Rk, for flow parallel to fractures. 53
Figure 4.12. Chirlin layout for the explicit fracture representation study..... 54
Figure 4.13. Gridded 9 X 9 array with two edge fractures 55
Figure 4.14. Comparison of analytical solution and NNC simulation for the effective permeability of a periodic array of fractures with two fractures on the edge of the grid 55
Figure 4.15. Gridded 9 X 9 array with multiple fractures..... 56
Figure 4.16. Comparison of analytical solution and NNC simulation for the effective permeability of a periodic array of fractures with multiple fractures in the grid (h = 1.5). 57
Figure 4.17. Comparison of analytical solution and NNC simulation for the effective permeability of a periodic array of fractures with multiple fractures in the grid (h=0.5)..... 57
Figure 4.18. Values of R_k vs. strain, for all 7 realizations for a bed height of 10 m..... 58

Figure 4.19. Values of R_k vs. strain, for all 7 realizations for a bed height of 5 m 59
Figure 4.20. Mean and standard deviation of the effective permeability ratios for a bed height of 10 m. 59
Figure 4.21. Mean and standard deviation of the effective permeability ratios for a bed height of 5 m. 60
Figure 4.22. Average Rk vs. average total length (average of 7 realizations) 60
Figure 4.23. Average Rk vs. average mean length (average of 7 realizations) 61
Figure 4.24. Average Rk vs. average mean aperture (average of 7 realizations) 62
Figure 4.25. The effect of synkinematic cement on effective permeability for a SWCF simulated fracture pattern (realization 4) with a bed height of 10 m and SCC index of 40. 63
Figure 4.26. SWCF simulated fracture pattern (realization 4) with a bed height of 10 m and SCC index of 40 with an emergent threshold ratio of 0 and no degradation 64
Figure 4.27. SWCF simulated fracture pattern (realization 4) with a bed height of 10 m and SCC index of 40 with an emergent threshold ratio of 2..... 65
Figure 4.28. SWCF simulated fracture pattern (realization 4) with a bed height of 10 m and SCC index of 40 with a degradation index of 44 %..... 66
Figure 4.29. SWCF simulated fracture pattern (realization 4) with a bed height of 10 m and SCC index of 40 with a degradation index of 78 %..... 67
Figure 4.30. The effect of postkinematic cement on effective permeability for a SWCF simulated fracture pattern (realization 4) with a bed height of 10 m and SCC index of 40 67

List of Tables

Table 2.1. Data for test cases..... 22
Table 3.1. Test results of the Travis Peak Formation..... 35
Table 4.1. Mean values of the SCC index for six South Wasson Clear Fork samples. .. 45
Table 4.2. Input data to the crack growth simulator..... 45
Table 4.3. Simulation results using the explicit fracture-representation method and a cell size of 0.05 ft for a staggered array of four fractures..... 54
Table 4.4. Simulation results using the explicit fracture-representation method and a cell size of 0. 025 ft for a staggered array of four fractures..... 54
Table 4.5. Microcrack observations from South Wasson Clear Fork thin sections. 66

Executive Summary:

This report summarizes the work carried out during the period of September 29, 2001 to September 28, 2002 under DOE Research Contract No. DE-FC26-00BC15308. All of the work described has been performed at the University of Texas at Austin.

Observational verification of the emergent threshold (Task 1) is largely complete (Year 1 report); however, our studies lead to a new hypothesis of how cementation and fracture growth interact. Thus we have continued to study to microstructures associated with fractures near the emergent threshold as these features hold evidence useful for guiding the selection of appropriate mechanics properties for fracture growth modeling.

We have completed a mathematical model to simulate the geochemical controls on fracture mineralization (Task 2), and have demonstrated its implications with regard to calcite mineralization in fractures. The fluid convection, diffusion and precipitation-dissolution (PD) reaction inside a finite space are solved as a simplified representation of natural fracture mineralization. Through this test case of a calcite precipitation problem, we present a process of the fracture mineralization. With certain geologic conditions, the process can be classified as convection- or reaction-dominated using Peclet number and Damkohler number. The model shows that to have a relatively uniform deposition of calcite within a fracture, the velocity of supersaturated solution must be very high or the solution must be only slightly supersaturated with respect to calcite.

We have made significant progress in our fracture mechanics testing of subsurface reservoir rocks, and we have postulated a preliminary model to explain the dependence of subcritical crack index on lithologic and diagenetic parameters (Task 3). Grain size, cement content, and porosity dominate the subcritical index value, given the same chemical environment. Subcritical index decreases with increase in grain size as proposed by the theory for polycrystalline materials. For small carbonate percentages the subcritical index increases with increase in carbonate cement content. However for large carbonate percentage the trend is reversed and subcritical index decreases with carbonate content.

We have made significant accomplishments related to the fluid flow analysis for fractured reservoirs (Task 4). Firstly, we have established a procedure for estimating permeability in fractured reservoir blocks (This work was done in collaboration with DOE Contract No. DE-AC26-98BC15105). Using subcritical crack growth measurements from a West Texas dolomite reservoir and our fracture propagation model, we generated natural fracture networks that were imported into a reservoir simulator. We found that reservoir block permeability depended not only on the intensity of fracturing (as measured by the cumulative length of fractures per area), but also the degree of clustering and the average length of the individual fracture segments in a population. This type of modeling at the outcrop scale will be a stepping stone to determining effective simulation block permeability for field scale modeling. Secondly, we have developed a technique by which communication between injectors and producers can be quantified using only well rate data. Using multivariate linear regression analysis, high permeabilities trends can be identified as well as the location of permeability barriers.

Finally, we have effectively transferred our technology through our industry consortium review meetings, theses and several publications, documentation of which are included as appendices to this report.

1. Introduction

This report has been organized in a topical fashion to document progress on the following research tasks as originally proposed to the Department of Energy for this project:

- Task 1: Observational verification of emergent threshold, a characteristic fracture size (aperture) below which natural fractures are completely mineralized by cements precipitated concurrently with fracture opening and above-which fractures may preserve porosity and would be expected to be conduits for flow in the absence of later cements.

- Task 2: Theoretical investigation of the geochemical controls on fracture mineralization, how fracture aperture size can affect the amount of preserved porosity in natural fractures, and how large fractures (above emergent threshold) can become closed by cements.

- Task 3: Quantification of the fracture mechanics properties, particularly subcritical crack growth parameters, in oil reservoir rock types, and investigating the role of diagenesis in controlling the change of these parameters through time (over the burial history of a reservoir).

- Task 4: Fluid flow analysis of fracture network realizations generated using a geomechanical model that depends on subcritical index as a key input parameter and that incorporates diagenetic modification of fracture apertures.

Observational verification of the emergent threshold (Task 1) is largely complete (Year 1 report); however, our studies lead to a new hypothesis of how cementation and fracture growth interact. Thus we have continued to study to microstructures associated with fractures near the emergent threshold as these features hold evidence useful for guiding the selection of appropriate mechanics properties for fracture growth modeling. Significant progress has been made in Tasks 2 through 4, the focus of research during this report period. This progress is described below.

2. Geochemical Modeling of Mineral Precipitation in Fractures

2.1. Influence of saturation states and flow velocity

Mineral-filled or mineral-lined fractures (veins) are nearly ubiquitous in rocks that have experienced even slight deformation. They are present in otherwise undeformed, flat-lying petroleum reservoir rocks, where mineral-lined fracture may provide essential permeability enhancement, but sealed fractures may not. The presence of cement in fractures indicates that: (1) fluids were both present and perhaps moving during and after the deformation event, carrying sufficient mass of fracture constituents in solution to precipitate the observed fracture void volume, and (2) dilation of the rock took place for fractures to be both open and provide pathways for fluid flow. Because some fracture-filling minerals may have precipitated from the fluid that existed during deformation whereas others precipitated later when fractures were not opening, fractures may provide

an important record of several parameters: (a) deformation kinematics, *i.e.* how the rock surrounding a fracture moved during deformation, from structures within cements in fractures (vein fabrics), (b) mechanics, *i.e.* the stress which caused this motion, from deformation textures, (c) pressure and temperature within the fluid, important for determining both rock strength and P-T-t paths, from fluid inclusions and other methods, and (d) fluid composition, needed to understand fluid sources, from fracture mineral composition (Lee et al., 1996).

Our studies show that in siliciclastic rocks and in many carbonate rocks, the main phase sealing large fractures is a carbonate mineral (calcite, ferroan dolomite, ankerite). The kinetics of calcite precipitation in subsurface environments is uncertain. Although extensive studies on calcite reaction kinetics have been done in seawater (Morse, 1983; Mucci and Morse, 1983; Mucci, 1986), the precipitation kinetics of calcite in fresher groundwater are largely unknown. In the kinetic models of calcite dissolution and precipitation in seawater, the simple first-order reaction kinetics cannot be applied because the carbonate reaction is complex. Several different processes are usually involved during calcite precipitation/dissolution reaction such as adsorption, diffusion and desorption (Morse, 1983). The precipitation kinetics of calcite is a large reaction order surface controlled process (usually $1 < n < 3$). Morse and Machenzie (1993) in their paper on geochemical constraints on calcium carbonate mass transport in subsurface environments, proposed a coupled, chemical kinetic-hydrodynamic model that has potential application to conditions similar to those that may exist during fracture filling by calcite. Their calculations showed that the rate of precipitation is related to the flowrate as well as to the saturation state in a given subsurface open system. This model may give basic information about both how much fluid is necessary and how much time is needed to fill up an open space in the subsurface.

Estimation of the expected time and amount of fluid needed to produce mineral filling in fractures has been a largely unresolved problem because of a lack of data on precipitation kinetics in subsurface environments. Fyfe et al. (1978) and Fournier and Potter (1982) have calculated the volume of fluid required to fill a quartz vein opening as a function of temperature change in an upward flowing fluid based on the temperature-solubility relationship of quartz. Fisher and Brantley (1992) developed various models for quartz overgrowths in fractures related to episodic fluid migration which were compared to natural syntectonic fractures in the Kodiak Formation. In their crack-seal vein models, the time required for one crack-and-seal event was estimated to be about 100 years. However, few attempts have been made for describing precipitation by which fractures filled by calcite, especially in terms of precipitation kinetics (Morse and Machenzie, 1990; 1993). The precipitation kinetics of fracture-filling calcite is controlled by not only time and fluid volume required for the precipitation of a certain mass of fracture mineral, but also the precipitation pattern inside a fracture opening. The precipitation kinetics of calcite in fracture openings with a continuous fluid flow is still poorly understood. Identification of both chemical and physical parameters controlling the precipitation of calcite such as pressure, temperature, partial pressure of CO_2 (P_{CO2}), flow velocity, and co-precipitating ions provides important constraints on establishing conceptual models for calcite precipitation in fractures (Mucci and Morse, 1983; Sjöberg and Richard, 1984; Mucci, 1986; Reddy, 1986; Burton and Walter, 1987; Dromgoole and Walter, 1990;

Morse and He, 1993; Andritsos et al., 1997).

Studies of the nucleation and growth of calcite in fractures can contribute to the understanding of fracture filling processes in nature (Dickson, 1992; Clark et al, 1995). Factors controlling the kinetics of calcite nucleation and growth, such as saturation state, temperature and pressure, density of surface-controlled nucleation, concentration of dissolved ions, influence of growth inhibitors, and flow velocity can influence the morphology and growth rate of calcite (Nancollas and Reddy, 1971; Lahann, 1978; Mucci and Morse, 1983; Arnórsson, 1989; Dromgoole and Walter, 1990; Gonzalez et al., 1992; Keysar et al., 1994; Andritsos et al., 1997).

Nucleation of calcite was initiated on crystallographic-controlled sites that might be dislocations or have a different angle of the axis with respect to the surface (Dickson, 1992). Further crystal growth preferentially occurs on the newly nucleated calcite. This is probably because of the increased surface area (Morse and Machenzie, 1993) as well as the favorable crystallographic orientation (Dickson, 1992) of the nucleated calcite for further crystal overgrowth.

By directly measuring the amount of calcite precipitation, Lee and Morse (1999) showed that both the saturation state and fluid flow velocity are two very important factors influencing calcite precipitation in fractures. The precipitation of calcite is controlled by high order reaction kinetics and influenced by flow velocity. In their experimental results, the pattern and amount of precipitated calcite were presented for faster and slower flow velocities at the same degree of saturation state in Figure 2.1. At a faster flow velocity, aggregates of very fine-grained calcite overgrew with some intergranular space and the amount of calcite precipitation was less than at slow velocity. At the slow flow velocity, most of the inlet surface is covered with a precipitated calcite layer. The surface of the calcite layer was very irregular. Individual calcite crystals were too small to be identified by optical microscopy. Therefore, a large amount of calcite precipitated near the inlet portion at a relatively slow flow velocity.

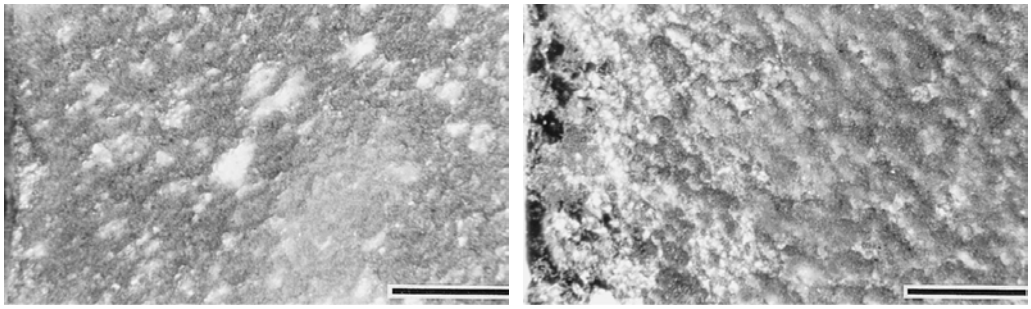

(a) Calcite precipitation at high velocity (b) Calcite precipitation at low velocity

Figure 2.1. Photomicrographs of a channel surface near the inlets of experiments showing different amounts of calcite precipitate with respect to changes in fluid velocity and saturation state. Scale bars are 150 micron. Here white spots are calcite precipitation.

A major problem in understanding fracture filling is a realistic estimation of the volume

of fluid and time required to fill a given vein volume. Several major factors influence the amount of calcite precipitated from a given volume of solution. At constant temperature and pressure, these factors include saturation state, P_{CO2}, the activity coefficients of ions, relative concentrations of dissolved components, and presence of reaction inhibitors (Morse and Machenzie, 1990). Based on the model by Lee et al. (1996), various solution/calcite volume ratios required for synthetic vein formation were calculated at different initial saturation states of the solution. The solution/calcite volume ratio dramatically decreases with increasing solution saturation state at a constant flow velocity. This implies that extremely large volumes of fluid are required to precipitate calcite at low saturation states. When fracture fillings develop by fracture-channelized fluid flow, either the fluids must be slightly supersaturated with respect to calcite or the flow velocity must be very fast to prevent uneven distribution of calcite along a fracture. Therefore, the expected fluid/calcite volume ratio in natural veins might be very large, sometimes more than 10^6.

The distribution of calcite is also problematical. As the fluid flows out of the high-pressure reservoir, it becomes supersaturated with respect to calcite through a combination of fluid pressure drop, decrease in partial pressure of dissolved gases (*e.g.* CO_2) and perhaps mixing with fresher water. Large calcite-filled fractures should not occur if cracks and faults are simple fluid conduits (Morse and Machenzie, 1993). The implication of this is that simple conduits should fill at the inlet, effectively plugging them to further fluid flow. In the field this should appear as partially filled fractures, the filling occurring asymmetrically, namely thicker toward the inlet and thinner toward the outlet. The great preponderance of observation on veins shows that fillings are largely symmetrical with respect to the plane of symmetry of the vein and that vugs or openings are relatively rare.

Lee et al. (1996) presented the results of their model, which include the calculated flow velocities required to produce a relatively uniform distribution of fracture-filling calcite. Here relatively uniform means the rate of deposition at exit of vein equals 90% of that at vein entrance. The two variables used in Figure 2.2 are solution saturation state and fracture length with 0.2 cm aperture. Here SI is the saturation index with respect to calcite, which represents saturation states of injected fluid.

$$SI = \frac{a_{Ca^{2+}} a_{C0_3^{2-}}}{K_{sp}} \qquad (2\text{-}1)$$

where a is the thermodynamic activity and K_{sp} is the thermodynamic solubility product of calcite. As is reasonably expected, the required flow velocity increases approximately in proportional to vein length at moderate to high supersaturations.

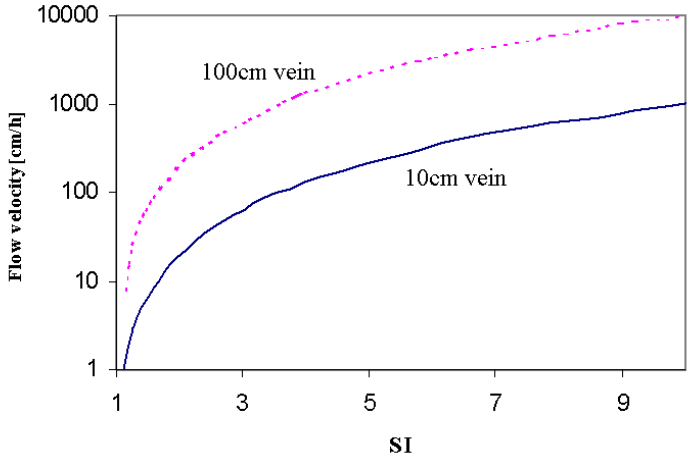

(a)

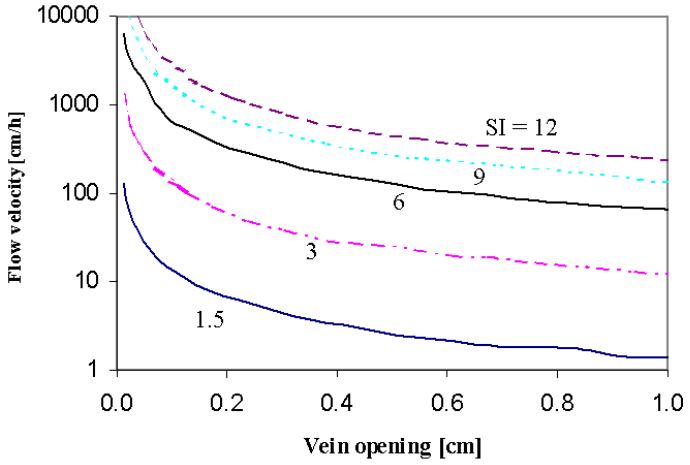

(b)

Figure 2.2. (a) The relationship between solution saturation index with respect to calcite, and the flow velocity required to produce a 10 % change in precipitation rate in 10 and 100 cm fractures under the experiment condition. (b) The relationship between the aperture size and the flow velocity required to produce a 10\% change in precipitation rate at different supersaturations (numbers next to curves) with respect to calcite.

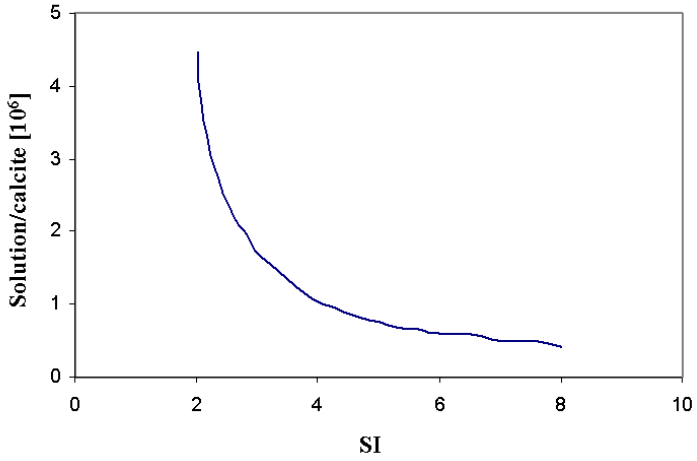

Figure 2.3. Relationship between solution/calcite volume ratio and saturation state with respect to calcite at 6.7 cm/h

The aperture of a fracture determines the solution volume to fracture surface area ratio and thus influences the relationship between required solution flow velocity and solution saturation state with respect to calcite necessary to produce the previously described change in calcite deposition rate. This relationship is shown in Figure 2.3 for a 10 cm long fracture and different initial solution saturation states. There is a rapid increase in required flow velocities for fracture aperture less than 0.2 cm. The flow velocity is required to go to infinity as the aperture goes to zero. Again at all but low degrees of supersaturation relatively high flow velocities *e.g.* greater than 10 cm/h are required even at aperture up to 1 cm in size.

To have a relatively uniform deposition of calcite in a vein, either a low degree of supersaturation with respect to calcite must exist in the solution or its flow velocity must be high. Although little information is available on fluid flow velocities in veins under subsurface conditions, such high flow velocities are probably not common. Therefore fracture-filling calcite is probably often deposited from only slightly supersaturated flows. The less supersaturated the solution is, the greater is the volume of solution required to produce a given amount of fracture filling calcite.

In most cases, fracture mineralization probably occurs at elevated pressure ad temperature, and most likely with considerable gradient in P and T. Changes in P and T not only can affect solution saturation state, but are also likely to influence rates of precipitation at a given saturation state, P and T.

Solution/calcite volume ratio can vary with several factors influencing precipitation rate of calcite in subsurface environments, such as rate constant k, solution carrying capacity and aperture size. In nature, therefore, the estimated time period for fracture filling for a given flow velocity could vary by at least an order of magnitude. Also, if the calcite volume increases hundreds of times for meter-scale fractures, the time required for producing the calcite volume in the fractures could similarly increase to about 10^2 years. This range of estimated time scales may be reasonable, and is comparable to the 10^3 to

10^6 year estimate of Fisher and Brantley (1992) for the formation of a millimeter-scale thickness crack-seal fracture. Also, they estimated that micron-scale crack-and-seal episode in crack-seal fractures could occur within 10^3 to 10^4 years. It is, therefore, proposed that most natural veins develop over thousands to sometimes millions of years, which is quite slow.

2.2. Convection, diffusion and surface reaction in a fracture

Groundwater flow frequently causes cementation and dissolution. Cements of calcite, quartz, pyrite, dolomite or ankerite are often deposited within fractures. Partially cemented fractures are created if this cementation fails to completely and totally fill the fracture with cement or if subsequent dissolution leaches out some of the mineralization. In this way, a highly conductive fluid path can exist. In carbonates, fracture permeability can be created by similar processes or through the dissolution of the host rock on the fracture faces. Natural fluids are not always in equilibrium with solid phases with which they are in temporary or permanent contact. The deviation from equilibrium is usually small and the reaction kinetics under this condition is often very sensitive to environmental factors and solution composition.

The hydrological cycle interacts with the cycle of rocks. Minerals dissolve in or react with the water. Under different conditions, minerals are precipitated and accumulate on the ocean floor or porous media. Precipitation and dissolution reactions (PD) impart of the water constituents that modify its chemical properties. Most common basis is a consideration of the equilibrium relations (Stumm and Morgan, 1996). PD reactions are generally slower than reactions among dissolved species, but it is quite difficult to generalize about rates of precipitation and dissolution. Frequently, the solid phase formed incipiently is metastable with respect to a thermodynamically stable solid phase. Examples are provided by the occurrence under certain conditions of aragonite instead of stable calcite or by the quartz oversaturation of most natural waters. This oversaturation occurs because the rate of attainment of equilibrium between silicic acid and quartz is extremely slow.

The solubility of many inorganic salts increase with temperature, but a number of compounds of interest in natural waters (*e.g.* $CaCO_3$, $CaSO_4$) decrease in solubility with an increase in temperature. Pressure dependence of solubility is slight but must be considered for the extreme pressures encountered at ocean depths. For example, the solubility product of $CaCO_3$ will increase with increased pressure.

Relations used to describe precipitation and dissolution reaction rates usually describe the reaction of solid and aqueous species in the following way,

$$\tau T \underset{k}{\longleftrightarrow} \alpha A + \beta B \,, \qquad (2\text{-}2)$$

where k_1, the forward reaction rate constant, is for dissolution and k_2, the backward reaction rate constant, is for precipitation. The two aqueous species are A (*e.g.*, Ca^{2+}) and B (*e.g.*, CO_3^{2-}), and T (*e.g.*, $CaCO_3$) is a single-phase solid. The stoichiometric coefficients (α, β and τ) indicate the number of moles of each species in the reaction. At

equilibrium, there is no net reaction; the forward and backward reactions are equal, $k_1\ a_T = k_2\ a_A\ a_B$. Rearranging terms, we have

$$\frac{k_1}{k_2} = \frac{a_A a_B}{a_T} = a_A a_B = K_{sp} \tag{2-3}$$

where a_j is the molal activity of component j. The reaction is assumed to be elementary and reversible, and the rate law for species T in terms of the surface activitiy of the species, which is indicated by superscript s, is,

$$r_T = -k_1 (a_T^s)^\tau + k_2 (a_A^s)^\alpha (a_B^s)^\beta \tag{2-4}$$

The reaction rates of each component are related by

$$r_T = -\frac{\tau}{\alpha} r_A = -\frac{\tau}{\beta} r_B \tag{2-5}$$

Supersaturation of solid T is defined as the state when the ion activity product (IAP) of its component in a solution is greater than what is allowed by true equilibrium. The term *true* equilibrium refers to the thermodynamic equilibrium state that makes $r_T = 0$. Supersaturation is quantified by a saturation index (SI), which is defined by $SI=IAP/K_{sp}$. For SI > 1, the solution is *supersaturated* and precipitation takes place.

Since molal activity of component j is defined by $a_j = \gamma_j C_j$, the ion activity product is related to the ion concentration product by the activity coefficient (γ) product. For example,

$$C_A C_B = \frac{a_A a_B}{\gamma_A \gamma_B} \tag{2-6}$$

$$SI = \frac{\prod_{j=1}^{J} a_j^{\eta_j}}{K_{sp}} = \frac{(\gamma_A C_A)^\alpha (\gamma_B C_B)^\beta}{K_{sp}} \tag{2-7}$$

where η is a stoichiometric coefficient. γ is related to the ionic strength of the aqueous phase through several models (Stumm and Morgan, 1996). When $\gamma = 1$ for all components, activities and concentrations become equal and the aqueous phase is an ideal solution. Consequently, change in SI is not the same as change in the ion concentration product associated with dissolution or precipitation. Additionally, activity coefficients depend on solution composition.

Since the pure solid is generally assigned an activity of unity, Eq. (2-3) could be expressed by the first order reaction kinetics.

$$r_T = k_1 (SI - 1) \tag{2-8}$$

In reality, solid precipitation is not a spontaneous reaction. Crossing the saturation line (SI=1) is not sufficient to cause precipitation but energy barrier must be overcome. The energy barrier is the level of Gibb's free energy and is associated with a critical point on the supersaturation line (SI=SI*) above which a solid starts to nucleate new crystals (Nielsen, 1981).

Nucleation is the formation of new crystal for a specific solid phase. Heterogeneous nucleation, which is the process occurred on the surface of any already existing solid, is often considered in the flow through permeable media. Heterogeneous nucleation involves three different physical phenomena: (1) adsorption of the solid molecule onto a solid surface, (2) diffusion jumps of those adsorbed molecules along a diffusion path, and (3) crystal growth at a nucleation site. Since the precipitation is initiated at a smaller SI* in heterogeneous nucleation than that in the homogeneous nucleation, the energy barrier is not considered in this study.

Several different mechanisms occur in a reaction between a solid and a solution. A typical sequence would be: diffusion of a reactant through a stagnant boundary layer to the surface, adsorption of the reactant on the surface, diffusion on the surface to a reactive or high energy site (such as a dislocation), reaction of the reactant with the solid, diffusion of products away from the reaction site, desorption of products, and the diffusion of products to bulk solution (Araque, 2001). A basic idea in the study of reaction kinetics is that under a given set of conditions, one mechanism will be slower than the others. This step is then the rate-controlling mechanism. Generally, surface reactions are most important near equilibrium, while transport control of reaction rates becomes more important as distance from equilibrium increases.

Simple first order reaction kinetics in Eq. (2-8) cannot be applied to the precipitation dissolution reaction for carbonate precipitation (Morse, 1983). Therefore, the mineral precipitation rate has most frequently been expressed by an empirical rate law of the form (Morse, 1983)

$$r_T = k_1 (SI - 1)^n \qquad (2\text{-}9)$$

$$\log r_T = n \log (SI - 1)^n + \log k_1 \qquad (2\text{-}10)$$

where n is the empirical reaction order.

Plummer et al. (1978) made the first successful attempt to derive a mechanistic expression for calcite dissolution kinetics in simple solutions. Three parallel elementary reactions were combined to represent the overall reaction, and their representative rate constants were determined:

$$CaCO_3 + H^+ \leftrightarrow Ca^{2+} + HCO_3^- \qquad (2\text{-}11)$$

$$CaCO_3 + H_2CO_3 \leftrightarrow Ca^{2+} + 2HCO_3^- \qquad (2\text{-}12)$$

$$CaCO_3 + H_2O \leftrightarrow Ca^{2+} + HCO_3^- + OH^- \quad (2\text{-}13)$$

However, difficulties were encountered when this reaction control model was applied to the crystal growth of calcite (Busenberg and Plummer, 1986). Inskeep and Bloom (1985) conducted a series of calcite precipitation experiments to examine kinetic models, including the Plummer et al. (1978) mechanistic model. They concluded that calcite precipitation kinetics under their experimental conditions was best represented by a simple elementary reaction:

$$Ca^{2+} + CO_3^{2-} \leftrightarrow CaCO_3 \quad (2\text{-}14)$$

Zhong and Mucci (1993) presented the experimental results of calcite precipitation in seawater. From their measurements, when P_{CO2}=0.0031 atm and $C_{Ca^{2+}} \approx 10.5$ mmol/kg of seawater at 25°C the calcite dissolution rate constant obtained in seawater is 0.29 μmol/m^2h, which is significantly smaller than that of Chou et al. (1989), 2324.4 μmol/m^2h in dilute solution. This is in agreement with observations that the calcite dissolution rate is significantly slower in seawater than in low ionic strength $CaCl_2$ + $MgCl_2$ solutions at identical degrees of undersaturations and close to equilibrium (Walter, 1986).

2.3. Development of mathematical model

Fluid convection, diffusion and PD reactions inside a finite parallel plate are solved as a simplified representation of natural fracture mineralization. The problem involves mass transfer within the fluid accompanied by chemical reaction at the fracture surface.

The surface condition associated with flow and precipitation / dissolution (PD) reaction is nonlinear and generally depends on more than two ionic components. Unlike a single-component mass transfer processes, at least two mass-conservation equations are needed in PD problems, and these must be coupled at the fracture surface through the reaction rate term. (Noh, in progress) When the inlet concentration is greater than the equilibrium concentration, precipitation will occur by reaction at the fracture surface and decrease the fracture aperture. The cementation of carbonate is an example of crystal growth by precipitation. For dissolution, however, the aperture will be increased.

Figure 2.4 shows a schematic diagram of flow and PD. The finite parallel plate will represent a single fracture. When a solute flows through the plate, it diffuses to the solid surface where a PD reaction takes place. The reaction rate at the surface strongly influences the outlet solute concentration.

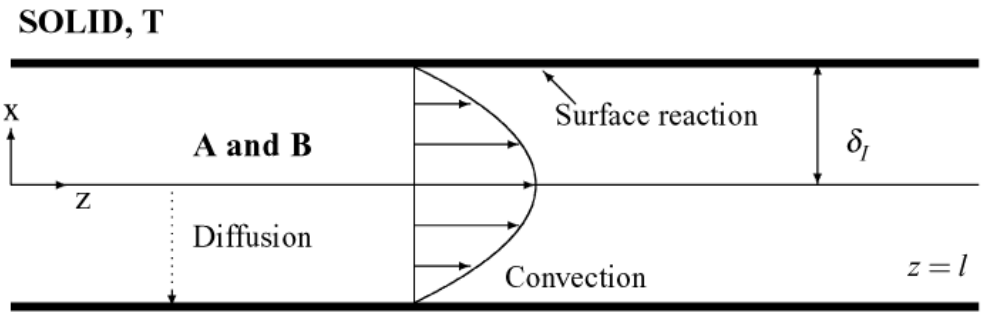

Figure 2.4. Schematic picture of precipitation/dissolution reaction in a single fracture

We simplify the problem by considering convective and diffusive mass transfer and reaction as an extended work of Wu (1992). Several assumptions are made such as (1) uniform initial concentration, (2) uniform and constant temperature, (3) the PD reaction occurs only at the solid surface, (4) single-phase flow, (5) incompressible, laminar flow in the fracture, (6) only two reactive components in dilute concentrations, (7) convection in the z-direction (parallel to flow), and (8) diffusion only in the x-direction (perpendicular to flow). Additional simplifications follow from assuming a dilute solution: concentrations and activities and equal, and diffusion coefficients are isotropic and independent of concentration.

We solve the transient flow and PD problem with variable aperture along the parallel plate and investigate the change of aperture size with time. Early work on this problem (Wu, 1992) used a radial geometry such as tube flow. The mass conservation equations for the two species are,

$$\frac{\partial C_A}{\partial t} = -v_z \frac{\partial C_A}{\partial z} + D_A \frac{\partial^2 C_A}{\partial x^2} \quad 0 \le x \le \delta(z,t) \;\; 0 \le z \le l \;\; t > 0 \tag{2-15}$$

$$\frac{\partial C_B}{\partial t} = -v_z \frac{\partial C_B}{\partial z} + D_B \frac{\partial^2 C_B}{\partial x^2} \quad 0 \le x \le \delta(z,t) \;\; 0 \le z \le l \;\; t > 0 \tag{2-16}$$

The fluid velocity distribution is determined by the equation of motion for a Newtonian fluid with constant density and viscosity (Bird et al., 2002).

$$\rho \frac{D\vec{v}}{Dt} = -\nabla p + \mu \nabla^2 \vec{v} + \rho \vec{g} \tag{2-17}$$

From the equation above, we only allow the convection in the z-direction and it depends on x. Therefore, Eq. (2-17) is rewritten as

$$\mu \frac{\partial^2 v_z}{\partial x^2} = \frac{\partial p}{\partial z} \tag{2-18}$$

With two boundary conditions at the center of the fracture and the fracture wall,

$$v_z = 0 \text{ at } x = \delta, \ \frac{\partial v_z}{\partial x} = 0 \text{ at } x = 0 \tag{2-19}$$

The x-direction fluid velocity distribution is represented by

$$v_z = \frac{\Delta P \delta^2}{2\mu l}\left[1 - \left(\frac{x}{\delta(z,t)}\right)^2\right] = \frac{3}{2}\left(\frac{q(t)}{2\delta(z,t)W}\right)\left[1 - \left(\frac{x}{\delta(z,t)}\right)^2\right] \tag{2-20}$$

where l is the length of a single fracture and W is the width of a fracture. A mass balance on mineral T at the fracture surface is

$$\frac{\partial \delta(z,t)}{\partial t} = -\frac{M_T}{\rho_T} r_T \tag{2-21}$$

Here M_T is the molecular weight and ρ_T is the density of solid T. To complete the formulation, the boundary and initial conditions are,

$C_j = C_{jJ}$ at z = 0, where j = A, B

$\frac{\partial C_j}{\partial x} = 0$ at x = 0

$D_j \frac{\partial C_j}{\partial x} = r_j$ at x = δ(z,t)

$C_j = C_{jI}$ at t = 0

$\delta = \delta_I$ at t = 0

Here the subscripts *i* and *j* represent initial and injection values, respectively.

Realistic, practical boundary conditions are needed. Groundwater is flowing because of a pressure gradient in flow field. If a fracture is located in a reservoir, the pressure gradient applied to the rock matrix will be the same as that applied to the fracture of the same length. Therefore, we assume the overall pressure drop (ΔP) of fracture is constant throughout the simulation and the flowrate is a function of time. When precipitation occurs, the aperture size of a fracture decreases. Using the assumption of constant ΔP, the average flux also decreases with time. As shown in Eqs. (2-15) and (2-16), low fluid velocity reduces the transport of supersaturated fluid. Therefore, the aperture size near the outlet (Region 3) is larger than that of the inlet (Region 1) as shown in Figure 2.5. For a large ΔP or low SI (a slightly supersaturated fluid) the aperture size difference between inlet and outlet will be small.

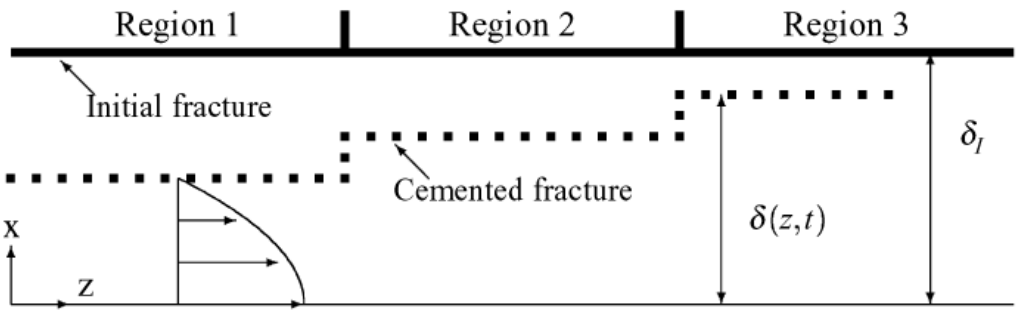

Figure 2.5. Fracture shape with precipitation

Because of precipitation at the surface, the aperture size, δ(z,t), is a function of position and time. As indicated by Eq. (2-20) the flow velocity is large where the aperture size δ(z,t) is small and small where δ(z,t) is large. This phenomena will be important to our results because the relative importance of reaction and flow with change along the fracture. The volumetric flow rate, q(t), the product of the average velocity and aperture size, is independent of z, because of the incompressibility of the fluids. However, q(t) decreases with time because of the overall shrinkage of the aperture.

In a finite difference approximation, the flowrate is a constant within each segment of calculation time, even though it is time-dependent overall. For example, for the three grids in the domain shown in Figure 2.5, the dotted line is a possible fracture aperture distribution after certain time. Since the precipitation reaction occurs only at the fracture surfaces, the concentrations are always getting smaller in the z-direction. Higher concentration at the fracture surface causes more precipitation in Eq. (2-21), so that the aperture size at high concentration portion (Region 1) is small. During the next time step, we calculate pressure gradient (Δp(z,t)/Δz) of each grid using successive substitution.

$$\frac{\Delta p}{\Delta p_I}\left(\frac{\delta(z,t)}{\delta_I}\right)^3 = \text{constant} \qquad (2\text{-}22)$$

With constant flow rate, Δp is inversely proportional to $\delta^3(z,t)$. If the aperture size of Region 1 is much smaller than Region 2 and 3, Δp_1 takes the most of the pressure drop ($\Delta p_1 \approx \Delta P$). In an extreme case, there is almost zero pressure drop and no fluid movement in Region 2 and 3, so that δ_2 and δ_3 remain constants and δ_1 still goes down to zero.

Now we introduce dimensionless variables as follows:

$$C_{Dj} = \frac{C_j - C_{jI}}{C_{jJ} - C_{jI}} \qquad z_D = \frac{z}{l}$$

$$t_D = \frac{q_I t}{2\delta_I W l} = \frac{\delta_I^2 \Delta P}{3\mu l^2} t \qquad \delta_D = \frac{\delta(z,t)}{\delta_I}$$

$$x_D = \frac{x}{\delta(z,t)} \qquad q_D(t) = \frac{q}{q_I} = \Delta p_D \delta_I^3$$

$$\Delta p_D(z,t) = \frac{\Delta p(z,t)}{\Delta p_I} \qquad N_{Shj} = \frac{k_1 \delta_I}{\mathbf{D}_j (C_{jJ} - C_{jI})}$$

$$N_{Pej} = \frac{q_I \delta_I}{2Wl\mathbf{D}_j} = \frac{\delta_I^4 \Delta P}{3\mu l^2 \mathbf{D}_j}$$

$$N_{Da} = \frac{2Wl}{q_I}\frac{M_T}{\rho_T}k_1 = \frac{3\mu l^2}{\delta_I^3 \Delta P}\frac{M_T}{\rho_T}k_1 = \frac{N_{Shj}}{N_{Pej}}(C_{jJ} - C_{jI})$$

$$r_D = \frac{r_T}{k_1} = \left[-1 + \frac{C_A^\alpha C_B^\beta}{K_{sp}}\right]^N$$

$$= \left[-1 + \frac{K_{spI}}{K_{sp}}\left[1 + C_{DA}\left(\frac{C_{AJ}}{C_{AI}} - 1\right)\right]^\alpha \left[1 + C_{DB}\left(\frac{C_{BJ}}{C_{BI}} - 1\right)\right]^\beta\right]^N$$

where $K_{sp}=k_1/k_2$ is the solubility product and N is an empirical reaction order. ΔP is the overall pressure drop, which is a constant, and $\Delta p(z,t)$ is the local pressure drop. The dimensionless reaction rate, r_D, is positive for precipitation and negative for dissolution.

Using these dimensionless variables, Eqs. (2-15) and (2-16) can be rewritten as,

$$\frac{q_I}{2\delta_I Wl}\frac{\partial C_{Dj}}{\partial t_D} = -\frac{3}{2}\left(\frac{q(t)}{2\delta Wl}\right)\left[1 - x_D^2\right]\frac{\partial C_{Dj}}{\partial z_D} + \frac{\mathbf{D}_j}{\delta^2}\frac{\partial^2 C_{Dj}}{\partial x_D^2} \tag{2-23}$$

Since $q/q_I = \Delta p_D \, \delta_D^3$, the dimensionless form of the PDE is,

$$\frac{\partial C_{Dj}}{\partial t_D} = -\frac{3}{2}\Delta p_D \delta_D^2 \left(1 - x_D^2\right)\frac{\partial C_{Dj}}{\partial z_D} + \frac{\mathbf{1}}{\delta_D^2 N_{Pej}}\frac{\partial^2 C_{Dj}}{\partial x_D^2},\ 0 \le x_D \le 1,\ 0 \le z_D \le 1 \tag{2-24}$$

$$\frac{\partial \delta_{Dj}}{\partial t_D} = -N_{Da} r_D \tag{2-25}$$

The dimensionless boundary conditions are,

$C_{Dj} = 1$ at $z_D = 0$, where j = A, B

$\frac{\partial C_{Dj}}{\partial x_D} = 0$ at $x_D = 0$

$\frac{\partial C_{Dj}}{\partial x_D} = -\frac{\eta_j}{\tau} N_{Shj} \delta_D r_D$ at $x_D = 1$

$C_{Dj} = 0$ at $t_D = 0$

$\delta_D = 1$ at $t_D = 0$

Here η_j is a stoichiometric coefficient, which can be α or β for components A and B. Therefore, we solve 3 partial differential equations, Eqs. (2-24) – (2-25) using the finite difference method. To solve the partial differential equations, we follow the general procedure of implicit, cell centered finite differencing in two dimensional space to resolve the nonlinearity at boundaries of the fracture wall. The basic idea is to generate an expansion of the derivatives with respect to primary variables in the conservation equations. Discretization is performed in a rectangular grid system using one point upstream weighting scheme for the convection terms. For time and space discretization an implicit finite difference method is used (Aziz and Settari, 1979; Noh, 1999).

$$\frac{C_{Dj,ik}^{n+1} - C_{Dj,ik}^{n}}{\Delta t_D} = -\frac{3}{2}\Delta p_D \left(\delta_D^n\right)^2 \left(1 - x_D^2\right) \left[\frac{C_{Dj,ik} - C_{Dj,ik-1}}{\Delta z_D}\right]^{n+1} + \frac{\mathbf{1}}{\left(\delta_D^n\right)^2 N_{Pej}} \left[\frac{C_{Dj,i+1k} - 2C_{Dj,ik} + C_{Dj,i-1k}}{\Delta x_D^2}\right]^{n+1} \tag{2-26}$$

$$\frac{\delta_D^{n+1} - \delta_D^n}{\Delta t_D} = -N_{Da} r_D^{n+1} \tag{2-27}$$

where *i* is the x-component index and *k* is the z-component index. *n* is time level.

2.4. Results and discussion

The solution yields equations for the transient surface reaction rate along the fracture as a function of aperture size, inlet concentration and a set of dimensionless groups. The solutions are based on finite difference schemes with a fixed number of nodes in the x and z directions. Initially, the fracture, made of mineral T, is at equilibrium with aqueous species A and B. It is then disturbed by injected aqueous species A and B of supersaturated fluid, so that it is no longer at equilibrium.

As discussed with Figure 2.4, higher concentrations will always occur at the center of the fracture because the fluid velocity is largest. The large velocity will tend to carry the injected (unreacted) components the farthest. The smallest concentrations will occur at the fracture wall because (a) there is no flow (the no-slip condition) and (b) the reaction is taking place. A very large reaction rate will make the dimensionless concentrations at the surface approach zero. On the other hand, diffusion will tend to equalize the centerline and fracture wall concentrations. The reaction at the fracture wall surface is always positive, causing a precipitate to form.

Figure 2.6 - Figure 2.8 show solution concentration profiles for species A with various N_{Sh}, N_{Pe} and time using SI = 10 and N = 1. The three-dimensional plots have concentration on the vertical axis and the space coordinates on the other two. Ranges of dimensionless concentrations are shown by the shading in the legend. The other lines on the surfaces are lines of constant z_D. By definition,

$$N_{Pe} = \frac{Convection\ rate}{Diffusion\ rate}, \qquad N_{Sh} = \frac{Reaction\ rate}{Diffusion\ rate}$$

Figure 2.6 shows that the concentration of species A changes in both the x- and z-directions with time. Since N_{Sh} is zero, there is no reaction in this case. The concentration profile is created only by convection and diffusion. The reaction-free cases should approach the so-called Taylor limit (Lake and Hirasaki, 1981; Lake, 1989; Taylor, 1953), given a small enough N_{Pe} or a long enough flowing time.

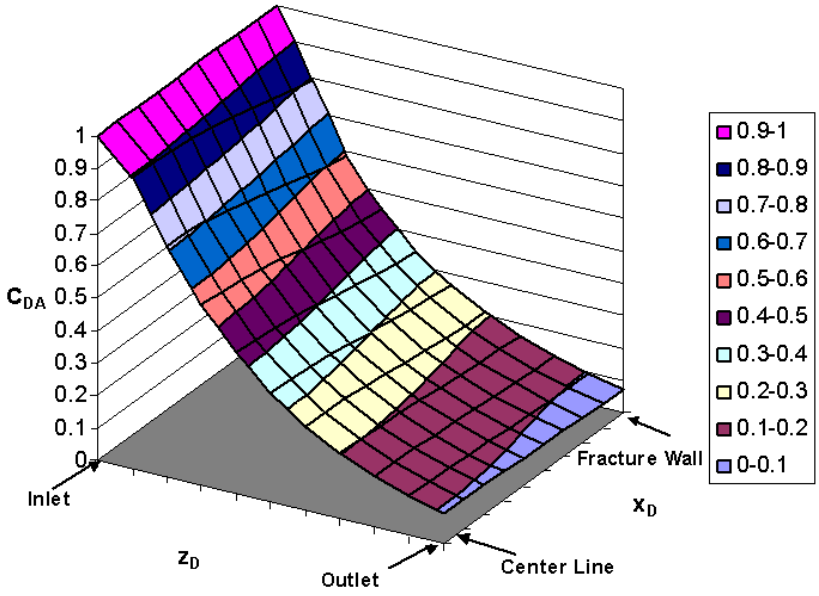

(a) $t_D = 0.5$

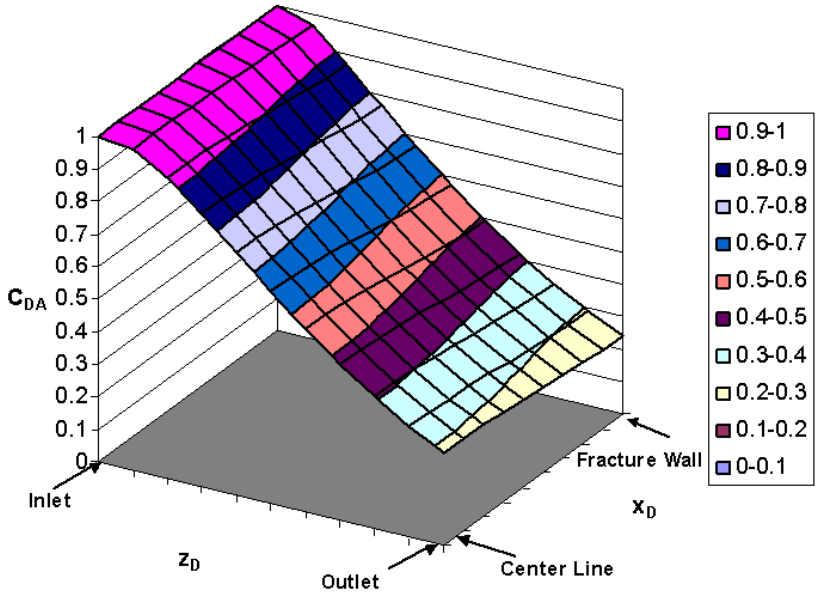

(b) $t_D = 1$

Figure 2.6. Concentration history with $N_{Pe} = 100$, $N_{Sh} = 0$

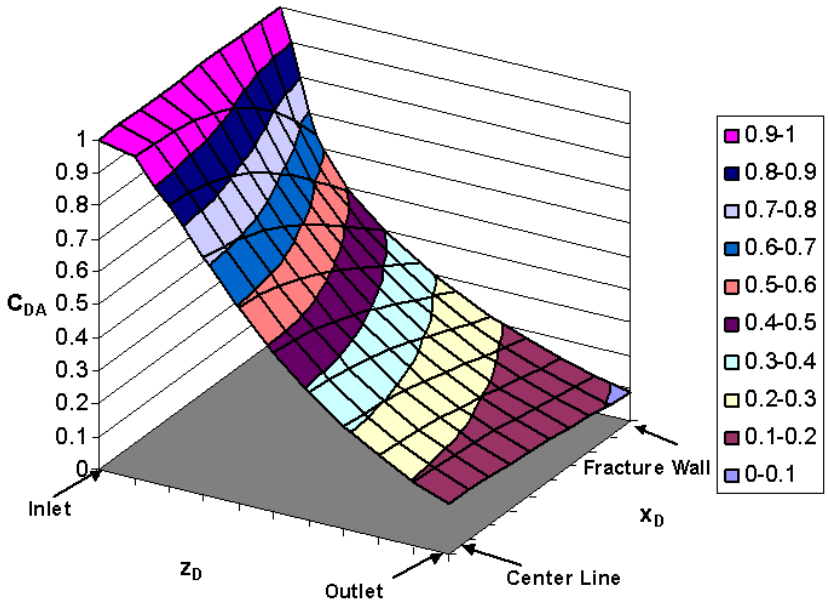

(a) $N_{Pe} = 100$, $N_{Sh} = 2$

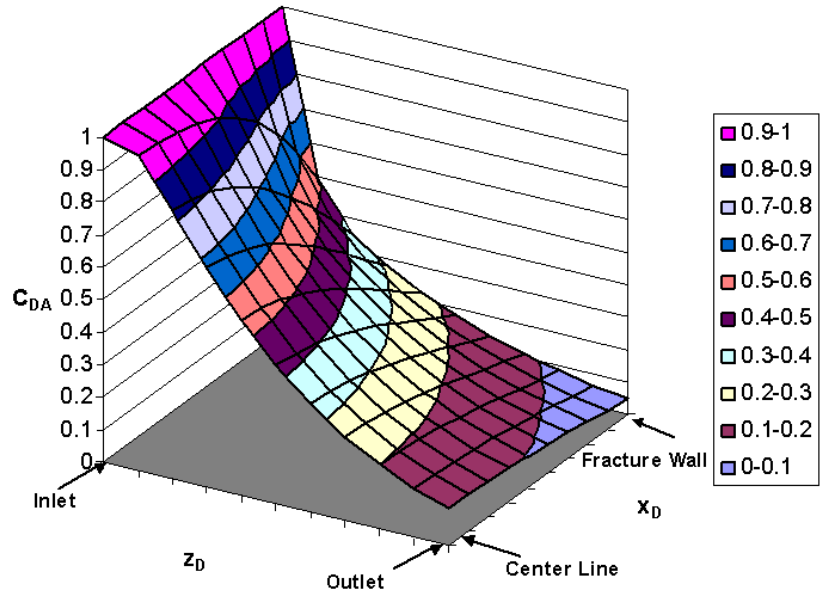

(b) $N_{Pe} = 100$, $N_{Sh} = 4$

Figure 2.7. Concentration profile with various N_{Sh} at $t_D = 1$ pore volume of supersaturated fluid injected.

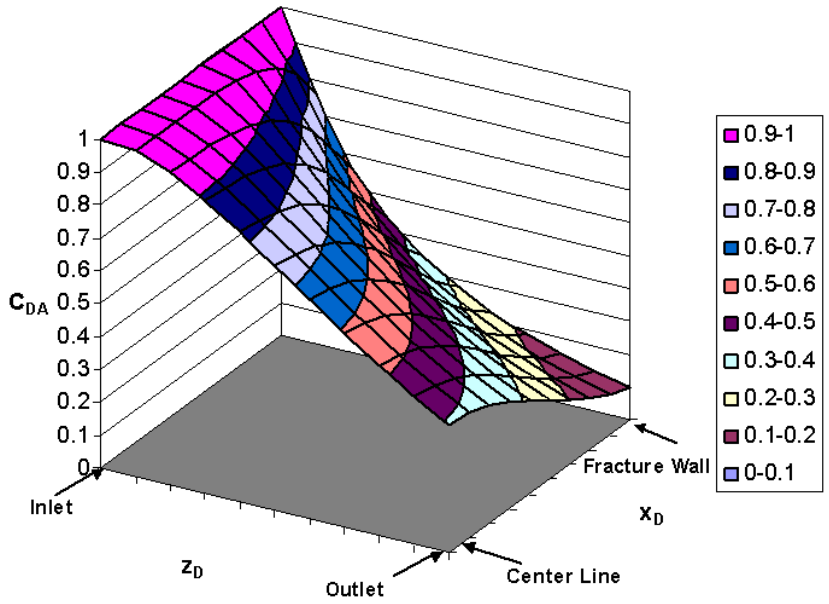

(a) $N_{Pe} = 1000$, $N_{Sh} = 2$

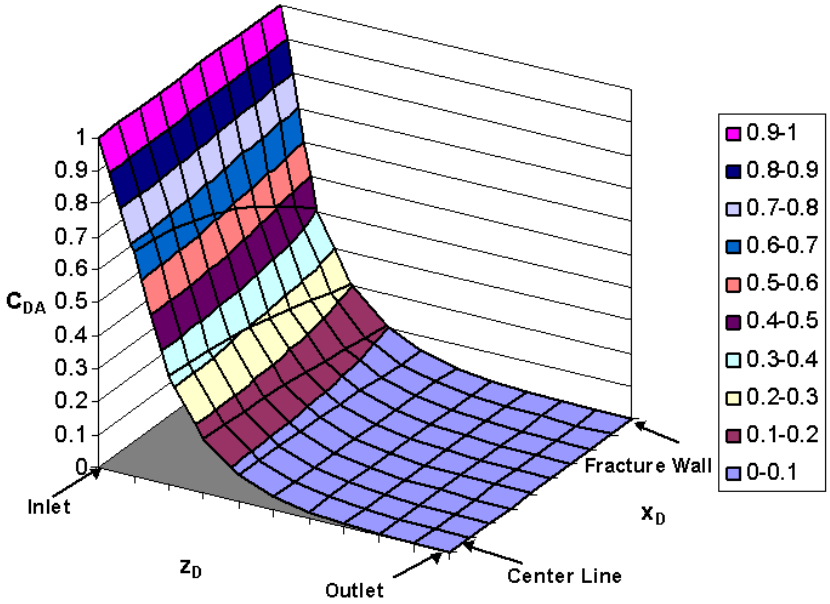

(b) $N_{Pe} = 10$, $N_{Sh} = 4$

Figure 2.8. Concentration profile with various N_{Pe} at $t_D = 1$ pore volume of supersaturated fluid injected

As shown in Figure 2.7, a large N_{Sh} means higher reaction at the fracture surface, so that concentration near the fracture wall decreases with N_{Sh} compared to Figure 2.6(b). Diffusion in the x-direction makes a lower concentration of A at the center of the fracture when N_{Sh} is high. Figure 2.8 shows concentration profiles with various N_{Pe}. With high N_{Pe}, the concentration at the center of fracture is higher than that of Figure 2.7. Since the diffusion rate is relatively low and convection is the dominant process for this case, the

concentration at the fracture wall is not much different than that in Figure 2.7. When N_{Pe} is reduced to 10, the concentration gradient in x-direction becomes smaller as shown in Figure 2.8(b). This is because the x-directional mass transfer rate becomes more migrated than the convective transport rate.

We now discuss the aperture size distribution in the z-direction. N_{Da} is defined by

$$N_{Da} = \frac{Reaction\ rate}{Convection\ rate}$$

and calculated from N_{Pe} and N_{Sh} as shown above. A large Peclet number will lead to a small Damkohler number. It also causes relatively uniform precipitation reaction because a large concentration passes going entirely through the end of the fracture. That means the concentration gradient in the z-direction is small, which results in relatively uniform dimensionless reaction rate, r_D. As presented in Eq. (2-25), we expect the same amount of precipitation if the reaction rate is the same with constant Damkohler number.

When the Damkohler number is large, we can assume that solid phase is everywhere in equilibrium with a flowing phase. This assumption is called the local equilibrium assumption (LEA). LEA is likely to occur in a flow problem in a porous media. However, the flow inside a fracture is not an appropriate example of LEA because the flow velocity is high compared to that in the rock matrix.

Since the concentration gradient in the z-direction is not exactly zero, there will be a difference in aperture size between the inlet and outlet of the fracture. At this point, however, a small aperture at the outlet can be expected with large Peclet number. If the Sherwood number is large, there is also a high precipitation reaction by definition. This will show an aperture profile similar to the small Peclet number case.

As we discussed in Figure 2.5, the pressure drops of each grid block are changed with decreasing aperture size. Figure 2.9 shows the dimensionless pressure drop for each grid and velocity profiles associated with the aperture profile in Figure 2.10. Assuming the overall pressure difference as a constant, we have a high pressure drop near the inlet when the aperture is relatively small. The constant flowrate within each timestep causes a small pressure drop at the outlet. Since we have a small pressure drop and the low flux at the outlet region, the aperture does not change very much.

Here we use the time variable as the pore volume injected (PV), which is the cumulative volume of fluid running through the void space. In this study, pore volume is defined based on the initial properties. In this example, 1000 pore volume is equivalent to 2.8 hours of real time.

Figure 2.10 - Figure 2.12 show three precipitation examples of fracture aperture profiles at different values of N_{Pe} and N_{Sh} with SI = 10 and N = 1. Since Figure 2.9 has larger N_{Sh} than Figure 2.11, Figure 2.10 has more precipitation at the inlet. That causes a high concentration gradient along the flow direction and reduces precipitation reaction near the outlet of the fracture.

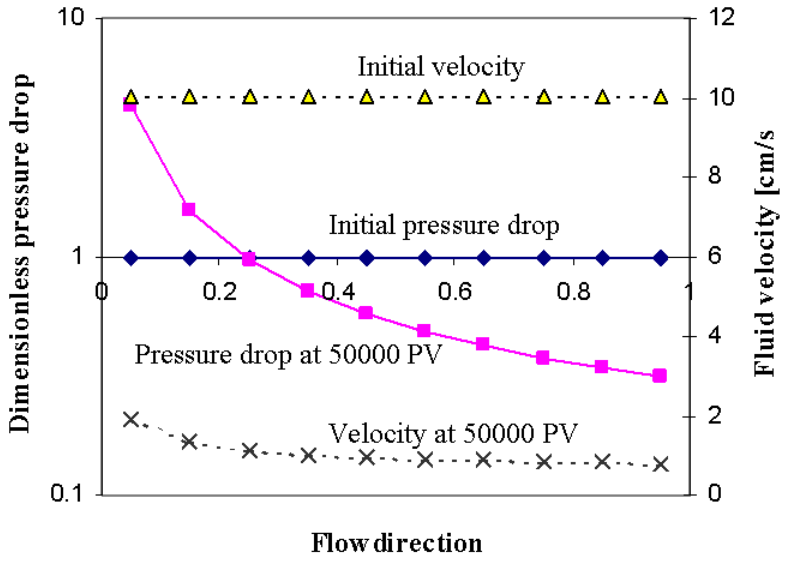

Figure 2.9. Dimensionless pressure difference profile with $N_{Pe} = 100$, $N_{Sh} = 2$

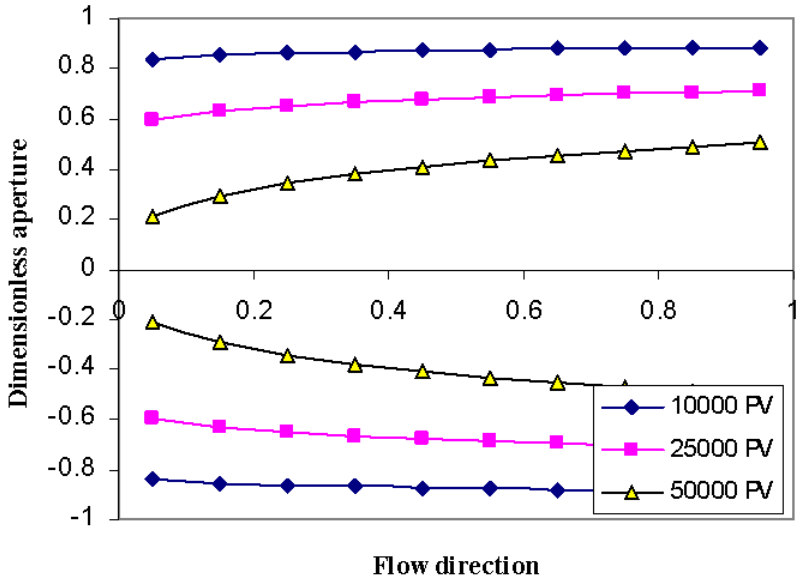

Figure 2.10. Dimensionless aperture profile with $N_{Pe} = 100$, $N_{Sh} = 2$

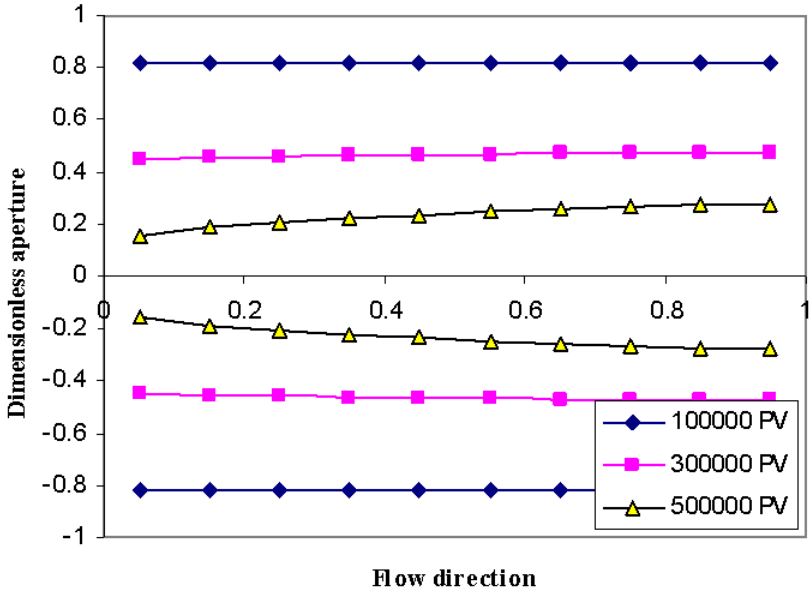

Figure 2.11. Dimensionless aperture profile with N_{Pe} = 100, N_{Sh} = 0.2

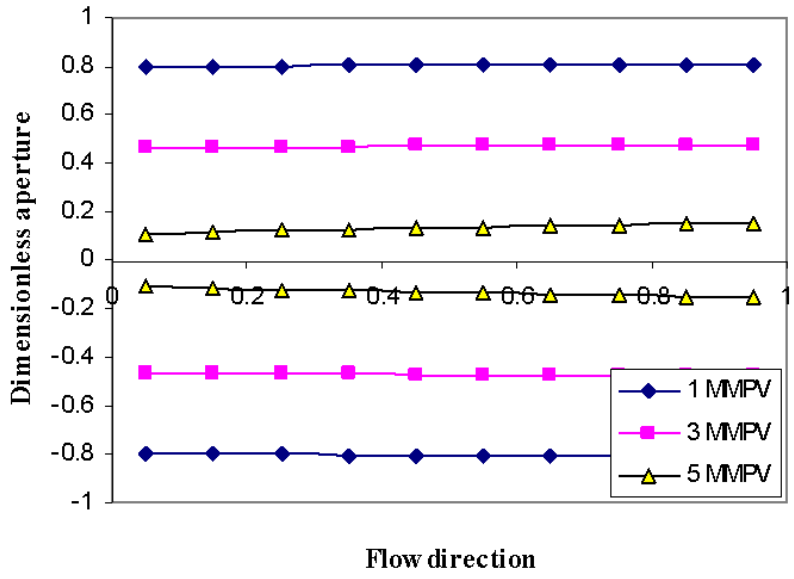

Figure 2.12. Dimensionless aperture profile with N_{Pe} = 1000, N_{Sh} = 0.2

In Figure 2.11 - Figure 2.12, the aperture shrinks uniformly at early time. After a certain amount of cementation, the flow rate of the injected supersaturated fluid decreases because of the constant overall pressure drop and the fracture inlet is getting closing. However, with a large Sherwood number, shown in Figure 2.10, the excess mineral T is mostly created in a relatively short time period and the remaining aperture, which is the aperture at the outlet, is larger than in Figure 2.11. As we discussed with Figure 2.5, high reaction rate at the inlet will cause different pressure drops for each segment. The

supersaturated fluid moves slower at large z-direction.

Figure 2.12 shows an aperture distribution with higher N_{Pe}, which means a higher flux or a larger initial aperture. In this figure, we have uniform precipitation along the z-direction until about 3 million pore volumes. Since the Damkohler number is 10 times smaller than that in Figure 2.11, we have the less reaction so that more pore volumes of supersaturated solution are needed for the same amount of cementation.

Keeping the overall pressure difference constant, the fluid flux within the fracture is much higher than in the rock matrix. For example, the flux of in a fracture with 2 mm aperture is 3.38×10^{7} times higher than 10 md rock matrix. Here, we assume fluid flows only because of hydraulic gradient.

The concentration of the injected fluid can be determined from the saturation index using Eq. (2-7). For example, the solubility product of the calcite precipitation reaction is $10^{-8.48}$ (Stumm and Morgan, 1996), so that injected concentration (C_J) is 8.14×10^{-5}gmol/cm^3 with SI = 2 in an ideal solution.

Zhong and Mucci (1993) showed a calcite dissolution rate constant, k_1 = 0.29 μgmol / m^2-hr (= 8.06×10^{-14}gmol/cm^2-s) and an empirical reaction order of N = 3 in seawater. With those results, we calculate reasonable dimensionless numbers (N_{Pe}, N_{Sh} and N_{Da}) from the values shown in Table 2.1 for a test case.

Table 2.1. Data for test cases

Parameter	Value
Number of grids	10×10 in x, z
Fracture length, l	100 [cm]
Fracture width, W	20 [cm]
Initial aperture size	0.1 [cm]
Dip angle, β	10°
Overall pressure drop, Δ P	17035 [dyne/cm^2]
Fluid flux	56.78 [cm/s]
Density, ρ_T	2.71 [g/cm^3]
Molecular weight, M_T	100 [g/gmol]
Viscosity, μ	1 [mPa-s]
Diffusion coefficient, D	10^{-5} [cm^2/s]
Reaction rate constant, k_1	8.06×10^{-14} gmol/cm^2 s
Empirical reaction order, N	3 ± 0.05
Saturation index, SI	2

Using these data, N_{Pe}, N_{Sh} and N_{Da} are calculated as 567.83, 3.38×10^{-5} and 5.25×10^{-11} respectively. The very small Damkohler number indicates that the flow is at an opposite extreme of local equilibrium assumption.

The aperture profile is presented in Figure 2.13. As we have seen before, a large N_{Pe} and a small N_{Sh} create the low reaction rate on the fracture wall so that many pore volumes are needed for the complete cementation of this fracture. From these results, we can determine the dominant process of each case from the initial and boundary conditions. In a convection-dominated process, which has a high fluid velocity, relatively uniform precipitation occurs because the concentrations at the fracture wall along the z-direction are almost same. Otherwise, it is reaction-dominated. To define how relatively uniformly precipitation can occur, we can use the difference of an aperture size between the ends of the fracture.

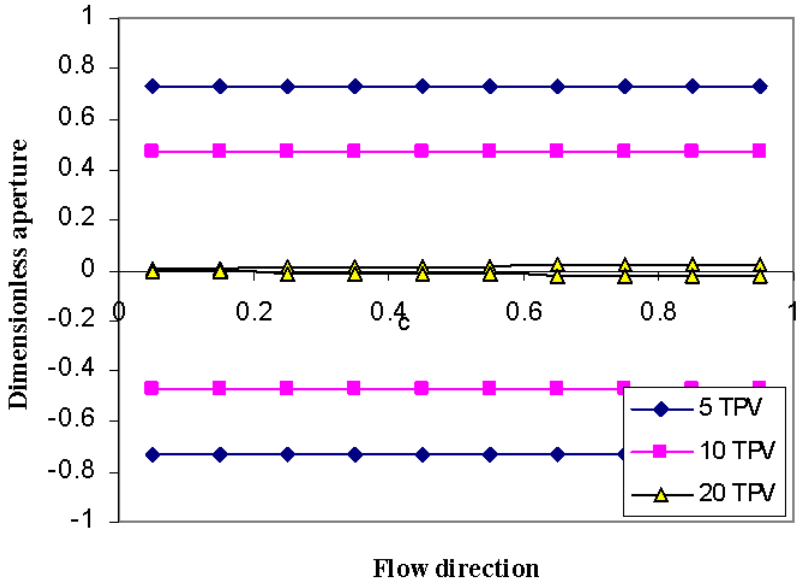

Figure 2.13. Dimensionless aperture profile with N_{Pe} = 567.83, N_{Sh} = 3.38×10-5

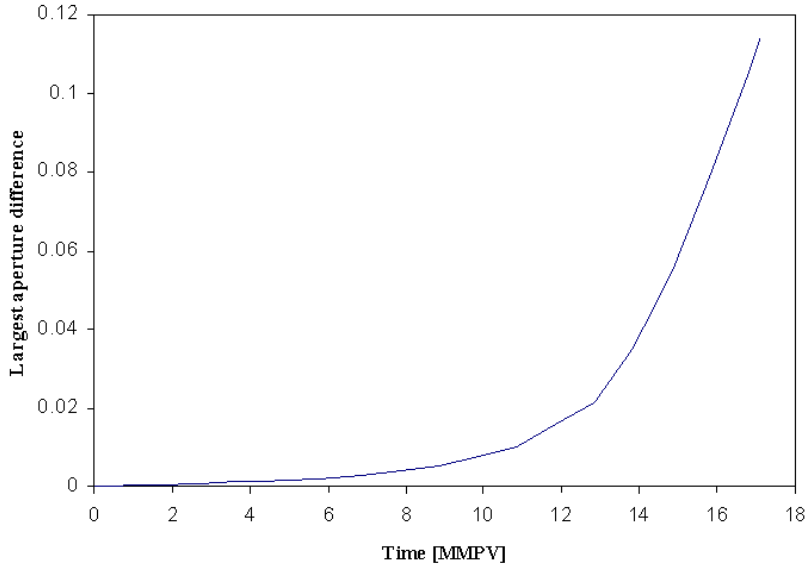

Figure 2.14. Largest aperture difference history with N_{Pe} = 567.83, N_{Sh} = 3.38×10-5

Figure 2.14 shows a history of the aperture size differences between the inlet and the outlet of the fracture associated with Figure 2.13. Aperture size differences are very small and gradually increases until 18.4×10^9 pore volumes of the supersaturated fluid injected: then the difference increases rapidly. From this figure, we can determine that less than the 0.15% of aperture difference (less than 18.4×10^9 pore volumes) can be approximated as a uniform precipitation.

As we have mentioned before, uniform precipitation is an indication of a convection-dominated process. With a high Damkohler number or a low Peclet number, we will see a reaction-dominated result. In Figure 2.14, for example, there is a convection-dominated process before 18.4×10^9 PV, then the precipitation reaction becomes a controlling process. If we have the higher concentration of the injected fluid, which means a large SI, this curve goes left and has less curvature. Small SI or high dip angle makes it move to the right.

With a number of runs of various initial apertures, dip angles and saturation indexes, Figure 2.15 is obtained. The curve represents critical pairs of N_{Pe} and N_{Da}. For example, in Figure 2.14, a Peclet number and a Damkohler number are recalculated using the average aperture at 18.4×10^9 PV. That aperture (*e.g.* $\delta_D = 0.035$ in this example) is critical for SI = 2 and a 10° dip angle. Since N_{Pe} is defined by convection rate over diffusion rate and N_{Da} as reaction rate over convection rate, we can present the upper right area as reaction-dominated. Otherwise, the flow is convection-dominated.

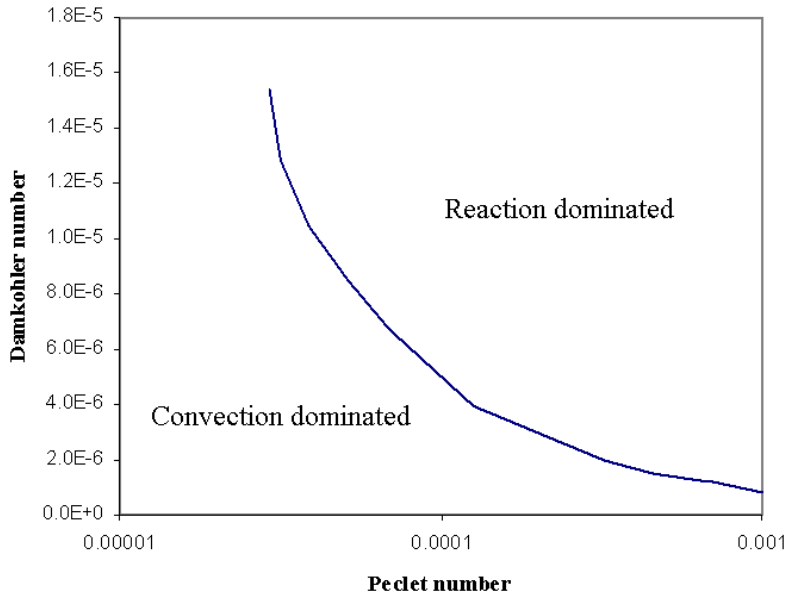

Figure 2.15. Boundary of convection dominant vs. reaction dominant process

2.5. Conclusions

Characterization of fractures is an important issue in many reservoir engineering applications and field performance studies. Although outcrop study, core and well log data combined with seismic interpretation are used to describe fracture systems, these studies typically do not account for the sealing of fractures, although this process could have a fundamental impact on the role fractures play in reservoir performance, an impact on reservoir fluid flow can only be imperfectly assessed by reservoir performance data. Well productivity and the breakthrough behavior combined with insight about processes that seal fractures would be useful performance parameters.

We present a mathematical model to simulate hydrodynamics and fluid-mineral reactions. The intent of this model is to show the time evolution of fracture aperture shrinkage patterns from PD reactions. The fluid convection, diffusion and PD reaction inside a finite space are solved as a simplified representation of natural fracture mineralization. The problem involves mass transfer within the fluid accompanied by chemical reaction at the fracture surface. Mass-conservation equations for each component in fluid are solved in this problem, and these are coupled with the chemical reaction at the fracture surface.

Concentration profiles along the fracture show that the high reaction at the fracture surface makes low concentration values. A high Peclet number, which means a high convection rate results in a high concentration along the fracture. When N_{Pe} is low, concentrations depend more on diffusion so that the concentration gradient in the x-direction becomes small. The local equilibrium assumption implies the flowing phase is in equilibrium with the solid phase at all positions. For this to happen, the Damkohler number must be large. Large N_{Da} implies a large reaction constant or a small convection rate. Since we have large convection and small reaction in the previous example as shown in Table 2.1, the Damkohler number is low and this problem is the opposite of local equilibrium flow.

The precipitation rate along the fracture becomes relatively uniform with a high Peclet number. As the aperture is closing, the fluid flux decreases because of a constant overall pressure drop assumption. When it is at the critical value, the effect of convection decreases and the reaction becomes dominant. Relatively high reaction causes a rapid shrinkage at the inlet. Eventually the inlet of a fracture is closed partially cemented fracture is created. This model has a limitation to show a fully cemented fracture because cementation at the inlet is always greater than at the outlet.

Through this test case of a calcite precipitation problem, we present a process of the fracture mineralization. With certain geologic conditions, the process can be classified as convection- or reaction-dominated using Peclet number and Damkohler number. The model shows that to have a relatively uniform deposition of calcite within a fracture, the velocity of supersaturated solution must be very high or the solution must be only slightly supersaturated with respect to calcite.

The diagenetic processes of dissolution and partial cementation are key controls on the creation and distribution of natural fractures within hydrocarbon reservoirs. Even with extensive data collection, fracture permeability still creates uncertainty in reservoir description and the prediction of well performance. Data on the timing and stages of diagenetic events can provide explanation as to why, when and where natural fractures will be open and permeable.

2.6. References

Araque, A. (2001) Moldeling the effects of geochemistry on well impairment. Ph.D. dissertation, The University of Texas at Austin.

Arnórsson, S. (1989). Deposition of calcium carbonate minerals from geothermal waters –theoretical considerations. *Geothermics* 18, 33–39.

Aziz, K., and Settari, A. (1979) Petroleum reservoir simulation. Amsterdam: Elsevier.

Bird, R. B., Stewart, W. E., and Lightfoot, E. N. (2002). *Transport phenomena*. New York, NY: John Wiley & Sons, Inc.

Burton, E. A. and Walter, L. M. (1987). Relative precipitation rates of aragonite and mg calcite from seawater: temperature or carbonate ion control? *Geology* 5, 111–114.

Busenberg, E. and Plummer, L. N. (1986). A comparative study of the dissolution and crystal growth kinetics of calcite and aragonite. *Studies in Diagenesis (ed. F. A. Mumpton) USGS Bull. 1579*, 139–168.

Chou, L., Garrels, R. M., and Wollast, R. (1989). Comparative study of the kinetics and mechanisms of dissolution of carbonate minerals. *Chem. Geol. 78*, 269–282.

Clark, M. B., Brantley, S. L., and Fisher, D. M. (1995). Power-law vein-thickness distributions and positive feedback in vein. *Geology 23*, 975–978.

Dickson, J. A. D. (1992). Crystal growth diagrams as an aid to interpreting the fabrics of calcite aggregates. *J. Sed. Petrol. 63*, 1–17.

Dromgoole, E. L. and Walter, L. M. (1990). Inhibition of calcite growth rates by Mn^{2+} in $CaCl_2$ solutions at 10, 25, and 50 °C. *Geochim. Cosmochim. Acta 54*, 2991–3000.

Fisher, D. M. and Brantley, S. L. (1992). Models of quartz overgrowth and vein formation: deformation and episodic fluid flow in an ancient subduction zone. *J. Geophys. Res. 9*7, 20043–20061.

Fournier, R. O. and II, R. W. P. (1982). An equation correlating the solubility of quartz in water from 25°C to 900°C at pressures up to 10,000 bars. *Geochim. Cosmochim. Acta* 6, 1969–1973.

Fyfe, W. S., Price, N. J., and Thompson, A. B. (1978). *Fluids in the Earth's Crus*t. Amsterdam: Elsevier.

Inskeep, W. P. and Bloom, P. R. (1985). An evaluation of rate equations for calcite precipitation kinetics at *PCO* = less than 0.01 atm and ph greater than 8. *Geochim. Cosmochim. Acta 4*9, 2165–2180.

Keysar, S., Semiat, R., Hasson, D., and Yahalom, J. (1994). Effect of surface roughness on the morphol-ogy of calcite crystallizing on mild steel. *J. Colloid Interface Sci. 162*, 311–319.

Lahann, R. W. (1978). A chemical model for calcite crystal growth and morphology control. *J. Sed. Petrol. 48*, 337–344.

Lake, L. W. and Hirasaki, G. J. (August 1981). Taylor's dispersion in stratified porous

media, *Soc. Pet. Eng. J.*, 70-84.
Lake, L. W. (1989) Enhanced oil recovery. Prentice Hall, NJ.
Lee, Y. J. and Morse, J. W. (1999). Calcite precipitation in synthetic veins: implications for the time and fluid volume necessary for vein filling. *Chem. Geol.* 156, 151–170.
Lee, Y. J., Morse, J. W., and Wiltschko, D. V. (1996). An experimentally verified model for calcite precipitation in veins. *Chem. Geol.* 130, 203–215.
Lucia, F. J. (1999). *Carbonate reservoir characterization*. Germany: Springer-Verlag Berlin Heidelberg.
Morse, J. W. (1983). The kinetics of calcium carbonate dissolution and precipitation, in carbonates: Mineralogy and chemistry, reviews, in mineralogy, ii. *Mineralogical Society of America, Washington, DC edited by R. J. Reeder*, 227.
Morse, J. W. and He, S. (1993). Influences of *T*, *S* and P_{CO2} on the pseudo-homogeneous precipitation of caco3 from seawater: implications for whiting formation. *Mar. Chem. 41*, 291–297.
Morse, J. W. and Machenzie, F. T. (1990). *Geochemistry of Sedimentary Carbonates*. Amsterdam: Elsevier.
Morse, J. W. and Machenzie, F. T. (1993). Geochemical constraints on $CaCO_3$ transport in the subsur-face. *Chem. Geol. 105*, 181–196.
Mucci, A. (1986). Growth kinetics and composition of magnesian calcite overgrowths precipitated from seawater: quantitative influence of orthophosphate ions. *Geochim. Cosmochim. Acta 50*, 2255–2265.
Mucci, A. and Morse, J. W. (1983). The incorporation of $Mg^{2+}$and Sr^{3+} into calcite overgrowth: influences of growth rate and solution composition. *Geochim. Cosmochim. Acta 47*, 217–223.
Nancollas, G. H. and Reddy, M. M. (1971). The crystallization of calcium carbonate: Ii. calcite growth mechanism. *J. Colloid Interface Sci. 37*, 824–830.
Nielsen, A. E. (1981). Theory of electrolyte crystal growth the parabolic rate law. *Pure & Appl. Chem. 53*, 2025–2039.
Noh, M. H. (1999) Fully coupled air-water flow model in unsaturated porous media, M.S. thesis, The University of Texas at Austin.
Noh, M. H. (in progress) Geochemical modeling of naturally fractured reservoir. Ph.D. dissertation, The University of Texas at Austin.
Plummer, L. N., Wigley, T. M. L., and Parkhurst, D. L. (1978). The kinetics of calcite dissolution in CO_2-water systems at 5°C to 60°C and 0.0 to 1.0 atm *CO2*. *Amer. J. Sci. 278*, 179–216.
Reddy, M. M. (1986). Effect of magnesium ions on calcium carbonate nucleation and crystal growth in dilute aqueous solutions at 25°C. *US Geol. Sur. Bull. 1578*, 169–182.
Sjöberg, E. L. and Richard, D. T. (1984). Temperature dependence of calcite dissolution kinetics between 1 and 62°C at ph 2.7 to 8.4 in aqueous solutions. *Geochim. Cosmochim. Acta* 8, 485–493.
Stumm, W. and Morgan, J. (1996). *Aquatic Chemistry*. New York: John Wiley & Sons, Inc.
Taylor, G. (1953). Dispersion of soluble matter in solvent flowing slowly through a tube, *Proc., Roy. Soc. London*, 219, 186-203.
Walter, L. M. (1986). Relative efficiency of carbonate dissolution and precipitation

during diagenesis: Aprogress report on the role of solution chemistry. *Roles of Organic Matter in Sediment Diagenesis (ed. D. L. Gautier), SEPM Spec. Publ. 38*, 1–11.

Wu, G. (1992). *Pore network evolution induced by interaction between minerals and migrating fluids*. Ph.d. dissertation, The University of Texas at Austin.

Zhong, S. and Mucci, A. (1993). Calcite precipitation in seawater using a constant addition techniques: a new overall reaction kinetic expression. Geochim. Cosmochim. Acta 57, 1409–1417.

3. Fracture Mechanics Attributes of Sandstones – An Example from the Travis Peak Formation

3.1. Introduction

Fractures control fluid flow in low permeability formations. The prediction of fracture patterns and fracture attributes has been the subject of many studies (e.g. La Pointe and Hudson, 1985; Rives et al., 1992). Conventional studies gather data on fracture attributes and use geostatistics to obtain fracture distributions (e.g. Rives et al., 1992; Marrett, 1997). A wide range in distributions has been reported, from negative exponential, exponential, log normal to power law for fracture spacing and length, and from log normal to power law for fracture aperture (e.g. Snow, 1970; Panek, 1985; Rives et al., 1992; Marrett, 1997). However, significant data collection and correlation are required to estimate fracture pattern distributions within a region. The correlations are limited not only to the region under investigation, but also to surface formations. Subsurface fracture data are sparse; vertical wellbores do not often intersect vertical fractures because of large fracture spacing and small borehole size (Laubach et al., 2000). Hence the use of conventional data gathering techniques to predict subsurface fracture patterns is time consuming if at all possible. We propose an alternative method which allows for subsurface fracture pattern prediction without abundant sampling.

The proposed method is twofold. First the fracture pattern length, spacing and clustering distribution are predicted using a geomechanical model. This numerical model uses rock properties and geological boundary conditions as input data. Secondly, we examine the micro-fractures in the rock from which we can establish orientation and openness of the fractures (Laubach, 1997; Laubach et al., 2000; Laubach, submitted). The combination of these two methods provides a means for estimating flow in subsurface fracture systems without extensive sampling The present discussion will focus on the geomechanical modeling parameters. Specifically, we will investigate the subcritical index value, a rock property, which exerts control on fracture pattern development (Olson 1993; Renshaw and Pollard, 1994; Renshaw, 1996; Olson, 1997). This study will investigate systematic variations of the subcritical index with several other rock properties using a material science model developed for metals and ceramics as a guide.

3.2. Subcritical fracture model

The geomechanical model used to predict subsurface fracture patterns is based on subcritical fracture growth. In the case of critical fracture growth, a fracture will propagate at a rupture velocity near the shear wave velocity of the material whenever the stress intensity (K_I) at the fracture tip exceeds the fracture toughness of the material (K_{Ic}). However, fractures can develop and propagate at much lower velocities under long term loading conditions, even though the stress intensity is less than the fracture toughness (e.g. Atkinson, 1984; Segall, 1984). This condition, in which a fracture propagates at stress intensity values below the fracture toughness but above a threshold stress intensity factor (K_I^*), is called subcritical fracture growth.

Multiple competing mechanisms can cause subcritical fracture growth. Of these, stress corrosion crack growth is the most well-known (Atkinson and Meredith, 1989a). In this process, strained atomic bonds are further weakened by the presence of water or another chemical reactive agent (Atkinson and Meredith, 1989a). This weakening of the bonds permits fracture propagation at stress intensity factors below the critical fracture toughness. Significant progress has been made in the development of subcritical fracture growth theory, explaining many previously confusing observations (Atkinson and Meredith, 1989b).

Fracture propagation velocity is correlated to stress intensity through the following empirical relation:

$$v = A\left(\frac{K_I}{K_{Ic}}\right)^n \quad \text{..... (3-1)}$$

where

v = Fracture propagation velocity
K_I = Mode I stress intensity factor
K_{Ic} = Fracture toughness
A = Critical fracture propagation velocity (constant)
n = Subcritical fracture index (constant)

The critical fracture propagation velocity (rupture velocity), A, and the subcritical fracture index, n, can be measured in the laboratory. Subcritical index values have been determined for glass, single crystal, polycrystalline ceramics and rocks (e.g. Atkinson, 1984). It has been shown that subcritical index values vary with rock type (Atkinson and Meredith, 1989b). Likewise, it has been shown that subcritical fracture index exerts control on fracture attributes such as length, spacing (Olson 1993; Renshaw and Pollard, 1994) and connectivity (Renshaw, 1996; Olson, 1997). This is illustrated by the output of the geomechanical model (Figure 3.1). Increasing the subcritical index from n=5 to n=80, but keeping all other conditions equal, increases fracture clustering and spacing. Fracture length increases from n=5 to n=20, but decreases with further increase in subcritical index value.

The subcritical index is a material/rock property, and we expect characteristic fracture patterns to develop under identical loading histories within one rock type. From experimental data based on single crystals and polycrystalline ceramics we know that the following 6 factors influence subcritical fracture growth (Atkinson and Meredith, 1989b): 1) strain energy release rate, 2) temperature, 3) chemical environment, 4) pressure, 5) rock microstructure and 6) residual internal strains. These influencing factors are based on results obtained from metals, ceramics and glass. However, sedimentary rock is inherently different from these materials. Rocks have porosity, grain size distributions, cement volume and composition, and thus a wide range in microstructure. Therefore, the first step in our investigation of the systematics of subcritical index variations is an assessment of how microstructure influences subcritical index values. A second step is the investigation of the chemical environment. Subcritical growth is a chemical process that depends on the fluid type present (Atkinson and Meredith, 1981). Within petroleum

reservoirs fluid saturation and fluid distribution is variable, which may change the subcritical index value and, in turn, may alter the ultimate fracture pattern.

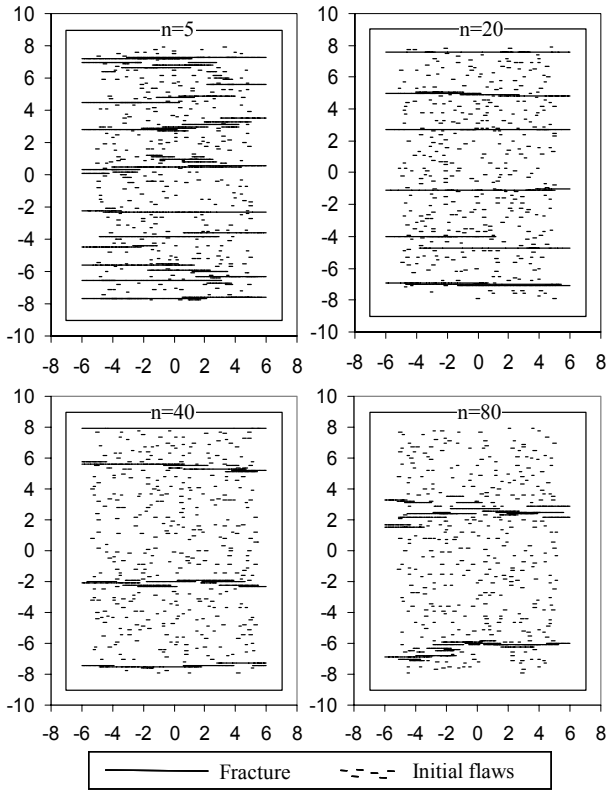

Figure 3.1: Fracture trace maps for numerical subcritical crack propagation simulations for different subcritical crack indices, using 400 initial flaws. Each case used an identical crack-perpendicular extensional strain rate. Note increasing fracture density with decreasing n, and fracture clustering for n=40 and n=80. From Olson et al. (2001).

In the following sections we will discuss a theory proposed for metals and ceramics. Although this theory has not been developed for sedimentary rock, we will use it to guide our assessment of systematic variations within sedimentary rock samples. Whether or not our results fall within the expected analytical trend(s) will provide insight into the validity of the material science theory to sedimentary rock.

Microstructure

The energy required to create a fracture is proportional to the fracture surface area and its specific surface energy (Lawn and Wilshaw, 1975). Within granular material three processes have been observed to take place that increase the energy necessary for fracture propagation: 1) fracture wandering: due to intergranular fracturing the crack-path is not straight and therefore longer than a comparable planar feature (Wu et al., 1978; Gesing and Bradt, 1983); 2) microcracking: within the cracktip stress field, numerous micro cracks develop (Gesing and Bradt, 1983; Han and Suresh, 1989); and 3) fracture

branching: fractures have been observed to form two or more separate branches (Wu et al., 1978). Fracture branching is associated with fast or critical fracture growth (Lawn and Wilshaw, 1975) and is not addressed in this discussion.

Whether a fracture grows intergranular (fracture propagates along the grain boundaries through the material present between the grains) or transgranular (fracture propagates through the grain) in polycrystalline materials depends on flaw/grain size ratio (Rice et al., 1980; Mussler et al., 1982). For intergranular fracture growth the grains remain intact, whereas for transgranular fracture growth the grains are fractured. Thus in intergranular fracture growth the grains remain intact, whereas in transgranular fracture growth the grains are fractured. As the ratio of flaw/grains size increases, the proportion of intergranular fracture with respect to transgranular fracture increases (Rice et al., 1980; Mussler et al., 1982). Scanning electron microscope secondary electron images reveal that most of the fracture propagation occurs intergranular in sedimentary rock (Olson et al., 2001). We assume intergranular growth provides a lower resistance path than transgranular fracturing and will be the dominant fracture process. Accordingly, we postulate that cement present between the detrital grains plays an important role in subcritical fracture growth within sedimentary rock.

The theory as postulated by Gesing and Bradt (1983) assumes that flaws ahead of the fracture tip are linked as grain boundaries lose cohesion. The crack extension force that has to be applied to the main crack in order to extend a flaw, a, can be calculated from the stress field analysis around the crack tip. The main fracture is assumed to only propagate if the apparent extension force provides sufficient energy to propagate all micro-flaws in the crack-tip stress field. Thus the macro-fracture will only propagate when the local stress intensity factor at all the micro-flaws exceeds the stress intensity necessary for the micro-flaws to propagate. This condition is satisfied when the apparent crack extension force equals the average extension force for all micro-flaw sizes. The flaws, which link to form the main crack, are always one grain facet, d, away from the crack tip since the crack is assumed to propagate along the grain boundaries. These assumptions and the assumption the crack extends, on average, with subcritical fracture velocity until the local fracture toughness is exceeded, lead to the following equation (Gesing and Bradt, 1983):

$$n = c \times \frac{a}{d} \times \frac{G}{G_0} \quad \text{..... (3-2)}$$

where a is flaw length, d is facet or grain size, G is the applied crack extension force, G_0 is critical crack extension force (a material property) and c is a constant.

Equation 2 provides for preliminary predictions of subcritical index within sedimentary materials. We expect the subcritical index of a material to decrease when the grain size of the material increases without changing the microstructure or the chemical environment of the material. This is illustrated in Figure 3.2 by a decrease in slope on a log-log plot of normalized stress intensity vs. subcritical fracture velocity. Likewise, a decrease in surface energy, which we postulate corresponds to a change in cement type from quartz cement (surface energy = 1.34 J m^{-2} , Atkinson and Avdis, 1980) to calcite cement

(surface energy = 0.27 J. m^{-2}, Atkinson and Avdis, 1980) is expected to increase the subcritical index value.

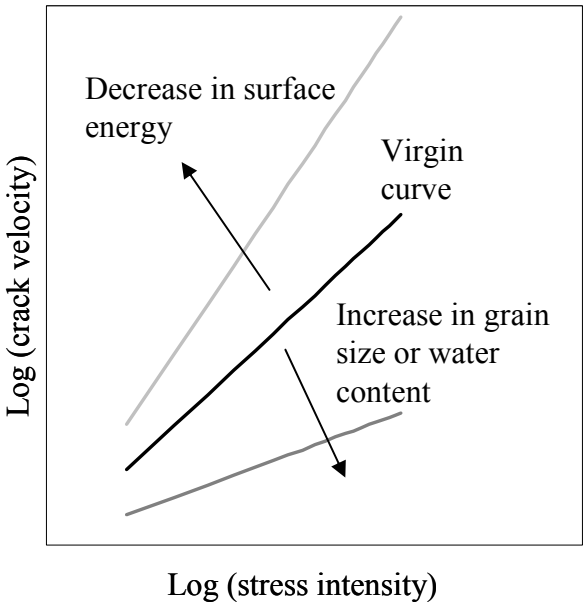

Figure 3.2: Log of stress intensity vs. log of fracture velocity. The slope of this line (n = subcritical index value) is hypothesized to decrease with increase in grain size and water content and increase with a decrease in surface energy.

Reactive environment: water saturation

As noted, the reactive environment at the crack-tip influences subcritical fracture growth. Reactive agents such as water can excite the bonds, and these excited bonds are easier to break than non-excited bonds (Atkinson and Meredith, 1989b). For example Scholz (1972) and Martin (1972) proposed that silica bonds undergo the following weakening in a water rich environment:

$$H-O-H+\left[\equiv Si-O-Si\equiv\right]\leftrightarrow\equiv Si-OH\cdot HO-Si\equiv\leftrightarrow 2\left[Si-OH\right] \quad \text{.. Reaction 1}$$

where the reaction speed depends on the availability and accessibility of water. This bond excitation is not restricted to silica. Similar results have been found in other materials, but the reaction taking place is not as well characterized as Reaction 1 (Atkinson and Meredith, 1989b).

The accessibility of water to the silica bonds is another important factor for subcritical fracture growth, so understanding the distribution of water within pores is important. Minerals have a natural wettability, which is the tendency for one fluid to spread on or adhere to a solid surface in the presence of other immiscible fluids. Almost all reservoir minerals are strongly water-wet (Gant and Anderson, 1988). However, exposure to different pore fluids can alter this state to preferentially oil-wet. When sandstone is preferentially water-wet, any water present will adhere to the mineral surface, thereby making the rock more susceptible to bond excitation. In oil-wet rock, accessibility of

water to the bonds is reduced, thus bond excitation is diminished. As Holder et al. (2001) noted, we expect a relationship between wettability and subcritical index; oil-wet rock should have a higher subcritical index than water-wet rock.

3.3. Experimental measurements

Our next step is to experimentally determine to what extent sedimentary rocks follow the theories derived for metals and ceramics. A constant displacement double torsion testing procedure was used to determine subcritical index values (Evans, 1972; Williams and Evans, 1973). This testing procedure is widely used for subcritical fracture growth measurements, because the stress intensity is independent of fracture length. This feature simplifies data reduction and provides for measurements on opaque samples. Modifications in the testing procedures proposed by Holder et al. (2001) were used, in order to minimize testing complication due to the compliant and heterogeneous nature of sedimentary rocks.

The test samples were selected from the Travis Peak Formation. The sandstones in this sand rich, Lower Cretaceous, fluvial-deltaic deposit have a wide range of grain size, quartz and carbonate cement (Dutton et al., 1988). After testing, thin sections of the samples were made and inspected with a petrographic microscope to collect data on grain size, cement, porosity, and detrital grains. Suites of subcritical experiments were performed on the specimens (Table 3.1). In the following, we discuss the results in light of the theory from polycrystalline materials, starting with grain size and cement type and concluding with the chemical aspects.

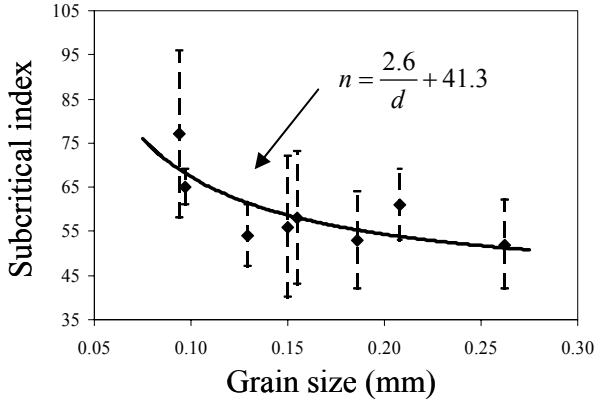

Figure 3.3: Grain size (mm) vs. subcritical index plot. The curve fit shows that the results follow the predictions based on polycrystalline materials, where subcritical index is inversely proportional to grain size (d).

Grain size

Values of subcritical index vary from rock type to rock type as well as within one rock type (Holder et al., 2001). In order to delineate variations with grain size only, we isolate specimens with similar mineral composition (Table 3.1). Within this subset, we find that subcritical index decreases when grain size increases (Figure 3.3), conforming to the

theory proposed by Gesing and Bradt (1983) and as seen in polycrystalline material (e.g. Navarette et al., 1976; Gesing and Bradt, 1983).

Table 3.1. Test results of the Travis Peak Formation.

Well*	Depth	Detrital quartz grains	Quartz Cement	Carbonate Cement	Grain size	Subcritical index		
	(ft)	(%)	(%)	(%)	(mm)	Dry	Wet	Oil
1	5962	59	20	10	0.105	50±12	--	--
1**	6206	60.5	16.5	2.5	0.097	65±4	66±5	--
1	6270	72	10.25	14.5	0.102	61±14	54±16	--
1	6295	52	19	18	0.097	51±12	--	--
1**	7457	76.25	14.25	0	0.150	56±16	56±9	--
1**	7506	72.75	18.75	0	0.155	58±15	70±8	--
2**	5952	68.5	12	1.5	0.208	61±8	70±7	--
2**	6244	68.25	13.75	0.75	0.129	54±7	52	--
3	6633	67	10.5	11.5	0.108	81±17	--	--
4	7737	70.3	17.3	1	0.058	42±7	63±9	--
5**	10141	74.75	11.75	3.25	0.094	77±19	54±16	--
6**	9817	73.7	17.3	0	0.186	53±11	60±15	--
6	9837	73.5	9.5	12.5	0.222	69±8	--	82±4
6**	9880	74.75	18	0	0.262	52±10	--	70±1

* Wells: 1) Holditch Howell #5, 2) Mobil Cargill #14, 3) Marshall Werner Sawmill #5, 4) Arkla #1 J.O. Pate, 5) Ashland #1 SFOT, and 6) Holditch SFE #2.
** Samples used for grain size correlation.

Unfortunately, smaller grain sizes within the Travis Peak have systematically higher clay content. Because clay is chemically charged and has a large surface area, we expect the subcritical index to vary significantly with clay content. Therefore, extension of samples to the smaller grain size regime is impeded. The correlation between subcritical index and clay content has not yet been investigated.

Carbonate content

According to the Gesing and Bradt (1983) correlation, we expect an increase in index value with decreasing quartz cement, increasing carbonate cement, decreasing grain size and increasing pore size for constant chemical environment (Figure 3.2). However, we do not expect this correlation to hold if the rock contains a large percentage of carbonate cement. Large cement content will change the microstructure of the rock: porosity will decrease and pore size and shape will change. This change in microstructure will alter the energy balance and thus the subcritical index. Large carbonate cement percentages may alter the sample too much to be compared to samples containing small or no carbonate cement percentages.

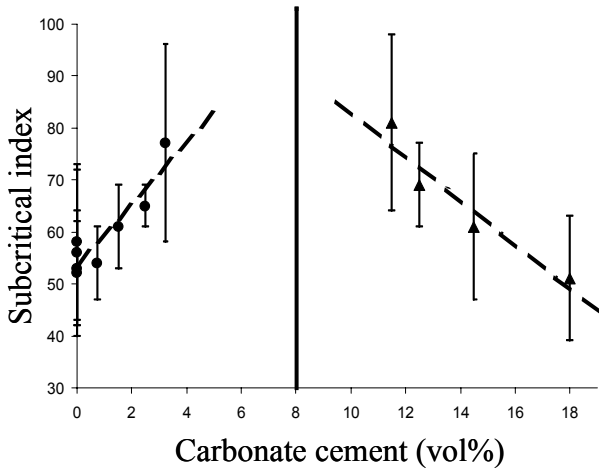

Figure 3.4. Variation in subcritical index with carbonate cement (vol%). For carbonate values below 8 vol% samples follow the predictions as specified for polycrystalline materials (Gesing and Bradt, 1983). For values larger than 8 vol%, samples behave in the opposite sense.

The results show (Figure 3.4) that for small (< 8 vol%) volume percentages of carbonate, variations in subcritical index follows the Gesing and Bradt (1983) trend. The subcritical index increases as carbonate content increases. However, for large values of carbonate volume percentage (> 8 vol%) we see that the trend reverses (Figure 3.4), which we attribute to a change in microstructure of the rock.

The model we have used only takes into account the amount of carbonate cement present in the rock and assumes the detrital grains of the samples to be identical. However, some specimens contain variable amounts of clays and feldspars in addition to variations in their detrital quartz grains. These clay and feldspar variations will change the overall trend and obscure systematic changes within the trend. Also grain sizes vary among samples with different carbonate cement percentages, and some of the variation shown in Figure 3.4 may be related to these grain size variations.

Artificial cement

In order to investigate the effects of cement on subcritical index, artificial cement was introduced into some of the rock samples. This artificial cement mimics secondary carbonate cement, but is more controllable than natural cement variations. Two cements were used: salol (Salicylic Acid, $C_6H_4(OH)CO_2H$) which melts at temperatures above 40 ºC and is solid for temperatures below this threshold, and sodium silicate (Na_4O_4Si), a water soluble compound. The low-viscosity molten salol penetrates the pores of the sample and reduces porosity, whereas water-soluble sodium silicate is deposited by evaporation. Salol has a hydroxyl group which could influence subcritical fracture growth as described in reaction 1, but sodium silicate does not. Samples bathed in salol showed a marked reduction in subcritical index from 53±11 to 14±6, and samples soaked in sodium silicate yielded a value of 25±3. The larger reduction with salol cement is consistent with the added chemical effect from the hydroxyl ion.

An additional suite of tests was carried out using a single test specimen. By re-using the same specimen, sample-sample variations in microstructure are avoided. Four tests were carried out on the sample, which was prepared using standard methods. The sample was tested twice under dry conditions and then was soaked in salol. After treatment with salol, the sample was tested again. As before, the subcritical index decreased (from 56±3 to 14±6). A clear increase in rock strength as well as a reduction in subcritical index is observed in the velocity-stress intensity plot (Figure 3.5).

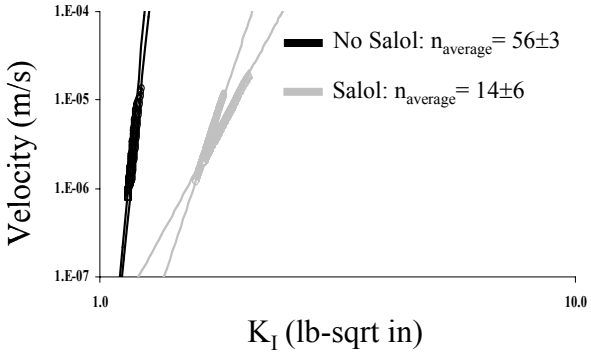

Figure 3.5. Subcritical fracture velocity vs. stress intensity. Four tests were carried out on one sample from a depth of 9817 ft. First the sample was tested in air after a standard preparation procedure (black curves). After these tests were completed the sample was soaked in Salol and dried. The sample was tested again (light grey curves) and a marked reduction in subcritical index was observed. The thin black and grey lines are trend lines fitted through the data. The thicker part on the curve corresponds to the data collected.

We conclude that artificial cementation with either salol or sodium silicate decreases the subcritical index value. This decrease is consistent with the response of natural samples to large carbonate cement content (Figure 3.4). The amount of artificial cement added in these tests is not controlled. Samples are submerged in the cement, taken out and then left to solidify. We expect to have filled most of the pore space with the artificial cement, and we postulate that this corresponds to large amounts of secondary carbonate cement within a natural sample. We see that after treatment with both cements the subcritical index decreases. A possible cause for this decrease in subcritical index is a decrease in porosity, which would correspond to decreasing pore/flaw size. Returning to the theory for polycrystalline materials we see that a smaller flaw size corresponds to a smaller subcritical index value. Further testing is required to fully understand and quantify this trend.

Water saturation

Another factor controlling subcritical index is the chemical environment, especially water content. In order to characterize this effect samples were tested both under dry (ambient air) conditions and submerged in water. Water is a reactive fluid as described in Reaction 1, thus we expect a decrease in subcritical index as samples are submerged (Atkinson and

Meredith, 1989b). Accordingly, the value of dry (ambient air) subcritical index value minus wet subcritical index value (n_{dry}-n_{wet}=Δ) should be positive. However, as Figure 3.6 shows, these specimens do not always follow this trend. The plot of Δ vs. grain size (Figure 3.6) shows that grain size plays an important role in this correlation. A part of this dependence can be attributed to the surface area of a sample. When samples are tested in ambient air, a small quantity of water is available to weaken the atomic bonds. If the surface area of the sample is large (e.g. small grain size samples), insufficient water is present to weaken all the bonds. On the other hand, when submerging these small grain size samples, sufficient water is present to weaken the bonds, and a pronounced change (large positive Δ) in subcritical index is expected. Likewise for large grain sizes we expect enough water to be present while testing in ambient air to weaken the bonds. Thus when submerged in water the correlation will be less pronounced. This however does not explain the negative values for Δ obtained.

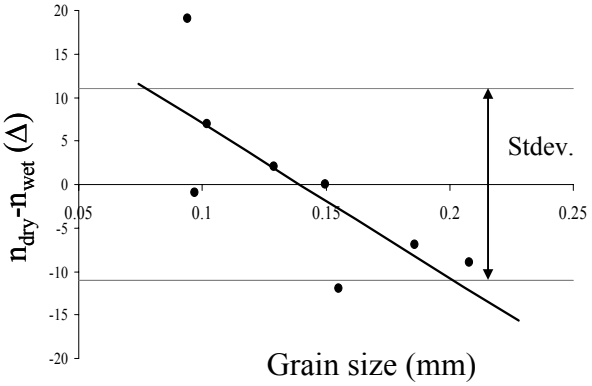

Figure 3.6. Difference between dry subcritical index value and submerged subcricital index value (Δ) vs. grain size. According to the literature this value should be positive since subcritical index decreases with increase in water content. However, we find this not to be true for large grain size values.

For specimens from two depths, samples were soaked in toluene and then soaked in oil (Table 3.1). These samples were tested in air, and both showed an increase in subcritical index beyond the one standard deviation range. Oil droplets decrease the accessibility of water to the silica bonds, thus allowing less of the bonds to be excited, and an increase in the subcritical index is expected. It should be noted that samples of depth 9837 ft contain 12.5 vol% carbonate cement. We conclude that despite this change in rock constituents the correlation with oil content still holds.

From these tests it is apparent that microstructure can impact the effects of chemical environment on subcritical index values. Subcritical index generally increases with oil content. Subcritical index decreases with water content (Atkinson and Meredith, 1989b), but grain size alters the dependence of subcritical index on water content (Figure 3.6). Further testing is required to quantify whether microstructure or chemical environment is dominant in subcritical index measurements on sedimentary rock.

3.4. Discussion: Controls on subcritical index

The subcritical index depends on a number of parameters, and trend analysis in rock is difficult because variations in one parameter can overprint another. Sample selection is such that sample attributes are only known after testing. It is virtually impossible to keep all variables but one constant for natural samples. However, some trends can be identified.

For the same chemical environment, we expect a higher index value in fine-grained materials than in coarse-grained materials. This observation, combined with the geomechanical model simulation of fracture pattern attributes (Figure 3.1), enables us to predict that fracture families in coarser grained material will be shorter and more closely spaced than fracture families in fine grained materials. Many sedimentary environments show a gradation in grain size, and we expect that the fracture spacing, length and connectivity will not remain constant within such a stratigraphic heirarchy.

Rocks consist of many different minerals, each with their specific surface activity. Because chemical environment influences subcritical index differently for various minerals, rocks with dissimilar grain composition cannot be directly compared. A sample consisting of carbonate grains and quartz cement will behave differently than a sample consisting of quartz grains and carbonate cement. However, we expect that the deviations from the virgin curve will trend similarly (Figure 3.2). A virgin curve is a curve that represents rock samples that consist of only one mineral type.

We have assumed that cementation occurs as overgrowths, and that the surface area created by the overgrowth correlates with grain size. Quartz cement is more likely to be deposited as overgrowths on detrital quartz grains (Pettijohn, 1975). Carbonate cement in quartz-rich sandstones typically does not occur as overgrowths but may show a variety of microstructural shapes because the mineralogy of the cement is different from the mineralogy of the detrital grains (Pettijohn, 1975). Due to these textural differences, microstructure within carbonate-cemented sandstones is highly variable. Subcritical index trends with varying volumes of carbonate cement are thus more difficult to predict.

3.5. Micro-fractures as proxies for macro-fractures

Subsurface flow behavior not only depends on fracture length, spacing and clustering, but also on the degree of fracture filling. The overall subsurface flow pattern depends on whether fractures are open or closed to flow, and estimates of fracture filling must accompany prediction of fracture patterns in order to fully characterize the flow pattern. For this purpose micro-fractures and diagenetic observations can be used as proxies for macro-fractures (Laubach et al., 2000; Laubach, submitted). Micro-fractures have previously been shown to be good predictors of fracture strike in the Travis Peak Formation (Laubach, 1997).

The process by which large fractures seal is discussed in section 2. The degree to which large fractures are sealed by late cements can be inferred from cement patterns because cements that are contemporaneous with fracturing events do not completely fill macro-

fractures. For a given burial history and time of fracturing there is a threshold below which fractures are completely filled, and above which fractures are partly to completely open (Laubach et al., 2000; Lander et al., 2002). Hence, late (or postkinematic) cement precipitation after the fracturing event is the main cause of fracture closure for large fractures (Laubach, submitted), and fracture openness can be predicted by estimating the amount of cement precipitated after the fractures were formed (= postkinematic cement; Laubach, submitted) using observations of those cements present in the rock mass (not the fractures). If large amounts of the pore space are filled, macro-fracture openness has degraded considerably and the fracture will not be open. Likewise, if small amounts of pore space are filled with postkinematic cement, macro-fractures should be open.

By dividing the postkinematic cement volume by the post fracture pore volume we obtain a degradation index (Dg) (Laubach et al., 2000) that predicts fracture openness (Figure 3.7). If values are larger than 50% we expect macro-fractures to be closed, whereas for values below 50% we expect macro-fractures to be at least partly open. As part of a larger study, we measured degradation at several depths in the same wells where we collected subcritical crack index data. Overall, degradation in the Travis Peak is highly variable, but in this area the samples mostly have degradation values less than 50% (Figure 3.7). Four depths (depth of 154 ft, 410 ft, 1825 ft and 1838 ft below the top of the Travis Peak Formation) show degradation values in excess of 50% (Figure 3.7). Only fractures present in these four depths are predicted to be closed to flow. In the area where we collected subcritical crack index samples, Travis Peak fractures should be open to fluid flow, and the dominant control on flow patterns should be fracture distributions such as those predicted by the geomechanical model.

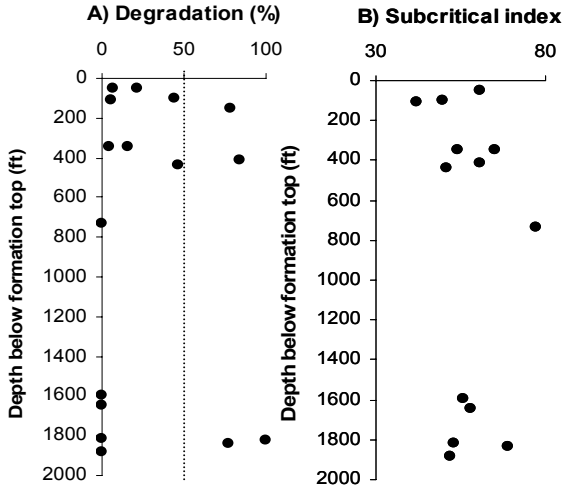

Figure 3.7. A) Degradation vs. depth below formation top. Large degradation values correspond to sealed micro-fractures indicating that macro-fractures will be largely non conductive. Values below 50% indicate mostly open fractures (Degradation analysis by Stephen Laubach). B) Subcritical index vs. depth below formation top. Combination of the two methods allows for subsurface fracture pattern prediction.

3.6. Conclusions

Grain size, cement, and porosity dominate the subcritical index value, given the same chemical environment. Subcritical index decreases with increase in grain size as proposed by the theory for polycrystalline materials. For small carbonate percentages the subcritical index increases with increase in carbonate cement content. However for large carbonate percentage the trend is reversed and subcritical index decreases with carbonate content. We attribute this decrease to a decrease in flaw size that reduces the subcritical index (Gesing and Bradt, 1983). This hypothesis is substantiated by the observation that subcritical index decreases with introduction of large volumes of artificial cement. Furthermore, samples with small grain sizes show a pronounced decrease in subcritical index with water content, whereas large grain size samples do not.

We conclude that the Travis Peak Formation has a subcritical index value of 50 to 60. If geological boundary conditions such as strain values are estimated accurately, this information allows for prediction of a general subsurface fracture pattern within the Travis Peak as depicted in Figure 3.1. Cement in the fracture system will modify these trace patterns, reducing apertures (and thus trace lengths) and in some cases entirely closing fractures, as is locally observed in the Travis Peak Formation (Laubach, 1989). The most damaging cements are postkinematic phases that tend to close large fractures. The presence of these cements can be quantified even where fractures have not been sampled (Laubach, submitted). Thus prediction of fracture flow in the Travis Peak Formation as well as other formations can be constrained by using mechanical modeling to derive a characteristic fracture pattern, and then modifying the pattern with independent evidence about fracture openness. This approach provides a quantitative basis for prediction of subsurface fracture-assisted fluid flow.

3.7. References

Atkinson, B.K., and V. Avdis, 1980, Technical note, fracture mechanics parameters of some rock-forming minerals determined using an indention technique: International Journal of Rock Mechanics, Mining Science & Geomechanics Abstracts, v. 17, p. 383-386.

Atkinson, B.K., 1984, Subcritical crack growth in geological materials: Journal of Geophysical Research, v. 89, no. B6, p. 4077-4114.

Atkinson , B.K., and P.G. Meredith, 1981, Stress corrosion cracking of quartz: a note on the influence of chemical environment: Tectonophysics, v. 77, p. T1-T11.

Atkinson, B.K., and P.G. Meredith, 1989a, The theory of subcritical crack growth with applications to minerals and rocks: Fracture mechanics of rock, B. K. Atkinson (editor), Academic press geology series, London, p. 111-166.

Atkinson, B.K., and P.G. Meredith, 1989b, Experimental Fracture mechanics data for rocks and minerals: Fracture mechanics of rock, B. K. Atkinson (editor), Academic press geology series, London, p. 477-526.

Dutton, S.P., and L.S. Land, 1988, Cementation and burial history of a low-permeability quartzarenite, Lower Cretaceous Travis Peak Formation, East Texas: Geological Society of America Bulletin, v. 100, no. 8., p. 1271-1282.

Evans, A.G., 1972, A method for evaluating the time-dependent failure characteristics of

brittle materials and its application to polycrystalline alumina: Journal of Material Science, v. 7., p. 1137-1146.
Gant, P.L., and W.G. Anderson, 1988, Core cleaning for restoration of native wettability: SPE Formation Evaluation, v. 3, no. 1, p. 131-138.
Gesing, A.J., and R.C. Bradt, 1983, A microcrack model for the effect of grain size on slow crack growth in polycrystalline AL_2O_3: Fracture mechanics of Ceramics, v. 5, R.C. Bradt, A.G. Evans, D.P.H. Hasselman, and F.F. Lange (editors), Plenum Press, New York, p. 569-590.
Han, L.X., and S. Suresh, 1989, High-temperature failure of an alumina-silicon carbide composite under cyclic loads: mechanisms of fatigue crack-tip damage: Journal of the American Ceramic Society, v. 72, no. 7, p. 1233-1238.
Holder, J., J.E. Olson, and Z. Philip, 2001, Experimental determination of subcritical crack growth parameters in sedimentary rock: Geophysical Research Letters, v. 28, no. 4, p. 599-602.
Lander, R.H., J.F.W. Gale, S.E. Laubach, and L.M. Bonnell, 2002, Interaction between quartz cementation and fracturing in sandstone (abs.): AAPG Annual Convention Program, v. 11, p. A98-A99.
La Pointe, P.R., and J.A. Hudson, 1985, Characterization and interpretation of rock mass joint patterns: Geological Society of America Special Paper 199, 37 p.
Laubach, S.E., submitted, Practical approaches to predicting open and sealed fractures: AAPG Bulletin.
Laubach, S.E., 1997, A method to detect natural fracture strike in sandstones: AAPG Bulletin, v. 81, no. 4, April, p. 604-623.
Laubach, S.E., 1989, Fracture analysis of the Travis Peak Formation, western flank of the Sabine Arch, East Texas: The University of Texas at Austin Bureau of Economic Geology Report of Investigations No. 185, 55 p.
Laubach, S.E., R. Marrett, and J. Olson, 2000, New directions in fracture characterization: The Leading Edge, v. 19, no. 7, July, p. 704-711.
Lawn, B.R., and T.R. Wilshaw, 1975, Fracture of brittle solids, Cambridge University Press, Cambridge, 204 p.
Marrett, R., 1997, Permeability, porosity, and shear-wave anisotropy from scaling of open fracture populations: Fractured reservoirs; characterization and modeling, E. Thomas (editor), p. 217-226.
Martin, R.J., III, 1972, Time-dependent crack growth in quartz and its applications to the creep of rocks: Journal of Geophysical Research, v. 77, no.8, p. 1406-1419.
Mussler, B., M.V. Swain, and N. Claussen, 1982, Dependence of fracture toughness of alumina on grain size, and test technique: Journal of The American Ceramic Society, v. 65, no. 11, p. 566-572.
Navarette-Guijosa, A., W.P. Minnear, and R.C. Bradt, 1976, Effect of grain size on subcritical crack growth in alumina: Presented at the Am. Ceram. Soc. Annual Meeting, Cincinatti, Ohio, 1-6 May.
Olson, J.E., 1993, Joint pattern development: effects of subcritical crack growth and mechanical crack interaction: Journal of Geophysical Research, v. 98-B7, p. 12251-12265.
Olson, J.E., 1997, Natural fracture pattern characterization using a mechanically-based model constrained by geologic data – moving closer to a predictive tool: 36th U.S.

Rock Mechanics Symposium.
Olson, J.E., Y. Qiu, J. Holder, and P. Rijken, 2001, Constraining the spatial distribution of fracture networks in naturally fractured reservoirs using fracture mechanics and core measurements: SPE Annual Technical Conference and Exhibition: New Orleans, LA.
Panek, L.A., 1985, Estimating fracture trace length from censored measurements on multiple scanlines: Proceedings of the international Symposium on Fundamentals of Rock Joints/ Björkliden/15-20 September, p. 13-23.
Pettijohn, F.J., 1975, Sedimentary rocks: Third Edition, Harper & Row, Publishers, New York, 628 p.
Renshaw, C.E., 1996, Influence of subcritical fracture growth on the connectivity of fracture networks: Water Resources Research, v. 32, no. 6., p. 1519-1530.
Renshaw, C.E., and D.D. Pollard, 1994, Numerical simulation of fracture set formation: a fracture mechanics model consistent with experimental observations: Journal of Geophysical Research, v. 99-B5, p. 9359-9372.
Rice, R.W., S.W. Freiman, and J.J. Mecholsky Jr., 1980, The dependence of strength-controlling fracture energy on the flaw-size to grain-size ratio: Journal of The American Ceramic Society, v. 63. no. 3-4, p. 129-136.
Rives, T., M. Razack, J.-P. Petit, and K.D. Rawnsley, 1992, Joint spacing: analogue and numerical simulations: Journal of structural Geology, v. 14, no. 8/9, p. 925-937.
Scholz, C.H., 1972, Static fatigue of quartz: Journal of Geophysical Research, v. 77, no. 11, p. 2104-2114.
Segall, P., 1984, Rate-dependent extensional deformation resulting from crack growth in rock: Journal of Geophysical research, v. 89, no. B6, June 10, p. 4185-4195.
Snow, D.T., 1970, The frequency and apertures of fractures in rock: International Journal of Rock Mechanics and Mining Science, v. 7, p. 23-40.
Williams, D.P., and A.G. Evans, 1973, A simple method for studying slow crack growth: Journal of Testing and Evaluation, v. 1, p. 264-270.
Wu, C. Cm., S.W. Freiman, R.W. Rice, and J.J. Mecholsky, 1978, Microstructural aspects of crack propagation in ceramics: Journal of Materials Science, v. 13, p. 2659-2670.

4. Permeability Estimation for Geomechanically Generated Fracture Patterns

Subcritical crack growth parameters were measured from representative rock samples of various reservoir rocks including the Cretaceous Dakota sandstone (tight gas sandstone, San Juan Basin, Colorado) and the Permian Clear Fork dolomite (South Wasson field, West Texas). We focus on results form the dolomite study. These measurements along with other inferred parameters such as the strain and Young's modulus were used with a geomechanical crack growth simulator (Olson, 2001) to generate fracture patterns at a series of increasing strain levels. The resulting fracture patterns exhibited total fracture lengths, mean fracture lengths, and cluster spacing dependent on strain level, bed height, and subcritical crack index. Fluid-flow simulations were conducted to estimate effective permeability in the simulated fracture patterns using two different approaches representing fractures (1) explicitly with high-permeability grid cells and (2) indirectly with nonneighbor connections between matrix grid cells.

The ratio of effective permeability to matrix permeability, R_k, was found to increase with strain level, total fracture length, and mean fracture length. For a given strain level R_k depended on the subcritical crack index and bed height. Fracture aperture, however did not affect R_k. The reduction of effective permeability by the filling of fractures with diagenetic cements was also studied.

4.1. Introduction

In conventional reservoir simulation, grid-block permeabilities must frequently be assigned values systematically larger than those observed in core measurements or inferred from well logs in order to obtain reasonable history matches. Even then, accuracy with regard to some aspects of the performance such as water or gas cuts, breakthrough times, and sweep efficiencies may be inadequate. This could be due to a substantial part of the flow taking place through fractures not accounted for in the simulation.

High-permeability fracture networks in a matrix system can create high-conductivity channels for the flow of fluids through a reservoir, producing larger flow rates and larger apparent permeabilities than those in the matrix alone. The presence of fractures can also lead to poorer sweep efficiencies for flooding operations with large portions of the reservoir remaining untouched by the displacing fluid. A better understanding of reservoir performance may be obtained by including the physics of fluid flow in fractures in reservoir flow modeling.

4.2. Geomechanical Simulation

Simulation Parameters: South Wasson Clear Fork Case Study

The SCC index has been measured with the dual-torsion-beam apparatus (Williams and Evans, 1973; Pletka and others, 1979) for samples from six representative layers of the South Wasson Clear Fork reservoir (Holder and others, 2001; Table 4.1). In these measurements the SCC index ranges from 40 to 80. We have used these two extreme

values as our case study scenarios. A Young's modulus of 40,000 MPa for this formation was estimated from a typical porosity of 10 percent using a published correlation for dolomites. A strain of 0.00725 was inferred from fracture-aperture measurements at an outcrop of the Victorio Peak Formation (a Clear Fork equivalent), Apache Canyon, West Texas. The geometric mean of the apertures observed from the outcrop is 0.212 mm. A typical thickness for rock-fabric flow layers in the South Wasson Clear Fork field is 5 m and for high-frequency cycles is 10 m. These thicknesses were used in the crack simulation. Owing to crack simulation limitations the inferred strain of 0.00725 could not be applied. Therefore a value of strain was applied such that the resultant geometric mean aperture obtained was fairly close to that observed in the outcrop. The input data used to generate fracture patterns are given in Table 4.2.

Table 4.1. Mean values of the SCC index for six South Wasson Clear Fork samples.

Sample depth (ft)	Type of test	No. of tests	Average SCC index
6,091	Dry	7	43
	Wet	5	37
6,138	Dry	11	40
	Wet	3	34
6,367	Dry	6	60
	Wet	12	53
6,385	Dry	6	81
	Wet	3	70
6,484	Dry	5	43
	Wet	1	37
6,520	Dry	8	38
	Wet	10	30

Table 4.2. Input data to the crack growth simulator.

Parameter	**Value**
Area of study	50 × 50 m
Young's modulus, E	40,000 MPa
Critical stress intensity factor	1.5 MPa(m)$^{1/2}$
Threshold stress intensity factor	0.15 MPa(m)$^{1/2}$
Displacement increment	0.00005 m
No. of increments	83
Total strain	7.33E-5
Time	19.7 million years
Strain rate	2.30E-19 1/s
No. of initial flaws	2,000

Four case scenarios were studied combining two bed heights, 5 and 10 m, and two SCC indices, 40 and 80. For each case, seven different realizations were studied, each realization with a different set of random starter cracks. Thus, a total of 28 different geomechanical simulations were performed. A sample set of fracture patterns obtained

for each of the four cases (realization 3) is shown in Figure 4.1 through Figure 4.4. For all other parameters remaining constant, the subcritical index of 80 produces a fracture pattern with a larger number of smaller fractures as compared with the subcritical index of 40. Further, for everything else remaining constant, we see that the bed height of 5 m causes fracture patterns in which the fracture clusters are more closely spaced than when the bed height is 10 m.

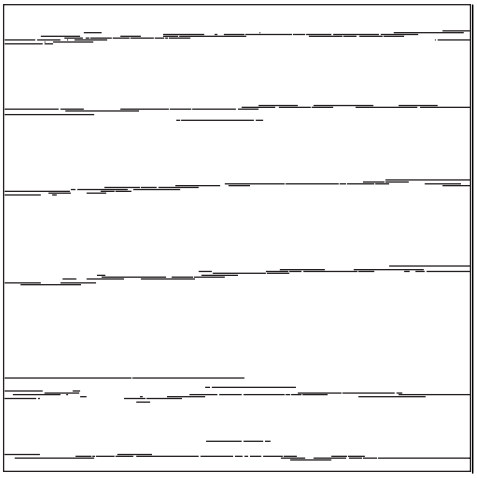

Figure 4.1. SWCF simulated fracture pattern (Realization 3) with a bed height of 10 m and SCC index of 40.

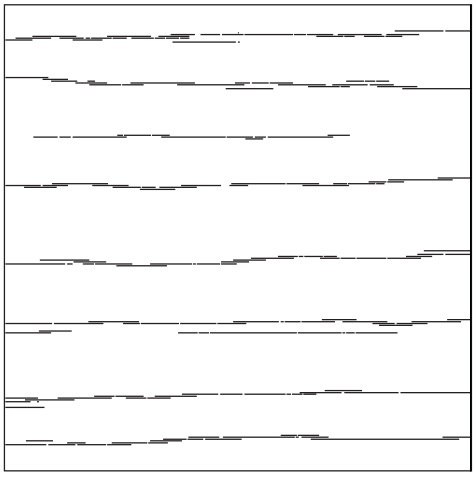

Figure 4.3. SWCF simulated fracture pattern (Realization 3) with a bed height of 5 m and SCC index of 40.

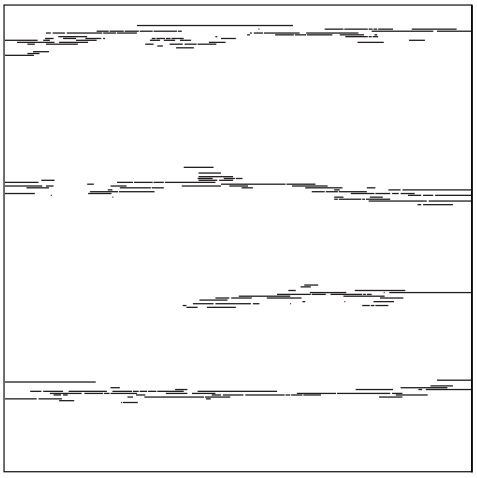

Figure 4.2. SWCF simulated fracture pattern (Realization 3) with a bed height of 10 m and SCC index of 80.

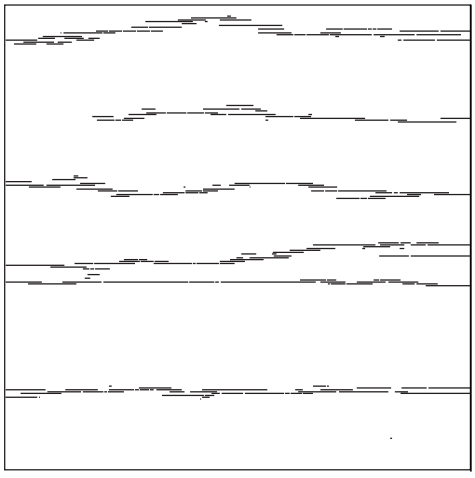

Figure 4.4. SWCF simulated fracture pattern (Realization 3) with a bed height of 5 m and SCC index of 80.

4.3. Flow Modeling

Explicit Fracture Representation

The geomechanical simulation produces a list of patches with location and aperture information. Each fracture is made up of a series of patches lying end to end. The greater the number of patches associated with a particular crack the greater is the length of that particular crack. Thus a fracture can have varying apertures along its length. For a flow simulation, the flow area is gridded to the same resolution as the geomechanical simulation. In this study the geomechanical simulation area was 50 × 50 m square, and the patches were 0.1 m in length. Therefore, the flow simulations were performed on the same 50 × 50 m area with 500 × 500 = 250,000 cells of equal x and y dimension (0.1 m). This ensures that each patch can be represented by one cell in the flow simulation. The z direction cell size was 0.5 m.

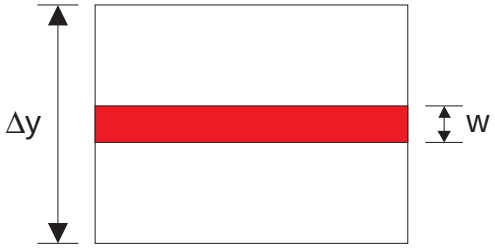

Figure 4.5. Grid cell representation of a fracture patch, showing the cell dimension and fracture aperture.

The permeability of a fracture patch, k_{frac}, with uniform aperture w (Figure 4.5), can be computed using (Halihan and others, 1999)

$$k_{frac} = \frac{w^2}{12} \tag{4-1}$$

The permeability of a cell in the flow simulation containing a patch can be computed using

$$k_{cell} = \frac{\left(k_{frac} w + k_{mat}\left(\Delta y - w\right)\right)}{\Delta y}, \tag{4-2}$$

where k_{cell} is the permeability of a flow simulation cell containing a fracture patch, and k_{mat} is the matrix permeability. The width of the simulation cell perpendicular to the flow direction is Δy. A matrix permeability of 1 md was used for all flow simulations.

Each cell in the flow simulation was assigned a unique permeability on the basis of the location and aperture of the patches. The *y* and *z* direction permeabilities were unchanged because the geomechanical simulations were constrained to produce fractures only in the *x* direction. A Fortran program was written to create lists of cell permeabilities from the patch coordinates and aperture information obtained from the geomechanical simulations.

Nonneighbor Connections

Flow through fractures can also be modeled using nonneighbor connections (NNC) in a traditional finite-difference simulator (Hearn and others, 1997). In this approach the fractures are assumed to have infinite conductivity, making fracture aperture information irrelevant. The fracture patterns are gridded such that the fractures lie at the boundaries between grid cells.

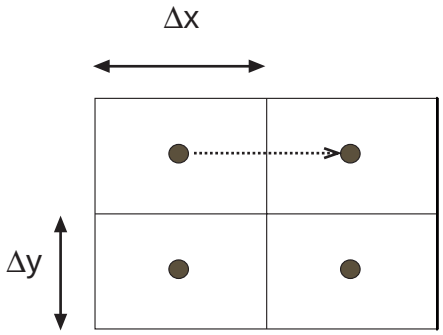

Figure 4.6. Schematic of grid, depicting cell dimensions and x direction permeability.

The matrix flow transmissibility between any two grid cells is

$$T_{x(mat)} = \frac{k_x A_x}{\Delta x}, \tag{4-3}$$

where A_x is the area perpendicular to flow in the x direction, $\Delta y \Delta z$, and k_x is the permeability in the x direction (**Figure 4.6**).

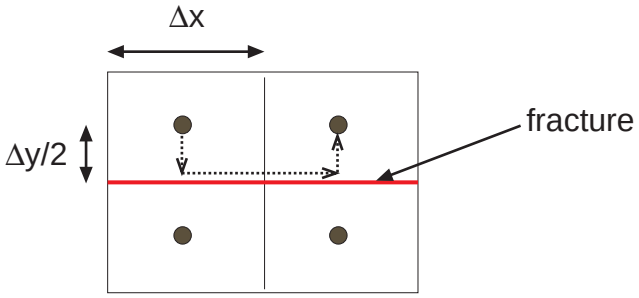

Figure 4.7. Schematic of grid, depicting the location of, and x direction permeability due to, a fracture.

If there is a fracture between the cells as shown in Figure 4.7, an additional transmissibility for fracture flow can be assigned using

$$T_{x(frac)} = \frac{k_y A_y}{2\left(\Delta y / 2\right)} = \frac{k_y A_y}{\Delta y}, \tag{4-4}$$

where A_y is the area perpendicular to flow in the y direction, $\Delta x \Delta z$, and k_y is the permeability in the y direction. The total x direction transmissibility, accounting for both matrix and fracture flow, is

$$T_{x(total)} = T_{x(mat)} + T_{x(frac)} = \frac{k_x A_x}{\Delta x} + \frac{k_y A_y}{\Delta y} \quad . \tag{4-5}$$

The transmissibility between adjacent cells due to matrix flow is computed automatically by the simulator, connecting cell i to cells i-1 and i+1. The transmissibility between cells due to fracture flow can be entered explicitly using NNC, connecting cell i to cells i-1 and i+1 as well as to all other cells on that same fracture. The NNC between cell i and its neighbors i-1 and i+1 is in addition to that due to matrix flow. Thus, a fracture extending between cells 1 and n connects cell 1 to cells 2 through n, cell 2 to cells 3 through n, and so on (**Figure 4.8**).

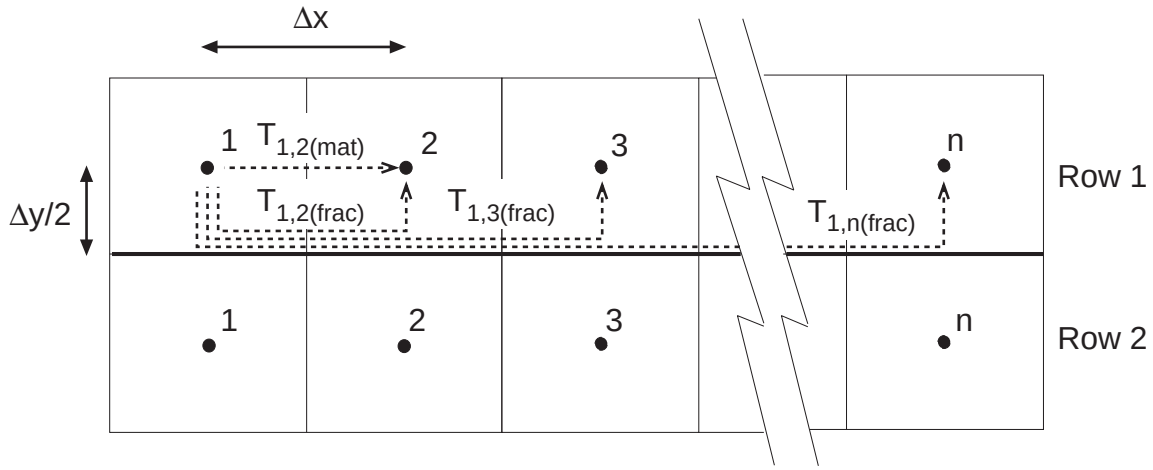

Figure 4.8. Schematic of grid, depicting non-neighbor connections between cells, to model flow due to a fracture.

The total number of NNC per fracture is

$$\left(\frac{n(n-1)}{2}\right)2 = n(n-1) \quad . \tag{4-6}$$

The multiplication by 2 accounts for cells on both sides of the fracture. A Fortran program was written to create a list of NNC transmissibilities from the endpoint locations of fractures in a fracture pattern simulation. A fracture between rows 1 and 2 extending from cells 1 to n results in the following nonneighbor transmissibilities for connections between cell 1 and the others in row 1:

$$T_{1,2}, T_{1,3}, ..., T_{1,n(frac)} = \frac{k_y(\Delta x \Delta z)}{\Delta y} \quad . \tag{4-7}$$

Likewise the nonneighbor transmissibilities between cell 2 and cells 3 through *n* are

$$T_{2,3}, T_{2,4}, ..., T_{2,n(frac)} = \frac{k_y(\Delta x \Delta z)}{\Delta y}, \quad (4\text{-}8)$$

and so on, for cells 3 through *n*. The transmissibilities for cell connections in row 2 are computed similarly. The corresponding matrix transmissibilities are computed automatically by the simulator.

Flow Simulation Methodology

A finite difference simulator, Eclipse 100, (Schlumberger, 1995, 1997) was used to perform 2-D, single-phase flow simulations. Constant pressure boundaries were maintained on two opposing sides while the other two sides were no-flow boundaries. Constant pressure was maintained by assigning to each of the cells on a particular side producing wells on pressure control, and to each of the cells on the opposing side injector wells on pressure control. Thus the number of producers and injectors was each equal to the number of rows in the flow grid.

Water was used as the flowing phase, both with and without tracer. Tracers were used only for flow visualization and do not otherwise affect the simulation. The flow simulation was performed till a steady-state flow rate, q, was obtained. Knowing q, the pressures at both the ends, P_1 and P_2, the distance between the constant pressure conditions, L - (2(Δx)/2), and the fluid properties, one can obtain an effective permeability for the fractured grid as follows,

$$k_{eff} = \frac{q\mu(L - \Delta x)}{A(P_1 - P_2)}, \quad (4\text{-}9)$$

where μ is the fluid viscosity, and A, the area perpendicular to flow, is the product of Δy, Δz, and the number of cells in the y direction.

4.4. Verification

Effective permeability estimates from flow simulations using explicit fracture representations and NNC were verified by comparison with analytical solutions for (1) a single finite aperture fracture extending across the entire simulation grid, and (2) the Chirlin solution for a staggered periodic array of infinite-conductivity fractures (Chirlin, 1985; Nakashima and others, 2000).

Single-Fracture Analytical Solution

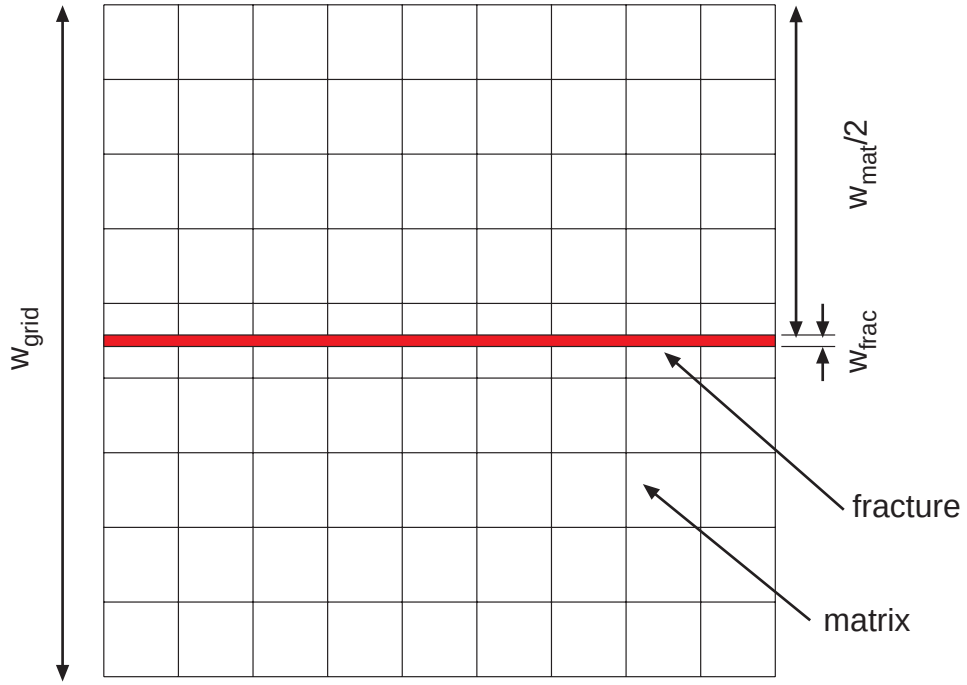

Figure 4.9. Plot showing an embedded fracture extending from end to end in a simulation grid.

The analytical solution for the effective permeability of a rectangle with a single fracture extending across the entire area is (**Figure 4.9**)

$$k_{anal} = \frac{k_{frac} w_{frac} + k_{mat} w_{mat}}{w_{grid}} \quad . \tag{4-10}$$

Flow simulations were conducted using the explicit fracture method for two different grid cell sizes of 0.5 m and 0.05 m and a series of fracture widths ranging from 1 to 10,000 microns. The effective permeabilities obtained from the flow simulations agreed to within 0.5 percent of the effective permeabilities obtained using the analytical solution for all fracture apertures studied and for both grid sizes.

The NNC method does not give a good match with the analytical solution for the case of a fracture going all the way across the simulation grid. The reason for this is that in the flow simulation the boundary conditions are established with constant pressures and fluid injection or production at the midpoints of the left and right columns of grid cells. However, in the NNC approach the fractures are assumed to lie in between the grid cells, and the flow resistance from the midpoint of a boundary cell to its edge at both ends of the fracture is sufficient to cause a substantial discrepancy between the simulated and analytical effective permeabilities. This problem does not occur in the explicit fracture approach because the constant pressure boundaries can be applied directly to both ends of the fracture.

4.5. Chirlin Solution

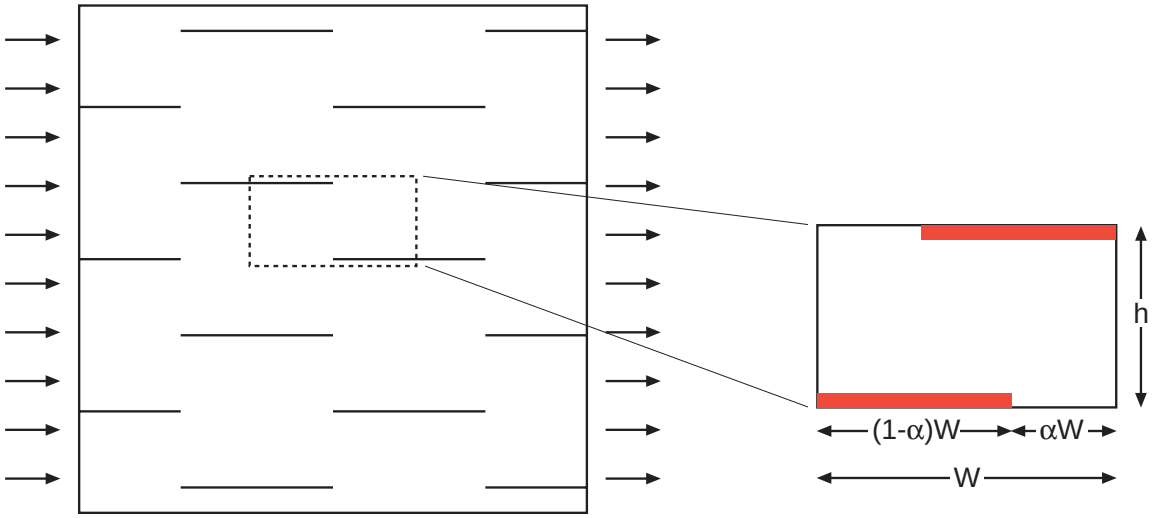

Figure 4.10. Periodic staggered array of fractures depicting parameters used in the Chirlin solution

An analytical solution for the effective permeability in a staggered periodic array (Figure 4.10) of infinite conductivity fractures gives the effective permeability ratio R_k as follows:

$$R_k = \frac{k_{eff}}{k_{mat}} = \frac{2WG(r)}{hG\left(\sqrt{1-r^2}\right)}, \tag{4-11}$$

where $G(r)$ is the complete elliptic integral of the first kind. In the mathematical literature the symbol $K(r)$ is usually used for this function, but $G(r)$ will be used here to avoid potential confusion with permeability, k. The modulus, r , of the elliptic integral is given by

$$\frac{1}{r} = \frac{2m(P-1)^2}{(mP+1)^2} + 1 + \sqrt{\left[\frac{2m(P-1)^2}{(mP+1)^2} + 1\right]^2 - 1}, \tag{4-12}$$

where

$$\frac{1}{P} = dn\left[\alpha G\left(\sqrt{1-m^2}\right), \sqrt{1-m^2}\right], \tag{4-13}$$

dn is a Jacobian elliptic function, and m is the modulus of elliptic integral, obtained by solving

$$\frac{G\left(\sqrt{1-m^2}\right)}{G(m)} = \frac{2W}{h} \quad . \tag{4-14}$$

These equations have been implemented in Mathematica (Wolfram, 1999), and the solution is plotted in **Figure 4.11**.

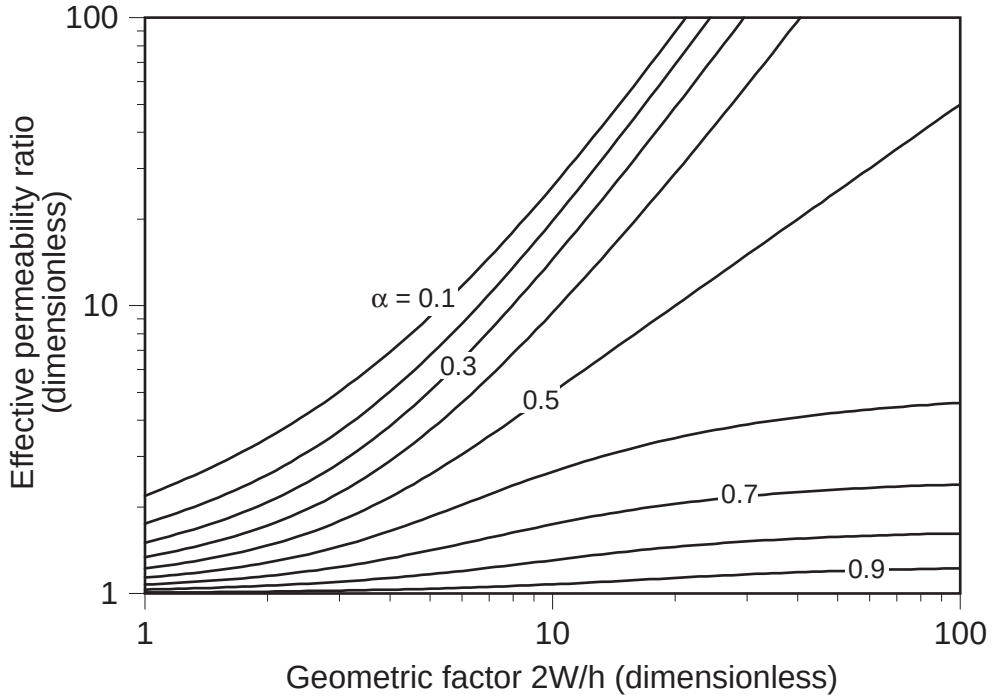

Figure 4.11. The Chirlin solution for Effective Permeability Ratio, Rk, for flow parallel to fractures.

Flow simulations for this arrangement of fractures were run until steady-state flow conditions were achieved and the resulting values of R_k were compared with those obtained from the analytical solution. For the explicit-fracture-representation case we studied an array with four fractures—two on the edge and two completely embedded in the grid (Figure 4.12). This ensured that the north and south edges were no-flow boundaries, whereas the east and west edges were constant-pressure boundaries. We used a width W of 4.5 ft, a fracture spacing h of 1.5 ft, and an α value of 1/3, giving 2W/h = 6 and an analytical solution for the effective permeability ratio R_k=5.8404.

The results for two different grid cell sizes of 0.05 ft and 0.025 ft are as shown in the Table 4.3 and Table 4.4. The effective permeability ratios obtained from the flow simulations approach the Chirlin solution for infinite conductivity fractures as the fracture aperture increases. The accuracy improves with grid refinement.

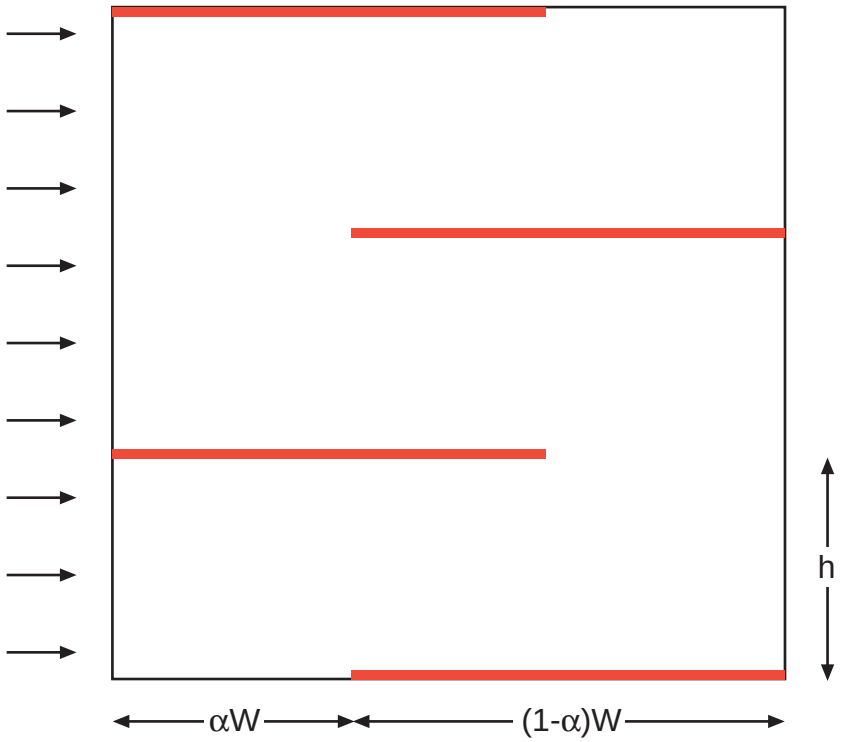

Figure 4.12. Chirlin layout for the explicit fracture representation study

Table 4.3. Simulation results using the explicit fracture-representation method and a cell size of 0.05 ft for a staggered array of four fractures.

Fracture aperture (microns)	Fracture permeability (md)	Grid effective *k* ratio (R_k)
1	8.44E+01	1.0055
10	8.44E+03	1.0991
100	8.44E+05	4.7088
1,000	8.44E+07	4.8399
10,000	8.44E+09	4.8399

Table 4.4. Simulation results using the explicit fracture-representation method and a cell size of 0. 025 ft for a staggered array of four fractures.

Fracture aperture (microns)	Fracture permeability (md)	Grid effective *k* ratio (R_k)
1	8.44E+01	1.0109
10	8.44E+03	1.1096
100	8.44E+05	5.1643
1,000	8.44E+07	5.3290
10,000	8.44E+09	5.3290

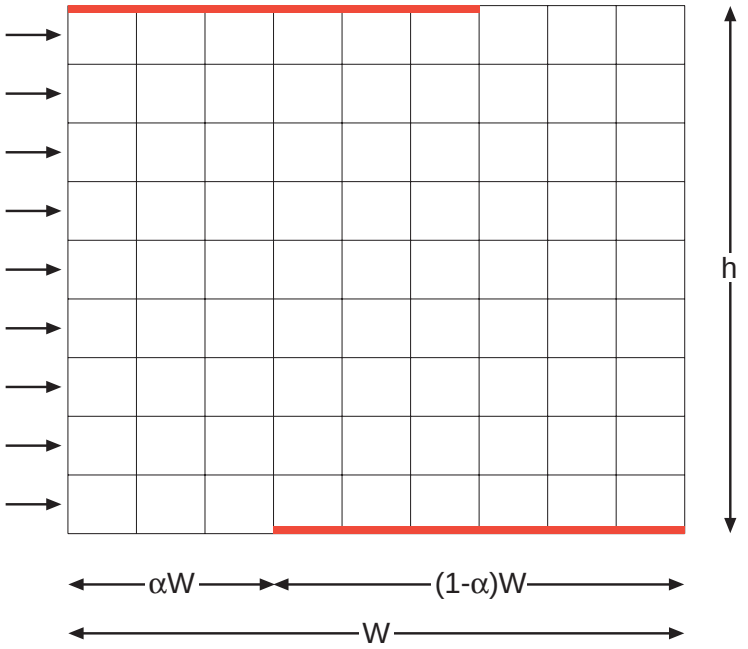

Figure 4.13. Gridded 9 X 9 array with two edge fractures

We applied the NNC method to two periodic fracture cases. For the first case, we used a width, W, of 4.5 ft, a fracture spacing, h, of 4.5 ft, and an α of 1/3 (Figure 4.13), giving 2W/h = 2 and an analytical solution of R_k=1.947 (Figure 4.11). As the grid becomes finer in resolution, the effective permeability obtained by the flow simulation gets closer to the analytical solution (Figure 4.14).

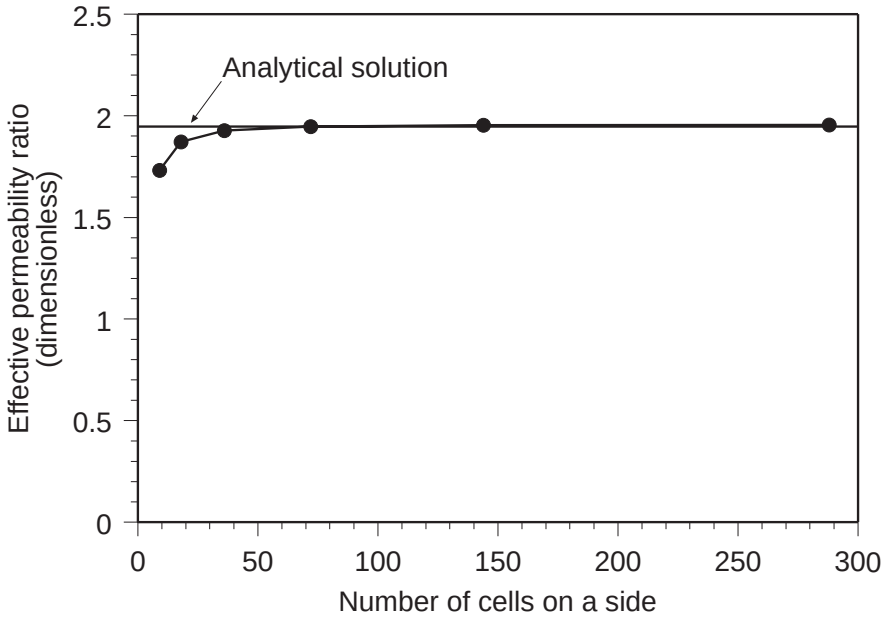

Figure 4.14. Comparison of analytical solution and NNC simulation for the effective permeability of a periodic array of fractures with two fractures on the edge of the grid

For the second test we had multiple fractures inside the gridded region (**Figure 4.15**). The dimensions were the same as for the previous case, with a width, W, of 4.5 ft and an αW of 1.5 ft, giving an α of 1/3. The fracture spacing, h, however, varied depending on the number of fractures. We studied this scenario for two values of h. For the first case the number of fractures was 4, giving a value of 1.5 for h, and for the second case the number of fractures was 10, giving a value of 0.5 for h. For a given α and W, as h decreases the effective k ratio increases. Thus, for $h = 1.5$ the analytical solution is $R_k = 5.8402$, and for h=0.5 the analytical solution is $R_k = 34.944$. We modeled both these cases with six gridding schemes increasing grid resolution from 9×9 to 288×288 numbers of cells.

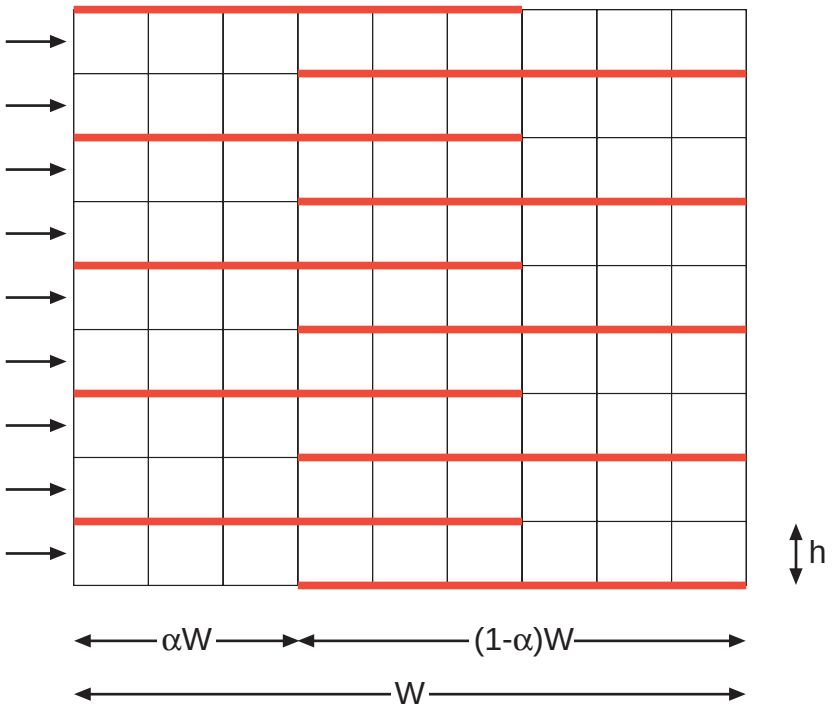

Figure 4.15. Gridded 9 X 9 array with multiple fractures

The simulation results for both cases are shown in Figure 4.16 and Figure 4.17. With increasing grid resolution the effective permeability ratio, R_k, obtained from the simulation gets very close to the analytical solution. One gets to within 5 percent of the analytical solution if there are 12 cells between fractures and to within 2 percent of the analytical solution if there are 24 cells between fractures. The difficulty with the NNC approach that occurred when simulating a single fracture extending across the entire simulation grid did not occur when simulating a periodic array of fractures because the fractures extend only two-thirds of the way across the simulation grid. The additional resistance due to an extra half-matrix cell at one end of each fracture is small compared with the resistance due to the unfractured matrix beyond the other end of each fracture.

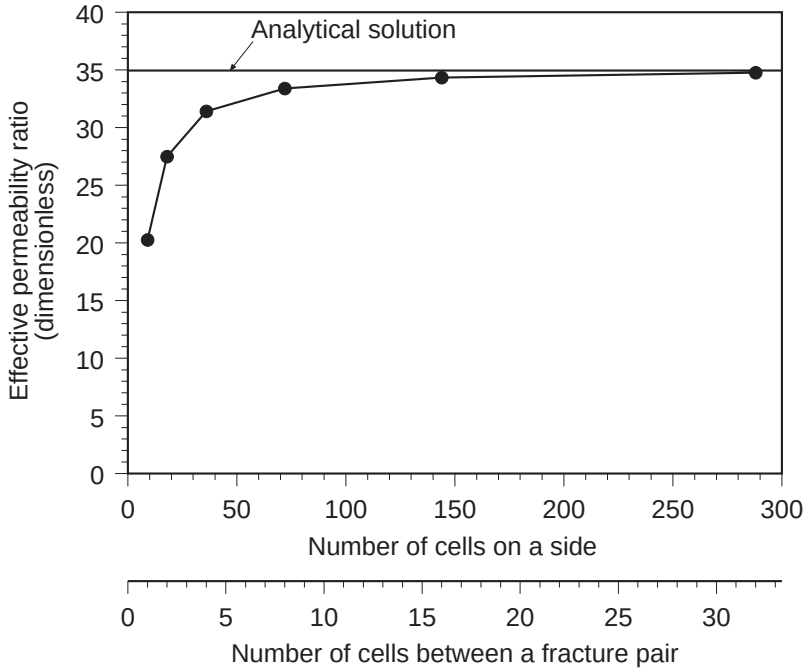

Figure 4.16. Comparison of analytical solution and NNC simulation for the effective permeability of a periodic array of fractures with multiple fractures in the grid (h = 1.5).

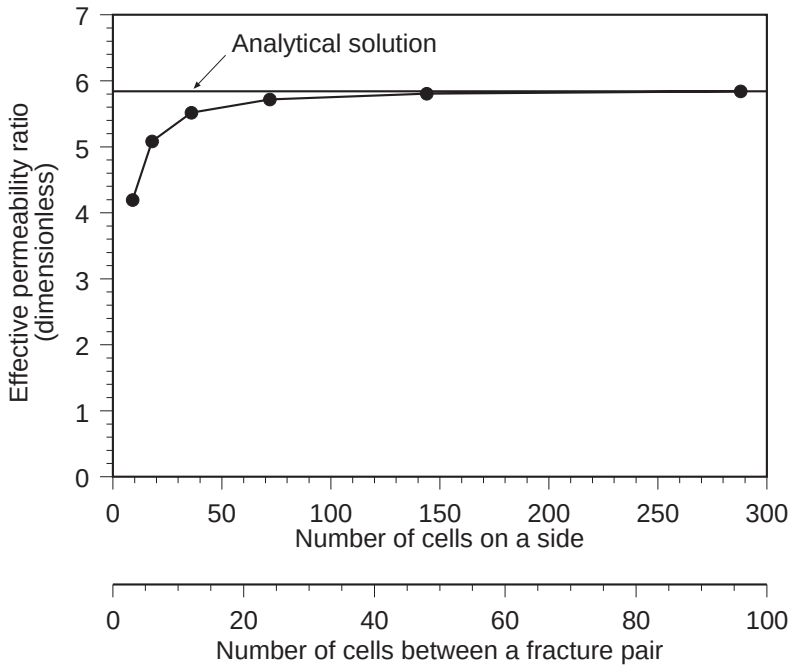

Figure 4.17. Comparison of analytical solution and NNC simulation for the effective permeability of a periodic array of fractures with multiple fractures in the grid (h=0.5).

4.6. Flow Modeling of Simulated Fracture Patterns

A fracture pattern was obtained for each run of the fracture simulation and each displacement increment. From these patterns the cell permeabilities for input to the eclipse simulator were computed. The total fracture length, mean fracture length, and geometric mean fracture aperture were also computed. For each strain level, steady-state flow simulations were performed and the effective *k* ratio, R_k, was computed. Thus, for each of the four cases of a particular combination of bed height and subcritical index and for each strain level the average R_k of seven realizations was obtained. This procedure was repeated for increasing values of strain.

Explicit Fracture Representation

Values of R_k vs. strain obtained for each of the runs and for the individual bed heights of 5 m and 10 m are plotted in Figure 4.18 and Figure 4.19. The R_k values depend on both the bed height and the subcritical index with a large degree of variability between the different realizations. The means and standard deviations of R_k from the seven realizations for each of the four combinations of bed height and subcritical index are shown in Figure 4.20 and Figure 4.21. In subsequent analysis and figures, we shall be referring to only the average of the seven realizations.

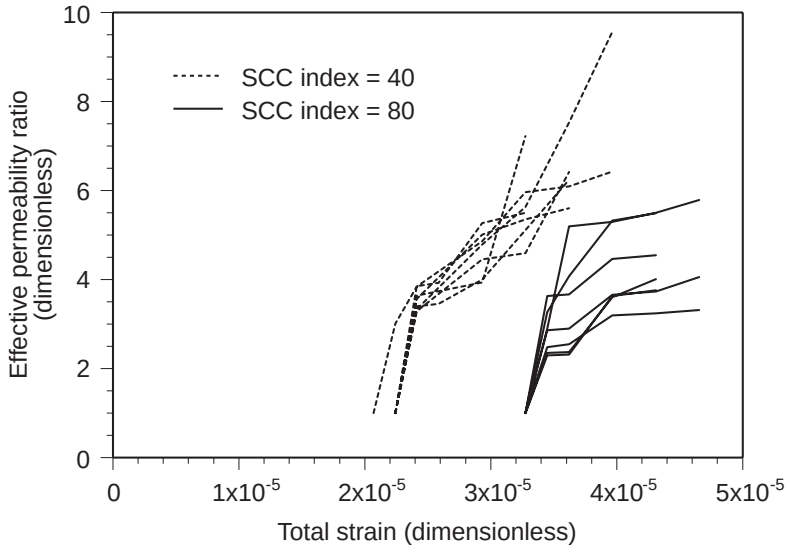

Figure 4.18. Values of R_k vs. strain, for all 7 realizations for a bed height of 10 m.

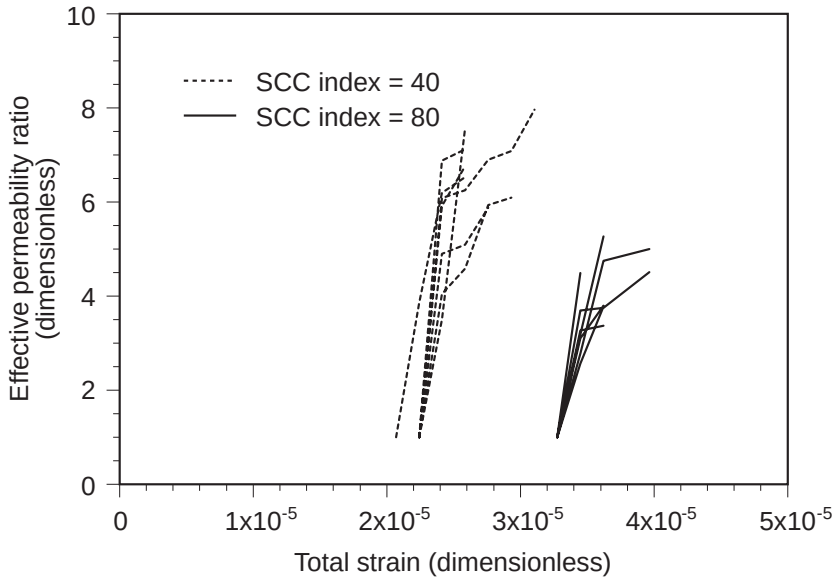

Figure 4.19. Values of R_k vs. strain, for all 7 realizations for a bed height of 5 m

In Figure 4.20 and Figure 4.21 we can see the effect of strain on the effective permeability ratio, R_k. As expected, an increase in the strain causes an increase in R_k. The first significant fractures appear at a strain 2.0E-5 for the index of 40, but at a larger strain of 3.2E-5 for the index of 80 because the larger SCC index produces a smaller crack propagation velocity. Furthermore, for a given strain the total fracture length and the R_k is larger for the lower index.

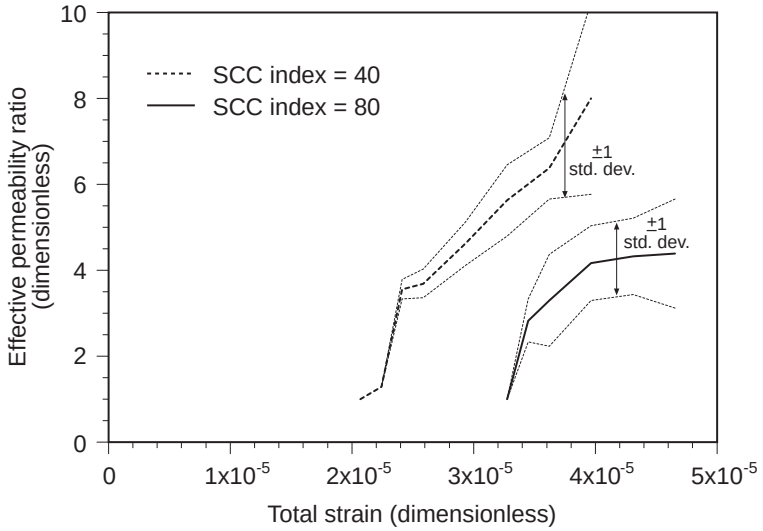

Figure 4.20. Mean and standard deviation of the effective permeability ratios for a bed height of 10 m.

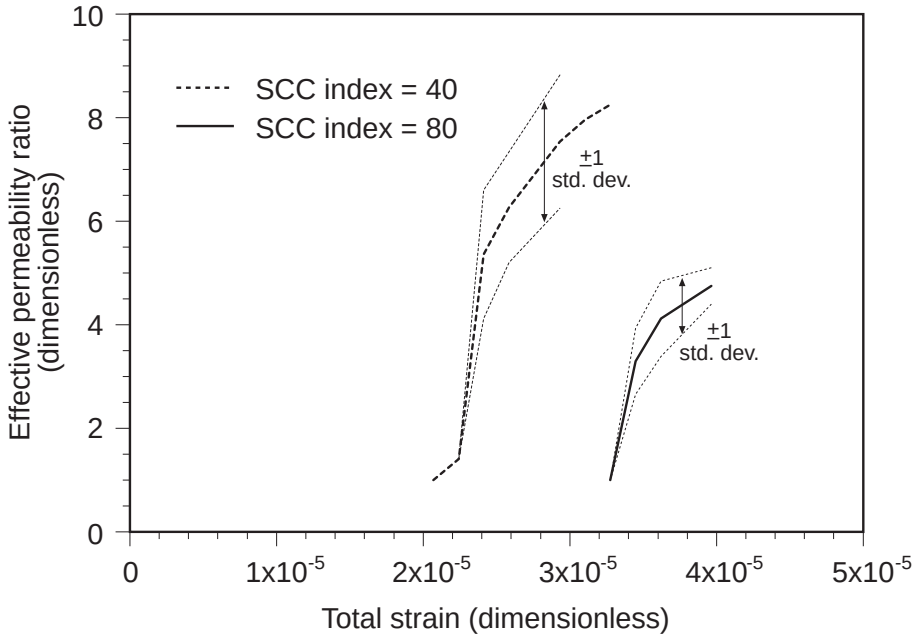

Figure 4.21. Mean and standard deviation of the effective permeability ratios for a bed height of 5 m.

It is also evident from Figure 4.20 and Figure 4.21 that for a given index, the rate of increase in R_k is higher for the bed height of 5 m compared with the bed height of 10 m. This is because for the smaller bed height at a particular strain, a larger number of starter flaws develop into fractures, leading to a larger total fracture length. The smaller bed height also causes a closer spacing in the fracture clusters (Figure 4.1 through Figure 4.4), but that factor probably does not by itself cause an increase in R_k.

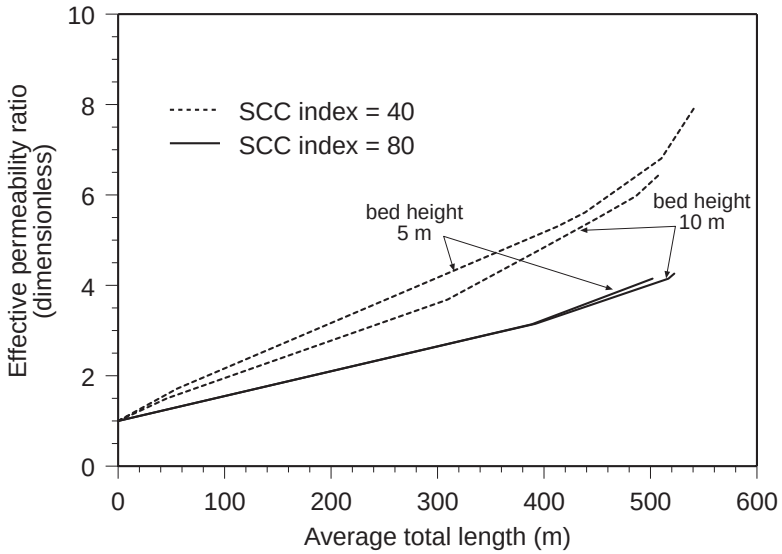

Figure 4.22. Average Rk vs. average total length (average of 7 realizations)

For each combination of bed height and index for each strain level, the average total fracture length of seven realizations was computed. As expected, the total fracture length

increases with the strain; therefore, the effective *k* ratio, R_k, also increases with the strain (Figure 4.22). For the same total length, the case with the index of 40 has a higher R_k than that with an index of 80. This is because an index of 40 in the geomechanical simulations leads to fracture patterns with a smaller number of larger fractures compared with cases with an index of 80.

Further, we see in this figure that there is no strong dependence of R_k on the bed height. There is a slight dependence for the lower index value of 40 but no dependence for the index of 80. The larger R_k for a lower bed height (Figure 4.20 and Figure 4.21) was due to the larger fracture length at the same strain.

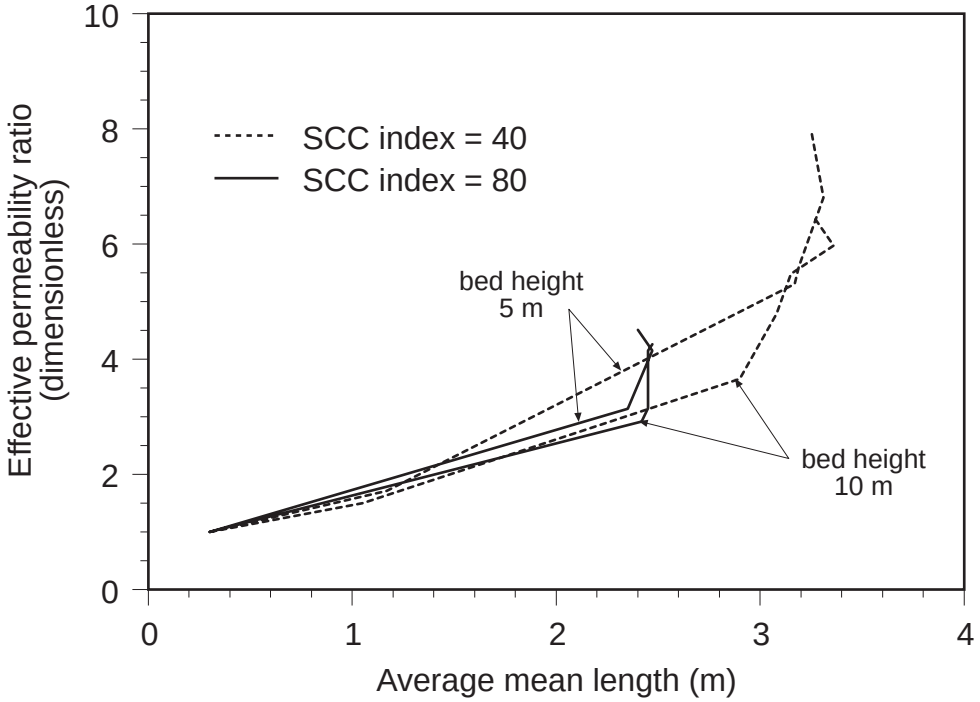

Figure 4.23. Average Rk vs. average mean length (average of 7 realizations)

Similarly, for each strain level, the average mean length of seven realizations was also computed. The effective *k* ratio, R_k, increases with an increase in the fracture mean length (Figure 4.23). For the initial part of the curve, that is, for values of mean length below about 2.5 m, there is no difference in the R_k values obtained for the different indices or bed heights. However, toward the end of the crack growth simulation, the index of 40 does produce fractures with an average mean length (~3.5 m) larger than that produced by the index of 80 (~2.5 m).

In Figure 4.23, the sharp increase in the R_k values at the end of the simulations for both the indices of 40 and 80 is due to the increase in the number of fractures of the same mean length. There is not much of a dependence on bed height. The previous observation of R_k dependence on bed height (Figure 4.20 and Figure 4.21) at a given strain is due to differences in fracture total length and fracture mean length and not due to the closer

spacing between fracture clusters. The spacing between the fracture clusters does not appear to have an effect on R_k.

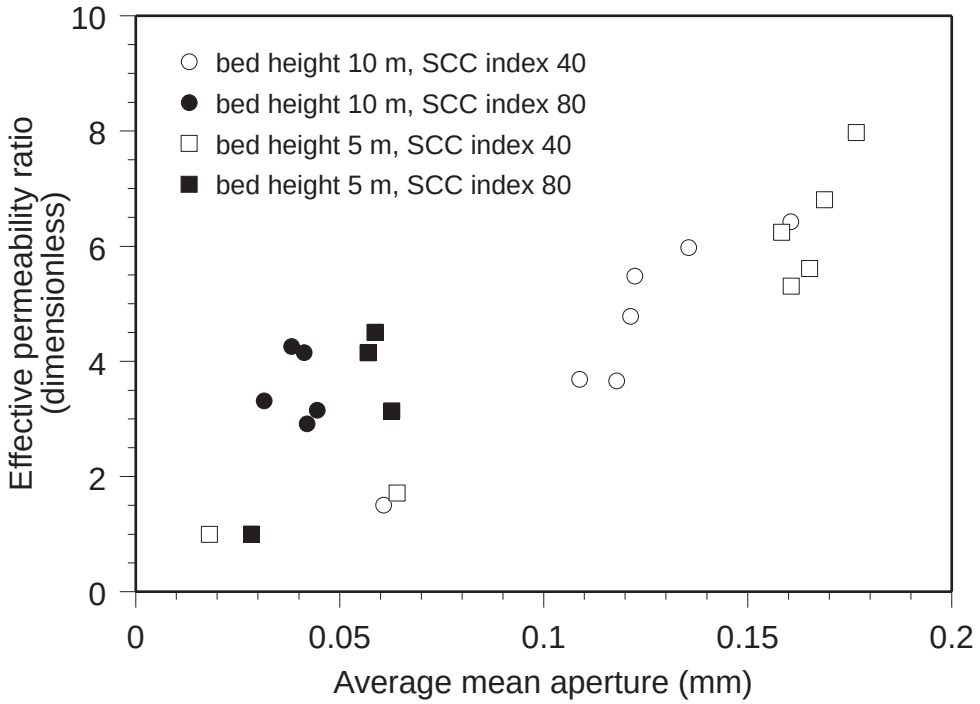

Figure 4.24. Average Rk vs. average mean aperture (average of 7 realizations)

A plot of the effective *k* ratio, R_k, vs. average mean aperture is shown on Figure 4.24. At first glance, it appears that R_k does increase with the average mean aperture. However, it is to be noted that each marker point represents a different strain level. Therefore, with a change in the mean aperture, the total length and mean length are also changing. The apparent increase in R_k with the mean aperture for the index of 40 is probably due to an increase in the fracture total length and/or mean length.

Further, for seven realizations of one of the cases (bed height 10 m and index 40) the fracture cell permeabilities were increased by a factor of 10 and the flow simulations repeated. The resultant grid permeabilities, however, went up only 6 percent. Thus, the effective permeability ratio is not very sensitive to the fracture aperture when the fracture permeabilities are much larger than the matrix permeability.

Nonneighbor Connection Fracture Representation

Flow simulations for one set of runs (realization 1) for both bed heights (5 m and 10 m) and both indices (40 and 80) were repeated using the NNC approach. The effective permeabilities are similar to those obtained using explicit fracture representations except that in the NNC approach the R_ks are bigger by about 30 percent because the fractures are assumed to be infinitely conductive. Nevertheless, the similarity of results from the two methods indicate that effective permeability is more sensitive to the fracture pattern than fracture conductivity.

The fluid-flow simulations were performed using the fully implicit method. The memory and run-time requirements for the NNC approach depend on the number of fractures and were much higher than that required for the explicit fracture representation method. The memory required ranged from about 1.5 to 3 times that of the explicit fracture representation method, whereas the CPU run time ranged from about 15 to 30 times that of the explicit fracture representation method.

4.7. Other Factors Affecting Fracture Permeability

Synkinematic Cement

In some cases cement is precipitated on the walls of the fracture as the fractures form, thus reducing the fracture aperture everywhere by a constant amount. Cement that is precipitated in conjunction with fracture propagation is called synkinematic cement. The constant amount by which the aperture is reduced is defined as the emergent threshold, e_t (Laubach and others, 2000). In the South Wasson Clear Fork reservoir the emergent threshold is estimated at 100 μm (see Gale and others, this report). To examine the effect of the partial filling of fractures by cement, we define an emergent threshold ratio, e_r, such that

$$e_r = \frac{e_t}{w_{gm}} \quad , \tag{4-15}$$

where w_{gm} is the geometric mean of the simulated apertures.

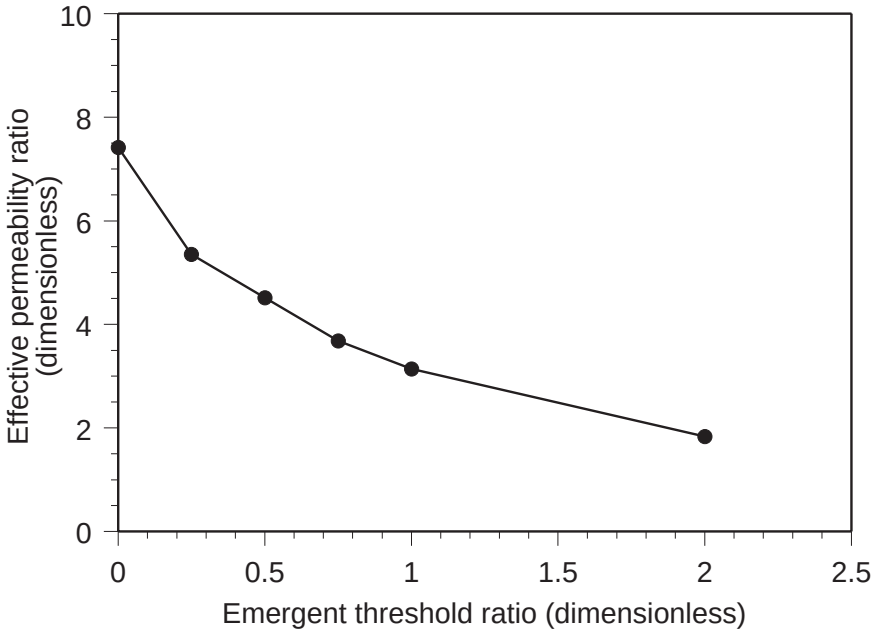

Figure 4.25. The effect of synkinematic cement on effective permeability for a SWCF simulated fracture pattern (realization 4) with a bed height of 10 m and SCC index of 40.

Fractures, or portions of them, that have apertures less than the emergent threshold are completely filled in. The effect of the emergent threshold was studied on a sample run (realization 4) with a bed height of 10 m and SCC index of 40. The emergent threshold ratio was varied from 0 (that is, no reduction in aperture) to 2. The effective k ratio, R_k, was computed for each of the cases studied. We see that as the emergent threshold increases, R_k decreases (Figure 4.25).

However, this decrease in R_k is not so much due to the decrease in the fracture apertures as to the change in the fracture pattern and interconnectivity. Fracture patterns for an emergent threshold ratio, e_r, of 0 and 2 are shown in Figure 4.26 and Figure 4.27. All the fractures in Figure 4.27 with an aperture less than the e_r of 2 are filled, causing a change in the fracture pattern.

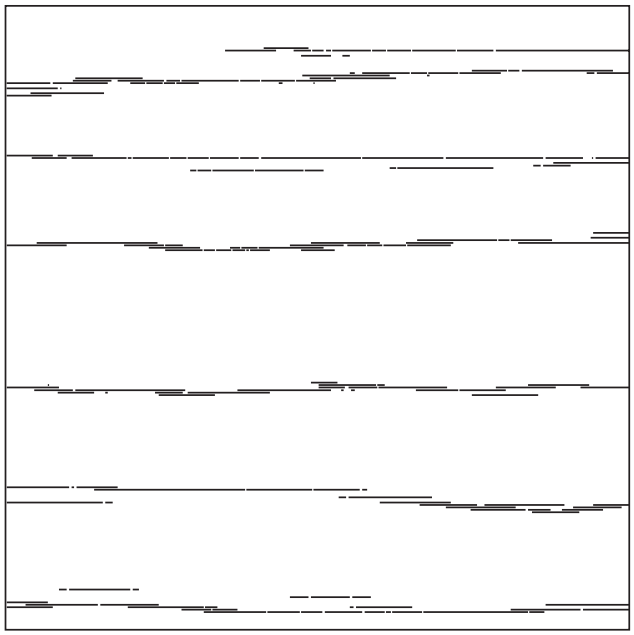

Figure 4.26. SWCF simulated fracture pattern (realization 4) with a bed height of 10 m and SCC index of 40 with an emergent threshold ratio of 0 and no degradation

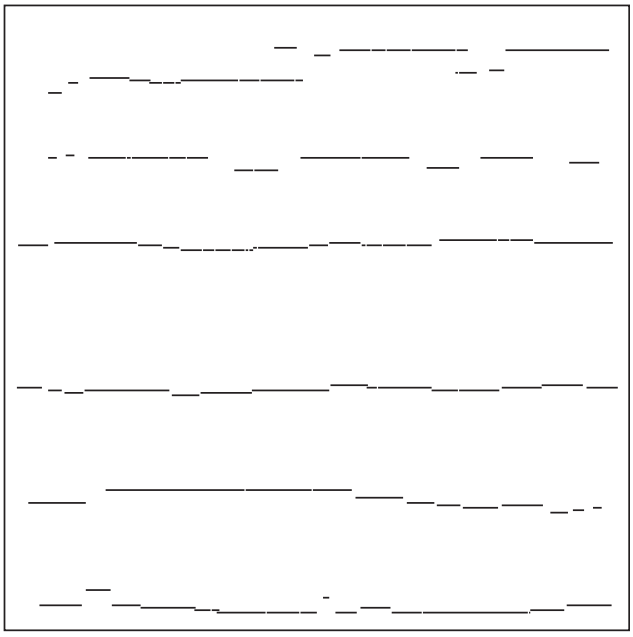

Figure 4.27. SWCF simulated fracture pattern (realization 4) with a bed height of 10 m and SCC index of 40 with an emergent threshold ratio of 2.

Further, because the permeability of the grid cells containing fractures is much higher (on the order of hundreds of Darcys) than the permeability of the matrix cells (1 md), a reduction of the aperture by even a fairly large amount would still result in fracture grid cells having a high permeability. Only if the fractures are completely filled in would the permeability of the fracture grid cells drop to the matrix permeability.

Postkinematic Cement

In some cases, cement is precipitated after fractures are formed. This cement randomly fills in all kinds of porosity including fracture porosity. Cement that is precipitated after fracture propagation is called postkinematic cement. Processes controlling these cements in fractures are discussed in section 2. Unlike synkinematic cement, where there is a constant reduction in fracture aperture (defining the emergent threshold, see Task 1), postkinematic cement causes some fractures to be completely filled, regardless of their aperture. The effect of varying values of postkinematic cement was also studied on a sample run (realization 4) with a bed height of 10 m and an SCC index of 40 by randomly eliminating some of the fractures independent of their length. Because petrographic data suggested that large fractures were filled heterogeneously at a range of scales, we represented this process as random fracture sealing. However, actual patterns in reservoirs may follow patterns that can be understood and predicted (see section 2) or mapped (Laubach, submitted).

It is possible from point-count data of thin sections to obtain the fraction of pore-space filled in with postkinematic cement, termed the degradation index. This often correlates well with the percentage of fractures filled in microfracture observations and hence is frequently used to predict the amount of filled macrofractures (Laubach and others,

2000). However, in the South Wasson Clear Fork reservoir, the percentage of microfractures filled and the distribution of postkinematic cement are variable on the scale of a thin section (centimeters). Therefore, instead of a degradation index we used the extent of microfracture filling obtained directly from thin-section. The partly filled fractures were treated as fully open in case 1 and as fully closed in case 2.

Table 4.5. Microcrack observations from South Wasson Clear Fork thin sections.

Open fractures	8
Partly filled fractures	12
Filled fractures	16
Total fracture observations	36

Case 1: Percent of fractures filled = 16/36 = 44%
Case 2: Percent of fractures filled = (16+12)/36 = 78%

The fracture pattern with no filled fractures is shown in Figure 4.26. The final fracture patterns obtained for both cases are shown in Figure 4.28 and Figure 4.29. It is evident that fracture filling also changes the fracture pattern. Higher filling reduces fracture total length and interconnectivity. The effective k ratio, R_k, was computed for each case. As expected the permeability decreases with increasing fracture filling (Figure 4.30).

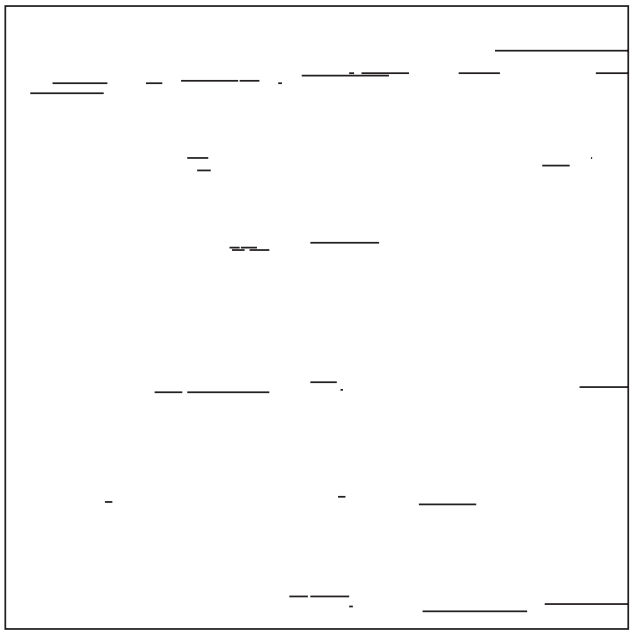

Figure 4.28. SWCF simulated fracture pattern (realization 4) with a bed height of 10 m and SCC index of 40 with a degradation index of 44 %.

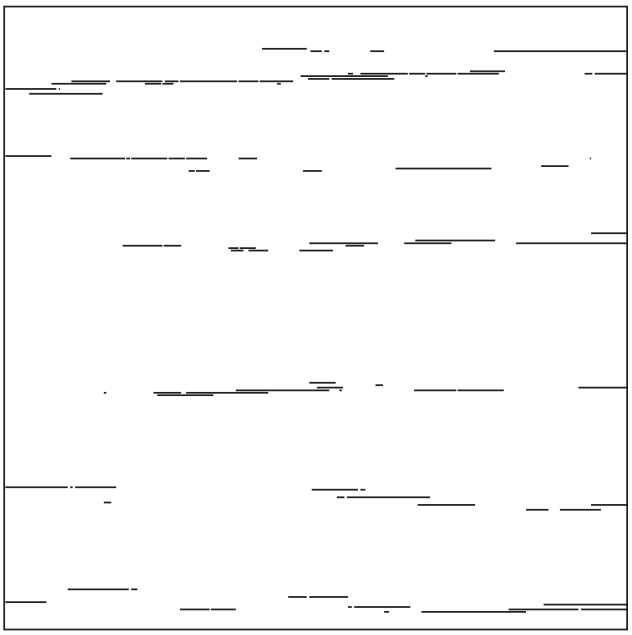

Figure 4.29. SWCF simulated fracture pattern (realization 4) with a bed height of 10 m and SCC index of 40 with a degradation index of 78 %.

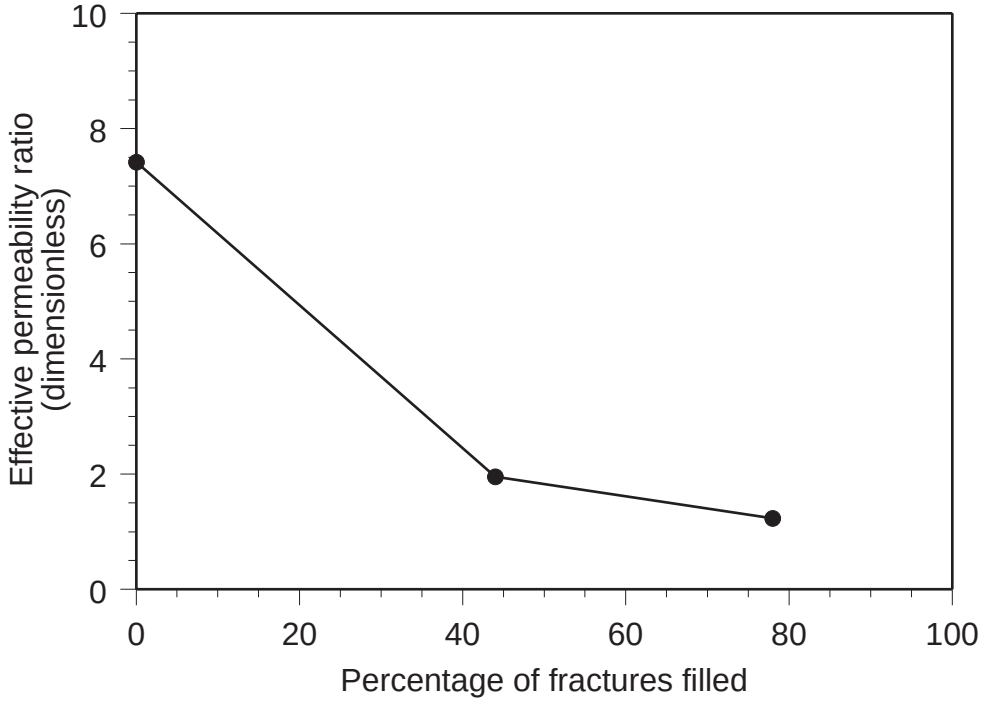

Figure 4.30. The effect of postkinematic cement on effective permeability for a SWCF simulated fracture pattern (realization 4) with a bed height of 10 m and SCC index of 40

4.8. Conclusions

Traditional models of the South Wasson Clear Fork reservoir underpredict injectivity. An improved model removes some of the discrepancy by using a carefully controlled power-averaging scale-up method, but there is still a shortfall in the observed permeability by a factor of 2. One reason for this could be the presence of fractures, which are known to exist in carbonate reservoirs and which are abundant in core from this reservoir. This study indicates that the effective grid permeability due to the presence of fractures is enhanced by a factor of between 2 and 10. This is substantially lower than the 1,000- or 10,000-fold increase that one would expect by simply computing the fracture permeability, but it is more than enough to explain the discrepancy between the observed and modeled injectivity. The small size and heterogeneous distribution of open fractures (owing to low emergent threshold and heterogeneous postkinematic cement on a centimeter scale) also indicates that measurements of porosity and permeability from laboratory core plugs are likely in part measuring the effects of fractures. This effect may be difficult to discern because on the core plug scale the open microfractures are poorly interconnected (in the same way that we modeled larger fractures) and thus the effect of fractures or laboratory measurements could go unrecognized.

In future studies, careful measurements that include detailed mapping of fractures with a particular emphasis on fracture connectivity are needed to meaningfully include the presence of fractures in reservoir modeling. Aperture information is not critical as critical as length information, except for modeling fracture filling by synkinematic cement. Further, for flooding operations, breakthrough times and sweep efficiencies could probably be better understood by the incorporation of fractures into the flow analysis.

The simulation studies done for this study have demonstrated improved fracture modeling methods and provided guidance for future research in fractured reservoir studies. It is possible to include fractures in reservoir simulation both explicitly and using NNC. Both methods give reasonable results with the accuracy of the solution improving with grid refinement. However, the NNC approach cannot be reliably used for fractures that extend across a simulation grid. Further, the NNC approach assumes that the fractures are infinitely conductive, whereas in explicit fracture representation, fracture width and hence fracture permeability information can be incorporated. The NNC approach also requires much higher CPU time and memory compared with the explicit fracture representation.

Although fracture permeability is highly sensitive to fracture aperture, the resultant effective permeability is not unless the fracture network is completely connected. It is more sensitive to fracture pattern and connectivity. The reason for this is that fracture permeability is usually so much larger (on the order of hundreds of Darcys) than the matrix permeability (on the order of millidarcys) that an increase in the fracture aperture does not produce an equivalent increase in the grid effective permeability. The matrix portions of the grid act as “bottlenecks,” reducing the flow. This observation is supported by the fact that the NNC approach yields effective permeability ratios that are only 30 percent higher than those obtained using the explicit-fracture representation.

The effective permeability ratio increases with total fracture length and mean fracture length. An increase in the fracture length decreases the matrix portion of the grid, thereby reducing the "bottlenecks". The rate of increase of the effective permeability ratio increases as the fracture length or mean length increased. This is because as the fracture length increases the probability that two fractures link up or become very close to one another increases.

Beds having a higher subcritical index tend to have a lower effective permeability than those having lower indices because they tend to have fractures with smaller mean lengths. This is because a higher index has a lower velocity of subcritical crack propagation. Therefore, visible crack growth is delayed, and the stresses are also released at a lower rate for the higher index. When cracks eventually do start to form, more cracks tend to grow at the same time, leading to a lower mean length.

Grid effective permeability is highly sensitive to fracture filling by synkinematic and postkinematic cements. Both types of cement close a portion of the fracture network and reduce the effective permeability. It is to be emphasized that both types of cement lower the effective permeability by changing the fracture pattern and reducing fracture interconnectivity.

4.9. References

Atkinson, Barry Kean "Subcritical Crack growth in Geological Materials," J. of Geophysical Research, Vol 89, No. B6, pp 4077-4114, June 10, 1984.

Atkinson, B.K., and Meredith, P.G., "The theory of subcritical crack growth with applications to minerals and rocks," in Fracture Mechanics of Rock, edited by B. K. Atkinson, pp. 111-166, Academic, San Diego, Calif., 1987.

Chirlin, G. R., "Flow Through a Porous Medium with Periodic Barriers or Fractures," SPEJ (June 1985), pp. 358-362.

Freund, L.B., Dynamic Fracture Mechanics, 563 pp., Cambridge University Press, Cambridge, 1990.

Halihan, Todd, John M. Sharp, Jr., and Robert E. Mace, "Interpreting flow using permeability at multiple scales", in Karst modeling edited by Palmer, A.R., Palmer, M.V., and Sasowsky, I.D., Karst Waters Institute Special Publication No. 5, Charlottesville, VA, p.82-96.

Hearn, Charles L., SPE, Occidental Petroleum of Qatar Ltd., Al-Emadi, Ismail A. Abdulla, SPE, Qatar General Petroleum Corp., Worley, Paul L.H. and Taylor, Robert D., SPE, Occidental Petroleum of Qatar, Ltd., SPE 38908 – "Improved Oil Recovery in a Tight Reservoir with Conductive Faults, ISND Shuiaba, Qatar," presented at the 1997 SPE Annual Technical Conference and Exhibition, San-Antonio, TX, USA, 5-8 Oct, 1997.

Holder, Jon, Jon E Olson and Zeno Philip, "Experimental determination of subcritical crack growth parameters in sedimentary rock," Geophysical Research letters, Vol 28, No 4, pp 599-602, Feb 15, 2001.

Ingraffea, A.R., "Theory of Crack initiation and propagation in rock, in Fracture Mechanics of Rock, edited by B. K. Atkinson, pp71-110, Academic, San Diego, Calif, 1987.

Laubach, Steve, Randy Marrett and Jon Olson, "New directions in fracture characterization", The Leading Edge, July 2000.
Nakashima, T., SPE, Waseda University, Sato, K., SPE, The University of Tokyo, Arihara, N., SPE, Waseda University, and Yazawa, N., SPE, JNOC, SPE 64286 – "Effective Permeability Estimation for Simulation of Naturally Fractured Reservoirs," presented at the SPE Asia Pacific Oil and Gas Conference and Exhibition held in Brisbane, Australia, 16-18 Oct, 2000.
Olson, J. E., "Fracture mechanics analysis of joints and veins," Ph.D. dissertation, 174 pp., Stanford Univ., Stanford, Calif., 1991.
Olson, Jon E., "Joint Pattern Development: Effects of Subcritical Crack Growth and Mechanical Crack Interaction," Journal of Geophysical Research, Vol. 98, No B7, pp 12,251-12,265, July 10, 1993.
Olson, Jon E., Yuan Qiu, Jon Holder and Peggy Rijken, " Constraining the Spatial Distribution of Fracture Networks in Naturally Fractured Reservoirs using Fracture Mechanics and Core Measurements", presented at the 2001 SPE Annual Technical Conference and Exhibition held in New Orleans, Louisiana, 30 Sept-3 Oct 2001.
Olsson W.A., and S.S. Peng, " Micro-crack nucleation in marble," Int. J. Rock Mech. Min. Sci., 13, 53-59,1976.
Pletka, B.J., Fuller, E.R., Jr., and Koepke, B.G., "An Evaluation of Double-Torsion Testing – Experimental," Fracture Mechanics Applied to Brittle Materials. ASTM STP 678, S. W. Freiman, Ed., American Society for Testing and Materials, 1979, pp. 19-37.
Renshaw, Carl E., "Influence of Subcritical fracture growth on the connectivity of fracture networks," Water Resources Research, Vol 32, no 6, pp 1519-1530, June 1996.
Schlumberger, "The Eclipse 100 Reference Manual, 96A", 1995.
Schlumberger, "The Eclipse 100 Technical Description, 97A", 1997.
Tapponier, P., and W. F Brace, "Development of Stress induced micro-cracks in Westerly granite," Int J Rock Meh Min Sc., 13,102-112,1976.
Williams, D. P. and Evans, A.G., "A Simple Method for Studying Slow Crack Growth," Journal of Testing and Evaluation, JTEVA, Vol. 1, No. 4, July 1973, pp. 264-270.
Wang H. F. and H.C. Heard, "Prediction of elastic moduli via crack density in pressurized and thermally stressed rock," J. Geophys. Res., 90, 10,342-10,350, 1985.
Wolfram, Stephen, "The Mathematica Book", fourth edition, 1999, Cambridge University Press.

5. Technology Transfer

Results of work to date have been transferred to the public via technical papers that have been published and or that are submitted and in review, and by technical presentations at professional meetings and specialized workshops we held. A listing of papers and key presentations is appended. We held a major review of progress on the project in June, 2002, which was attended by representatives of more than a dozen companies.

6. Plans for Next Research Steps

In the context of the timetable described in our research plan (Table 7-1), we are making good research progress. We have completed the observation verification of the emergent threshold (Task 1). We have delineated two processes for fracture mineralization, identified the process that has the greatest impact on the large fractures that affect flow in petroleum reservoirs. The geochemical modeling of these processes is essentially finished, as described in previous sections of this report (Task 2). We have made considerable progress in testing rock for the subcritical index, and continue to add to our database of results (Task 3). Finally, we have established a procedure for estimating permeability based on geomechanically generated fracture patterns (Task 4).

Table 7-1. List of Tasks and Timeline.

	Year 1	Year 2	Year 3
Task 1 - Observational verification of emergent threshold			
Task 2 - Geochemical investigation of fracture mineralization			
Task 3 - Fracture mechanics testing and modeling			
Task 4 - Fluid flow analysis of fracture networks			

7. Appendix 1: Publications and Presentations

The following are papers and presentations from the second year of the project.

Technical meeting papers and presentations:

Albertoni, Alejandro, and Lake, Larry W., 2002, "Inferring Interwell Connectivity from Well-rate Fluctuations in Waterfloods," 2002 SPE/DOE Thirteenth Symposium on Improved Oil Recovery, Tulsa, Oklahoma, April 13-17.

Laubach, S. E., Reed, R. M., Olson, J., Ortega, Orlando, and Stowell, J. F. W., 2001, "Fracture-surrogate analysis methods applied to Spraberry, Bone Spring, and Canyon cores: preliminary results, in The Permian Basin: microns to satellites, looking for oil and gas at all scales": West Texas Geological Society Fall Symposium, West Texas Geological Society Publication 01-110, p. 75–79.

Noh, Myeong, and Lake, Larry W., 2002, "Geochemical Modeling of Fracture Filling," 2002 SPE/DOE Thirteenth Symposium on Improved Oil Recovery, Tulsa, Oklahoma, April 13-17.

Philip, Z., J. W. Jennings, Jr., J. E. Olson, and J. Holder, 2002, "Modeling coupled fracture-matrix fluid flow in fracture patterns generated using a geo-mechanical crack growth simulator": Naturally Fractured Reservoir Conference, University of Oklahoma and Oklahoma Geological Survey, Norman, OK, June 3-4.

Philip, Zeno, Jennings, James, Olson, Jon and Holder, Jon, 2002, "Modeling Coupled Fracture-Matrix Fluid Flow in Fracture Patterns Generated using a Geo-Mechanical Crack Growth Simulator," 2002 SPE Annual Technical Conference and Exhibition, San Antonio, TX, September 29 – October 2.

Archival Publications:

Laubach, S. E., (in press), "Practical approaches to identifying sealed and open fractures," American Association of Petroleum Geologists Bulletin (Accepted September 2002).

Olson, J.E., (invited, in review), "Fracture swarms: A mechanical paradox?," in Mechanisms of Jointing in the Crust, edited by J. W. Cosgrove and T. Engelder, Geological Society of London Special Publication.

Theses and Dissertations

Albertoni, Alejandro, 2002, "Inferring Interwell Connectivity from Well-rate Fluctuations in Waterfloods," The University of Texas at Austin, M.S. Thesis, 187 pages.

Qiu, Yuan, 2002, “Natural Fracture Modeling and Characterization,” The University of Texas at Austin, Ph.D. dissertation, 169 pages.

SPE 75225

Inferring Interwell Connectivity From Well-Rate Fluctuations in Waterfloods

Alejandro Albertoni and Larry W. Lake, The University of Texas at Austin

This paper was prepared for presentation at the SPE/DOE Thirteenth Symposium on Improved Oil Recovery held in Tulsa, Oklahoma, 13–17 April 2002.

Abstract

This paper presents a practical technique to quantify communication between wells in a reservoir using only production and injection rate data. The technique combines a constrained multivariate linear regression analysis with diffusivity filters to provide information about permeability trends and the presence of transmissibility barriers. The method was developed and tested using a numerical simulator and then applied to a waterflooded field in Argentina. The simulation results indicate that the connectivity between wells is described by coefficients that only depend on geology and relative position between wells; they are independent of injection/production rates. The results of this work can be used to improve the performance of an existing waterflood by suggesting how well patterns might be changed or managed. They could also be used to model flow in the reservoir.

Introduction

Production and injection rates usually based on monthly well tests are the most abundant data available in any waterflooding project. Valuable and useful information can be obtained from the analysis of these data. Typically, reservoir description and characterization together with observation of injection and production rates is used to determine the influence of each injector on producers. Ultimately, the final objective is the optimization of operations and economics and the maximization of oil recovery of existing waterfloods. This may include changes in injection patterns, assignment of priorities in operations, recompletion of wells, and in-fill drilling.

There have been previous statistical approaches that compared the rate performance of a production well with that of the surrounding injectors. Heffer *et al.*[1] used Spearman rank correlations to relate injector/producer pairs and associated these relations with geomechanics. Refunjol[2] also used Spearman analysis to determine preferential flow trends in a reservoir. She related injection wells with their adjacent producers and used time lags to find an extreme coefficient value. Sant'Anna Pizarro[3] validated the Spearman rank technique with numerical simulation and pointed out its advantages and limitations. Panda and Chopra[4] used artificial neural networks to determine the interaction between injector/producer pairs within a pattern. Soeriawinata and Kelkar[5], who also used Spearman rank analysis, suggested a statistical approach to relate injection wells and their adjacent producing wells. They applied the superposition principle to introduce concepts of constructive and destructive interference. Additional reference can be found in Araque-Martinez's work[6].

The main objectives of this work are to quantitatively determine the communication between wells in a waterflood and to perform the analysis field-wide, analyzing multiple well influences in a single step. This work shows that distant injectors (from different patterns) can significantly affect production.

We view the reservoir as a system that processes a stimulus (injection) and returns a response (production). In a waterflood, there are typically several injectors and producers acting at the same time; moreover, the effect of the reservoir on the input signal (injection) will depend on the location and the orientation of each stimulus-response pair. Taking this into account, the technique presented here uses different statistical approaches based on constrained multiple linear regression to infer connectivity. In addition, we use diffusivity filters to account for the time lag and attenuation that occurs between stimulus and response.

The technique is first applied to two synthetic fields of different sizes and then to a real field in Argentina.

Procedure

The technique uses the liquid (oil and water) production rates and the injection rates of every well in a waterflood as input data. Both rates are in reservoir volumes. The gas rate is not included in the analysis; periods with no significant free gas production must be selected for the analysis. The reason for this will be discussed later. The location of the wells must also be provided. The simplicity of the method and the

always-available production and injection data makes this technique a very practical tool.

Two different approaches aimed at solving this problem are presented in this paper: multivariate linear regression (MLR) and balanced multivariate linear regression (BMLR). The use of one or other approach will depend on the type of waterflood and the data that is being analyzed. First, both MLR and BMLR approaches are explained without the use of diffusivity filters; then, later in this section, the concept of diffusivity filters is presented.

Multivariate linear regression (MLR). We say that a waterflood is unbalanced when the field-wide injection rate is significantly different from field-wide liquid production rate. If this is the case, the MLR approach must be used.

In this model, the estimated production rate of a producer j is given by:

$$\hat{q}_j(t) = \beta_{0j} + \sum_{i=1}^{I} \beta_{ij} i_i(t) \qquad (j = 1, 2, \ldots N)$$

where N is the total number of producers and I is the number of injectors. This equation states that at any time the total production rate at well j is a linear combination of the rates of every injector plus a constant term, β_{0j}. The factors β_{ij} are the weighting factors and the constant term β_{0j} accounts for the unbalance. If the injection rates are known, the coefficients β_{ij} and the term β_{0j} need to be determined.

Jensen *et al.* (Ref.7, p.255) present the solution of a multivariate linear regression problem. To solve this overdetermined system the variance

$$Var\left(\hat{q}_j - q_j\right)$$

is minimized. This minimization leads to the following set of I linear equations:

$$\begin{pmatrix} \sigma_{11}^2 & \sigma_{12}^2 & \cdots & \sigma_{1I}^2 \\ \sigma_{21}^2 & \sigma_{22}^2 & \cdots & \sigma_{2I}^2 \\ \vdots & \vdots & \ddots & \vdots \\ \sigma_{I,1}^2 & \sigma_{I2}^2 & \cdots & \sigma_{II}^2 \end{pmatrix} \times \begin{pmatrix} \beta_{1j} \\ \beta_{2j} \\ \vdots \\ \beta_{Ij} \end{pmatrix} = \begin{pmatrix} \sigma_{1j}^2 \\ \sigma_{2j}^2 \\ \vdots \\ \sigma_{Ij}^2 \end{pmatrix} \quad \ldots\ldots\ldots\ldots\ldots\ldots\ldots\ldots\ldots\ldots (1)$$

which can be solved by standard means. The constant term β_{0j} is given by:

$$\beta_{0j} = \bar{q}_j - \sum_{i=1}^{I} \beta_{ij} \bar{i}_i \quad \ldots\ldots\ldots\ldots\ldots\ldots\ldots\ldots\ldots\ldots\ldots\ldots\ldots\ldots\ldots\ldots (2)$$

where the symbol $\bar{}$ indicates an average.

In the case of MLR, a set of I+1 equations and I+1 unknowns must be solved for each producer (Equations 1 and 2). The weighting coefficients β_{ij} obtained from the solution of the N systems of equations provide a quantitative expression of the influence of each injector i on each producer j; the larger the β_{ij}, the greater the influence

As stated before, the MLR approach is to be used when the field is unbalanced. However, this is not the only case when it should be applied. If only a portion of the waterflooding project is being analyzed, there will be flow across the open boundaries of the selected area. In this case, MLR must be again used without any modification in the injection rates of the wells close to the boundaries. There will be boundary effects, though.

Balanced multivariate linear regression (BMLR). If the waterflood is balanced (the field injection rate is approximately equal to the total production rate) the BMLR approach must be used.

In this model, the production rate of a certain well j is given by:

$$\hat{q}_j(t) = \sum_{i=1}^{I} \lambda_{ij} i_i(t) \qquad (j = 1, 2, \ldots N)$$

Again, this equation states that at any time, the total production rate at well j is a linear combination of the injection rates of every injector, where λ_{ij} are the weighting factors. In the BMLR approach, there is no constant additive term.

The average balance condition is given by:

$$\bar{q}_j = \sum_{i=1}^{I} \lambda_{ij} \bar{i}_i \qquad (j = 1, 2, \ldots N)$$

To include the balance condition constraint we make use of Lagrange multipliers (μ_j) as is done in Kriging. Then, we minimize the term

$$Var\left(\hat{q}_j - q_j\right) - 2\mu_j \left[\bar{q}_j - \sum_{i=1}^{I} \lambda_{ij} \bar{i}_i \right]$$

After deriving this expression with respect to each of the unknowns and setting these derivations equal to zero, the final set of equations is given by:

$$\begin{pmatrix} \sigma_{11}^2 & \sigma_{12}^2 & \cdots & \sigma_{1I}^2 & \bar{i}_1 \\ \sigma_{21}^2 & \sigma_{22}^2 & \cdots & \sigma_{2I}^2 & \bar{i}_1 \\ \vdots & \vdots & \ddots & \vdots & \vdots \\ \sigma_{I1}^2 & \sigma_{I2}^2 & \cdots & \sigma_{II}^2 & \bar{i}_1 \\ \bar{i}_1 & \bar{i}_2 & \cdots & \bar{i}_I & 0 \end{pmatrix} \times \begin{pmatrix} \lambda_{1j} \\ \lambda_{2j} \\ \vdots \\ \lambda_{Ij} \\ \mu_j \end{pmatrix} = \begin{pmatrix} \sigma_{1j}^2 \\ \sigma_{2j}^2 \\ \vdots \\ \sigma_{Ij}^2 \\ \bar{q}_j \end{pmatrix} \quad \ldots\ldots\ldots\ldots\ldots (3)$$

which can be solved for the λ_{ij} by standard means. Again, a set of I+1 equations and I+1 unknowns must be solved for each producer.

Diffusivity filters. We define dissipation as the inverse of diffusivity. In other words, a small permeability, a large porosity, a large viscosity and a large total compressibility contribute to a large dissipation. If there were no dissipation in the reservoir, a change in the injection rate would cause an equivalent and instantaneous change in the production rate, regardless of the distance between injector and producer. The use of diffusivity filters accounts for the time lag and attenuation of the changes that occur between the stimulus

(injection) and the response (production). Filters become more important for large distances between injectors and producers and for large dissipation of the medium.

We applied diffusivity filters to injection rates. Their shapes are defined by two factors: the diffusivity constant (which depends on the medium) and the distance between the injector and the producer. The basic shape of the filter is obtained from the impulse propagation equation[8] (transient solution to the diffusivity equation superimposed in time). There is one diffusivity constant η_{ij}, for each pair of injector/producer wells in the medium. In the procedure, the values of η_{ij} are obtained after an iterative process that minimizes the error between the modeled and the observed production rates.

The filters basically transform the injection rates affecting a certain producer so that they take the form of the response in an incompressible medium. This results in a convoluted or effective injection rate at a certain time. For example, for the BMLR model, the modeled production rate in well *j* would be given by:

$$\hat{q}_j(t) = \sum_{i=1}^{I} \lambda_{ij} i_{ij}^e(t)$$

where

$$i_{ij}^e(t) = \sum_{n=0}^{11} \alpha_{ij}^{(n)} i_i(t-n)$$

is the effective injection rate of injector *i* affecting producer *j* at time *t*. The filters are discretized by sweeping the effects of the most recent 12 months of injection. The $\alpha_{ij}^{(n)}$ are the twelve filter coefficients obtained from the discretization of the filter function. More than 12 filter coefficients may be needed if the dissipation is large. See the Appendix.

However, the diffusivity filters only solve the transient problem partially, because the superposition effect is only addressed from the injector and not from the producer standpoint. Periods that are highly dominated by transient flow must be avoided simply by omitting those points from the analysis. These periods will be characterized by sharp peaks in injection that become more relevant in reservoirs with large dissipation. Often, all the data points can be used, but care should be taken when selecting periods with severe transients for the analysis.

Results

The method was developed and tested through its application to two synthetic fields and then to a field in Argentina. The results of these applications are presented and discussed in this section.

Application to synthetic fields. BMLR and MLR approaches, with and without diffusivity filters, were applied to two numerically simulated fields (Synfields) with a five-spot injection pattern: one of 5 injectors and 4 producers (the 5x4 Synfield) and one of 25 injectors and 16 producers (the 25x16 Synfield). They both are flowing undersaturated oil. The injector-producer distance is 800 ft for the 5x4 Synfield and 890 ft for the 25x16 Synfield. The oil-water mobility ratio is equal to one, and the oil, water, and rock compressibility are $5x10^{-6}$, $1x10^{-6}$ and $1x10^{-6}$ psi^{-1} respectively. Both synfields have vertical wells. The characteristics of the synthetic fields are similar to those of the real case to which the technique was applied later.

5x4 Synfield. Several cases were analyzed for this field. Actual injection data was used as input in the numerical simulation to provide temporally uncorrelated and realistic injection rates. This injection data was randomly selected from different wells in a real field and proportionally modified to be in agreement with the Synfield injectivity. The simulation extends for 100 months (3000 days approximately), which represent a history of 100 data points of rate. **Figure 1** and **Figure 2** show the injection rates of the five injectors and the total injection rate, respectively.

Homogeneous reservoir. The first and simplest case is of a single-layered homogeneous reservoir with an isotropic permeability of 40md. **Table 1** shows the numerical values of the weighting coefficients obtained from BMLR. In **Figure 3** the weighting coefficients (λ_{ij}) are represented by inverted arrows that start from the i^{th} injector and point to the j^{th} producer. The larger the arrow, the larger the value of the coefficient and the connectivity between the two wells.

Several things can be noted in **Figure 3**. As expected, the λs are larger for near well pairs (e.g. λ_{11}, λ_{12}) than for more separated well pairs (e.g. λ_{13}, λ_{14}). Another important characteristic is the symmetry. Since the reservoir is homogeneous and the wells are symmetrically located, the field has several planes of symmetry. The fact that the injection rates are uncorrelated together with the excellent symmetry shown by the calculated λs, suggests that λs do not depend on injection rates. Indeed, further tests performed in this and in other synthetic fields verified that the weighting coefficients, λ, only depend on the reservoir properties and the relative location of the wells[9]. They are independent of injection rates.

Figure 4 shows a comparison between the modeled total production rate using the BMLR approach and the total production rate observed in the numerical simulation. Without diffusivity filters, the coefficient of determination (Ref.7, p.226) R^2 = 0.969; the use of diffusivity filters improved the correlation to R^2 = 0.993 as shown in the figure.

With the sole purpose of comparison, the injection of non-reactive tracers was also simulated in the synthetic field. **Figure 5** shows a representation of the tracer results. The length of the arrows in the figure is proportional to the fraction of tracer injected in the i^{th} injector that was produced in the j^{th} producer. Unlike the λs, the tracer response is not symmetric. In other words, tracer response does depend on injection rate. While the λ estimation is determined from the analysis of the fluctuation of injection and production rates, the tracer response is determined by rate averages. For example, the average rates of injectors I01 and I02 are approximately 60%

larger than those ones of injectors I04 and I05. Thus, the tracer injected in I03 is more likely to be produced in P04 than in P01 (see **Figure 5**). On the one hand, tracers tell us where each barrel of injected water is being produced; on the other hand, the weighting coefficients obtained from BMLR tell us what is the connectivity between each injector-producer pair. The following example illustrates this fact: none of the water injected in I04 reaches P01, but, from the λ results, we know that 17 percent of its injection is influencing P01 (see **Table 1**).

Anisotropic reservoir. In this case, the permeability in the *y* direction was set to be 1/40th of the permeability in the *x* direction. The MBLR approach was applied. **Figure 6** shows that, as expected, the larger weighting coefficients occur in the *x* direction, clearly showing the preferential permeability orientation. In this case, the use of diffusivity filters is more important than for the isotropic case. The lower transmissibility makes the changes in injection rate be much more diffused in the *y* direction before they reach the producers. Without the diffusivity filters the modeled total production rate yields $R^2 = 0.670$; while using the filters, gives $R^2 = 0.996$. **Figure 7** shows these results.

Presence of a sealing fault. When a sealing fault is introduced into the simulated reservoir and the BMLR model is applied, results are just as expected. The presence of transmissibility barrier can also be easily inferred from the weighting coefficients in **Figure 8**. The technique estimates the values of λ corresponding to pairs of wells located on each side of the fault (e.g. λ_{11}, λ_{13}, λ_{22}, λ_{24}) to be either zero or very close to zero. This shows no communication between these wells based only on the analysis of the field injection and production rates.

Other cases. We furthered studied the application of the BMLR to the 5x4 Synfield introducing more complications to the reservoir properties[9]. We analyzed multi-layered reservoirs, with Dykstra-Parsons coefficients of 0.8 and 0.9 and different average permeabilities with satisfactory results. The cases of a large permeability channel (areal heterogeneity) and partially sealing fault also yielded excellent results. On the other hand, when the dissipation of the reservoir was increased 30 times in the homogeneous-isotropic synfield, the technique yielded poorer symmetry, or poorer coefficients. Diffusivity filters that sweep more than 12 months may be needed.

25x16 Synfield. The sensitivity of the technique to a larger number of wells in the field was analyzed using a homogeneous reservoir. Like in the 5x4 Synfield, the injection rates here are temporally uncorrelated and were modified from actual data; but in this case, a history of 65 data points was initially used. This synthetic field is also used for comparison with the application of the technique to a real case.

Homogeneous reservoir. **Figure 9** and **Figure 10** show the results for the BMLR approach to the 25x16 Synfield. For comparison, only the total production of the four producers at the center of the field is plotted. Since, the reservoir is homogeneous and the field has several planes of symmetry, one would expect the weighting coefficients to be symmetric across these planes. Even though the $R^2 = 0.999$, the symmetry is poorer than that obtained in the 5x4 Synfield. **Figure 11** also shows that the λs, as expected, are smaller for more distant well pairs, but some of the weighting coefficients are negative, which has no physical meaning. Using 65 data points in 25x16 Synfield, results are not as good as using 100 points in the 5x4 Synfield. The use of fewer data points and more injectors are the cause for the unsatisfactory results. These reasons are discussed in the following paragraphs.

Overdetermination. In a bivariate linear regression model of the type $\hat{q}_j = \beta_{0j} + \beta_{1j} i_1$, the variability of the slope is determined by

$$s^2_{\beta_{1j}} = \frac{1}{(M-2)} \times \frac{\sum_{m=0}^{M} \left(q_j^{(m)} - \hat{q}_j^{(m)}\right)^2}{\sum_{m=0}^{M} \left(i_1^{(m)} - \bar{i}_1\right)^2} \quad \text{.....(4)}$$

where *M* is the total number of data points (Ref.7, p.213). The ratio of the two summations does not strongly depend on *M*, thus the variability of β_{1j} is approximately inversely proportional to (*M*-2). Extending this analysis to the multivariate linear regression (either balanced or unbalanced), the variability of the weighting coefficients will be inversely proportional to (*M*-*I*-1). In other words, the more data points, the more precise the determination of the weighting coefficients. Furthermore, the results will be more precise with fewer injectors.

Let's apply this concept to the 25x16 Synfield. In the MLR and the BMLR models (Equations 1, 2, and 3), the number of unknowns per producer (β_{ij} or λ_{ij}) is given by the number of injector-producer pairs plus one independent term (β_{0j} in MLR or μ_j in BMLR). There are (*I*+1) unknowns per producer. In the 25x16 Synfield, the first 25 data points were not used for the analysis because of the highly transient-dominated nature of that portion of the data. So, the effective number of data points is 41. Then, since we have 25 injectors, we have 26 (25 + 1) unknowns and 41 data points to solve the problem. The system is overdetermined.

We define an overdetermination coefficient (O_d) of a system as the number data points divided by the number of unknowns, or

$$O_d = \frac{M}{(I+1)}$$

For a homogeneous reservoir with several planes of symmetry, the λs should be symmetric across these planes. For the 5x4 Synfield, taking symmetry into account, we can find three groups of λ_{ij} coefficients: corner injectors and adjacent producers (8 pairs, $\lambda = 0.33$, group a), corner injectors with non-adjacent producers (8 pairs, $\lambda = 0.17$, group b), and center injector and adjacent producers (4 pairs, $\lambda = 0.25$, group c). Similarly, in the 25x16 Synfield, taking symmetry into

account, 55 groups of λ_{ij} coefficients (out of a total number of 400 λs) can be found. To quantify the goodness (or badness) of the coefficients we define a term that describes the variability of the weighting coefficients, λ. The asymmetry coefficient (A) is the square root of the sum of the variances of λ of the group, weighted by the number of well pairs in each group. In the case of the 5x4 Synfield, that has 3 groups (a, b and c) and a total of 20 λ coefficients, the asymmetry coefficient would be

$$A = \sqrt{\frac{8\,\mathrm{var}_a(\lambda) + 8\,\mathrm{var}_b(\lambda) + 4\,\mathrm{var}_c(\lambda)}{20}}$$

A is similarly defined for the 25x16 Synfield. To put it simply, A is an inverse measure of the goodness of the results for a homogeneous reservoir. The more symmetric λs, the smaller A, and the better the results.

For the 25x16 Synfield, with 41 effective data points, we calculate O_d = 1.58 and the application of the BMLR model yields A = 0.05. According to Equation 4 and its extension to multivariate linear regression, an increase in the number of data points or, equivalently, an increase in O_d, should give better symmetry. **Figure 12** and **Figure 13** show the results obtained when using 390 effective data points (O_d = 15). The symmetry observed in the figure is excellent and the asymmetry coefficient has been lowered to A = 0.004. The weighting coefficients are smaller for more distant pairs of wells and there are no negative λs. The coefficient of determination for this case is R^2 = 0.995.

Following this analysis, the effect of having different levels of overdetermination was studied for both the 5x4 and 25x16 Synfields. The different values of O_d were obtained by changing the number of data points. **Figure 14** clearly shows that results improve for larger overdetermination. For O_d > 6, the asymmetry significantly levels-off, yielding very good results. Both the 5x4 and 25x16 Synfield plots lie practically on the same curve. Thus, given a five-spot waterflood, this plot can be used to quantitatively estimate the confidence one can have in the results of the application of the BMLR technique. Furthermore, the log-log plot of A vs. O_d gives an approximate straight line of slope -1, showing that A is inversely proportional to O_d, which is in agreement with the application of Equation 4 to multivariate linear regression.

Application to real field data. The technique was applied to the Chihuido de la Sierra Negra (ChSN) Field in Argentina. The field is undergoing a waterflood on a five-spot pattern. We analyzed only a portion of the field, with 25 injectors and 16 producers. The reservoir conditions are similar to those of the synthetic fields. Since only a portion of the field was analyzed and the boundaries are open, the MLR approach is applied. For simplicity, from this point on, we will refer to this portion of the field as ChSN field.

Figure 15 shows the production rate, injection rate and gas oil ratio of the ChSN field. Injection started on month 50, causing the GOR to sharply decrease. By month 75, the GOR was at its lowest level and only dissolved gas was being produced. Injection and production rates are in acceptable balance. Thus, the analysis is performed using the data starting in month 75 using 51 effective data points. With 51 effective points and 25 injectors, we get O_d = 1.96. From **Figure 14**, with O_d = 1.96 we know in advance that we will obtain less than optimal results and the estimated weighting coefficients will be imprecise. However, some general features can be inferred.

Figure 16 shows a map of ChSN field and the representation of the positive estimated weighting coefficients. A structural map obtained from the operator is overlain in **Figure 17**. Injectors in the north present smaller weighting coefficients than those in the south. Four injectors (F14, F18, E14 and E18), particularly, seem to have little influence on inner producers. The orientation of the coefficients in wells C14 and C15 (and even in C16 and C17) seem to be in good agreement with the presence of a fault slightly south of C14 and C15. However, some coefficients relate the southern-most injectors to inner producers, which is in disagreement with the presence of this fault. This error could be attributed to a boundary effect, together with the small O_d (which causes errors in the estimation of the weights). Another explanation is that the fault may not be completely sealing.

Since we have a relatively small overdetermination, we expect the occurrence of some negative weighting coefficients. **Figure 18** shows the values of β versus distance. Reasonable values of β are obtained for the closest well pairs, but very large and even negative coefficients are obtained for more distant pairs. **Figure 19** shows a comparison of the liquid production rate observed in the field and the modeled liquid production rate for the four center wells. The four center wells were chosen for this comparison to minimize the effects of the boundaries. The model has R^2 = 0.971.

Discussion. This section discusses the assumptions, the possible sources of errors, the properties of the weighting coefficients, the proper selection of data points and the use of the technique presented as a predictive tool.

Assumptions. There are several assumptions for the application of this technique. The general assumption is that within the period of time selected for the analysis, all the parameters in the field must be constant, with the obvious exception of the injection and production rates. From a more detailed perspective, the assumptions can be enumerated as the following:

No new wells: The number and location of wells must remain constant within the analyzed period. The drilling of new injection or producing wells implies a complete new set of weighting coefficients.

Constant producing bottom-hole pressure: Changes in injection rate will cause changes in pressure in the surrounding of a producer. The technique assumes that every change in the production rate is exclusively caused by changes in injection rates. Bottom-hole production pressure and operation conditions are assumed to be constant[9].

Constant well productivity: This assumption is related to the previous one. No major changes in skin or in other well properties should occur in the producers within the analyzed period of time.

Constant gas-oil ratio (GOR): Changes in the reservoir gas saturation will cause changes in GOR. A change in gas saturation represents a change in the reservoir total compressibility, and consequently in the reservoir diffusivity. So, for best results, the GOR should be constant and equal to the dissolved gas-oil ratio in the analyzed period. Normally, changes in water and oil saturations will not significantly affect the reservoir properties unless the compressibility difference is extremely large.

No new completions: No new layers should be completed during the analyzed period.

Constant non-waterflooding production: In the MLR approach, the production accounted for by non-waterflooding reasons (mainly primary production) is assumed to be constant.

Sources of error. The possible sources of error in the estimation of the weighting coefficients are the following:

Deviation from assumptions: Deviations from the stated assumptions will introduce errors.

Small overdetermination: As discussed before, the overdetermination coefficient O_d must be greater than 6 to obtain best results. The use of distance cut-off to include fewer injection wells in each calculation will tend to improve (increase) the O_d. But the error introduced by ommitting distant injection wells is significant[9]. Distance cut-offs are not a solution for small O_d.

Data quality: The technique is relatively sensitive to the quality of the injection and production rate measurements. An error sensitivity analysis was performed introducing a relative error (uncorrelated, zero mean and normally distributed) to the observed injection and production data before using the BMLR. For each level of error introduced, we ran 100 cases. **Figure 20** shows a plot of R^2 from BMLR vs. the error in measurement. For example, if a normally distributed error of standard deviation of 10% is observed in the measurements, the R^2 is expected to drop from 0.993 (no error) to 0.795 in average (+/- 0.04).

Open boundaries: Boundary effects will be large in the estimation of weighting coefficients for wells close to open boundaries.

Injection losses: Water injected in non-productive layers will introduce an error in the estimations.

Properties of the weighting coefficients. As discussed before, the weighting coefficients only depend on the relative location of the wells and the reservoir properties. From the results in the 5x4 and 25x16 Synfield cases, the coefficients for each injector approximately add up to one in a balanced waterflood. We also studied a third type of approach where the balance condition is given by

$$\sum_{j=1}^{N} \lambda_{ij} = 1 \qquad (i = 1, 2, \ldots I)$$

and where the weighting coefficients are determined by solving an Nx(I+1) by Nx(I+1) system of linear equations in one single step[9]. This third type of approach was applied to the 5x4 Synfield with similar results to those obtained with MLR and BMLR.

Figure 21 shows a cross plot between the rates of injector I02 and producer P03 in the 5x4 Synfield with homogeneous reservoir. The correlation between this two rates is very poor (R^2 = 0.063) and negative. However, the BMLR yielded λ_{23} = 0.33. Here, the concepts of constructive and destructive interference must be considered. The rates between an injector-producer pair may be uncorrelated (or even negatively correlated) just because of the effect of other injectors; but it is important to remark that the correlation alone between rates of well pairs is not an indicator of the connectivity (weights) between wells.

Selection of data points: The selection of the appropriate period of time to apply the technique is very important. Special attention must be paid to minimize the deviation from the assumptions when selecting the data. As commented before, periods that are highly dominated by transient flow must be avoided.

Use as a predictive tool. This technique can be used to predict the total production rate in each producer using the injection rates as input. **Figure 22** shows the comparison between the BMLR model and the production observed in the 5x4 Synfield homogeneous reservoir using the first 45 data points to estimate the λs and the last 45 data points to test the prediction. Using 45 training data-points yields O_d = 7.5, which is greater than 6, so the excellent results (R^2 = 0.991) obtained in the prediction were expected. Testing the predictive capability of this technique in the other cases also yielded very good results[9].

R^2 measures the quality of the correlation between observed and modeled production, but it provides only a weak description of the goodness of the results. As Jensen *et al.* (Ref.7, p.226) state, the coefficient of determination does not measure the appropriateness of the model. In the case of the synthetic homogeneous reservoirs, the asymmetry coefficient is a much better indicator. For example, in some of the cases studied when testing predictions, λs that yielded higher R^2 when applied to the training period, resulted in poorer predictions than cases that had yielded smaller R^2 in the respective training period. This doesn't occur with the asymmetry coefficient in homogeneous Synfields. A small asymmetry coefficient in the training period always results in good predictions.

Conclusions

We developed a practical technique to quantify communication between wells in a reservoir using only production and injection rate data. The connectivity between wells is described by coefficients that only depend on geology and relative position between wells; they are independent of injection/production rates. The technique is useful for determining permeability trends and the presence of

permeability barriers. In addition, it can be used to predict total production from given injection rate.

The technique works in anisotropic media and media with vertical and spatial heterogeneity. The use of diffusivity filters improves the results and extends its range of application. Besides, the quality of the expected results can be determined before the application of this method to a five-spot waterflooding, by a simple calculation based on the number of available data points and the number of injectors. The use of a small number of data points and a large number of injectors lead to poor results.

The weighting coefficients obtained from this technique were compared with the response of the injection of non-reactive tracers in a synthetic field. On the one hand, tracers tell where each barrel of injected water is being produced, but they depend on injection rates. On the other hand, the weighting coefficients describe the connectivity between injector-producer pairs and the effective influence of each barrel of injected water on each producer.

The technique was applied to a waterflood in Argentina, and even when the overdetermination of the problem is smaller than that recommended, some features could be inferred. The validation of these results is very difficult; however, our results do seem to agree with the presence of known geological features.

Acknowledgements

The authors of this paper would like to thank Repsol-YPF for providing the data and their permission to publish this paper. We would also like to thank Dr. Carlos Torres-Verdin for his valuable contribution to the diffusivity filter work.

Nomenclature

A = asymmetry coefficient
C_1 = proportionality constant
C_2 = proportionality constant
d = dissipation constant
GOR = gas oil ratio
I = total number of injection wells
i_i = observed injection rate (rb/d)
$\bar{i}_j$ = average injection rate (rb/d)
i^c_{ij} = convoluted injection rate (rb/d)
k = permeability
M = total number of data points
N = total number of production wells
O_d = overdetermination coefficient
$\overline{P}$ = average pressure
P_{wf} = bottom-hole flowing pressure
q_j = observed liquid production rate (rb/d)
$\hat{q}_j$ = modeled liquid production rate (rb/d)
$\overline{q}_j$ = average liquid production rate (rb/d)
J = productivity index
r = injector-producer distance
R^2 = coefficient of determination
$s^2_{\beta 1j}$ = variability of regression parameter β_{1j}
t = time (days or months)
$\alpha^{(n)}_{ij}$ = diffusivity filter coefficient
β_{ij} = weighting coefficient in MLR
β_{0j} = additive constant term in MLR
ΔP = pressure change
Δq = production rate change (rb/d)
η_{ij} = diffusivity constant
λ_{ij} = weighting coefficient in BMLR
μ_j = Lagrange multiplier
σ^2_{ii} = injector-injector covariance
σ^2_{ij} = injector-producer covariance

Subscripts and superscripts

i = injector index
j = producer index
m = observed data point
n = time

References

1. Heffer, K.J., Fox, R.J., and McGill, C.A.: "Novel techniques show links between reservoir flow directionality, earth stress, fault structure and geomechanical changes in mature waterfloods," paper SPE 30711 presented at the SPE ATCE, Dallas, October 22-25, 1995.
2. Refunjol, B.T.: Reservoir characterization of North Buck Draw field based on tracer response and production/injection analysis," MSc. Thesis, The University of Texas at Austin, 1996.
3. De Sant'Anna Pizarro, J.O.: "Estimating injectivity and lateral autocorrelation in heterogeneous media," Ph.D. Thesis, The University of Texas at Austin, 1998.
4. Panda, M.N. and Chopra, A.K.: "An integrated approach to estimate well interactions," paper SPE 39563 presented at SPE India Oil and Gas Conference and Exhibition, New Delhi, India, February 17-19, 1998.
5. Soeriawinata, T. and Kelkar, M.: "Reservoir management using production data," paper SPE 52224 presented at the SPE Mid-Continent Operation Symposium, Oklahoma City, Oklahoma, March 28-31, 1999.
6 Araque-Martinez, A.N.: "Estimation of autocorrelation and its use in sweep efficiency calculation," M.S. Thesis, The University of Texas at Austin, 1993.
7. Jensen, J.L., Lake, L.W., Corbett, P.W.M. and Goggin, D.J.: *Statistics for petroleum engineers and geoscientists*, Prentice-Hall Inc., Upper Saddle River, New Jersey (1997).
8. Sabet, M.A.: *Well test analysis*, Gulf Publishing Company, Houston, Texas (1991) 40.
9. Albertoni, A.: "Inferring interwell connectivity from well-rate fluctuations in waterfloods, " M.S. Thesis, The University of Texas at Austin, May, 2002.

SI Metric Conversion Factors

bbl x $1.589873 \times 10^{-1} = m^3$
ft x 3.048×10^{-1}* = m
ft^3 x $2.831685 \times 10^{-2} = m^3$
*Conversion factor is exact

Appendix. Diffusivity filters.

This appendix describes the development and use of diffusivity filters in the MLR and BMLR techniques.

The pressure change (ΔP) at any point of an infinite reservoir, caused by a change in an injection rate, can be expressed as:

$$\Delta P = C_1 \times Ei\left(-d\frac{r^2}{t}\right)$$

where C_1 is a constant, Ei is the exponential integral function, r is the distance from the point to the well, t is time and d is the dissipation of the medium where $d = 1/\eta$. Using the superposition principle, the change in pressure caused by an impulse of a unit of time can be expressed as:

$$\Delta P = \begin{cases} C_1 \times Ei\left(-d\dfrac{r^2}{t}\right) & for \quad t \le 1 \\ C_1 \times \left[Ei\left(-d\dfrac{r^2}{t}\right) - Ei\left(-d\dfrac{r^2}{(t-1)}\right)\right] & for \quad t > 1 \end{cases}$$

If we use a linear model of the form

$$q = J \times \left(\overline{P} - P_{wf}\right)$$

for the production rate of a well at a distance r from the injector, we can write the change in production rate caused by a unit injection impulse as:

$$\Delta q = \begin{cases} C_2 \times Ei\left(-d\dfrac{r^2}{t}\right) & for \quad t \le 1 \\ C_2 \times \left[Ei\left(-d\dfrac{r^2}{t}\right) - Ei\left(-d\dfrac{r^2}{(t-1)}\right)\right] & for \quad t > 1 \end{cases}$$

where C_2 is a new constant of proportionality.

Now, if we consider a fluctuating injection rate as the sum of unit injection impulses, we can use this equation to generate a filter function that lets us, given an injection rate history, determine the production rate at any time and at any point in a production well. The filter function transforms the injection rate so that the response at the producer is equivalent to that one occurring in an incompressible medium. We call the last equation the continuous filter function. Considering that field injection data is discrete (typically in months) we develop a discrete filter function that sweeps the effect for one year (12 months) of injection. We determine the 12 normalized filter coefficients of the discrete filter function as:

$$\alpha^{(n)} = \frac{\int_{t=n}^{t=n+1} \Delta q dt}{\int_{t=0}^{t=12} \Delta q dt} \qquad (n = 1, 2, \ldots 12)$$

More coefficients can be used if necessary. The normalization of the coefficients determines that the $\alpha^{(n)}$s are independent of the proportionality constant C_2, they are less or equal to one, and the sum of all the coefficients is equal to one. The discrete filter function ($\alpha^{(n)}$ coefficients) is characterized by the distance from the injector r, the time t and the dissipation d. For known locations of the wells and times, d can be guessed or determined by minimizing the error in the MLR or the BMLR techniques. The filters are applied only to the injectors and do not contain or seek information about the connectivity between the wells. The regression (MLR or BMLR) takes care of that.

The following examples illustrate the application of the filters. Let's analyze the case of one injector and one producer separated by a distance r. If there were no dissipation in the reservoir, an impulse in the injector would be instantaneously produced in the producer as shown in **Figure A-1**. The filter coefficient $\alpha^{(0)}$ is equal to one and the remaining coefficients are equal to zero. If there is some dissipation in the reservoir (see **Figure A-2**), an impulse occurring at time zero will not have its entire effect instantaneously on the producer ($\alpha^{(0)} \neq 1$). Some dissipated effect will remain for some months. In other words, the production at time t, will be the sum of the effects of injection in the previous months. **Figure A-3** illustrates the case of even larger dissipation (or a more distant production well) where the dissipation makes the production peak be much more attenuated and occur one month later than the impulse.

When the filters are applied to an injection history, the convoluted or effective injection rate at a time t is expressed as:

$$i_{ij}^{c}(t) = \sum_{n=0}^{11} \alpha_{ij}^{(n)} i_i(t-n)$$

Figure A-4 shows a comparison between the original rate of injector I03 and the convoluted injection rate of this well affecting producer P01 in the anisotropic reservoir case (5x4 Synfield).

Table 1. 5x4 Synfield, homogeneous reservoir. Weighting coefficients, λ. See Figure 3.

	P01	P02	P03	P04
I01	0.33	0.33	0.17	0.17
I02	0.33	0.17	0.33	0.17
I03	0.24	0.25	0.25	0.26
I04	0.17	0.33	0.17	0.33
I05	0.17	0.16	0.34	0.33

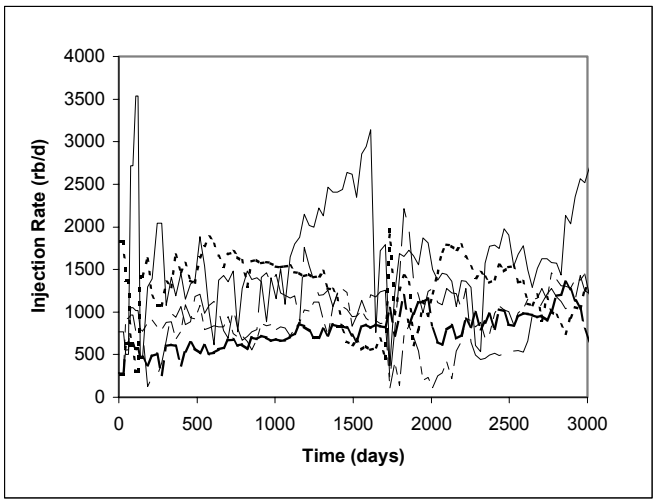

Figure 1. Rates for five injectors. 5x4 Synfield.

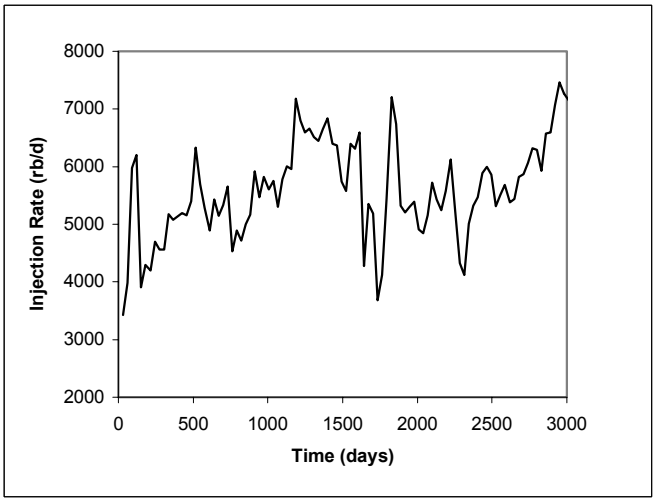

Figure 2. 5x4 Synfield. Total injection rate.

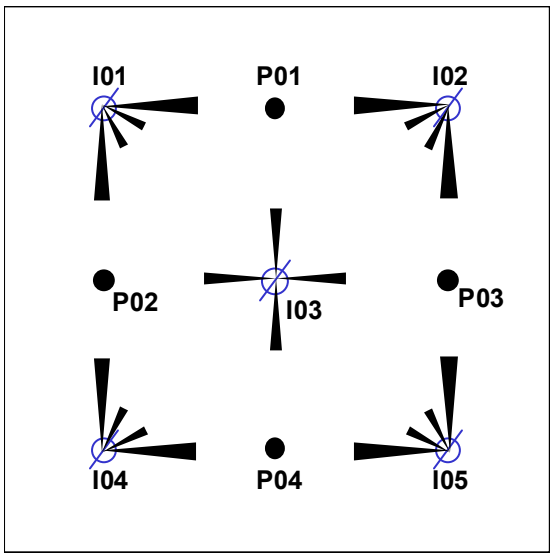

Figure 3. Representation of the weighting coefficients λ, shown in Table 1. The length of the arrow is proportional to the value of the coefficient. 5x4 Synfield, homogeneous reservoir.

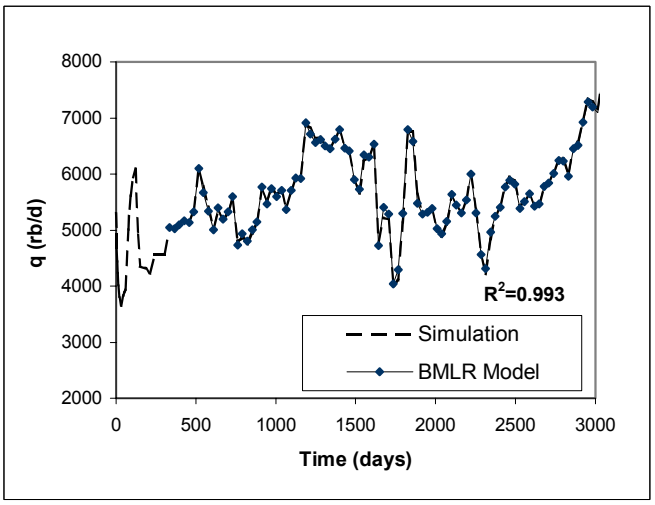

Figure 4. Comparison between modeled total production rate using Balanced Multivariate Linear Regression (BMLR) and the total production rate observed in the simulation. 5x4 Synfield, homogeneous reservoir.

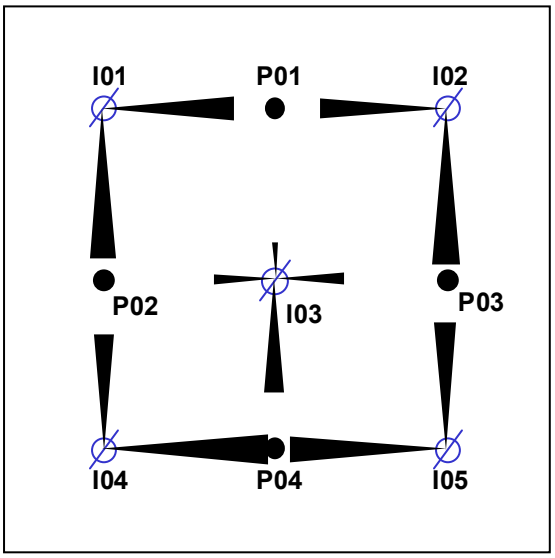

Figure 5. Representation of the tracer results. Fraction of the non-reactive tracer injected in the i^{th} injector produced in the j^{th} producer. The length of the arrow is proportional to the fraction. 5x4 Synfield, homogeneous reservoir.

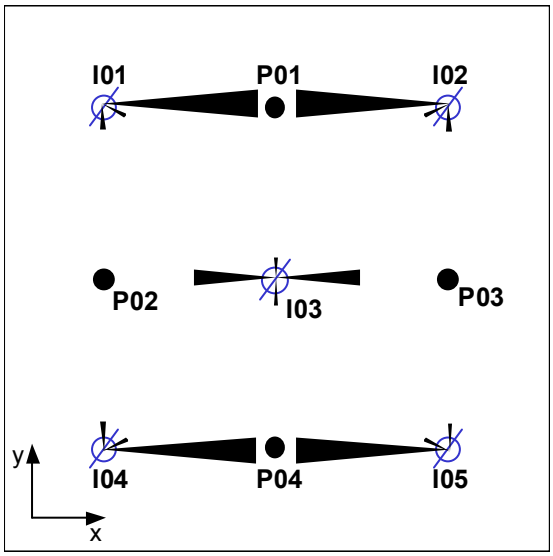

Figure 6. Representation of the weighting coefficients λ. 5x4 Synfield, anisotropic reservoir (k_x/k_y=40).

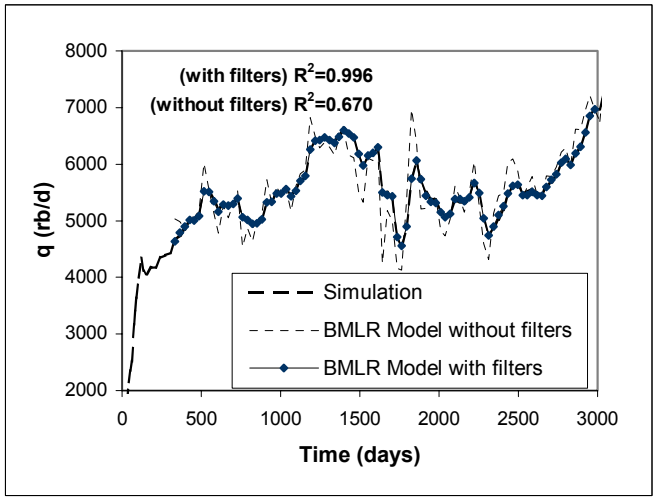

Figure 7. Comparison between modeled total production rate using BMLR (with and without diffusivity filters) and the total production rate observed in the simulation. 5x4 Synfield, anisotropic reservoir.

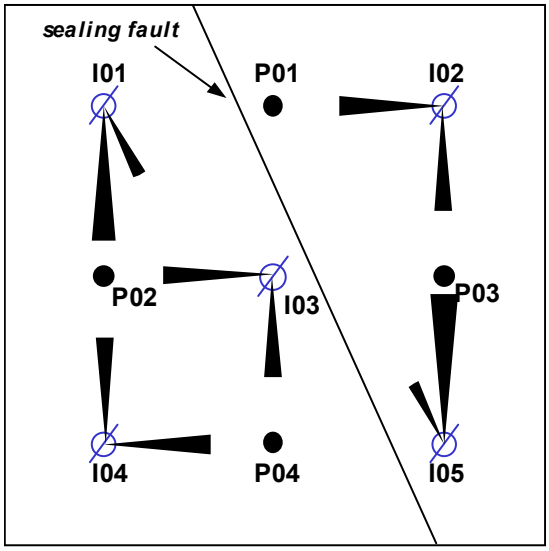

Figure 8. 5x4 Representation of the weighting coefficients λ. 5x4 Synfield, reservoir with a sealing fault (diagonal line).

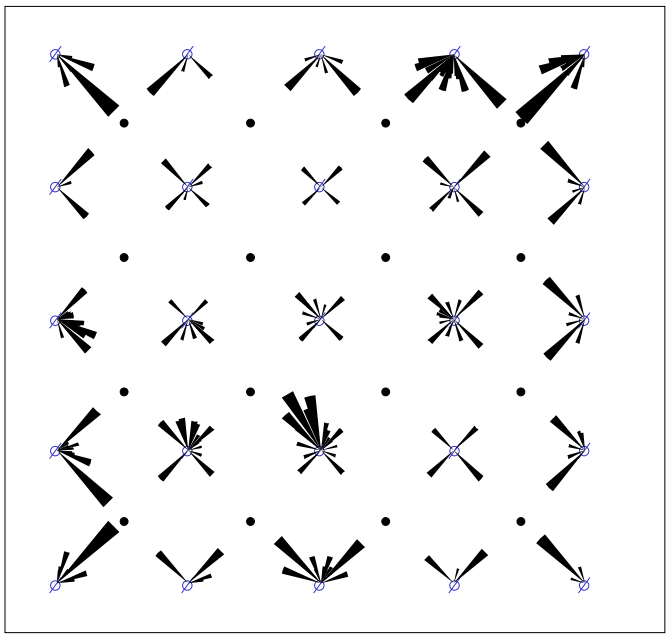

Figure 9. Representation of the weighting coefficients λ, using 65 data points. 25x16 Synfield, homogeneous reservoir, with O_d = 1.58.

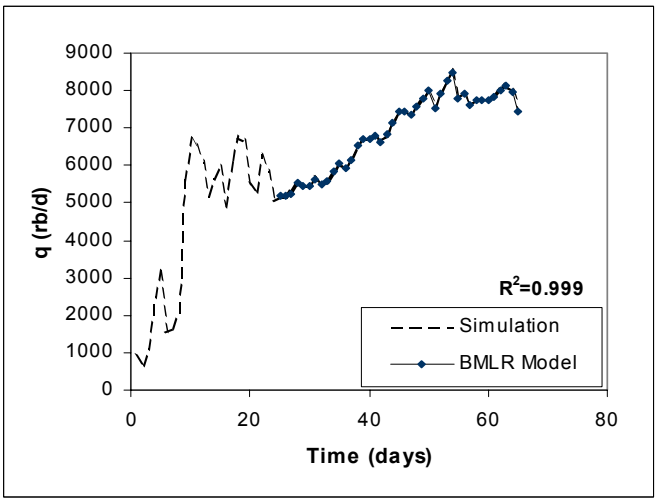

Figure 10. Comparison between modeled total production rate using BMLR and the total production rate of the four center production wells observed in the simulation. 25x16 Synfield, homogeneous reservoir, with O_d = 1.58.

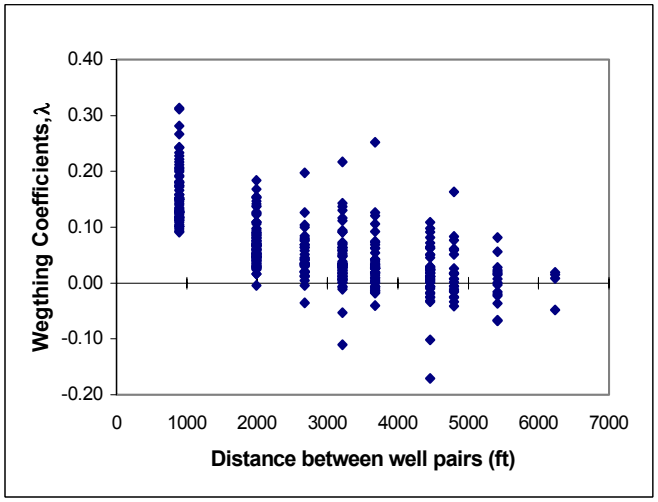

Figure 11. Weighting coefficients, λ, versus distance, using 65 data points. 25x16 Synfield, homogeneous reservoir, with O_d = 1.58.

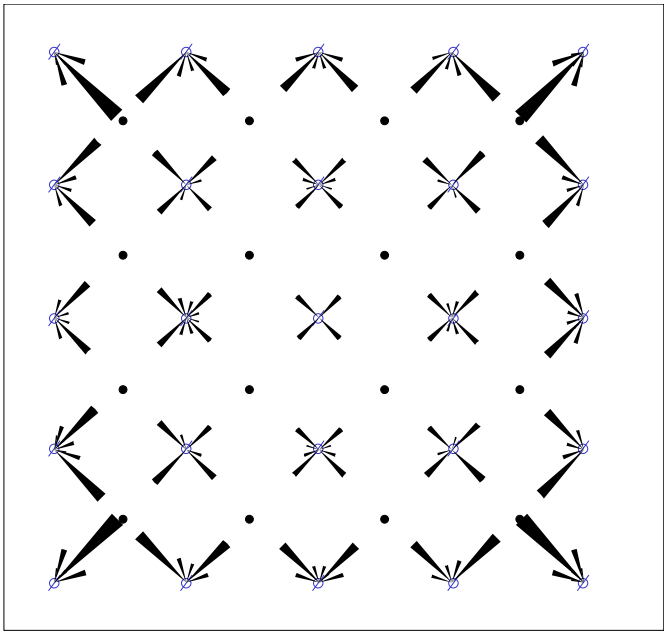

Figure 12. Representation of the weighting coefficients λ, with O_d = 15. 25x16 Synfield, homogeneous reservoir.

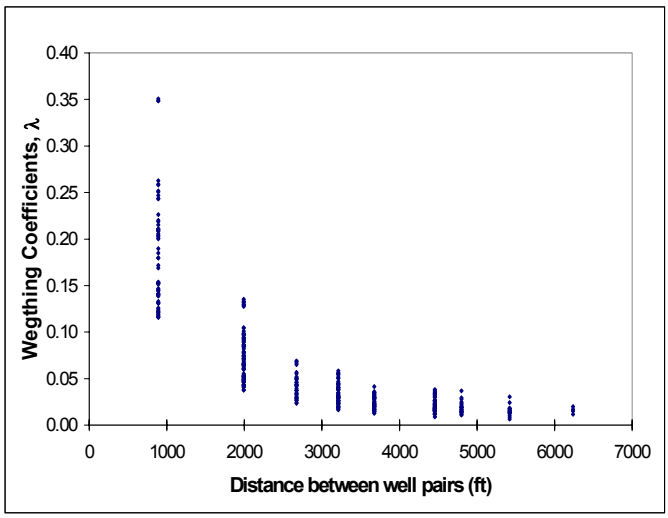

Figure 13. Weighting coefficients, λ, versus distance, with O_d = 15. 25x16 Synfield, homogeneous reservoir.

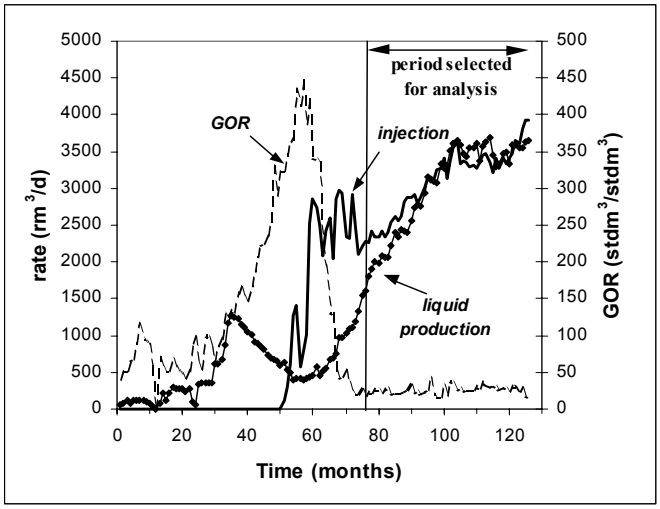

Figure 15. Chihuido de la Sierra Negra (ChSN) Field. Injection rate, production rate and gas-oil ratio (GOR) of the selected portion of the field. The period starting in month 75 was selected for the analysis.

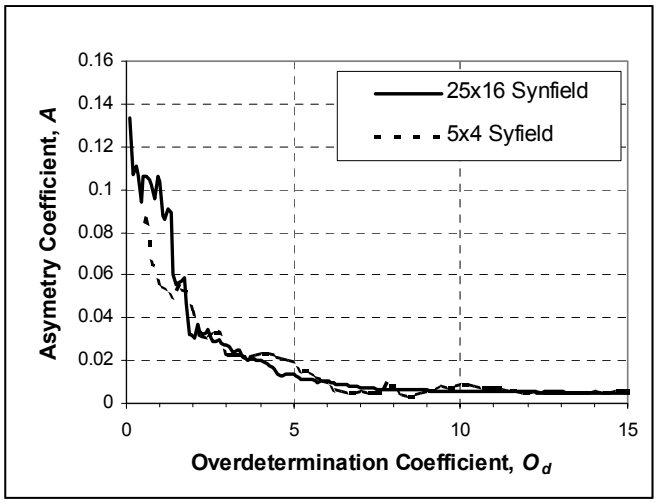

Figure 14. Effect of the overdetermination on the asymmetry coefficient.

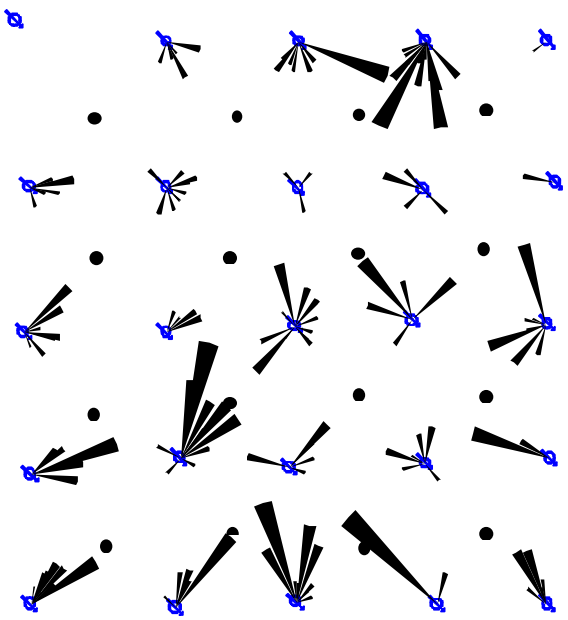

Figure 16. Application of MLR to the Chihuido de la Sierra Negra field. Representation of the positive weighting coefficients, β.

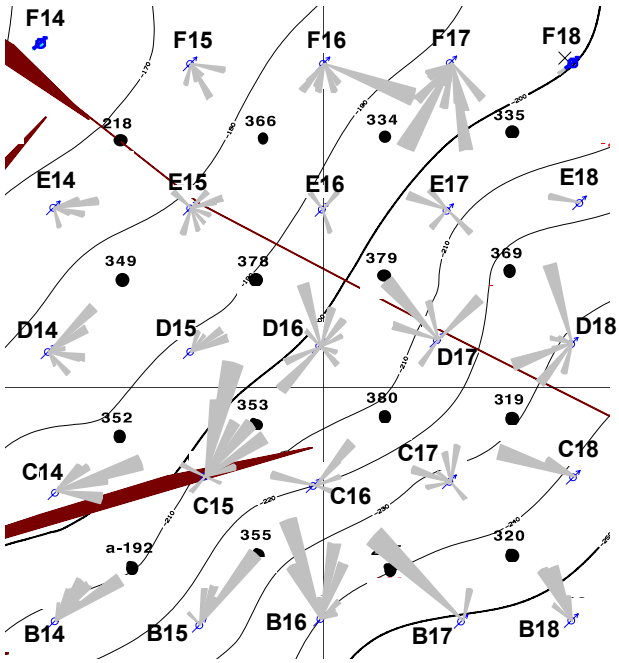

Figure 17. Representation of the positive weighting coefficients β in ChSN field and comparison with known geological features. A structural map is overlain. Coefficients are in gray, faults are in black.

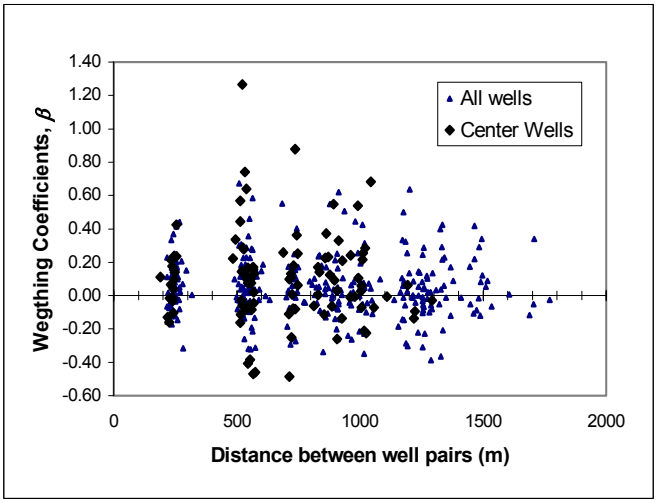

Figure 18. Application of MLR to the ChSN field with small O_d. Weighting coefficients, β, versus distance.

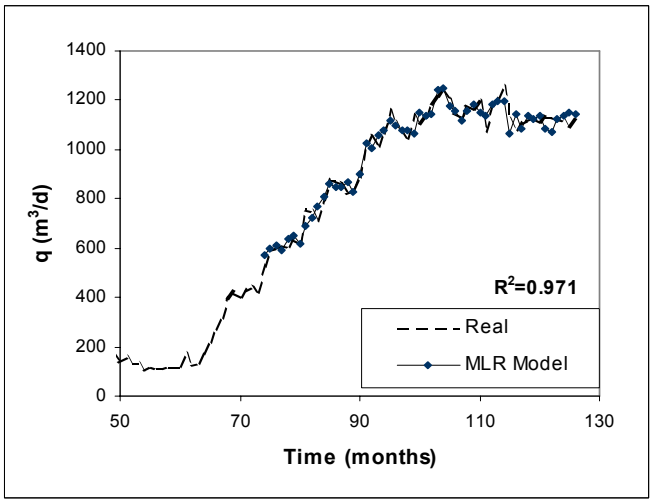

Figure 19. Application of MLR to the ChSN field. Comparison between modeled liquid production rate using MLR and the liquid production rate of the four center production wells in ChSN field.

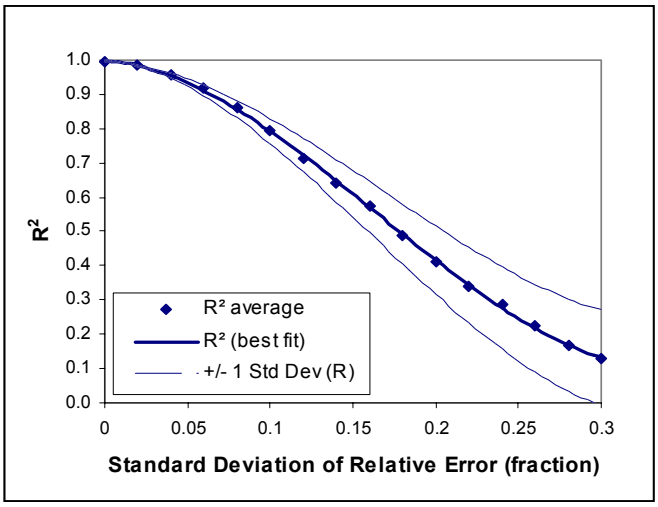

Figure 20. Effect of poor data quality on the coefficient of determination. 5x4 Synfield, homogeneous reservoir.

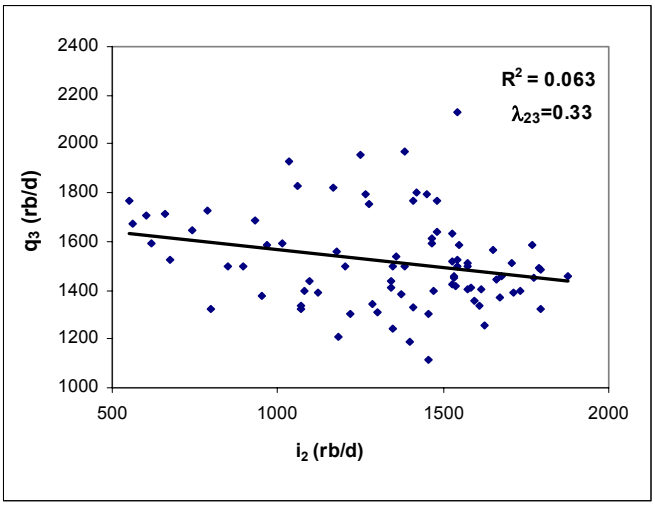

Figure 21. Cross plot of injector I02 and producer P03 rates in the 5x4 Synfield, homogeneous reservoir where λ_{23} = 0.33 (see Table 1 and Figure 3). A poor and even negative correlation between the rates of the two wells is not an indicator of lack of connectivity.

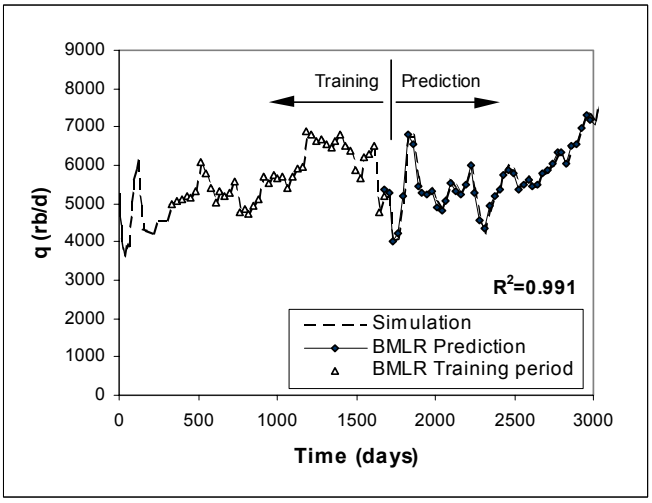

Figure 22. Comparison between modeled total production rate using BMLR and the total production rate observed in the simulation. The weighting coefficients were obtained using a training period of 45 data points and the rest is predicted. 5x4 Synfield, homogeneous reservoir.

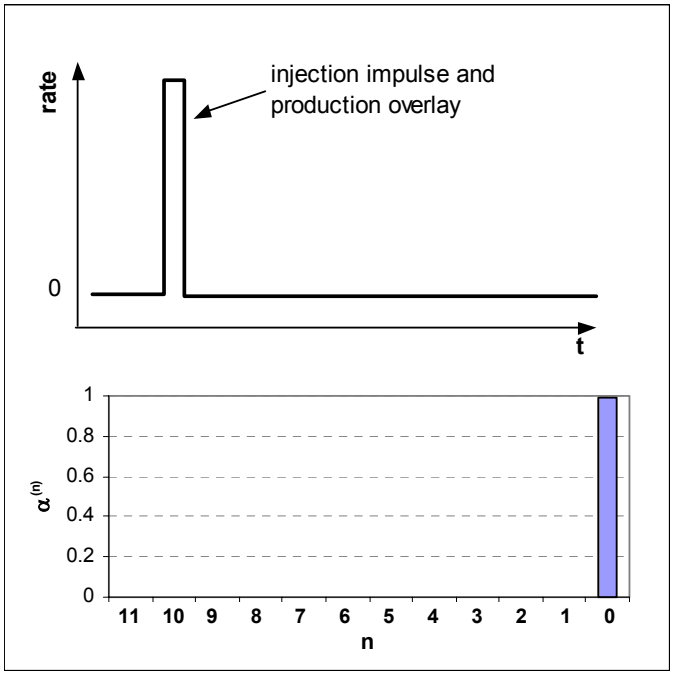

Figure A-1. Injection impulse and production rate in a producer at distance *r* in a reservoir with no dissipation. The discrete filter function (lower plot) has only one effective coefficient, $\alpha^{(0)}$ = 1, all the rest are null.

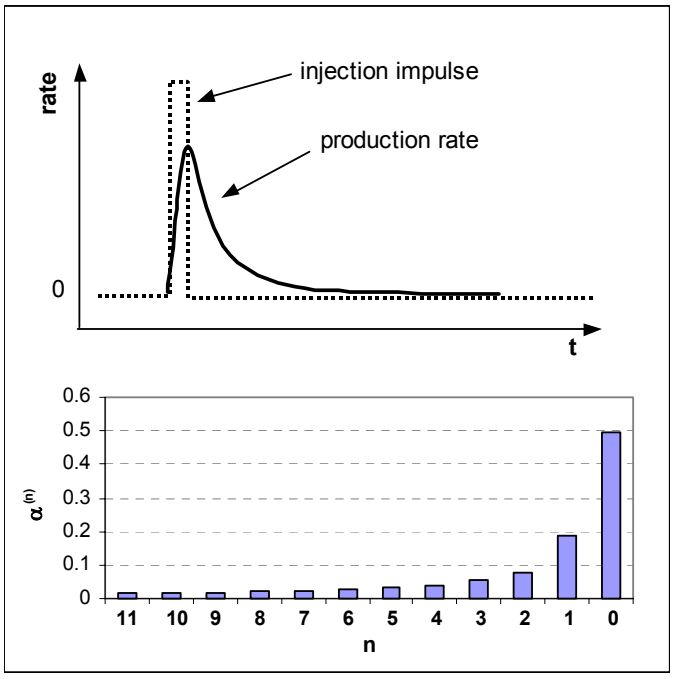

Figure A-2. Injection impulse and production rate in a producer at distance *r* in a reservoir with moderate dissipation. Lower plot is the discrete filter function.

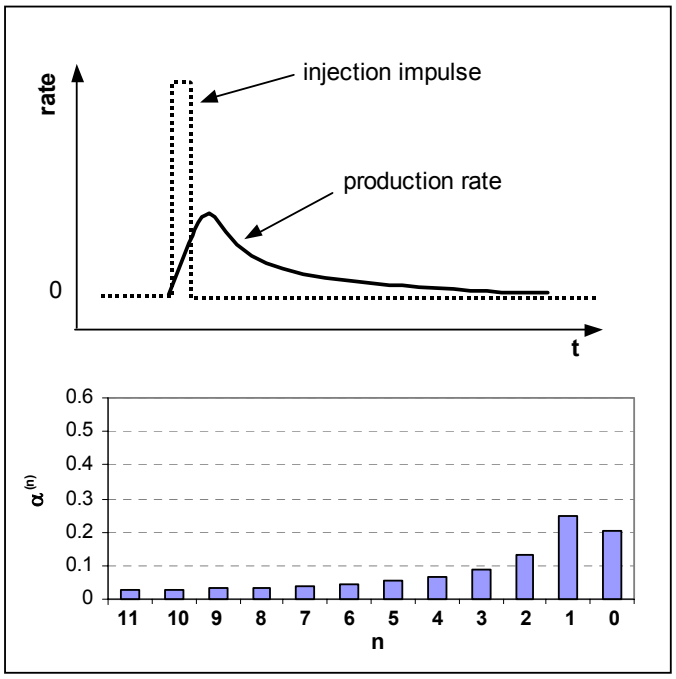

Figure A-3. Injection impulse and production rate in a producer at distance *r* in a reservoir with large dissipation. Lower plot is the discrete filter function.

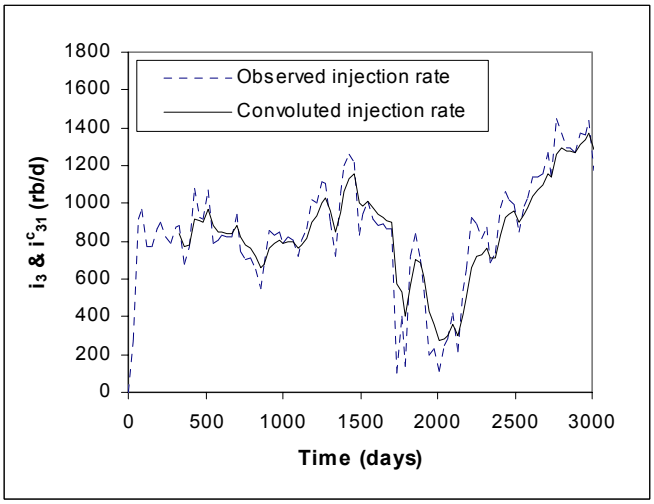

Figure A-4. Comparison between the observed rate of injector I03 and its effective (convoluted) injection rate affecting producer P01. Effect of attenuation and time lag in the 5x4 Synfield, anisotropic reservoir.

WTGS Fall Symposium

Fracture-Surrogate Analysis Methods Applied to Spraberry, Bone Springs, and "Canyon" Cores: Preliminary Results

S. E. Laubach, R. Reed, Bureau of Economic Geology; R. Marrett, Department of Geological Sciences; J. E. Olson, Department of Petroleum and Geosystems Engineering; O. Ortega, J. F. W. Gale, Bureau of Economic Geology, The University of Texas at Austin.

Abstract

Large fractures (macrofractures) produce the greatest impact on fluid flow through fractured rock, however they are orders of magnitude less abundant than microscopic fractures. Macrofractures in subsurface reservoirs typically are poorly represented by data acquired with conventional techniques. Due to the abundance of microfractures, they can be well studied even in small samples from the subsurface. We are exploring the hypotheses that micro- and macrofractures are different size fractions of the same fracture sets, and that microfractures can be used to predict the critical characteristics (in terms of fluid flow) of associated macrofractures. In this paper we report preliminary application of some of these methods to the Spraberry, Bone Springs, and Canyon sandstone plays.

The Fracture Sampling Challenge

Uncertainties about *subsurface* fracture attributes are generally greater than for almost any other important geologic parameter because it is difficult to sample fracture networks in a meaningful way with well bores. Adequate fracture assessments are commonly lacking because the critically important large fractures that primarily govern flow are rarely intersected by wells where they can be measured.

For example, in petroleum reservoirs, where well bores are typically near vertical and many fractures have steep to near-vertical attitudes, the chances of a well bore penetrating large fractures in a given horizon are less than 10 percent for most fracture distributions. Even the most successful sampling provides little information on fracture size distribution and connectivity, as well as other vital parameters.

The basic fact of inadequate sampling arising from typical fracture network and well bore architecture is the primary reason currently deployed fracture evaluation techniques usually fail at the level of completeness required for rigorous assessment of fracture attributes.

In this paper we present examples of techniques that overcome this sampling hurdle from West Texas siliciclastic reservoirs.

Microfracture Observation

Microfractures are structures that are so small that a microscope is required to observe them. Previously invisible microfractures are readily observed and characterized when light emitted from the cements filling them (cathodoluminescence) is imaged using scanning electron microscopy (SEM-based CL, or scanned CL) (Milliken and Laubach, 2000). This facilitates determination of the orientations, timing (relative to diagenetic events), and sizes of the numerous microfractures typically present in prospective fractured reservoirs. Because microfractures are filled with authigenic cement, there is no danger of mistaking them for drilling, coring, or sample handling artifacts (Laubach, 1989; 1997).

Microfracture observations may be made systematically on a bed-by-bed basis. Orientations and timing of microfractures commonly compare favorably with those of associated macrofractures (Laubach, 1997), as do fracture size distributions (Marrett et al., 1999).

On Using Sealed Microfractures

As illustrated in figures 1 through 3, we have empirical evidence that in some areas the sampling predicament can be overcome through observation of micron- to millimeter-scale cement-filled microfractures. These microfractures are useful guides, or surrogates, for difficult-to-sample large fractures.

Except for size, these microfractures share many attributes with, but are not necessarily localized near, large fractures (Laubach, 1989, 1997; Olson et al., 1998; Ortega and Marrett, 2000; and unpublished studies). Such fractures are potentially of great importance for describing and mapping fracture flow pathways in deeply buried rocks.

That microfractures are cement filled should pose a question about the practical use of these structures in the petroleum industry. Who is interested in sealed fractures? After all, open fractures are the ones that can assist producibility. The ability to use sealed microfractures to predict the attributes of large, open fractures is the essential element of this approach. Empirical evidence shows that the assumption is justified (Laubach, 1997; Marrett et al, 1999). Recent diagenetic modeling work corroborates that under various widespread

diagenetic scenarios, microfractures will seal whereas larger fractures will retain porosity (Lander, 2001).

The interplay of fracture and diagenetic processes and the large size range that typifies natural fractures is the reason microfractures are good guides to large fractures, even though microfractures may have negligible porosity. Although small and large fractures are frequently merely different size fractions of the same fracture sets, some attributes of small fractures differ in systematic ways from the attributes of large fractures. The degree of porosity preservation is one attribute that typically differs between large and small fractures. Small fractures tend to seal rapidly with the expected ambient cements in a rock-dominated rock-fluid system owing to their small volume and large surface area (Laubach, in preparation; Lander, 2001), whereas large fractures can preserve porosity for millions of years even at relatively great depth (10,000 ft or more) because of slow rates of authigenic cement precipitation (Lander and Walderhaug, 1999).

Yet these large fractures can also be rapidly sealed if the local diagenetic situation changes. Such changes are challenging to predict from first principles, but the occurrence of late cements can frequently be recognized from samples that lack macrofractures. This is the basis for a surrogate for fracture 'openness preservation' based on fracture timing information (as opposed to direct fracture porosity observation), as described below.

Microfracture Surrogates

The attributes of macrofractures that can be inferred from microfracture observation include:

1. Presence of fractures,
2. Number of fracture sets,
3. Fracture strike,
4. Size distribution of fractures—a measure of average spacing or intensity, and
5. Timing of fracture opening relative to authigenic cement precipitation (indirectly, a measure of the potential for open fractures).

Applications

In "blind" tests, we have successfully used microfractures to predict the orientation, size distribution, and degree and type of mineral fill, of fractures that are as much as three orders of magnitude larger. Observations in more than 50 formations demonstrate the widespread occurrence of microfracture arrays, so the approach is widely applicable.

The surrogate approach to fracture characterization has been tested in several formations in West Texas. A companion paper (Gomez et al., this volume) describes an application in Ellenburger dolomite. In addition, we have deployed the technique in several siliciclastic reservoirs including the Spraberry, Bone Springs, and various "Canyon" and "Wolfcamp" sandstones. Here we briefly review the results of some of these tests in West Texas siltstone and sandstone reservoirs.

Fracture Strike? Spraberry Example

In the Midland Basin, Permian Spraberry Formation is an oil-producing unit in fine-grained turbidites. As part of a DOE project, Pioneer Natural Resources collected more than 395 ft of core in two horizontal Spraberry sidetracks in the E.T O'Daniel No. 28 well (McDonald et al., 1997). The 1U sandstone is stratigraphically near the top of the Floyd submarine fan at ~7089 ft, while the 5U sandstone is located near the top of the Driver submarine fan at ~7238 ft. Cores were drilled out from the vertical using minimal dogleg severity to prevent damage to core during retrieval. The radius of curvature was ~400 ft and both horizontal legs were drilled to the south (158 and 167 degrees, respectively).

Since the 1950's, permeability anisotropy with a generally NE trend has been recognized in the Spraberry. Cores from the sidetracks document three distinct fracture sets, striking NNE, NE, and ENE (McDonald et al., 1997). NE-striking fractures, found only in the 1U reservoir, commonly contain quartz and barite. NNE- and ENE-striking fractures occur in the 5U reservoir. Fractures were interpreted to be a mixture of shear and opening-mode fractures (McDonald et al., 1997).

Using three 2.5 cm core plugs taken from the 1U horizontal core, we measured sealed microfractures to estimate the strike of large fractures in the sidetrack. Information about the core and any large fractures in it was withheld during analysis so that our method could be tested without possibility of bias.

The three core plugs contain quartz-filled microfractures having lengths of generally less than 50 microns and kinematic apertures of less than 0.10 microns. Kinematic aperture is the distance fracture walls have moved apart. Owing to mineral fill, kinematic aperture is almost always greater than the open aperture available for fluid flow. Microfractures strikes were measured along five short traverses (A though G; Figure 1). The number of microfractures per traverse ranged from 19 to 64.

In the classification scheme of Laubach (1997), all of the Spraberry microfractures used in the orientation analysis have ratings of 'd' (or lower), which is to say, they are so small and ambiguous in their patterns that the recommended procedure would be to reject these fractures for orientation analysis. Resolution limits on fracture characterization have improved since this analysis was conducted in 1996. Yet the recommended procedure when faced with low-rated microfractures is to image larger areas with the aim of acquiring more high 'rating' and more reliable fractures. The optimum size of image area is dictated by fracture population scaling.

The area available for analysis in the Spraberry thin sections is about 490 mm^2. Microtraverses (at 350x magnification) were as much as 2000 microns long and only ~200 microns wide. Thus only a small part of the available sample area was used. The data set reflects both low rated microfractures and small sample area. Coincidentally all but one of the microtraverses was oriented at a low angle to the dominant microfracture trend. This is evidence that the sampling strategy does not cause observed orientation patterns.

Despite the low quality of the microfracture data, orientation analysis was carried out and consistent preferred orientations of microfractures were detected in all three 1-inch core plugs. Overall, a main NE-striking set was found (040°±20 degrees) with apparent subsidiary maxima at 350 and 050 degrees. Averaging all microfracture strikes (that is, neglecting the subsidiary maxima) gives a mean strike of ~020 degrees. Given the dispersion in strikes, subsidiary directions, low data quality, and small sample area we can only specify that the dominant fracture trend have a NE strike that falls between 020 and 050 degrees. A subsidiary fracture set, probably older based on ambiguous crosscutting microfracture relations, likely strikes NNW.

As shown in Figure 1, the average macrofracture strike we infer from microfractures is consistent with the traditional NE permeability anisotropy direction in the Spraberry (reported to range from 020 to 050 degrees). Moreover, the measured microfracture strike (and 99-percent confidence angle) overlaps with our evaluation of average macrofracture strikes in the upper cored interval of the horizontal well, ~035°±8 degrees as well as published results for the upper cored zone (043 degrees)(McDonald et al., 1997).

Overlap in average fracture strikes for micro- and macrofractures in this data set is evidence that microfractures are tracking the strike of macrofractures. Microfracture strike populations (or individual microfractures) do not necessarily have the same strikes as the nearest macrofracture, as fractures of various sizes within a population may not grow at exactly the same time in a fracture 'event' or under the influence of identical local stresses (Olson et al., 2001). Moreover, macrofracture populations frequently also exhibit dispersion in strike that may not be apparent in horizontal core.

Macrofractures in the lower cored zone are reported to have strikes of 032 degrees and 070 degrees (McDonald et al., 1997). The microfracture approach was only applied to one of the cored Spraberry intervals, 1U. Consequently, a comparison is unwarranted with the slightly contrasting NE-striking fracture patterns in the 5U interval reported by McDonald et al. (1997). Bed-to-bed variability in fracture strikes and patterns is to be expected in regional fracture sets.

The subsidiary NW fracture set in our microfracture data could be an artifact of a small and low-quality microfracture dataset. However, it is substantially parallel to direction of the horizontal laterals and it would be fortuitous to find large fractures having this strike in the horizontal core. Moreover, if this direction marks an older group of fractures, as the microanalysis data suggests, these fractures would have experienced a longer diagenetic history and thus be more prone to seal and play a lesser role in reservoir response.

In principle, sampling of large fractures using expensive horizontal core should provide a more nuanced fracture interpretation than data from specimens the size of a relatively inexpensive sidewall core. This case study as well as previous and subsequent work (Laubach, 1997; Gomez et al, this volume) shows that valuable fracture strike data can be obtained from small samples collected and analyzed prior to the expensive step of drilling horizontal laterals.

Fracture Intensity? Ozona Canyon Example

Microfractures are sufficiently abundant in the numerous fractured units we have studied that the size distributions can be readily quantified. Under special circumstances, the sizes (i.e., kinematic apertures and/or lengths) of both micro- and macrofractures can be reliably measured in the same fractured rock volume. The spatial frequency of fractures, as a function of fracture size, follows power-law distributions over at least 4 to 5 orders of magnitude in these cases (Marett et al., 1999). This confirms that microfracture sizes can be used to quantitatively predict spatial frequencies of associated macrofractures.

This approach was applied to core of the Mobil Blackney Kruger No. 1, an Ozona sandstone well, West Texas (Marrett et al., 1999)(Figure 2). Cores taken from subvertical beds in the hanging wall of a thrust fault contain carbonate and quartz-filled fractures at a high angle to bedding. More than 300 kinematic apertures were measured visually along fracture-perpendicular scanlines in these subvertical beds. Microfracture aperture data were collected from scaned CL traverses along scanlines in the same orientation as the scanlines in the cores.

Macrofracture apertures range from less than one tenth of a millimeter to nearly one centimeter, and the microfractures range from tenths of a micron to tenths of a millimeter.

Size distributions of micro- and macrofracture data are each well modeled using a power-law. Normalization of aperture size distributions by lengths of the scanlines allows direct comparison of fracture frequencies in both data sets (Figure 2). The results represent over four orders of magnitude in fracture aperture and strongly suggest that the micro- and macrofractures are expressions of the same fracture system at two different scales of observation.

This implies that the prediction of macrofracture frequency based on microfracture data is possible, at least up to the scale of fractures that span the mechanical layer.

Microfracture population statistics can be used to predict the distribution of fractures having much larger kinematic apertures than those sampled. In this case, larger fractures, although not used in the initial analysis, are present in the core, permitting a fracture intensity prediction to be tested. As Figure 2 shows there is an excellent fit between microfracture data used for prediction and the macrofracture data observed in the core.

Are Fractures Open? Bone Springs Example

Whether fractures are open or sealed may dictate if fractures enhance reservoir permeability or not. A surrogate for direct observation of open fractures is evidence for the timing of fracture formation relative to diagenesis. A description of a thorough test of this approach on two Wolfcamp sandstone wells from Pakenham Field, where whole core and image log data are available, is provided elsewhere (Laubach, in preparation).

Here we report fracture quality data from two Bone Springs Formation wells, the University 18-34 No. 1 and the University 19-20B. Sandstones of the Permian Bone Springs Formation are oil reservoirs in the Delaware Basin. These wells provide a test of surrogate methods to predict whether fractures are open or sealed (Figure 3). In this example, the 'ground truth' is production data from two wells that in every respect except fracture quality, appear to be quite similar. The analysis was performed on 14 sidewall cores.

The analysis used microfractures to determine the time of fracture formation (Laubach et al., 2000). Using conventional paragenetic sequence data for cements and point-count data for cement volumes, the amount of cement post-dating fracture opening was calculated. This postkinematic cement is the material available to seal large fractures (Laubach, 1988; Laubach, in preparation). This information was used as a surrogate for fracture observation to infer whether natural fractures likely provide a permeability assist in either well.

The ratio of postkinematic cement to available rock volume, the degradation index, is a predictor of whether large fractures are sealed or not. High values of degradation (near 100) predict sealed fractures. In cases where this technique is calibrated against macrofracuture observations, degradation values less than 20 percent frequently correspond to open fractures, whereas degradation values >50 percent commonly have partly to completely sealed fractures. In the Bone Springs test, well University 19-20B, with high degradation values, lacks a permeability assist from open fractures (matrix porosity values from porosity logs are low – less than 10% but for the two wells are essentially indistinguishable).

This example illustrates the approach in a West Texas example. Other types of data sets, as described elsewhere, verify that sealed macrofractures exist where high degradation is detected.

Fluid-Flow Modeling

The orientations, time of formation relative to diagenetic minerals (and thus potential for fracture porosity), and sizes of macrofractures are important factors for understanding fluid flow in fractured rock. Although discrete-fracture modeling provides the most realistic portrayal of fluid flow through fractured rock, this technique is usually computationally infeasible for simulation of the large volumes in a fractured hydrocarbon field. Dual-porosity simulation is the dominant technique for this reason. We are developing a blended approach to simulation that is both cost effective and grounded on local fracture observation (Rossen et al., 2000).

Using fracture predictions from surrogate patterns, multiple discrete-fracture models may be generated for each bed. With suitable data density, maps representing volumes comparable to those of cells in dual-porosity simulations can be generated. Fluid-flow simulations in discrete-fracture models provide a quantitative, observation-based understanding of fluid-flow characteristics and spatial heterogeneity for each bed. These results can then be used to construct a dual-porosity simulation for large regions in the subsurface. Quantitative testing of this approach with subsurface flow data is ongoing.

Discussion and Conclusions

On a bed-by-bed basis, microfracture observations can be used to make statistical predictions of essential macrofracture attributes: orientation, intensity, porosity and the potential for transmitting fluid. Because data can be obtained from most samples, this approach potentially has great value as a means to collect information for fracture attribute maps. As is demonstrated here and elsewhere, sealed microfractures are good guides to the attributes of large fractures that may be open (Laubach, in preparation).

Examples from mature oil and gas fields in West Texas silt- and sandstones demonstrate that the method can be used to obtain fracture data (Figures 1 through 3). In turn, these results can guide development and re-exploration strategies.

Acknowledgments

Our research on reservoir fracture issues is supported by members of the Fracture Research and Application Consortium, including Barrett Resources Inc./Williams Exploration & Production, BG Group, Chevron USA, Conoco Inc., Devon Energy Corporation, Enron Global, EOG Resources, Japan National Oil Corp., Lariat Petroleum Inc., Marathon Oil, Pemex Exploración y Producción, Petroleos de Venezuela, Petrobras, Repsol-YPF-Maxus, TotalFinaElf, and

by U.S. Department of Energy Contract No. DE-FC26-00BC15308. We are grateful to Dave Scolman for access to the Bone Springs core suite and interpretation of associated porosity log and production data. We are grateful to Tim Hunt, University Lands, for the invitation to present this paper. Publication authorized by the Director, Bureau of Economic Geology, The University of Texas at Austin.

References

Gomez, L.A., Gale, J.F.W., Ruppel, S.C., and Laubach, S.E., this volume, Fracture characterization using rotary-drilled sidewall cores: an example from the Ellenburger Formation, West Texas: West Texas Geological Society Fall Symposium.

Lander, R.H., 2001, Quantitative prediction of petrophysical properties using diagenetic models (abs.): AAPG program, Denver Convention, on CD.

Lander, R.H., and Walderhaug, O., 1999, Porosity prediction through simulation of sandstone compaction and quartz cementation: AAPG Bulletin, v. 83, p. 433-449.

Laubach, S.E., 1988, Subsurface fractures and their relationship to stress history in East Texas basin sandstone: Tectonophysics, v. 156, p. 37-49.

Laubach, S.E., 1989, Paleostress directions from the preferred orientation of closed microfractures (fluid-inclusion planes) in sandstone, East Texas Basin, U.S.A., Journal of Structural Geology, v. 11, no. 5, p. 603-611.

Laubach, S.E., 1997, A method to detect natural fracture strike in sandstone: AAPG Bulletin, v. 81, p. 604-623.

Laubach, S.E., Marrett, R., and Olson, J.E., 2000, New directions in fracture characterization: The Leading Edge, v. 19, no. 7, p. 704-711.

McDonald, P., Lorenz, J.C., Sizemore, C., Schechter, D.S., and Sheffield, T., 1997, Fracture characterization based on oriented horizontal core from the Spraberry Trend reservoir: a case study: SPE 38664, p. 231-239.

Marrett, R., Ortega, O., and Kelsey, C., 1999, Extent of power-law scaling for natural fractures in rock: Geology, v. 27, no. 9, p. 799-802.

Milliken, K.L., and Laubach, S.E., 2000, Brittle deformation in sandstone diagenesis as revealed by cathodoluminescence imaging with application to characterization of fractured reservoirs, Chapter 9: in Pagel, M, Barbin, V., Blanc, P., and Ohnenstetter, D., eds., Cathodoluminescence in Geosciences, Springer-Verlag, p. 225-244.

Olson, J.E., Qiu, Y., Holder, J., and Rijken, P., 2001, Constraining the spatial distribution of fracture networks in naturally fractured reservoirs using fracture mechanics and core measurements: SPE 71342.

Olson, J.E., Hennings, P.H., and Laubach, S.E., 1998, Integrating well-bore data and geomechanical modeling for effective characterization of naturally fractured reservoirs: EUROCK '98, Society of Petroleum Engineers, p. 475-485.

Ortega, O., and Marrett, R., 2000, Prediction of macrofracture properties using microfracture information, Mesaverde Group sandstones, San Juan Basin, New Mexico: Journal of Structural Geology, v. 22, no. 5, p. 571-588.

Rossen, W.R., Gu, Y., and Lake, L.W., 2000, Connectivity and permeability in fracture networks obeying power-law statistics: SPE 59720.

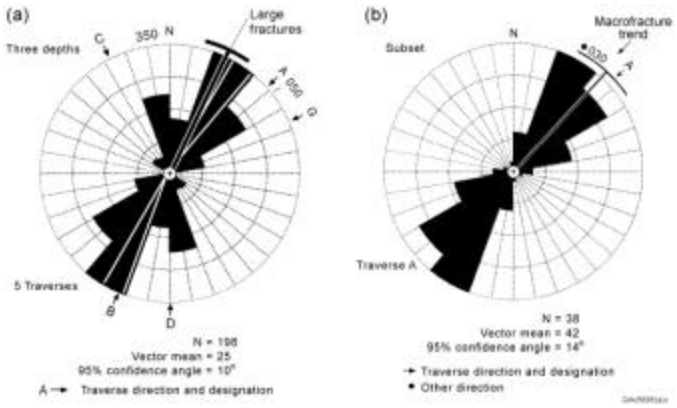

Figure 1. Fracture strike determined in a blind test using microfractures (rose diagrams). Samples obtained from a horizontal core were analyzed for microfracture strike then compared with strike of large fractures recovered in the horizontal core. Rose diagrams show average microfracture strikes weighted using the method of Laubach (1997), as well as the mean and 95–percent confidence angle of macrofractures. Shown here are (a) all data and (b) one subset (from 7664.9 ft).

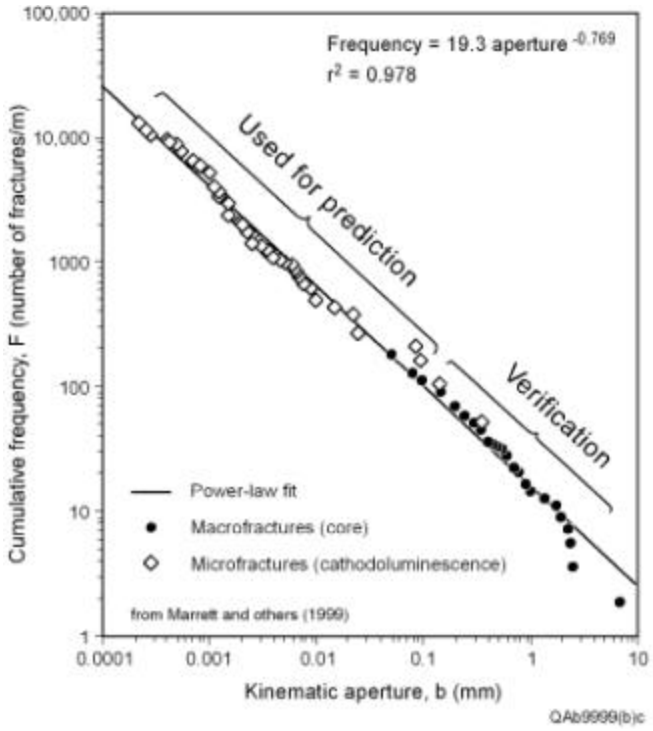

Figure 2. Fracture size distribution prediction, based on scaling patterns of microfractures. Predictions were confirmed in this case by using data on large fracture from a core cut perpendicular to fractures (Modified from Marrett et al., 1999). Mobil Blakeney Kruger No. 1 well, core depth 4453.2 to 4457.0 ft.

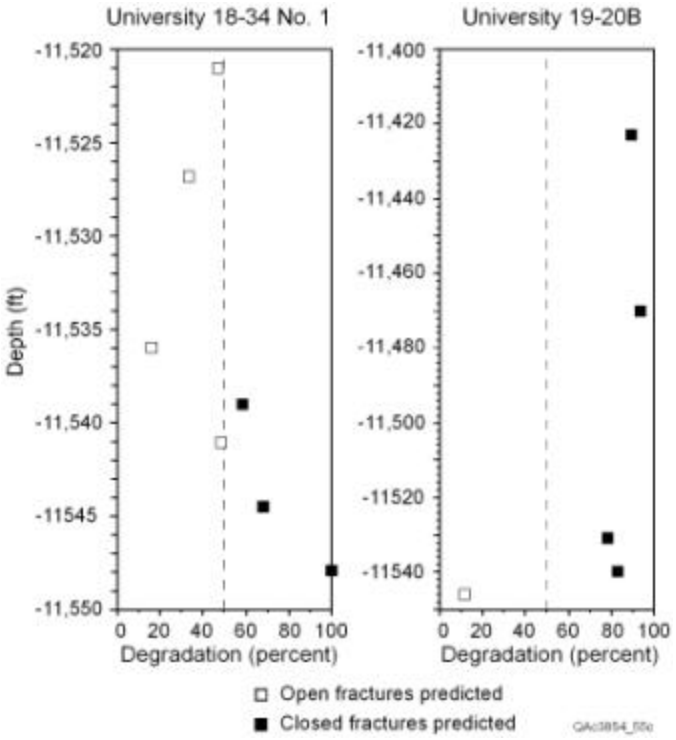

Figure 3. Fracture quality in two Bone Springs wells: Are fractures open or closed? In this example, fracture quality in two wells is estimated based on observations of microfractures and diagenesis patterns. Results predict that open fractures enhance reservoir permeability in the University 18-34 No. 1, but not in the University 19-20B. Some fracture quality heterogeneity is apparent in both wells.

SPE 75245

Geochemical Modeling of Fracture Filling

Myeong H. Noh, Larry W. Lake, SPE, The University of Texas at Austin

This paper was prepared for presentation at the SPE/DOE Thirteenth Symposium on Improved Oil Recovery held in Tulsa, Oklahoma, 13–17 April 2002.

Abstract

This paper reports on a mathematical model to simulate hydrodynamics and fluid-mineral reactions in the fracture within a permeable media. Fluid convection, diffusion and precipitation / dissolution (PD) reaction inside a finite space are solved as a simplified representation of natural fracture mineralization. The problem involves mass transfer within the fluid accompanied by chemical reaction at the fracture surface. Mass-conservation equations for components in the fluid are solved in this problem, and these are coupled with chemical reaction at the fracture surface. The intent of this model is to show the time evolution of fracture aperture shrinkage patterns caused by PD reactions. We present the aperture distribution along the fracture with various boundary conditions. Partially cemented fractures are created if cementation fails to completely fill the fracture or if subsequent dissolution leaches out some of the mineral.

Introduction

A fracture has been recognized as a fluid conduit that has high permeability relative to that of the surrounding rock matrix in a fractured reservoir. To characterize the reservoirs, core and well log data can be investigated. However, only a few fractures can be observed by the direct measurements; determining which particular fractures are controlling fluid flow and by which mechanisms the wells in fractured media produce are difficult tasks. Often, the most reliable way of characterizing the response of a fractured reservoir is through the analysis of reservoir production behavior, such as well productivity and breakthrough data.

The reservoir quality of sedimentary rocks is closely related to diagenesis, a process involving post-depositional alteration of previously deposited sediments. Rock properties such as porosity, permeability, pore-size distribution, reservoir heterogeneity and spatial correlation can be the product of diagenetic modification of original properties. One of the most important mechanisms of diagenetic processes is chemical reaction between minerals and migrating fluids.

Fluid-mineral reactions are dynamic processes that involve many effects: complex fluid flow, pore space changes, surface chemistry, and the mineral composition. We have developed a simple precipitation / dissolution (PD) model for the flow in a finite parallel plate that represents a single fracture. The idea behind the model is to approximate the description of a variable fracture aperture, surface reaction, and diffusion by a set of parameters and simple rules governing the alteration of fractures. Fracture aperture can either grow or shrink as chemical reaction proceeds at the fracture surface. In this study, we solve mass conservation equations for the components of aqueous and solid phases simultaneously and show the fracture aperture size distribution with time. Calcite cementation is as the form of precipitation considered.

Characterization of Fractured Reservoir

The spatial variations of fracture properties, such as aperture size and orientation, are complicated and irregular so that the characterization of a fractured reservoir is more difficult than that of an unfractured reservoir. One way to approach the characterization is to start from a local characterization of a single fracture and proceed to fracture systems. Parameters for the characterization of fractures include fracture property distributions, fracture density and the size and the shape of matrix blocks.

Especially in low permeability reservoirs, natural fracture permeability is an important issue. In crystalline rocks, the system permeability is almost entirely the result of the fracture network even though the matrix contains most of the reservoir fluid.

In general, the two rock surfaces that bound a fracture are rough. The degree of roughness can be a function of the fracture aperture and the fluid properties within the fractures. Fractures can be partially or fully-filled by mineral precipitation. The nature of a fracture is reservoir-specific, depending on mineral composition, tectonic stress history, diagenesis and petrophysical properties. One purpose of this work is to put some of these connections into a quantitative understanding.

Diagenesis of sedimentary rocks

Diagenesis is the process of physical and chemical changes in sediment, after deposition, that converts it to consolidated rock.

Common minerals, dissolved in or precipitated from an aqueous phase can be grouped into those that are relatively reactive or inert in that their dissolution or precipitation rates are fast or slow, respectively, relative to the flow rate of the aqueous phase.[24] Berner[3] has outlined the consequences of variations in reaction rates relative to flow rate of the fluid in which the minerals are reacting. The minerals can be further grouped according to simple and complex stoichiometry. Those minerals with complex stoichiometry are much less likely to reach the solubility equilibrium than those with simple stoichiometry. For example, it is well known that simple ionic solids with high solubilities (such as halite, mirabilite, and carnallite) will reach solubility equilibrium more quickly than complex solids with a much more covalent character and low solubility. Since calcite is a reactive mineral and has simple stoichiometry, it is considered as an example of water-rock reaction problem in this study.

Carbonate diagenesis

Generally, diagenesis of carbonate rocks includes all the processes on the sediments after their initial deposition. High temperatures and pressures at the subsurface create minerals and structures by metamorphism. Physical, chemical, and organic processes begin acting on carbonate sediments after their deposition, leaving an influence on the mineral composition and structure. Diagenesis typically changes porosity, permeability and capillary pressure characteristics. The porosity of modern sediments varies from 40 to 70% and the porosity of carbonate reservoirs in the USA ranges from 9 to 17%.[25] The permeability of carbonate reservoirs is also reduced with porosity. Therefore, an understanding of diagenetic processes is important for carbonate reservoir characterization.

Early cementation processes require fluid flow to import calcium and carbonate into the system, but the fluid flow is closely tied to the depositional environment through permeability. Late or burial cementation may occur by chemical compaction and thus be linked to a depositional environment, or it may require regional transport of ions by groundwater. In a sense, it is possible to generalize that the composition of subsurface fluid and the flowrate as the prime determinants in diagenesis. Thus the interpretation of the diagenetic history of a carbonate rock is an interpretation of fluid flow history. For example, the presence of vugs in a carbonate rock implies that large volume of water of markedly different composition has moved through the rock. Many significant advances of diagenetic processes have resulted from chemical studies of the sedimentary material and the reactions that occur between these materials and groundwater.

Cementation of carbonate

Cementation in carbonate rocks normally refers to the growth of crystals into a void space from carbonate rock surfaces. The new crystal occupies space that formerly was occupied by fluid. The composition of the carbonate cements depends on the composition of the fluid from which the crystals grow. In general, when the cementing crystals grow from seawater or a similar solution, aragonite and sometimes high-magnesium calcite form. These are unstable minerals and are subsequently replaced by more stable forms. Aragonite, for example, can be precipitated from seawater, but it is unstable at the Earth's surface temperature and pressure, and can persist metastably because of kinetic reasons. This can be explained by the difference of Gibbs free energy that indicates the reaction should proceed from aragonite to calcite at standard condition.[18] When the cement grows from a freshwater solution, calcite forms.

A characteristic of all cements is that they propagate from pore walls into pore space and therefore reduce pore size. In the case of uniformly distributed cement, the pore size is reduced in proportion to the amount of cement precipitated.[15] The reduction in pore size accounts for the changes in porosity, permeability and capillary pressure.

Unevenly distributed calcite cement will produce small-scale heterogeneity. The total porosity of the sample will be reduced, but the porosity and pore size of the noncemented portions will remain unchanged. Because permeability and capillary pressure are principally functions of pore size, unevenly distributed cementation will make them less than they would be if the same volume of cement were evenly distributed.

We assume that an undersaturated solution takes up $CaCO_3$ from one place and, after moving through porous sediment, becomes supersaturated. Then it loses $CaCO_3$ as precipitated cement. Because of the slow movement of the formation fluid within the rock matrix, equilibrium is completely reached between the surfaces of the particles and the solution in contact with that surface. Weyl[28] presented experimental results that showed that the limiting factor of reaction is the rate of transport of ions by diffusion and convection away from the dissolving surface. Hasson *et al.*[9] also noted the importance of the rate of diffusion in controlling the rate of precipitation of $CaCO_3$ in their study of the growth of $CaCO_3$ scale in the water pipes of industrial heat exchangers.

Influence of saturation states and flow velocity on the amount of calcite precipitated

Fractures are nearly ubiquitous in rocks that have experienced even slight deformation and most of these are mineral filled. Their presence indicates that: (1) dilation of the rock took place for fractures to be both open and provide pathways for fluid flow and (2) fluid was present and perhaps moving during and after the deformation event, and it carried sufficient mass of fracture constituents in solution to precipitate in the observed fracture void space.[14]

The kinetics of calcite precipitation in subsurface environments is uncertain. Although extensive studies on

calcite reaction kinetics have been done in seawater,[16, 20, 21] the precipitation kinetics of calcite in fresher groundwater is largely unknown. The kinetic models of calcite dissolution and precipitation in seawater are too complex to be modeled with a simple first-order reaction model.[16] Several different processes are usually involved during calcite precipitation / dissolution reaction such as adsorption, diffusion and desorption. The precipitation kinetics of calcite is a high reaction order, surface controlled process (usually 1 < *reaction order* < 3). Morse and Machenzie,[19] proposed a coupled chemical kinetic-hydrodynamic model that applies to conditions similar to those that might exist during fracture filling by calcite. Their calculations showed that the rate of precipitation is related to the fluid flow rate as well as to the saturation state in a given subsurface system. This model may give basic information about both how much fluid is necessary and how much time is needed to fill up an open space in the subsurface. The work discussed here makes the estimates also.

Estimation of the expected time and amount of fluid for mineral filling in fractures has been a largely unresolved problem because of a lack of data on precipitation kinetics in subsurface environments. Fyfe *et al.*[8] and Fournier and Potter[7] have calculated the volume of fluid required to fill a quartz vein opening as a function of temperature change in an upward flowing fluid based on the temperature-solubility relationship of quartz. Fisher and Brantley[6] developed various models for quartz overgrowths in fractures related to episodic fluid migration. However, few attempts have been made for describing precipitation of fractures filled by calcite, especially in terms of precipitation kinetics.[18, 19] The precipitation kinetics of fracture-filling calcite is controlled by not only time and fluid volume required for the precipitation of a certain mass of fracture mineral, but also the precipitation pattern inside a fracture opening.[19] Identification of both chemical and physical parameters controlling the precipitation of calcite such as pressure, temperature, partial pressure of CO_2, flow velocity, and co-precipitating ions provides constraints on establishing conceptual models for calcite precipitation in fractures.[4, 5, 17, 20, 21]

By directly measuring the amount of calcite precipitation, Lee and Morse[13] showed that both the saturation state and fluid flow velocity are two very important factors influencing calcite precipitation in fractures. Controlled by high order reaction kinetics, the precipitation of calcite is influenced by flow velocity. Their experimental results gave the pattern and amount of precipitated calcite for fast and slow flow velocities at the same degree of saturation. At a faster flow velocity, aggregates of very fine-grained calcite overgrown with some intergranular space and the amount of calcite precipitation s less than at slow velocity. At the slow velocity, most of the inlet surface is covered with a precipitated calcite layer.

A major problem in understanding fracture filling is a realistic estimation of the volume of fluid and time required to fill a given fracture space. Several major factors influence the amount of calcite precipitated from a given volume of solution. At constant temperature and pressure, these factors include saturation state, partial pressure of CO_2, the activities of ions, relative concentrations of dissolved components, and presence of reaction inhibitors.[18] Based on the model by Lee *et al.,*[14] extremely large volumes of fluid are required to precipitate calcite at low saturation states. When fracture fills in the presence of fluid flow, either the fluid must be slightly supersaturated with respect to calcite or the flow velocity must be very fast to prevent uneven distribution of calcite along a fracture.

The distribution of calcite is also problematical. Large calcite-filled fractures should not occur if cracks and faults are simple fluid conduits.[19] Simple conduits should fill at the inlet, and effectively plug it to further fluid flow. In the field, this should appear as partially filled fractures. We have observed, however, that many field fractures are completely filled. Explaining the causes of this observation is another objective of this work.

Convection, diffusion and surface reaction in a fracture

Groundwater flow frequently causes cementation and dissolution. Cements of calcite, quartz, pyrite, dolomite or ankerite are often deposited within fractures. Partially cemented fractures are created if this cementation fails to completely and totally fill the fracture with cement or if subsequent dissolution leaches out some of the mineralization. In this way, a highly conductive fluid path can exist. In carbonates, fracture permeability can be created by similar processes or through the dissolution of the host rock on the fracture faces.

The kinetics of precipitation and dissolution

Relations used to describe precipitation and dissolution reaction rates usually describe the reaction of solid and aqueous components in the following way.

$$\tau T \underset{k}{\longleftrightarrow} \alpha A + \beta B \qquad (1)$$

Here k_1, the forward reaction rate constant, is for dissolution and k_2, the backward reaction rate constant, is for precipitation. The two aqueous components are A (*e.g.*, Ca^{2+}) and B (*e.g.*, CO_3^{2-}), and T (*e.g.*, $CaCO_3$) is a single-phase solid. The stoichiometric coefficients (α, β and τ) indicate the number of moles of each component in the reaction. The reaction is assumed to be elementary and reversible, and the rate law for component *T* in terms of the surface activities of the components, which is indicated by superscript *s*, is,

$$r_T = -k_1 (a_T^s)^\tau + k_2 (a_A^s)^\alpha (a_B^s)^\beta \qquad (2)$$

Supersaturation of solid *T* is defined as the state when the ion activity product (IAP) of its component in a solution is greater than what is allowed by *true equilibrium* or when r_T = 0. Supersaturation is quantified by a saturation index (SI), which is defined by SI = IAP/K_{sp}. For SI > 1, the solution is *supersaturated* and precipitation takes place.

Since the molal activity of component *j* is defined by the product of the ion concentration and the molal activity coefficient, SI can be expressed as

$$SI = \frac{(\gamma_A C_A)^{\alpha}(\gamma_B C_B)^{\beta}}{K_{sp}} \quad (3)$$

where γ, the average molal activity coefficient, is related to the ionic strength of the aqueous phase through several models.[26] When γ = 1 for all components, activities and concentrations become equal and the aqueous phase is an ideal solution. Consequently, change in SI is not the same as a change in the ion concentration product associated with dissolution or precipitation.

Several different mechanisms occur in a reaction between a solid and a solution. A typical sequence would be: diffusion of a reactant through a stagnant boundary layer to the surface, adsorption of the reactant on the surface, diffusion on the surface to a reactive or high energy site (such as a dislocation), reaction of the reactant with the solid, diffusion of products away from the reaction site, desorption of products, and the diffusion of products to bulk solution.[1] A basic idea in the study of reaction kinetics is that under a given set of conditions, one mechanism will be slower than the others. This step is then the *rate-controlling* mechanism. Generally, surface reactions are most important near equilibrium, while transport control of reaction rates becomes more important as distance from equilibrium increases.

Simple first-order reaction kinetics cannot be applied to the PD reaction for carbonate precipitation.[16] Therefore, the mineral precipitation rate has frequently been expressed by an empirical rate law[16] of the form

$$r_T = k_1(SI - 1)^n \quad (4)$$

where *n* is the empirical reaction order.

Inskeep and Bloom[10] conducted a series of calcite precipitation experiments to examine kinetic models. They concluded under their experimental conditions that calcite precipitation kinetics was best represented by a simple elementary reaction:

$$Ca^{2+} + CO_3^{2-} \leftrightarrow CaCO_3$$

Zhong and Mucci[30] presented the experimental results of calcite precipitation in seawater. From their measurements, when partial pressure of CO_2 is 0.0031atm and $C_{Ca^{2+}} \approx$ 10.5mmol/kg of seawater at 25°C, the calcite dissolution rate constant obtained in seawater is 0.29 μmol/m^2-hr.

Development of mathematical model

The surface condition associated with flow and precipitation / dissolution (PD) reaction is nonlinear because it usually depends on more than two ionic components. At least two mass-conservation equations are needed in PD problems, and these must be coupled at the fracture surface through the reaction rate term.[23] When the inlet concentration is greater than the equilibrium concentration, precipitation will occur by reaction at the fracture surface and subsequently decrease the fracture aperture. The cementation of carbonate is an example of crystal growth by precipitation. For dissolution, however, the aperture will increase.

Figure 1 shows a schematic diagram of flow and PD. The finite parallel plates shown represent a single fracture. When a solute flows between the plates, it diffuses to the solid surface where a PD reaction takes place. The reaction rate at the surface strongly influences the outlet solute concentration. The region outside of the plates is the reservoir matrix.

We simplify the problem by considering convective, diffusive mass transfer and reaction as an extended work of Wu.[29] Several assumptions are made such as (1) uniform initial concentrations, (2) uniform and constant temperature, (3) the PD reaction occurs only at the solid surface, (4) flow is single-phase, (5) the flow incompressible, laminar in the fracture, (6) only two reactive components are present and these occur in dilute concentrations, (7) convection occurs only in the z-direction (parallel to the fracture surface), and (8) diffusion occurs only in the x-direction (perpendicular to the fracture). Additional simplifications follow from assuming a dilute solution (6): concentrations and activities are equal, and diffusion coefficients are isotropic and independent of concentration. We further take the diffusion coefficient to be equal for all components.

We solve the transient flow and PD problem and investigate the change of aperture size with time. Early work on this problem[29] used a radial geometry such as tube flow. The mass conservation equations for the two species are,

$$\frac{\partial C_j}{\partial t} = -v_z \frac{\partial C_j}{\partial z} + D_j \frac{\partial^2 C_j}{\partial x^2}$$

$$0 \le x \le \delta(z,t),\ 0 \le z \le l,\ t > 0 \quad (5)$$

where *j* is the aqueous components *A* and *B*.

The x-direction fluid velocity distribution is represented by

$$v_z = \frac{3}{2}\left(\frac{q(t)}{2\delta(z,t)W}\right)\left[1 - \left(\frac{x}{\delta(z,t)}\right)^2\right] \quad (6)$$

where *l* is the length of a single fracture and *W* is the width of a fracture. Equation (6) implies that parabolic (laminar) flow occurs in the fracture at all values of the aperture size. A mass balance on mineral *T* at the fracture surface is

$$\frac{\partial \delta(z,t)}{\partial t} = -\frac{M_T}{\rho_T} r_T \quad (7)$$

Here M_T is the molecular weight and ρ_T is the density of solid *T*.

Realistic and practical boundary conditions are needed. We assume the total pressure drop (ΔP) across the fracture is constant throughout the simulation; this makes the volumetric flowrate decrease with time as the fracture fills. The average flux also decreases with time and this affects the interplay between the convective rate and the reaction rate.

Because of precipitation at the surface, the aperture size, $\delta(z,t)$, is a function of position and time. As indicated by Eq. (6), q(t) is not a function of position, and the flow velocity is large where the aperture size $\delta(z,t)$ is small and small where $\delta(z,t)$ is large. This phenomenon will be important to our results because the relative importance of reaction and flow with change along the fracture. The volumetric flow rate, q(t), the product of the aperture size, width and the average velocity, is independent of z, because of the incompressibility of the fluids. However, q(t) decreases with time because of the overall shrinkage of the aperture at constant pressure drop.

In a finite difference approximation, the flowrate is a constant within each segment of calculation time, even though it is time-dependent overall. For example, for the three grids in the domain shown in Figure 2, the dotted line is a possible fracture aperture distribution after a certain time. Since the precipitation reaction occurs only at the fracture surface, the fluid concentrations always decrease in the z-direction. A large concentration at the fracture surface causes more precipitation, Eq. (7), so that the aperture size in the high concentration portion (Region 1) is small. During the next time step, we calculate the local pressure gradient ($\Delta p(z,t)/\Delta z$) of each grid using successive substitution and based on the aperture size at the previous time levels.

$$\frac{\Delta p}{\Delta p_I}\left(\frac{\delta(z,t)}{\delta_I}\right)^3 = \text{constant}$$

With constant flow rate, Δp is inversely proportional to $\delta^3(z,t)$. If the aperture size of Region 1 is much smaller than Region 2 and 3, Δp_1 takes the most of the pressure drop ($\Delta p_1 \approx \Delta P$). In an extreme case, there is almost zero pressure drop and no fluid movement in Region 2 and 3, so that δ_2 and δ_3 remain constant and δ_1 still decreases.

Now we introduce dimensionless variables as follows:

$$C_{Dj} = \frac{C_j - C_{jI}}{C_{jJ} - C_{jI}} \qquad z_D = \frac{z}{l}$$

$$t_D = \frac{q_I t}{2\delta_I W l} = \frac{\delta_I^2 \Delta P}{3\mu l^2} t \qquad \delta_D = \frac{\delta(z,t)}{\delta_I}$$

$$x_D = \frac{x}{\delta(z,t)} \qquad q_D(t) = \frac{q}{q_I} = \Delta p_D \delta_I^3$$

$$\Delta p_D(z,t) = \frac{\Delta p(z,t)}{\Delta p_I} \qquad N_{Shj} = \frac{k_1 \delta_I}{D_j (C_{jJ} - C_{jI})}$$

$$N_{Pej} = \frac{q_I \delta_I}{2WlD_j} \qquad N_{Da} = \frac{2Wl}{q_I}\frac{M_T}{\rho_T} k_1$$

$$r_D = \frac{r_T}{k_1}$$

where $K_{sp}=k_1/k_2$ is the solubility product. ΔP is the constant overall pressure drop, and $\Delta p(z,t)$ is the local pressure drop. The dimensionless reaction rate, r_D, is positive for precipitation and negative for dissolution.

Using these dimensionless variables, Eq. (5) and (7) can be rewritten as,

$$\frac{\partial C_{Dj}}{\partial t_D} = -\frac{3}{2}\Delta p_D \delta_D^2 \left(1 - x_D^2\right)\frac{\partial C_{Dj}}{\partial z_D} + \frac{\mathbf{1}}{\delta_D^2 N_{Pej}}\frac{\partial^2 C_{Dj}}{\partial x_D^2},$$
$$0 \le x_D \le 1,\ 0 \le z_D \le 1 \qquad (8)$$

$$\frac{\partial \delta_{Dj}}{\partial t_D} = -N_{Da} r_D \qquad (9)$$

Therefore, we solve 3 partial differential equations, Eqs. (8) – (9), using the finite difference method. To solve these partial differential equations, we follow the general procedure of implicit, cell centered finite differencing in two-dimensional space to resolve the nonlinearity at boundaries of the fracture wall. The basic idea is to generate an expansion of the derivatives with respect to primary variables in the conservation equations. Discretization is performed in a rectangular grid system using one point upstream weighting scheme for the convection terms. The grid system distorts (the number of cells is constant) as the aperture decreases. For time and space discretization, an implicit finite difference method is used.[2, 22]

The concentration of the injected fluid can be determined from the saturation index. For example, the solubility product of the calcite precipitation reaction is $10^{-8.48}$, [26] so that the injected concentration (C_J) is 8.14×10^{-5}gmol/cm^3 with SI = 2 in these ideal solutions.

Results and discussion

The solution yields transient concentrations of the two components. The concentrations lead to a transient surface reaction rate along the fracture as a function of aperture size, inlet concentration and a set of dimensionless groups. Initially, the fracture, made of mineral *T*, is at equilibrium with aqueous components *A* and *B*. It is then disturbed by the injected aqueous solution containing components *A* and *B* that are supersaturated, so that the fracture is no longer at equilibrium. As we discuss the solution, we quantitatively compare the calculated results to those of Lee *et al.*[13] as a way of validating and confirming the conclusions of this work.

As discussed with Figure 1, higher concentrations will always occur at the center of the fracture because the fluid velocity is largest there. The large velocity will tend to carry the injected (unreacted) components the farthest. The smallest concentrations will occur at the fracture wall because (a) there is no flow (the no-slip condition) and (b) the reaction is taking place. A very large reaction rate will make the dimensionless concentrations at the surface approach zero. On the other hand, diffusion will tend to equalize the centerline and fracture

wall concentrations. The reaction at the fracture surface is always positive, causing a precipitate to form.

Figure 3 - Figure 5 show solution concentration profiles for component A with various N_{Sh}, N_{Pe} and time using SI = 10 and n = 1. The three-dimensional plots have concentration on the vertical axis and the space coordinates on the other two. Ranges of dimensionless concentrations are shown by the shading in the legend. The other lines on the surfaces are lines of constant z_D. The dimensionless groups are expressing the following ratios:

$$N_{Pe} = \frac{Convection\ rate}{Diffusion\ rate}, \qquad N_{Sh} = \frac{Reaction\ rate}{Diffusion\ rate}$$

Figure 3 shows that the concentration of component A changes in both the x- and z-directions with time. Since N_{Sh} is zero, there is no reaction in this case and the concentration profile is created only by convection and diffusion. The reaction-free cases should approach the so-called Taylor limit,[11, 12, 27] given a small enough N_{Pe} or a long enough flowing time.

As shown in Figure 4, a large N_{Sh} means higher reaction at the fracture surface, so that the concentration near the fracture wall decreases with N_{Sh} compared to Figure 3(b). Diffusion in the x-direction reduces the concentration of A at the center of the fracture. Figure 5 shows concentration profiles with various N_{Pe}. With large N_{Pe}, the concentration at the center of fracture is larger than that of Figure 4(a). Since the diffusion rate is relatively small, convection is the dominant process for this case, and the concentration at the fracture wall is not much different from that in Figure 4. When N_{Pe} is reduced to 10, the concentration gradient in x-direction becomes smaller as shown in Figure 5(b). This is because the x-directional mass transfer rate becomes much higher than the convective transport rate.

We now discuss the aperture size distribution in the z-direction. We characterize this flow with a Damkohler; N_{Da} is defined by

$$N_{Da} = \frac{Reaction\ rate}{Convection\ rate}$$

N_{Da} is calculated from N_{Pe} and N_{Sh} as shown above. A large Peclet number will lead to a small Damkohler number. It also causes relatively uniform precipitation reaction because a large concentration passes almost entirely through the end of the fracture under these conditions. That means the concentration gradient in the z-direction is small, which results in relatively uniform dimensionless reaction rate, and uniform filling of the fracture.

When the Damkohler number is large, the solid phase is everywhere in equilibrium with the flowing phase. This assumption is called the local equilibrium assumption (LEA). LEA is likely to occur in flow through porous media under typical pressure gradients of flow in a reservoir. However, the flow inside a fracture is not likely to satisfy LEA because the flow velocity is much larger compared to that in a matrix. For example, the flux in a fracture with 2 mm aperture is 3.38×10^7 times higher than 10 md rock matrix under the same constant hydraulic gradient.

Since the concentration gradient in the z-direction, though it can be small, is never exactly zero, there will always be a difference in aperture size between the inlet and outlet of the fracture. However, the remaining aperture size at the outlet will be small if the Peclet number is large. If the Sherwood number is large, there is also a high precipitation reaction by definition. This will show an aperture profile similar to the small Peclet number case.

As we discussed in Figure 2, the local pressure drops across each grid block change with decreasing aperture size even though the overall pressure drop is constant. Figure 6 shows the dimensionless pressure drop for each grid and velocity profiles associated with the aperture profile in Figure 7. Since the overall pressure difference is constant, there is a large pressure drop near the inlet when the aperture is relatively small. The flowrate being constant within each timestep causes a small pressure drop at the outlet. Since we have a small pressure drop and the low flux in the outlet region, the aperture changes slowly there.

Here we use as a time variable the pore volumes injected (PV), which is the cumulative volume of fluid running through the void space divided by the initial volume of the fracture. In this example, 1000 pore volume is equivalent to 0.49 hours of elapsed time assuming typical aperture sizes and hydraulic gradients. This value is similar to that reported experimental by Lee and Morse.[13]

Figure 7 - Figure 9 show three precipitation examples of fracture aperture profiles at different values of N_{Pe} and N_{Sh} with SI = 2 and n = 1. Since Figure 7 has a larger N_{Sh} than Figure 8, Figure 7 has more precipitation at the inlet. That causes a high concentration gradient along the flow direction and reduces the precipitation rate near the outlet of the fracture.

In Figure 7 - Figure 9, the aperture shrinks relatively uniformly at early time. After a certain amount of cementation, the flow rate of the injected supersaturated fluid decreases because of the constant overall pressure drop and the fracture inlet closes. However, with a large Sherwood number, shown in Figure 7, the excess mineral T is mostly created in a relatively short time period and the remaining aperture at the outlet, is larger than in Figure 8. As we discussed with Figure 2, a high reaction rate at the inlet will cause different pressure drops for each segment. The supersaturated fluid moves slower at large z.

Figure 9 shows an aperture distribution with large N_{Pe}, which means a higher flux or a larger initial aperture. In this figure, we have uniform precipitation along the z-direction until about 3 million pore volumes have passed through the fracture. Since the Damkohler number is 10 times smaller than that in Figure 8, we have the less reaction so that more pore volumes of supersaturated solution are needed for the same amount of cementation.

To get some idea about how reasonable the calculations are, we calculate some realistic values for the dimensionless groups. Zhong and Mucci[30] reported a calcite dissolution rate constant, $k_1 = 0.29$ μgmol / m^2 h (=8.06×10^{-14}gmol/cm^2 s) and an empirical reaction order of n = 3 in seawater. With those results, we calculate dimensionless numbers (N_{Pe}, N_{Sh} and N_{Da}) from the values shown in Table 1 for a test case.

Using these data, N_{Pe}, N_{Sh} and N_{Da} are calculated as 567.83, 3.38×10^{-5} and 5.25×10^{-11} respectively. The very small Damkohler number indicates that the flow is at an opposite extreme of local equilibrium assumption.

The aperture profile for these values is in Figure 10. As we have seen before, a large N_{Pe} and a small N_{Sh} create the low reaction rate on the fracture wall so that many 1000s of pore volumes are needed for the complete cementation of this fracture. This observation is consistent with those of Lee and Morse. [13] In circumstances in which fractures are completely filled, it appears that these conditions--large Peclet number and small Sherwood number (Damkohler number)--prevail.

From these results, we can determine the dominant process of each case from combinations of the initial and boundary conditions. In a convection-dominated process, which has a high fluid velocity, relatively uniform precipitation occurs because the concentrations at the fracture wall along the z-direction are almost same. Otherwise, it is reaction-dominated. To quantify how relatively uniform precipitation can occur, we can use the difference of an aperture size between the ends of the fracture.

Figure 11 shows a history of the aperture size differences between the inlet and the outlet of the fracture associated with Figure 10. Aperture size differences are very small (this means that the fracture is filling uniformly) and gradually increases until 18.4×10^9 pore volumes of the supersaturated fluid has been injected: then the difference increases rapidly.

As discussed above, uniform precipitation is an indication of a convection-dominated process. With a large Damkohler number or a small Peclet number, we will see a reaction-dominated result. In Figure 11, for example, there is a convection-dominated process before 18.4×10^9 PV, then the precipitation reaction becomes the controlling process. If we have a higher concentration of the injected fluid, which means a large SI, this curve moves to the left and has less curvature. A small SI, therefore, has the effect of making the process less reaction-dominated (more convection-dominated), which in turn makes the filling more uniform.

We obtain Figure 12 from a number of runs of various initial apertures, dip angles and saturation indexes. The curve represents critical pairs of N_{Pe} and N_{Da}. For example, in Figure 11, a Peclet number and a Damkohler number are recalculated using the average aperture at 18.4×10^9 PV. That aperture (*e.g.* $\delta_D = 0.035$ in this example) is critical for SI = 2 and a 10° dip angle. Since N_{Pe} is defined by convection rate over diffusion rate and N_{Da} as reaction rate over convection rate, we can present the upper right area as reaction-dominated. Otherwise, the flow is convection-dominated. This means that the upper right region of the Figure 12 would lead to nonuniform fracture filling and the lower left to uniform filling.

Summary and conclusions

Characterization of fractures is important to many reservoir engineering applications and field performance studies. Although outcrop study, core and well log data combined with seismic interpretation are used to describe fracture systems, the impact of those studies on reservoir fluid flow can only be assessed by reservoir performance data.

We present a mathematical model to simulate hydrodynamics and fluid-mineral reactions. The intent of this model is to show the time evolution of fracture aperture shrinkage patterns from PD reactions. The fluid convection, diffusion and PD reaction inside a finite space are solved as a simplified representation of natural fracture mineralization. The problem involves mass transfer within the fluid accompanied by chemical reaction at the fracture surface. Mass-conservation equations for each component in fluid are solved in this problem, and these are coupled with the chemical reaction at the fracture surface.

Some conclusions of this work are,

1. Concentration profiles along the fracture show that the high reaction rates at the fracture surface makes low concentration values there. A high Peclet number, which means a high convection rate, results in high and uniform concentrations along the fracture. When N_{Pe} is low, concentrations depend more on diffusion so that the concentration gradient in the x-direction becomes small.
2. Our predictions show that several thousands of pore volumes must pass through a fracture before it is complete filled. This is in qualitative agreement with observation.
3. The local equilibrium assumption implies the flowing phase is in equilibrium with the solid phase at all positions. For this to happen, the Damkohler number must be large. Large N_{Da} implies a large reaction constant or a small convection rate. Since we have large convection and small reaction in the previous example as shown in Table 1, the Damkohler number is small and this problem lies at the opposite extreme of local equilibrium flow.
4. The precipitation rate along the fracture becomes relatively uniform with a high Peclet number. As the aperture is closing, the fluid flux decreases because of a constant overall pressure drop assumption. Examples show the aperture size uniformly decreases until a critical value pore volumes injected occurs. When the aperture attains a critical value, the effect of convection is relatively small and the reaction becomes dominant. High reaction causes a rapid shrinkage at the inlet. Eventually the inlet of a fracture is closed and a partially cemented fracture is created. This model will never show a fully cemented fracture because cementation at the inlet is always greater than at the outlet.
5. Through this test case of calcite precipitation problem, we present a process of the fracture mineralization. With certain geologic conditions, the process can be classified as convection- or reaction-dominated using Peclet number and

Damkohler number. The model shows that to have a relatively uniform deposition of calcite within a fracture, the velocity of supersaturated solution must be very high or the solution must be only slightly supersaturated with respect to calcite.

The diagenetic processes of dissolution and partial cementation are key controls on the characterization of natural fractures within hydrocarbon reservoirs. Even with extensive data, the permeability of a fracture system still creates uncertainty in reservoir description. Study on the diagenetic events can provide explanation as to why, when and where natural fractures will be open and permeable.

Acknowledgements

We acknowledge the support of the Bureau of Economic Geology Fracture Research Consortium, the U.S. Department of Energy (Award No. DE-FC26-00BC15308), and several helpful insights from Dr. Jon E. Olson.

Nomenclature

T = Solid component
A, B = Aqueous components
α, β, τ = stoichiometric coefficients
r, k = reaction rate and rate constant
γ = molal activity coefficient
K_{sp} = solubility product
n = reaction order
v, q = velocity and flow rate of fluid
C = concentration
z, x = longitudinal and transverse coordinates
t = time
D = transverse diffusion coefficient
δ = aperture size
l, W = length and width of a fracture
ΔP, Δp = overall and local pressure drop
μ = viscosity
M, ρ = molecular weight and density
N_{Pe}, N_{Sh}, N_{Da} = Peclet, Sherwood and Damkohler number

Superscripts
s = at surface

Subscripts
I, J = initial and injection
j = component
D = dimensionless variable

References

1. Araque, A. (2001) Moldeling the effects of geochemistry on well impairment. Ph.D. dissertation, The University of Texas at Austin.
2. Aziz, K., and Settari, A. (1979) Petroleum reservoir simulation. Amsterdam: Elsevier.
3. Berner, R. A. (1978). Rate control of mineral dissolution under earth surface conditions. *Am. J. Sci.* 278, 1235–1252.
4. Burton, E. A. and Walter, L. M. (1987). Relative precipitation rates of aragonite and mg calcite from seawater: temperature or carbonate ion control? *Geology* 5, 111–114.
5. Dromgoole, E. L. and Walter, L. M. (1990). Inhibition of calcite growth rates by Mn^{2+} in $CaCl_2$ solutions at 10, 25, and 50 °C. *Geochim. Cosmochim. Acta* 54, 2991–3000.
6. Fisher, D. M. and Brantley, S. L. (1992). Models of quartz overgrowth and vein formation: deformation and episodic fluid flow in an ancient subduction zone. *J. Geophys. Res.* 97, 20043–20061.
7. Fournier, R. O. and II, R. W. P. (1982). An equation correlating the solubility of quartz in water from 25°C to 900°C at pressures up to 10,000 bars. *Geochim. Cosmochim. Acta* 6, 1969–1973.
8. Fyfe, W. S., Price, N. J., and Thompson, A. B. (1978). Fluids in the Earth's Crust. Amsterdam: Elsevier.
9. Hasson, D., Aviriel, M., Resnick, W., Rozeman, T., and Windreich, S. (1968). Mechanism of calcium carbonate scale deposition on heat-transfer surfaces. *Ind. Eng. Chem.* 7, 59–65.
10. Hill, A. C. and Thomas, G. W. (Dallas, Feb. 1985). A new approach for simulating complex fractured reservoir. paper SPE 13537 presented at the SPE reservoir simposium, 10–13.
11. Lake, L. W. and Hirasaki, G. J. (August 1981). Taylor's dispersion in stratified porous media, *Soc. Pet. Eng. J.*, 70-84.
12. Lake, L. W. (1989) Enhanced oil recovery. Prentice Hall, NJ.
13. Lee, Y. J. and Morse, J. W. (1999). Calcite precipitation in synthetic veins: implications for the time and fluid volume necessary for vein filling. *Chem. Geol*. 156, 151–170.
14. Lee, Y. J., Morse, J. W., and Wiltschko, D. V. (1996). An experimentally verified model for calcite precipitation in veins. *Chem. Geol*. 130, 203–215.
15. Lucia, F. J. (1999). Carbonate reservoir characterization. Germany: Springer-Verlag Berlin Heidelberg.
16. Morse, J. W. (1983). The kinetics of calium carbonate dissolution and precipitation, in carbonates: Mineralogy and chemistry, reviews, in mineralogy, ii. Mineralogical Society of America, Washington, DC edited by R. J. Reeder, 227.
17. Morse, J. W. and He, S. (1993). Influences of T, S and P_{CO_2} on the pseudo-homogeneous precipitation of $CaCO_3$ from seawater: implications for whiting formation. *Mar. Chem*. 41, 291–297.
18. Morse, J. W. and Machenzie, F. T. (1990). Geochemistry of Sedimentary Carbonates. Amsterdam: Elsevier.
19. Morse, J. W. and Machenzie, F. T. (1993). Geochemical constraints on $CaCO_3$ transport in the subsur-face. *Chem. Geol.* 105, 181–196.
20. Mucci, A. (1986). Growth kinetics and composition of magnesian calcite overgrowths precipitated from seawater: quantitative influence of orthophosphate ions. *Geochim. Cosmochim. Acta* 50, 2255–2265.

21. Mucci, A. and Morse, J. W. (1983). The incorporation of $Mg^{2+}$and Sr^{3+} into calcite overgrowth: influences of growth rate and solution composition. *Geochim. Cosmochim. Acta* 47, 217–223.
22. Noh, M. H. (1999) Fully coupled air-water flow model in unsaturated porous media, M.S. thesis, The University of Texas at Austin.
23. Noh, M. H. (in progress) Geochemical modeling of naturally fractured reservoir. Ph.D. dissertation, The University of Texas at Austin.
24. Nordstrom, D. K. and Munoz, J. L. (1994). Geochemical Thermodynamics. Oxford, England: Blackwell Scientific Publications.
25. Schmoker, J. W., Krystinic, K. B., and Halley, R. B. (1985). Selected characterristics of limestone and dolomite reservoirs in the united states. *AAPG Bull.* 69(5), 733–741.
26. Stumm, W. and Morgan, J. (1996). Aquatic Chemistry. New York: John Wiley & Sons, Inc.
27. Taylor, G. (1953). Dispersion of soluble matter in solvent flowing slowly through a tube, *Proc., Roy. Soc. London*, 219, 186-203.
28. Weyl, P. K. (1958). The solution kinetics of calcite. *J. Geol.* 66, 163–176.
29. Wu, G. (1992). Pore network evolution induced by interaction between minerals and migrating fluids. Ph.D. dissertation, The University of Texas at Austin.
30. Zhong, S. and Mucci, A. (1993). Calcite precipitation in seawater using a constant addition techniques: a new overall reaction kinetic expression. *Geochim. Cosmochim. Acta* 57, 1409–1417.

Tables

Table 1: Data for test cases

Parameter	Value
Number of grids	10×10 in x, z
Fracture length, l	100 [cm]
Fracture width, W	20 [cm]
Initial aperture size	0.1 [cm]
Dip angle, β	10°
Overall pressure drop, Δ P	17035 [dyne/cm^2]
Fluid flux	56.78 [cm/s]
Density, ρ_T	2.71 [g/cm^3]
Molecular weight, M_T	100 [g/gmol]
Viscosity, μ	1 [mPa-s]
Diffusion coefficient, D	10^{-5} [cm^2/s]
Reaction rate constant, k_1	8.06×10^{-14} gmol/cm^2 s
Empirical reaction order, N	3 ± 0.05
Saturation index, SI	2

Figures

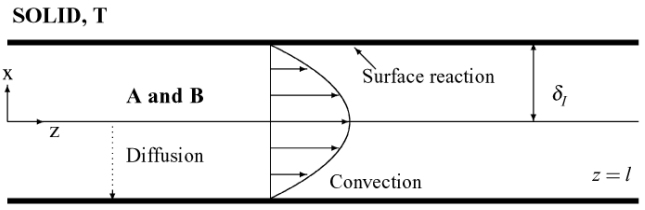

Figure 1: Schematic picture of precipitation/dissolution reaction in a single fracture

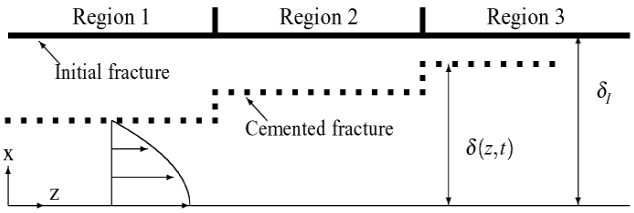

Figure 2: Fracture shape with precipitation

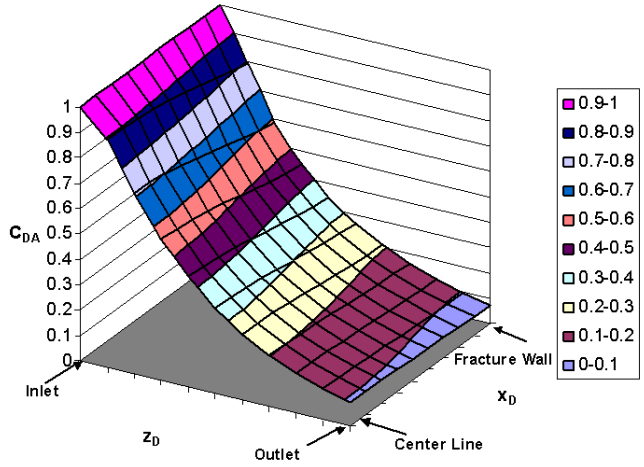

(a) $t_D = 0.5$

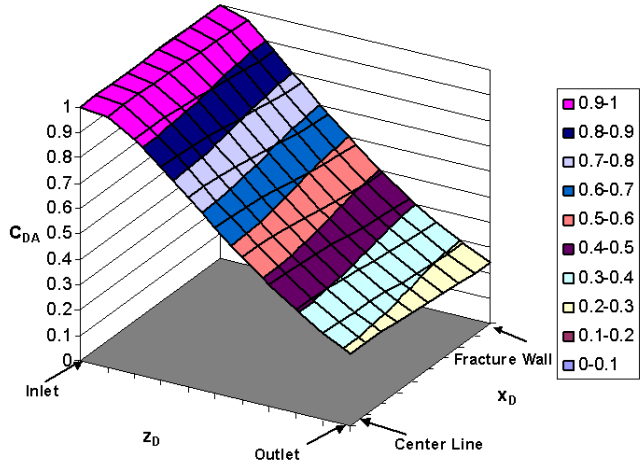

(b) $t_D = 1$

Figure 3: Concentration profile with $N_{Pe} = 100$, $N_{Sh} = 0$

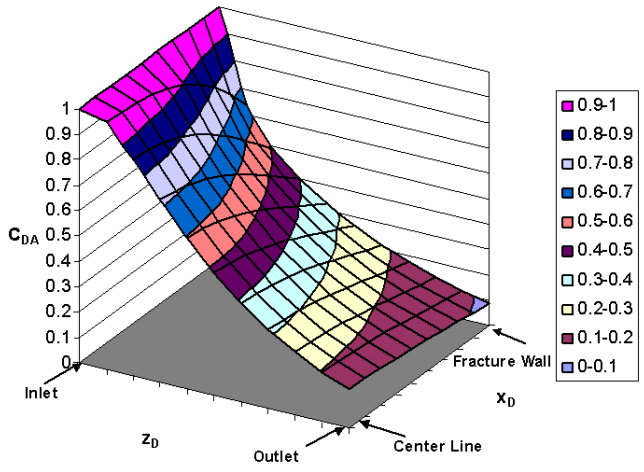

(a) $N_{Pe} = 100$, $N_{Sh} = 2$

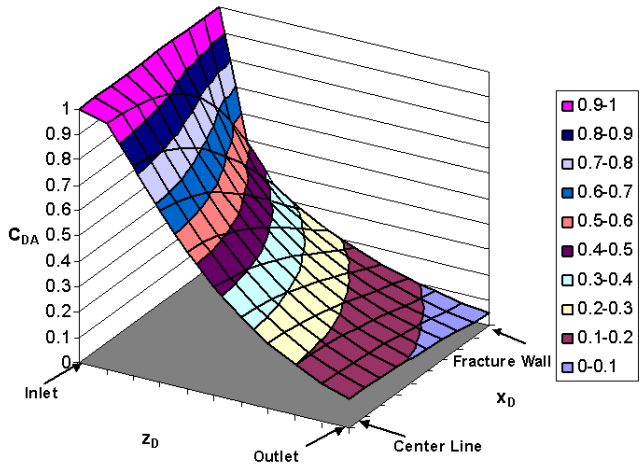

(b) $N_{Pe} = 100$, $N_{Sh} = 4$

Figure 4: Concentration profile with various N_{Sh} at t_D = 1 pore volume of supersaturated fluid injected

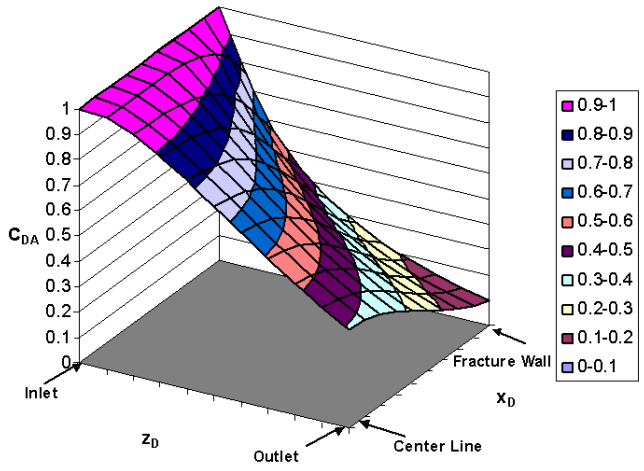

(a) $N_{Pe} = 1000$, $N_{Sh} = 2$

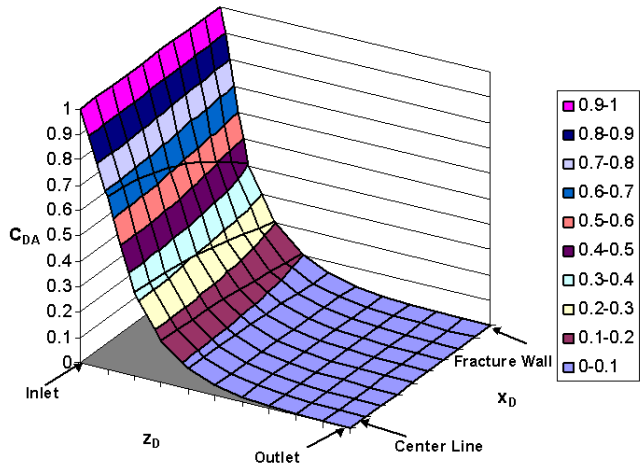

(b) $N_{Pe} = 10$, $N_{Sh} = 4$

Figure 5: Concentration profile with various N_{Pe} at t_D = 1 pore volume of supersaturated fluid injected

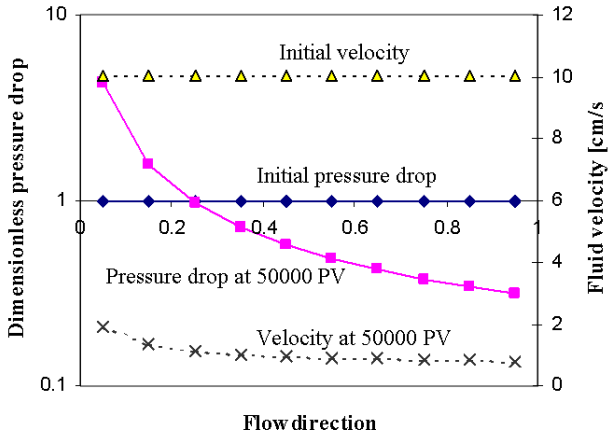

Figure 6: Dimensionless pressure drop and velocity profile with $N_{Pe} = 100$, $N_{Sh} = 2$

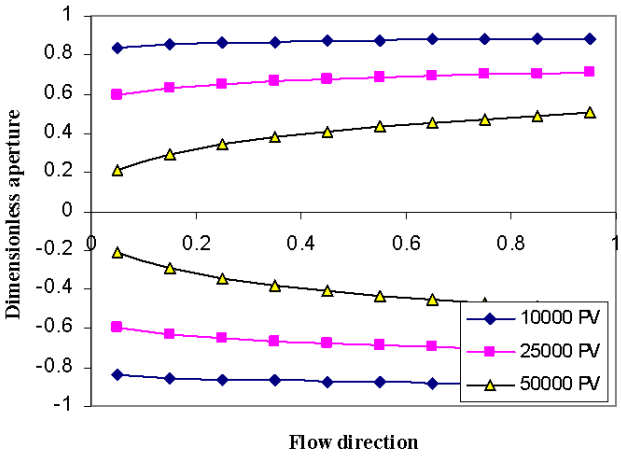

Figure 7: Dimensionless aperture profile with $N_{Pe} = 100$, $N_{Sh} = 2$

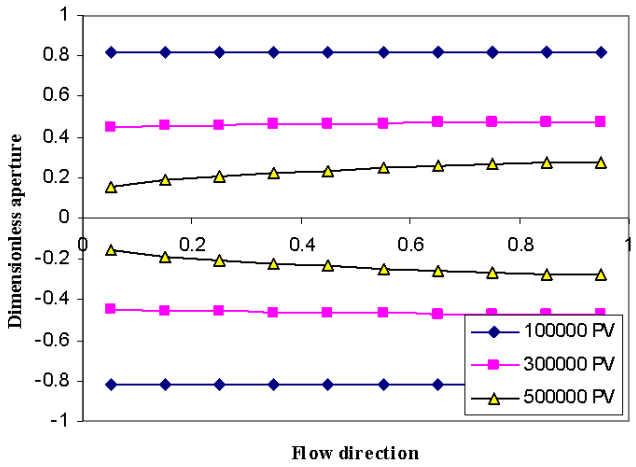

Figure 8: Dimensionless aperture profile with N_{Pe} = 100, N_{Sh} = 0.2

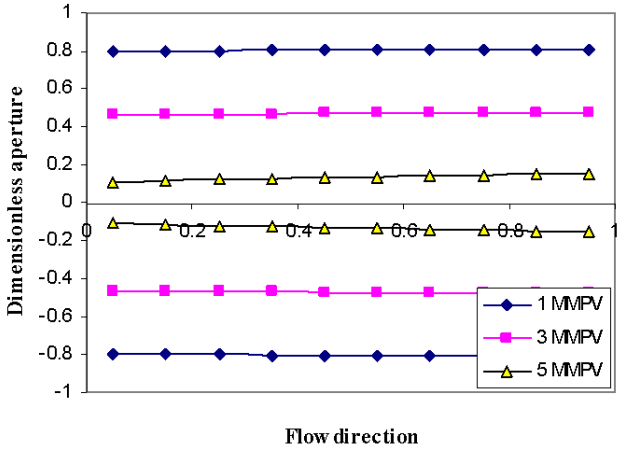

Figure 9: Dimensionless aperture profile with N_{Pe} = 1000, N_{Sh} = 0.2

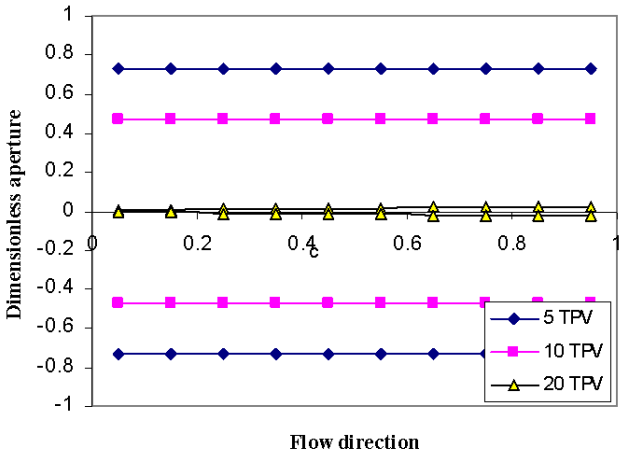

Figure 10: Dimensionless aperture profile with N_{Pe} = 567.83, N_{Sh} = 3.38×10^{-5}

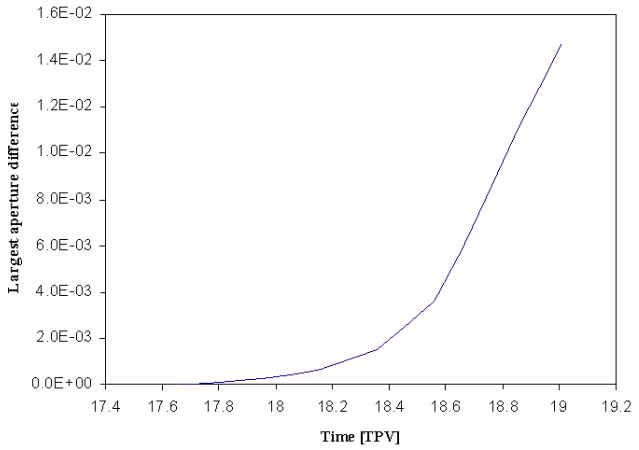

Figure 11: Largest aperture difference history with N_{Pe} = 567.83, N_{Sh} = 3.38×10^{-5}

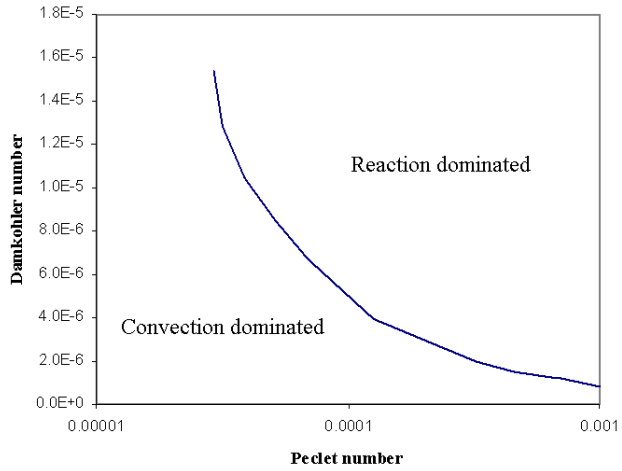

Figure 12: Boundary of convection dominant vs. reaction dominant process

A paper presented at the

Naturally Fractured Reservoir Conference

June 3-4, 2002
Oklahoma City, Oklahoma

Sponsored by the

University of Oklahoma

and the

Oklahoma Geological Survey

Presented at: Naturally Fractured Reservoirs Conference, Oklahoma City, OK, sponsored by University of Oklahoma and Oklahoma Geological Survey, Jun 3-4, 2002.

Modeling Coupled Fracture-Matrix Fluid Flow in Geomechanically Simulated Fracture Networks

Zeno G. Philip, James W. Jennings, Jr., Jon E. Olson, Jon Holder, The University of Texas at Austin

Abstract

In conventional reservoir simulations, grid block permeabilities must frequently be assigned values systematically larger than those observed in core measurements to obtain reasonable history matches. Even then, accuracy with regard to some aspects of the performance such as water or gas cuts, breakthrough times, and sweep efficiencies may be inadequate. In some cases this could be due to the presence of substantial flow through natural fractures unaccounted for in the simulation. In this paper we present a numerical investigation into the effects of coupled fracture-matrix fluid flow on grid equivalent permeability.

A fracture mechanics based crack growth simulator, rather than a purely stochastic method, was used to generate fracture networks with realistic clustering, spacing and fracture lengths dependent on the Young's modulus, the subcritical crack index, the bed height and tectonic strain. Coupled fracture-matrix fluid flow simulations of the resulting fracture patterns were performed using a finite-difference simulator to obtain equivalent permeabilities that can be used in a coarser scale flow simulation. Fractures were represented in finite-difference simulators both explicitly as grid cells and implicitly using non-neighbor connections between grid cells.

The results indicate that even though fracture permeability is highly sensitive to the fracture aperture, the computed equivalent permeabilities are more sensitive to fracture patterns and connectivity. The effects of diagenetic cements completely filling smaller aperture fractures and partially filling larger aperture fractures were also studied.

Introduction

High-permeability fracture networks in a matrix system can create high-conductivity channels for the flow of fluids through a reservoir, producing larger flow rates and therefore larger apparent permeabilities. The presence of fractures can also cause earlier breakthrough of the displacing fluid and lead to poorer sweep efficiencies in displacement processes. A better understanding of reservoir performance in such cases may be obtained by including the details of the fluid flow in fractures in a coupled fracture-matrix reservoir flow model.

It is impossible to accurately quantify interwell fracture network geometries in sufficient detail to directly model their effect on reservoir behavior. Thus, most modeling approaches have been statistical, using data from outcrop and well-bore observations to determine distributions for fracture attributes such as fracture length, spacing, and aperture to randomly populate a field. In this paper we present a geomechanics-based approach where a model of the fracturing process is used in predicting fracture characteristics.

Opening mode (mode 1) fractures propagate in a plane perpendicular to the least compressive stress.[1] Such fractures may propagate when the fluid pressure inside them exceeds the local least compressive stress or when the local stress becomes tensile. Although this is a necessary condition for fracture propagation, it is not sufficient. Fracture propagation from an existing flaw also requires a sufficiently large stress intensity factor, K_I, to exceed the rock's fracture strength. The mode I stress intensity factor, K_I, for a uniformly loaded isolated crack of length $2c$ is defined as

$$K_I = \Delta\sigma_I \sqrt{\pi c} \quad \text{..... (1)}$$

and

$$\Delta\sigma_I = P_p - \sigma_{min}, \quad \text{..... (2)}$$

where $\Delta\sigma_I$ is the driving stress, P_p is the pore pressure in the rock, and σ_{min} is the in situ least compressive stress.

Material failure typically occurs when the stress intensity factor is greater than a quantity defined as the critical stress intensity factor, K_{IC}, also known as the fracture toughness. This is called critical crack propagation. However, in cases of long-term loading in corrosive or liquid-saturated environments, cracks have been known to propagate at stress intensities much below the critical stress intensity but above a minimum threshold value[2], $K_I^* \sim K_{IC}/10$. This type of fracture propagation, called subcritical crack growth, is thought to be representative of most natural fracturing processes in subsurface rocks[2,3,4]. The velocity of subcritical crack propagation is much slower than that for critical crack propagation and has been observed to follow an empirical power law,

$$V = V_{\max}\left(\frac{K_I}{K_{IC}}\right)^n, \quad \text{..... (3)}$$

where V_{max} is the maximum (critical) propagation velocity at $K_I = K_{IC}$, and n is the subcritical crack index.

As the cracks grow they continually change the stress field in the region. Thus subcritical crack growth coupled with interactions among cracks can lead to different fracture patterns in rocks with different mechanical properties even though the starting fracture patterns are identical.[5,6] Details of the final fracture patterns for a given strain depend on the bed height, critical stress intensity factor, subcritical index and rock Young's modulus.[7,8]

Geomechanical Simulation:
Case Study of the South Wasson Clear Fork reservoir

Although fracture initiation in rock is often non-linear[9], linear elastic fracture mechanics is a good approximation when the fracture length is large relative to the inelastic process zone at the fracture tip.[5] A linear elastic fracture mechanics based crack growth simulator based on the boundary element method[8] was used in the present study. The subcritical crack index has been measured with the dual-torsion-beam apparatus[10,11] for samples from six representative layers of the South Wasson Clear Fork (SWCF) reservoir.[12] The results are presented in table 1.

In these measurements, the subcritical crack index varies from 40 to 80. These two extreme values have been used in the case study. A Young's modulus of 40,000 MPa for this formation was estimated from a typical porosity of 10 percent using a published correlation for dolomites. The geometric mean of the apertures observed from the outcrop is 0.212 mm and was used in constraining the strain applied to the reservoir bed. Typical thicknesses for rock-fabric flow layers in the SWCF field are 5 m and 10 m.[13]

Four case scenarios were studied combining two bed heights, 5 m and 10 m, and two subcritical crack indices, 40 and 80. Other geomechanical simulation parameters used to generate the fracture patterns are presented in table 2. For each case, 7 different realizations were studied, each realization with a different set of random starter cracks (flaws). Thus a total of 28 different geomechanical simulations were performed, each producing a series of fracture patterns for a sequence of increasing strains. Final fracture patterns obtained for one of the realizations (realization 3), for each of the four cases, are presented in **Fig. 1**.

Flow Simulation

The geomechanical simulation produces a list of fractures represented by patches with location and aperture information. Each fracture is made up of a series of patches lying end to end. A fracture can therefore have varying apertures along its length. The fractures have been constrained to grow in only one direction, i.e., the x direction (East-West). They can therefore, be represented easily in a finite difference simulator. Two methods have been used for this purpose - explicit fracture representation and using non neighbor connections (NNC).

Explicit Fracture Representation

The flow area is divided into grid cells with the same resolution as the geomechanical simulation. Each patch from the geomechanical simulation can be represented by one grid cell in the flow simulation. In this study the geomechanical simulation was 50 x 50 m square and the patches were 0.1 m in length. Thus there were 500 x 500 = 250000 cells of equal x and y dimensions (0.1 m). The z direction cell size was 0.5 m.

The permeability of a fracture patch, k_{frac}, with uniform aperture w (**Fig. 2**), can be computed using the parallel plate law[14]

$$k_{frac} = \frac{w^2}{12} \quad \text{..... (4)}$$

The permeability of a cell in the flow simulation, containing a fracture patch and matrix of permeability k_{mat} can be computed as

$$k_{cell} = \frac{\left(k_{frac} w + k_{mat}\left(\Delta y - w\right)\right)}{\Delta y} \quad \text{..... (5)}$$

where Δy is the width of the simulation cell perpendicular to the flow direction. A matrix permeability of 1 md was used for all flow simulations.

Thus, each cell in the flow simulation was assigned a unique permeability on the basis of the location and aperture of the patches. The y and z direction permeabilities were unchanged because the geomechanical simulations were constrained to produce fractures in only the x direction.

Non-neighbor Connections

Flow through fractures can also be modeled using non-neighbor connections (NNC) in a traditional finite difference simulator.[15] In this approach, the fractures are assumed to have infinite conductivity, making fracture aperture information irrelevant. The flow area is gridded such that the fractures lie at the boundaries between grid cells. The matrix flow transmissibility in the x direction, $T_{x(mat)}$, between any two grid cells is

$$T_{x(mat)} = \frac{k_x A_x}{\Delta x}, \quad \text{..... (6)}$$

where A_x is the area perpendicular to flow in the x direction, ($\Delta y \Delta z$), and k_x is the permeability in the x direction (**Fig. 3**). If there is a fracture between the cells as shown in Fig. 3, an additional transmissibility for fracture flow, $T_{x(frac)}$, can be assigned using

$$T_{x(frac)} = \frac{k_y A_y}{2\left(\Delta y / 2\right)} = \frac{k_y A_y}{\Delta y}, \quad \text{..... (7)}$$

where A_y is the area perpendicular to flow in the y direction, ($\Delta x \Delta z$), and k_y is the permeability in the y direction. The total x direction transmissibility, $T_{x(total)}$, accounting for both matrix and fracture flow, is therefore,

$$\begin{aligned} T_{x(total)} &= T_{x(mat)} + T_{x(frac)} \\ &= \frac{k_x A_x}{\Delta x} + \frac{k_y A_y}{\Delta y} \end{aligned} \quad \text{..... (8)}$$

The transmissibility between adjacent cells due to matrix flow is computed automatically by the simulator, connecting cell i to cells i-1 and i+1. The transmissibility between cells due to fracture flow can be entered explicitly using NNC, connecting cell i to cells i-1 and i+1 as well as to all other cells on that same fracture. The NNC transmissibility between cell i and its neighbors i-1 and i+1 is in addition to that due to matrix flow. Thus, a fracture extending between cells 1 and m connects cell 1 to cells 2 through m, cell 2 to cells 3 through m, and so on. The total number of NNC per fracture is

$$\left(\frac{m(m-1)}{2}\right)2 = m(m-1) \quad \text{..... (9)}$$

The multiplication by 2 accounts for cells on both sides of the fracture. A fracture between rows 1 and 2 extending from cells 1 to *m* results in the following non-neighbor transmissibilities for connections between cell 1 and the others in row 1:

$$T_{1,2}, T_{1,3}, ..., T_{1,m(frac)} = \frac{k_y \Delta x \Delta z}{\Delta y} \quad \text{..... (10)}$$

Likewise the non-neighbor transmissibilities between cell 2 and cells 3 through *m* are

$$T_{2,3}, T_{2,4}, ..., T_{2,m(frac)} = \frac{k_y \Delta x \Delta z}{\Delta y}, \quad \text{..... (11)}$$

and so on, for cells 3 through *m*. The transmissibilities for cell connections in row 2 are computed similarly.

A finite difference simulator, Eclipse 100,[16,17] was used to perform 2-D, single-phase flow simulations. Constant pressure boundaries were maintained on two opposing sides while the other two sides were no-flow boundaries. Constant pressure was maintained by assigning to each of the cells on a particular side producing wells on pressure control, and to each of the cells on the opposing side injector wells on pressure control. Thus the number of producers and injectors was each equal to the number of rows in the flow grid. The flow simulation was performed till a steady-state flow rate, q, was obtained. Knowing q, the pressures at both the ends, (P_1 and P_2), the distance between the constant pressure conditions, (L - (2(Δx)/2)), and the fluid properties, one can obtain an equivalent permeability for the fractured grid as follows,

$$k_{eqv} = \frac{q\mu(L-\Delta x)}{A(P_1 - P_2)}, \quad \text{..... (12)}$$

where μ is the fluid viscosity, and A, is the area perpendicular to flow, (i.e. the product of Δy, Δz, and the number of cells in the y direction.) The equivalent permeability can also be expressed in dimensionless form using an equivalent permeability ratio, R_k,

$$R_k = \frac{k_{eqv}}{k_{mat}} \quad \text{..... (13)}$$

Verification

The equivalent permeability estimates from the single-phase flow simulations using both methods, i.e., explicit fracture representation and NNC were verified by comparison with an analytical solution for flow through a staggered, periodic array of infinite conductivity fractures.[18,19] For such an array (**Fig. 4**) an analytical solution for the equivalent permeability ratio, R_k, as a function of the fracture array spacing, h, and half-length, (1-α)W, is presented in **Fig. 5**.

Results of the comparison between the analytical solution and simulation results for two array scenarios are presented in **Fig. 6** and **Fig. 7**. For the explicit fracture case (Fig. 6), the simulation results approach the analytical solution as the fracture aperture increases. For the NNC case (Fig. 7) the simulation results approach the analytical solution as the grid resolution increases.

Flow Modeling of Simulated Fracture Networks:

Results and Discussion

In this section we present results obtained using the explicit fracture representation method. The NNC approach yielded similar results for one set of realizations studied, with the equivalent permeability ratios being approximately 30 % larger. However, the CPU run time and memory requirements were approximately 30 times and 3 times larger, respectively. Moreover, fracture aperture information cannot be incorporated using the NNC method. So we prefer the explicit fracture approach.

Values of the equivalent permeability ratio, R_k, vs. strain obtained for each of the runs and for the individual bed heights of 5 m and 10 m are plotted in **Fig. 8**. The means and standard deviations of R_k from the seven realizations for each of the four combinations of bed height and subcritical crack index are also shown in **Fig. 9**. Although there appears to be a fairly large degree of variability between the realizations, there is a definite segregation in the R_k values based upon both the bed height and the subcritical crack index. In subsequent analysis and figures, we shall be referring to the average of the seven realizations.
In Fig. 9, the effect of strain on the equivalent permeability is evident. As expected, an increase in the strain causes an increase in R_k. The first significant fractures appear at a strain of 2.0E-5 for the subcritical crack index of 40, but at a larger strain of 3.2E-5 for the index of 80 because the larger subcritical crack index produces a smaller crack propagation velocity. Therefore, visible crack growth is delayed, and the stresses are also released at a lower rate for the larger index. Further, since the velocity of propagation is larger for the smaller index, for a given strain, the total fracture length is also larger for the smaller index. Thus, for other conditions remaining the same, R_k is larger for the smaller index than for the higher index.
It is also evident from Fig. 9 that for a given index, the rate of increase in R_k with strain is higher for the bed height of 5 m than for 10 m. This is because for thinner beds at a particular strain, a larger number of starter flaws develop into fractures, leading to a larger total fracture length. Thinner beds have a smaller volume for energy dissipation compared to thicker beds. Hence for a given strain, more fractures are formed in thinner beds.

For each combination of bed height and index and for each strain level, the average total fracture length of seven realizations was computed. As expected, the equivalent permeability ratio, R_k, increases with the total length (**Fig. 10**). However, for the same total fracture length, the case with the subcritical index of 40 has a higher R_k than that with an index of 80. This is because for the index of 40, the fractures have a larger mean length than for the index of 80. As visible crack growth is delayed for the larger index, when cracks eventually do start to form, more cracks tend to grow at the same time, leading to a smaller mean length.

Further, we see in Fig. 10 that there is no strong dependence of R_k on the bed height for a given total fracture length. The larger R_k for a smaller bed height at a given strain (Fig. 9) was due to the larger fracture length at that strain.

To study the effect of the mean aperture on R_k, the flow simulations were repeated for a set of 7 realizations of fracture networks with the permeability of the fracture cells increased by a factor of 10. The average R_k values, however, increased by only a factor of 1.06. Thus, the equivalent permeability ratio is not very sensitive to the fracture aperture in cases without a strongly interconnected fracture network, such as those investigated in this study. The reason for this is that fracture permeability is usually already so much larger (on the order of hundreds of Darcies) than the matrix permeability (on the order of millidarcies) that the overall resistance to flow is controlled more by the permeability and geometry of the matrix flow paths between the fractures, than by the permeabilities of the fractures themselves. This observation is also supported by the fact that the NNC approach which assumes infinite conductivity fractures, yields equivalent permeability ratios that are only 30 % higher than those obtained using the explicit fracture representation.

Other Factors Affecting Fractured Grid Permeability

In the subsurface, over geologic time scales, carbonate, quartz or other cement often precipitates on the fracture walls, thus reducing the fracture aperture available for flow.

Synkinematic Cement

Cement that is precipitated contemporaneous with fracture propagation is called synkinematic cement[20]. Observations suggest that fractures below a certain aperture size, termed the emergent threshold, e_t, are completely closed with cement. Fractures with larger apertures are only partially filled and can still conduct flow. To estimate the effect of this fracture mineralization process on permeability the aperture in each fracture patch was reduced by a constant amount. An emergent threshold ratio, e_r, is defined

$$e_r = \frac{e_t}{w_{gm}}, \quad \text{..... (14)}$$

where w_{gm} is the geometric mean of the simulated apertures.

The effect of the emergent threshold was studied on a sample run (realization 4) with a bed height of 10 m and subcritical crack index of 40. The emergent threshold ratio was varied from 0 (that is, no reduction in aperture) to 2. The equivalent permeability ratio, R_k, was computed for each case. It is evident that as the emergent threshold increases, R_k decreases (**Fig. 11**). However, this decrease in R_k is not so much due to the fact that the fracture apertures got smaller as to the fracture length reduction resulting from some fracture segments becoming completely filled. Fracture patterns for an emergent threshold ratio, e_r, of 0 and 2 are shown in **Fig. 12** and **Fig. 13**.

Postkinematic Cement

In some cases, cement is precipitated after fractures are formed and it is called postkinematic cement[20] This cement fills in all kinds of porosity including fracture porosity. Postkinematic cement is typically more heterogeneously distributed than synkinematic cement, so we estimated it in our reservoir simulations by applying it randomly to the fractures. The number of fractures eliminated from the flow simulation (i.e., fractures that were completely closed by postkinematic cement) was determined based on thin section microfracture data[21] (table 3). The partly filled fractures were treated as fully open in case 1 and as fully closed in case 2. Thus, for case 1, we obtained a microfracture percentage filling of 44 % (i.e., 16/36) and for case 2 we obtained a microfracture percentage filling of 78 % (i.e., (16+12)/36). The modified fracture patterns obtained for both cases are shown in **Fig. 14** and **Fig. 15**. Increased levels of postkinematic cementation also reduce total fracture length. The equivalent permeability ratio subsequently reduces with an increase in postkinematic cement (**Fig. 16**).

Conclusions

The equivalent permeability ratio increases with total fracture length and mean fracture length. For a given strain, beds having a lower subcritical index tend to have a higher equivalent permeability because they tend to have fractures with larger mean lengths.

The equivalent permeability of a weakly connected fracture network is not very sensitive to the fracture aperture. It is more sensitive to the fracture pattern. Equivalent permeability is also highly sensitive to fracture filling by synkinematic and postkinematic cements. Both types of cement close a portion of the fracture network, reducing the equivalent permeability by increasing the proportion of flow through the matrix.

This study indicates that the equivalent permeability in the SWCF reservoir is enhanced by a factor of between 2 and 10 due to the presence of fractures. This is substantially lower than the 1,000 or 10,000 fold increase that one would expect by assuming that all fractures completely cross the flow area of interest.

In future studies, careful observations of fracture patterns, i.e., details of how connected they are, are needed to meaningfully include the presence of fractures in reservoir modeling. Aperture information is not critical, except for modeling the effects of fracture filling by synkinematic cement.

Nomenclature

Variables

K_I = mode 1 stress intensity factor
K_{IC} = mode 1 critical stress intensity factor or material fracture toughness
$\Delta\sigma$ = driving stress, differential
P = pressure
σ = compressive stress
V = velocity of crack propagation
n = subcritical crack growth index
m = number of matrix cells in a row touching a particular fracture
c = half length of fracture
k = permeability
R_k = equivalent permeability ratio
T = transmissibility between two matrix cells
L = Length of flow region
w = fracture aperture
W = distance between midpoints of two adjacent fractures in the Chirlin staggered fracture array

α = fraction of W comprised of the matrix portion
h = perpendicular distance between two adjacent fractures in the Chirlin staggered fracture array
A = area perpendicular to flow
e_t = emergent threshold
e_r = emergent threshold ratio
Δx = dimension of grid cell in x direction
Δy = dimension of grid cell in y direction
Δz = dimension of grid cell in z direction

Subscripts

i = cell index
$frac$ = fracture
mat = matrix
eqv = equivalent
gm = geometric mean
x = x direction
y = y direction
z = z direction
p = pore
max = maximum
min = minimum
$cell$ = fracture cell

Acknowledgements

We thank Dr. Steve Laubach and Mr. F. Jerry Lucia of the Bureau of Economic Geology, The University of Texas at Austin, for valuable advice regarding the cementation parameters and geology of the South Wasson Clear Fork reservoir. This paper was prepared with the support of the U.S. Department of Energy, under Award No. DE-AC26-98BC15105 and DE-FC26-OOBC15308. However, any opinions, findings, conclusions, or recommendations expressed herein are those of the authors and do not necessarily reflect the views of the DOE.

Corresponding author

Jon E. Olson, Associate Professor
The Department of Petroleum and Geosystems Engineering
The University of Texas at Austin
jolson@mail.utexas.edu

References

1. Lawn, B.R., and Wilshaw, T.R., *Fracture of Brittle Solids*, Cambridge, Cambridge University Press, 204 p, 1975
2. Segall, P., “Formation and Growth of Extensional Fracture Sets”, *Geol. Soc. Am. Bull*., 95, 454-462, 1984
3. Atkinson, Barry Kean "Subcritical Crack growth in Geological Materials," *J. of Geophysical Research*, **Vol 89, No. B6**, pp 4077-4114, June 10, 1984
4. Atkinson, B.K., and Meredith, P.G., “The theory of subcritical crack growth with applications to minerals and rocks,” *Fracture Mechanics of Rock*, edited by B. K. Atkinson, pp. 111-166, Academic, San Diego, Calif., 1987
5. Olson, Jon E., “Joint Pattern Development: Effects of Subcritical Crack Growth and Mechanical Crack Interaction,” *Journal of Geophysical Research*, **Vol. 98, No B7**, pp 12,251-12,265, July 10, 1993.
6. Renshaw, Carl E., "Influence of Subcritical fracture growth on the connectivity of fracture networks," Water Resources Research, Vol 32, no 6, pp 1519-1530, June 1996
7. Olson, Jon E., Yuan Qiu, Jon Holder and Peggy Rijken, " Constraining the Spatial Distribution of Fracture Networks in Naturally Fractured Reservoirs using Fracture Mechanics and Core Measurements", presented at the 2001 SPE Annual Technical Conference and Exhibition held in New Orleans, Louisiana, 30 Sept-3 Oct 2001
8. Olson, J. E., "Fracture mechanics analysis of joints and veins," Ph.D. dissertation, 174 pp., Stanford Univ., Stanford, Calif., 1991.

9. Ingraffea, A.R., "Theory of Crack initiation and propagation in rock, *Fracture Mechanics of Rock*, edited by B. K. Atkinson, pp71-110, Academic, San Diego, Calif, 1987
10. Williams, D. P. and Evans, A.G., "A Simple Method for Studying Slow Crack Growth," *Journal of Testing and Evaluation, JTEVA*, **Vol. 1, No. 4,** July 1973, pp. 264-270.
11. Pletka, B.J., Fuller, E.R., Jr., and Koepke, B.G., "An Evaluation of Double-Torsion Testing – Experimental," Fracture Mechanics Applied to Brittle Materials. ASTM STP 678, S. W. Freiman, Ed., American Society for Testing and Materials, 1979, pp. 19-37
121. Holder, Jon, Jon E Olson and Zeno Philip, "Experimental determination of subcritical crack growth parameters in sedimentary rock," *Geophysical Research letters*, **Vol 28, No 4**, pp 599-602, Feb 15, 2001
13. Lucia, Jerry F. and James W. Jennings, "Calculation and Distribution of Petrophysical Properties in the South Wasson Clear Fork Field", Integrated Outcrop and Subsurface Studies of the Interwell Environment of Carbonate Reservoirs; Clear Fork (Leonardian-Age) Reservoirs, US DOE Technical Report, (contract no. DE-AC26-98BC15105), F. Jerry Lucia, editor.
14. Halihan, Todd, John M. Sharp, Jr., and Robert E. Mace, "Interpreting flow using permeability at multiple scales", Karst modeling edited by Palmer, A.R., Palmer, M.V., and Sasowsky, I.D., Karst Waters Institute Special Publication No. 5, Charlottesville, VA, p.82-96.
15. Hearn, Charles L., SPE, Occidental Petroleum of Qatar Ltd., Al-Emadi, Ismail A. Abdulla, SPE, Qatar General Petroleum Corp., Worley, Paul L.H. and Taylor, Robert D., SPE, Occidental Petroleum of Qatar, Ltd., SPE 38908 – "Improved Oil Recovery in a Tight Reservoir with Conductive Faults, ISND Shuiaba, Qatar," presented at the 1997 SPE Annual Technical Conference and Exhibition, San-Antonio, TX, USA, 5-8 Oct, 1997.
16. Schlumberger, "The Eclipse 100 Reference Manual, 96A", 1995
17. Schlumberger, "The Eclipse 100 Technical Description, 97A", 1997
18. Chirlin, G. R., "Flow Through a Porous Medium with Periodic Barriers or Fractures," *SPEJ* (June 1985), pp. 358-362.
19. Nakashima, T., SPE, Waseda University, Sato, K., SPE, The University of Tokyo, Arihara, N., SPE, Waseda University, and Yazawa, N., SPE, JNOC, SPE 64286 –"Effective Permeability Estimation for Simulation of Naturally Fractured Reservoirs," presented at the SPE Asia Pacific Oil and Gas Conference and Exhibition held in Brisbane, Australia, 16-18 Oct, 2000
20. Laubach, Steve, Randy Marrett and Jon Olson, "New directions in fracture characterization", *The Leading Edge*, July 2000
21. Gale, J. F. W., S. E. Laubach, R. M. Reed, J. G. Moros Otero, and L. Gomez, "Fracture Analysis of Clear Fork Outcrops in Apache Canyon and Cores from South Wasson Clear Fork Field", Integrated Outcrop and Subsurface Studies of the Interwell Environment of Carbonate Reservoirs; Clear Fork (Leonardian-Age) Reservoirs, US DOE Technical Report, (contract no. DE-AC26-98BC15105), F. Jerry Lucia, editor.

Sample Depth	Type of Test	No. of Tests	Average SCC index
6091 Grain-dominated dolopackstone	Dry	7	43
	Wet	5	37
6138 Dolomitic sandstone	Dry	11	40
	Wet	3	34
6367 Grain-dominated dolopackstone	Dry	6	60
	Wet	12	53
6385 Dolowackestone	Dry	6	81
	Wet	3	70
6484 Grain-dominated dolopackstone	Dry	5	43
	Wet	1	37
6520 Grain-dominated dolopackstone	Dry	8	38
	Wet	10	30

Table 1: Mean values of the subcritical crack (SCC) index for 6 South Wasson Clear Fork samples.

Parameter	Value
Area	50 x 50 m
Young's modulus	40,000 MPa
Critical Stress Intensity Factor	1.5 MPa $(m)^{1/2}$
Threshold Stress Intensity Factor	0.15 MPa $(m)^{1/2}$
Displacement Increment	0.00005 m
No. of increments	83
Total Strain	7.33E-5
Time	19.7 million years
Strain rate	2.30E-19 1/s
No. of initial flaws	2000

Table 2: Input data to the subcritical crack growth simulator.

Aperture Reduction by Postkinematic Cement	No. of fractures
None	8
Partially filled	12
Completely filled	16
Total fracture observations	**36**

Table 3: Microfracture observations from South Wasson Clear Fork thin sections; from Gale et al [21].

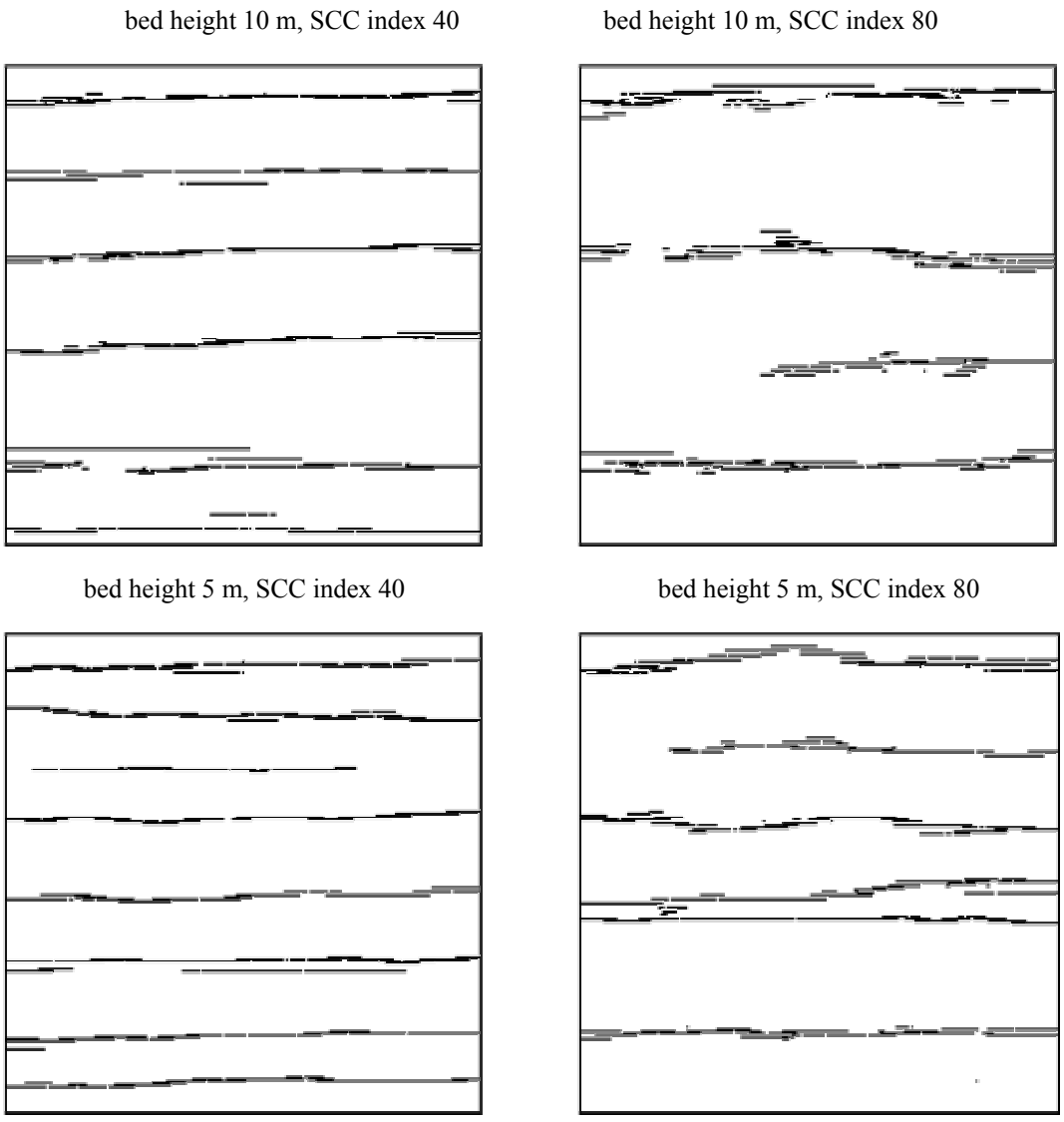

Figure 1: SWCF simulated fracture patterns (Realization 3) for bed heights of 10 m and 5 m and subcritical crack (SCC) indices of 40 and 80.

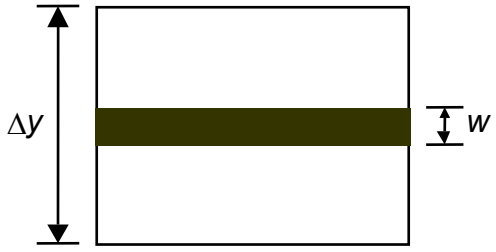

Figure 2: Grid cell representation of a fracture patch, showing the cell dimension and fracture aperture

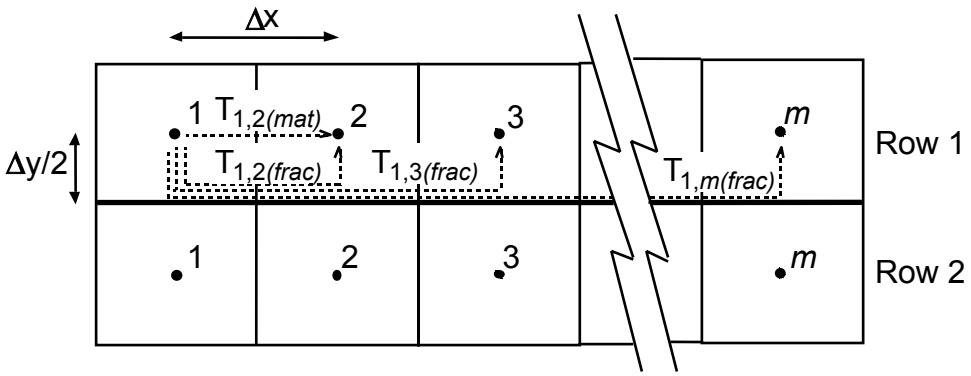

Figure 3: Schematic of grid, depicting non-neighbor connections between cells, to model flow due to a fracture.

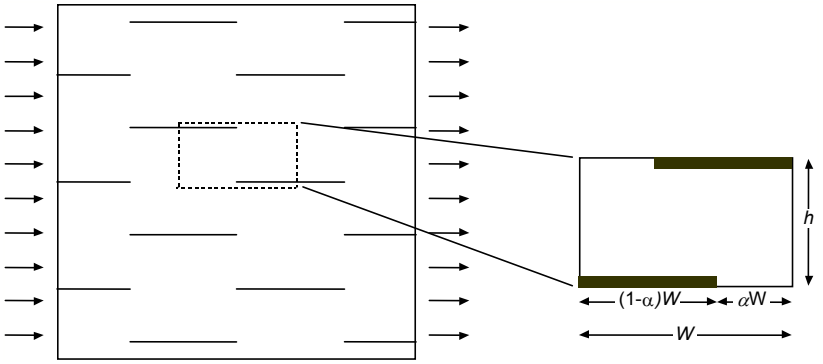

Figure 4: Periodic staggered array of fractures depicting parameters used in the Chirlin solution.

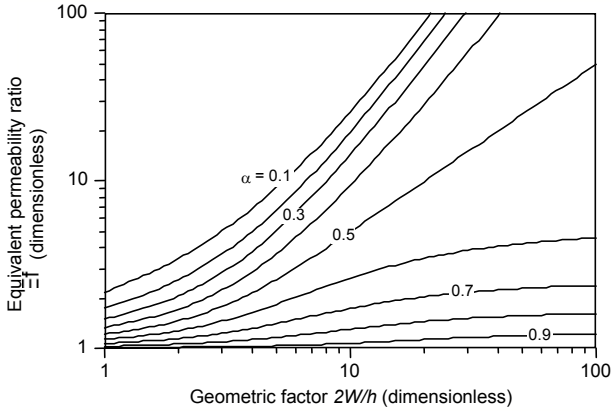

Figure 5: The Chirlin solution for equivalent permeability ratio, R_k, for flow parallel to fractures.

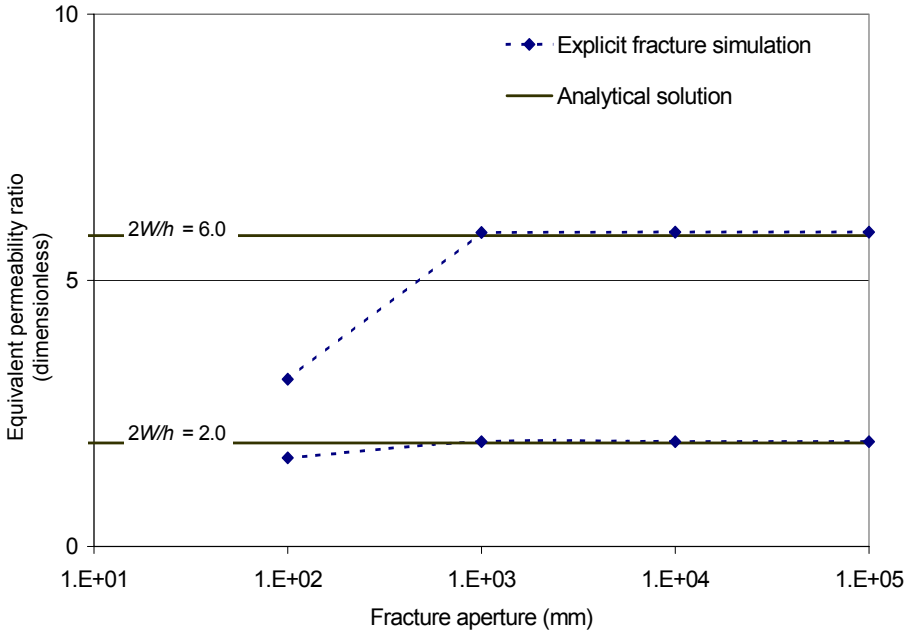

Figure 6: Comparison between results obtained from the flow simulation using explicit fracture representation and the Chirlin solution (500 x 500 cells of equal *x* and *y* dimension 0.1 m).

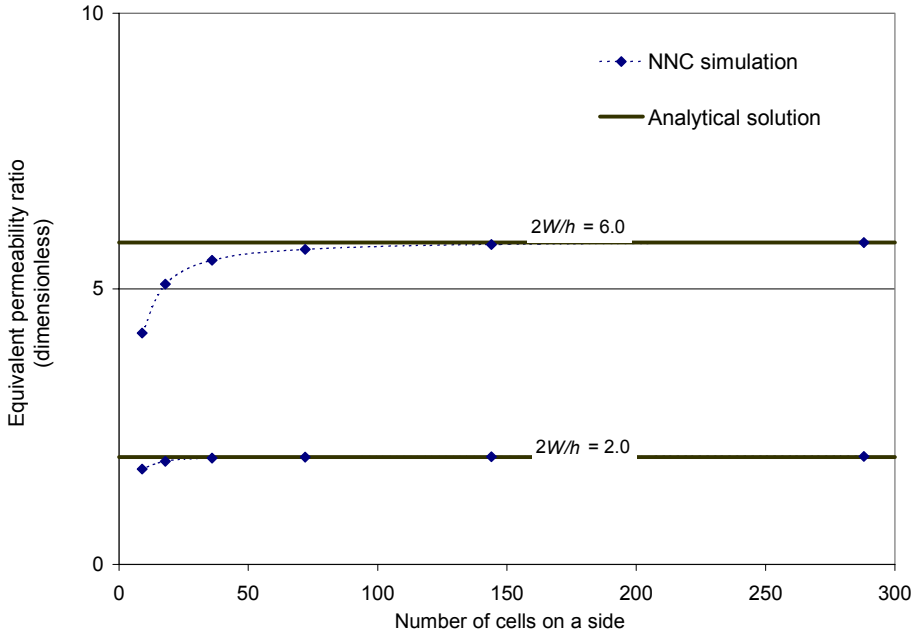

Figure 7: Comparison between results obtained from the flow simulation using non-neighbor connections and the Chirlin solution.

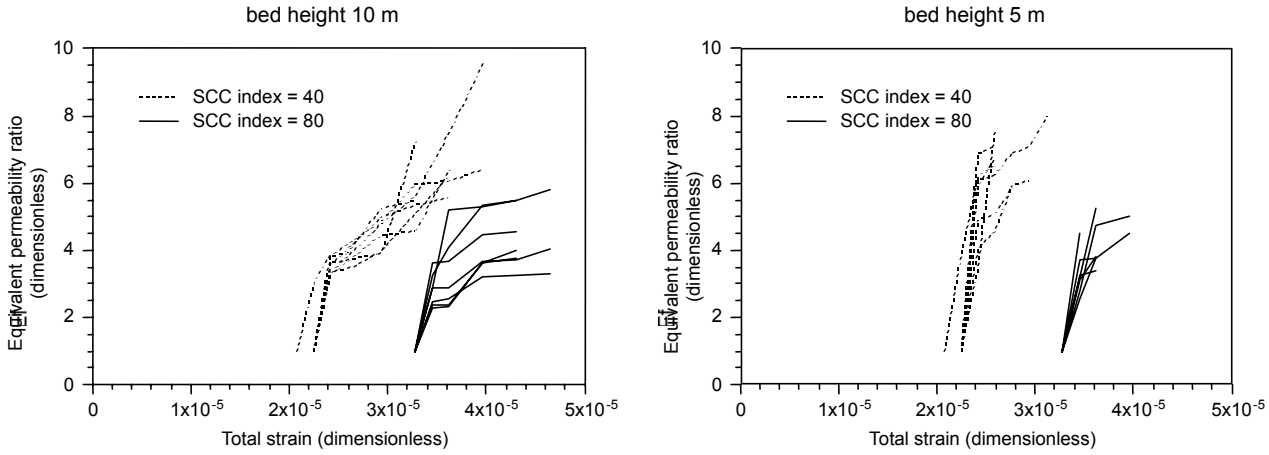

Figure 8: Values of equivalent permeability ratio, R_k, vs. strain, for all 7 realizations, for bed heights of 10 m and 5 m and subcritical crack (SCC) indices of 40 and 80.

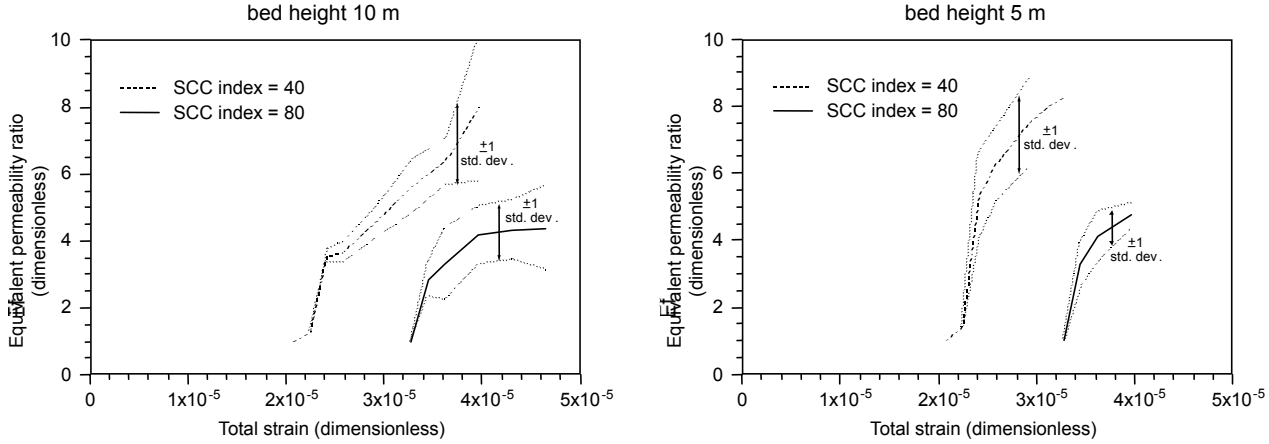

Figure 9: Mean and standard deviation of equivalent permeability ratio, R_k, vs. strain, for bed heights of 10 m and 5 m and subcritical crack (SCC) indices of 40 and 80.

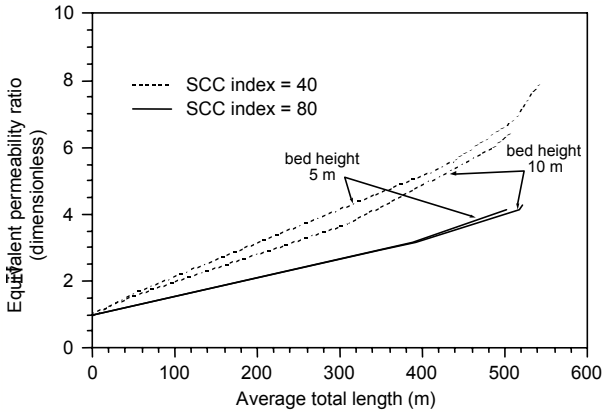

Figure 10: R_k vs. average total length.

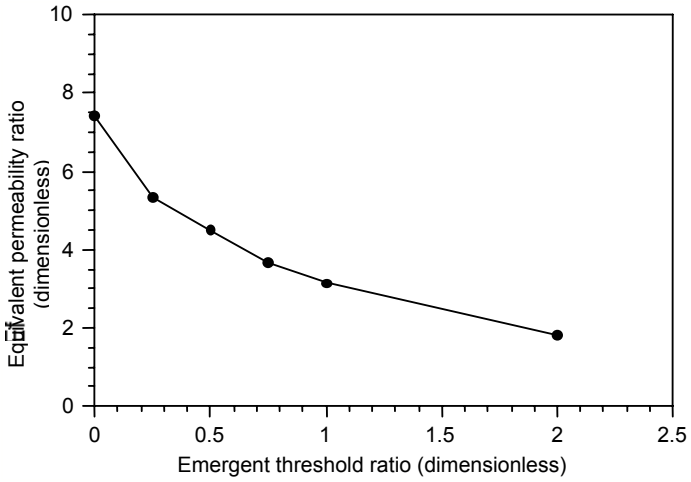

Figure 11: The effect of synkinematic cement on equivalent permeability for a SWCF simulated fracture pattern (realization 4) with a bed height of 10 m and subcritical crack index of 40.

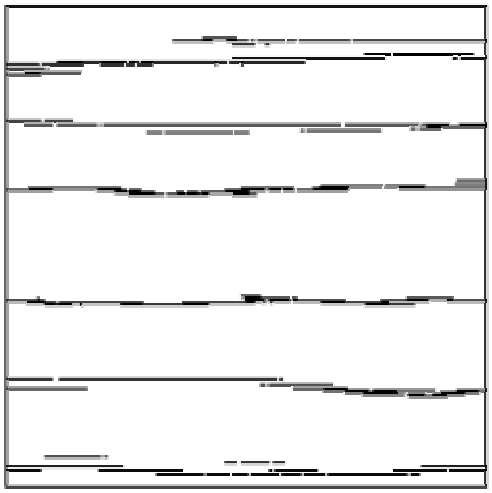

Figure 12: SWCF simulated fracture pattern (realization 4) with a bed height of 10 m and subcritical crack index of 40 with no synkinematic or postkinematic cement.

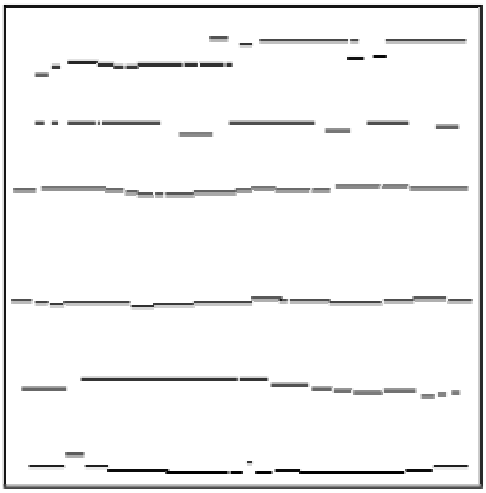

Figure 13: SWCF simulated fracture pattern (realization 4) with a bed height of 10 m and subcritical crack index of 40 with an emergent threshold ratio of 2.

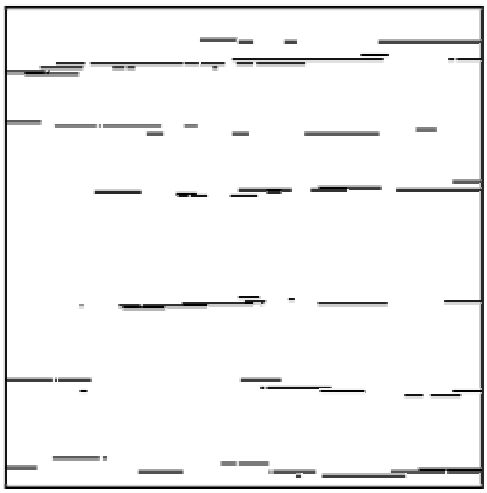

Figure 14: SWCF simulated fracture pattern (realization 4) with a bed height of 10 m and subcritical crack index of 40 with 44 % filling of fractures by postkinematic cement.

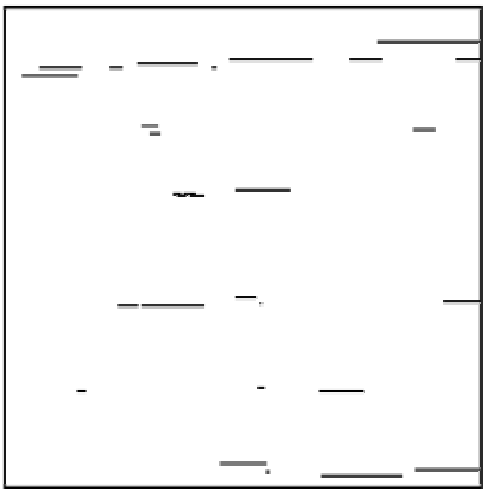

Figure 15: SWCF simulated fracture pattern (realization 4) with a bed height of 10 m and subcritical crack index of 40 with 78 % filling of fractures by postkinematic cement.

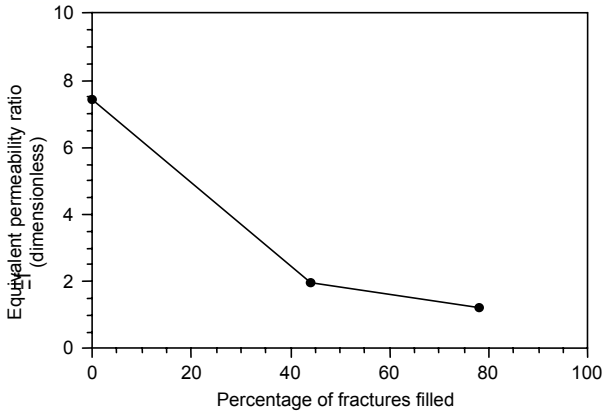

Figure 16: The effect of postkinematic cement on equivalent permeability for a SWCF simulated fracture pattern (realization 4) with a bed height of 10 m and subcritical crack index of 40.

SPE 77340

Modeling Coupled Fracture-Matrix Fluid Flow in Geomechanically Simulated Fracture Networks.

Zeno G. Philip, SPE, James W. Jennings, Jr., SPE, Jon E. Olson, SPE, Jon Holder, The University of Texas at Austin

This paper was prepared for presentation at the SPE Annual Technical Conference and Exhibition held in San Antonio, Texas, 29 September–2 October 2002.

Abstract

In conventional reservoir simulations, grid block permeabilities are frequently assigned values larger than those observed in core measurements to obtain reasonable history matches. Even then, accuracy with regard to some aspects of the performance such as water or gas cuts, breakthrough times, and sweep efficiencies may be inadequate. In some cases this could be due to the presence of substantial flow through natural fractures unaccounted for in the simulation. In this paper we present a numerical investigation into the effects of coupled fracture-matrix fluid flow on equivalent permeability.

A fracture-mechanics-based crack growth simulator, rather than a purely stochastic method, was used to generate fracture networks with realistic clustering, spacing and fracture lengths dependent on the Young's modulus, the subcritical crack index, the bed thickness, and tectonic strain. Coupled fracture-matrix fluid flow simulations of the resulting fracture patterns were performed using a finite-difference simulator to obtain equivalent permeabilities that can be used in a coarser scale flow simulation. Fractures were represented in finite-difference simulators both explicitly as grid cells and implicitly using nonneighbor connections between grid cells.

The results indicate that even though fracture permeability is highly sensitive to fracture aperture, the computed equivalent permeabilities are more sensitive to fracture patterns and connectivity. The effects of diagenetic cements completely filling smaller aperture fractures and partially filling larger aperture fractures were also studied.

Introduction

High-permeability fracture networks in a matrix system can create high-conductivity channels for the flow of fluids through a reservoir, producing larger flow rates and therefore larger apparent permeabilities. The presence of fractures can also cause earlier breakthrough of the displacing fluid and lead to poorer sweep efficiencies in displacement processes. A better understanding of reservoir performance in such cases may be obtained by including the details of the fluid flow in fractures in a coupled fracture-matrix reservoir flow model.

It is impossible to accurately quantify interwell fracture network geometries in sufficient detail to directly model their effect on reservoir behavior. Thus, most modeling approaches have been statistical, using data from outcrop and well-bore observations to determine distributions for fracture attributes such as fracture length, spacing, and aperture to randomly populate a field. In this paper we present a geomechanics-based approach where a model of the fracturing process is used in predicting fracture characteristics.

Opening-mode (mode I) fractures propagate in a plane perpendicular to the least compressive stress.[1] Such fractures may propagate when the fluid pressure inside them exceeds the local least compressive stress or when the local stress becomes tensile. Although this is a necessary condition for fracture propagation, it is not sufficient. Fracture propagation from an existing flaw also requires a sufficiently large stress intensity factor, K_I, to exceed the rock's fracture strength. The mode I stress intensity factor, K_I, for a uniformly loaded isolated crack of length $2c$ is defined as

$$K_I = \Delta\sigma_I \sqrt{\pi c} \quad , \quad \text{.....(1)}$$

and

$$\Delta\sigma_I = P_p - \sigma_{min} \quad , \quad \text{.....(2)}$$

where $\Delta\sigma_I$ is the driving stress, P_p is the pore pressure in the rock, and σ_{min} is the in situ least compressive stress.

Material failure typically occurs when the stress intensity factor is greater than a quantity defined as the critical stress intensity factor, K_{IC}, also known as the fracture toughness. This is called critical crack propagation. However, in cases of long-term loading in corrosive or liquid-saturated environments, cracks have been known to propagate at stress

intensities smaller than the critical stress intensity but above a minimum threshold value,[2] $K_I^* \sim K_{IC}/10$. This type of fracture propagation, called subcritical crack growth, is thought to be representative of most natural fracturing processes in subsurface rocks.[2–4] The velocity of subcritical crack propagation is much slower than that for critical crack propagation and has been observed to follow an empirical power law,

$$V = V_{max}\left(\frac{K_I}{K_{IC}}\right)^n \quad , \quad \text{.....(3)}$$

where V_{max} is the maximum (critical) propagation velocity at $K_I = K_{IC}$, and n is the subcritical crack index.

As the cracks grow they continually change the stress field in the region. Thus subcritical crack growth coupled with interactions among cracks can lead to different fracture patterns in rocks with different mechanical properties even if the starting fracture patterns are identical.[5,6] Details of the final fracture patterns for a given strain depend on the bed thickness, critical stress intensity factor, subcritical index, and Young's modulus.[7,8]

Geomechanical Simulation

Although fracture initiation in rock is often nonlinear,[9] linear elastic fracture mechanics is a good approximation when the fracture length is large relative to the inelastic process zone at the fracture tip.[5] A linear elastic fracture-mechanics-based crack growth simulator[8] based on the boundary element method was used in the present study. The subcritical crack index has been measured with the dual-torsion-beam apparatus[10,11] for samples from six representative layers of the South Wasson Clear Fork (SWCF) reservoir.[12] The results are presented in table 1.

In these measurements, the subcritical crack index ranges from 38 to 81 for dry sample tests. Values of 40 and 80 have been used in the case study. A Young's modulus of 40,000 MPa for this formation was estimated from a porosity of 10% using a published correlation for dolomites. The geometric mean of the apertures observed from the outcrop is 0.212 mm and was used in constraining the strain applied to the reservoir bed. Typical thicknesses for rock-fabric flow layers in the SWCF field are 5 m and 10 m.[13]

Four case scenarios were studied combining two bed thicknesses, 5 m and 10 m, and two subcritical crack indices, 40 and 80. Other geomechanical simulation parameters used to generate the fracture patterns are presented in table 2. For each case, seven different realizations were studied, each realization with a different set of random starter cracks (flaws). Thus a total of 28 different geomechanical simulations were performed, each producing a series of fracture patterns for a sequence of increasing strains. Final fracture patterns obtained for one of the realizations (realization 3), for each of the four cases, are presented in **Fig. 1**.

Flow Simulation

The geomechanical simulation produces a list of fractures represented by patches with location and aperture information. Each fracture is made up of a series of patches lying end to end. A fracture can therefore have varying apertures along its length. The fractures have been constrained to grow in only the x direction (east-west) and can be represented easily in a finite difference simulator. Two methods have been used for this purpose—explicit fracture representation and use of nonneighbor connections (NNC).

Explicit Fracture Representation. The flow area is divided into grid cells with the same resolution as the geomechanical simulation. Each patch from the geomechanical simulation can be represented by one grid cell in the flow simulation. In this study the geomechanical simulation was 50 × 50 m square and the patches were 0.1 m in length. Thus there were 500 × 500 = 250000 cells of equal x and y dimensions (0.1 m). The z direction cell size was 0.5 m.

The permeability of a fracture patch, k_{frac}, with uniform aperture w (**Fig. 2**), can be computed using the parallel plate law[14]

$$k_{frac} = \frac{w^2}{12} \quad . \quad \text{.....(4)}$$

The permeability of a cell in the flow simulation containing a fracture patch and matrix of permeability k_{mat} can be computed as

$$k_{cell} = \frac{\left(k_{frac}w + k_{mat}\left(\Delta y - w\right)\right)}{\Delta y} \quad , \quad \text{.....(5)}$$

where Δy is the width of the cell perpendicular to the flow direction. A matrix permeability of 1 md [9.9 E-04 μm^2] was used for all flow simulations.

Thus, each cell in the flow simulation was assigned a unique permeability on the basis of the location and aperture of the patches. The y and z direction permeabilities were unchanged.

Nonneighbor Connections. Flow through fractures can also be modeled using nonneighbor connections (NNC) in a traditional finite-difference simulator.[15] In this approach, the fractures are assumed to have infinite conductivity, making fracture aperture information irrelevant. The flow area is gridded such that the fractures lie at the boundaries between grid cells. The matrix flow transmissibility in the x direction, $T_{x(mat)}$, between any two grid cells is

$$T_{x(mat)} = \frac{k_x A_x}{\Delta x} \quad , \quad \text{.....(6)}$$

where A_x is the area perpendicular to flow in the x direction, ($\Delta y \Delta z$), and k_x is the permeability in the x direction (**Fig. 3**). If there is a fracture between the cells as shown in Fig. 3, an additional transmissibility for fracture flow, $T_{x(frac)}$, can be assigned using

$$T_{x(frac)} = \frac{k_y A_y}{2(\Delta y/2)} = \frac{k_y A_y}{\Delta y} \quad , \quad \text{.....(7)}$$

where A_y is the area perpendicular to flow in the y direction, ($\Delta x \Delta z$), and k_y is the permeability in the y direction. The total x direction transmissibility, $T_{x(total)}$, accounting for both matrix and fracture flow, is therefore

$$T_{x(total)} = T_{x(mat)} + T_{x(frac)} = \frac{k_x A_x}{\Delta x} + \frac{k_y A_y}{\Delta y} \quad . \quad \text{.....(8)}$$

The transmissibility between adjacent cells due to matrix flow is computed automatically by the simulator, connecting cell i to cells i-1 and i+1. The transmissibility between cells due to fracture flow can be entered explicitly using NNC, connecting cell i to cells i-1 and i+1 as well as to all other cells on that same fracture. The NNC transmissibility between cell i and its neighbors i-1 and i+1 is in addition to that due to matrix flow. Thus, a fracture extending between cells 1 and m connects cell 1 to cells 2 through m, cell 2 to cells 3 through m, and so on. The total number of NNC per fracture is

$$\left(\frac{m(m-1)}{2}\right)2 = m(m-1) \quad . \quad \text{.....(9)}$$

The multiplication by 2 accounts for cells on both sides of the fracture. A fracture between rows 1 and 2 extending from cells 1 to m results in the following nonneighbor transmissibilities for connections between cell 1 and the others in row 1:

$$T_{1,2}, T_{1,3}, ..., T_{1,m(frac)} = \frac{k_y \Delta x \Delta z}{\Delta y} \quad . \quad \text{.....(10)}$$

Likewise the nonneighbor transmissibilities between cell 2 and cells 3 through m are

$$T_{2,3}, T_{2,4}, ..., T_{2,m(frac)} = \frac{k_y \Delta x \Delta z}{\Delta y} \quad , \quad \text{.....(11)}$$

and so on, for cells 3 through m. The transmissibilities for cell connections in row 2 are computed similarly.

A finite-difference simulator[16,17] was used to perform 2-D, single-phase flow simulations. Constant pressure boundaries were maintained on two opposing sides, whereas the other two sides were no-flow boundaries. Constant pressure was maintained by assigning to each of the cells on a particular side producing wells on pressure control, and to each of the cells on the opposing side injector wells on pressure control. Thus the number of producers and injectors was each equal to the number of rows in the flow grid. The flow simulation was performed till a steady-state flow rate, q, was obtained. Knowing q, the pressures at both the ends, (P_1 and P_2), the distance between the wells, (L - (2(Δx)/2)), and the fluid properties, one can obtain an equivalent permeability for the fractured grid as follows,

$$k_{eqv} = \frac{q\mu(L - \Delta x)}{A(P_1 - P_2)} \quad , \quad \text{.....(12)}$$

where μ is the fluid viscosity, and A is the area perpendicular to flow (the product of Δy, Δz, and the number of cells in the y direction). The equivalent permeability can also be expressed in dimensionless form using an equivalent permeability ratio, R_k,

$$R_k = \frac{k_{eqv}}{k_{mat}} \quad . \quad \text{.....(13)}$$

Verification

The equivalent permeability estimates from the single-phase flow simulations using both methods, i.e., explicit fracture representation and NNC were verified by comparison with an analytical solution for flow through a staggered, periodic array of infinite conductivity fractures.[18,19] For such an array (**Fig. 4**) an analytical solution for the equivalent permeability ratio, R_k, as a function of the fracture array spacing, h, and half-length, (1-α)W, is presented in **Fig. 5**.

Results of the comparison between the analytical solution and simulation results for two array scenarios are presented in **Fig. 6** and **Fig. 7**. For the explicit fracture case (Fig. 6), the simulation results approach the analytical solution as the fracture aperture increases. For the NNC case (Fig. 7) the simulation results approach the analytical solution as the grid resolution increases.

Flow Modeling of Simulated Fracture Networks

In this section we present results obtained using the explicit fracture representation method. The NNC approach yielded similar results for one set of realizations studied, with the equivalent permeability ratios being approximately 30% larger. However, the CPU run time and memory requirements were approximately 30 times and 3 times larger, respectively. Moreover, fracture aperture information cannot be incorporated using the NNC method. So we prefer the explicit fracture approach.

Values of the equivalent permeability ratio, R_k, vs. strain obtained for each of the runs and for the individual bed thicknesses of 5 m and 10 m are plotted in **Fig. 8**. The means and standard deviations of R_k from the seven realizations for each of the four combinations of bed thickness and subcritical crack index are also shown in **Fig. 9**. Although there appears to be a fairly large degree of variability between the realizations, there is a definite segregation in the R_k values based upon both the bed thickness and the subcritical crack index. In subsequent analysis and figures, we shall be referring to the average of the seven realizations.

In Fig. 9, the effect of strain on the equivalent permeability is evident. As expected, an increase in the strain causes an increase in R_k. The first significant fractures appear at a strain of 2.0E-5 for the subcritical crack index of 40, but at a larger strain of 3.2E-5 for the index of 80. This is because the larger

subcritical crack index produces a smaller crack propagation velocity delaying visible crack growth (Eq. 3). Further, since the velocity of propagation is larger for a smaller index the total fracture length is also larger at a given strain. Thus, for other conditions remaining the same, R_k is larger for the smaller index than for the higher index.

It is also evident from Fig. 9 that for a given index, the rate of increase in R_k with strain is higher for the bed thickness of 5 m than for 10 m. This is because for thinner beds at a particular strain, a larger number of starter flaws develop into fractures, leading to a larger total fracture length. Thinner beds have a smaller volume for energy dissipation compared with thicker beds. Hence, for a given strain, more fractures are formed in thinner beds.

For each combination of bed thickness and index and for each strain level, the average total fracture length of seven realizations was computed. As expected, the equivalent permeability ratio, R_k, increases with the total length (**Fig. 10**). However, for the same total fracture length, the case with the subcritical index of 40 has a higher R_k than that with an index of 80. This is because, for a given total length, for the index of 40, the fractures have a larger mean length than for the index of 80. Because crack growth is delayed for the larger index causing the stresses to be released at a smaller rate, more cracks tend to grow at the same time, leading to a smaller mean length.

Further, we see in Fig. 10 that there is no strong dependence of R_k on the bed thickness for a given total fracture length. The larger R_k for a smaller bed thickness at a given strain (Fig. 9) was due to the larger total fracture length at that strain.

To study the effect of the mean aperture on R_k, the flow simulations were repeated for a set of seven realizations of fracture networks with the permeability of the fracture cells increased by a factor of 10. The average R_k values, however, increased by only 6%. Thus, the equivalent permeability ratio is not very sensitive to the fracture aperture in cases without a strongly interconnected fracture network, such as those investigated in this study. The reason for this is that fracture permeability is usually already so much larger (on the order of hundreds of Darcys) than the matrix permeability (on the order of millidarcys) that the overall resistance to flow is controlled more by the permeability and geometry of the matrix flow paths between the fractures than by the permeabilities of the fractures themselves. This observation is also supported by the fact that the NNC approach, which assumes infinite conductivity fractures, yields equivalent permeability ratios that are only 30% higher than those obtained using the explicit fracture representation.

Other Factors Affecting Fractured Grid Permeability

In the subsurface, over geologic time scales, carbonate, quartz or other cement often precipitates on the fracture walls, thus reducing the fracture aperture available for flow.

Synkinematic Cement. Cement that is precipitated contemporaneous with fracture propagation is called synkinematic cement.[20] Observations suggest that fractures below a certain aperture size, termed the emergent threshold, e_t, are completely closed with cement. Fractures with larger apertures are only partially filled and can still conduct flow. To estimate the effect of this fracture mineralization process on permeability the aperture in each fracture patch was reduced by a constant amount. An emergent threshold ratio, e_r, is defined

$$e_r = \frac{e_t}{w_{gm}} \quad , \qquad \text{.....(14)}$$

where w_{gm} is the geometric mean of the simulated apertures.

The effect of the emergent threshold was studied on a sample run (realization 4) with a bed thickness of 10 m and subcritical crack index of 40. The emergent threshold ratio was varied from 0 (that is, no reduction in aperture) to 2. The equivalent permeability ratio, R_k, was computed for each case. It is evident that as the emergent threshold increases, R_k decreases (**Fig. 11**). However, this decrease in R_k is not so much due to the fact that the fracture apertures were reduced as to the fracture length reduction resulting from some fracture segments becoming completely filled. Fracture patterns for an emergent threshold ratio, e_r, of 0 and 2 are shown in **Fig. 12** and **Fig. 13**.

Postkinematic Cement. Cement that is precipitated after fractures are formed is called postkinematic cement.[20] This cement fills in all kinds of porosity including fracture porosity. Postkinematic cement is typically more heterogeneously distributed than synkinematic cement, so we estimated it in our reservoir simulations by applying it randomly to the fractures. The number of fractures eliminated from the flow simulation (i.e., fractures that were completely closed by postkinematic cement) was determined from thin-section microfracture data[21] (table 3). The partly filled fractures were treated as fully open in case 1 and as fully closed in case 2. Thus, for case 1, we obtained a microfracture percentage filling of 16/36 = 44%, and for case 2 we obtained a microfracture percentage filling of (16+12)/36 = 78%. The modified fracture patterns obtained for both of these cases are shown in **Fig. 14** and **Fig. 15**. Increased levels of postkinematic cementation also reduce total fracture length. The equivalent permeability ratio subsequently reduces with an increase in postkinematic cement (**Fig. 16**).

Conclusions

The equivalent permeability ratio increases with total fracture length and mean fracture length. For a given strain, beds having a lower subcritical index tend to have a higher equivalent permeability because they tend to have fractures with larger mean lengths.

The equivalent permeability of a weakly connected fracture network is not very sensitive to the fracture aperture. It is more sensitive to the fracture pattern. Equivalent permeability is also highly sensitive to fracture filling by synkinematic and postkinematic cements. Both types of

cement close a portion of the fracture network, reducing the equivalent permeability by increasing the proportion of flow through the matrix.

This study indicates that the equivalent permeability in the SWCF reservoir is enhanced by a factor of between 2 and 10 because of the presence of fractures. This is substantially lower than the 1,000- or 10,000- fold increase that one would expect by assuming that all fractures completely cross the flow area of interest.

In future studies, careful observations of fracture patterns and connectivity are needed to meaningfully include the presence of fractures in reservoir modeling. Aperture information is not critical, except for modeling the effects of fracture filling by synkinematic cement.

Nomenclature

K_I = mode I stress intensity factor
K_{IC} = mode I critical stress intensity factor or material fracture toughness
$\Delta\sigma$ = driving stress, differential
P = pressure
σ = compressive stress
V = velocity of crack propagation
n = subcritical crack growth index
m = number of matrix cells in a row touching a particular fracture
c = half length of fracture
k = permeability
R_k = equivalent permeability ratio
T = transmissibility between two matrix cells
L = length of flow region
w = fracture aperture
W = distance between midpoints of two adjacent fractures in the Chirlin staggered fracture array
α = fraction of W composed of the matrix portion
h = perpendicular distance between two adjacent fractures in the Chirlin staggered fracture array
A = area perpendicular to flow
e_t = emergent threshold
e_r = emergent threshold ratio
Δx = dimension of grid cell in x direction
Δy = dimension of grid cell in y direction
Δz = dimension of grid cell in z direction

Subscripts

i = cell index
$frac$ = fracture
mat = matrix
eqv = equivalent
gm = geometric mean
x = x direction
y = y direction
z = z direction
p = pore
max = maximum
min = minimum
$cell$ = fracture cell

Acknowledgments

We thank Dr. Steve Laubach and Mr. F. Jerry Lucia of the Bureau of Economic Geology, The University of Texas at Austin, for valuable advice regarding the cementation parameters and geology of the South Wasson Clear Fork reservoir. This paper was prepared with the support of the U.S. Department of Energy, under Award No. DE-AC26-98BC15105 and DE-FG26-OOBC15308. However, any opinions, findings, conclusions, or recommendations expressed herein are those of the authors and do not necessarily reflect the views of the DOE.

The fluid flow simulations were conducted with software provided by Schlumberger Geoquest. The figures were prepared by the Bureau of Economic Geology graphics department under the direction of Joel L. Lardon. The manuscript was edited by Susann V. Doenges. Publication was authorized by the Director, Bureau of Economic Geology, The University of Texas at Austin.

References

1. Lawn, B.R., and Wilshaw, T.R.: *Fracture of Brittle Solids*, Cambridge University Press, Cambridge, (1975).
2. Segall, P.: "Formation and Growth of Extensional Fracture Sets," *Geol. Soc. Am. Bull*., (1984), **95**, 454–462.
3. Atkinson, B.K.: "Subcritical Crack growth in Geological Materials," *Journal of Geophysical Research*, (June 1984), **89** (B6), 4077–4114.
4. Atkinson, B.K., and Meredith, P.G.: "The Theory of Subcritical Crack Growth with Applications to Minerals and Rocks," *Fracture Mechanics of Rock*, B.K. Atkinson (ed.), Academic, San Diego, Calif., (1987), 111–166.
5. Olson, J.E.: "Joint Pattern Development: Effects of Subcritical Crack Growth and Mechanical Crack Interaction," *Journal of Geophysical Research*, **98** (B7), (July 1993), 12,251–12,265.
6. Renshaw, C.E.: "Influence of Subcritical Fracture Growth on the Connectivity of Fracture Networks," *Water Resources Research*, **32** (6), (June 1996), 1519–1530,
7. Olson, J.E., Qiu Y., Holder J., and Rijken, P.: "Constraining the Spatial Distribution of Fracture Networks in Naturally Fractured Reservoirs Using Fracture Mechanics and Core Measurements," paper SPE 71342 presented at the 2001 SPE Annual Technical Conference and Exhibition, New Orleans, Louisiana, 30 Sept-3 Oct.
8. Olson, J.E.: "Fracture Mechanics Analysis of Joints and Veins," Ph.D. dissertation, Stanford Univ., Stanford, Calif., (1991).
9. Ingraffea, A.R.: "Theory of Crack Initiation and Propagation in Rock," *Fracture Mechanics of Rock*, B.K. Atkinson, (ed.), Academic, San Diego, Calif., (1987), 71–110
10. Williams, D.P. and Evans, A.G.: "A Simple Method for Studying Slow Crack Growth," *Journal of Testing and Evaluation, JTEVA*, **1** (4), (July 1973), 264–270.
11. Pletka, B.J., Fuller, E.R., Jr., and Koepke, B.G.: "An Evaluation of Double-Torsion Testing–Experimental," *Fracture Mechanics Applied to Brittle Materials*, ASTM STP 678, S. W. Freiman (ed), American Society for Testing and Materials, (1979), 19–37.
12. Holder, J., Olson, J.E., and Philip, Z.: "Experimental Determination of Subcritical Crack Growth Parameters in Sedimentary

Rock," *Geophysical Research letters*, **28** (4), (Feb 2001), 599–602.
13. Lucia, F.J., and Jennings, J.W.: "Calculation and Distribution of Petrophysical Properties in the South Wasson Clear Fork Field," *Integrated Outcrop and Subsurface Studies of the Interwell Environment of Carbonate Reservoirs: Clear Fork (Leonardian-Age) Reservoirs, West Texas and New Mexico*, F.J. Lucia, (ed.), final report, Contract No. DE-AC26-98BC15105, U.S. DOE (2002), 95–142.
14. Halihan, T., Sharp, J.M., Jr., and Mace, R.E.: "Interpreting Flow Using Permeability at Multiple Scales," *Karst modeling*, A.R. Palmer, Palmer, M.V., and Sasowsky, I.D., (eds.) Karst Waters Institute Special Publication No. 5, Charlottesville, VA, 82–96.
15. Hearn, C.L., Al-Emadi, I.A.A., Worley, P.L.H., and Taylor, R.D.: "Improved Oil Recovery in a Tight Reservoir with Conductive Faults, ISND Shuiaba, Qatar," paper SPE 38908 presented at the 1997 SPE Annual Technical Conference and Exhibition, San Antonio, TX, USA, 5–8 Oct.
16. Schlumberger: *The Eclipse 100 Reference Manual, 96A*, (1995).
17. Schlumberger: *The Eclipse 100 Technical Description, 97A*, (1997).
18. Chirlin, G.R.: "Flow Through a Porous Medium with Periodic Barriers or Fractures," *SPEJ* (June 1985), 358–362.
19. Nakashima, T., Sato, K., Arihara, N., and Yazawa, N.: "Effective Permeability Estimation for Simulation of Naturally Fractured Reservoirs," paper SPE 64286 presented at the 2000 SPE Asia Pacific Oil and Gas Conference and Exhibition held in Brisbane, Australia, 16–18 Oct.
20. Laubach, S., Marrett, R., and Olson, J., "New Directions in Fracture Characterization," *The Leading Edge*, (July 2000), 704–711.
21. Gale, J.F.W., Laubach S.E., Reed, R.M., Moros Otero J.G., and Gomez, L.: "Fracture Analysis of Clear Fork Outcrops in Apache Canyon and Cores from South Wasson Clear Fork Field," *Integrated Outcrop and Subsurface Studies of the Interwell Environment of Carbonate Reservoirs: Clear Fork (Leonardian-Age) Reservoirs, West Texas and New Mexico*, F.J. Lucia, (ed.), final report, Contract No. DE-AC26-98BC15105, U.S. DOE (2002), 191–226.

SI Metric Conversion Factors

md x 9.9 E-04 = μm^2

Sample Depth	No. of Tests	Average SCC index
6091 Grain-dominated dolopackstone	7	43
6138 Dolomitic sandstone	11	40
6367 Grain-dominated dolopackstone	6	60
6385 Dolowackestone	6	81
6484 Grain-dominated dolopackstone	5	43
6520 Grain-dominated dolopackstone	8	38

Table 1: Mean values of the subcritical crack (SCC) index for six South Wasson Clear Fork samples.

Parameter	Value
Area	50 x 50 m
Young's modulus	40,000 MPa
Critical stress intensity factor	1.5 MPa $(m)^{1/2}$
Threshold stress intensity factor	0.15 MPa $(m)^{1/2}$
Displacement increment	0.00005 m
No. of increments	83
Total strain	7.33E-5
Time	19.7 million years
Strain rate	2.30E-19 1/s
No. of initial flaws	2000

Table 2: Input data to the subcritical crack growth simulator.

Aperture Reduction by Postkinematic Cement	No. of fractures
None	8
Partially filled	12
Completely filled	16
Total fracture observations	**36**

Table 3: Microfracture observations from South Wasson Clear Fork thin sections[21].

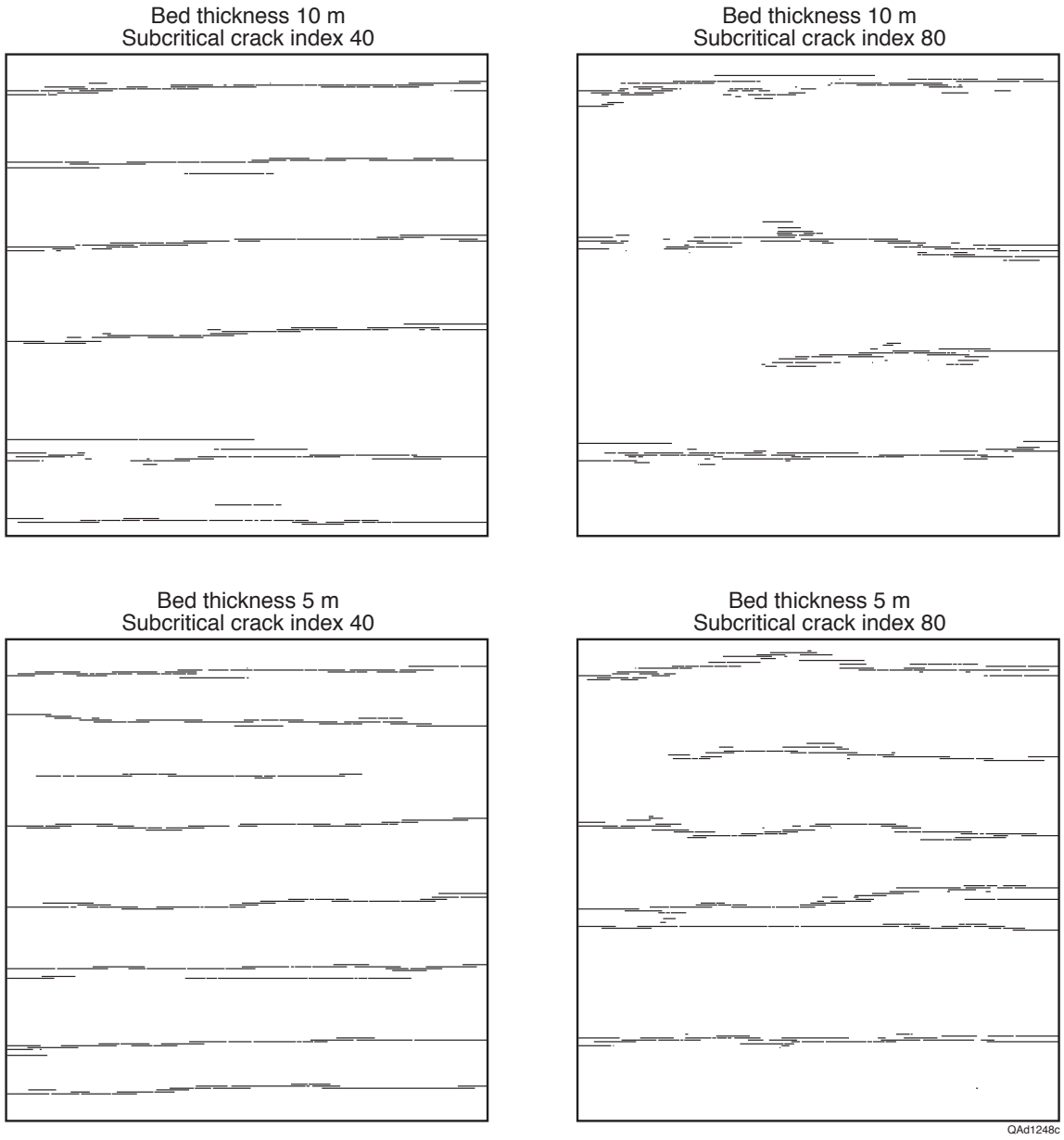

Figure 1: SWCF simulated fracture patterns (realization 3) for bed thicknesses of 10 m and 5 m and subcritical crack (SCC) indices of 40 and 80.

Figure 2: Grid cell representation of a fracture patch, showing the cell dimension and fracture aperture.

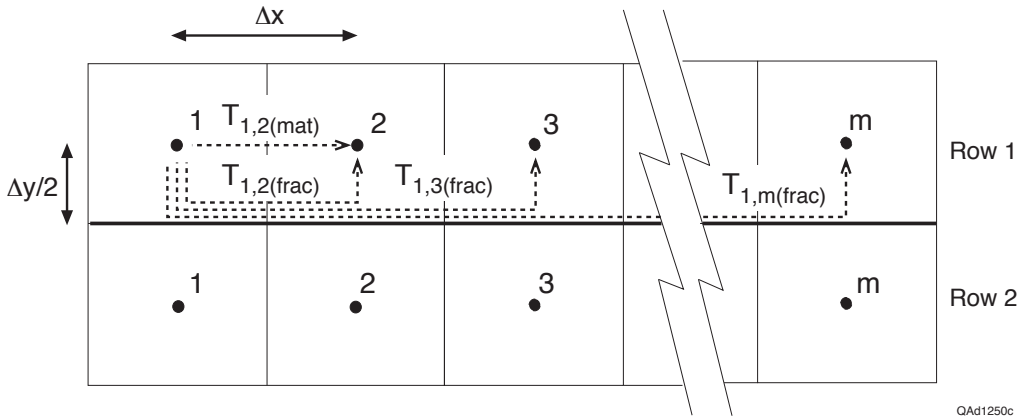

Figure 3: Schematic of grid, depicting nonneighbor connections between cells to model flow due to a fracture.

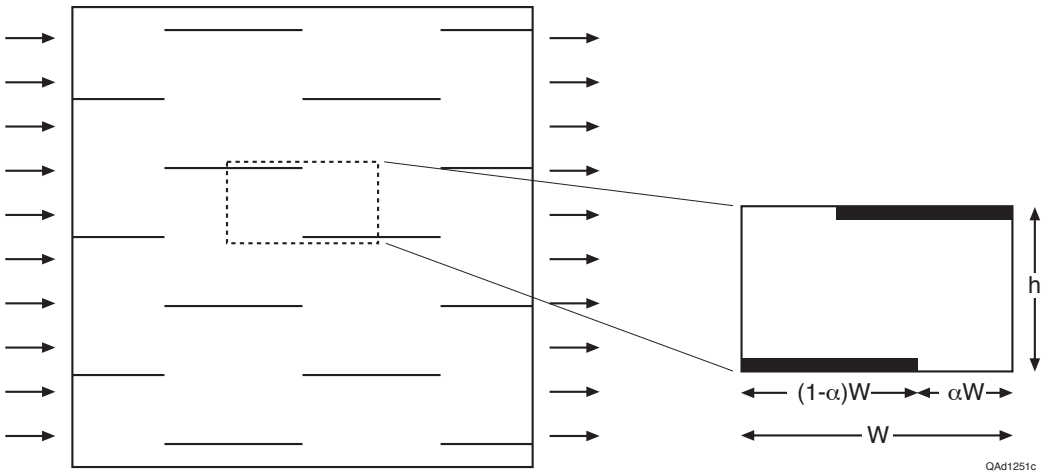

Figure 4: Periodic staggered array of fractures depicting parameters used in the Chirlin solution.

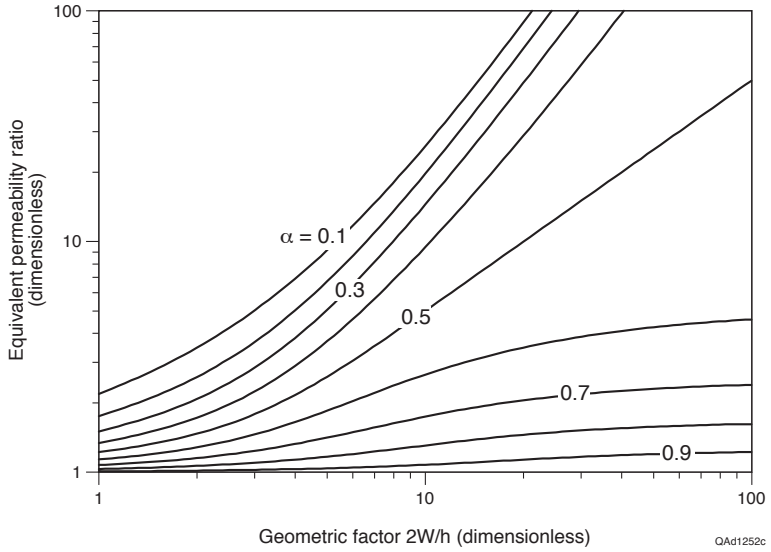

Figure 5: The Chirlin solution for the equivalent permeability ratio for flow parallel to fractures.

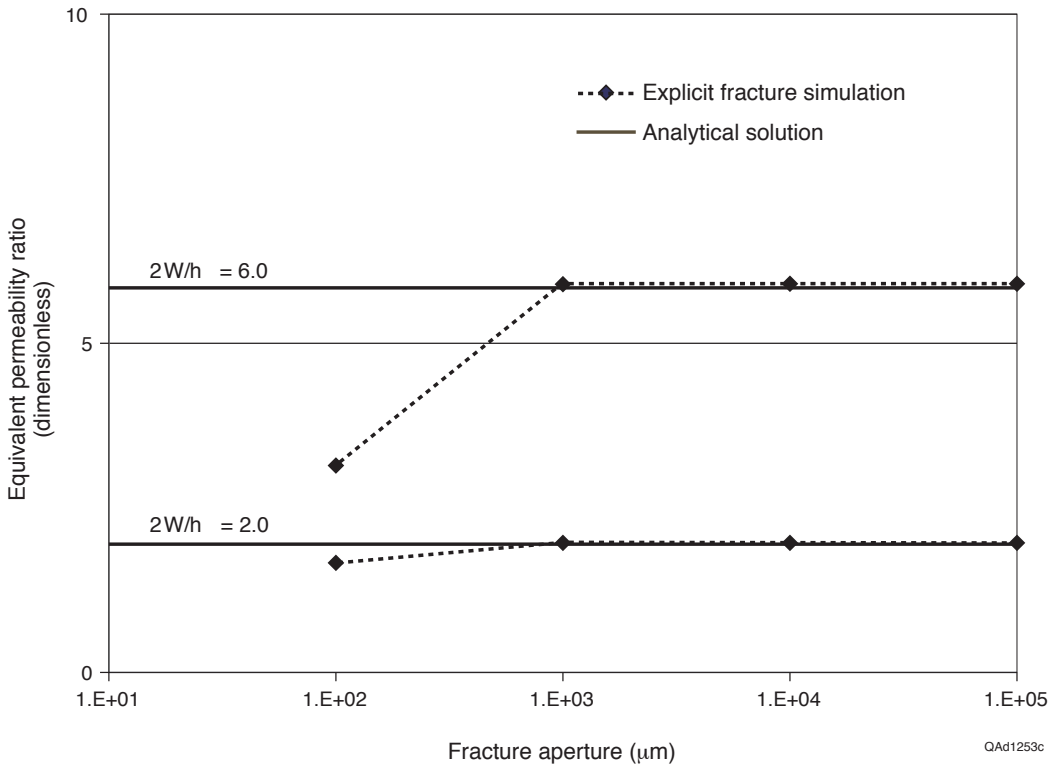

Figure 6: Comparison between results obtained from the flow simulation using explicit fracture representation and the Chirlin solution (500 × 500 cells of equal *x* and *y* dimension 0.1 m).

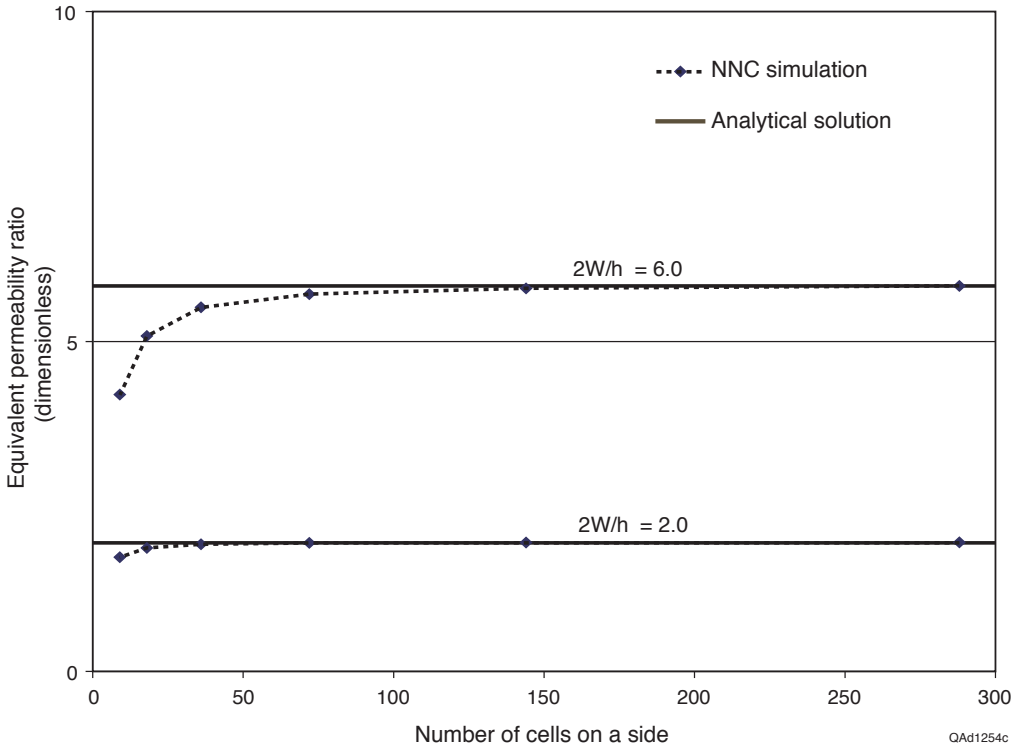

Figure 7: Comparison between results obtained from the flow simulation using nonneighbor connections and the Chirlin solution.

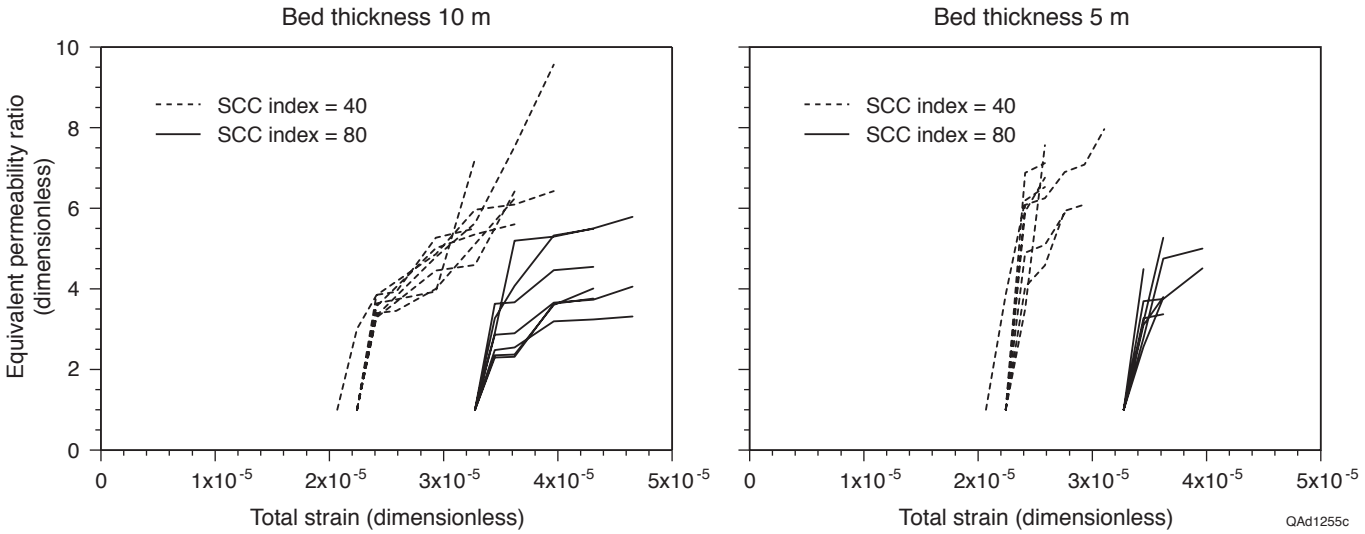

Figure 8: Values of equivalent permeability ratio vs. strain, for all seven realizations, for bed thicknesses of 10 m and 5 m and subcritical crack (SCC) indices of 40 and 80.

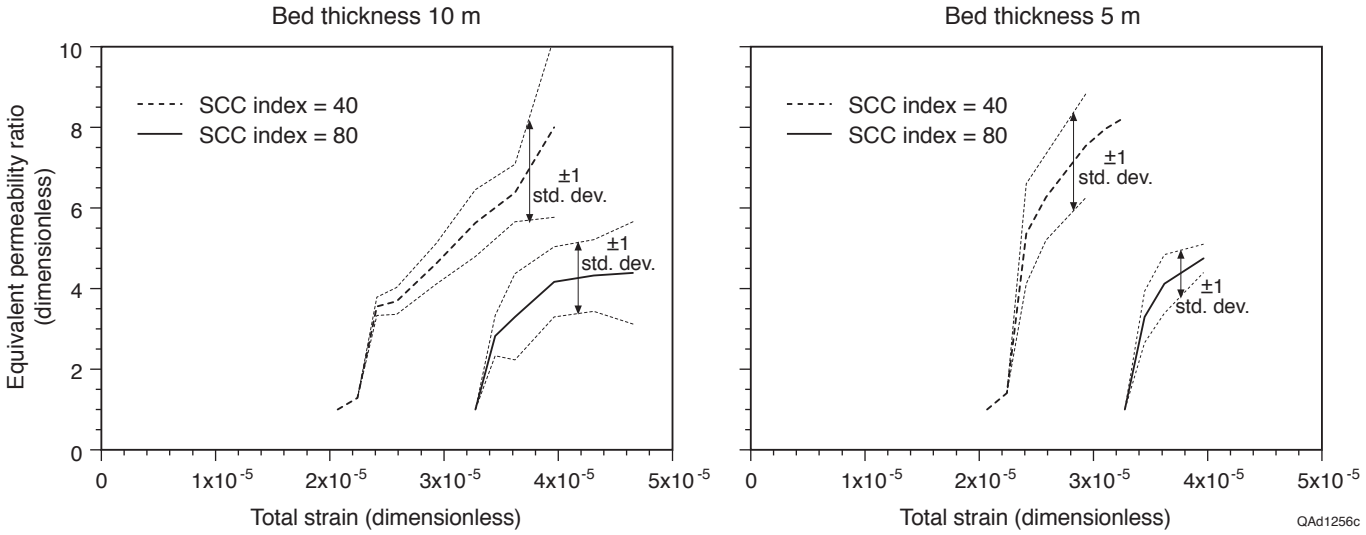

Figure 9: Mean and standard deviation of equivalent permeability ratio vs. strain, for bed thicknesses of 10 m and 5 m and subcritical crack (SCC) indices of 40 and 80.

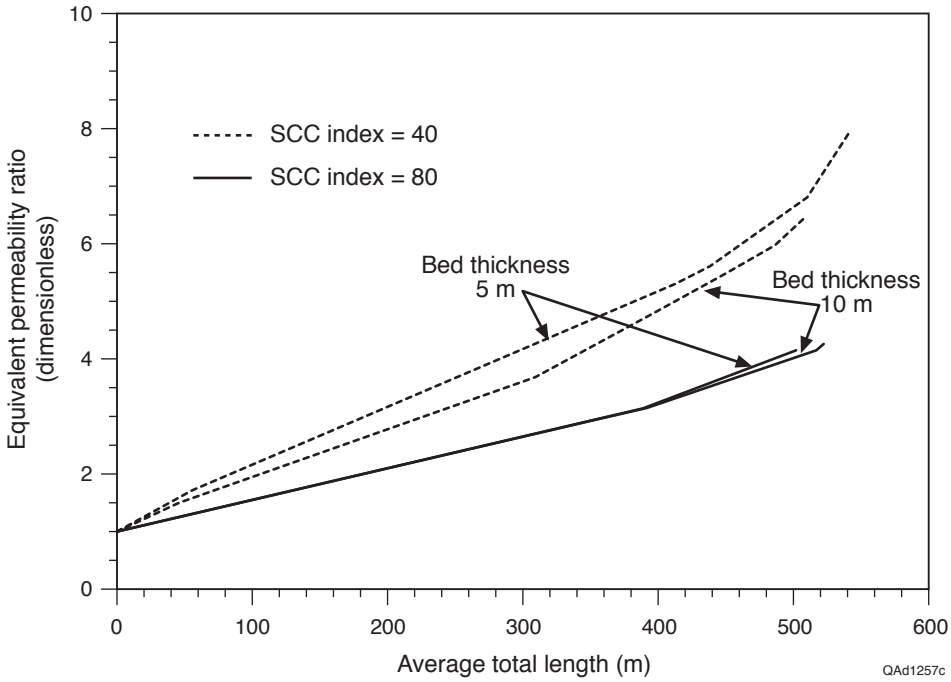

Figure 10: The effect of average total fracture length on the equivalent permeability for given SCC indices and bed thicknesses.

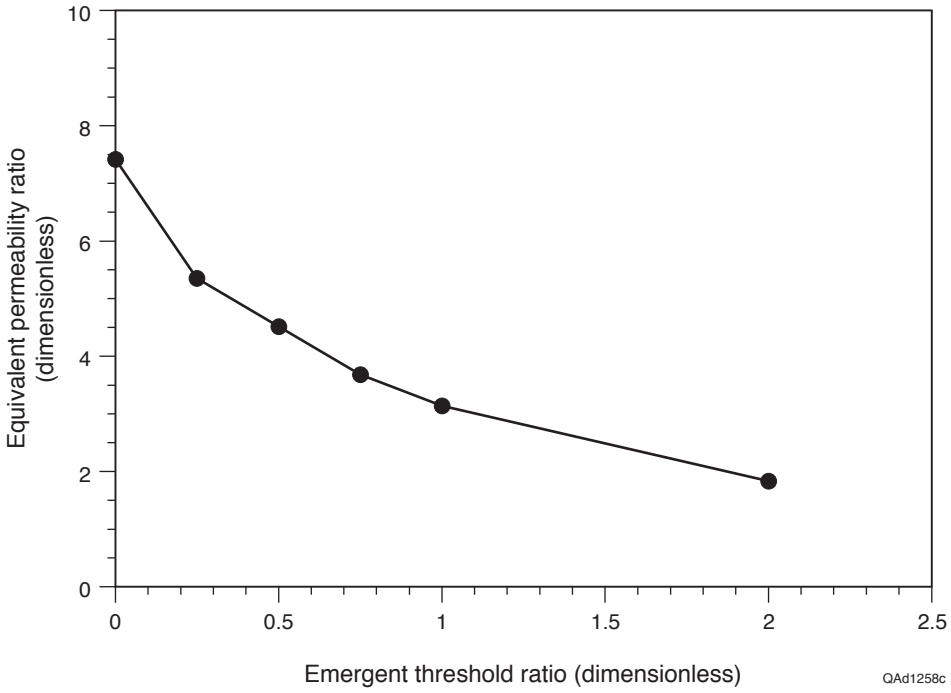

Figure 11: The effect of synkinematic cement on equivalent permeability for a SWCF simulated fracture pattern (realization 4) with a bed thickness of 10 m and subcritical crack index of 40.

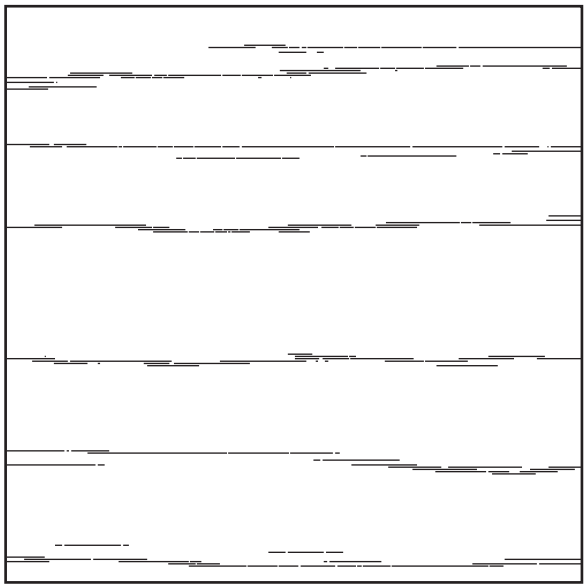

Figure 12: SWCF simulated fracture pattern (realization 4) with a bed thickness of 10 m and subcritical crack index of 40 with no synkinematic or postkinematic cement.

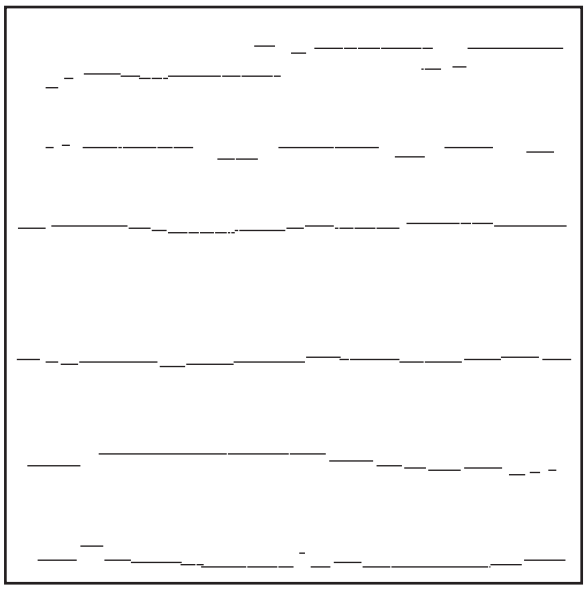

Figure 13: SWCF simulated fracture pattern (realization 4) with a bed thickness of 10 m and subcritical crack index of 40 with an emergent threshold ratio of 2.

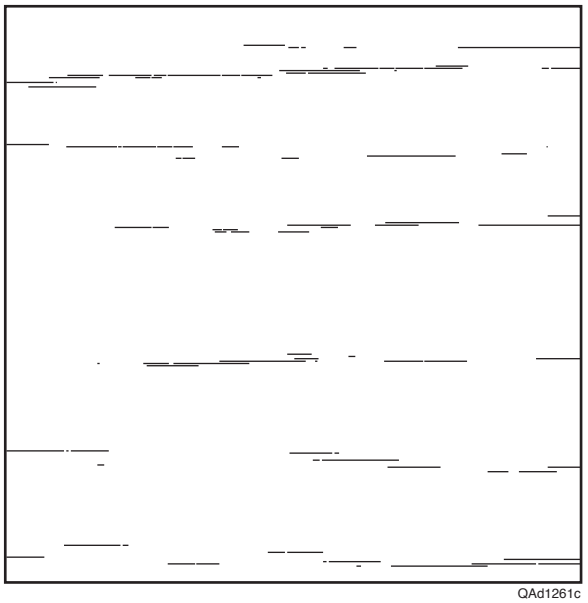

Figure 14: SWCF simulated fracture pattern (realization 4) with a bed thickness of 10 m and subcritical crack index of 40 with 44% filling of fractures by postkinematic cement.

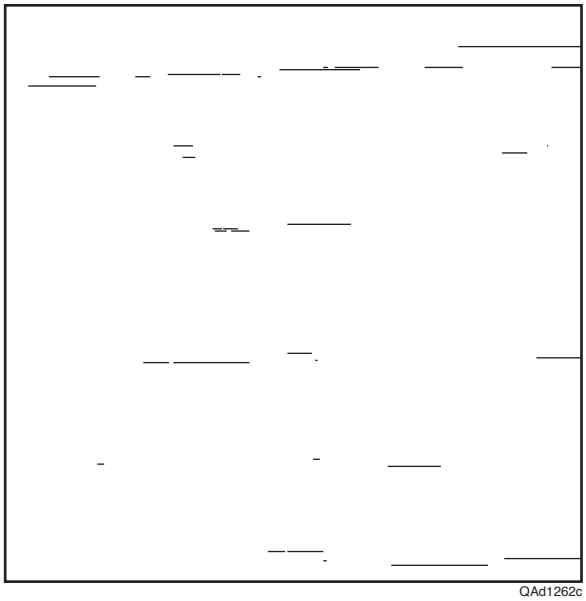

Figure 15: SWCF simulated fracture pattern (realization 4) with a bed thickness of 10 m and subcritical crack index of 40 with 78% filling of fractures by postkinematic cement.

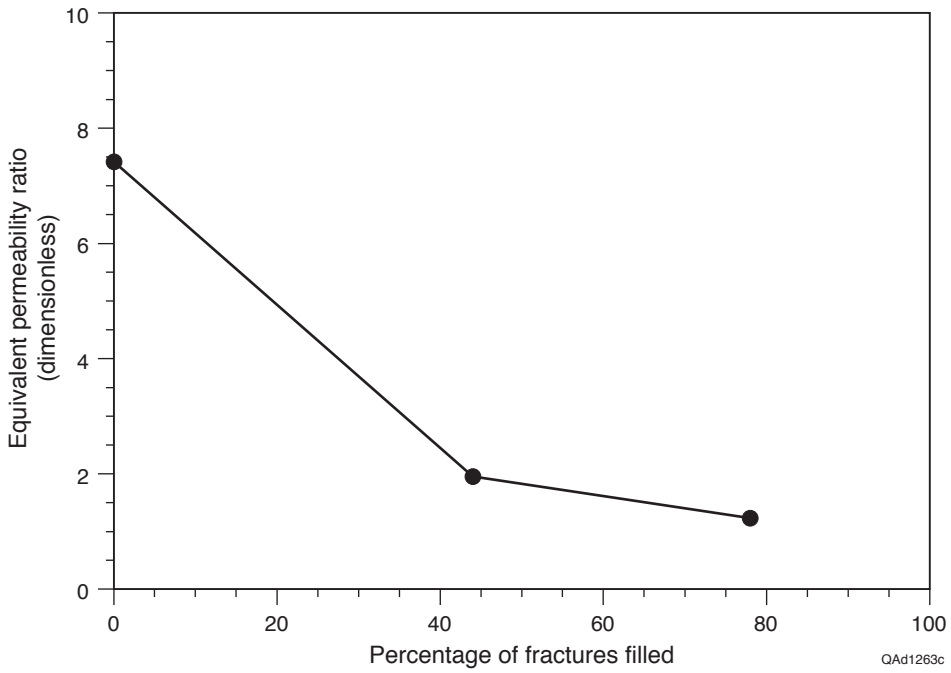

Figure 16: The effect of postkinematic cement on equivalent permeability for a SWCF simulated fracture pattern (realization 4) with a bed thickness of 10 m and subcritical crack index of 40.

Practical Approaches to Identifying Sealed and Open Fractures

Stephen E. Laubach

ACKNOWLEDGMENTS

Partly supported by U.S. Department of Energy Contract No. DE-FC26-00BC15308 and by industrial associates of the Fracture Research and Application Consortium: Barrett Resources, BG Group, Chevron USA, Conoco Inc., Devon Energy Corporation, Enron Global, EOG Resources, Japan National Oil Corporation, Lariat Petroleum, Inc., Marathon Oil, Pemex Exploración y Producción, Petroleos de Venezuela, Petrobras, Repsol-YPF, Schlumberger, Tom Brown, Inc., TotalFinaElf, and Williams Exploration & Production. We are grateful to associates for sample suites used in this study. R. Reed collected scanned CL images and A. Ozkan and A. Makowitz contributed to petrography. L. Bonnell, J. Gale, R. Lander, R. Manceda, R. Marrett, K. Milliken, W. Narr, J. Olson, and R. Reed influenced development of these concepts. Publication authorized by Director, Bureau of Economic Geology.

ABSTRACT

Knowledge of where natural fractures are open and capable of transmitting fluid would aid exploration, development, and management of many petroleum reservoirs. Yet this information is usually lacking because conventional analysis of vertical well bores provides only nonsystematic and incomplete samples of fracture arrays. More systematic and complete data can be acquired by substituting other observations as surrogates for direct fracture measurements. For one essential ingredient of permeable fracture networks—degree of fracture pore space preservation—I show how the inherent fracture sampling challenge can be overcome by measuring abundance of rock-mass cement that precipitated after fractures ceased opening. Analysis of a diverse core database shows that a high proportion of postfracture cement relative to postfracture intergranular volume ("degradation") correctly predicts where fractures having apertures of >1 mm are sealed. This "bad cholesterol" surrogate for observing fractures circumvents sampling limitations because it is readily measured in small rock samples, including sidewall cores and cuttings, permitting site-specific diagnosis of the capacity of fractures to transmit fluid over a wider range of sample depths than conventional methods allow.

Essential information on timing of fracture opening relative to paragenetic sequence can be obtained in two ways. First, evidence of fracture movement history and cement sequences in sparse large fractures can be extrapolated to areas having only readily acquired cement data. Alternately, where no large fractures are sampled, evidence of fracture timing can be acquired from crosscutting, sealed, µm-scale fractures and cements. Tests in wells having similar geology and engineering but differing degrees of natural damage to fractures show the surrogate accurately forecast fracture attributes and production response. Late cements decrease flow in large fractures by reducing connectivity of fracture networks or effective fracture length or by closing fractures altogether. Distribution of damaging cements is frequently heterogeneous (from bed to bed and location to location) in siliciclastic and carbonate rocks. But because it cannot be delineated using fracture observations alone, surrogates have practical value for production fairway mapping and other

applications in which identifying open fractures is essential. This study highlights the vital interplay among structural and diagenetic processes for fracture porosity preservation or destruction.

SEEKING OPEN FRACTURES

Many reservoirs having low porosity are known to be productive largely because natural fractures enhance hydrocarbon delivery to well bores. Yet exploration and development decisions must often be made in the face of great uncertainty about the contribution of fractures to production. This uncertainty stems, in part, from lack of data on fracture attributes. The role of fractures is commonly deciphered from well tests and from discrepancies between observed and expected production rather than from site-specific observations of fracture porosity, size, and connectivity. Fracture observations are frequently sparse or ambiguous. Repercussions of severely limited fracture data include foregone exploration and development opportunities and risk of surprises in production response. Undiagnosed fracture-system heterogeneity can cause unexpected exploration and development outcomes even where horizontal drilling is employed.

Thanks to the advent of logging tools that image fractures in the well-bore wall and coring procedures that maintain core integrity in fractured rock, log- and core-based methods usually provide some information on fracture attributes. Yet data are commonly incomplete because meaningful samples of fracture networks are inherently difficult to obtain. This difficulty occurs because the probability of intercepting vertical fractures with vertical wells is exceedingly small, approximately the ratio of well-bore diameter to average fracture spacing (Terzaghi, 1965; Narr, 1991; Lorenz and Hill, 1992). For the many areas where large fractures are moderately to widely separate or are arrayed in swarms, even the most complete logging and coring program will frequently miss large fractures. Consequently, a central challenge of subsurface fracture characterization is obtaining data on essential fracture attributes where direct observation is unlikely.

What properties make fractures effective fluid conduits and how can these be identified? Fracture permeability is proportional to the cube of aperture. Effective fracture permeability also depends on length and connectivity (lateral persistence) of fracture porosity. Apertures and lengths of fractures remaining open and effective for fluid flow reflect fracture growth, modern state of stress, and diagenesis. Of these, structural diagenesis—mineral precipitation and dissolution within fractures and host rocks—has received little systematic study. Current-day effective stress is widely viewed as a prime control on variation in fracture aperture (and fracture closure) (Crampin, 1994; Barton et al., 1995; Heffer et al., 1997). Yet in many petroleum provinces, orientation and location of open fractures are indifferent to stress regime (Dyke, 1995; Stowell et al., 2000).

Mineral deposits can preserve or destroy fracture-system permeability. Mineral deposits in fractures are widespread, ranging from isolated crystals lining open fractures to massive cements that completely fill fractures (Table A-1) (Nelson, 1985; Laubach, 1988; Dyke, 1995). It would be surprising if fractures that formed in the subsurface, in the presence of high temperatures and reactive fluids, were not subject to the same dissolution and precipitation phenomena that affect other pores in these rocks, and, as described later, fracture and host-rock diagenesis are frequently closely linked. Moreover, great heterogeneity is present in

the distribution of fracture-filling minerals within subsurface rocks, presenting an opportunity for targeting fractures that contribute to fluid flow and avoiding those that do not.

Microstructural surrogates for large fractures have previously been used to assess fracture strike (Laubach, 1997) and fracture intensity (Marrett et al., 1999). However, µm-scale fractures readily seal with cements that differ from those that close large fractures, and so alone they are inadequate guides to porosity preservation in large fractures (Figure 1). The purpose of this paper is to show how information on the volume and timing of cement precipitated in the rock mass itself (not in fractures) can be used as a proxy for direct fracture observation to predict whether large fractures are open or not. Empirical evidence from siliciclastic rocks, dolomite, and a few limestones shows patterns that are sufficiently systematic to allow sealed or open fractures to be inferred from a combination of observed host-rock microstructures and cements. I summarize evidence of these patterns in regional opening-mode fracture sets and show how they allow the fracture-sampling problem to be circumvented.

Models that quantify feedback between fracture growth, diagenetic reactions, rock-property evolution, and pore-pressure changes (Olson et al., 2001; Lander et al., 2002; Milliken, 2002; Noh and Lake, 2002) are beyond the scope of this paper. Much remains to be learned before linked diagenetic and mechanical models can make reliable fracture porosity predictions in advance of sampling in a given location. Fortunately, without sophisticated process-oriented models but with inexpensive site-specific petrographic *observations*, accurate and useful qualitative fracture predictions for the vicinity of the sample are feasible now.

DATA AND METHODS

Our data sets, methods, and terminology are described in Appendix 1. Most samples are from siliciclastic and carbonate rocks (primarily dolomite) in oil and gas reservoirs at depths of 6,000 to 14,000 ft (1,828 to 4,267 m) with some samples from outcrops and some from depths to 21,000 ft (6,400 m). Fractures are typical opening-mode (extension) fractures (Nelson, 1985). They are mostly inclined at close to right angles to bedding, so that they are nearly vertical in flatlying beds. Sets are marked by consistent preferred orientations over wide areas (approximately kilometers). Results are therefore most applicable to regional opening-mode fractures in siliciclastic rocks and dolomite that experienced moderate to deep and/or protracted burial. Owing to space limitations, illustrations and discussion in this paper focus on sandstones.

Two essential aspects of cement patterns in fractures and rock mass are evident only through extensive imaging using SEM-based cathodoluminescence (scanned CL, Appendix 1). By illuminating subtle chemical differences in cement and rock composition, scanned CL demonstrates widespread, previously mostly invisible µm-scale sealed fractures (Figure 2). Images also reveal crack-seal textures in large fractures (Figures 3, 4), formerly only documented in a few regional fracture systems (Laubach, 1988). Crack-seal texture defines fracture-opening history relative to cement sequence.

PATTERNS IN FRACTURE SEALING

Diagenesis refers to chemical and mechanical processes that convert sediment to rock. In many rocks, cement precipitation is a dominant process. Under moderate to deep burial, freshly broken fracture surfaces

are highly favorable sites for cement growth. Sedimentary rocks are porous, permeable media, so shared precipitation (and dissolution) in rock and fracture network is unsurprising. To a certain extent, fractures fill with cement in the same way that other pores fill. Yet fracture opening processes, timing, and size are critically different between fractures and pores.

Figure 1 generalizes two patterns in preservation or destruction of fracture porosity. In the first pattern, although small and large fractures frequently share initial stages of a sequence of cementation, microfractures preferentially fill with cement. Owing to their smaller size, larger surface area-to-volume ratios, and possibly also to less frequent reopening, pore space in small fractures is readily destroyed. Microfractures are thus readily sealed, whereas large fractures might remain open. In siliciclastic rocks and dolomite, for fractures having apertures less than ~ 0.1 mm, destruction of porosity is frequently nearly complete; large aperture size >~1 mm is crucial to porosity preservation. The most voluminous cement phases in the rock mass are frequently contemporaneous with fracture opening (synkinematic): quartz in siliciclastic rock, dolomite in dolomites, and calcite in limestone. Yet synkinematic cements are rarely the most prevalent in large fractures.

In the second pattern, pores are preserved in some large fractures but not in others because of late cements. Large size is no guarantee that fracture porosity is preserved. Late cements have uniform or heterogeneous distributions in both fractures and rock mass. Our data set shows that situations in which large fractures are sealed typically involve cements that precipitated in static rather than opening fractures. Moreover, traces of the late fracture-sealing cements are normally present in the rock mass as well as in fractures. Fracture porosity preservation above a certain threshold size defined by synkinematic cement implies that the culprit closing *large* fractures is cement that precipitates *after fractures cease opening*. At that stage, fractures are merely another variety of pore to be filled, and fracture quality depends on the volume of cement available to clog the fracture system: postkinematic cement. Where postkinematic cement is prevalent, flow in fractures should be impeded.

The surrogate for observing fractures that might be open or sealed is thus (1) fracture-timing information relative to diagenetic sequence, which identifies postkinematic cement, and (2) the volume of postkinematic cement. In the absence of *any* macrofracture observations, fracture timing can be obtained from sealed microfractures owing to a systematic transition from sealed microfractures to potentially open macrofractures (a transition size called “emergent threshold”). The following section illustrates these patterns.

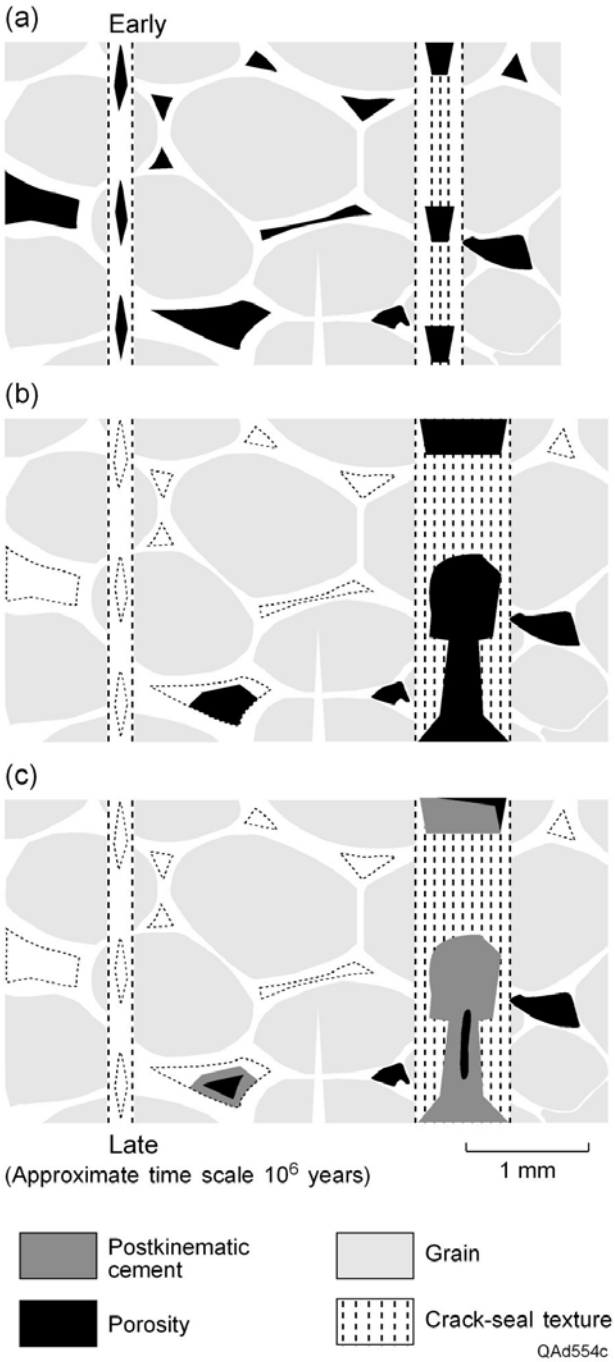

Figure 1. **Two ways that opening-mode fractures seal. (a through c) Microfractures sealed concurrently with fracture opening (synkinematic cement), whereas porosity is preserved in large fracture. (d) Large fractures lined by synkinematic cement but sealed by postkinematic cement, which is in both fractures and host rock. Fracture timing information and cement data combine to make a surrogate for fracture observation. See appendix for explanation of terminology. Diagram based on dataset in Table A-1, Laubach (1988) and models by Rob Lander.**

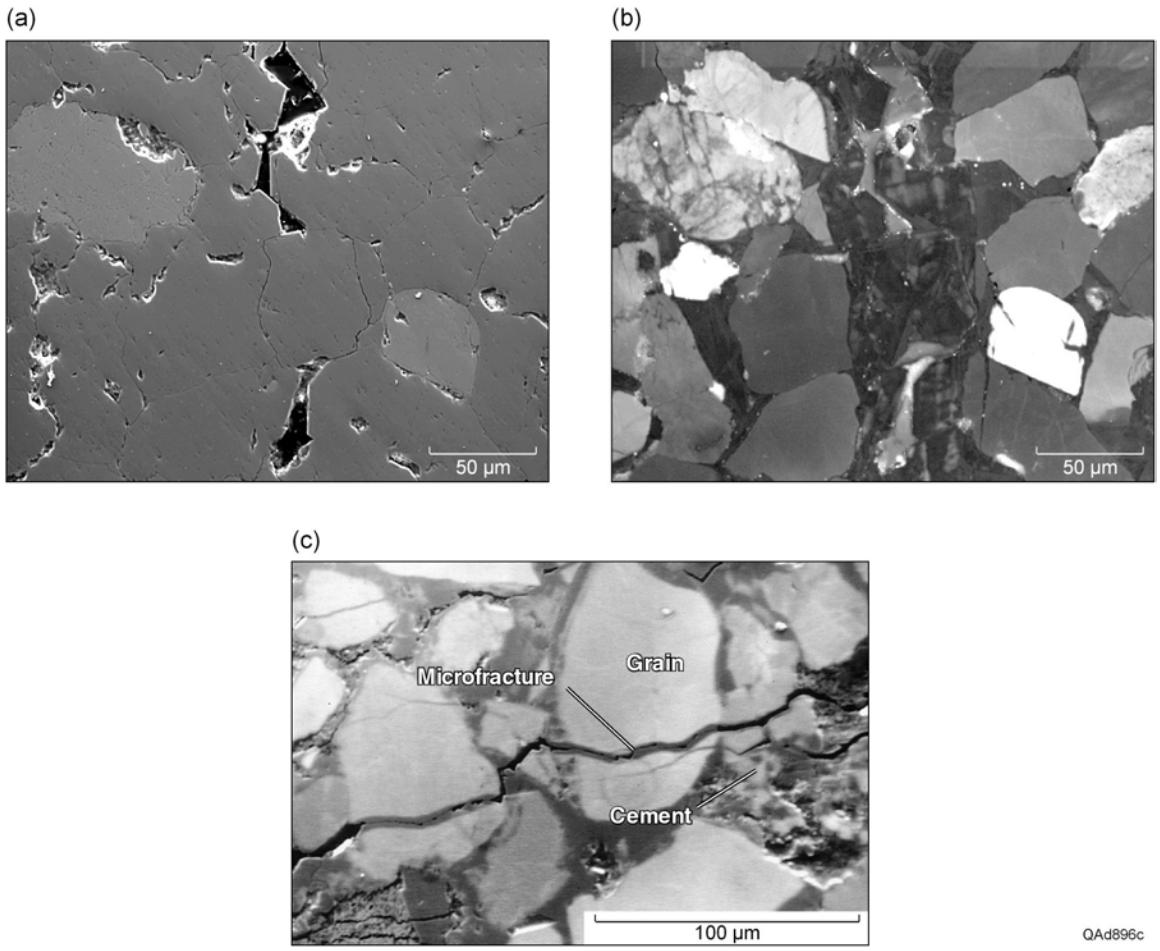

Figure 2. **Sealed microfractures detected using scanned CL. (a) Microfractures, Cambrian Flathead Sandstone, Wyoming. Secondary electron (SEI) image. Fractures are not visible. Black areas are porosity. (b) Scanned CL of same area, fracture is visible. Authigenic quartz is black, porosity and grains are grey. (c) Pennsylvanian Davis Sandstone, Fort Worth Basin. Superposed scanned CL and SEI image. Note trace porosity (black).**

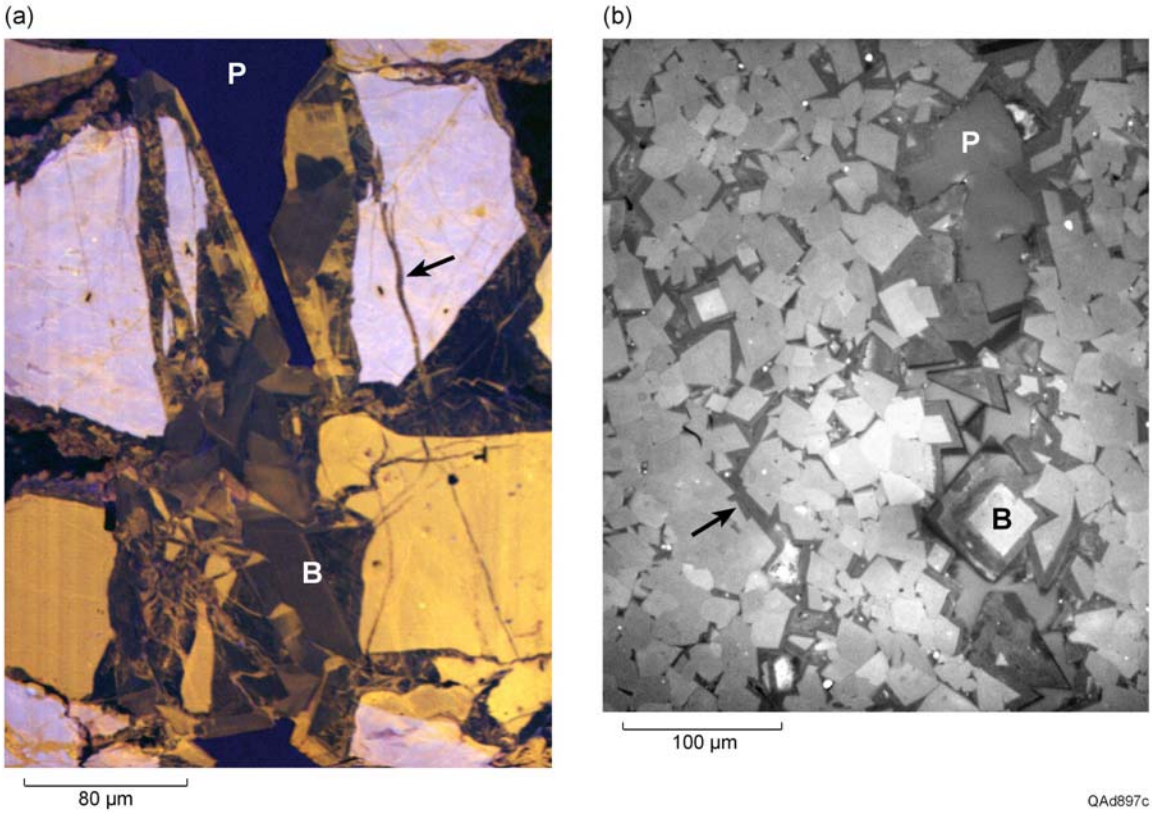

Figure 3. **Large and small fractures. (a) Open, bridged fracture and associated sealed microfractures (arrow), Cretaceous Lance Formation, Green River Basin, Wyoming. P, porosity. Note crack-seal texture in bridge, B. (b) Bridged, B, macrofracture having porosity, P, and sealed microfracture (arrow), Permian Ellenburger dolomite, Barnhart field, West Texas (Gomez et al., 2001). Scanned CL image.**

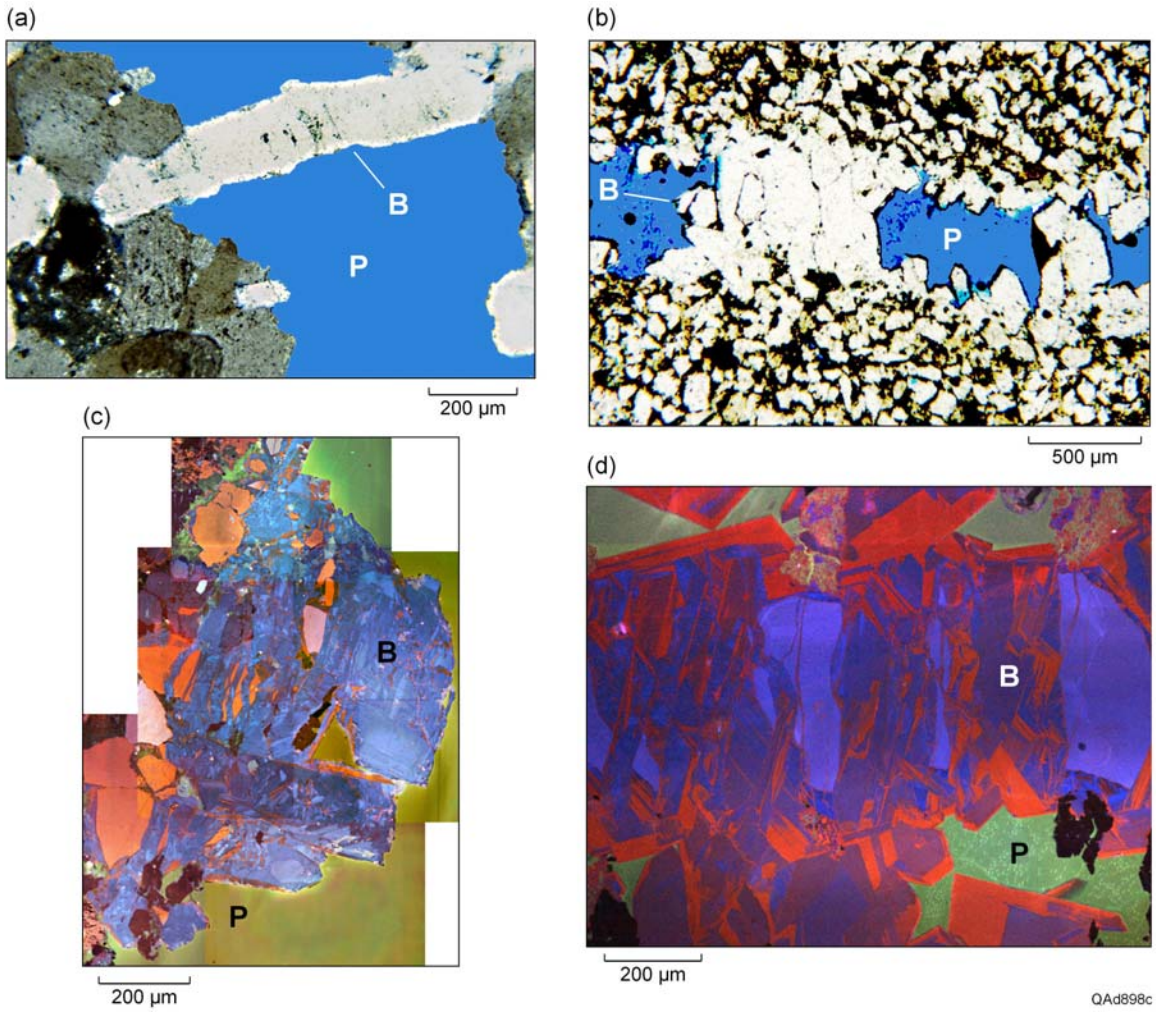

Figure 4. **Bridges and crack-seal texture. (a) Narrow quartz bridge, B, and open fracture, P, Cretaceous Travis Peak Formation, East Texas. Transmitted light. (b) Wide quartz bridge, B, and porosity, P, Cretaceous Travis Peak Formation, East Texas. Transmitted light. (c) Bridge, B, having crack-seal texture and porosity, P, Cretaceous Williams Fork Formation, Colorado. Scanned CL. (d) Narrow bridge, B, with crack-seal texture and residual porosity, P, Cretaceous Frontier Formation, Wyoming. Depth ~20,000 ft. Scanned CL images by Rob Reed.**

Fracture Internal Structure

Cements line or fill most fractures in our data set (Figures 2-7). Cement fill may be obvious or so subtle that detection requires a microscope and careful sample handling to preserve veneers fractions of a millimeter thick. Fracture pore shapes range from isolated and equant (including minute fluid inclusions in microfractures), through discontinuous and anastomosing channels, to continuous and tabular. Crystal morphology provides evidence of growth conditions. Faceted (euhedral) and massive (anhedral) to blocky crystal habits are common. Where they line otherwise open fractures, inward-projecting faceted crystals mark growth into open pores (Figures 3-5). Crystals projecting inward may increase in size but decrease in number toward fracture centers (cockade texture) because some crystals crowd out others as growth proceeds. A common texture is faceted crystals surrounded by anhedral crystals, marking cement growth into open space succeeded by infilling during fracture closure. Subhedral and anhedral crystals may also record etching and dissolution of fracture-filling minerals. Although abundant blocky mineral filling in

fractures is often the most obvious (and abundant) cement, inconspicuous µm- to mm-thick veneers of authigenic cement are prevalent and may be the only cements present in otherwise open fractures.

Cement spans some fractures, forming mineral bridges that range from isolated, narrow (<0.05 mm) pillars to wide, semicontinuous masses having contact areas on fracture walls of tens of mm^2 or more (Figure 4). Bridge substrates range from individual grains that have nucleated cement growth to areas much larger than those of individual grains. In many cases thickness (and volume) of cement within a bridge is considerably larger than thickness of the same phase lining adjacent areas of fracture. Bridges are common in siliciclastic rocks, dolomite, and limestone over a range of fracture sizes. Some bridges result from incomplete cement fill in static fractures, but many are a consequence of cement precipitation in opening fractures. As discussed in the next section, they contain compelling evidence of fracture-opening history.

Evidence of Fracture-Opening History

Crack seal is a deformation mechanism in which small increments of extension repeatedly occur across a planar discontinuity, followed by repeated sealing by cement (Hulin, 1929; Ramsay, 1980). Crack-seal texture records fracture history marked by progressive reopening and filling of breaks within fill as fractures grow (Figures 1, 4). Crack seal is ubiquitous in cemented, moderately to deeply buried siliciclastic rocks, even in unstructured rocks distant from large folds and faults.

Some fracture-fill fabrics are layered, banded or, rarely, fibrous, with layers paralleling fracture walls and crystal bands or fibers aligned at a high angle to walls. Layered fabrics are frequently faint or obscure under transmitted light. Scanned CL shows that layering and banding in fracture-filling cements is crack-seal texture. This texture is marked by lamination parallel to fracture walls defined by wall-rock inclusions, broken cement inclusions, cement zoning cut by fractures, and fluid-inclusion planes (Figures 3, 4). The crack-seal process also produces inclusion trails and apparent “stretched crystals” oriented at high angles to fracture walls. The latter result from fills in crystallographic continuity with wall-rock grains. In quartz and dolomite, stretched crystals and bridges commonly have alternating wide and narrow segments (serrate structure) that reflect cement growth from broken wall-rock particles and connecting cement.

Crack-seal texture is common in isolated single crystals or clusters of crystals that span or that formerly spanned a fracture. These cement bridges are contemporary with fracture opening (Figure 4). Euhedrally terminated crystals growing into fractures (partial bridges and fracture-lining material) commonly show crack-seal texture at their bases. Wide fractures may lack bridges in their centers because cement precipitation rates (or durations) were insufficient to bridge during fracture growth. These fractures have only relict crack-seal texture near formerly bridged segments. Bridges having crack-seal texture mark mineral growth sufficient, locally, to connect opposite fracture walls. Intact bridges are evidence of cessation of fracture widening; more fracture growth would have broken the bridge. Cements in fractures that postdate intact bridges must therefore have precipitated in dormant fractures. However, faceted crystals that grew into open cavities cannot record fracture wall movement.

Crack-seal texture identifies which cements precipitated during fracture opening. In siliciclastic rocks, crack-seal texture is common in isolated fracture-bridging quartz nucleated on broken quartz grains. Some crystals and bridges show dozens to hundreds of µm-scale, sealed fractures. Crack-seal texture is present, although generally less obvious, in dolomite bridges in fractured dolomites and in calcite lining fractures in limestone because textures in carbonate minerals are challenging to discern using existing CL imaging methods (Reed and Milliken, submitted). In these rocks bridges having serrate structure mark crack-seal processes.

Crack-seal texture is present in microfractures as narrow as 35 µm. Many of the smallest fractures lack crack-seal texture, partly owing to limits of imaging resolution, partly because many filled after only one increment of opening. Crosscutting and overlapping relations among microfractures and cements (Reed and Laubach, 1996) show that these small and widely separate fractures formed and filled progressively as cement precipitated, recording fracture-timing information in the rock far from large fractures.

Bridges and Porosity

Association of crack-seal texture with discontinuous bridges implies that bridges and porosity developed concurrently. Bridges are either flanked by porosity or by cements deposited after fracture growth ceased. Fractures having bridges, crack-seal texture, and adjacent areas of porosity (or later cement) are widespread (Figures 3, 4). This association most likely reflects low solute concentrations (per volume fluid) at moderate temperature and burial depths. Precipitation may be a rate-limiting factor; models show that precipitation on numerous subparallel, fresh fracture surfaces can account for greater cement thickness in bridges than can the same phase lining adjacent fracture walls (Lander et al., 2002). Rapid cement growth on new fracture surfaces and repeated renewal of surfaces result in positive feedback for bridge growth. Crack-seal texture shows that fracture-pore-space retention with increasing aperture size results partly from competition between fracture opening and sealing that large fractures win (that is, they retain open pore space). Crack-seal texture is compatible with overall cement precipitation patterns that are broadly episodic or essentially continuous.

Bridges in siliciclastic rock or dolomite having crack-seal texture are frequently surrounded by a veneer of unfractured quartz or dolomite, marking cement precipitation after last increments of opening. Fractures may also be bridged or filled by quartz, dolomite, calcite or other phases that lack crack-seal texture, marking cements that filled static fractures, as described in the section on cement sequence.

Fracture-Size Effect

Fracture size is an important variable for understanding fracture porosity preservation. Shared cements and textures that reflect fracture opening (as well as orientation and size-distribution) link micro- and macrofractures. Yet fractures of contrasting size may differ markedly in their porosity.

It is convenient to approximate fracture size with kinematic aperture, the distance fracture walls have moved apart (Marrett, 1996; Marrett et al., 1999). Because of cement, kinematic aperture is usually greater

than any open gaps (which are absent if fractures are sealed). Aperture sizes were measured on high-resolution (>200×) CL images, with micrometers on transmitted light microscopes and using graduated aperture comparators (Marrett et al., 1999). In terms of kinematic aperture, sampled fracture size in sandstones and dolomites ranges from μm to tens of centimeters, but most fractures in our data set have apertures of a few millimeters or less. According to outcrop studies, lateral persistence (length, connectivity) has dimensions of μm to as much as kilometers.

Fractures having apertures of less than 0.1 mm usually require magnification to observe, and I call these *microfractures*. Some reflect processes operating only at microscale, and others in clastic rocks are inherited (Laubach, 1997). In many rocks, however, both micro- and macrofractures have a spectrum of sizes that follow systematic patterns (Marrett, 1996). Where these size distributions are quantified, they have many small and fewer large fractures; populations can be described with power laws over a wide range of sizes (Marrett et al., 1999; Ortega and Marrett, 2000; Stowell, 2000; Gillespie et al., 2001; Ortega et al., 2001). Arrays have timing and orientation that match associated large fractures. In many respects micro- and macrofractures are merely different-size fractions of the same fracture sets.

Yet microfractures tend to be sealed, or they have only small, discontinuous areas of porosity, whereas large fractures of the same set may be open (Laubach, 1997; Milliken and Laubach, 2000) (Figures 2, 3). Size-dependent porosity is most evident where μm- to millimeter-scale fractures and large fractures of the same set are present (observed in more than 55 siliciclastic units). As width diminishes, many fractures show increasing bridging along their traces, with partial to complete fill more prevalent near tips, where apertures are smaller. Typically a single phase is responsible for sealing microfractures (i.e., quartz, dolomite, or calcite). In a single set, cement that fills smaller fractures lines or bridges larger fractures.

Size-Dependent Fill and Emergent Threshold

For cements associated with fracture opening, as fracture size increases, degree of contemporaneous cement fill decreases. Size-dependent fill is evident for cements that form crack-seal texture. A transition—the emergent threshold—marks the fracture size where porosity predominates over synkinematic cement contemporaneous with fracture opening. For cements precipitated during fracture opening (marked by crack-seal texture), transitions from sealed to open fractures generally occur over aperture-size ranges of ~0.01 to 1 mm in the siliciclastic rocks and dolomite we studied (Table A-1). In limestone limited data suggest a similar pattern, but with transitions from sealed to open fractures at larger aperture sizes (~1 to ~10 mm or more), possibly owing to rich sources of $CaCO_3$ in solution in limestone undergoing burial and pressure solution.

Although cement volumes and precipitation rates are sensitive to ambient temperature, solute concentration, and rock type, under uniform precipitation rates, μm- to millimeter-scale fractures will seal first, whereas more time is needed for accumulating cement sufficient to fill larger fractures owing to large surface areas relative to volumes of narrow versus wide fractures. Because large fractures may have been

subject to numerous opening events, competition between fracture and sealing, as well as fracture size, could possibly help conserve voids in large fractures.

Amongst sandstones there are regional differences in emergent threshold size. For example, in Cretaceous sandstones in a passive margin setting in East Texas, at depths of ~3,000 m, microfractures having apertures between 0.1 and 1 mm preserve pore space. In contrast, some open, quartz-lined microfractures having apertures of 0.001 mm or less are open in Cretaceous sandstones from South American foreland basins at similar depths. These differences could merely reflect different times of fracture formation. The South American microfractures may be of recent origin in this tectonically active area. In general, regional differences could reflect burial and fracture history, rock type, fluid geochemistry, and other factors (Lander et al., 2002).

The transition from sealed to open fractures for synkinematic cements is apparent in many data sets partly because it occurs in microfractures and small fractures that are well represented in core. Transitions are constrained to within about an order of magnitude in fracture size partly because they are gradational. For late cements in large fractures, evidence of size-dependent fill is sparse owing to the narrow size range of large fractures in most data sets. Moreover, late-cement quantities vary abruptly and are absent in some areas.

Emergent threshold is more than a fracture-porosity threshold because cement that precipitated during fracture opening defines the transition. Moreover, in polymineralic fractures, late cements may substitute for porosity, preserving evidence of shifts from sealed to open fractures defined by early cement (Figure 5). An emergent threshold is present in fossilized form in these fractures. Fractures above the threshold may be open or sealed, depending on volume of late cements present. Transition sizes are generally measurable, and those large fractures that could have the biggest impact on flow are generally well above the threshold.

The emergent threshold is important because microfractures having sizes below the threshold are not evidence that larger fractures of the same set are sealed. For a workable surrogate, microfractures can specify when fractures formed in a rock's diagenetic history. Yet they cannot record cements that could damage large fractures because μm-scale fractures rarely preserve polymineralic relations (these are locally apparent in millimeter-scale fractures) or porosity. Microfractures alone therefore cannot be proxy for degree of occlusion in large fractures. Information about polymineralic cement sequences from another source is needed. The other key to a useful surrogate is polymineralic cement patterns in a rock's pore space.

Cement Sequence and Closure of Large Fractures

Many fractures are lined or filled with a single phase (for example, quartz, dolomite, calcite), whereas others contain two or more phases that may show overlapping and crosscutting relations defining co-precipitation or, most commonly, precipitation sequence (Figures 5, 6). Overlapping relations among phases mark sequence of precipitation and dissolution (paragenetic sequence). In sedimentary rocks, cements in opening-mode fractures are frequently the same as those in the inter- and intragranular volume.

Where millimeter- to centimeter-scale fractures having several generations of cement are present, sequences in fractures and host rock are commonly closely similar. Fractures thus share the diagenetic imprint of porous host rocks.

A rock's intra- and intergranular volume can provide evidence of late cements that is lacking within microfractures (Figure 7). Although microfractures have length dimensions that are larger than or comparable to those of many pores, they typically have slotlike aspect ratios that assure small volume relative to surface area as compared with that of pores. They are thus more prone to seal under the same burial conditions. Moreover, because microfracture surfaces are initially mostly fresh and, hence, disposed to cement nucleation, primary and secondary pores in siliciclastic and carbonate rocks can potentially more faithfully record postfracture deposits in the rock—and in nearby large fractures.

Many fractures that we studied are probably not in physical contact in a network, although they are connected for flow via rock pores. Within our samples, envelopes on fractures made of narrow zones of disseminated cement are absent. This situation contrasts with that of some faults, which may localize their own fluid environment, as well as fractures in impervious rocks such as granites, in which cement phases are localized within or near interconnected fracture systems. Moreover, although differing widely in burial history, most fracture arrays that we sampled are in rocks buried to substantial depths where they have remained. Consequently, evidence of exposure to near-surface loading and fluid conditions is underrepresented. In outcrop and under cool, near-surface conditions, cements may not precipitate and fractures can remain barren (e.g., joints), undergo dissolution, or they may be filled only much later as rock and fractures undergo burial or near-surface cementation. Cement dissolution in fractures, although certainly important in some systems, is rare or has been obscured by overprinting cements in most fractures that we studied.

In our sample suite, early cements in fractures tend to be the same phases as those that dominate in the substrate. In siliciclastic rocks, fracture-lining cement is predominantly quartz (locally, authigenic feldspar), in dolomite rock, dolomite, and in limestone, calcite. These are the same phases, respectively, that are most abundant as cement in associated rocks. Congruence between initial fracture cement and overall rock composition holds mostly even where early (prekinematic) cements differ. For example, initial quartz along fractures is evident in siliciclastic rocks having moderate amounts (~20 percent) of prefracture calcite and dolomite cements, although it is not noticeable in sandy limestones. Initial dolomite precipitation is apparent in dolomites having abundant prefracture anhydrite and calcite cements. This pattern also holds where more than one fracture set is present, even where polymineralic fracture fill exists in early-formed fracture sets. These patterns suggest that rock composition influences initial cement precipitated in new fractures. This fact is not surprising if fracturing is a relatively rare event and rock-dominated geochemical conditions prevail during burial.

Textures in fractures also reflect substrate composition. Fracture-lining quartz tends to grow in crystallographic continuity with grains, leading to fracture linings in sandstone and siltstone that resemble overgrowth cement. Substrate control on cement nucleation is also apparent for minor phases such as

authigenic feldspar on feldspar substrates. Crystal sizes, at least initially, are similar to grain size, and in some cases c-crystallographic axes of broken wall-rock grains govern orientation of elongate crystal growth into fracture pore space. Similar patterns are evident in some dolomite-lined fractures in dolomite, but possibly owing to finer substrate crystal size or fine cockade texture, early cements in dolomite and limestone fractures can appear layered. For many fracture surfaces veneers of new mineral growth are localized on—and crystals are about the same size as—host-rock grains or crystals. In large fractures, thickness of initial mineral fill is generally small but variable, depending partly on burial history and identity of the phase. Quartz and dolomite linings are normally less than 1 mm and commonly only a few μm thick, whereas calcite in limestone frequently fills fractures having apertures of several millimeters to centimeters.

The first cement to precipitate in most fracture arrays can be identified with confidence. Within fractures in siliciclastic rocks, sharp, broken walls of fractures are frequently visible, preserved under a veneer of the first cements to precipitate. Commonly this initial phase is quartz. Similar, although in many cases less definitive, evidence of sharp fracture-cement contacts in dolomites suggests that authigenic dolomite also mostly precipitated on fresh fracture surfaces in examples that we studied. Association with crack-seal texture is compelling evidence that these cements partly precipitated while fractures opened.

Although the same early phase typically lines large fractures of a given set, late cements commonly have heterogeneous distributions, and they may be absent. These patterns show that late cements do not uniformly affect all fractures in an area to the extent that early cements do. Abrupt variations in presence and abundance of these cements from bed to bed, formation to formation, and well to well are common. In the rock, late cements are frequently present in small volumes (<10 percent) and may be rare (<1 percent) or absent.

First cements to precipitate frequently seal millimeter-scale and smaller fractures, but larger fractures (above emergent threshold) have porosity or several generations of cements (polymineralic fractures). Large fractures of about the same size, age, and orientation may thus be sealed or open. Typical late cements include calcite, ferroan calcite to ankerite, barite, anhydrite, and various clay minerals. Late cements typically fill pore spaces having shapes defined by initial cement (for example, mineral bridges), as well as by fracture geometry. Distributions range from patchy to tabular, depending on size and shape of available pore space and cement volume. Where they occur together, late cements overlap early cements or fill voids between intact bridges that contain crack-seal texture (Figure 6). This pattern shows that late cements mostly precipitated in static (not opening) fractures.

Paragenetic sequence, as well as fluid-inclusion and isotopic data, link fracture and host cements (e.g., Pitman and Sprunt, 1986; Laubach, 1989; Stone and Siever, 1996; Montañez, 1997). Diagenetic patterns may be complex, reflecting thermal and fluid history, and therefore difficult to understand and predict. Unlike large fractures, however, there is no challenge in sampling and describing polymineralic cements because these pervade the rock mass. Although many rocks contain several fracture sets formed at different times, as well as complex and, in some cases, repetitive sequences of cements, to the extent that diagenesis

affects both rock and fractures, cements in the rock mass provide evidence of cements that may be in fractures.

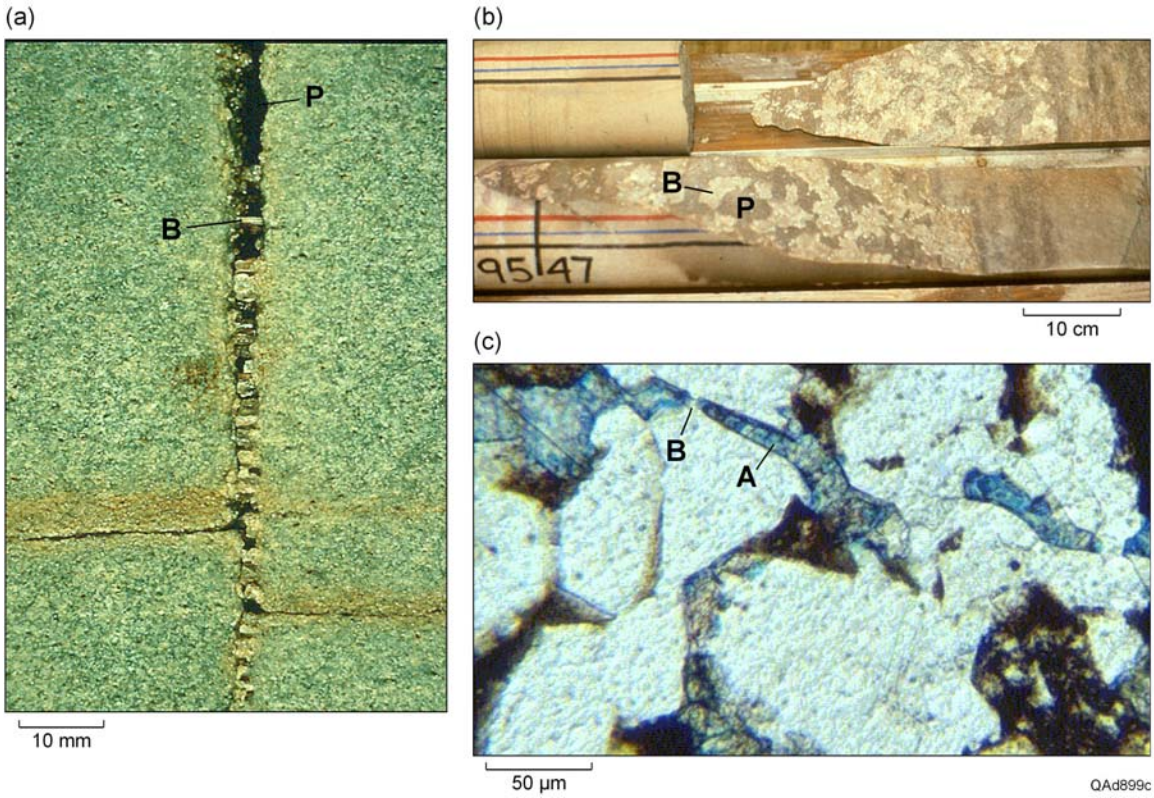

Figure 5. Cement deposits in fractures. (a) Increased fill percentage and bridging, B, near fracture tip, synkinematic quartz in open, P, fracture, Cretaceous Travis Peak Formation. (b) Quartz lined open fracture, P, having later, partial ferroan dolomite infill, P. (c) Quartz bridges, B, surrounded by later Fe-dolomite (A, blue stain), Lance Formation. Transmitted light. (d) Quartz and Fe-dolomite sealing fracture in Permian Weber Sandstone, Rangeley field, scanned CL. Note microfractures sealed with quartz, crack-seal texture, and late Fe-dolomite.

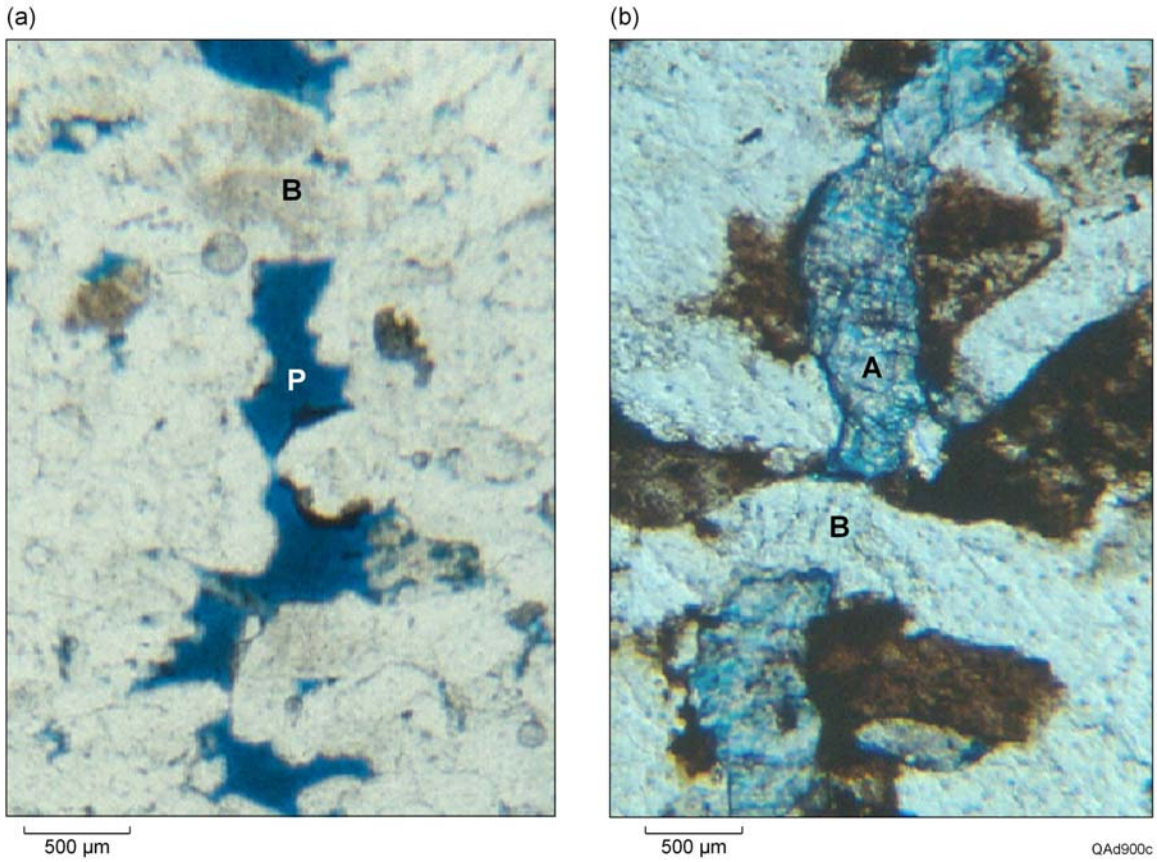

Figure 6. **Open and sealed fractures and associated cements. (a) Open bridged fracture, B, and porosity, P, Jurassic Cotton Valley sandstone, East Texas. Fracture is above emergent threshold. (b) Bridged fracture, B, sealed with postkinematic ferroan dolomite, A, Cretaceous Cody Sandstone, Wyoming. Fracture is above emergent threshold but sealed by later cement. Emergent threshold is fossilized by late Fe-dolomite cement.**

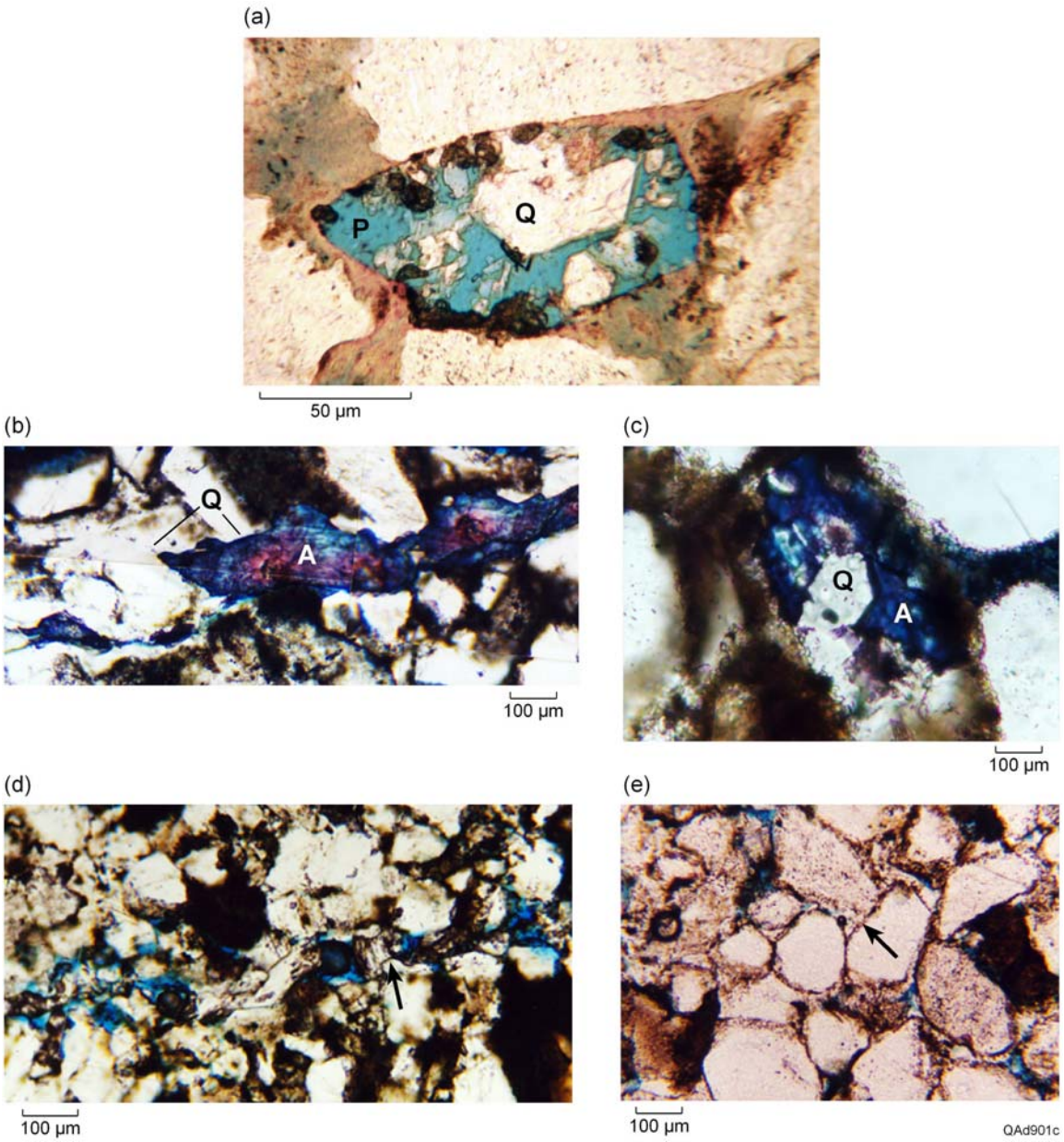

Figure 7. **Pore surrogates for fractures. (a) Secondary pore lined with quartz, Q, and containing porosity, P, Cretaceous Lance Sandstone. Compare, figure 3a. (b-e) Permian Wolfcamp sandstone, Texas. (b) Quartz-lined fracture, Q, sealed with Fe-dolomite, A. (c) Secondary pore lined with quartz, Q, and overlapped and filled with Fe-dolomite, A, same unit and depth. (b) Quartz-lined open fracture, arrow. (d) Pore lined with quartz, arrow, same unit and depth as (b). All samples are from same well and fractures have same strike. Transmitted light.**

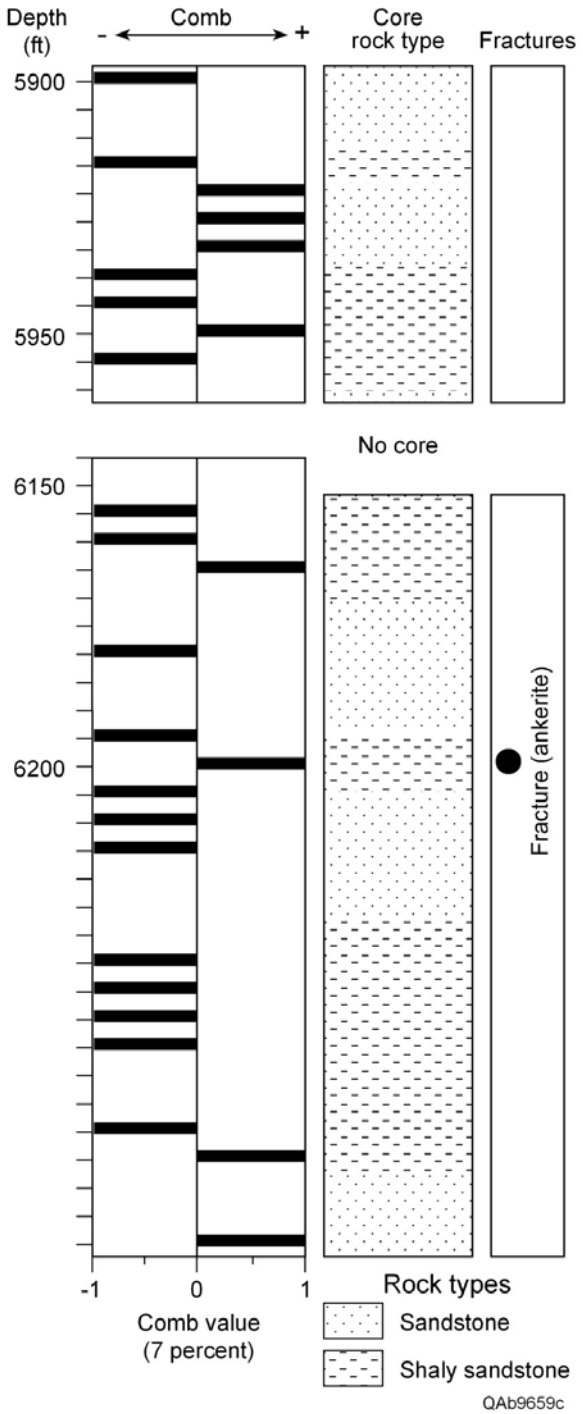

Figure 8. **Postkinematic cement abundance versus depth, Cotton Valley sandstone core. (a) Comb plot flags abundances greater than specified value (here, 7 percent). (b) Cement and porosity percentages. Capacity to record late cement is shown by ratio of postkinematic cement to residual pore space. Length of bars indicates postfracture inter- and intragranular volume. Some samples are filled to capacity yet contain less than "comb" rock mass postkinematic cement values. (c) Same data plotted as degradation.**

APPLYING AND TESTING THE SURROGATE

Judging by regional fracture sets in cores (Table A-1), synkinematic cements line large fractures, but cements that postdate fracture opening—postkinematic cements deposited in static fractures—seal large

fractures (Figure 6). Because large fractures are most likely to influence fluid flow on production time scales, the essential surrogate to replace observation of damage to large fractures is rock-mass postkinematic cement volume. Postkinematic cement is the surrogate for degree of porosity retention in large fractures, the "bad cholesterol" factor that predicts damage. The objective of rock measurements is to identify postkinematic cements and quantify their volumes. Herein I show how to translate this idea into a usable surrogate and compare predictions in several test cases to fracture observations.

Postkinematic Cement and Degradation

What is the best way to quantify postkinematic cement volume and how does a given amount of cement translate into damage to fractures? Once fracture timing is discovered from macro- or microfracture observations, whole-rock volumes of postkinematic cements in inter- and intragranular volume (IGV) can be obtained readily and accurately from point counts. In siliciclastic rocks, common postkinematic cements include calcite, ferroan calcite and ferroan dolomite, ankerite, barite, and clay minerals. In dolomites, common postkinematic cements are anhydrite, calcite, and ferroan dolomite. Useful damage predictors include absolute abundance of postkinematic cement and ratios of postkinematic cement to some measure of rock volume into which late cements are precipitated. These predictors could be labeled fracture-cementation or fracture-fill indices, but they are derived from the rock mass, and do not involve fracture observation.

Plots of postkinematic cement volume, or indicators based on volumes, can be informative. Figure 8 shows data from a well in which one large, sealed fracture (aperture ~2 mm) was sampled. It is lined with synkinematic quartz but filled with postkinematic ankerite. Corresponding whole rock volume of postkinematic cement is 7 percent. The plot flags depths that have postkinematic cement volumes above or below a specified value (in this case, 7 percent). Values for flags can be selected using fracture or production observations. This plot shows how surrogate use can guide geologic interpretation. Although a sealed fracture was sampled, how representative is it? Postkinematic cement volumes overall are generally low in the cored interval, and elsewhere in this formation, open fractures are present where rock-mass postkinematic cement values are low. The sealed fracture could thus be misleading.

Owing to large amounts of synkinematic cement, in many cases IGV available for postkinematic cement is small (typically <20 percent and in many cases only a few percent), and rocks have limited and variable capacity to record postkinematic cement. In Figure 8 and in most rocks we sampled, postkinematic cement volumes are low. For example, 15 East Texas Jurassic Cotton Valley sandstone samples have average volumes of postkinematic ankerite slightly over 3 percent, ranging from 0 to slightly more than 9 percent. Porosity values are similar (average ~3 percent, range 0 to 8 percent). Because capacity to record is variable, cement volumes alone are problematic for use as a surrogate.

An alternate is to normalize postkinematic cement volume to space available (postfracture IGV). This normalization facilitates comparison of samples having variable postfracture IGV. *Degradation index (Dg, percent)* is the ratio, in the rock mass, of cement that postdates fracture opening to available rock-mass porosity (postfracture inter- and intragranular volume) (Figure 9). Plots of this ratio versus depth are

convenient for intra- and interwell comparisons. High degradation (values near 100) implies sealed fractures (Figure 10). Although many samples having high degradation also have low porosity, it is not always the case, for example, where secondary porosity postdates and does not affect fracture fills. However, degradation is most valuable for discriminating rocks having low porosity owing to synkinematic cement and rocks having lower porosity owing to traces of postkinematic cement. Only in the latter case is damage to the fracture system indicated.

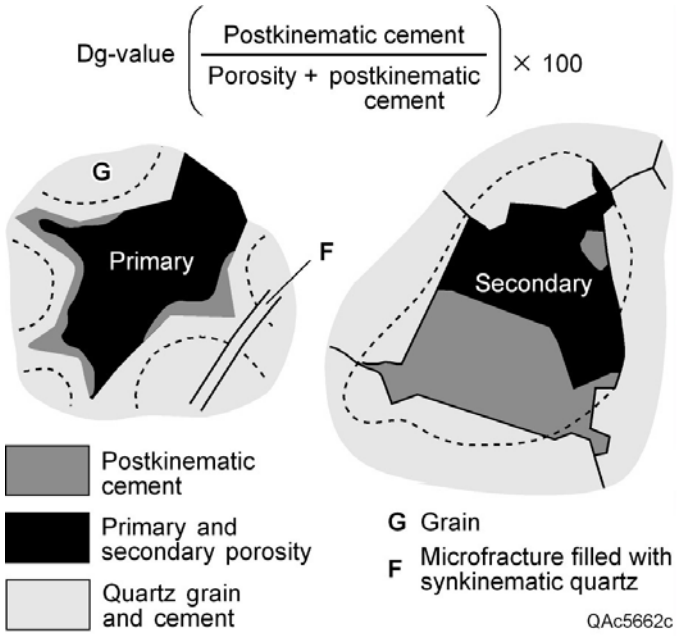

Figure 9. **Degradation (Dg), a measure or fracture quality (likelihood of porosity preservation). Possible values range from 0 to 100 percent. Where postkinematic cement is absent, Dg is zero, and large fractures should be open (albeit with linings and bridges of synkinematic cement), even if rock-mass porosity is small. Increasing postkinematic cement implies that large fractures contain fill that would be absent if degradation was low. Values near 100 percent predict sealed fractures. Because Dg is a measure of rock-mass properties rather than of fractures themselves, degradation is not a fracture-fill or fracture-cementation index.**

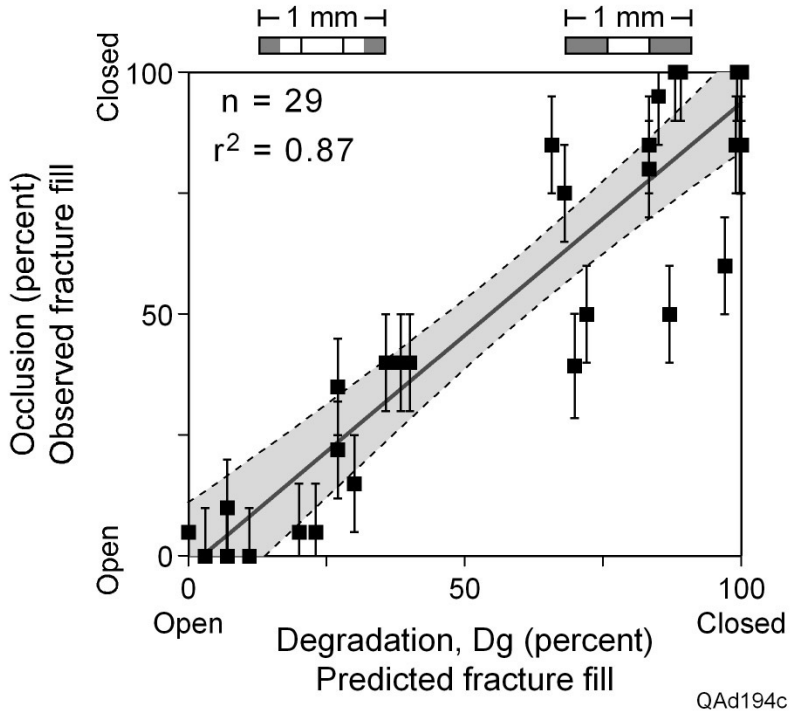

Figure 10. **Fracture observations (occlusion) versus surrogate predictions (degradation). Data are from sandstones from four formations having thorough estimates of pore space lost for fractures above emergent threshold (Wolfcamp, Weber, Cotton Valley, Lance). Error bars mark qualitative uncertainty measuring potential macrofracture void space. In a larger data set where fracture observations are subdivided into fewer categories (open, partly open, and sealed), apparent agreement is stronger between predictions and observations, which shows that a limitation in testing the surrogate is sparse accurate occlusion data.**

Testing the Surrogate

Tests compare predictions of degree of fracture fill (degradation) with observed infill (occlusion) in large fractures (Figures 10-12). In 42 units, postkinematic cement was the culprit in sealing large fractures (Table A-1). Data from sandstones show that low postkinematic cement volumes correspond to open fractures and high postkinematic cement values correspond to sealed fractures for fractures above emergent-threshold aperture size. Numbers of intact large fractures and uncertainty in estimates of pore space or postkinematic cement volume in fractures limit tests. Although there is agreement between surrogate predictions and fracture observations, particularly at high and low values, at intermediate values there is considerable scatter. This difference is partly due to difficulty in accurately measuring filled or open pore space in small macrofractures.

Shifts in postkinematic cement volumes within a single formation and fracture set correspond to variable preservation of open fractures. Degradation values derived from the rock mass correctly predict filled versus open fractures. In Weber Sandstone, Rangeley field, fracture observations corroborate heterogeneous fracture quality (Figure 11). But by deriving surrogate predictions from core that lacks large fractures, we can discern the *pattern* of fracture quality. Although good core coverage allowed numerous degradation measurements, in this well only four large fractures were sampled. As predicted, large fractures are lined with synkinematic quartz, and large fractures filled with postkinematic cement are in rocks having

high degradation. Evidence of cement heterogeneity is widespread, implying that fracture quality is also locally highly variable, in agreement with observed fractures.

Fracture occlusion patterns are evident in large core suites. In 8 Lower Cretaceous Travis Peak Formation wells having more than 2,099 ft of core (average 260 ft/well, range 84 ft to >570 ft) 118 macroscopically visible fractures were described, fewer than 0.1 fractures per foot of core (Laubach, 1989). Average kinematic aperture is only 0.1 mm. Of 118 fractures, 41 are so narrow that they are entirely filled with synkinematic quartz; these are below emergent threshold. Of remaining fractures, 32 are open but quartz lined and 45 contain polymineralic cements and are partly to completely sealed. Postkinematic cements are primarily ferroan dolomite and ankerite. For 251 analyses, average postkinematic cement volume is a mere 3.4 percent. Comparing open, partly sealed, and filled fractures with nearby degradation estimates shows that 98 percent of predicted open fractures correspond to open fractures and 93 percent of predicted partly sealed and sealed fractures correspond to fractures having appropriate attributes. The source of discrepancies is core damage, heterogeneity of postkinematic cement distribution, and inaccurate macrofracture porosity description.

Horizontal wells provide another perspective on fracture-sealing patterns. More than 1 dozen fractures range from sealed to open in about 30 ft of Cretaceous sandstone core cut subparallel to bedding and at a high angle to fracture strike. Postkinematic cement is uniformly low throughout this core, correctly predicting that large fractures are open. Synkinematic quartz seals closed fractures, which are near or below emergent threshold, having apertures between 0.1 and 0.01 mm or less, and lines open fractures. Yet in vertical core from adjacent wells in slightly shallower sandstones, sealed fractures are found in rocks having high degradation.

High degradation correctly predicted sealed macrofractures in all four dolomites that we studied (Table A-1). For example, Cretaceous Cupido dolomite contains several fracture sets delineated by micro- and macrofractures. Synkinematic dolomite, an emergent threshold, and postkinematic calcite sealing large fractures are all present (Monroy et al., 2001). The surrogate approach is therefore feasible in carbonate rocks but can be challenging owing to problems in discriminating pre- and postkinematic phases, which include calcite, anhydrite, and dolomite (Gomez et al., 2001; Monroy et al., 2001).

Well Pairs

Evidence that high degradation results in impeded fluid flow in fractures was found in well pairs where geologic and engineering parameters are similar and effects of fractures can be isolated. Low degradation and fracture-enhanced production and the reverse are evident in well pairs from Cretaceous and Paleozoic sandstones from foreland and passive margin settings where fractures are inferred to provide intrareservoir flow pathways (Table A-1). Because these paired wells have similar depositional environment and stimulation, surrogates apparently detect fracture-quality differences affecting fluid flow. The most complete match in engineering procedures and data completeness is in two wells from Paleozoic sandstone in West Texas. Here degradation values are systematically lower in well A than in well B, suggesting that open fractures should predominate in well A (Figure 12), as is observed.

Each well was cored through the same turbidite sandstone unit, and initial grain compositions and paragenetic sequences of cements are identical. Completion and stimulation procedures in both wells were similar. Porosity data from these wells are statistically indistinguishable, probably because synkinematic quartz cement is volumetrically dominant in both cored intervals. A slight decrease in average porosity in the well having higher average degradation values reflects slightly higher postkinematic cement volumes relative to porosity in well B. Despite both cored intervals having approximately 10 percent prekinematic carbonate cement, large fractures are lined and locally bridged with quartz, which is synkinematic judging by the presence of crack-seal textures in bridges. Postkinematic cements are ferroan dolomite, calcite, and barite.

Both wells intercepted large fractures having identical strike that formed concurrently with quartz cement. Differences in postkinematic cement volumes account for contrasts in fracture quality. In well A, six open fractures and three sealed fractures were accurately predicted by degradation index. In well B, six sealed fractures were correctly predicted. Well A, with low overall degradation, is a producer having probable fracture-enhanced permeability, whereas well B, with high degradation, is uneconomic owing to low permeability. The surrogate thus correctly predicts both open or sealed fractures and production response.

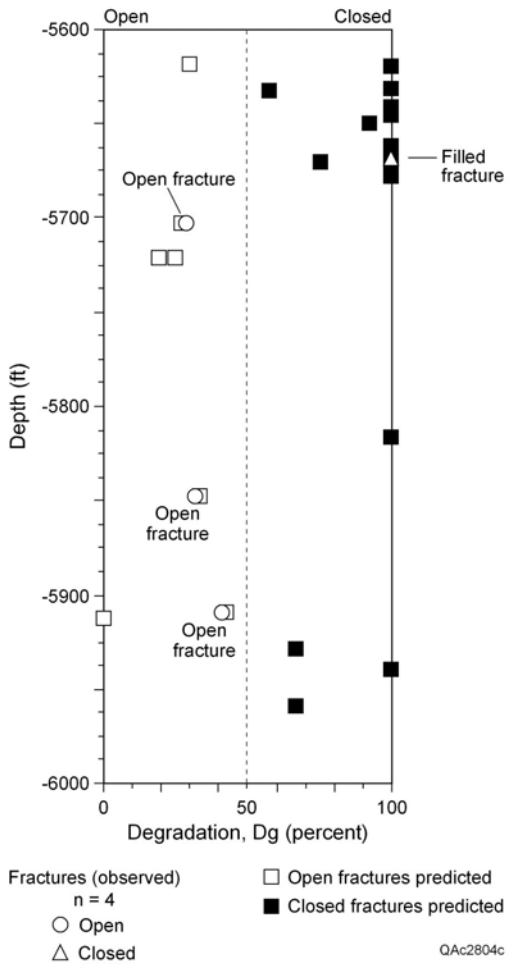

Figure 11. Fracture-quality predictions (degradation) versus depth compared with fracture observations, Weber Sandstone, Rangeley field, Colorado. Open fractures have thin (microns) veneers of synkinematic quartz.

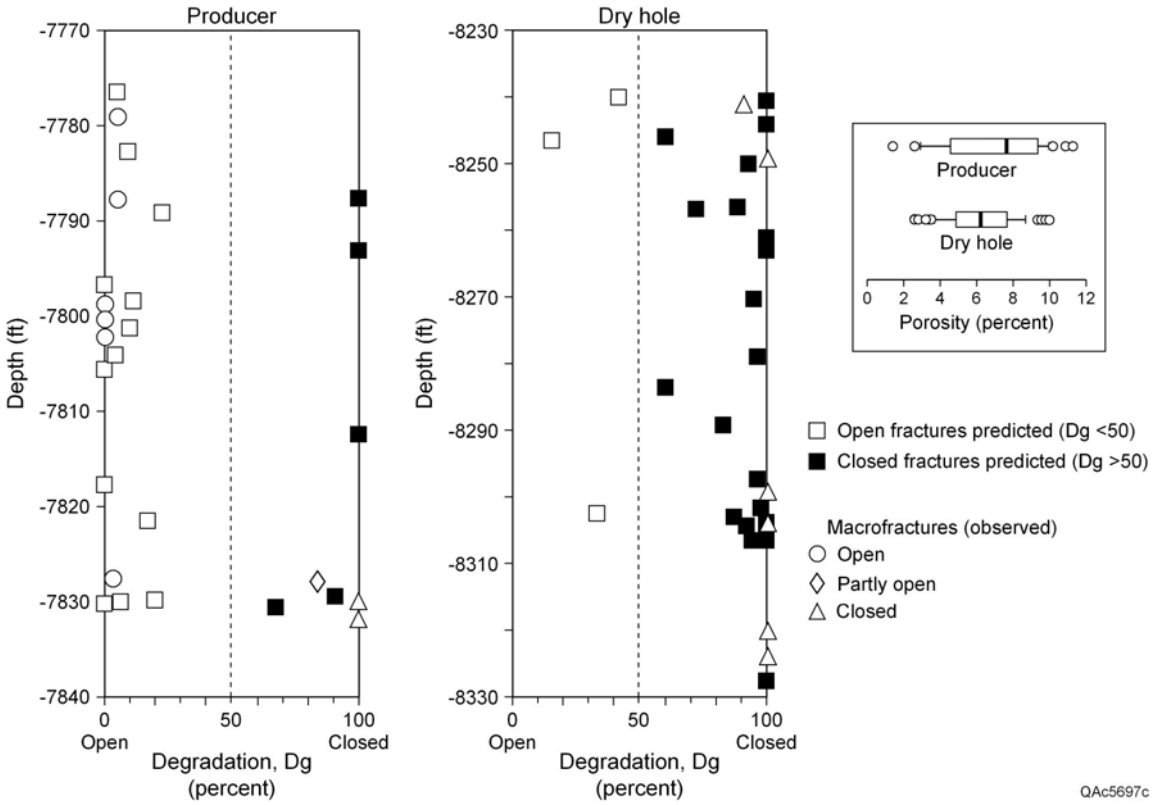

Figure 12. **Fracture-quality predictions (degradation) versus depth compared with fracture observations, Permian Wolfcamp Sandstone, West Texas. Ratio of postfracture cement to postfracture IGV (degradation index) identified open and sealed fractures, as well as cements filling large fractures. Note that well having mostly sealed fractures has no fracture-enhanced permeability (dry hole). Inset shows box plot of laboratory helium porosity measurements.**

Interpreting Degradation Values

Degradation is a *qualitative* predictor of fracture occlusion. Because it measures abundance of postkinematic cement in rock pore space, it accounts for neither synkinematic cement in fractures nor fracture-size distribution and connectivity. Neither size-dependent filling of large fractures by postkinematic cement nor up-scaling from arrays of small pores to infilling of large fractures is taken into account. Although porous rock has a finite capacity to record abundant deleterious cements, small pores might fill more readily than large fractures, so high degradation may over- or underpredict sealing in fractures of a given size.

Moreover, although these examples show that the surrogate correctly predicts sealing of fractures above a minimum size, amounts of postkinematic cement required to damage a particular fracture system depend on number and sizes of fractures and how they are interconnected. The surrogate does not specify these plumbing attributes, which need to be measured separately. Some fracture-size attributes can be extrapolated from microfracture size distributions (Marrett, 1996; Marrett et al., 1999), but fracture abundance and sizes, as well as connectivity and spatial distribution, are usually unknown. A small amount of postkinematic cement may be sufficient to damage connectivity if connections are narrow, and a large amount may be needed to seal large fractures.

Because pre- and synkinematic cements are voluminous, they influence rock-mass porosity more than postkinematic cements, yet traces of postkinematic cement are the phases available to damage large fractures. Rocks having contrasting degradation may thus have indistinguishable porosity. Similar values of porosity but differences in fracture damage could account for the efficacy in predicting production response of otherwise inexplicable porosity cutoff rules-of-thumb. Because both postkinematic cement volumes and porosity are low in many rocks, degradation is frequently a ratio of small numbers. Consequently, shifts in porosity and postkinematic cement can have large effects on degradation, amplifying signals present in rock-mass porosity that are not obvious owing to scatter in porosity values caused by other factors (e.g., grain size, secondary pores, etc).

Degradation values are therefore like a blood test for a factor that predicts clogged arteries. An independent measure of the arteries' capacity is needed to quantify how a specific value of degradation affects flow. Critical values might vary with fracture intensity, size distribution, or other variables. Within a region or play, impact of a given degradation value should be calibrated against observed fractures or production.

Extending Scope of Fracture Data

Because small samples can be used to observe microfractures and accurately quantify cement paragenesis and volumes, the types of samples that yield fracture data are greatly expanded. Sidewall cores are an economical source of data where no conventional core is available. Large cuttings that can be tied to depth may also be a source of fracture-quality data (Figure 13). Because a wider range of samples yields predicted fracture attributes, it is feasible to construct fracture quality "logs," cross sections (Figure 14) and maps (Figure 15) of wells having no other fracture data. Among other applications, these logs and maps are useful for targeting depths having favorable fracture attributes, calibrating well logs, identifying fracture "sweet spots," and testing remote-fracture detection results.

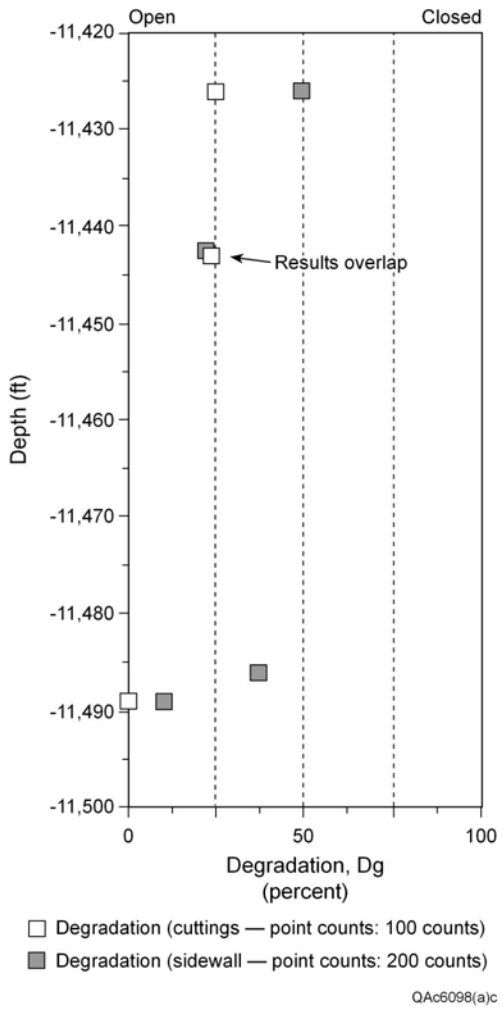

Figure 13. **Degradation values derived from sidewall cores (stippled boxes) consistent with values measured from cuttings. Permian sandstone, Val Verde Basin, Texas.**

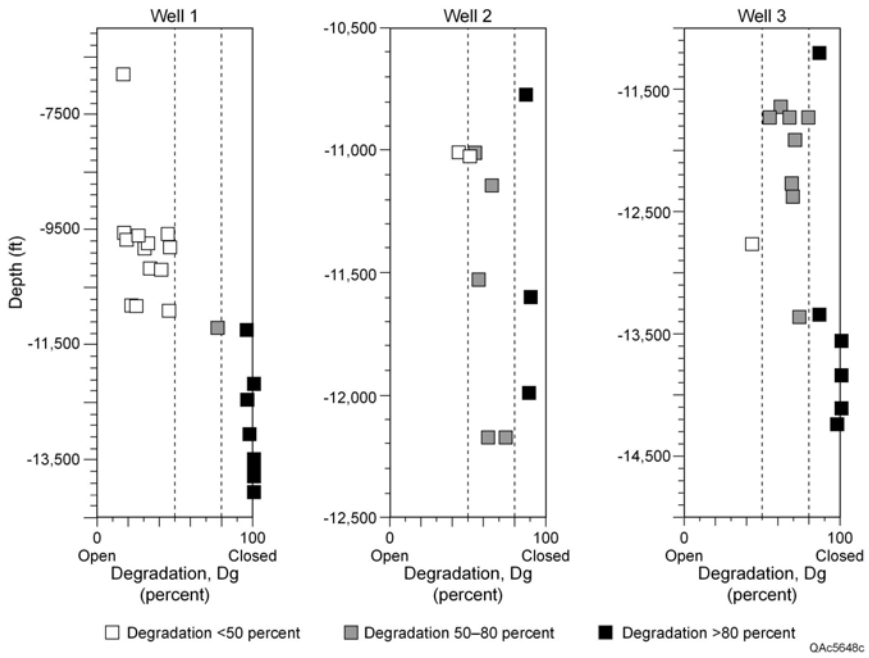

Figure 14. **Predicted fracture quality (degradation) versus depth for three wells penetrating Cretaceous sandstones, Wind River Basin, Wyoming. Surrogate data from drilled sidewall cores.**

IMPLICATIONS

Diagenesis patterns are readily sampled and diagenesis and fracturing are linked processes. Understanding these links is key to deciphering fracture attributes from limited observations. Fractures of interest to the petroleum industry develop during burial histories in which complex diagenetic reactions are well attested. Interplay between structural and diagenetic processes is probably inevitable, and the importance of these interactions is beginning to be appreciated. This study shows that preservation of porosity in fractures from a wide range of settings reflects interacting mechanical and chemical processes integrated over geologic timescales. Yet some repeated and relatively simple patterns are evident. (1) Cements that precipitate synchronously with fracture opening rarely seal large fractures but instead form thin, inconspicuous veneers and local bridges on fracture walls. These cements are found throughout a given set, and they are responsible for sealing numerous but petrographically invisible microfractures. (2) Later cements that can seal large fractures are heterogeneously distributed on a range of scales and are present in trace amounts in rock-mass pore space.

Because these patterns are widespread, effective predictive models may not require (generally unknowable) details of basin history. This modeling endeavor is in its infancy, and a discussion is beyond the scope of this paper. Here I mention a few implications as a point of departure for additional study. Although any mineral phase could accompany or postdate fracture opening, in practice certain phases are commonly synkinematic. On the basis of association with crack-seal structure, common synkinematic cements are found to be quartz in siliciclastic rocks, dolomite in dolomites, and calcite in limestone. This pattern persists even where multiple fracture sets are present. Do these patterns imply that conditions favoring quartz, dolomite, or calcite precipitation are causally linked to fracture growth? For example,

fracture is sensitive to pore-fluid pressure, so pore-fluid-pressure fluctuations and fracture could be linked by feedback loops. Rapid quartz or dolomite precipitation could promote fracture by elevating pore-fluid pressure (Laubach, 1988; Lander, 1998; Wangen, 2001). Or do patterns of synkinematic cement merely reflect prevalence of rock-dominated geochemistry through much of a rock's burial history, including times when conditions are amenable for fracture growth? Synkinematic cements, such as quartz, could merely be the most likely to precipitate through a protracted loading history (Lander and Walderhaug, 1999; Lander et al., 2002). Possibly both processes play a role.

An emergent threshold may develop in which synkinematic cement volume is limited by precipitation rate and substrate surface area (Lander et al., 2002). When a surface area is large relative to volume, µm- to mm-scale fractures readily seal in a few million years under precipitation rates expected in many basins, but long residence at high temperature is required for cement sufficient to fill large fractures to accumulate under these circumstances. Such rock-dominated geochemical conditions may typify fluid and thermal histories that many rocks have experienced for much of their history—the default is thus for large fractures to remain open. This situation accounts for widespread occurrence of crack-seal textures, bridges and residual fracture porosity, sealed microfracture arrays, and consistent synkinematic cements in many basins and tectonic settings.

For rocks confined to moderate to deep subsurface conditions in sedimentary basins, damaging cements in large opening-mode fractures mostly postdate fracture opening. Sources of elements for these cements are probably mostly derived from outside units in which they are deposited because discordant geochemistry of some late-stage fracture-filling minerals implies cross-formational flow and possibly long-distance transport during later diagenesis (Milliken, 2002). The largely postkinematic character of these cements implies that fluid-transport-limited processes operated after fractures formed under conditions where loading and pore-fluid pressure conditions do not promote fracture growth. Heterogeneous cement patterns could reflect a spectrum of flow pathways, including changing hydrologic regime (for example, paleo water levels), permeable carrier beds, or flow in or near conduits such as fracture swarms and faults, as well as detrital composition. Despite occurring in mostly low volumes, these hitherto largely neglected cements could provide important clues to spatial distributions of preserved fracture porosity.

Competition among processes that create and destroy fracture porosity governs how fracture permeability changes with time. Progressive fracture sealing is sensitive to duration and amount of heating, as well as composition and movement of aqueous solutions and hydrocarbons. Paragenetic sequences show that diagenesis is divisible; fracture timing can thus be referenced to progress of diagenetic reactions. This punctuation could reflect burial, uplift and temperature history, fluid flow patterns, chemical reactions, or other processes. Durations of cement precipitation "episodes" and the extent that they are punctuated on scales of tens of millions of years (or less) or are more gradual remain a matter of debate that information from fractures may help resolve.

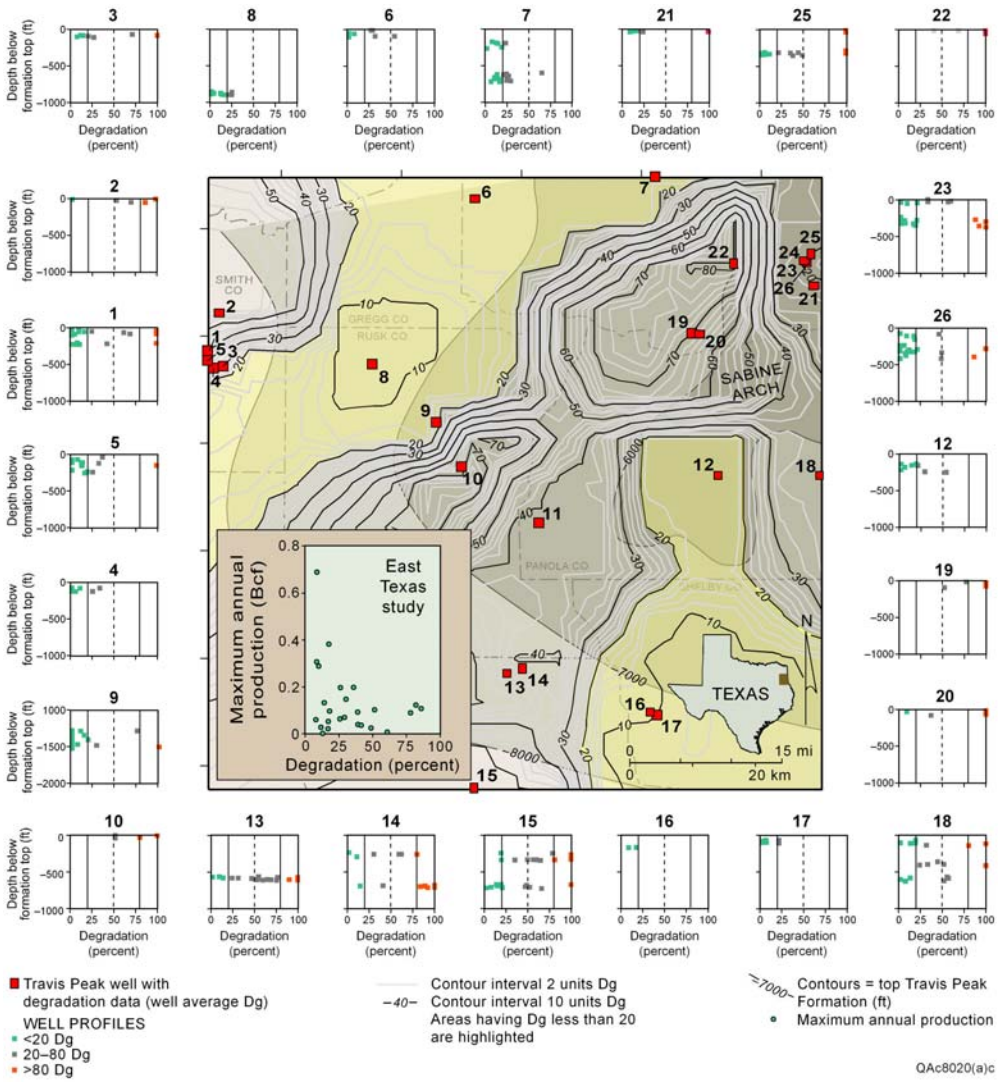

Figure 15. **Map and profiles of predicted fracture quality (degradation), Cretaceous Travis Peak Formation, East Texas, demonstrating that mapping fracture quality is possible. Map is superposed on structure, top Travis Peak Formation. More than 470 point counts were used to generate Dg profiles, which are all from wells having conventional core. Note that broad patterns are evident despite wide well spacing and averaging of degradation values by well that obscures fracture-quality heterogeneity. Inset shows a tendency for the highest maximum annual production to occur in wells having predicted open fractures (low average degradation).**

CONCLUSIONS

This paper emphasized a practical tool for exploration or development geologists or engineers. Surprisingly, a simple combination of easily made structural and diagenetic observations permits rapid prediction of whether fractures are open or sealed and how capable large fractures are of transmitting fluid, *even when large fractures have not been sampled*. Where suitable fracture samples are available for comparison, a surrogate accurately predicted open and sealed fractures. Production responses by wells having differing degrees of fracture damage suggest that fractures identified by surrogates as sealed *do* have a detrimental affect on fluid flow, and vice versa.

The ability to use widely available and relatively inexpensive rock samples makes this approach practical. The essential step is discerning postkinematic cements—the "bad cholesterol" of fracture systems—because where they are prevalent, flow is impeded. Fractures that require a microscope to detect are far more common than large fractures and, thus, more readily sampled, and these can provide fracture timing information. However, owing to their propensity to seal shortly after they form, microfractures generally lack postkinematic cement themselves, so they must be used in conjunction with data derived from the rock mass. Once identified, postkinematic cement volumes are readily quantified by conventional petrographic methods. Rare large fractures can confirm inferences based on microstructures, increasing confidence of extrapolations to areas where only cement samples are available. Unconventional use of widely available data thus provides surrogates for evaluation of fractures, without the need to observe the fractures themselves. A convenient measure of postkinematic cement incidence is the ratio of late cement to postfracture intergranular volume, degradation. This surrogate predicts degree of porosity retention or closure of fractures *above a specified size*, the emergent threshold.

Because inferences are based on site-specific observations of diagenesis and structure, the approach described herein can be used in subsurface studies without unraveling mechanical and geochemical interactions. This study does underline how important it is to understand these linked processes in order to improve predictions ahead of the bit.

Petroleum resources in fractured and diagenetically altered rocks are a growing target of U.S. and world exploration and development. For these plays, great uncertainty stems from highly heterogeneous, unpredictable, and difficult-to-diagnose fracture systems that govern fluid flow. Site-specific fracture information is essential. Locating depth intervals having fractures that might contribute to fluid flow using surrogates can help in measurement of exploration risk and guide development planning. Damaging postkinematic cements, frequently heterogeneous on a range of scales, cannot be delineated effectively using fracture observations alone, so surrogates have practical value for production-fairway mapping and other applications in which identifying open fractures is essential. Results of this study can be usefully incorporated in reservoir characterization procedures anywhere fractures may contribute to production.

APPENDIX 1. DATA SET, ANALYSIS METHODS, AND TERMINOLOGY

Core and Outcrop Data Sets

Our core and outcrop data include a wide range of geology, but discussion of each area or formation is beyond the scope of this paper. Samples are from siliciclastic and carbonate rocks in oil and gas reservoirs and from outcrops (Table A-1). Depths range from exposures to deep cores (>21,000 ft). Most observations are from depths of 6,000 to 14,000 ft in 24 siliciclastic formations (highlighted, Table A-1), 4 dolomite, and 3 limestone units. Because examples are mostly moderately to tightly cemented sandstone, it is to these rocks that results are most applicable.

Cores are mostly from North and South America. Within North America, data are from major producing regions, including Appalachian, Black Warrior, and Gulf Coast Basins; West Texas; and Rocky Mountain thrust belt and foreland basins. Most cores are from vertical wells, but there are 12 slant or

horizontal cores. In core, more than 1,000 fractures and associated rock properties were examined. Measured apertures in core and outcrop range from approximately 0.0001 mm to more than 1 m (Marrett et al., 1999; Ortega et al., 2001). Lengths are typically greater than heights because fractures are confined to layers that reflect mechanical stratigraphy. Sets have preferred orientation, as well as crosscutting and abutting relations.

For such diverse samples, it is challenging to generalize about geology and petrophysics. Oil and gas reservoirs are about equally represented. Sandstones range from litharenites to quartz arenites, and depositional settings range from fluvial/deltaic to deepwater. Dolomites, mostly Paleozoic or Cretaceous from platform settings, have extensive authigenic dolomite and variable porosity. Rocks have mostly low to moderate porosity (0 to 20 percent) and are either deeply buried (>2 km) or have been so in the past. A spectrum of burial histories is represented, but rocks not experiencing deep burial are mostly Paleozoic. Deep or protracted burial promotes cementation, and cement volumes are typically high (>15 percent). More than half are from foreland basins, with the rest from passive margins and platforms or cratons or from within fold-thrust belts. Forelands include both recent, active basins (Venezuela, Colombia, Bolivia) and older, inactive foreland basins (Appalachians, West Texas, Rocky Mountains).

Although some are from open folds, in general samples are from undeformed areas distant from tight folds or faults. In folds, where sufficient evidence is available, fractures largely or entirely predate folding (Laubach and Lorenz, 1992; Olson et al., 1998; Marrett and Laubach, 2001). Regional sets are responses to combinations of burial and tectonic loading and pore pressure changes. However, as is typical for opening-mode arrays, it is impossible to uniquely specify loading paths to fracture growth. Although Paleozoic rocks are represented, many are Cretaceous and may have experienced fracture in Late Cretaceous to Recent times. This diversity of compositions, burial histories, and settings results in differences in diagenesis and fracture history, yet patterns persist across this spectrum of geology.

	Formation/Unit	Age	Location/Setting	Depth (ft)#	Notes	Core Sets	Well Pair	Micro fractures	Emergent threshold	Crack-Seal	Synk. Bridge	Postk. Seal	Surrogate Prediction
	Capaya	L. Miocene	Venezuela/Foreland	15919-15922		a		Yes	Yes		Yes		Yes
	Frio	L. Oligocene	S. Texas/Passive	`15620				Yes					Yes
	Fontainebleau	Oligocene	France/Paris Basin	OC				Yes					
	Queen City	M. Eocene	S. Texas/Passive	~7779				Yes	Yes				
	Sandstone	Eocene	Poland/Foldbelt	OC				Yes		Yes	Yes		
	Lobo Wilcox	Paleocene	S. Texas/Passive	7645-8854		a		Yes	Yes			Yes	Yes
	Sandstone	Paleogene	Venezuela/Foreland	17482-17533				Yes	Yes		Yes		Yes
	Lance	U. Cretaceous	Rockies/Foreland	13433-13591	1	a		Yes	Yes	Yes	Yes	Yes	Yes
	Meeteetsee	U. Cretaceous	Rockies/Foreland	~10853				Yes	Yes		Yes	Yes	Yes
	Almond	U. Cretaceous	Rockies/Foreland	~9970		a		Yes	Yes	Yes	Yes	Yes	Yes
	Williams Fork	U. Cretaceous	Rockies/Foreland	OC-10000	1	b		Yes	Yes	Yes	Yes	Yes	Yes
	Cozzette	U. Cretaceous	Rockies/Foreland	~5894	1*	a		Yes	Yes	Yes	Yes	Yes	Yes
	Cliff House	U. Cretaceous	Rockies/Foreland	OC-5038		a		Yes	Yes		Yes	Yes	Yes
	Menefee	U. Cretaceous	Rockies/Foreland	~7900		a	x	Yes	Yes	Yes	Yes	Yes	Yes
	Point Lookout	U. Cretaceous	Rockies/Foreland	OC-6008				Yes	Yes		Yes	Yes	Yes
	Pictured Cliffs	U. Cretaceous	Rockies/Foreland	Core & OC				Yes	Yes	Yes	Yes	Yes	Yes
	Frontier	U. Cretaceous	Rockies/Foreland	OC-20487	1*	b	x	Yes	Yes	Yes	Yes	Yes	Yes
	Cody	U. Cretaceous	Rockies/Foreland	~13600	1	a		Yes	Yes	Yes	Yes	Yes	Yes
	Sandstone	Cretaceous	Colombia/Foldbelt	OC				Yes	Yes	Yes	Yes	Yes	Yes
	Dakota	L. Cretaceous	Rockies/Foreland	7068-16865	1	b		Yes	Yes	Yes	Yes	Yes	Yes
	Fall River	L. Cretaceous	Rockies/Foreland	12384-12446				Yes	Yes	Yes	Yes	Yes	Yes
	Travis Peak	L. Cretaceous	Texas/Passive	6119-10141	1	b	x	Yes	Yes	Yes	Yes	Yes	Yes
	Cox	L. Cretaceous	Texas/Platform	OC				Yes	Yes		Yes	Yes	
	Barranquin	L. Cretaceous	Venezuela/Foreland	11040	2			Yes	Yes	Yes	Yes		Yes
	Rio Negro	Cretaceous	Venezuela/Foreland	9144				Yes	Yes		Yes		Yes
	Cotton Valley	U. Jurassic	Texas/Passive	7099-7100	1	a	x	Yes	Yes	Yes	Yes	Yes	Yes
	Brae	U. Jurrasic	North Sea/Basin	11500-19000				Yes	Yes				
	Etjo	Jurassic	Namibia/Rift	OC				Yes					
	Sandstone	Triassic(?)	China/Platform	Core	2			Yes	Yes		Yes		Yes
Siliciclastic Rocks	Breathit	Pennsylvanian	East U.S./Foreland	OC				Yes	Yes		Yes		
	Spraberry	L. Permian	Texas/Foreland	7665-7685	1*			Yes	Yes	Yes	Yes	Yes	Yes
	Bone Spring	L. Permian	Texas/Foreland	3397-3697	3	a	x	Yes			Yes	Yes	Yes
	Ozona	L. Permian	Texas/Foreland	4449-6402		b	x	Yes	Yes	Yes	Yes	Yes	Yes
	Sonora	L. Permian	Texas/Foreland	5971-6384		b	x	Yes	Yes	Yes	Yes	Yes	Yes
	Wolfcamp	L. Permian	Texas/Foreland	7828-8305	1*	b	x	Yes	Yes	Yes	Yes	Yes	Yes
	Weber	Penn-Permian	Rockies/Foreland	OC-8305	2	b	x	Yes	Yes	Yes	Yes	Yes	Yes
	Tensleep	Pennsylvanian	Rockies/Foreland	OC				Yes	Yes		Yes	Yes	Yes
	Spiro	Pennsylvanian	Oklahoma/Foreland	~11000-12000				Yes	Yes				Yes
	Strawn	Pennsylvanian	Texas/Foreland	~3932				Yes	Yes		Yes		Yes
	Davis/Atoka	L. Pennsylvanian	Texas/Foreland	4397.5-4399.5	2			Yes	Yes	Yes	Yes	Yes	Yes
	Smithwick	L. Pennsylvanian	Texas/Foreland	OC				Yes			Yes		
	Pottsville	L. Pennsylvanian	East U.S./Foreland	3453-4240	1	a	x	Yes	Yes	Yes	Yes	Yes	Yes
	Berea	L. Mississippian	East U.S./Foreland	OC-3366				Yes					
	Sandstone	Devonian	Texas/Platform	Core				Yes	Yes		Yes		
	Iquiri	U. Devonian	Bolivia/Foreland	10167-10210	3			Yes	Yes		Yes	Yes	Yes
	Huamampampa	M. Devonian	Bolivia/Foreland	13737-16086				Yes	Yes	Yes	Yes	Yes	Yes
	Thorold	Silurian	East U.S./Foreland	OC-6568	1	a	x	Yes	Yes		Yes	Yes	Yes
	Grimsby	Silurian	East U.S./Foreland	6381-6611	1	a	x	Yes	Yes		Yes	Yes	Yes
	Whirlpool	Silurian	East U.S./Foreland	6462-6467	1	a	x	Yes	Yes	Yes	Yes	Yes	Yes
	Massanutten	L.Silurian	East U.S./Foreland	OC				Yes	Yes	Yes	Yes		Yes
	Bromide	M. Ordovician	Oklahoma/Foreland	12995-13110	1	a		Yes	Yes	Yes	Yes	Yes	Yes
	Tulip Creek	M. Ordovician	Oklahoma/Foreland	13303-13384	2	a		Yes	Yes		Yes	Yes	Yes
	St. Peter	Ordovician	Illinois/Platform	Core	2			Yes	Yes	Yes	Yes	Yes	Yes
	Bliss	C.-Ordovician	Texas/Platform	OC				Yes	Yes	Yes	Yes		Yes
	Ironton	U. Cambrian	Illinois/Platform	~3152	2			Yes	Yes		Yes		
	Galesville	U. Cambrian	Illinois/Platform	~3177	2			Yes	Yes		Yes	Yes	Yes
	Mt. Simon	U. Cambrian	Illinois/Platform	3743-3793	2			Yes	Yes		Yes	Yes	Yes
	Wilberns	U. Cambrian	Texas/Platform	OC				Yes	Yes				
	Hickory	U. Cambrian	Texas/Platform	OC				Yes					
	Sandstone	M. Cambrian	E. European/Platform	OC				Yes	Yes		Yes		
	Flathead	M. Cambrian	Wyoming/Thrustbelt	OC				Yes	Yes	Yes	Yes	Yes	Yes
	Basal Qzite	Cambrian	Scotland/Foreland	OC				Yes	Yes	Yes	Yes		Yes
Dolomite	**Cupido**	Cretaceous	Mexico/Platform	OC				Yes	Yes	Yes	Yes	Yes	Yes
	Clear Fork	Permian	Texas/Platform	OC-8000	2	a		Yes	Yes		Yes	Yes	Yes
	Ellenburger	Ordovician	Texas/Platform	~5000	1	a		Yes	Yes		Yes	Yes	Yes
	Knox	Ordovician	East U.S./Foreland	Core	1	a		Yes	Yes		Yes	Yes	Yes
Limestone	Austin Chalk	Cretaceous	Texas/Passive	OC-13000	1*	a		Yes	Yes		Yes		Yes
	Apon	Cretaceous	Venezuela/Foreland	OC-11000				Yes	Yes		Yes		

Core: 1, Whole & sidewall. *, Slant or horizontal. 2, Whole. 3, Sidewall. Wells: a, 2 or more. b, 10 or more. OC, Outcrop. Syk., Synkinematic. Postk., Postkinematic.
#Depths indicated are for CL analysis; conventional petrography and sample descriptions cover wider depth ranges. **Bold** indicates main units for surrogate testing

Table A-1. Data set used for investigating fracture sealing.

Fracture and Microstructure Characterization Methods

Owing to small aperture sizes, sensitive imaging of chemical contrasts afforded by SEM-based cathodoluminescence (scanned CL) is essential for discerning cement and microstructure patterns. A Philips XL-30 scanning electron microscope (SEM) with high-resolution cathodoluminescence (CL) detector is our primary instrument (Reed and Laubach, 1999; Reed and Milliken, submitted). Images were also collected using photomultiplier-based CL detectors on JEOL T330A and T300 SEM's (Milliken and Laubach, 2000). Elemental analysis included an SEM-based EDS system supplemented by microprobe analysis.

Fracture and cement attributes were measured in selected thin sections using conventional microscopy and scanned CL images (~200× to ~1,000×). Areas of as much as ~several mm^2 were imaged at approximately 200×, digitally stitched into mosaics and interpreted using commercial and in-house software. Sample composition and paragenetic sequence were determined using point counts (typically 200 to 300 counts; locally 1,000 counts) of stained thin sections (in sandstones, an alizarin stain for Fe-carbonate minerals is useful). In some core sets, fluid inclusion and stable isotope measurements on selected suites of minerals in fractures and hosts corroborate paragenetic relations derived from petrography or CL imaging. For most subsurface data sets, well log, production data, and porosity and permeability measurements are available. For practical deployment of a surrogate-based approach, such complete core coverage and data on fractures will rarely be available and in principle should not be required.

Fracture-Based Cement Classification

To identify where large fractures are likely to be sealed, it is helpful to define cement sequences relative to fracture growth. New terms provide shorthand for an array of attributes related to opening processes, timing, and size.

Cements can be divided into those that predate, accompany, and postdate fracture opening (Laubach 1988). The terms pre-, syn-, and postkinematic focus attention on links between fracture-movement history (kinematics) and rock and fracture diagenesis, underlining the role that fracture timing plays in porosity preservation. Rocks may have several fracture-opening events, as well as complex and repetitive sequences of precipitation and dissolution. Terms therefore refer to a specific fracture-opening event, and a postkinematic phase for one fracture set is pre- or synkinematic for the next. The classification refers to cements in fractures *and* the rock mass.

Prekinematic cements precipitate before fractures open. These cements, and compaction, can give rocks induration necessary to support fractures. Such cements can govern fracture patterns through influence on fracture growth velocities or other rock properties (Olson et al., 2001). By definition, however, prekinematic cement cannot occur within later fractures. *Synkinematic* cement precipitates during fracture opening. Microscopic evidence includes crack-seal texture and microfracture arrays. In many fractures diagnostic textures may be absent or restricted to near fracture walls or tips if cements grew into open pore space without spanning or if a given fracture was not reactivated. Of course precipitation and fracturing are rarely exactly coincident, so that quartz, for example, is typically partly pre- or postkinematic. *Postkinematic* cements precipitate after fracture opening ceases, filling voids within static fractures. A bridge of synkinematic cement containing crack-seal structures surrounded by postkinematic cements is diagnostic. In the rock, these cements are mainly distinguished by position within a paragenetic sequence, except that postkinematic cements are not cut by microfractures filled with synkinematic cement.

REFERENCES CITED

Barton, C.A., Zoback, M.D., and Moos, D., 1995, Fluid flow along potentially active faults in crystalline rock: Geology, v. 23, p. 683-686.

Crampin, S., 1994, The fracture criticality of crustal rocks: Geophysics Journal International, v. 118, p. 428-438.

Dyke, C.C., 1995, How sensitive is natural fracture permeability at depth to variation in effective stress? In Myer, L.R., Cook, N.G.W., Goodman, R.E., and Tsang, C.-F., eds., Fractured and Jointed Rock Masses: Balkema, p. 81-88.

Gillespie, P.A., Walsh, J.J., Watterson, J., Bonson, C.G., and Manzocchi, T., 2001, Scaling relationships of joint and vein arrays from The Burren, Co. Clare, Ireland: Journal of Structural Geology, v. 23, p. 183-201.

Gomez, L.A., Gale, J.F.W., Ruppel, S.C., and Laubach, S.E., 2001, Fracture characterization using rotary-drilled sidewall coves: an example from the Ellenburger Formation. In West Texas Proceedings, West Texas Geological Society Fall Meeting, WTGS publication, 01-110, p. 81-89.

Heffer, K.J, Fox, R.J., McGill, C.A., Koutsabeloulis, N.C., 1997, Novel techniques show links between reservoir flow directionality, earth stress, fault structure and geomechanical changes in mature waterfloods: SPE Journal, v. 2, p. 91-98.

Hulin, C.D., 1929, Structural control of ore deposition: Economic Geology: v. 24, p. 15-49.

Lander, R.H., 1998, Effect of sandstone diagenesis on fluid overpressure development (abs.): AAPG Conference and Exhibition, Salt Lake City, Utah.

Lander, R.H., 2001, Quantitative prediction of petrographic properties using diagenetic models (abs.): AAPG Annual Convention Official Program, v. 10 (CD).

Lander, R.H., Gale, J.F.W., Laubach, S.E., and Bonnell, L.M., 2002, Interaction between quartz cementation and fracturing in sandstone (abs.): AAPG Annual Convention Program, v. 11, p. A98-A99.

Lander, R.H., Helset, H.M., Bonnell, L.M., and Matthews, J.C., 1999, Implications of sandstone diagenesis for fluid overpressure development and seal failure (abs.): AAPG Annual Meeting Program, v. 8, p. A76.

Lander, R.H., and Walderhaug, O., 1999, Porosity prediction through simulation of sandstone compaction and quartz cementation: AAPG Bulletin, v. 83, p. 433-449.

Laubach, S.E., 1988, Subsurface fractures and their relationship to stress history in East Texas basin sandstone: Tectonophysics, v. 156, p. 37-49.

Laubach, S.E., 1989, Paleostress directions from the preferred orientation of closed microfractures (fluid-inclusion planes) in sandstone, East Texas Basin, U.S.A.: Journal of Structural Geology, v. 11, no. 5, p. 603-611.

Laubach, S.E., 1997, A method to detect fracture strike in sandstone: AAPG Bulletin, v. 81, no. 4, p. 604-623.

Laubach, S.E., and Lorenz, J., 1992, Preliminary assessment of natural fracture patterns in Frontier Formation sandstones, southwestern Wyoming. In Mullen, C.E., ed., Rediscover the Rockies: Wyoming Geological Association, 43rd Field Conference Guidebook, p. 87-96.

Lorenz, J., and Hill, R., 1992, Measurement and analysis of fractures in core. In Schmoker, J.W., Coalson, E.B., and Brown, C.A., eds., Geological Studies Relevant to Horizontal Drilling: Examples from Western North America: Rocky Mountain Association of Geologists, p. 47-57.

Marrett, R., 1996, Aggregate properties of fracture populations: Journal of Structural Geology, v. 18, nos. 3/4, p. 169-178.

Marrett, R., and Laubach, S.E., 2001, Burial, tectonic, and exhumational fracturing. In Marrett, R., ed., Genesis and Controls of Reservoir-Scale Carbonate Deformation, Monterrey Salient, Mexico: The University of Texas at Austin Bureau of Economic Geology Guidebook 28, p. 109-122.

Marrett, R., Ortega, O., and Kelsey, C., 1999, Extent of power-law scaling for natural fractures in rock: Geology, v. 27, no. 9, p. 799-802.

Milliken, K.L., 2002, Petrography of ankerite cement, grain replacement, and fracture fill in foreland sandstones of the Central Rocky Mountains, AAPG Annual Convention Program, v. 11, p. A123.

Milliken, K.L., and Laubach, S.E., 2000, Brittle deformation in sandstone diagenesis as revealed by cathodoluminescence imaging with application to characterization of fractured reservoirs, Chapter 9. In Pagel, M., Barbin, V., Blanc, P., and Ohnenstetter, D., eds., Cathodoluminescence in Geosciences: Springer-Verlag, p. 225-244.

Monroy, F., Laubach, S.E., Marrett, R., 2001, Preliminary diagenetic and stable isotope analysis of fractures in the Cupido Formation, Sierra Madre Oriental. In Marrett, R., ed., Genesis and Controls of Reservoir-Scale Carbonate Deformation, Monterrey Salient, Mexico: The University of Texas Bureau of Economic Geology Guidebook 28, p. 83-105.

Montañez, I.P., 1997, Secondary porosity and late diagenetic cements of the Upper Knox Group, Central Tennessee Region: A temporal and spatial history of fluid flow conduit development within the Knox regional aquifer. In Montañez, I.P, Gregg, J.M., and Shelton, K.L., eds., Basin-Wide Diagenetic Patterns: Integrated Petrologic, Geochemical, and Hydrological Considerations: SEPM Special Publication No. 57, p. 101-118.

Narr, W., 1991, Fracture density in the deep subsurface; techniques with application to Point Arguello oil field: AAPG Bulletin, v. 75, no. 8, p. 1300-1323.

Nelson, R.A., 1985, Geologic Analysis of Naturally Fractured Reservoirs: Gulf Publishing Company.

Noh, M.H., and Lake, L.W., 2002, Geochemical modeling of fracture filling: Society of Petroleum Engineers, SPE 75245.

Olson, J.E., Hennings, P.H., and Laubach, S.E., 1998, Integrating well-bore data and geomechanical modeling for effective characterization of naturally fractured reservoirs. In EUROCK '98, Society of Petroleum Engineers, p. 475-485.

Olson, J.E., Yuan Qiu, Holder, J., and Rijken, P., 2001, Constraining the spatial distribution of fracture networks in naturally fractured reservoirs using fracture mechanics and core measurements: SPE 71342, p. 1-12.

Ortega, O., and Marrett, R., 2000, Prediction of macrofracture properties using microfracture information, Mesaverde Group sandstones, San Juan Basin, New Mexico: Journal of Structural Geology, v. 22, no. 5, p. 571-588.

Ortega, O.O., Marrett, R., Laubach, S.E., Milliken, K., Olson, J., and Reed, R., 2001, Outcrop analogs for fractured reservoir characterization: Rangeley field, Colorado (abs.): AAPG Annual Convention Program CD.

Pitman, J.K., and Sprunt, E.S., 1986, Origin and distribution of fractures in Lower Tertiary and Upper Cretaceous Rocks, Piceance basin, Colorado, and their relation to the occurrence of hydrocarbons, In Spencer, C.W., and Mast, R.F., eds., Geology of Tight Gas Reservoirs: AAPG Studies in Geology, No. 24, p. 221-234.

Ramsay, J.G., 1980, The crack-seal mechanism of rock deformation: Nature (London), v. 284, no. 5752, p. 135-139.

Reed, R.M., and Laubach, S.E., 1996, The role of microfractures in the development of quartz overgrowth cements in sandstone: new evidence from cathodoluminescence studies (abs.): Geological Society of America Abstracts with Programs, v. 28, no. 7, p. A-280.

Reed, R.M., and Milliken, K.L., submitted, How to overcome imaging problems associated with carbonate minerals on SEM-based cathodoluminescence systems: Journal of Sedimentary Petrology.

Stone, W.N., and Siever, R., 1996, Quantifying compaction, pressure solution and quartz cementation in moderately- and deeply-buried quartzose sandstones from the Greater Green River basin. In Crossey, L.J., Loucks, R., and Totten, M.W., eds., Siliciclastic Diagenesis and Fluid Flow: Concepts and Applications: SEPM Special Publication No. 55, p. 129-150.

Stowell, J.F.W., 2000, Specifying lengths of horizontal wells in fractured reservoirs: Society of Petroleum Engineers, SPE 65458.

Stowell, J.F.W., Laubach, S.E., and Olson, J.E., 2001, Effect of modern state of stress on flow-controlling fractures: a misleading paradigm in need of revision. In Elsworth, D., Tinucci, J.P. and Heasley, K.A., eds., Rock Mechanics in the National Interest: Proceedings, 38th Annual U.S. Rock Mechanics Symposium: Balkema, v.1, p. 691-698.

Terzaghi, R., 1965, Sources of error in joint surveys: Geotechnique, v. 15, p. 287-297.

Wangen, M., 2001, A quantitative comparison of some mechanisms generating overpressure in sedimentary basins: Tectonophysics, v. 334, p. 211-234.

Fracture swarms - A mechanical paradox?

Jon E. Olson

Petroleum and Geosystems Engineering Department, The University of Texas at Austin, Austin, TX 78746, USA

ABSTRACT

Fracture spacing in layered rock is often observed to vary systematically with the thickness of the fractured layer. Experimental and numerical studies suggest a lower limit on fracture spacing equal to layer thickness, but there are many examples of fracture patterns in rock that violate this expectation. In particular, there are instances where spacing can be significantly closer than the magnitude of layer thickness in what have been termed fracture swarms or clusters. Fracture spacing within the cluster can be very small relative to bed thickness, while spacing between clusters may be highly variable. Such cases cannot be readily explained with conventional fracture spacing models or concepts, and are actually contradictory to static, two-dimensional, fracture stress analyses. These limitations can be overcome with a time-dependent fracture propagation model based on the subcritical crack growth mechanism that can capture the wide ranging nature of fracture spatial organization seen in layered rock. Based on results from this model, a new mechanism is proposed that can predict fracturing clustering as a result of mechanical interaction.

INTRODUCTION

A common attribute of opening mode fractures (Pollard and Aydin, 1988) in sedimentary rock sequences is that observed fracture spacing is proportional to layer thickness (Bai and Pollard, 2000b; Narr and Suppe, 1991; Wu and Pollard, 1994). Two dimensional, plane-strain, static analysis demonstrates how the stress relief around a pre-existing crack can create a

propagation "exclusion" zone (Pollard and Segall, 1987). Olson (1993) showed how this stress shielding can develop in an areal sense as multiple fractures grow in length and their stress shadows overlap, diminishing the stress available for additional parallel fractures to grow. Recent work (Bai and Pollard, 2000b) has shown that in well-bonded, layered materials under crack-normal, extensional loading, the crack-normal stress between closely spaced, parallel fractures (spacing ≤ layer thickness) actually becomes compressive (Figure 1). This surprising result dictates that increasing the remotely applied extensional strain will not promote the propagation of additional cracks between the pre-existing ones, but will only cause the existing cracks to open more to accommodate the added extension. Thus, a minimum spacing approximately equal to layer thickness is expected for parallel, equally-spaced opening-mode fractures, and such a fracture set is termed "saturated," as there is no room for additional fractures to grow (Rives et al., 1992; Wu and Pollard, 1994).

This well-established stress relief analysis explains much of what is observed in fracture patterns in rock and other layered materials, but it cannot explain fracture swarms or other situations where local fracture spacing is significantly less than layer thickness (Figure 2). Bai and Pollard (2000) proposed that fracture spacing closer than bed thickness can be attributed to the vertical growth of flaws located near the intersection of fractures with layer boundaries. Their model predicted a minimum spacing to layer thickness ratio of ~0.3. This work describes an analogous model except that lateral fracture growth (along the bed rather than vertically through it) is taken as the main fracture propagation mechanism, and the time history of growth of all fractures from the flaw size to macro-scale is explicitly modeled using a subcritical crack growth model. The model addresses the mechanics of fracture swarms (and other closely spaced fractures) and shows how subcritical crack growth properties can be used to predict swarm

occurrence. This incorporation of time-dependent crack propagation and additional three-dimensional effects can explain a wide range of fracture spacing distributions, as well as predict whether minimum fracture spacing will be equal to or less than mechanical layer thickness based on a measurable rock property, the subcritical fracture index.

FRACTURE PROPAGATION IN LAYERED ROCKS

A model has been constructed that simulates lateral fracture propagation along a layer assuming the fractures have already propagated vertically across the layer from top to bottom. This treatment of lateral propagation is crucial to understanding fracturing in mechanically layered materials, as the shortest dimension of fractures in layered material will be their vertical (or layer-perpendicular) extent or height (Olson, 1993). Consequently, most of the fracture propagation in bedded rock involves increasing the lateral dimension of the fracture (length as measured along the layer). Figure 3 depicts a roadcut example of fractured, interbedded sandstone and shale. The photograph depicts the vertical outcrop face, which is a composite surface made up of coplanar but non-continuous fracture segments. The central brittle sandstone bed is bounded by thin, more ductile shale layers. The plumose structure on the fracture can be used to determine that the fracture in this bed propagated from right to left, and was bounded in its propagation between the shale stringers indicated in the figure (Kulander and Dean, 1995). The fracture breached the entire layer thickness early in its growth history, and most of the subsequent propagation involved increasing the fracture length (lateral propagation), resulting in a fracture length that greatly exceeds the height. A two-dimensional, cross-sectional analysis (which would be done in the x-z plane) would be inadequate for analyzing the more dominant lateral fracture propagation along the y-direction. Only propagation in the vertical (z) direction

can be adequately represented in such a cross-sectional geometry. However, as suggested above, height growth is early-time behavior that is only a small part of fracture network development.

A more appropriate geometric configuration for modeling this type of fracture propagation analysis is to look at the x-y plane, capturing the sequence of lateral propagation and fracture interaction. The conceptual framework of the fracture propagation model presented here assumes that the initial starter flaws in a layer already extend across the full thickness of the layer, and the modeled propagation is the addition of fracture length caused by some manner of extensional loading. This model is similar to previous work by Olson (1993) and Renshaw and Pollard (1994) except for the fact that it represents the three-dimensional effects of fracture height contained by bed thickness.

SUBCRITICAL CRACK GROWTH

In order to analyze the simultaneous propagation of multiple fractures, both a failure criterion and a propagation velocity model are required. Brittle fracture strength is influenced by environmental factors such as relative humidity and chemical reactivity that can weaken the bonds between material grains (Atkinson, 1984; Swanson, 1984). For instance, most rock and ceramic material exhibit maximum fracture resistance (termed critical fracture toughness) when tested in a vacuum, and that strength is significantly reduced in the presence of water or water vapor. Fracture propagation under critical conditions is catastrophic and occurs at velocities comparable to the elastic wave speed of the material (Lawn and Wilshaw, 1975). Fracture propagation below the critical toughness, termed subcritical crack propagation, occurs at lower stress levels and much lower velocities. A useful attribute of subcritical crack growth is that propagation velocity, v, can be related to opening mode stress intensity at the crack tip, K_I, with

an empirically quantifiable, power-law relationship (Atkinson, 1984; Swanson, 1984; Olson, 1993),

$$v = A\left(\frac{K_I}{K_{Ic}}\right)^n \quad (1)$$

where K_{Ic} is the critical fracture toughness, n is the subcritical index, and A is a proportionality constant. The power-law exponent, n, can vary widely depending on environmental conditions (such as dry versus wet) and rock type. Reported values for carbonates and sandstones vary from 20 or less for tests done in water to greater than 100 under dry conditions (Atkinson and Meredith, 1987; Holder et al., 2001).

FRACTURE PROPAGATION MODEL

Two dimensional, plane strain modeling of the development of fracture networks utilizing subcritical crack growth conditions has shown that the value of the subcritical index, n, exerts a strong influence on the spatial arrangement and length distribution of fractures (Segall, 1984; Olson, 1993; Renshaw and Pollard, 1994). Results in Olson (1993) demonstrated how subcritical index controls fracture spacing to bed thickness ratio when modeling vertical fracture propagation across a bed under plane strain conditions. A very low subcritical index (n=1) garnered a spacing to bed thickness ratio of 0.25, while a higher index (n=15) resulted in a spacing/thickness ratio of 0.875. The Olson (1993) numerical results also demonstrated a mechanism for fracture cluster growth that had been postulated for joints in sandstone by Dyer (1983). The idea is that a propagating joint causes the stresses ahead of the tip to be more tensile, promoting the growth of nearby fractures in a manner similar to the process zone often observed around igneous dikes, where the intensity of dike-parallel joints is found to be very high close to the dike (Delaney et al., 1986; Pollard, 1987). The new, three dimensional

simulations presented here more clearly delineate how variation in the subcritical parameter *n* can determine whether the fracture pattern will exhibit clustered or more regular spacing. We also show, contrary to previous theorizations (Olson, 1993; Renshaw and Pollard, 1994), that fracture pattern development at very high subcritical index values ($n > 40$) can be materially different than results generated at moderately high subcritical index values ($n = 20$).

The simulations in this paper were performed with a model modified from Olson (1993) which is based on the conceptual formulation for joint growth as postulated by Segall (1984) and implemented using the displacement discontinuity method of Crouch (1976). The fractures are represented by series of equi-length boundary elements. Fracture pattern development is strongly influenced by the mechanical interaction between neighboring fractures throughout the fracture growth history. This interaction is manifested by the opening or shearing of one fracture perturbing the stress field acting of other fractures. Mathematically, the normal stress acting on an *ith* fracture element (σ_n^i) due to shearing and opening displacement discontinuities on the *jth* fracture element (D_s^j and D_n^j, respectively) can be given by the equation (modified after Crouch (1976))

$$\sigma_n^i = \sum_{j-1}^{N} F^{ij} A_{ns}^{ij} D_s^j + \sum_{j-1}^{N} F^{ij} A_{nn}^{ij} D_n^j \qquad (2)$$

where A_{ns}^{ij} is the plane-strain, elastic influence coefficient giving the normal stress at element *i* due to a shear displacement discontinuity at element *j*, and A_{nn}^{ij} gives the normal stress at element *j* due to an opening displacement discontinuity at element *j*. An analogous equation can be written for shear stresses. The fundamental integral for determining the influence coefficients *A* is presented by (Crouch, 1976). The difference here as compared to Olson (1993) and Crouch (1976) is the factor F^{ij}, given by

$$F^{ij} = 1 - \frac{d_{ij}^3}{\left[d_{ij}^2 + \left(h/2 \right)^2 \right]^{3/2}} \quad , \qquad (3)$$

where d_{ij} is the distance between the centers of elements *i* and *j*, and *h* is the fracture height (assumed equal to bed thickness). This correction factor is modeled after the analytical equation for normal stress perpendicular to a vertical, plane-strain crack, where the infinite (out of plane) dimension is the fracture length (Pollard and Segall, 1987). As d_{ij} gets large relative to *h*, F^{ij} goes to zero, meaning fractures that are widely spaced relative to bed thickness have no mechanical influence on one another. Thus, equation (3) is an approximate three-dimensional correction factor that asymptotically approaches *1* at small *d/h* and approaches *0* at high d/h.

NUMERICAL RESULTS

The simulation results demonstrate the role of subcritical index, layer thickness, and initial flaw density on fracture spacing and length (Figure 4). The initial set of simulations were run with 800 starter flaws, randomly located in a finite body with an x-dimension of 24 meters, a y-dimension of 34 meters and a layer thickness of 8 meters. To prevent unwanted edge effects between the propagating fractures and the boundaries of the finite body, initial flaws were excluded from a 2 meter thick border around the body perimeter, and subsequent growth was excluded from a slightly thinner 1 meter thick border. Straight crack propagation was imposed to simplify calculations, but such a geometry is reasonable if a strong horizontal stress anisotropy is assumed (Olson and Pollard, 1989). Crack growth was induced by a constant strain rate (2×10^{-20}/s) extension in the y-direction of final magnitude 9×10^{-5}. (Because of the greater fracture propagation for the n=5 case, the simulations was run in a body of half the size with half the flaws and the same imposed strain to reduce computing time and memory requirements. However, the loading conditions and flaw intensity were exactly the same.)

At the beginning of a simulation, the flaw with the highest stress intensity propagates first, and the magnitude of the propagation velocity contrast between the higher and lower stress intensity cracks is defined by the power-law relationship of equation 1. Previous work has shown that for very low subcritical index values ($n < 10$) (Olson, 1993; Holder et al., 2001; Olson et al., 2001), many cracks propagate roughly at the same time and at the same velocity. Even flaws that are initially close together relative to the layer thickness increase in length at a comparable rate, penetrating one another's propagation exclusion zones prior to the stress relief being fully developed. Using n=5, a fracture pattern was generated having a wide distribution of fracture lengths and an average spacing much less than the bed thickness where spacing is highly irregular (Figure 4A). Increasing the subcritical index to 20 significantly reduced the number of fractures that propagated and the amount of total fracture length created (Figure 4B), but more very long fractures grew. The spacing became more regular and systematic. This pattern development was characterized by fractures that grew one at a time as a consequence of a large relative velocity contrast between fractures of even slightly different K_I values as defined by equation 1.

Finally, the subcritical index case of n=80 gave some surprising results (Figure 4B). Instead of resulting in just a more sparsely fractured version of the n=20 case, the fracturing mechanism seemed to completely change to the growth of widely spaced fracture clusters. There were again less fractures that propagated (a consistent result for increasing n), but because of the clustering, the spacing distribution had many small values. Because of the very close spacing within clusters, there was an increase in fracture interaction that reduced the ability of a given fracture to reach great length, resulting in a pattern with fewer long fractures than the n=20 case. This represents a reversal in trend - moving from very low to moderate subcritical index, the

fracture lengths increase for the same external loading, but when moving from moderate to very high subcritical index, fracture lengths go back down (due to stronger clustering).

The fracture length and spacing data for Figure 4 are displayed in Figures 5 and 6. The change in fracture length distribution with changing subcritical index shows that the *n=5* case is not that different from the *n=20* case, but with *n=80*, there is a significant reduction in fracture lengths achieved (Figure 5). The clustered nature of the fracture pattern at *n=80* is the reason for this decrease in fracture lengths, as the stronger mechanical interaction within the cluster limits length development. Another feature of the length distributions from these simulations is that the cumulative frequency is very well described by a negative exponential function. This characteristic has been shown to be theoretically predicted if fracture length is limited by crack to crack mechanical interaction (Olson et al., 2001).

The cumulative frequency distribution of spacing values (Figure 6) shows that changing the subcritical index from *n=5* to *n=20* causes a significant increase in fracture spacing, changing the median value from 2 meters to almost 6 meters. Although the data is too sparse to make definitive statistical statements, there is a small degree of clustering (very small spacings) for *n=5* not present in the data for *n=20*. It is the intermediate subcritical index values that are most likely to give the fracture spacing roughly proportional to bed thickness. Since one fracture grows at a time at this subcritical index, each fracture can fully develop its stress shadow before neighboring fractures get a chance to compete for propagation energy, and the spacing scales with the size of the fully developed fracture's stress perturbation (Pollard and Segall, 1987). In the *n=80* case, spacing is bi-modal, with an average spacing of less than 0.5 meters within clusters and about 10 meters between clusters.

Additional simulations were run to demonstrate the effects of varying bed thickness and initial flaw density (Figures 7 through 9). These simulations were run only for the condition of *n=80*, under the same strain boundary conditions but with only half the initial flaw density (400 instead of 800 flaws) and with bed thickness varying from 2 to 8 meters. All of the trace maps show some degree of fracture clustering (Figure 7), but clustering is weakest for the thinnest bed (b=2 meters). This is because of the limited mechanical interaction between fractures in thin beds when interaction is restricted to a distance proportional to fracture height. As bed thickness increases, the mechanical interaction between fractures increases and clustering is more fully developed. However, even though the trace maps for the different bed thickness cases look substantially different, the fracture length cumulative frequency data for all cases follow virtually the same exponential curve (Figure 8). This suggests that subcritical index has a much stronger effect on length distribution than does bed thickness. However, comparing the exponent for the negative exponential fit in Figure 8 (-0.3678) to the exponent for the n=80 case in Figure 5 (-1.011) shows that the initial flaw density has a very strong influence on fracture length distribution. The steeper slope for the higher fracture density case (Figure 5) shows that more flaws cause additional length growth hindrance. Even though both cases were run to the same final strain and had the same bed thickness (cases c800b8n80 and c400b8n80), the maximum length for the higher flaw density case is 5 meters while for the lower density case it is almost 10 meters. This strong dependence of length development on flaw density is similar to that found in Olson et al. (2001).

As evident in the tracemaps, the fracture spacing distributions are strongly affected by bed thickness, even though the fracture length distribution is relatively independent of it (Figure 9). Conclusions based on this spacing data can only be qualitative as the limited extent of the

body perpendicular to fracture strike makes for a rather sparse data set, particularly for the bed thickness of 8 case (the body is only 4 bed thicknesses long in the y-direction). Also, the minimum fracture spacing value is an artifact of the minimum spacing of the grid on which the original flaws were laid out, but beyond these limitations, there are still some real differences that can be observed in the cumulative spacing frequency data. The observation based on the tracemaps that the thin bed case is less clustered seems to be supported by the fact that the median spacing (spacing at a cumulative frequency of 0.5) of about 2 meters represents the spacing between clusters and not within clusters. The spacing within clusters is represented by the cumulative frequency data above 0.75, where spacing is at the minimum possible value of 0.2 meters. Looking at the tracemap itself (Figure 7), it is evident that most of the fracture "clusters" are overlapped en echelon pairs of fractures. Only rarely is there a cluster of three or more closely-spacing fractures.

For both the 4 and 8 meter bed thickness cases (Figure 9), the median spacing appears to be the intra-cluster spacing, and this spacing within clusters becomes smaller with increasing bed thickness (*1.1 m* for *b=4 m* as compared to *0.4 m* for *b=8 m*). This decrease in minimum fracture spacing seems counter-intuitive at first, but reflects the stronger fracture clustering at greater bed thickness due to three dimensional effects. Thicker beds allow for stronger mechanical crack interaction and more stress elevation in the crack tip region, causing the growth of more fractures in the "process zone" that ultimately leaves behind the fracture swarm. The maximum spacing, conversely, which represents spacing between clusters, increases with increasing bed thickness, more consistent with traditional fracture spacing theories.

DISCUSSION

As mentioned earlier, the mechanism of fracture clustering can be likened to a process zone propagating across the body. The reason for clustering to occur in the high subcritical index cases is related to the stress intensity factor values when propagation occurs. Since fracture propagation velocities for the highest n value cases are initially very lower due to the power-law nature of equation 1, propagation is delayed in the high subcritical index case until more strain has accumulated. Consequently, when fracture growth finally occurs, it is at higher stress intensity values that approach or exceed critical values. Since stress scales linearly with stress intensity factor in the near tip region (Lawn and Wilshaw, 1975), the tensile stress perturbation around the crack tip is increased by high K_I values and the propagation of flaws in the crack tip region is enhanced for high *n* cases. The clusters or fracture swarms essentially record the movement of a process zone across the rock body, and because of the higher stress intensity factor values, the propagation mechanism is not subcritical but critical ($K_I \geq K_{Ic}$). This mechanism is similar to the process zone fracturing seen in dikes (Delaney et al., 1986; Pollard, 1987) and at the microscale around joints (Labuz et al., 1987; Nolen-Hoeksema and Gordon, 1987).

Looking at the sequence of development of fracture aperture and stress intensity factor in a growing cluster helps illustrate the cluster growth mechanism. Figure 10 shows the time sequence of fracture growth for the cluster located around *y=8* meters from the *n=80* case in Figure 4, mapping fracture opening at each boundary element in the simulation (fractures are made up of contiguous series of elements 0.1 meters in length) and stress intensity factor at every crack tip. Fracture opening is represented by the diameter of the white circles located at each fracture patch center. (Fracture aperture exaggeration is approximately 450 times – the

maximum aperture in the final plot of the sequence, Figure 10H, is approximately 1.75 mm located at *x=0 m, y=8.4 m*). The stress intensity factor is proportional to the diameter of the dark gray circles which are located at the center of every crack tip element. The scale for stress intensity factor magnitude is the large, dark circle centered at *(0,0)* on each plot, whose size represents a stress intensity factor value of 10 MPa-$m^{1/2}$.

In Figure 10A, only a small amount of fracture growth has occurred, starting at the cracks with the largest initial K_I values. None of the cracks in the simulation have any visible fracture aperture except for the crack whose tips are indicated to have the highest K_I on the plot. After additional growth has occurred (Figure 10B), the fracture aperture for the main crack is clearly visible, and the K_I values are rising for this main growing crack as well as for some of its close neighbors. The fracture cluster growth (or the process zone) is well-developed by Figure 10C, where several cracks are propagating ahead of the left tip of the main crack. It is interesting to note that the cracks in the cluster have elevated K_I values at both tips, suggesting that they are both propagating out ahead of the main crack (to the left) as well as back toward it (to the right). Eventually, the crack interaction of the overlapping en echelon crack tips will hinder growth of the clustered fractures toward the right and the main crack toward the left, causing arrest at some tips and providing a limitation on length growth (Pollard et al., 1982; Olson and Pollard, 1989).

Another aspect of crack interaction can be seen by comparing Figures 10 A and D. While there is fracture propagation enhancement ahead of the tip of the main propagating cracks, there is propagation hindrance to either side of the main body of the crack as pointed out in the Figure 10D. The propagation hindrance is exemplified by the diminished K_I values of the pre-existing flaws in that area as compared to their initial state. Further propagation of the fracture cluster completely across the body is shown in Figures 10 E through H. Further development of

the stress shadow or propagation suppression zone is evident, as well as the tapered, non-elliptical displacement profiles at the tips for many of the overlapping, en echelon fractures. Although the fracture opening solution for a uniformly loaded, isolated crack predicts an elliptical opening distribution (Pollard and Segall, 1987), it has been shown that non-uniform loading or fracture interaction in a linear elastic model will modify this distribution (Olson and Pollard, 1991; Pollard, 1976; Pollard, 1987). Although non-elastic failure (as implied by cohesive crack tip models) will generate similar tapered displacement distributions in the neartip area (Cowie and Scholz, 1992; Vermilye and Scholz, 1995), such a mechanism is not required.

Comparing the final fracture aperture map with the trace map (Figure 11) show that not all fractures that propagate are left with an appreciable aperture at the end of the deformation cycle. The figure clearly shows that although there are many fractures that propagated in the cluster (Figure 11B), there are a few dominant ones that have the largest aperture at the expense of their neighbors. Comparing the initial state to the final state but increasing the scale of the K_I values emphasizes the stress shadow or propagation suppression effects around an open fracture or cluster of fractures (Figure 12). This K_I suppression extends almost 6 meters to either side of the open fracture zone (the bed thickness for this case was 8 meters). Surprisingly, however, there is still some K_1 left on the overlapped tips of the fractures within the cluster, a location where one would expect very strong stress shadow effects. These non-trivial stress intensity values may be related to an overall weakening of the body due to the fracture zone that may enhance opening or propagation.

CONCLUSION

This work shows that spacing of fractures in layered, sedimentary rock depends not only on the static stress distribution around a fracture but also on fracturing dynamics and the three

dimensional nature of lateral fracture propagation. The two-dimensional, static analysis of a layer cross-section implying a minimum fracture spacing approximately equal to layer thickness is only one end-member of fracture spacing behavior. This relationship is reproduced in dynamic, pseudo-3d propagation simulations for materials with intermediate magnitude subcritical indices ($n \cong 20$). Another regime of propagation behavior exists for very low subcritical index materials ($n \cong 5$), where fractures tend to have spacing that is very irregular and much less than bed thickness. This spacing could be called clustered, but the clusters themselves are very close to one another relative to bed thickness. Finally, at very high subcritical index ($n \cong 80$), fracturing is also very clustered, but the clusters are very widely spaced and the fracture growth is actually critical. These fracture swarms propagate like a process zone across a rock body.

Although fracture height as constrained by bed thickness has an influence on fracture spacing, simulations show little impact of bed thickness on the cumulative frequency of fracture length. The key parameters controlling fracture length development appear to be subcritical index and flaw density in the body. Another unusual result related to bed thickness effects was found in the $n=80$ cases. Although increasing bed thickness increased the maximum observed spacing between fractures for a given pattern, which seems to be consistent with stress shadow ideas, the median spacing of the distribution actually decreased as bed thickness was increased. This behavior is attributed to the stronger mechanical crack interaction for larger bed thickness cases, causing more intense fracturing in the neartip region of a propagating crack. For a thin bed, the zone of elevated stress is less well-developed around the propagating crack tip, and thus fracture clusters are less significant and median spacing is broader.

ACKNOWLEDGEMENTS

This material is based in part on work supported by the US Department of Energy under Award No. DE-FC26-00BC15308, the Texas Advanced Technology Program and by The Fracture Research and Application Consortium of The University of Texas at Austin.

REFERENCES

Atkinson, B.K., 1984, Subcritical Crack Growth in Geological Materials: Journal of Geophysical Research, v. 89, p. 4077-4114.

Atkinson, B.K., and Meredith, P.G., 1987, Experimental Fracture Mechanics Data for Rocks and Minerals, *in* Atkinson, B.K., ed., Fracture Mechanics of Rock: London, Academic Press, p. 477-525.

Bai, T., and Pollard, D.D., 2000a, Closely spaced fracture in layered rocks: initiation mechanism and propagation kinematics: Journal of Structural Geology, v. 22, p. 1409-1425.

—, 2000b, Fracture spacing in layered rocks: a new explanation based on the stress transition: Journal of Structural Geology, v. 22, p. 43-57.

Cowie, P.A., and Scholz, C.H., 1992, Displacement-Length Scaling Relationship for Faults: Data Synthesis and Discussion: Journal of Structural Geology, v. 14, p. 1149-1156.

Crouch, S.L., 1976, Solution of Plane Elasticity Problems by the Displacement Discontinuity Method: International Journal for Numerical Methods in Engineering, v. 10, p. 301-343.

Delaney, P.T., Polllard, D.D., Ziony, J.L., and Mckee, E.H., 1986, Field Relations Between Dikes and Joints: Emplacement Processes and Paleostress Analysis: Journal of Geophysical Research, v. 91, p. 4920-4938.

Dyer, J.R., 1983, Jointing in sandstones, Arches National Park, Utah [Ph. D. dissertation thesis], Stanford University.

Holder, J., Olson, J.E., and Philip, Z., 2001, Experimental determination of subcritical crack growth parameters in sedimentary rock: Geophysical Research Letters, v. 28, p. 599-602.

Kulander, B.R., and Dean, S.L., 1995, Observations on fractography with laboratory experiments for geologists, *in* Ameen, M.S., ed., Fractography: fracture topography as a tool in

fracture mechanics and stress analysis, Volume 92: Geological Society Special Publications: London, Geological Society of London, p. 59-82.

Labuz, J.F., Shah, S.P., and Dowding, C.H., 1987, The fracture process zone in granite; evidence and effect: International Journal of Rock Mechanics and Mining Sciences & Geomechanics Abstracts, v. 24, p. 235-246.

Lawn, B.R., and Wilshaw, T.R., 1975, Fracture of Brittle Solids: Cambridge, Cambridge University Press, 204 p.

Narr, W., and Suppe, J., 1991, Joint Spacing in Sedimentary Rocks: Journal of Structural Geology, p. 1037-1048.

Nolen-Hoeksema, R.C., and Gordon, R.B., 1987, Optical Detection of Crack Patterns in the Opening-Mode Fracture of Marble: Int. J. Rock Mech. Min. Sci. and Geomech. Abstr., v. 24, p. 135-144.

Olson, J., and Pollard, D.D., 1989, Inferring paleostresses from natural fracture patterns: A new method: Geology, v. 17, p. 345-348.

Olson, J.E., 1993, Joint Pattern Development: Effects of Subcritical Crack-Growth and Mechanical Crack Interaction: Journal of Geophysical Research, v. 98, p. 12,251-12,265.

Olson, J.E., and Pollard, D.D., 1991, The initiation and growth of en echelon veins: Journal of Stuctural Geology, v. 13, p. 595-608.

Olson, J.E., Qiu, Y., Holder, J., and Rijken, P., 2001, Constraining the Spatial Distribution of Fracture Networks in Naturally Fractured Reservoirs Using Fracture Mechanics and Core Measurements, 2001 SPE Annual Technical Conference and Exhibition: New Orleans, LA.

Pollard, D.D., 1976, On the Form and Stability of Open Hydraulic Fractures in the Earth's Crust: Geophysical Research Letters, v. 3, p. 513-516.

—, 1987, Elementary fracture mechanics applied to the structural interpretation of dykes, *in* Halls, H.C.e., and Fahrig, W.F.e., eds., Mafic dyke swarms; a collection of papers based on the proceedings of an international conference, Volume 34: Mississauga, ON, Canada, p. 5-24.

Pollard, D.D., and Aydin, A., 1988, Progress in Understanding Jointing Over the Past Century: Geological Society of America Bulletin, v. 100, p. 1181-1204.

Pollard, D.D., and Segall, P., 1987, Theoretical displacements and stresses near fractures in rock: with applications to faults, joints, veins, dikes and solution surfaces, *in* Atkinson, B.K., ed., Fracture Mechanics of Rock: London, Academic Press, p. 277-350.

Pollard, D.D., Segall, P., and Delaney, P.T., 1982, Formation and Interpretation of Dilatant Echelon Cracks: Geological Society of America Bulletin, v. 93, p. 1291-1303.

Renshaw, C.E., and Pollard, D.D., 1994, Numerical Simulation of Fracture Set Formation: A Fracture Mechanics Model Consistent with Experimental Observations: Journal of Geophysical Research, v. 99, p. 9359-9372.

Rives, T., Razack, M., Petit, J.P., and Rawnsley, K.D., 1992, Joint Spacing: Analogue and Numerical Simulations: Journal of Structural Geology, v. 14, p. 925-937.

Segall, P., 1984, Formation and Growth of Extensional Fracture Sets: Geological Society of America Bulletin, v. 95, p. 454-462.

Swanson, P.L., 1984, Subcritical Crack Growth and Other Time- and Environment-Dependent Behavior in Crustal Rocks: Journal of Geophysical Research, v. 89, p. 4137-4152.

Vermilye, J.M., and Scholz, C.H., 1995, Relation Between Vein Length and Aperture: Journal of Structural Geology, v. 17, p. 423-434.

Wu, H., and Pollard, D., 1994, An Experimental Study of the Relationship Between Joint Spacing and Layer Thickness: Journal of Structural Geology, p. 1-19.

Figure 1. A three layer composite, where the middle layer is fractured. When fracture spacing becomes less than or equal to layer thickenss (saturated spacing), the static 2-d analysis shows that the stress in the region between the fractures (σ_{xx}) becomes compressive, no matter how large the applied extension (ε_{xx}) perpendicular to the fractures (Bai and Pollard, 2000a).

Figure 2. Examples of fractures in rock with a spacing much less than layer thickenss. A) Regularly-spaced joints in Devonian shale where the average spacing, s, is less than 1/3 the minimum fracture height, h. B) A fracture cluster where three to five long fractures lie within a 20 cm wide zone. The inter-cluster spacing is approximately 10 meters, which is also the thickness of the fractured layer.

Figure 3. Three dimensional representation of a fractured roadcut exposure. The sandstone beds are separated by thin shale stringers that stopped the vertical growth of the fractures (see middle sandstone with 10 cm scale). The plumose markings on the fracture surface for the middle bed indicate the fracture grew from right to left, reaching a length many times the height, indicating the dominance of lateral versus vertical fracture propagation.

Figure 4. Examples of subcritical fracture growth for propagation indices of A) n=5, B) n=20 and B) n=80. All simulations started with the randomly located, parallel flaws, a layer thickness of 8.0 meters, and srain imposed by normal displacement, zero shear stress conditions at the top and bottom body boundaries, resulting in an ultimate strain perpendicular to the flaws of $9x10^{-5}$ at a strain rate of $2.0x10^{-20}$/s. The boundary conditions on the right and left boundaries of the body have zero normal displacement and zero shear stress. To reduce the computing burden for

the n=5 case, a smaller representative body was simulated, changing all parameters appropriately to keep simulations equivalent. The elastic properties of the rock were a Young's modulus of 20 GPa and a Poisson's ratio of 0.25.

Figure 5. Cumulative frequency diagram of fracture length for the patterns from Figure 4. Each plot has a best-fit negative exponential curve with an R^2 value to indicate goodness of fit.

Figure 6. Cumulative frequency diagram of fracture spacing for the fracture patterns in Figure 4 based on a scanline at *x=0.05 m*.

Figure 7. Fracture tracemaps for simulations run under similar conditions as those for Figure 4 except all cases have a subcritical index of 80, there are only 400 starter flaws instead of 800, and the bed thickness is varied from 2 to 4 to 8 meters.

Figure 8. Cumulative frequency diagram of fracture length for the patterns of Figure 7. Note that all three patterns have markedly similar length distributions.

Figure 9. Cumulative frequency diagram of fracture spacing for the fracture patterns in Figure 7 based on a scanline at *x=0.05 m*.

Figure 10. Sequence of fracture aperture and stress intensity factor development for the cluster from Figure 4 (case n=80) in the vicinity of y=8 m. The circle centered at (0,0) is the scale for K_I, showing the diameter appropriate for a value of 10 MPa-$m^{1/2}$. Each fracture segment

modeled has an opening represented by a white circle with a proportionate diameter. The fracture tip elements have a gray circle representing the magnitude of K_I. Frames A through H show the propagation of a cluster across the body, the stress shadow effects of growing fractures on other nearby fractures, and the tapered fracture opening shape approaching the crack tips for interacting fractures.

Figure 11. Comparison of the final fracture aperture distribution and tracemap of fractures that grew, showing that some fractures grow and then subsequently close or never reach an observable aperture.

Figure 12. Rescaled versions of Figure 10A and 10H, emphasizing the heterogeneity of K_I throughout the fractured body.

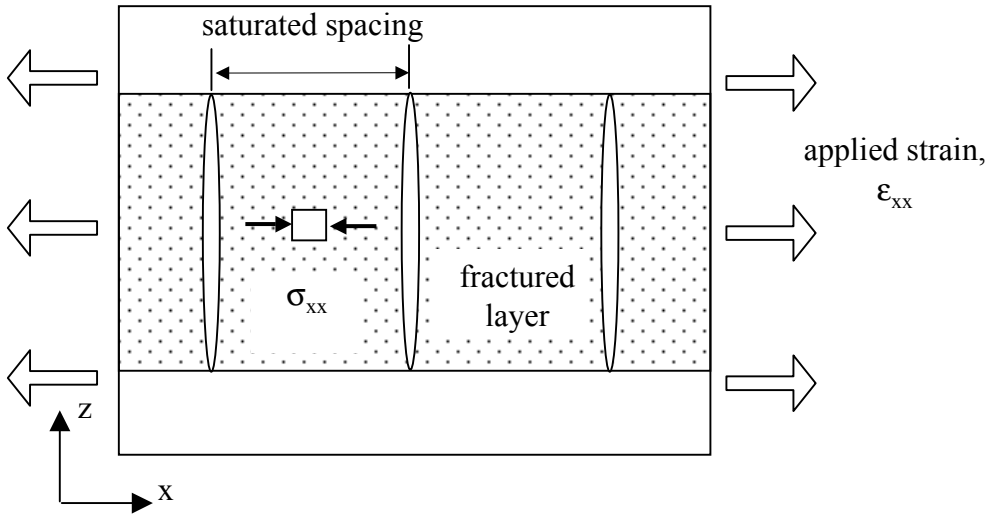

Olson

Figure 1

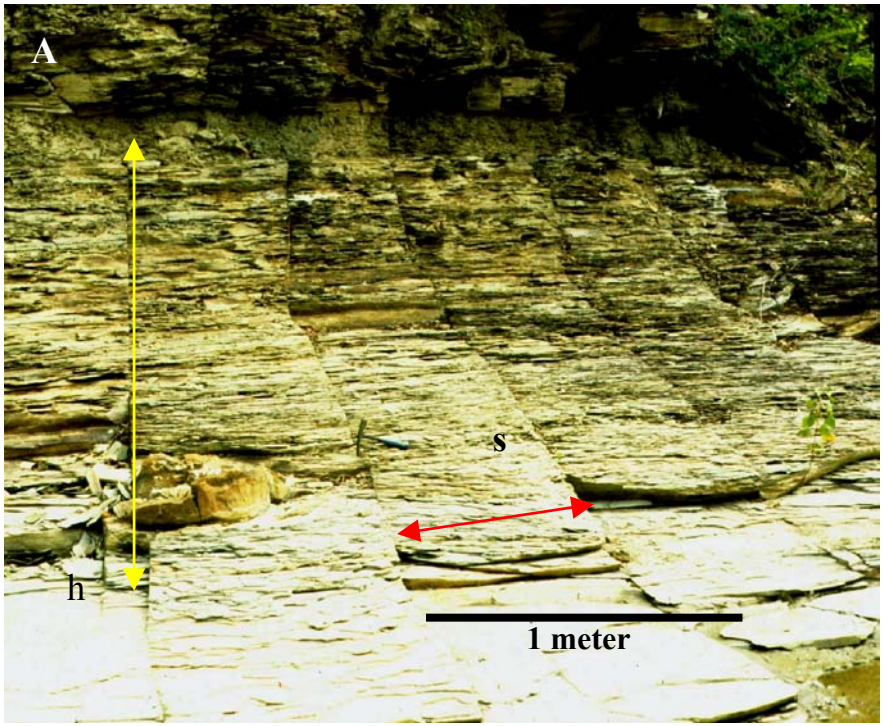

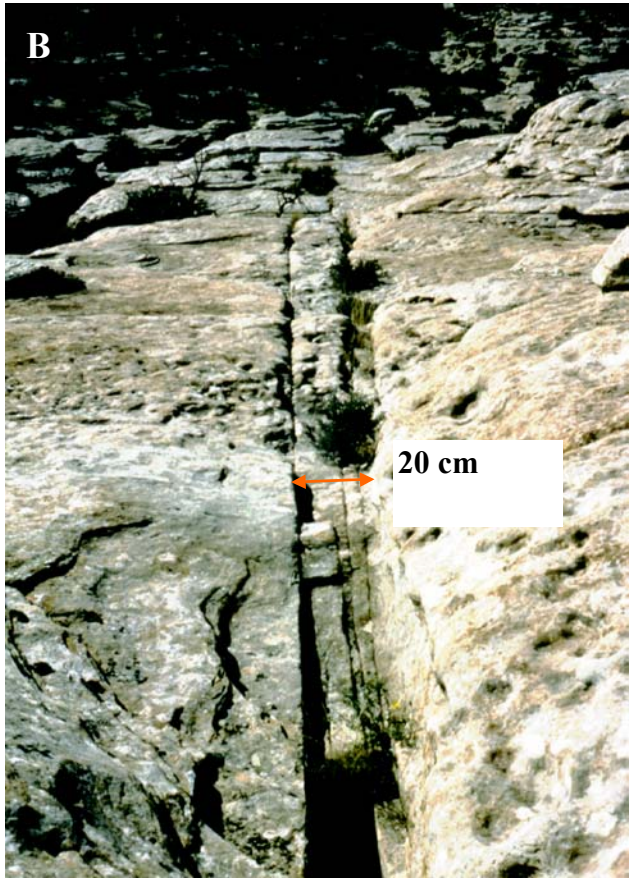

Olson

Figure 2

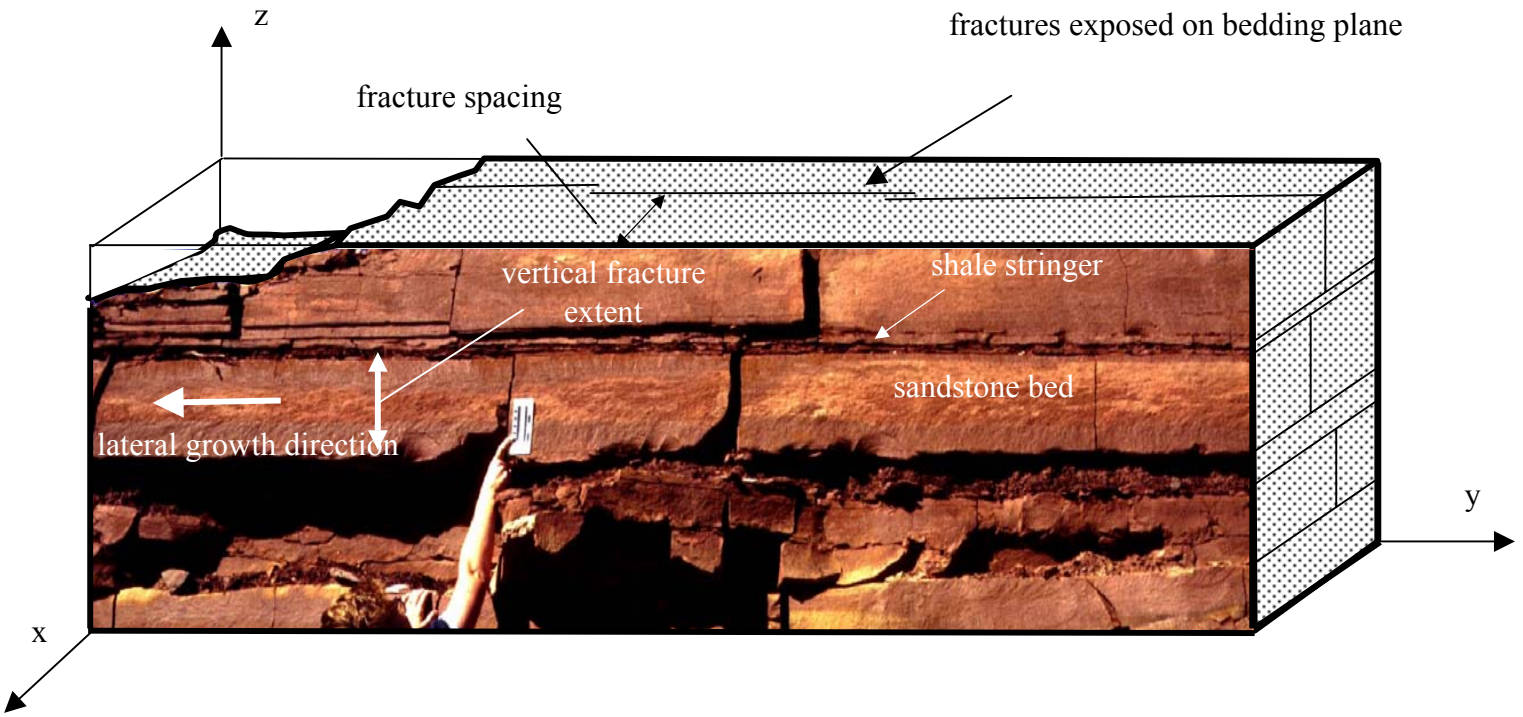

Olson

Figure 3

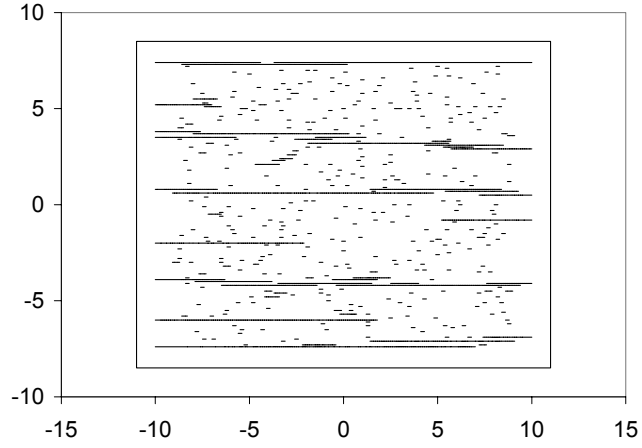
10
5
0
-5
-10
-15
-10
-5
0
5
10
15

n=5

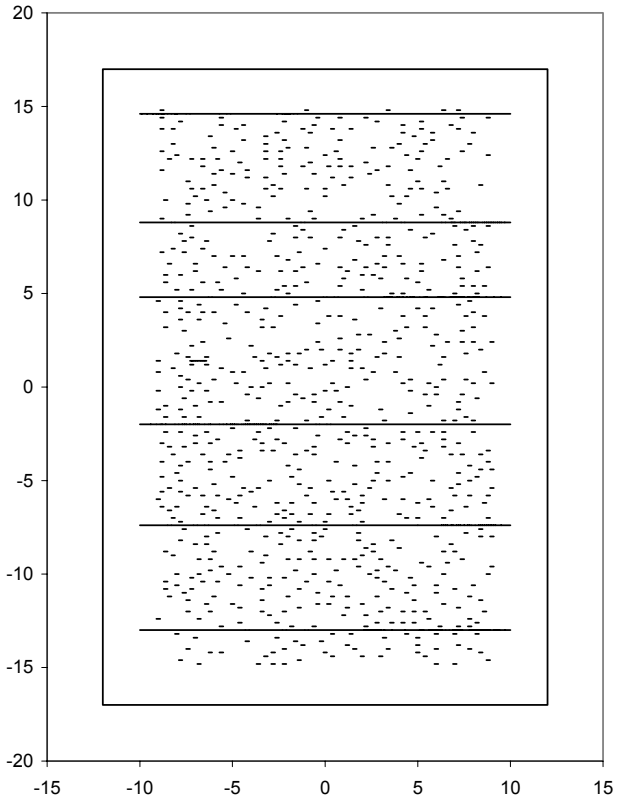
20
15
10
5
0
-5
-10
-15
-20
-15
-10
-5
0
5
10
15

n=20

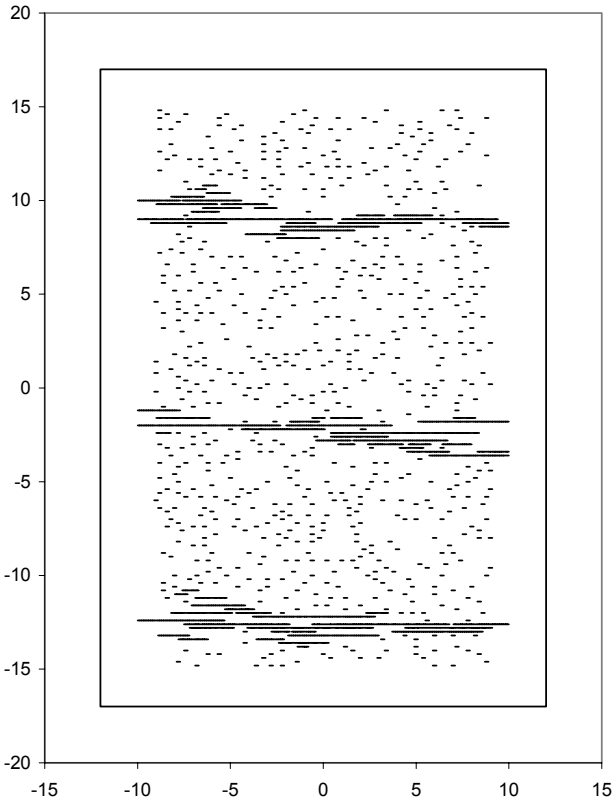
20
15
10
5
0
-5
-10
-15
-20
-15
-10
-5
0
5
10
15

n=80

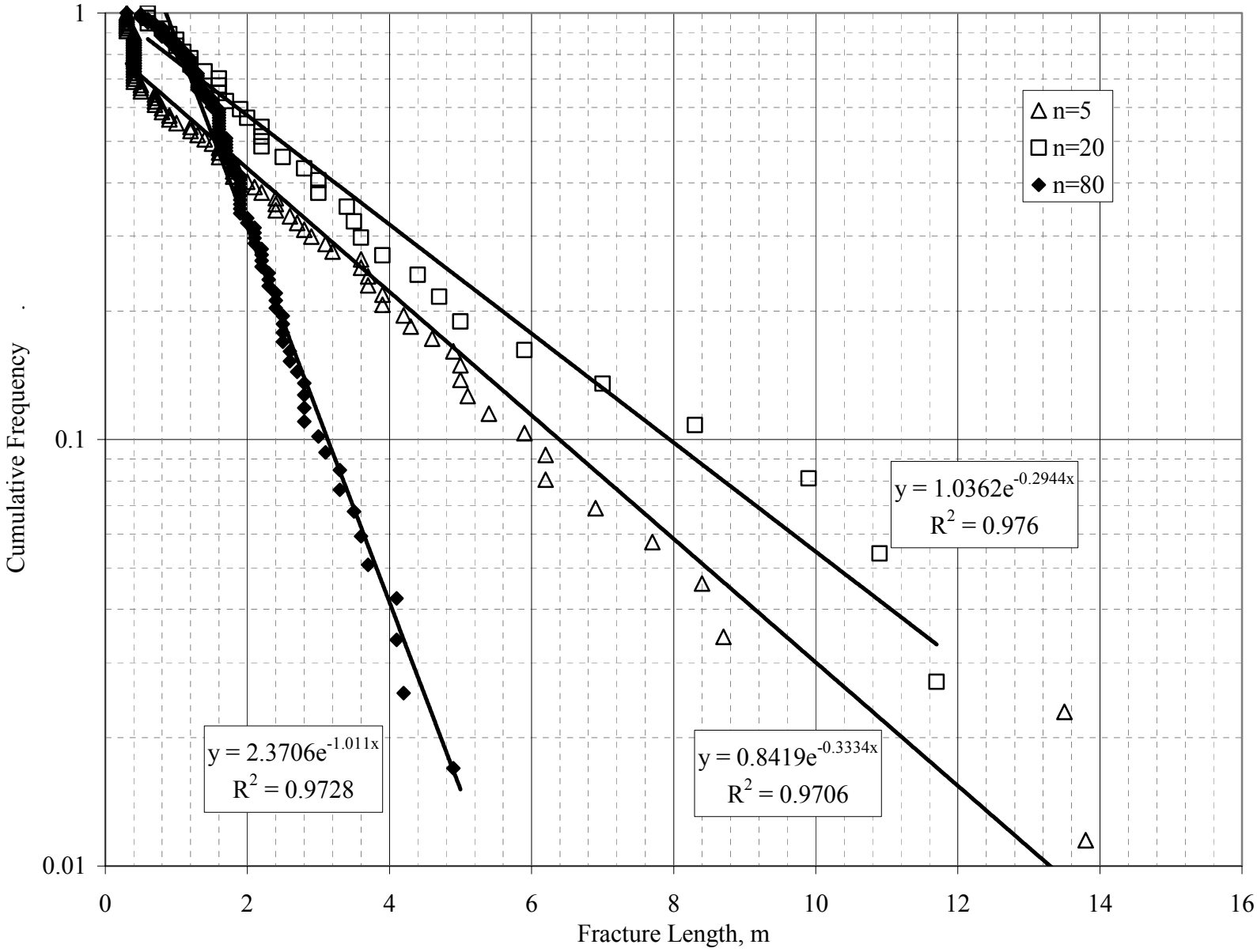

Olson

Figure 5

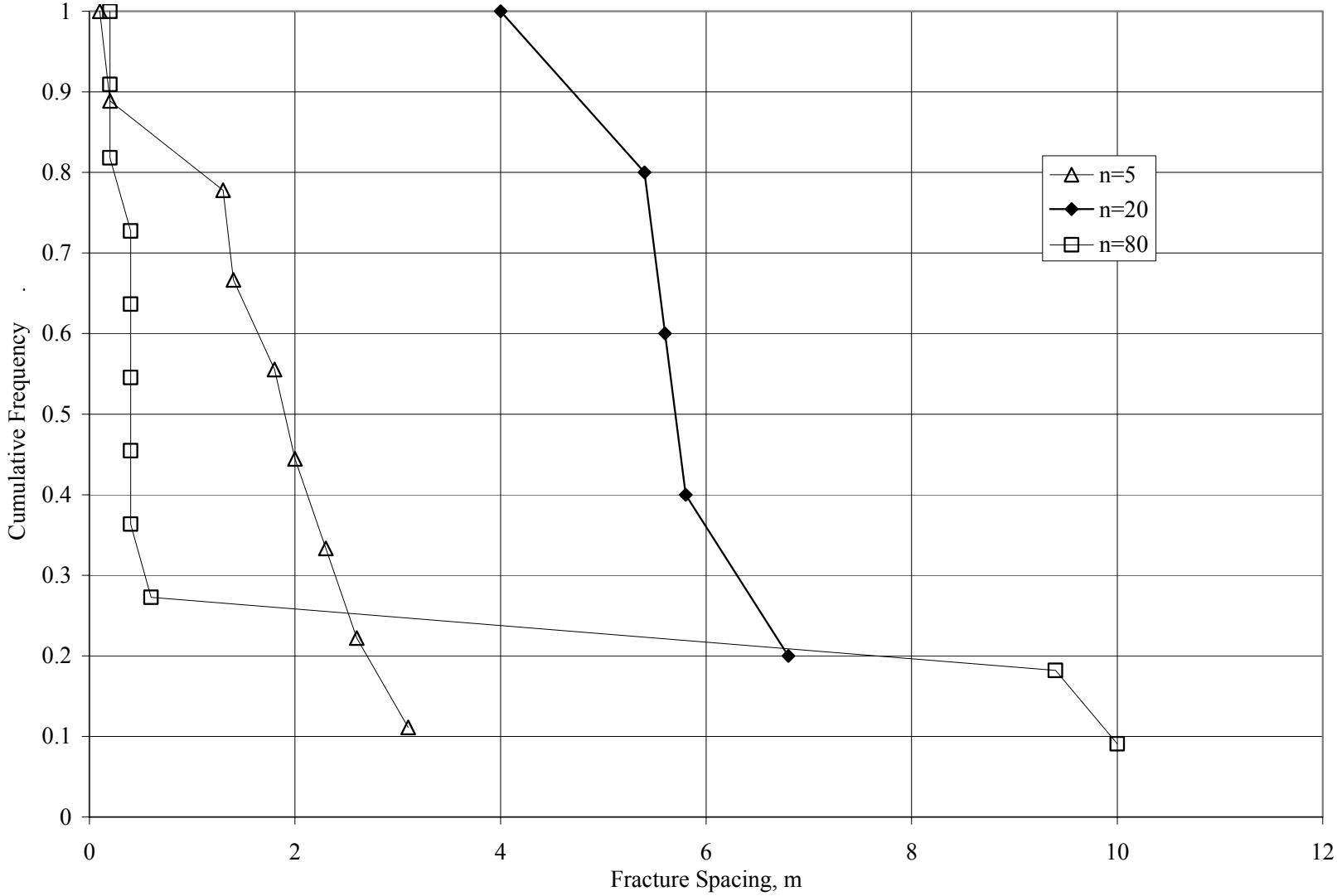

Olson

Figure 6

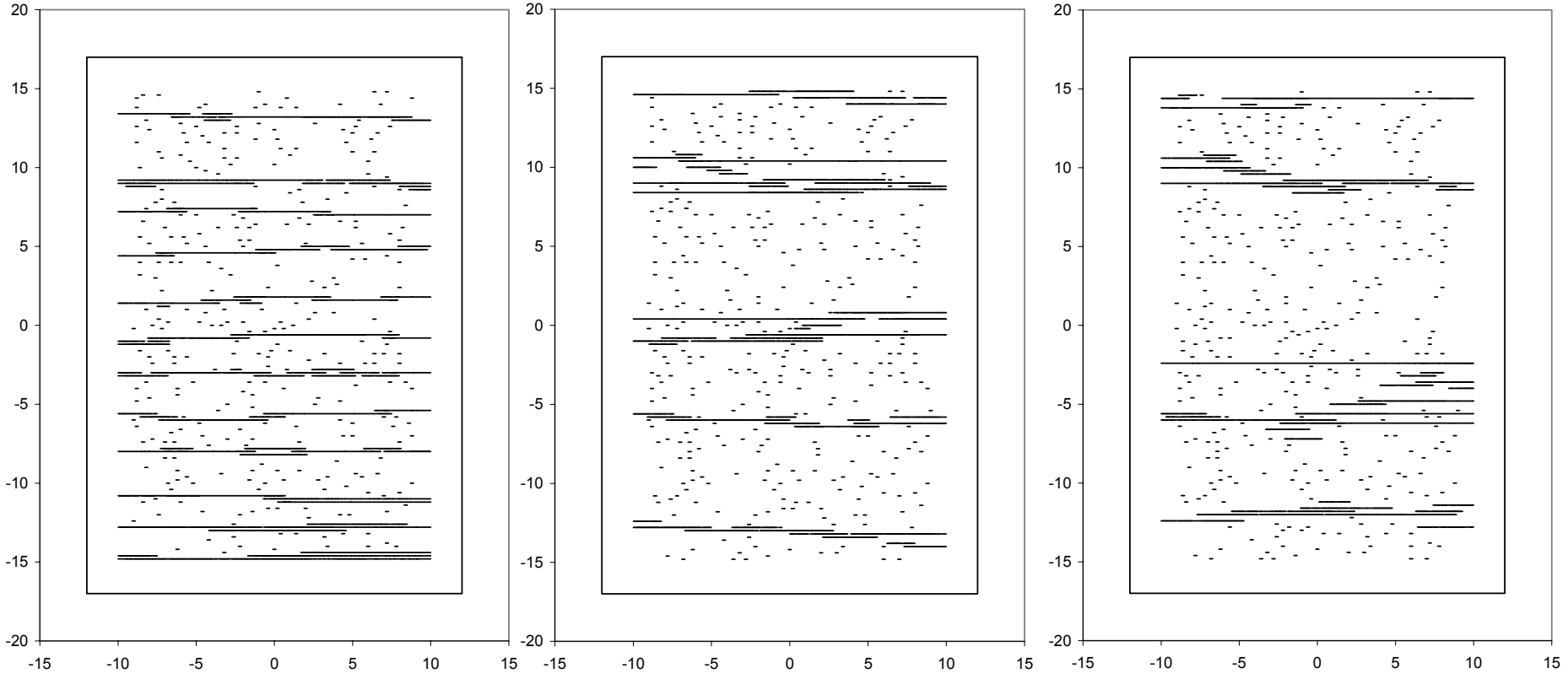

b=2 b=4 b=8

Olson Figure 7

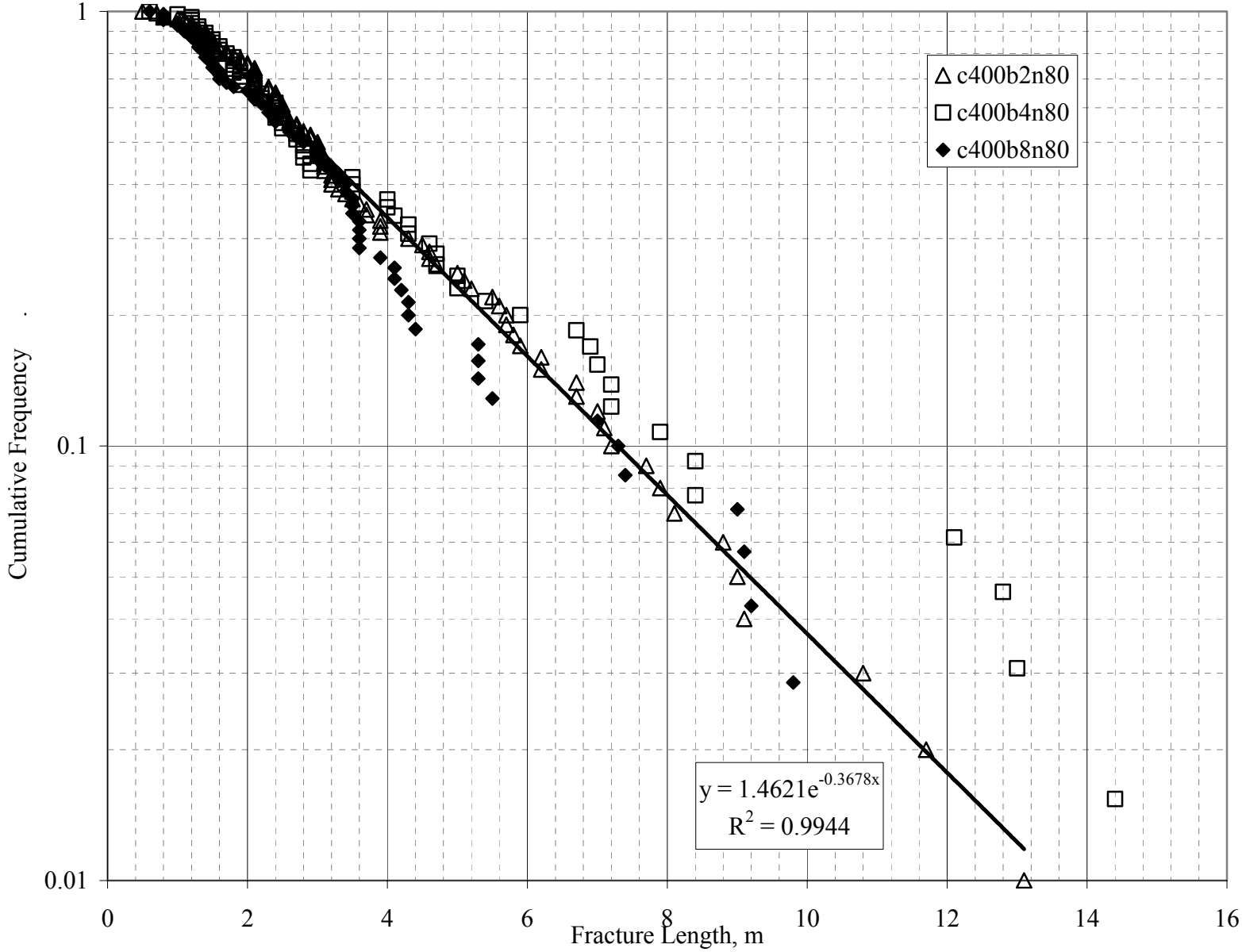

Olson

Figure 8

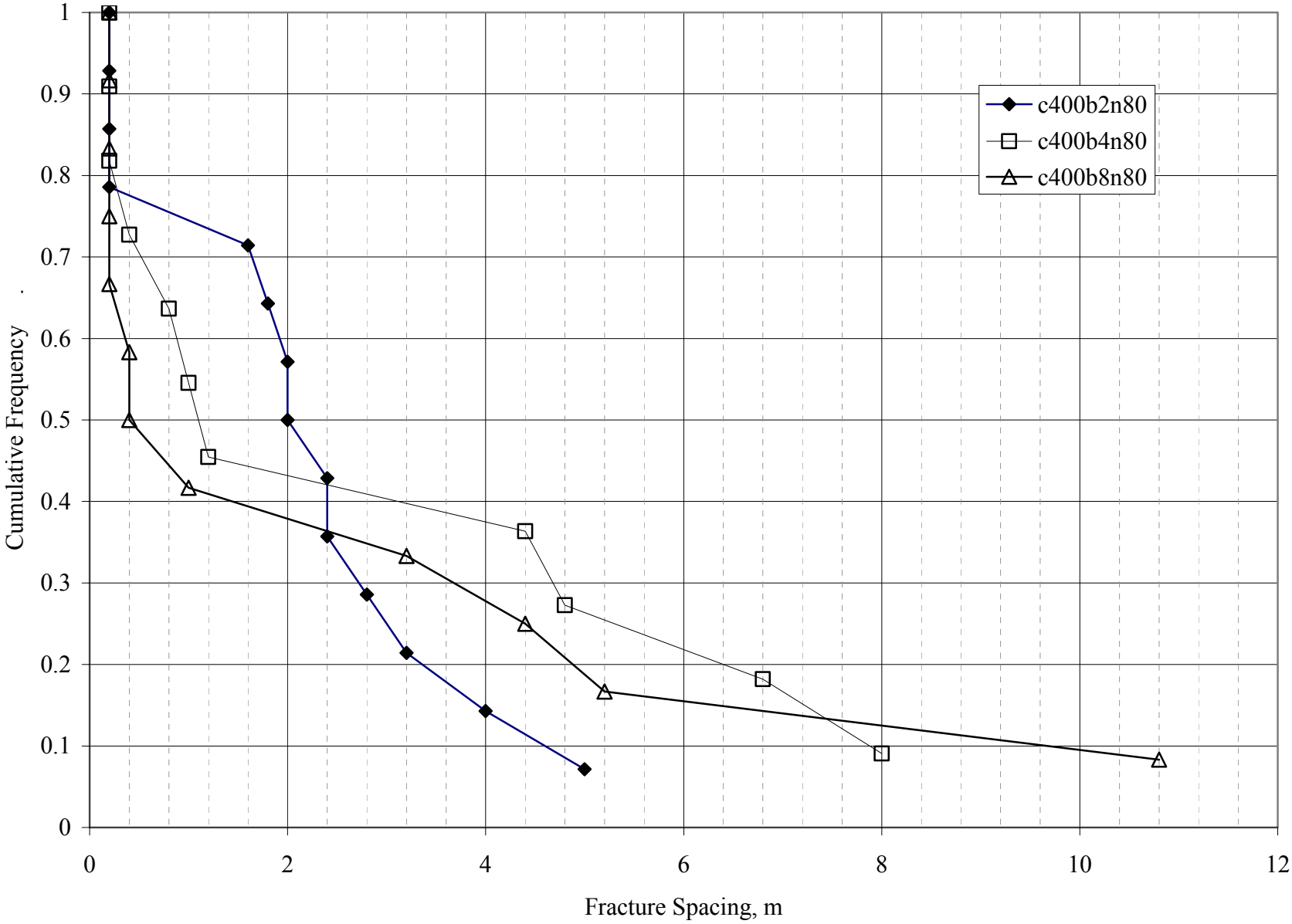

Olson

Figure 9

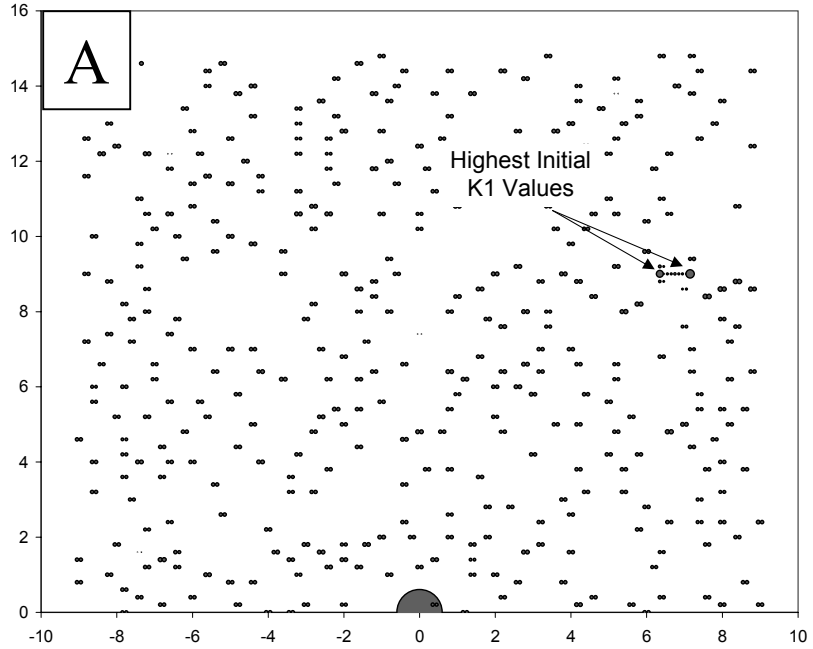

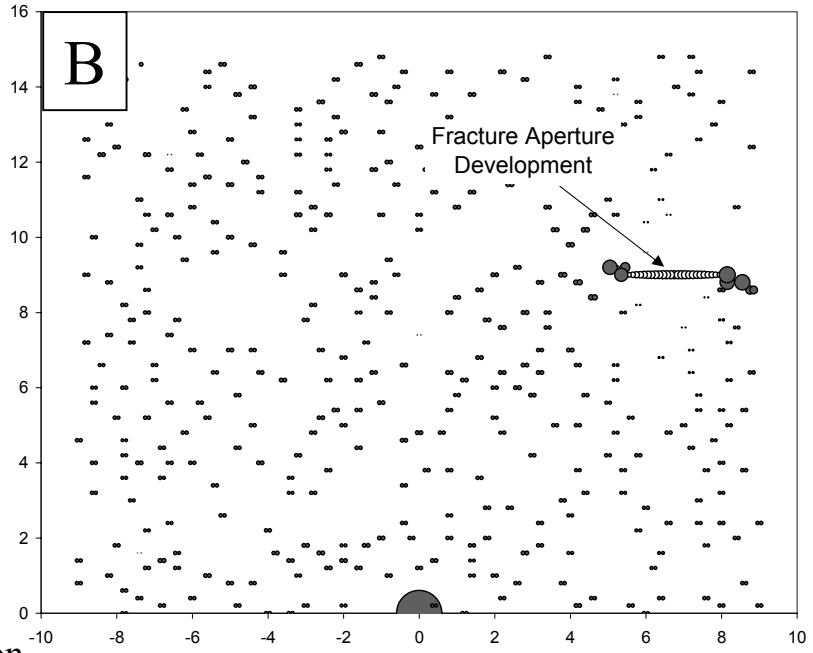

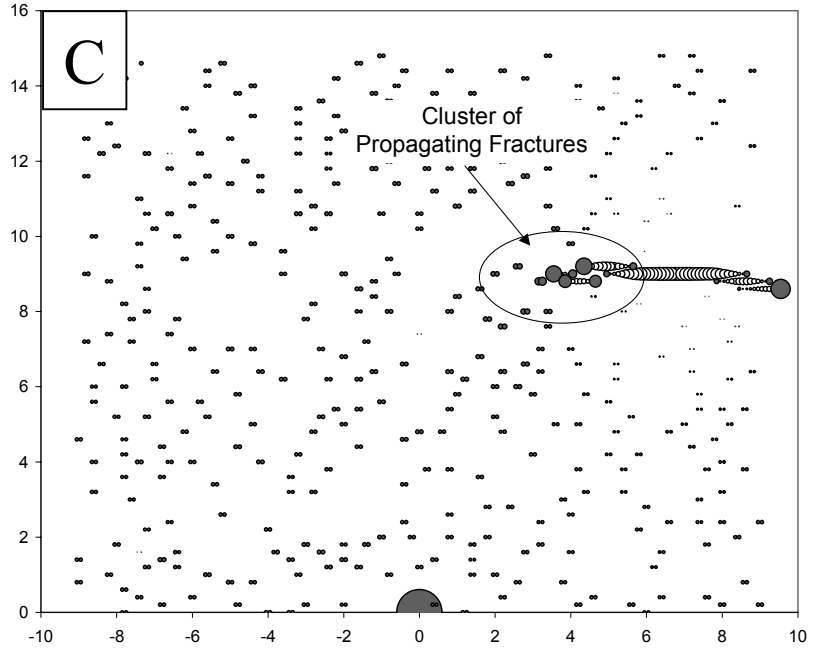

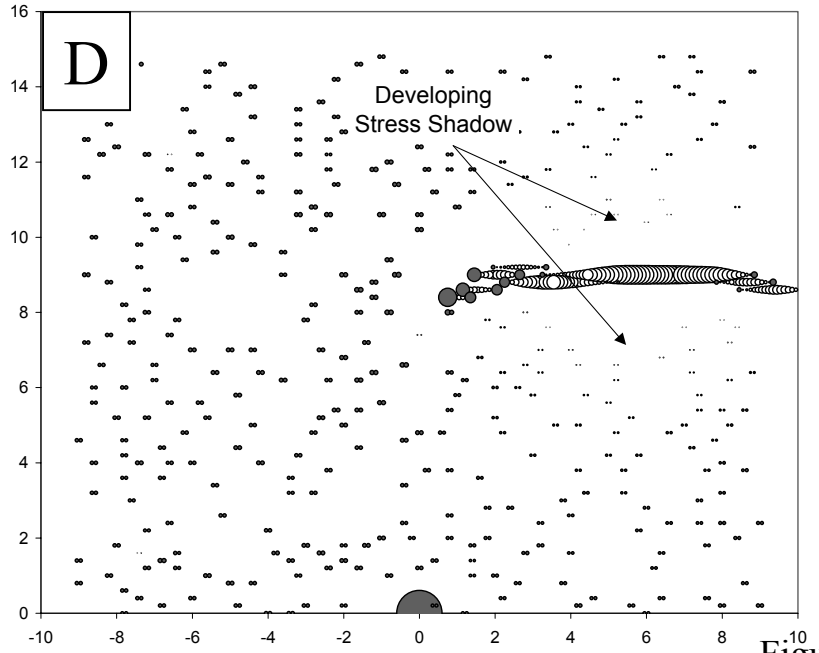

Olson

Figure 10

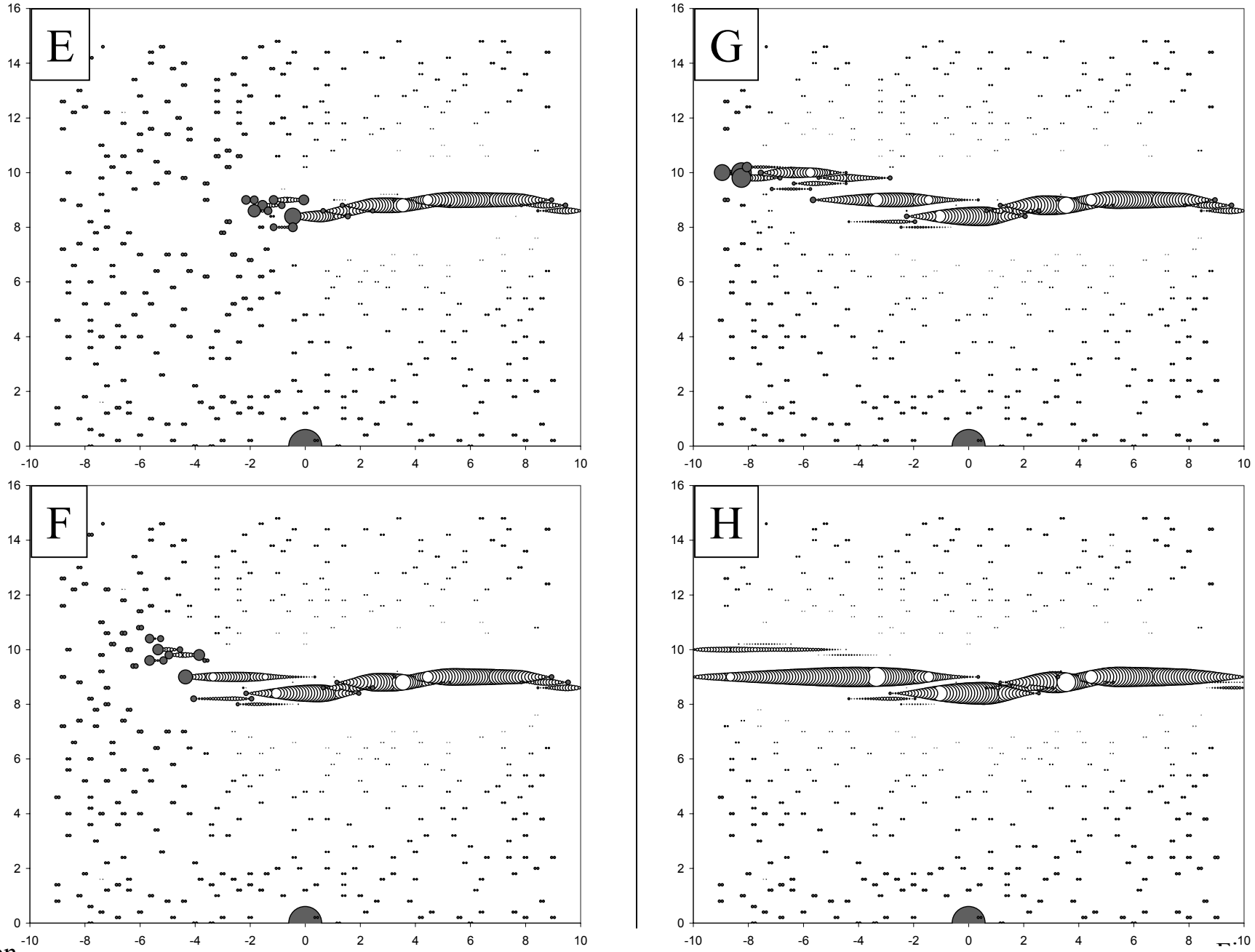

Olson

Figure 10

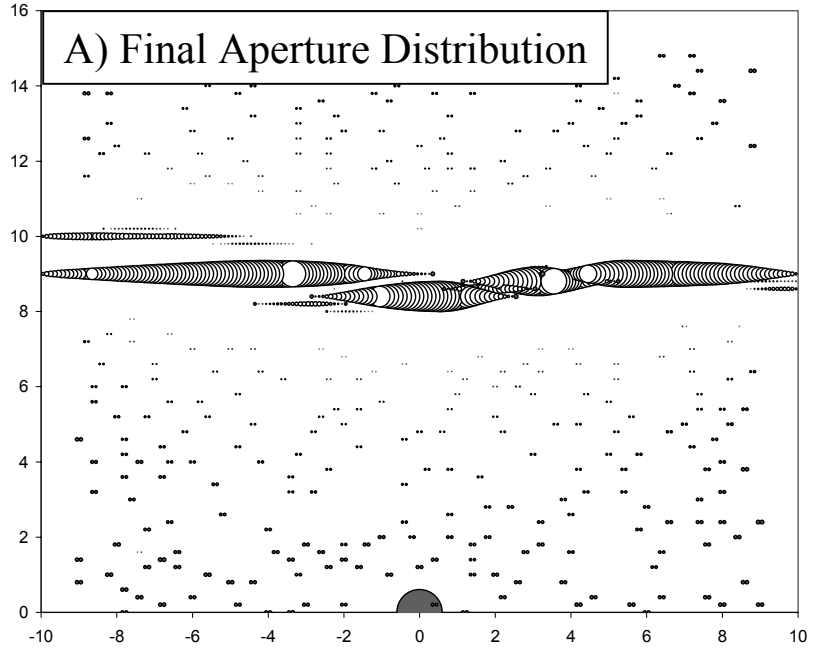

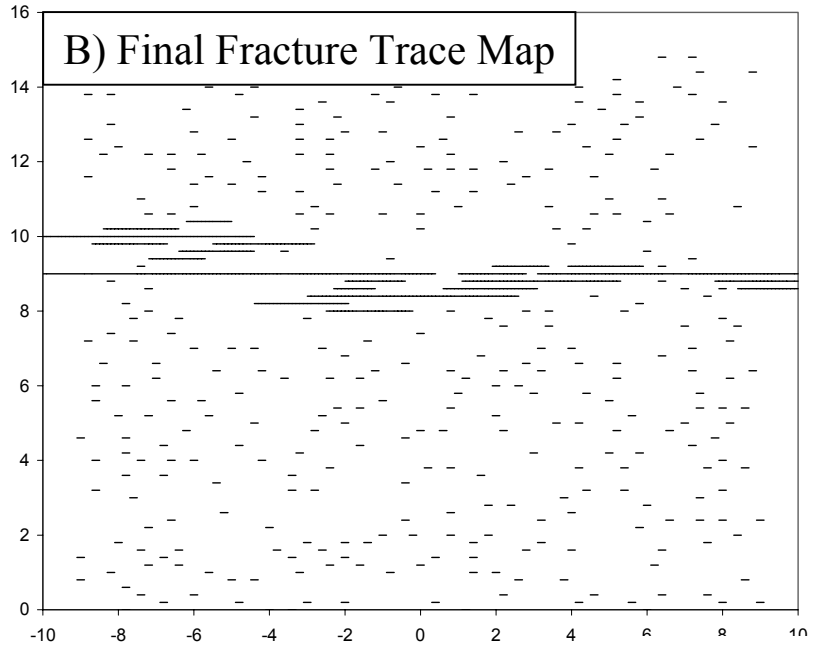

Figure 11

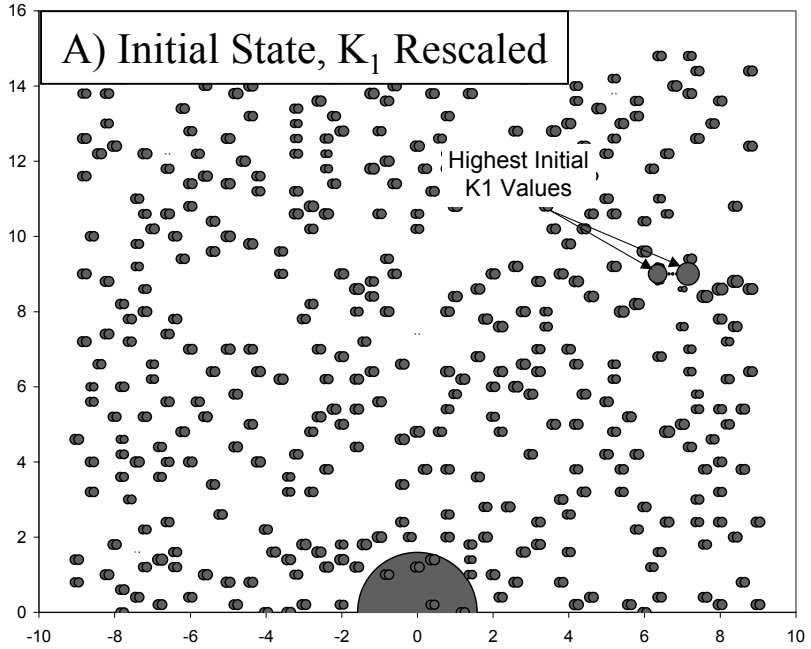

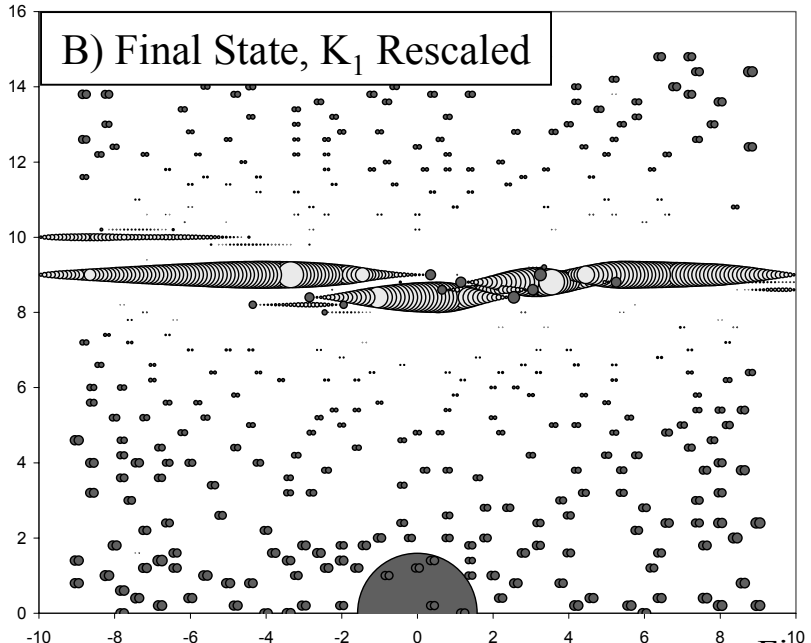

Figure 12

INFERRING INTERWELL CONNECTIVITY FROM WELL-RATE FLUCTUATIONS IN WATERFLOODS

by

ALEJANDRO ALBERTONI, B.S.

THESIS

Presented to the Faculty of Graduate School

of the University of Texas at Austin

in Partial Fulfillment

of the Requirements

for the Degree of

MASTER OF SCIENCE IN ENGINEERING

THE UNIVERSITY OF TEXAS AT AUSTIN

May 2002

INFERRING INTERWELL CONNECTIVITY FROM WELL-RATE FLUCTUATIONS IN WATERFLOODS

APPROVED BY
SUPERVISING COMMITTEE:

_____

Larry W. Lake

_____

Jon E. Olson

To Verónica,

for all her love, encouragement, and understanding.

ACKNOWLEDGEMENTS

I would like to express my deepest gratitude to my supervising professor Dr. Larry W. Lake for sharing his expertise and time with me throughout this research work. I praise him for his constant optimism, encouragement, and creativity. I particularly appreciate his invaluable advice and his ability to see the good things of unexpected results. I would also like to thank him for his patience and dedication when reading and reviewing this text.

I wish to express my gratitude to all the staff in the Petroleum Engineering Department. They made my days at the University of Texas very pleasant and helped me greatly enjoy my stay in Austin. I would like to specially thank Dr. Carlos Torres-Verdin for his help and comments, particularly in the development of the diffusivity filters. I also wish to thank Dr. Roberto Callarotti for his suggestions for future work, and Dr. Jon E. Olson who has taken the time to read and review my work.

Thanks are due to Repsol-YPF and BP for providing the data for the analysis; also to Saudi Aramco, the W.A. (Monty) Moncrief Chair in Petroleum Engineering, and the US Department of Energy (Award No. DE-FC26-00BC15308) for their financial support.

Finally, I want to thank my family: my parents, who have shown me the values of life, have provided me with a great education, and have taught me with love to always stay curious; Verónica, for her unconditional love, encouragement, and understanding; and Lucas, for his happiness.

ABSTRACT

INFERRING INTERWELL CONNECTIVITY FROM WELL-RATE FLUCTUATIONS IN WATERFLOODS

by

Alejandro Albertoni, M.S.E.

The University of Texas at Austin, 2002

Supervisor: Larry W. Lake

Reservoir characterization is one of the most important factors in successful reservoir management. The knowledge of reservoir heterogeneities and discontinuities is particularly relevant to the optimization of the operations and the economics of waterfloods. Moreover, developing efficient methods to appropriately describe the reservoir behavior has always been one of the most challenging goals in reservoir engineering because the information necessary for a good characterization is, most of the times, either scarce or very expensive to obtain and process.

This research project presents a practical technique to quantify communication between wells in reservoir using only production and injection rate data. The technique combines a constrained multivariate linear regression analysis

with diffusivity concepts to provide information about permeability trends and the presence of transmissibility barriers.

The technique presented in this research project calculates the fraction of flow in a producer caused by each of the injectors. This procedure also performs the analysis on a field-wide basis and analyzes multiple well influences in a single step. It uses filters to account for the time lag and attenuation that occurs between the stimulus (injection) and the response (production).

The method was developed and tested in synthetic fields using a numerical simulator and then applied to two waterflooded fields in Argentina. Application to numerically simulated fields reproduced input trends quite well. The simulation results indicate that the connectivity between wells is described by coefficients that only depend on geology and relative position between wells; they are independent of injection/production rates. Such validation on the field data is impossible; however, the results do seem to indicate the presence of known geological features.

The results of this work can be used to improve the performance of an existing waterflood by suggesting how well patterns might be changed or managed. They could also be used to model flow in the reservoir. Thus, valuable reservoir management and characterization tools are provided from the always-available measurements of production and injection rates at existing wells without the need for additional data. Several recommendations for further research on this topic are also presented.

TABLE OF CONTENTS

ACKNOWLEDGEMENTS ..... **V**

ABSTRACT ..... **VII**

TABLE OF CONTENTS ..... **IX**

LIST OF TABLES ..... **XII**

LIST OF FIGURES ..... **XV**

CHAPTER 1: INTRODUCTION **1**

1.1. Objectives & Hypotheses 4
1.2. Literature Review 4

CHAPTER 2: MATHEMATICAL APPROACHES **7**

2.1. Elements of Linear Regression and Definitions 7
2.2. Multivariate Linear Regression (MLR) 11
2.2.1. Mathematical Development 11
2.2.2. Uses of MLR 14
2.3. Average-rate Balanced Multivariate Linear Regression (ABMLR) 15
2.3.1. Balance Condition 15
2.3.2. Mathematical Development 16
2.3.3. Uses of ABMLR 18
2.4. Instantaneously Balanced Multivariate Linear Regression (IBMLR) 18
2.4.1. Balance Condition 18
2.4.2. Mathematical Development 19
2.4.3. Uses of IBMLR 24
2.5. Diffusivity Filters 24
2.5.1. Objectives of the Diffusivity Filters 26
2.5.2. Mathematical Development 27
2.5.3. Illustrative Examples 33

CHAPTER 3: APPLICATION TO SYNTHETIC FIELDS **41**

3.1. 5x4 Synfield 42
3.1.1. Homogeneous Reservoir 45

3.1.2. Discussion of Homogeneous Reservoir Results 57
3.1.3. Anisotropic Reservoir 67
3.1.4. Presence of a Sealing Fault 76
3.1.5. Vertical Heterogeneity 82
3.1.6. Spatial Heterogeneity 86
3.1.7. Other Cases 90
3.2. 25x16 Synfield 93
3.2.1. Homogeneous Reservoir 96
3.2.2. Using a Longer Injection History 104
3.2.3. Overdetermination Analysis 111
3.2.4. Distance Cut-off 115
CHAPTER 4: SCOPE OF APPLICATION 121
4.1. Assumptions 121
4.1.1. Constant Injection and Production Conditions 122
4.1.2. Constant Reservoir Conditions 125
4.2. Sources of Error 127
4.2.1. Deviations From Assumptions 128
4.2.2. Small Overdetermination 128
4.2.3. Data Quality 129
4.2.4. Data Sampling 130
4.2.5. Boundaries 131
4.3. Use as a Predictive Tool 132
4.3.1. Prediction of the Homogeneous 5x4 Synfield 133
4.3.2. Prediction of the Anisotropic 5x4 Synfield, Case B. 135
CHAPTER 5: APPLICATION TO FIELD DATA 137
5.1. Chihuido de la Sierra Negra Field 137
5.1.1. Field Description 137
5.1.2. Selection of Data Points 139
5.1.3. Results 140
5.1.4. Further Improvement of Results 147
5.2. Bloque I Field 153
5.2.1. Field Description 153
5.2.2. Selection of Data Points 154
5.2.3. Results of MLR 155
5.2.4. Further Improvement of Results (MLR) 158
5.2.5. Results of ABMLR 162
5.2.6. Further Improvement of Results (ABMLR) 164
5.3. General Procedure 167
CHAPTER 6: CONCLUSIONS AND FUTURE WORK 171
6.1. Conclusions 172

6.2. Future Work 175

NOMENCLATURE 180

Subscripts 182
Superscripts 183

REFERENCES 184

VITA 187

LIST OF TABLES

Table 2.1 Example of the application of diffusivity filters. Discrete filter function coefficients $a^{(n)}$.....37

Table 2.2 Example of the application of diffusivity filters. Injection history of 15 months for injector *i*.....38

Table 2.3 Example of the application of diffusivity filters. Convoluted injection history of 15 months for injector *i* affecting producer *j*.....39

Table 3.1 5x4 Synfield. Homogeneous reservoir. MLR without diffusivity filters. Weighting coefficients b_{ij}. See Figure 3.4.....46

Table 3.2 5x4 Synfield. Homogeneous reservoir. MLR with diffusivity filters. Weighting coefficients b_{ij}. See Figure 3.7.....51

Table 3.3 5x4 Synfield. Homogeneous reservoir. ABMLR with diffusivity filters. Weighting coefficients l_{ij}. See Figure 3.9.....53

Table 3.4 5x4 Synfield. Homogeneous reservoir. IBMLR with diffusivity filters. Weighting coefficients l_{ij}. See Figure 3.11.....55

Table 3.5 5x4 Synfield. Homogeneous reservoir. Well-pair groups determined by planes of symmetry. 58

Table 3.6 5x4 Synfield. Homogeneous reservoir. Comparison of results using MLR, ABMLR, and IBMLR 60

Table 3.7 Synfield 5x4. Injector-injector covariance matrix for a case without diffusivity filters. Covariances are in $(rb/d)^2$.....62

Table 3.8 5x4 Synfield. Homogeneous reservoir. Tracer results. Fraction of the non-reactive tracer injected in the i^{th} injector produced in the j^{th} producer. See Figure 3.14.....65

Table 3.9 5x4 Synfield. Anisotropic reservoir. k_y = 1/40 k_x, case a. ABMLR with diffusivity filters. Weighting coefficients l_{ij}. See Figure 3.18.....70

Table 3.10 5x4 Synfield. Anisotropic reservoir. k_y = 1/40 k_x, case b. ABMLR with diffusivity filters. Weighting coefficients l_{ij}. See Figure 3.19. 71

Table 3.11 5x4 Synfield. Reservoir with a sealing fault, case c. ABMLR with diffusivity filters. Weighting coefficients l_{ij}. See Figure 3.23. 76

Table 3.12 5x4 Synfield. Reservoir with a sealing fault, case d. ABMLR with diffusivity filters. Weighting coefficients l_{ij}. See Figure 3.26. 80

Table 3.13 5x4 Synfield. Vertically heterogeneous reservoir. V = 0.8, case e. ABMLR with diffusivity filters. Weighting coefficients l_{ij}. See Figure 3.29. 83

Table 3.14 5x4 Synfield. Vertically heterogeneous reservoir. V = 0.9, case f. ABMLR with diffusivity filters. Weighting coefficients l_{ij}. See Figure 3.31. 85

Table 3.15 5x4 Synfield. Spatially heterogeneous reservoir. ABMLR with diffusivity filters. Weighting coefficients l_{ij}. See Figure 3.33. 87

Table 3.16 25x16 Synfield. Homogeneous reservoir. Well-pair groups determined by planes of symmetry. Each group is denoted by two letters. Well pairs within the same group should have similar weighting coefficients. 98

Table 3.17 25x16 Synfield. Homogeneous reservoir. ABMLR with diffusivity filters using 65 data points, with O_d = 2.04 (see 3.2.2). Weighting coefficients l_{ij}. See Figure 3.40. 99

Table 3.18 25x16 Synfield. Homogeneous reservoir. ABMLR with diffusivity filters using 415 data points, with O_d = 15. Weighting coefficients l_{ij}. See Figure 3.45. 107

Table 4.1 5x4 Synfield. Homogeneous reservoir. ABMLR with diffusivity filters. Weighting coefficients l_{ij} obtained using 44 effective data points and used for prediction in Figure 4.2. 133

Table 4.2 5x4 Synfield. Anisotropic reservoir, case b. ABMLR with diffusivity filters. Weighting coefficients l_{ij} obtained using 44 effective data points and used for prediction in Figure 4.3. 135

Table 5.1 Chihuido de la Sierra Negra Field. MLR with diffusivity filters, with O_d = 2.04. Weighting coefficients b_{ij}. See Figure 5.3. 141

Table 5.2 Chihuido de la Sierra Negra Field. MLR with diffusivity filters, with O_d = 2.04. Weighting coefficients b_{ij} after the successive elimination of the negative weighting coefficients. See Figure 5.9. 148

Table 5.3 Bloque I Field. MLR with diffusivity filters, with O_d = 7.71. Weighting coefficients b_{ij}. See Figure 5.14. 156

Table 5.4 Bloque I Field. MLR with diffusivity filters, with O_d = 7.71. Weighting coefficients b_{ij} after the successive elimination of physically non-significant weighting coefficients. See Figure 5.17. 159

Table 5.5 Bloque I Field. ABMLR with diffusivity filters, with O_d = 7.71. Weighting coefficients l_{ij}. 163

Table 5.6 Bloque I Field. ABMLR with diffusivity filters, with O_d = 7.71. Weighting coefficients l_{ij} after the successive elimination of the physically non-significant coefficients. See Figure 5.23. 165

LIST OF FIGURES

Figure 2.1 Normalized continuous filter function. It shows the shape that an injection impulse of unit time length takes at a producer. The units of F_n and time are not particularly important. 29

Figure 2.2 Normalized continuous filter function. It shows the shape that an injection impulse of unit time length takes at a producer in a medium with more dissipation that the one shown in Figure 2.1. 30

Figure 2.3 Injection impulse and production rate in a producer at distance r in a reservoir with no dissipation. The discrete filter function (lower plot) has only one effective coefficient, $a^{(0)} = 1$, all the rest are null. 34

Figure 2.4 Injection impulse and production rate in a producer at distance r in a reservoir with moderate dissipation. The areas under the production rate (solid line) and the injection rate (dashed line) are equal. The lower plot is the discrete filter function. 35

Figure 2.5 Injection impulse and production rate in a producer at distance r in a reservoir with large dissipation. The areas under the production rate (solid line) and the injection rate (dashed line) are equal. The lower plot is the discrete filter function. 36

Figure 2.6 Comparison between the observed rate of an injector and its effective (convoluted) injection rate affecting a certain producer. The effect of attenuation and time lag is larger for large distances between injector and producer and for large dissipation in the medium. Convoluted rate is smoother. 40

Figure 3.1 5x4 Synfield. Base map, gridding, and well location. 43

Figure 3.2 5x4 Synfield. Rates for the five injectors and total injection rate. 44

Figure 3.3 5x4 Synfield. Homogeneous reservoir. Total injection and production rates. 45

Figure 3.4 5x4 Synfield. Homogeneous reservoir. MLR without diffusivity filters. Representation of the weighting coefficients b_{ij} shown in Table 3.1. The length of the arrow is proportional to the value of b_{ij}. 47

Figure 3.5 5x4 Synfield. Homogeneous reservoir. MLR without diffusivity filters. Comparison between modeled liquid production rate and the liquid production rate observed in simulation in the four producers. 48

Figure 3.6 5x4 Synfield. Homogeneous reservoir. MLR without diffusivity filters. Comparison between modeled total liquid production rate and the total liquid production rate observed in simulation. 49

Figure 3.7 5x4 Synfield. Homogeneous reservoir. MLR with diffusivity filters. Representation of the weighting coefficients b_{ij} shown in Table 3.2. 50

Figure 3.8 5x4 Synfield. Homogeneous reservoir. MLR with diffusivity filters. Comparison between modeled total liquid production rate and the total liquid production rate observed in simulation. 51

Figure 3.9 5x4 Synfield. Homogeneous reservoir. ABMLR with diffusivity filters. Representation of the weighting coefficients l_{ij} shown in Table 3.3. 53

Figure 3.10 5x4 Synfield. Homogeneous reservoir. ABMLR with diffusivity filters. Comparison between modeled total liquid production rate and the total liquid production rate observed in simulation. 54

Figure 3.11 5x4 Synfield. Homogeneous reservoir. IBMLR with diffusivity filters. Representation of the weighting coefficients l_{ij} shown in Table 3.4. 55

Figure 3.12 5x4 Synfield. Homogeneous reservoir. IBMLR with diffusivity filters. Comparison between modeled total liquid production rate and the total liquid production rate observed in simulation. 56

Figure 3.13 5x4 Synfield. Homogeneous reservoir. Injection rate-production rate crossplots. 64

Figure 3.14 5x4 Synfield. Homogeneous reservoir. Representation of the non-reactive tracer results (Table 3.8). Fraction of the non-reactive tracer injected in the i^{th} injector produced in the j^{th} producer. The length of the arrow is proportional to the fraction. 66

Figure 3.15 5x4 Synfield. Anisotropic reservoir. k_y = 1/40 k_x, case a. Rates for the five injectors and total injection rate. 68

Figure 3.16 5x4 Synfield. Anisotropic reservoir. k_y = 1/40 k_x, case a. Total injection and production rates. Production rate is delayed and smoothed with respect to the injection rate. 69

Figure 3.17 5x4 Synfield. Anisotropic reservoir. k_y = 1/40 k_x, case b. Total injection and production rates. 69

Figure 3.18 5x4 Synfield. Anisotropic reservoir. k_y = 1/40 k_x, case a. ABMLR with diffusivity filters. Representation of the weighting coefficients l_{ij} shown in Table 3.9. 71

Figure 3.19 5x4 Synfield. Anisotropic reservoir. k_y = 1/40 k_x, case b. ABMLR with diffusivity filters. Representation of the weighting coefficients l_{ij} shown in Table 3.10. 72

Figure 3.20 5x4 Synfield. Anisotropic reservoir. k_y = 1/40 k_x, case a. ABMLR with and without diffusivity filters. Comparison between modeled total liquid production rate and the total liquid production rate observed in simulation. 73

Figure 3.21 5x4 Synfield. Anisotropic reservoir. k_y = 1/40 k_x, case b. ABMLR with and without diffusivity filters. Comparison between modeled total liquid production rate and the total liquid production rate observed in simulation. 74

Figure 3.22 5x4 Synfield. Anisotropic reservoir. k_y = 1/40 k_x, case b. Representation of the non-reactive tracer results. Fraction of the non-reactive tracer injected in the i^{th} injector produced in the j^{th} producer. The length of the arrow is proportional to the fraction. 75

Figure 3.23 5x4 Synfield. Reservoir with a sealing fault, case c. ABMLR with diffusivity filters. Representation of the weighting coefficients l_{ij} shown in Table 3.11. 77

Figure 3.24 5x4 Synfield. Reservoir with a sealing fault, case c. ABMLR with diffusivity filters. Comparison between modeled total liquid production rate and the total liquid production rate observed in simulation. 78

Figure 3.25 5x4 Synfield. Reservoir with a sealing fault, case c. Representation of the non-reactive tracer results. 79

Figure 3.26 5x4 Synfield. Reservoir with a sealing fault, Case d. ABMLR with diffusivity filters. Representation of the weighting coefficients l_{ij} shown in Table 3.12. 81

Figure 3.27 5x4 Synfield. Reservoir with a sealing fault, Case d. Representation of the non-reactive tracer results. 81

Figure 3.28 5x4 Synfield. Reservoir with a sealing fault, Case d. ABMLR with diffusivity filters. Comparison between modeled total liquid production rate and the total liquid production rate observed in simulation. 82

Figure 3.29 5x4 Synfield. Vertically heterogeneous reservoir. V = 0.8, case e. ABMLR with diffusivity filters. Representation of the weighting coefficients l_{ij} shown in Table 3.13. 83

Figure 3.30 5x4 Synfield. Vertically heterogeneous reservoir. V = 0.8, case e. ABMLR with diffusivity filters. Comparison between modeled total liquid production rate and the total liquid production rate observed in simulation. 84

Figure 3.31 5x4 Synfield. Vertically Heterogeneous Reservoir. V = 0.9, case f. ABMLR With Diffusivity Filters. Representation of the weighting coefficients l_{ij} shown in Table 3.14. 85

Figure 3.32 5x4 Synfield. Vertically heterogeneous reservoir. V = 0.9, case f. ABMLR with diffusivity filters. Comparison between modeled total liquid production rate and the total liquid production rate observed in simulation. 86

Figure 3.33 5x4 Synfield. Spatially heterogeneous reservoir. The permeability in the shaded area is 5 times the permeability in the rest of the reservoir. ABMLR with diffusivity filters. Representation of the weighting coefficients l_{ij} shown in Table 3.15. 87

Figure 3.34 5x4 Synfield. Spatially heterogeneous reservoir. ABMLR with diffusivity filters. Comparison between modeled total liquid production rate and the total liquid production rate observed in simulation. 88

Figure 3.35 5x4 Synfield. Spatially heterogeneous reservoir. Total injection and production rates. 89

Figure 3.36 5x4 Synfield. Spatially heterogeneous reservoir. Representation of the non-reactive tracer results. 90

Figure 3.37 25x16 Synfield. Base map and well location. 94

Figure 3.38 25x16 Synfield. Homogeneous reservoir. History of 65 data points. Total injection and production rates. 95

Figure 3.39 25x16 Synfield. Planes of symmetry in homogeneous reservoir. There are 6 types of injectors and 3 types of producers in the field. 97

Figure 3.40 25x16 Synfield. Homogeneous reservoir. ABMLR with diffusivity filters using 65 data points, with O_d = 2.04 (see 3.2.2). Representation of the positive weighting coefficients l_{ij} shown in Table 3.17. 100

Figure 3.41 25x16 Synfield. Homogeneous reservoir. ABMLR with diffusivity filters using 65 data points, with O_d = 2.04 (see 3.2.2). Comparison between modeled liquid production rate and the liquid production rate observed in simulation in the four wells at the center of the Synfield. 101

Figure 3.42 25x16 Synfield. Homogeneous reservoir. ABMLR with diffusivity filters using 65 data points, with O_d = 2.04 (see 3.2.2). Comparison between modeled total liquid production rate and the total liquid production rate observed in simulation (four center wells). 102

Figure 3.43 25x16 Synfield. Homogeneous reservoir. ABMLR with diffusivity filters using 65 data points, with O_d = 2.04 (see 3.2.2). Weighting coefficients l, vs distance between wells. The large dots correspond to the four wells at the center of the Synfield. 103

Figure 3.44 25x16 Synfield. Homogeneous reservoir. History of 415 data points. Total injection and production rates. 106

Figure 3.45 25x16 Synfield. Homogeneous reservoir. ABMLR with diffusivity filters using 415 data points, with O_d = 15. Representation of the weighting coefficients l_{ij} shown in Table 3.18. 108

Figure 3.46 25x16 Synfield. Homogeneous reservoir. ABMLR with diffusivity filters using 415 data points, with O_d = 15. Comparison between modeled total liquid production rate and the total liquid production rate observed in simulation (four center wells). 109

Figure 3.47 25x16 Synfield. Homogeneous reservoir. ABMLR with diffusivity filters using 415 data points, with O_d = 15. Weighting

coefficients l, vs distance between wells. The large dots correspond to the four wells at the center of the Synfield. 110

Figure 3.48 Homogeneous reservoir. ABMLR with diffusivity filters. Effect of the overdetermination on the asymmetry coefficient. Both 5x4 Synfield and 25x16 Synfield results lie on the same curve. The larger the O_d, the better the results. 111

Figure 3.49 25x16 Synfield. Homogeneous reservoir. ABMLR with diffusivity filters. Log-log plot of A vs. $1/(M\text{-}I\text{-}1)$ with a slope of approximately 1. 112

Figure 3.50 Homogeneous reservoir. ABMLR with diffusivity filters. Log-log plot of A vs. O_d . Both 5x4 and 25x16 Synfields show a slope of approximately -1 for $O_d > 1$. 113

Figure 3.51 5x4 Synfield. Homogeneous reservoir. ABMLR with diffusivity filters. Plot of A vs. O_d for ABMLR with and without diffusivity filters, and IBMLR with diffusivity filters. A semi-log plot is used for easier comparison. 114

Figure 3.52 25x16 Synfield. Homogeneous reservoir. ABMLR with diffusivity filters using 41 effective data points and a distance cut-off of 1000 ft. A = 0.2290 with apparent O_d = 8.2. Representation of the weighting coefficients l_{ij}. 116

Figure 3.53 25x16 Synfield. Number of injectors included in the analysis for each producer group when applying distance cut-offs. 117

Figure 3.54 25x16 Synfield. History of 41 effective data points. Apparent O_d when applying distance cut-offs. 117

Figure 3.55 25x16 Synfield. Homogeneous reservoir. Weighting coefficients l, vs. distance between wells grouped by similar producers. 118

Figure 3.56 25x16 Synfield. Error introduced in the estimation of ls when applying distance cut-offs. 119

Figure 4.1 5x4 Synfield. Homogeneous reservoir. ABMLR with diffusivity filters. Sensitivity of the technique to data quality. Expected values of R^2 and A over 100 realizations for different levels of random relative error in the rate measurement. 130

Figure 4.2 5x4 Synfield. Homogeneous reservoir. ABMLR with diffusivity filters. Comparison between modeled total liquid production rate and the total liquid production rate observed in simulation. The first portion of the data is used as training period to estimate ls (see Table 4.1) and the last portion used to test the prediction. 134

Figure 4.3 5x4 Synfield. Anisotropic reservoir, case b. ABMLR with diffusivity filters. Comparison between modeled total liquid production rate and the total liquid production rate observed in simulation. The first portion of the data is used as training period to estimate ls (see Table 4.2) and the last portion used to test the prediction. 136

Figure 5.1 Chihuido de la Sierra Negra Field. Base map. 138

Figure 5.2 Chihuido de la Sierra Negra Field. Injection rate, production rate and gas-oil ratio (GOR) of the selected portion of the field. The period selected for the analysis starts on month 75 where injection and production rates are in approximate balance and only dissolved gas is produced. 140

Figure 5.3 Chihuido de la Sierra Negra Field. MLR with diffusivity filters, with O_d = 2.04. Representation of the positive weighting coefficients b_{ij} shown in Table 5.1. The size of the arrows is proportional to the value of the weighting coefficient. 142

Figure 5.4 Chihuido de la Sierra Negra Field. MLR with diffusivity filters, with O_d = 2.04. Representation of the positive weighting coefficients b_{ij} and comparison with known geological features. A structural map is overlain. 143

Figure 5.5 Chihuido de la Sierra Negra Field. MLR with diffusivity filters, with O_d = 2.04. Comparison between modeled liquid production rate and the observed liquid production rate in the four wells at the center of the field. 144

Figure 5.6 Chihuido de la Sierra Negra Field. MLR with diffusivity filters, with O_d = 2.04. Comparison between modeled total liquid production rate and the total observed liquid production rate (four center wells). 145

Figure 5.7 Chihuido de la Sierra Negra Field. MLR with diffusivity filters, with O_d = 2.04. Weighting coefficients b_{ij} vs injector-producer distance. The large dots correspond to the four wells at the center of the field. 146

Figure 5.8 Chihuido de la Sierra Negra Field. MLR with diffusivity filters, with O_d = 2.04. Comparison between modeled total liquid production rate and the total observed liquid production rate (four center wells), after the successive elimination of the negative weighting coefficients. 149

Figure 5.9 Chihuido de la Sierra Negra Field. MLR with diffusivity filters, with O_d = 2.04. Representation of the weighting coefficients b_{ij} (after the successive elimination of the negative weighting coefficients) shown in Table 5.2 and comparison with known geological features. A structural map is overlain. 150

Figure 5.10 Chihuido de la Sierra Negra Field. MLR with diffusivity filters, with O_d = 2.04. Effect of the successive elimination of the negative weighting coefficients on the R^2 corresponding to the 4 wells at the center of the field. The maximum and minimum weighting coefficient at each step of elimination are also plotted. 151

Figure 5.11 Chihuido de la Sierra Negra. MLR with diffusivity filters, with O_d = 2.04. Weighting coefficients b_{ij} vs injector-producer distance, after the successive elimination of the negative weighting coefficients. The large dots correspond to the four wells at the center of the field. 152

Figure 5.12 Bloque I Field. Base map. The horizontal and vertical axes show the coordinates, in meters. 153

Figure 5.13 Bloque I Field. Injection and production rates. Period selected for the analysis. 154

Figure 5.14 Bloque I Field. MLR with diffusivity filters, with O_d = 7.71. Comparison between modeled total liquid production rate and the total observed liquid production rate. 156

Figure 5.15 Bloque I Field. MLR with diffusivity filters, with O_d = 7.71. Representation of the positive weighting coefficients b_{ij} shown in Table 5.3. 157

Figure 5.16 Bloque I Field. MLR with diffusivity filters, with O_d = 7.71. Weighting coefficients b_{ij} vs injector-producer distance. 157

Figure 5.17 Bloque I Field. MLR with diffusivity filters, with O_d = 7.71. Representation of the positive weighting coefficients b_{ij} (after the

successive elimination of physically non-significant weighting coefficients) shown in Table 5.4. 159

Figure 5.18 Bloque I Field. MLR with diffusivity filters, with O_d = 7.71. Comparison between modeled total liquid production rate and the total observed liquid production rate, after the successive elimination of the physically non-significant weighting coefficients. 160

Figure 5.19 Bloque I Field. MLR with diffusivity filters, with O_d = 7.71. Weighting coefficients b_{ij} vs injector-producer distance after the successive elimination of the physically non-significant weighting coefficients. 161

Figure 5.20 Bloque I Field. MLR with diffusivity filters, with Od = 7.71. Effect of the successive elimination of the physically non-significant weighting coefficients on R^2. The maximum and minimum weighting coefficient at each step of elimination are also plotted. 162

Figure 5.21 Bloque I Field. ABMLR with diffusivity filters, with O_d = 7.71. Comparison between modeled total liquid production rate and the total observed liquid production rate. 163

Figure 5.22 Bloque I Field. ABMLR with diffusivity filters, with O_d = 7.71. Weighting coefficients l_{ij} vs injector-producer distance. 164

Figure 5.23 Bloque I Field. ABMLR with diffusivity filters, with O_d = 7.71. Representation of the positive weighting coefficients l_{ij} (after the successive elimination of physically non-significant weighting coefficients) shown in Table 5.6. 166

Figure 5.24 Bloque I Field. ABMLR with diffusivity filters, with O_d = 7.71. Comparison between modeled total liquid production rate and the total observed liquid production rate, after the successive elimination of the physically non-significant weighting coefficients. 166

Figure 5.25 Bloque I Field. ABMLR with diffusivity filters, with O_d = 7.71. Weighting coefficients l_{ij} vs injector-producer distance after the successive elimination of the physically non-significant weighting coefficients. 167

CHAPTER 1: INTRODUCTION

Much of the effort of geoscientists and reservoir engineers is devoted to characterizing the reservoir. A good model of the reservoir is a most valuable tool for a successful reservoir management. In waterfloods, the knowledge of reservoir heterogeneities and discontinuities is particularly relevant to the optimization of operations and to the maximization of oil recovery. Accurately determining the connectivity between wells can lead to decisions oriented to maximize the economics of the waterflood, such as changes in injection patterns, assignment of priorities in operations, recompletion of wells, or in-fill drilling.

Many of the methods used for reservoir description are based on geological studies, coring, seismic data, well testing, well logging, and fluid testing. This information is gathered during the entire life of the reservoir, starting in the very early stages of its development. However, the acquisition and processing of this data is expensive and, consequently, in many cases the information is not available. Indeed, the lack of information together with the time and money consumed by extensive modeling methods, such as numerical simulation, can become an obstacle for the reservoir engineering analysis.

Production and injection rates, usually based on monthly well tests, are the most abundant data available in any waterflooding project. Highly valuable and

useful information can be obtained from the analysis of these data. Typically, observation of injection and production rates together with reservoir description and characterization is used to qualitatively determine the influence of each injector on producers. These visually obtained results are non-unique, involve a time consuming process, and, in some occasions, they can be erroneous. Injector-producer pairs that show no correlation between their rates may be as connected through the reservoir as pairs that show good correlations. Likewise, injection is typically allotted by geometrical distribution in waterfloods, which is a simple technique but not always correct. This work presents a practical technique to quantify communication between wells in reservoir using only production and injection rate data.

The reservoir can be viewed as a system that processes a stimulus (injection) and returns a response (production). In a waterflood, there are typically several injectors and producers acting at the same time; moreover, the effect of the reservoir on the input signal (injection) will depend on the location and the orientation of each stimulus-response pair. Taking this into account, the technique presented here uses different statistical approaches, based on constrained multivariate linear regression, to infer connectivity and to provide information about permeability trends and the presence of transmissibility barriers. It analyzes the entire field in one single step, and using only production and injection rate data. In addition, the method uses diffusivity filters to account for the time lag and attenuation that occurs between

stimulus and response. The technique is first applied to two synthetic fields of different sizes and then to two fields in Argentina.

This chapter (Chapter 1) presents the main objectives of this work and a literature review on the use of statistical methods based on production and injection data aimed to determine the connectivity between well pairs. Chapter 2 presents the three different mathematical approaches developed to attain the proposed objectives and describes the development and use of diffusivity filters. Chapter 3 shows the application of these approaches to two numerically simulated reservoirs of different sizes. The technique was tested in synthetic fields (Synfields) with reservoirs of diverse characteristics, such as a homogeneous reservoir, an anisotropic reservoir, a spatially heterogeneous reservoir, and a vertically heterogeneous reservoir. The results of the application to Synfields and the effect and importance of large overdetermination are also discussed in this chapter. Chapter 4 enumerates the assumptions on which the application of the technique is based. It also provides a description of the possible sources of error and an analysis of the sensitivity of the results to the data quality. Chapter 5 contains the results of the application of the presented method to two fields in Argentina: Chihuido de la Sierra Negra Field and Bloque I Field. It also describes the appropriate selection of data points for the analysis and shows a simple method to further improve the output. Finally, Chapter 6 presents the conclusions and lists recommendations for future development of this technique.

1.1. OBJECTIVES & HYPOTHESES

The main hypotheses of this work are the following:

- It is possible to quantitatively determine the communication between wells in a waterflood using only production and injection rate data.
- Production rate in every producer can be predicted from given the injection rate.
- The information about inter-well connectivity can be used to map reservoir heterogeneities, preferential permeability trends, and transmissibility barriers.

1.2. LITERATURE REVIEW

Many of the reservoir description methods are based on integrated studies using a wide variety of information. Alabert and Modot enumerate and compare different probabilistic techniques used for modeling reservoir heterogeneity and connectivity (Alabert and Modot, 1992). Malik *et al.* show an integrated study of reservoir characterization, geostatistics, production performance and reservoir engineering that investigates the hydraulic interwell connectivity concept to characterize and estimate the reservoir connectivity (Malik *et al.*, 1993). Canas and Wu add the interwell flow capacity index and analyze interwell connectivity concepts to characterize the reservoir for waterflood performance evaluation (Canas and Wu,

1994). Hird and Dubrule indirectly incorporate dynamic production data constraints into geostatistically-derived reservoir descriptions (Hird and Dubrule, 1995).

On the other hand, there have been previous statistical approaches that compared the rate performance of a production well with that of the surrounding adjacent injectors. Heffer and McGill used Spearman rank correlations to relate injector/producer pairs and associated these relations with geomechanics (Heffer and McGill, 1995). Refunjol also used Spearman analysis to determine preferential flow trends in a reservoir and compared the results with injected tracer response. She related injection wells with their adjacent producers and used time lags to find an extreme coefficient value (Refunjol, 1996). Sant'Anna Pizarro validated the Spearman rank technique with numerical simulation and pointed out its advantages and limitations (De Sant'Anna Pizarro, 1998). Panda and Chopra used artificial neural networks to determine the interaction between injector/producer pairs within a pattern generating a multi-variate data set consisting of production, injection, and petrophysical information (Panda and Chopra, 1998). Jansen and Kelkar decompose the production data into a combination of their frequency components using the wavelet transformation. The frequency components can then be analyzed using other traditional cross correlation routines such as the Spearman Rank correlation, to determine the well influence on surrounding wells (Jansen and Kelkar, 1997, A). They also show how to introduce the interwell connectivity information obtained from production data directly into the interpolation routine to generate an

experimental variogram model for the estimation of reservoir properties (Jansen and Kelkar, 1997, B). Soeriawinata and Kelkar, who also used Spearman rank analysis, suggested a statistical approach to relate injection wells and their adjacent producing wells. They applied the superposition principle to introduce concepts of constructive and destructive interference (Soeriawinata and Kelkar, 1998). See also Araque-Martinez's work (Araque-Martinez, 1993) and Griffiths Barros' work (Griffiths Barros, 1998).

CHAPTER 2: MATHEMATICAL APPROACHES

This chapter begins with a brief review of the elements of linear regression and some definitions. Then, it presents three different statistical approaches used to quantify the connectivity between injectors and producers: multivariate linear regression (MLR), average-rate balanced multivariate linear regression (ABMLR) and instantaneously balanced multivariate linear regression (IBMLR). We first show the mathematical formulation and then describe the use of each of the three methods. The last section of this chapter presents the mathematical development of the diffusivity filters used to account for the time lag and attenuation that occurs between injectors and producers, and provides illustrative examples of their use.

2.1. ELEMENTS OF LINEAR REGRESSION AND DEFINITIONS

A regression procedure uses data to adjust a model. Typically, the model is later used to predict the behavior of a dependent variable as a function of known independent variables. This means that a model must exist prior to the application of a regression procedure. The most frequently used model is the linear model:

$$y = b_0 + \sum_{k=1}^{K} b_k x_k + e$$

where y is the dependent variable, x_k are the independent variables, e is a random error, and b_0 and b_k are the parameters to be adjusted or determined by the regression procedure. The error term e includes both inadequacies in the model and measurement errors. It is also very common to assume that the errors are normally distributed with zero mean ($E(e) = 0$). At this point, it is useful to recall that for a finite sample, the expected value is the same as the arithmetic average

$$E(x) = \frac{1}{M}\sum_{m=1}^{M} x^{(m)} = \bar{x}$$

where the superscript m is associated with each data point and M is the total number of data points.

To perform the regression we need data, which typically consist of measurements of both observed and predicted quantities. Furthermore, the determination of the unknown parameters consists of a method that inverts the role of the variables and the parameters in the model to determine the latter, based on these measurements (Jensen *et al.*, 1997).

In the case of a waterflood, the variable we want to predict is the liquid production rate of a well (dependent variable). We assume that it is a linear combination of the injection rates of every injector in the field (independent variables). If this is the case, then the linear model becomes

$$\hat{q}_j = b_{0j} + \sum_{i=1}^{I} b_{ij} i_i + e$$

where $\hat{q}_j$ is the modeled liquid production rate of well j, I is the total number of injectors in the field, i_i is the injection rate of the i^{th} injector, and b_{ij} are the parameters to be determined by the regression procedure. Both production and injection rates are in reservoir volumes. The physical meaning of the model is described in more detail in section 2.2.1.

Once the parameters are determined, the model can be used to predict the liquid production rate of a producer given the injection rates. Likewise, the numerical values of the determined parameters b_{ij} are of great importance and, as shown throughout this work, describe the connectivity between the producer and its related injector.

It is also important to recall the definition of the following terms that are used later in this work: variance, covariance, coefficient of determination, and variability of the slope.

The variance of q_j is defined as

$$Var(q_j) = s_j^2 = E\left\{\left[q_j - E(q_j)\right]^2\right\}$$

For discrete samples

$$Var(q_j) = s_j^2 = \sum_{m=1}^{M} \left[q_j^{(m)} - E(q_j)\right]^2$$

where

$$E(q_j) = \bar{q}_j = \frac{1}{M}\sum_{m=1}^{M} q_j^{(m)}$$

In our model, the superscript m is a time-like variable and M is the total number of data points. Besides, both the injection and production rates are assumed to be random variables normally distributed.

Similarly, the covariance between q_j and i_i is defined as

$$Cov(i_i, q_j) = s_{ij}^2 = E\{[i_i - E(i_i)] \times [q_j - E(q_j)]\}$$

The coefficient of determination (R^2) represents that proportion of the variability in q_j explained by the model (Jensen *et al.*, 1997). In other words, it measures the quality of the correlation between observed and modeled production. It is defined as

$$R^2 = 1 - \frac{\sum_{m=1}^{M} \left(\hat{q}_j^{(m)} - q_j^{(m)}\right)^2}{\sum_{m=1}^{M} \left(q_j^{(m)} - \bar{q}_j\right)^2} \qquad (2.1)$$

In a bivariate linear regression model of the type $\hat{q}_j = b_0 + b_{1j} i_1$, the variability of the slope is defined as (Jensen *et al.*, 1997):

$$s^2_{b_{1j}} = \frac{1}{(M-2)} \times \frac{\sum_{m=1}^{M} \left(q_j^{(m)} - \hat{q}_j^{(m)}\right)^2}{\sum_{m=1}^{M} \left(i_1^{(m)} - \bar{i}_1\right)^2} \tag{2.2}$$

2.2. MULTIVARIATE LINEAR REGRESSION (MLR)

2.2.1. Mathematical Development

In a field with N producers and I injectors, the linear model for the j^{th} producer is

$$\hat{q}_j(t) = b_{0j} + \sum_{i=1}^{I} b_{ij} i_i(t) \qquad (j = 1, 2, \ldots N) \tag{2.3}$$

This equation states that at any time the total production rate at well j is a linear combination of the rates of every injector plus a constant term, b_{0j}. The parameters b_{ij} are called the weighting coefficients and the constant term b_{0j} accounts for the possible unbalance in the field. In other words, the term b_{0j} takes care of the following two causes of unbalance: liquid production not associated with injected water (primary production), and injection losses to non-productive layers (water injection not affecting producers).

Actually, if $\sum_{j=1}^{N} b_{0j} = 0$ the total field is apparently balanced. Even more, $\sum_{j=1}^{N} b_{0j} = 0$ is necessary but not sufficient condition for a balanced field, because the effects of injection losses and primary production may cancel just by chance. So, in that case, b_{0j} can be different from zero for a particular producer j, meaning that there are some primary production or injection losses, but the total field still shows apparent balance. The most probable case is that when $b_{0j} \neq 0$ for any producer, the field shows unbalance; henceforth, for simplicity, we say that the field is unbalanced when $b_{0j} \neq 0$.

This model (Eq. 2.3) assumes steady state flow. So, changes in injection rate instantaneously produce changes in production rate. In a waterflood, the flow regimes continuously change from transient flow to flow patterns that approximate steady state flow. For simplicity, the steady state model is used and the diffusivity filters (see section 2.5) partially correct the effect of transient flow.

Given a set of observed data of production and injection rates, the variance of q_j

$$s^2_{MLR,j} = Var(\hat{q}_j - q_j) = E[(\hat{q}_j - q_j)^2] \tag{2.4}$$

is a measure of the error of the model for producer j. The minimization of this variance leads to the determination of the weighting coefficients b_{ij} and the constant

term b_{0j}. One remarkable characteristic of this type of regression is that it is robust even if there are deviations from the basic assumptions (Miller, 1986). So, first, we take the expectation of Eq. 2.3 to solve for b_{0j}. Since the average of the modeled liquid production rate must be equal to the average of the observed liquid production rate ($E(\hat{q}) = \bar{q}$), we get

$$b_{0j} = \bar{q}_j - \sum_{i=1}^{I} b_{ij} \bar{i}_i \tag{2.5}$$

where the symbol $^-$ indicates average in time over the interval selected for analysis.

After inserting the model (Eq. 2.3) and b_{0j} (Eq. 2.5) into Eq. 2.4 we get

$$s^2_{MLR,j} = s^2_j - 2\sum_{i=1}^{I} b_{ij} s^2_{ij} + \sum_{i=1}^{I}\sum_{h=1}^{I} b_{ij} b_{hj} s^2_{ih} \tag{2.6}$$

where σ_j^2 (j^{th} producer variance), σ_{ij}^2 (i^{th} injector-j^{th} producer covariance), and σ_{ih}^2 (i^{th} injector-h^{th} injector covariance) are known quantities. To minimize $\sigma^2_{MLR,j}$, we take the derivative of Eq. 2.6 with respect to each of the weighting coefficients and set it to zero:

$$\frac{\partial s^2_{MLR,j}}{\partial b_{ij}} = 0 \qquad (i = 1, 2, \ldots I)$$

which leads to

$$\sum_{h=1}^{I} b_{hj} s_{ih}^{2} = s_{ij}^{2} \qquad (i = 1, 2, \ldots I) \qquad (2.7)$$

Equation 2.7 can be written in matrix form as

$$\begin{pmatrix} s_{11}^{2} & s_{12}^{2} & \cdots & s_{1I}^{2} \\ s_{21}^{2} & s_{22}^{2} & \cdots & s_{2I}^{2} \\ \vdots & \vdots & \ddots & \vdots \\ s_{I,1}^{2} & s_{I2}^{2} & \cdots & s_{II}^{2} \end{pmatrix} \times \begin{pmatrix} b_{1j} \\ b_{2j} \\ \vdots \\ b_{Ij} \end{pmatrix} = \begin{pmatrix} s_{1j}^{2} \\ s_{2j}^{2} \\ \vdots \\ s_{Ij}^{2} \end{pmatrix} \qquad (2.8)$$

which can be solved for the b_{ij}s by standard means. The first term in this equation (square matrix) is called injector-injector covariance matrix, and the vector on the right side of the equation is called injector-producer covariance column vector.

We use the MLR approach to determine the weighting coefficients b_{ij} that relate a producer j to an injector i. A set of I+1 equations and I+1 unknowns must be solved for each producer (Eqs. 2.5 and 2.8). The weighting coefficients b_{ij} obtained from the solution of the N systems of equations provide a quantitative expression of the influence of each injector i on each producer j; the larger the b_{ij}, the greater the influence. The constant term b_{0j} represents amount of production on producer j not related to the injected water.

2.2.2. Uses of MLR

A waterflood is unbalanced when the field-wide injection rate is significantly different from field-wide liquid production rate. As stated before, the constant term

b_{0j} accounts for the possible unbalance in the field. So, the most obvious use of the MLR approach is when the waterflood is not in balance. However, this is not the only case when it should be applied. If only a portion of the waterflood is being analyzed, there will be flow across the open boundaries of the selected area. In this case, MLR must be again used without any modification in the injection rates of the wells close to the boundaries; however, since the water rate crossing the boundaries may not be actually constant (and b_{0j} is constant in the model), the production wells close to the boundaries may suffer some boundary effects.

2.3. AVERAGE-RATE BALANCED MULTIVARIATE LINEAR REGRESSION (ABMLR)

2.3.1. Balance Condition

If the waterflood is balanced on average (the field-wide injection rate is approximately equal to the total production rate) the ABMLR approach may be used. In this case, the constant term that accounts for the unbalance in Eq. 2.3 (b_{0j}) is set to zero and the model is given by:

$$\hat{q}_j(t) = \sum_{i=1}^{I} l_{ij} i_i(t) \qquad (j = 1, 2, \ldots N) \qquad (2.9)$$

where the weighting coefficients are denoted by l_{ij},. We use l_{ij}, instead of the b_{ij} used in MLR, simply to distinguish the balanced model from the unbalanced model. The meaning of the l_{ij}s and the b_{ij}s is basically the same, with the exception of the b_{0j} term.

The balance condition is given by

$$\bar{q}_j = \sum_{i=1}^{I} l_{ij} \bar{i}_i \qquad (j = 1, 2, \ldots N) \qquad (2.10)$$

This condition states that, on average, the liquid production rate is equal to the sum of the weighted injection rate, or that all the liquid production is due to water injection, on average. Equation 2.10 is analogous to Eq. 2.5 when the term b_{0j} is set to zero.

2.3.2. Mathematical Development

To determine the weighting coefficients in the ABMLR model we must minimize the variance of producer *j*

$$s^2_{ABMLR,j} = E\left[\left(\hat{q}_j - q_j\right)^2\right] \qquad (2.11)$$

After inserting the model (Eq. 2.9) and the balance condition (Eq. 2.10) into Eq. 2.11 we get the same expression as in MLR:

$$s^2_{ABMLR,j} = s^2_j - 2\sum_{i=1}^{I} l_{ij} s^2_{ij} + \sum_{i=1}^{I}\sum_{h=1}^{I} l_{ij} l_{hj} s^2_{ih}$$

To introduce the balance condition constraint in the equation we use the Lagrange multiplier (Bertsekas, 1982) m_j as follows

$$s^{2}_{ABMLR,j} = s^{2}_{j} - 2\sum_{i=1}^{I} l_{ij} s^{2}_{ij} + \sum_{i=1}^{I}\sum_{h=1}^{I} l_{ij} l_{hj} s^{2}_{ih} - 2m_j \left(\bar{q}_j - \sum_{i=1}^{I} l_{ij} \bar{i}_i \right) \qquad (2.12)$$

where the factor 2 before the multiplier is for mathematical simplicity.

Now we proceed as before, taking the derivative of Eq. 2.12 with respect to each of the variables l_{ij} and setting them to zero:

$$\frac{\partial s^{2}_{ABMLR,j}}{\partial l_{ij}} = 0 \qquad (i = 1, 2, \ldots I)$$

to get

$$\sum_{h=1}^{I} l_{hj} s^{2}_{ih} = s^{2}_{ij} - m\bar{i}_i \qquad (i = 1, 2, \ldots I)$$

which in matrix form, together with the balance condition (Eq. 2.10) can be written as

$$\begin{pmatrix} s^{2}_{11} & s^{2}_{12} & \cdots & s^{2}_{1I} & \bar{i}_1 \\ s^{2}_{21} & s^{2}_{22} & \cdots & s^{2}_{2I} & \bar{i}_1 \\ \vdots & \vdots & \ddots & \vdots & \vdots \\ s^{2}_{I1} & s^{2}_{I2} & \cdots & s^{2}_{II} & \bar{i}_1 \\ \bar{i}_1 & \bar{i}_2 & \cdots & \bar{i}_I & 0 \end{pmatrix} \times \begin{pmatrix} l_{1j} \\ l_{2j} \\ \vdots \\ l_{Ij} \\ m_j \end{pmatrix} = \begin{pmatrix} s^{2}_{1j} \\ s^{2}_{2j} \\ \vdots \\ s^{2}_{Ij} \\ \bar{q}_j \end{pmatrix} \qquad (2.13)$$

Again, the set of I+1 linear equations (Eq. 2.13) can be solved for the l_{ij} and m_j by standard means for each producer. Likewise, the weighting coefficients l_{ij}

obtained from the solution of the N systems of equations provide a quantitative expression of the influence of each injector i on each producer j.

2.3.3. Uses of ABMLR

We use ABMLR if the waterflood is balanced on average. This means that the data may show temporary or local differences between field-wide injection and production rates, but it must be in acceptable balance on average. In this model, the entire production rate of a producer is associated to the injection rates of the injectors.

2.4. INSTANTANEOUSLY BALANCED MULTIVARIATE LINEAR REGRESSION (IBMLR)

2.4.1. Balance Condition

The IBMLR must be used when the waterflood is in acceptable balance (the field-wide injection rate is approximately equal to the total production rate) at every time. The IBMLR model is identical to the ABMLR model:

$$\hat{q}_j(t) = \sum_{i=1}^{I} l_{ij} i_i(t) \qquad (j = 1, 2, \ldots N) \qquad (2.9)$$

The instantaneous balance in the field can be written as:

$$\sum_{j=1}^{N} \hat{q}_j(t) = \sum_{i=1}^{I} i_i(t)$$

Substituting for Eq. 2.9

$$\sum_{j=1}^{N}\sum_{i=1}^{I} l_{ij} i_i(t) = \sum_{i=1}^{I} i_i(t)$$

or

$$\sum_{i=1}^{I}\sum_{j=1}^{N} l_{ij} i_i(t) = \sum_{i=1}^{I} i_i(t)$$

which can be written as

$$\sum_{i=1}^{I} i_i(t)\left(\sum_{j=1}^{N} l_{ij}\right) = \sum_{i=1}^{I} i_i(t)$$

The only way that the above equation is true at every time is if

$$\sum_{j=1}^{N} l_{ij} = 1 \qquad (i = 1, 2, \ldots I) \qquad (2.14)$$

Equation 2.14 is the instantaneous balance condition. It states that the sum of the weighting coefficients for each injector is equal to one.

2.4.2. Mathematical Development

In the previous approaches (MLR and ABMLR) the minimization of the total variance of system is equivalent to the minimization of the variance of each producer. That happens because the estimation of the weighting coefficients for each producer is independent of the remaining producers. In this approach (IBMLR) we perform the minimization of the total variance of the system given by

$$s^{2}_{IBMLR} = \sum_{j=1}^{N} E\left[\left(\hat{q}_j - q_j\right)^2\right] \tag{2.15}$$

After inserting the model (Eq. 2.9) into Eq. 2.15 we get:

$$s^{2}_{IBMLR} = \sum_{j=1}^{N}\left[s^{2}_{j} - 2\sum_{i=1}^{I} l_{ij} s^{2}_{ij} + \sum_{i=1}^{I}\sum_{h=1}^{I} l_{ij} l_{hj} s^{2}_{ih} + \left(\bar{q}_j - \sum_{i=1}^{I} l_{ij} \bar{i}_i \right)^2 \right]$$

It is important to remark that even when the balance condition in IBMLR (Eq. 2.14) is different from that one in ABMLR (Eq. 2.10), Eq. 2.10 is still valid in IBMLR. IBMLR is nothing but a more restrictive case of ABMLR. In other words, if the balance condition is satisfied at every time, it is expected that the balance condition is satisfied in average.

Now, using the Lagrange multipliers n_i (one for each injector) to insert the balance condition constraint (Eq. 2.14) we get

$$s^{2}_{IBMLR} = \sum_{j=1}^{N}\left[s^{2}_{j} - 2\sum_{i=1}^{I} l_{ij} s^{2}_{ij} + \sum_{i=1}^{I}\sum_{h=1}^{I} l_{ij} l_{hj} s^{2}_{ih} + \left(\bar{q}_j - \sum_{i=1}^{I} l_{ij} \bar{i}_i \right)^2 \right]$$

$$+ \sum_{i=1}^{I} 2\nu_i \left(\sum_{j=1}^{N} l_{ij} - 1 \right) \tag{2.16}$$

To minimize the variance, we take the derivative of Eq. 2.16 with respect to each of the variables l_{ij} and set it to zero:

$$\frac{\partial s^{\,2}_{IBMLR}}{\partial l_{ij}} = 0 \qquad \begin{matrix}(i=1,\ 2,\ \ldots\ I)\\ (j=1,\ 2,\ \ldots\ N)\end{matrix}$$

to get

$$\sum_{h=1}^{I} l_{hj}\left(s^{\,2}_{ih} + \bar{i}_i \bar{i}_h\right) = s^{\,2}_{ij} + \bar{i}_i \bar{q}_j - n_i \qquad \begin{matrix}(i=1,\ 2,\ \ldots\ I)\\ (j=1,\ 2,\ \ldots\ N)\end{matrix} \qquad (2.17)$$

Equation 2.17 together with the balance condition (Eq. 2.14) can be written in matrix form as

$$\begin{pmatrix} S_{inj} + \overline{II} & 0 & \cdots & 0 & I_d \\ 0 & S_{inj} + \overline{II} & \cdots & 0 & I_d \\ \vdots & \vdots & \ddots & \vdots & \vdots \\ 0 & 0 & \cdots & S_{inj} + \overline{II} & I_d \\ I_d & I_d & \cdots & I_d & 0 \end{pmatrix} \times \begin{pmatrix} L_1 \\ L_2 \\ \vdots \\ L_N \\ N \end{pmatrix} = \begin{pmatrix} S_1 + \overline{IP_1} \\ S_2 + \overline{IP_2} \\ \vdots \\ S_N + \overline{IP_N} \\ U \end{pmatrix} \qquad (2.18)$$

where S_{inj} is the injector-injector covariance matrix:

$$S_{inj} = \begin{pmatrix} s^{\,2}_{11} & s^{\,2}_{12} & \cdots & s^{\,2}_{1I} \\ s^{\,2}_{21} & s^{\,2}_{22} & \cdots & s^{\,2}_{2I} \\ \vdots & \vdots & \ddots & \vdots \\ s^{\,2}_{I,1} & s^{\,2}_{I2} & \cdots & s^{\,2}_{II} \end{pmatrix}$$

$\overline{II}$ is the injector-injector average rate matrix:

$$\overline{II} = \begin{pmatrix} \bar{i}_1 \bar{i}_1 & \bar{i}_1 \bar{i}_2 & \cdots & \bar{i}_1 \bar{i}_I \\ \bar{i}_2 \bar{i}_1 & \bar{i}_2 \bar{i}_2 & \cdots & \bar{i}_2 \bar{i}_I \\ \vdots & \vdots & \ddots & \vdots \\ \bar{i}_I \bar{i}_1 & \bar{i}_1 \bar{i}_2 & \cdots & \bar{i}_I \bar{i}_I \end{pmatrix}$$

I_d is the identity matrix of dimensions IxI:

$$I_d = \begin{pmatrix} 1 & 0 & \cdots & 0 \\ 0 & 1 & \cdots & 0 \\ \vdots & \vdots & \ddots & \vdots \\ 0 & 0 & \cdots & 1 \end{pmatrix}$$

the L_js are the weighting coefficient column vectors:

$$L_j = \begin{pmatrix} l_{1j} \\ l_{2j} \\ \vdots \\ l_{Ij} \end{pmatrix}$$

N is the Lagrange multipliers column vector:

$$N = \begin{pmatrix} n_1 \\ n_2 \\ \vdots \\ n_I \end{pmatrix}$$

the S_js are the injector-producer covariance column vectors:

$$S_j = \begin{pmatrix} s_{1j}^2 \\ s_{2j}^2 \\ \vdots \\ s_{Ij}^2 \end{pmatrix}$$

the $\overline{IP}_j$ s are the injector-producer average rate column vectors:

$$\overline{IP_j} = \begin{pmatrix} \bar{i}_1 \bar{q}_j \\ \bar{i}_2 \bar{q}_j \\ \vdots \\ \bar{i}_I \bar{q}_j \end{pmatrix}$$

and U is the unit column vector:

$$U = \begin{pmatrix} 1 \\ 1 \\ \vdots \\ 1 \end{pmatrix}$$

Equation 2.18 is a block matrix equation that represents a system of Nx(I+1) equations that can be solved for the l_{ij} and the n_i by standard means. Again, the weighting coefficients l_{ij} provide a quantitative expression of the influence of each injector i on each producer j.

MLR, ABMLR and IBMLR methods show similarities with the Kriging statistical technique used to interpolate data (Jensen *et al.*, 1997). In fact, like Kriging, the approaches presented here are constrained multivariate linear regressions. In particular, the IBMLR approach balance constraint (Eq. 2.14) appears to be similar to ordinary Kriging's

$$\sum_{i=1}^{I} l_{ij} = 1$$

constraint. But the main difference is that in Kriging's constraint the sum of the l_{ij}s is equal to one over i, while in IBMLR, the sum of l_{ij}s is equal to one over j, which means that the l_{ij}s add up to one per injector.

2.4.3. Uses of IBMLR

The IBMLR approach must be used if the waterflood is in acceptable balance (field-wide injection rate approximately equal to total liquid production rate, in reservoir volumes) at every time. In this model, as in ABMLR, the entire production rate of the field is associated to the entire injection rate.

As shown below in Chapter 3, the IBMLR approach yields excellent results if the instantaneous balance condition is met. However, large reservoir dispersion may alter the instantaneous balance and, consequently, alter the results. This approach has not been completely tested and further research is suggested.

2.5. DIFFUSIVITY FILTERS

The diffusivity constant is defined by

$$h = \frac{k}{f m c_t}$$

Likewise, we define dissipation as the inverse of diffusivity

$$d = \frac{1}{h} = \frac{f m c_t}{k}$$

In other words, a small permeability, a large porosity, a large viscosity and a large total compressibility cause a large dissipation. If there were no dissipation in the reservoir, a change in the injection rate would cause an equivalent and instantaneous change in all production rates, regardless of the distance between injector and producer. But in some reservoirs this may not be a good assumption, because there is actually a time lag and an attenuation of the signal between the injector and the producer.

The speed at which a perturbation is transmitted in the reservoir depends on the fluid and reservoir properties. This is very much the same as the spread of sound waves through a medium. Sound travels faster in a denser medium. Analogously, a perturbation transmitted through a more permeable, less viscous, less compressible, and less porous medium will travel faster. So, the time lag between the signal (change in injection rate) and the response (change in production rate) may be significant depending on the medium properties. In addition, the porous and tortuous nature of the medium, local heterogeneities, and the different fluids filling the medium cause the signal to travel at different speeds within the reservoir. This second effect, together with the radial propagation of the perturbation, causes a signal to be attenuated and spread when it reaches the producer.

Diffusivity filters are applied to injection rates. The shapes of the filters are defined by two factors: the diffusivity constant (which depends on the medium) and the distance between the injector and the producer. The basic shape of the filter is

obtained from the impulse propagation equation (transient solution to the diffusivity equation superimposed in time) (Sabet, 1991). There is one diffusivity constant h_{ij}, for each injector-producer pair in the reservoir. In the procedure, the values of h_{ij} are obtained after an iterative process that minimizes the difference between the modeled and the observed production rates, maximizing R^2 (see Eq. 2.1). This means that values of h_{ij} are initially guessed, then the regression is performed to estimate the weighting coefficients, and R^2 is calculated using the total observed production rate and the total production rate of the statistical model. Then, the h_{ij}s are changed iteratively until R^2 is maximized. This process only involves the production rates in the estimation of R^2, but the production rates are not included in the diffusivity filters estimation.

2.5.1. Objectives of the Diffusivity Filters

The main objective of the diffusivity filters is to account for the time lag and attenuation that occurs between the stimulus (injection) and the response (production). The filters basically transform the injection rates affecting a certain producer so that they take the form of an equivalent injection rate acting in an incompressible medium, which results in a convoluted or effective injection rate at a certain time. Filters become more important for large distances between injectors and producers and for large dissipation in the medium.

2.5.2. Mathematical Development

The pressure change (*DP*) at any point of an infinite homogeneous reservoir of constant thickness, caused by a change in an injection rate (*Di*), can be expressed as:

$$\Delta P = C_1 \times E_i\left(-d\frac{r^2}{t}\right) \tag{2.19}$$

where C_1 is a constant, E_i is the exponential integral function, r is the distance from the point to the injection well, t is time and d is the dissipation of the medium.

Using the superposition principle, the change in pressure caused by an impulse that lasts a unit time (independently of the time units) can be expressed as:

$$DP = \begin{cases} C_1 \times E_i\left(-d\dfrac{r^2}{t}\right) & for \quad t \le 1 \\ C_1 \times \left[E_i\left(-d\dfrac{r^2}{t}\right) - Ei\left(-d\dfrac{r^2}{(t-1)}\right)\right] & for \quad t > 1 \end{cases} \tag{2.20}$$

Let's assume a linear model of the form

$$q = J \times \left(\overline{P} - P_{wf}\right) \tag{2.21}$$

for the production rate of a well at a distance r from the injector. If we assume that the change in $\overline{P}$ in the drainage area of the producer is proportional to *DP* ($D\overline{P} = C_2 \times DP$), we can combine Eqs.2.19 to 2.21 and write the change in production rate caused by a unit injection impulse as:

$$Dq = \begin{cases} C_3 \times E_i\left(-d\dfrac{r^2}{t}\right) & for \quad t \le 1 \\ C_3 \times \left[E_i\left(-d\dfrac{r^2}{t}\right) - Ei\left(-d\dfrac{r^2}{(t-1)}\right)\right] & for \quad t > 1 \end{cases} \tag{2.22}$$

where C_3 is a new constant of proportionality, which is unknown. The constant C_3 is defined by the size of the change in injection rate (*Di*), properties of the reservoir, and the distance *r* between wells.

If we consider a fluctuating injection rate as the sum of injection impulses, Eq. 2.22 could be used as a model to reproduce production rate. But this would be true only if the flow is 100 percent dominated by transient flow, which does not occurr in waterfloods. Besides, Eq. 2.22, and its hypothetical extension to several injectors, is much more complex than the suggested linear models (Eq. 2.3 or Eq. 2.9). So, this equation is only used to correct the proposed steady state models for transient effects.

We call Eq. 2.22 the continuous filter function because it can be used to generate a filter function that applied to an injection rate returns the production rate of a producer at a distance *r*. The filter function transforms the injection rate so that the response at the producer is equivalent to one occurring in an incompressible medium. But Eq. 2.22 is not useful in that form, because C_3 is unknown. Ultimately, we will use one of the multivariate linear regression procedures to determine C_3. To eliminate the constant C_3, which is unknown, we define the normalized filter function as

$$F_n = \frac{\Delta q}{\int_{t=0}^{t=\infty} \Delta q dt}$$

where the proportionality constant C_3 cancels because Dq appears both in the numerator and denominator. F_n describes the shape that an injection impulse of unit time length has at a producer. Depending only on h and r, F_n may take on more or less attenuated shapes. A couple of examples are shown in Figure 2.1 and Figure 2.2.

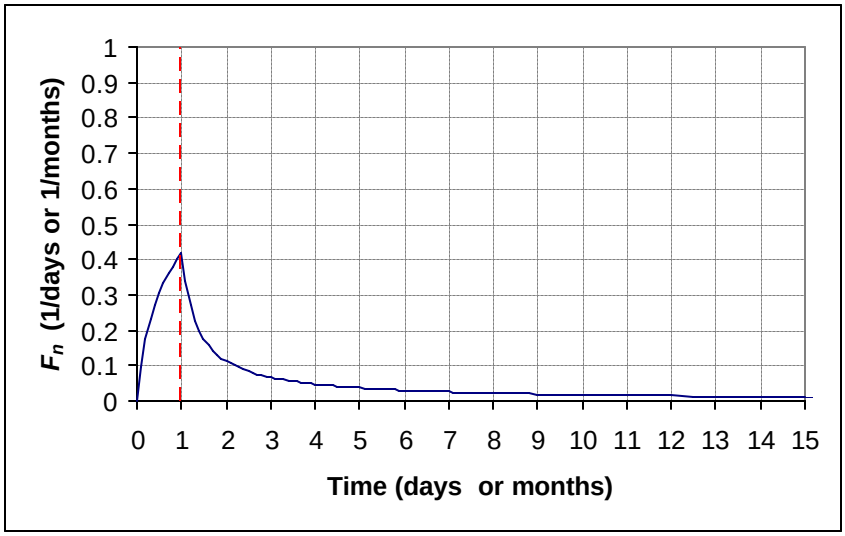

Figure 2.1 Normalized continuous filter function. It shows the shape that an injection impulse of unit time length takes at a producer. The units of F_n and time are not particularly important.

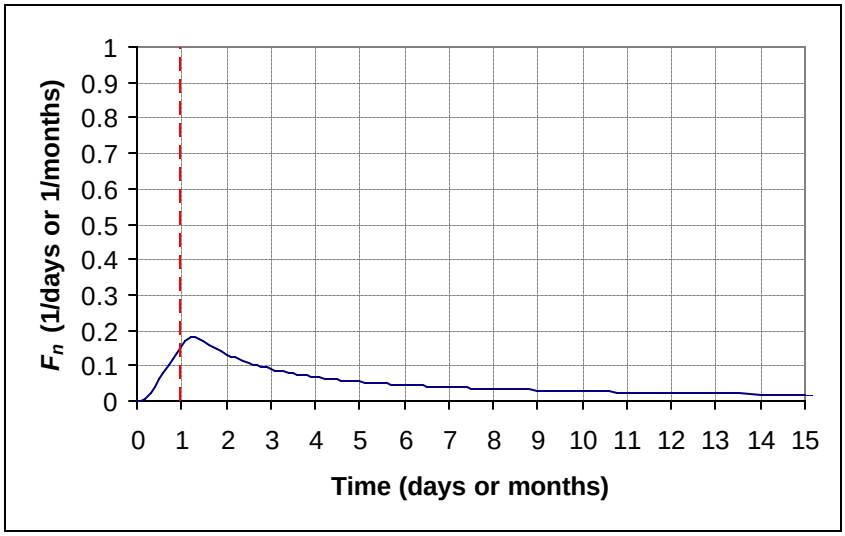

Figure 2.2 Normalized continuous filter function. It shows the shape that an injection impulse of unit time length takes at a producer in a medium with more dissipation that the one shown in Figure 2.1.

Considering that field injection and production data is discrete (typically in months) we must discretize F_n. The proposed normalized discrete filter function accounts for the effect of one year (12 months) of injection because, in most cases, the effect of a one-month injection impulse after one year is very small. We determine the 12 normalized filter coefficients of the discrete filter function as:

$$a^{(n)} = \int_{t=n}^{t=n+1} F_n dt = \frac{\int_{t=n}^{t=n+1} Dqdt}{\int_{t=0}^{t=12} Dqdt} \qquad (n = 1, 2, \ldots 12) \qquad (2.23)$$

More than 12 coefficients can be used if the dissipation is large. The normalized coefficients (Eq. 2.23) are independent of C_3, they are less than or equal to one, and the sum of the $a^{(n)}$s is equal to one.

The discrete filter function (with $a^{(n)}$ coefficients) is entirely characterized by the injector-producer distance r, the time t and the dissipation d. Then, for known locations of the wells and times, d can be guessed or determined by maximizing R^2 in the model. The filters are applied only to the injectors and do not contain or seek information about the connectivity between the wells. Only the regression procedure (MLR, ABMLR or IBMLR), after the injection rates have been transformed, seeks information about the connectivity between injector-producer pairs.

When the filters are applied to an injection history, the convoluted or effective injection rate of injector i affecting producer j at a time t is expressed as:

$$i_{ij}^{c}(t) = \sum_{n=0}^{11} \alpha_{ij}^{(n)} i_i(t-n) \tag{2.24}$$

meaning that the effect of injector i on j is determined not only by what the injection of i is at time t (n = 0), but also by what it was during the previous 11 months. An example of the application of the filters is presented in the next section. For example, for the ABMLR model (Eq. 2.9), the modeled production rate in well j using a diffusivity filter would be given by:

$$\hat{q}_j(t) = \sum_{i=1}^{I} \lambda_{ij} i_{ij}^c(t) \tag{2.25}$$

So, the procedure to obtain the diffusivity constants h_{ij} for each well pair and use the diffusivity filter is the following:

1. Initially guess values of d_{ij} (or $h_{ij} = 1/ d_{ij}$)
2. Estimate the discrete diffusivity filter function ($\alpha_{ij}^{(n)}$) using Eqs. 2.22 and 2.23.
3. Calculate the convoluted injection rates for each well pair
4. Perform the regression (MLR, ABMLR, or IBMLR) using the convoluted injection rates (e.g. using Eq.2.24 for the ABMLR approach) and determine the weighting coefficients
5. Calculate R^2 using the total observed production rate and the total production rate of the statistical model (Eq. 2.1).
6. Change the values of h_{ij} and repeat the process to calculate R^2 until R^2 is maximized.

However, the diffusivity filters only partially solve the transient problem, probably because the superposition effect is addressed only from the injector and not from the producer standpoint. In reservoirs with large dissipation, the transient effects of the producers may be significant. Besides, the statistical models are steady state models corrected for transient effects using the diffusivity filters, rather than

theoretical models that accounts for both transient and steady state flows. Results show that periods that are highly dominated by transient flow must be avoided simply by omitting those points from the analysis. Such periods will be characterized by sharp peaks in injection; their effects become more important in reservoirs with large dissipation. Often, all the data points can be used, but care should be taken when selecting periods with severe transients for the analysis

2.5.3. Illustrative Examples

The following examples illustrate the application of the filters. Let's analyze the case of one injector and one producer separated by a distance *r*. If there were no dissipation in the reservoir, an impulse in the injector would be instantaneously produced in the producer as shown in Figure 2.3**.** The filter coefficient $a^{(0)}$ is equal to one and the remaining coefficients are equal to zero, making the production rate change occur at the same time as the injection rate change, and the production rate is equal to the injection rate.

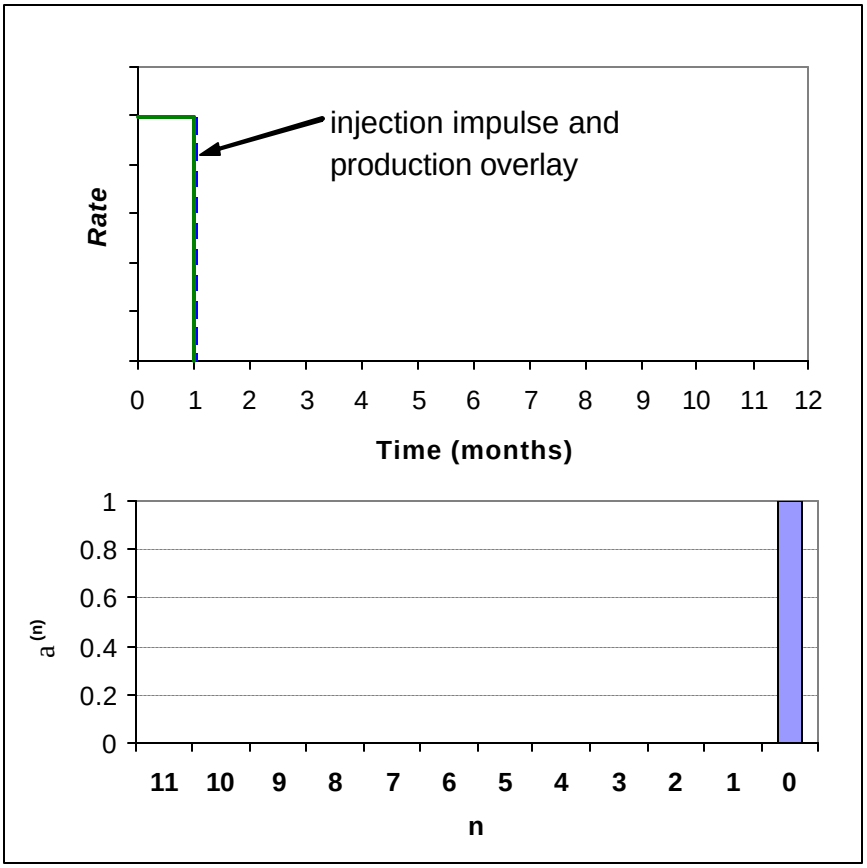

Figure 2.3 Injection impulse and production rate in a producer at distance *r* in a reservoir with no dissipation. The discrete filter function (lower plot) has only one effective coefficient, $a^{(0)} = 1$, all the rest are null.

If there is some dissipation in the reservoir (see Figure 2.4), an impulse occurring at time zero will affect the producer instantaneously but the effect will be attenuated ($a^{(0)}$? 1). Some dissipation will remain for a few months. In other words, the production at time *t* will be the sum of the effects of injection in the previous months. Note that the areas under the production rate curve (solid line) and the injection rate (dashed line) in the figure are equal. Likewise, the coefficients $a^{(n)}$,

calculated using Eq. 2.23 are proportional to the area under the production curve in the corresponding lapse. For example, $a^{(2)}$ is proportional to the area under the solid line (production rate curve) between t = 2 months and t = 3 months. The coefficients are displayed in inverse order because $a^{(0)}$ is applied to the current time t, and the other coefficients are applied to previous times (t -1, t – 2, etc.).

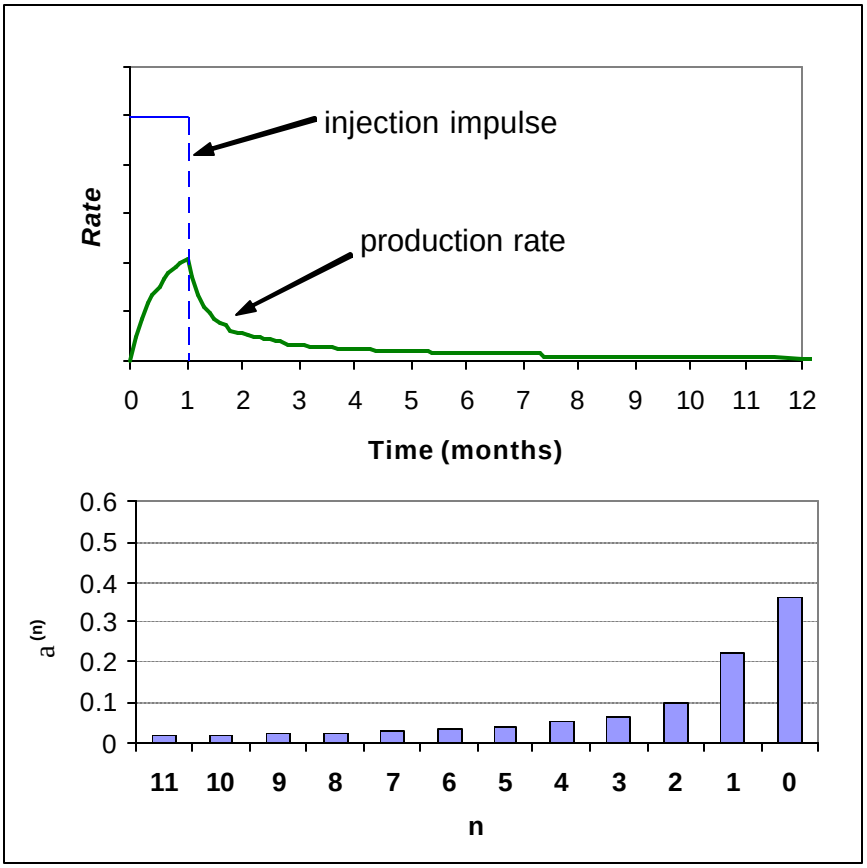

Figure 2.4 Injection impulse and production rate in a producer at distance r in a reservoir with moderate dissipation. The areas under the production rate (solid line) and the injection rate (dashed line) are equal. The lower plot is the discrete filter function.

Figure 2.5 illustrates the case of even larger dissipation (or a more distant production well) where the dissipation makes the production peak caused by an injection impulse of 1-month duration be much more attenuated and occur one month later than the impulse.

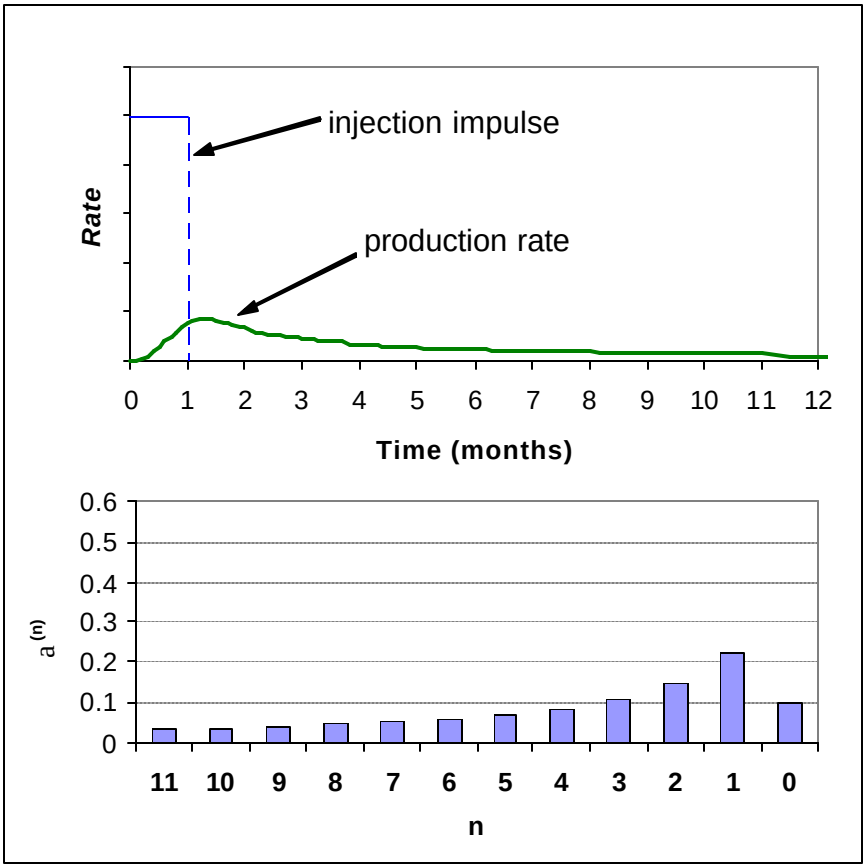

Figure 2.5 Injection impulse and production rate in a producer at distance *r* in a reservoir with large dissipation. The areas under the production rate (solid line) and the injection rate (dashed line) are equal. The lower plot is the discrete filter function.

An example of the application of the filters to a portion of an injection history follows. The $a^{(n)}$s showed in Figure 2.4 are used and presented in Table 2.1. A sample injection history of 15 months is presented in Table 2.2.

Table 2.1 Example of the application of diffusivity filters. Discrete filter function coefficients $a^{(n)}$.

$a_{ij}^{(11)}$	0.01823
$a_{ij}^{(10)}$	0.02030
$a_{ij}^{(9)}$	0.02253
$a_{ij}^{(8)}$	0.02531
$a_{ij}^{(7)}$	0.02907
$a_{ij}^{(6)}$	0.03388
$a_{ij}^{(5)}$	0.04060
$a_{ij}^{(4)}$	0.05069
$a_{ij}^{(3)}$	0.06756
$a_{ij}^{(2)}$	0.10200
$a_{ij}^{(1)}$	0.22804
$a_{ij}^{(0)}$	0.36178

Table 2.2 Example of the application of diffusivity filters. Injection history of 15 months for injector *i*.

t (months)	i_i (rb/d)
1	1678
2	1645
3	1715
4	1646
5	1544
6	1860
7	1797
8	1490
9	1369
10	1446
11	1434
12	1356
13	1061
14	1358
15	1352

Since the convoluted or effective injection rate of injector *i* affecting producer *j* at every time is caused by the previous 12 months of injection, we start estimating $i_{ij}^{c}(t)$ at t = 12 months. According to Eq. 2.24

$$i_{ij}^{c}(12)=\sum_{n=0}^{11} a_{ij}^{(n)} i_i(12-n)$$

or

$$i_{ij}^{c}(12)=a_{ij}^{(0)} i_i(12)+a_{ij}^{(1)} i_i(11)+a_{ij}^{(2)} i_i(10)+\ldots+a_{ij}^{(11)} i_i(1)$$

Using that expression we get $i_{ij}^{c}(12)$ = 1458 rb/d. Similarly, the effective injection rate of i affecting producer j at t = 13 is

$$i_{ij}^{c}(13) = a_{ij}^{(0)} i_i(13) + a_{ij}^{(1)} i_i(12) + a_{ij}^{(2)} i_i(11) + \ldots + a_{ij}^{(11)} i_i(2) = 1428 \text{ rb/d}$$

The $i_{ij}^{c}(t)$ history for this short injection history is shown in Table 2.3.

Table 2.3 Example of the application of diffusivity filters. Convoluted injection history of 15 months for injector *i* affecting producer *j*.

t (months)	i^{c}_{ij} (rb/d)
1	-
2	-
3	-
4	-
5	-
6	-
7	-
8	-
9	-
10	-
11	-
12	1458
13	1428
14	1394
15	1356

Finally, Figure 2.6 shows an example of a comparison between the observed injection rate and the convoluted injection rate corresponding to an injector-producer pair. The convoluted injection rate (solid line) is clearly smoother and slightly delayed with respect to the observed rate (dotted line).

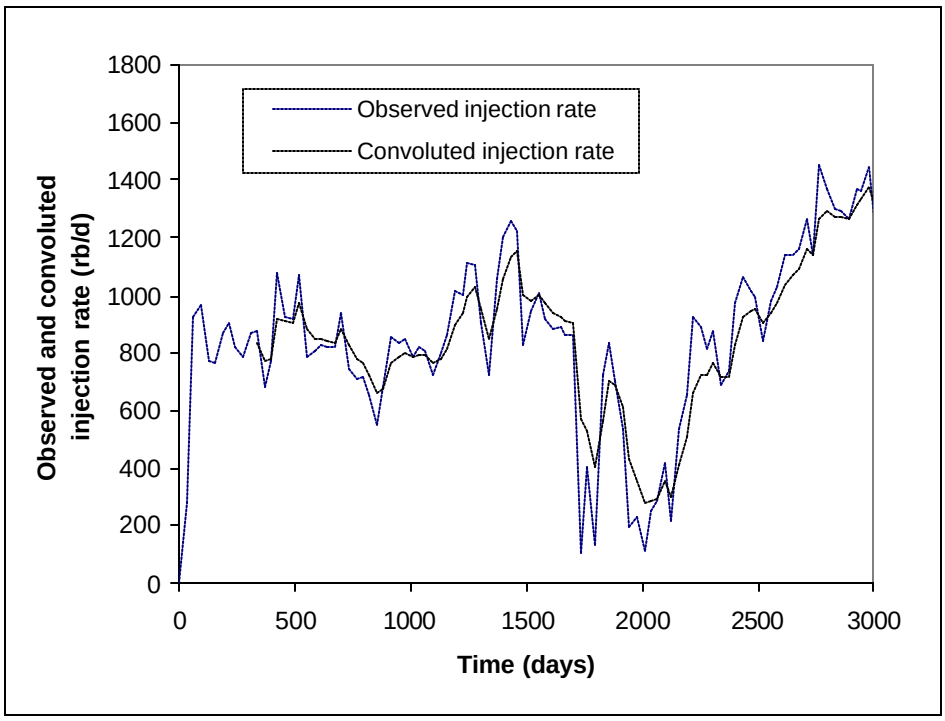

Figure 2.6 Comparison between the observed rate of an injector and its effective (convoluted) injection rate affecting a certain producer. The effect of attenuation and time lag is larger for large distances between injector and producer and for large dissipation in the medium. Convoluted rate is smoother.

CHAPTER 3: APPLICATION TO SYNTHETIC FIELDS

This chapter presents the application of MLR, ABMLR and IBMLR, with and without diffusivity filters, to numerically simulated fields (synthetic or Synfields). Fields of two types are studied: one of 5 injectors and 4 producers (the 5x4 Synfield) and one of 25 injectors and 16 producers (the 25x16 Synfield). They both are flowing water and undersaturated oil and have a five-spot injection pattern. The injector-producer distance is 800 ft for the 5x4 Synfield and 890 ft for the 25x16 Synfield. The oil-water mobility ratio is equal to one, and the oil, water, and rock compressibility are 5.0, 1.0 and 1.0 mips respectively. Both Synfields have vertical wells.

The first part of this chapter presents the application to the 5x4 Synfield. Reservoirs with different characteristics are studied. The results of the application of the three techniques proposed in Chapter 2 to a homogeneous reservoir are first presented. After the homogeneous reservoir results, we compare the three approaches, discuss the properties of the weighting coefficients, discuss the possible negative correlation between well pairs, and present a comparison between the results of non-reactive tracers and weighting coefficients. Then, we show the results of the application of the technique to other reservoirs such as anisotropic reservoirs, reservoirs with sealing faults, and vertically and spatially heterogeneous reservoirs.

The second part of this chapter discusses the results of the 25x16 Synfield with a homogeneous reservoir. The number of data points (production/injection history) and the number of injectors determine the overdetermination of the system and directly affect the quality of the results. An analysis of the overdetermination is presented in this section.

3.1. 5x4 SYNFIELD

Several cases were analyzed for this synthetic field of 5 injectors and 4 producers (see Figure 3.1). Actual injection data was used as input in the numerical simulation to provide weakly spatially correlated and realistic injection rates. This injection data was randomly selected from different wells in the Chihuido de la Sierra Negra Field, in Argentina, and proportionally modified to be in agreement with the Synfield injectivity. Figure 3.2 shows the injection rate of the five injectors in the field and the total injection rate. The simulation extends for 100 months (3000 days approximately), which represent a history of 100 data points of rate because the rate is constant within one month. The numerical simulator used is Eclipse 100, a finite difference simulator, the gridding is 31x31x5 (see Figure 3.1), and the gridblocks are 80 ft in x, by 80 ft in y, and 12 ft in z.

The output of the numerical simulator is the production data, which is to be analyzed using any of the three approaches described in Chapter 2.

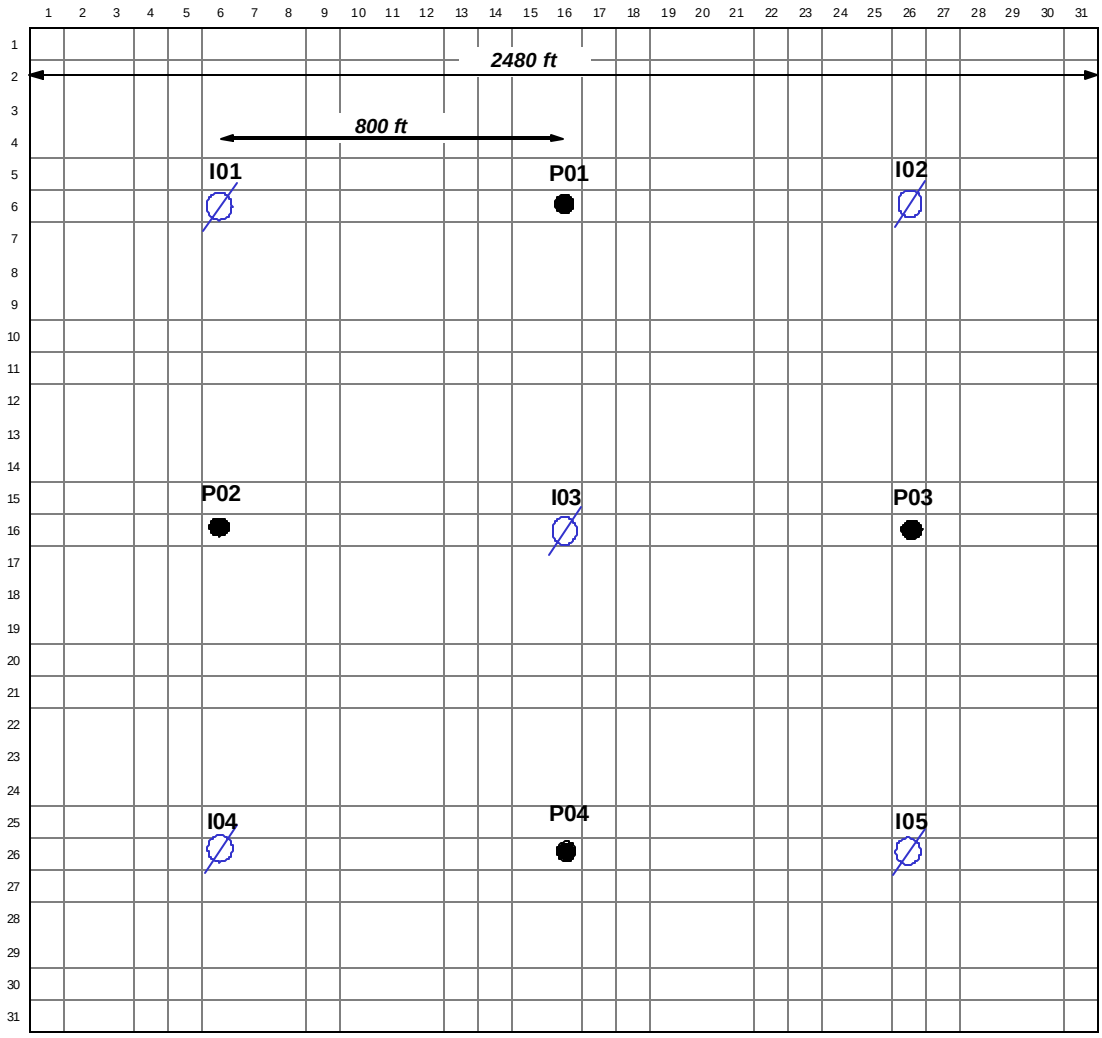

Figure 3.1 5x4 Synfield. Base map, gridding, and well location.

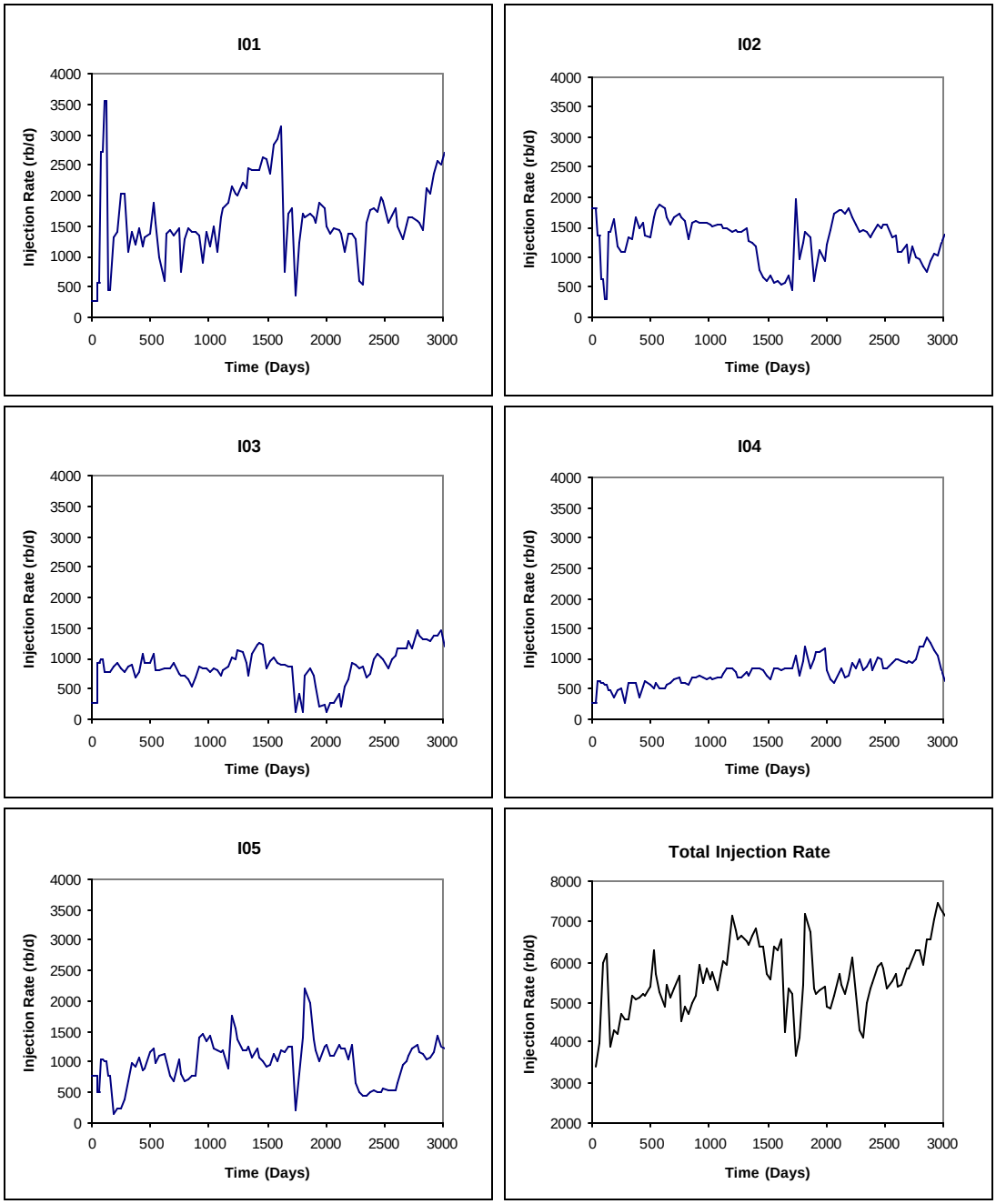

Figure 3.2 5x4 Synfield. Rates for the five injectors and total injection rate.

3.1.1. Homogeneous Reservoir

The first and simplest case is of a single-layered (the five layers in *z* have the same properties in the simulator) homogeneous reservoir with an isotropic horizontal permeability of 40md; the vertical permeability is 4md but it has no effect in the results.

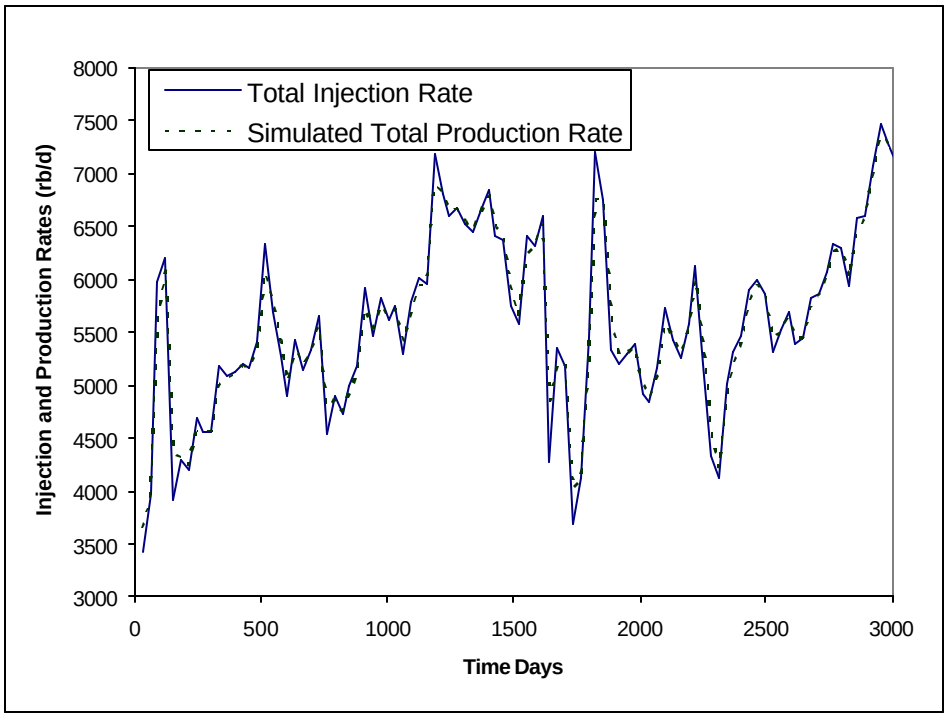

Figure 3.3 5x4 Synfield. Homogeneous reservoir. Total injection and production rates.

Figure 3.3 shows that the waterflood is clearly balanced at every time. According to the uses of the three proposed techniques, IBMLR (Instantaneously Balanced Multivariate Linear Regression) should be used. However, for comparison

purposes only, the three approaches MLR (Multivariate Linear Regression), ABMLR (Average-rate Balanced Multivariate Linear Regression), and IBMLR, with and without diffusivity filters were applied to this reservoir. As shown below in this section, we obtain best results using IBMLR with diffusivity filters.

a. Application of MLR

Table 3.1 shows the results of the application of MLR to the homogeneous 5x4 Synfield, without diffusivity filters. In Figure 3.4, the weighting coefficients (b_{ij}) are represented by inverted arrows that start from the i^{th} injector and point to the j^{th} producer. The larger the arrow, the larger the value of the coefficient and the connectivity between the two wells.

Table 3.1 5x4 Synfield. Homogeneous reservoir. MLR without diffusivity filters. Weighting coefficients b_{ij}. See Figure 3.4**.**

	P01	**P02**	**P03**	**P04**
I01	0.29	0.29	0.14	0.14
I02	0.28	0.12	0.28	0.13
I03	0.25	0.25	0.25	0.25
I04	0.13	0.29	0.13	0.29
I05	0.15	0.15	0.30	0.30
b_{0j} **(rb/d)**	185.68	177.60	177.61	169.49

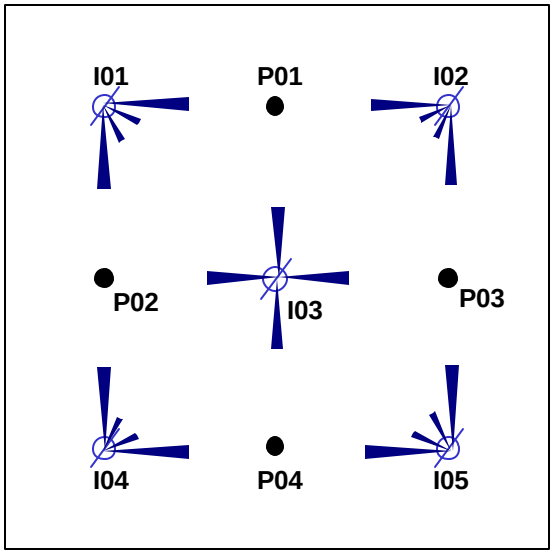

Figure 3.4 5x4 Synfield. Homogeneous reservoir. MLR without diffusivity filters. Representation of the weighting coefficients b_{ij} shown in Table 3.1. The length of the arrow is proportional to the value of b_{ij}.

Several things can be noted in Table 3.1 and Figure 3.4**.** As expected, the bs are larger for near well pairs (e.g. b_{11}, b_{12}) than for more separated well pairs (e.g. b_{13}, b_{14}). Another important characteristic is the symmetry. Since the reservoir is homogeneous and the wells are symmetrically located, the field has several planes of symmetry. The fact that the injection rates are weakly correlated (Figure 3.2) together with the symmetry shown by the calculated bs (Figure 3.4), suggests that bs do not depend on injection rates. The symmetry of the weighting coefficients is discussed in more detail below in this chapter.

MLR, does not force the modeled rates to be in balance. Hence, even when the field is in good balance, the constant term b_0 is not equal to zero for any of the

producers; it ranges from 161 to 174 rb/d, out of average production rates of 1450 rb/d approximately.

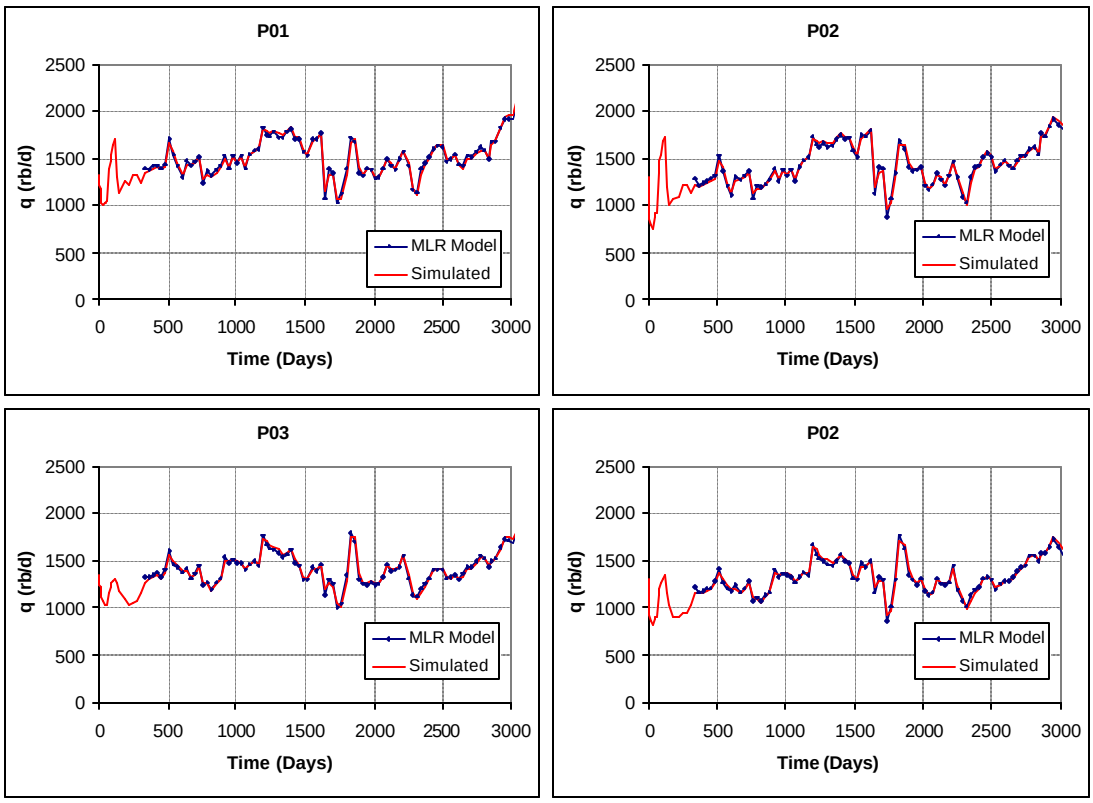

Figure 3.5 5x4 Synfield. Homogeneous reservoir. MLR without diffusivity filters. Comparison between modeled liquid production rate and the liquid production rate observed in simulation in the four producers.

Figure 3.5 shows a comparison between modeled liquid production rate using the coefficients shown in Table 3.1 and the liquid production rate observed in simulation in the four producers. Figure 3.6 shows the same comparison for the total liquid production rate in 5x4 Synfield. The model reproduces the observed liquid

production rates with excellent accuracy. The coefficient of determination (R^2) for the field is 0.977.

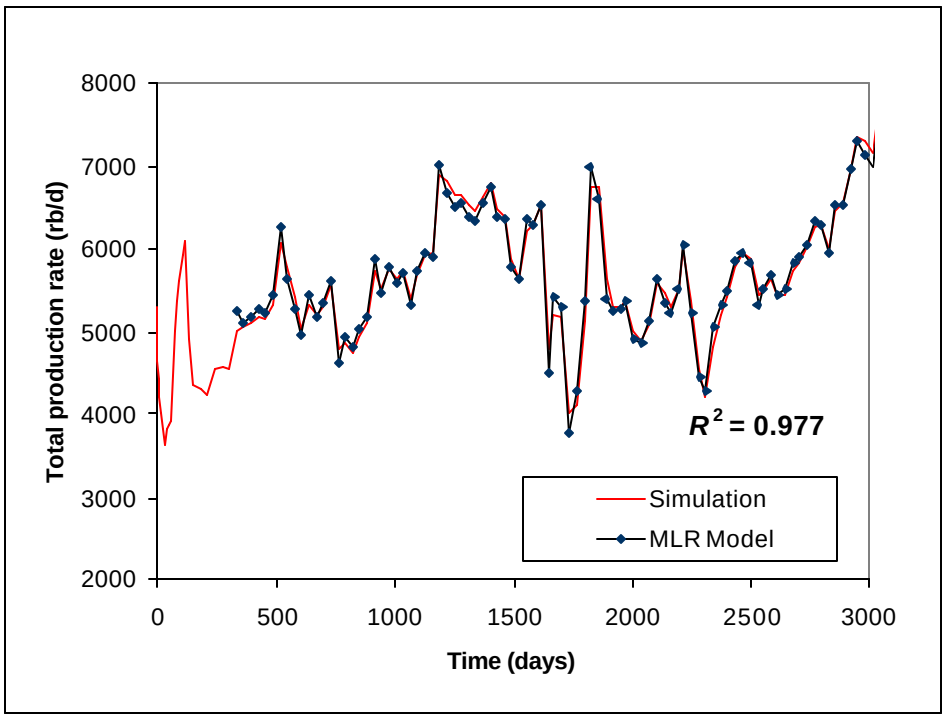

Figure 3.6 5x4 Synfield. Homogeneous reservoir. MLR without diffusivity filters. Comparison between modeled total liquid production rate and the total liquid production rate observed in simulation.

Results improve when we apply diffusivity filters. Figure 3.7 shows the b_{ij}s obtained when using MLR with diffusivity filters. The b_0s are smaller and negative. However, they are still not equal to zero, as should be in a field where the injection and production rates are balanced. The representation of the results (Figure 3.7) looks, at first glance, similar to the case without diffusivity filters (Figure 3.4); large

coefficients for close wells and small ones for more distant pairs. But the coefficients are, in general, slightly larger than those obtained without filtering; the negative b_0s compensate this effect. While symmetry remains basically unaffected, the most significant change occurs in modeled production: R^2 improves from 0.978 without diffusivity filters to 0.996 with diffusivity filters (see Figure 3.8).

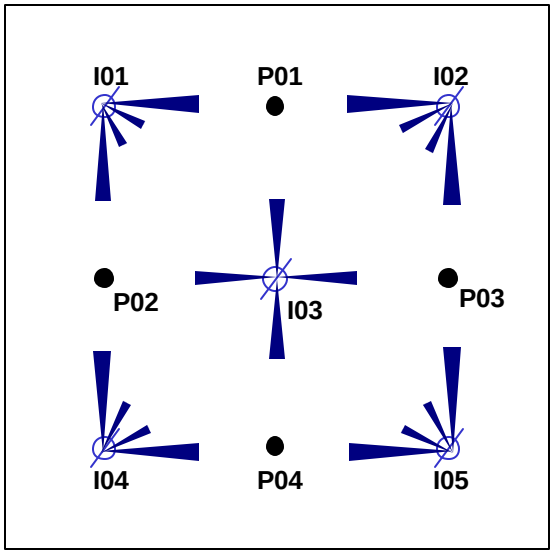

Figure 3.7 5x4 Synfield. Homogeneous reservoir. MLR with diffusivity filters. Representation of the weighting coefficients b_{ij} shown in Table 3.2.

Table 3.2 5x4 Synfield. Homogeneous reservoir. MLR with diffusivity filters. Weighting coefficients b_{ij}. See Figure 3.7.

	P01	P02	P03	P04
I01	0.34	0.34	0.16	0.16
I02	0.37	0.20	0.35	0.18
I03	0.28	0.28	0.28	0.29
I04	0.19	0.35	0.18	0.34
I05	0.19	0.19	0.36	0.36
b_{0j} **(rb/d)**	-124.63	-113.73	-78.03	-65.50

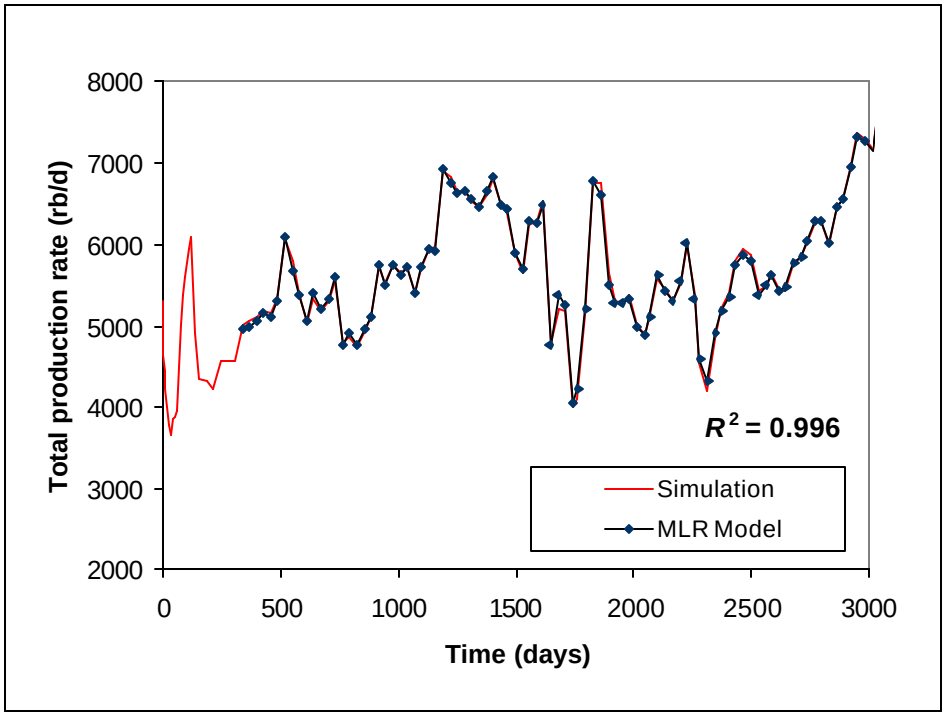

Figure 3.8 5x4 Synfield. Homogeneous reservoir. MLR with diffusivity filters. Comparison between modeled total liquid production rate and the total liquid production rate observed in simulation.

b. Application of ABMLR

The Synfield is in excellent balance (see Figure 3.3); thus, better results are expected when using the ABMLR approach instead of the MLR. Since the effects of the diffusivity filters in this homogeneous reservoir were presented above together with the application of the MLR approach, only the case with diffusivity filters is presented for ABMLR.

Table 3.3 and Figure 3.9 show the weighting coefficients obtained from the application of ABMLR. In this case, there is no constant term (it's set equal to zero by hypothesis) and, instead, the Lagrange multipliers m_j are presented. Again, the results look similar to those obtained with MLR (Table 3.2 and Figure 3.7). R^2 = 0.994 is slightly lower than that one obtained from MLR (0.996), but it is still very high (see Figure 3.10). The most important factor is that using ABMLR, we use a model that is much more appropriate than MLR because the field is balanced and we set the constant term to be equal to zero (there are no l_0 terms) at the expense of a very small decrease in R^2.

Table 3.3 5x4 Synfield. Homogeneous reservoir. ABMLR with diffusivity filters. Weighting coefficients l_{ij}. See Figure 3.9.

	P01	P02	P03	P04
I01	0.33	0.33	0.16	0.15
I02	0.33	0.17	0.33	0.16
I03	0.27	0.27	0.27	0.28
I04	0.15	0.32	0.16	0.32
I05	0.18	0.17	0.35	0.35
m_j **(rb/d)**	0.58	0.51	0.29	0.21

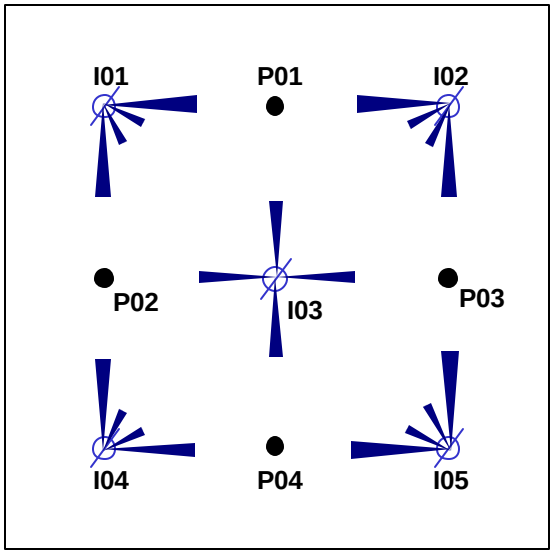

Figure 3.9 5x4 Synfield. Homogeneous reservoir. ABMLR with diffusivity filters. Representation of the weighting coefficients l_{ij} shown in Table 3.3.

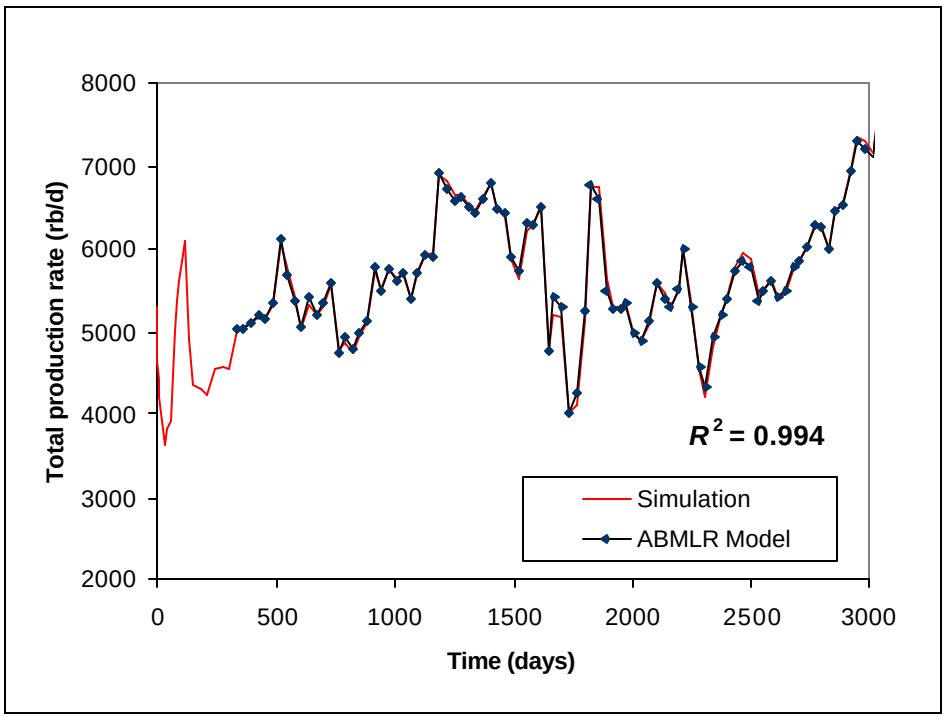

Figure 3.10 5x4 Synfield. Homogeneous reservoir. ABMLR with diffusivity filters. Comparison between modeled total liquid production rate and the total liquid production rate observed in simulation.

c. Application of IBMLR

Since the field is in excellent balance at every time (see Figure 3.3), the best results are expected when using the IBMLR approach, where we actually impose the instantaneously balance condition. And those expectations are met. Again, only the cases with diffusivity filters are presented for the IBMLR approach.

Table 3.4 5x4 Synfield. Homogeneous reservoir. IBMLR with diffusivity filters. Weighting coefficients l_{ij}. See Figure 3.11.

	P01	**P02**	**P03**	**P04**	S	n_i **(rb/d)**^{2}
I01	0.33	0.33	0.17	0.17	**1.00**	**3053.4**
I02	0.33	0.17	0.33	0.17	**1.00**	**3078.6**
I03	0.24	0.25	0.25	0.26	**1.00**	**3143.1**
I04	0.17	0.33	0.17	0.33	**1.00**	**1730.6**
I05	0.17	0.16	0.34	0.33	**1.00**	**2903.6**
S	**1.25**	**1.25**	**1.25**	**1.26**		

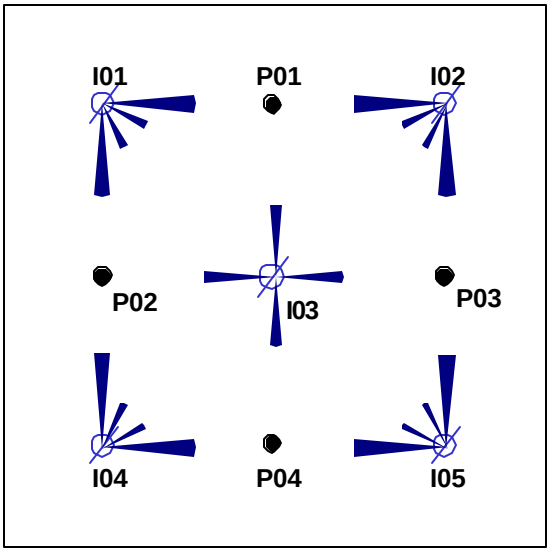

Figure 3.11 5x4 Synfield. Homogeneous reservoir. IBMLR with diffusivity filters. Representation of the weighting coefficients l_{ij} shown in Table 3.4.

In Table 3.4 the weighting coefficients and the Lagrange multipliers ν_i are shown. In addition, the sum of the coefficients per injector and per producer is also presented. We constrained the regression so that $\sum_{j=1}^{N} l_{ij} = 1$ (Eq. 2.14) for each

injector. The sum of l_{ij} is practically 1.25 for each producer. Figure 3.11 shows the representation of the l_{ij}s. The results show an excellent symmetry in the l_{ij}s. More discussion about symmetry and a comparison between MLR, ABMLR and IBMLR are presented in the next section. Figure 3.12 shows that R^2 = 0.992 is lower than in the MLR and the ABMLR cases, but still very high. In summary, we obtain a better symmetry, at the cost of a slightly lower R^2.

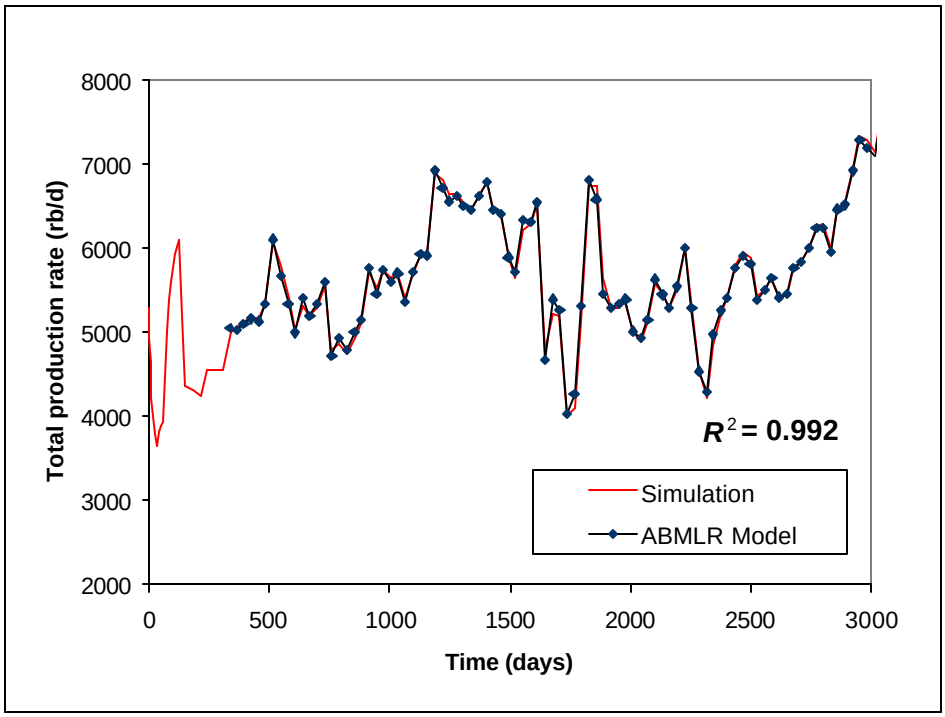

Figure 3.12 5x4 Synfield. Homogeneous reservoir. IBMLR with diffusivity filters. Comparison between modeled total liquid production rate and the total liquid production rate observed in simulation.

3.1.2. Discussion of Homogeneous Reservoir Results

The previous section, presented the results of the application of MLR, ABMLR and IBMLR to a homogeneous reservoir in the 5x4 Synfield. The weighting coefficients show symmetry with respect to the planes of symmetry in the field. There are basically two ways to compare the results: comparing symmetry and comparing R^2. The meanings of symmetry and R^2 are explained in this section where more detail and a comparison between the three approaches are shown. In addition, we also present a discussion of the properties of the weighting coefficients and a comparison between the weighting coefficient and non-reactive-tracer injection results.

a. Symmetry and R^2

As stated above, if the reservoir is homogeneous and the wells are symmetrically located, then the field has several planes of symmetry (see Figure 3.1). These planes of symmetry, determine three groups of injector-producer pairs with similar relative location; these groups are: (a) corner injectors with adjacent producers I01-P01, I01-P02, I02-P01, I02-P03, I04-P02, I04-P04, I05-P03, and I05-P04; (b) corner injectors with non-adjacent producers I01-P03, I01-P04, I02-P02, I02-P04, I04-P01, I04-P03, I05-P01, and I05-P02; and (c) center injector with adjacent producers I03-P01, I03-P02, I03-P03, and I03-P04 (see Table 3.5). Figure 3.7, Figure 3.9, and Figure 3.11 show that the weighting coefficients are similar in each of these

groups or, in other words, there is symmetry in the weighting coefficients. The fact that the injection rates are weakly correlated (Figure 3.2) together with the excellent symmetry shown by the calculated ls (or bs), suggests that ls (or bs) do not depend on injection rates. Indeed, further tests performed in other synthetic fields verify that the weighting coefficients only depend on the reservoir properties and the relative location of the wells. They are independent of injection rates.

Table 3.5 5x4 Synfield. Homogeneous reservoir. Well-pair groups determined by planes of symmetry.

	P01	P02	P03	P04
I01	a	a	b	b
I02	a	b	a	b
I03	c	c	c	c
I04	b	a	b	a
I05	b	b	a	a

To quantify the symmetry shown by the weighting coefficients we define a term that describes their variability in each similar group. The asymmetry coefficient (A) is the square root of the sum of the variances of ls (or bs) of the group, weighted by the number of well pairs in each group. Using ABMLR or IBMLR in the 5x4 Synfield, that has 3 groups (a, b and c) and a total of 20 l coefficients, the asymmetry coefficient is

$$A = \sqrt{\frac{8\,\mathrm{var}_a(l) + 8\,\mathrm{var}_b(l) + 4\,\mathrm{var}_c(l)}{20}} \tag{3.1}$$

Another way to compare the results is comparing R^2. Equation 2.1 defined R^2 where we said that it measures the quality of the correlation between observed and modeled production. But it provides only a weak description of the goodness of the results. As Jensen *et al.* state (1997), the coefficient of determination does not measure the appropriateness of the model. In the case of the synthetic homogeneous reservoirs with planes of symmetry, R^2 alone is not a good indicator; the asymmetry coefficient is a much better indicator and should be considered together with R^2 to evaluate the goodness of the results. However, in actual applications of the technique one must only use R^2 because symmetry is not expected from the results.

b. Comparison between MLR, ABMLR, and IBMLR

Table 3.6 shows a comparison of some of the parameters obtained using MLR, ABMLR, and IBMLR with and without diffusivity filters in the 5x4 Synfield with homogeneous reservoir. R^2 and A are presented. In addition, a field balance check is shown for all three approaches. The field balance check is the calculation of $\sum_{j=1}^{N} \bar{q}_j - \sum_{j=1}^{N}\sum_{i=1}^{I} \lambda_{ij}\bar{i}_i$. If the model is balanced in average, then this calculation (analogous to the calculation of $\sum_{j=1}^{N} b_{0j}$ using Eq. 2.5), must be zero. In both balanced models (ABMLR and IBMLR) b_0 is not part of the model, but it still can be calculated using as an average balance check. The calculation of b_0 as a field balance

check is performed after the regression procedure and does not affect the estimation of the weighting coefficients.

Table 3.6 5x4 Synfield. Homogeneous reservoir. Comparison of results using MLR, ABMLR, and IBMLR

	Diffusivity Filters	R^2	A	Field Balance check (rb/d)
MLR	No	0.977	0.00778	710.4
	Yes	0.996	0.01160	-381.9
ABMLR	No	0.972	0.01600	0.0
	Yes	0.994	0.00948	0.0
IBMLR	No	0.967	0.00214	-11.1
	Yes	0.992	0.00265	8.5

ABMLR is a constrained case of MLR. So, since an average balance constraint is imposed, R^2 is expected to be lower in ABMLR than in MLR. Similarly, IBMLR is an even more restrictive case of MLR because it uses a stronger condition, where the balance is forced at every time in the model. Thus, an even lower R^2 is expected for IBMLR. If we compare the three cases without diffusivity filters, R^2 decreases from 0.978 to 0.967 as we impose more restrictions, as expected. The same happens with the three cases with diffusivity filters, but the change is smaller (0.996 to 0.992).

On the other hand, among the cases with filters, the symmetry of the weighting coefficients improves (A is smaller) as we use more restrictive approaches. Knowing that in synthetic homogeneous reservoirs with planes of symmetry, the

asymmetry coefficient is a better indicator than R^2, the best results are obtained with IBMLR with diffusivity filters, where A = 0.00265. This indicates that for the homogeneous 5x4 Synfield, the IBMLR is the most appropriate model.

The field balance check is also presented in Table 3.6. These are the sum of the b_{0j}s over the producers for each approach. In MLR, b_{0j}s are calculated as part of the procedure and can be different from zero, because we do not use the balance condition constraint. The model is unbalanced in 710.4 and -381.9 rb/d out of an average total injection rate of 5722 rb/d, for the cases without and with diffusivity filters respectively. In both ABMLR and IBMLR, b_0 is not part of the model but we can still calculate it as a balance check using Eq. 2.5. In ABMLR, $b_0 = 0$ is the exact constraint we use, so we get $b_0 = 0$ for each producer. In IBMLR, the balance condition is given by instantaneous balance at every time, but not in average. Anyway, $b_0 \cong 0$ is also expected because if the model is balanced at every time, it is expected to be balanced in average. Applying the IBMLR, we obtain field balance checks that are very small (about -11.1 and 8.5 rb/d out of an average total injection rate of 5722 rb/d). The instantaneously balance condition is met ($\sum_{j=1}^{N} l_{ij} = 1$) and the average balance condition is satisfactorily met.

IBMLR is then the most appropriate model to use in the case of the homogeneous 5x4 Synfield. However, the IBMLR has not been completely tested and further research is suggested in that topic. For the remaining cases, only the

MLR and the ABMLR approaches, which still yield excellent results, are going to be used.

c. Properties of the weighting coefficients

The weighting coefficients show excellent symmetry using the IBMLR approach in the homogeneous 5x4 Synfield (see Table 3.4 and Figure 3.11). All the well-pairs in the same group determined by the planes of symmetry have almost the same weighting coefficient: 0.33 for group a (corner injectors with adjacent producers), 0.17 for group b (corner injectors with non-adjacent producers), and 0.25 for group c (center injector with adjacent producers). Since the injection rates are uncorrelated (Figure 3.2 and Table 3.7) or do not show a correlation pattern, we can conclude that the weighting coefficients are independent of injection rates. They only depend on the reservoir properties and the relative location of the wells.

Table 3.7 Synfield 5x4. Injector-injector covariance matrix for a case without diffusivity filters. Covariances are in $(rb/d)^2$.

	I01	**I02**	**I03**	**I04**	**I05**
I01	307812	-100388	69646	23225	43008
I02	-100388	129486	-33963	-29943	-18664
I03	69646	-33963	93602	12121	5232
I04	23225	-29943	12121	36070	1532
I05	43008	-18664	5232	1532	109734

In many occasions, the influence of an injector on a certain producer is evaluated by observation, simply by comparing the injection and production rates. An equivalent and quantitative way to directly compare injection and production rates making an injection rate-production rate crossplot and estimating the correlation coefficient r, where

$$r = \frac{Cov(i,q)}{\sqrt{Var(i)Var(q)}}$$

The determination of the influence of an injector on a certain producer through the correlation coefficient r may lead to significant errors.

Figure 3.13 shows the crossplots of the injection rates and the production rates in the 5x4 Synfield. r^2 is calculated for each crossplot. Some well pairs show high positive correlations (e.g. I01-P01, I05-P03), but others show negative correlations (e.g. I02-P01, I02-P04). Furthermore, the pair I02-P03 shows no correlation between the injection and the production rates (r^2 = 0.000). This is caused by constructive and destructive interference between injectors. The rates between an injector-producer pair may be uncorrelated (or even negatively correlated) just because of the effect of other injectors on the same producer; but it is important to remark that r^2 alone is not an indicator of the connectivity between wells. Moreover, we know that the field is homogeneous and, consequently, we expect the influence on similar well pairs to be similar. For example, the influence of I02 on P03 is not null, as suggested by r^2; it is expected to be similar to that one of the I05-P03 or the I04-P04 pairs. The IBMLR

yields l_{23} = 0.33, so 33 percent of the water injected in I02 affects P03. It also yields $l_{53} = l_{44}$ = 0.33, as expected (see Table 3.4).

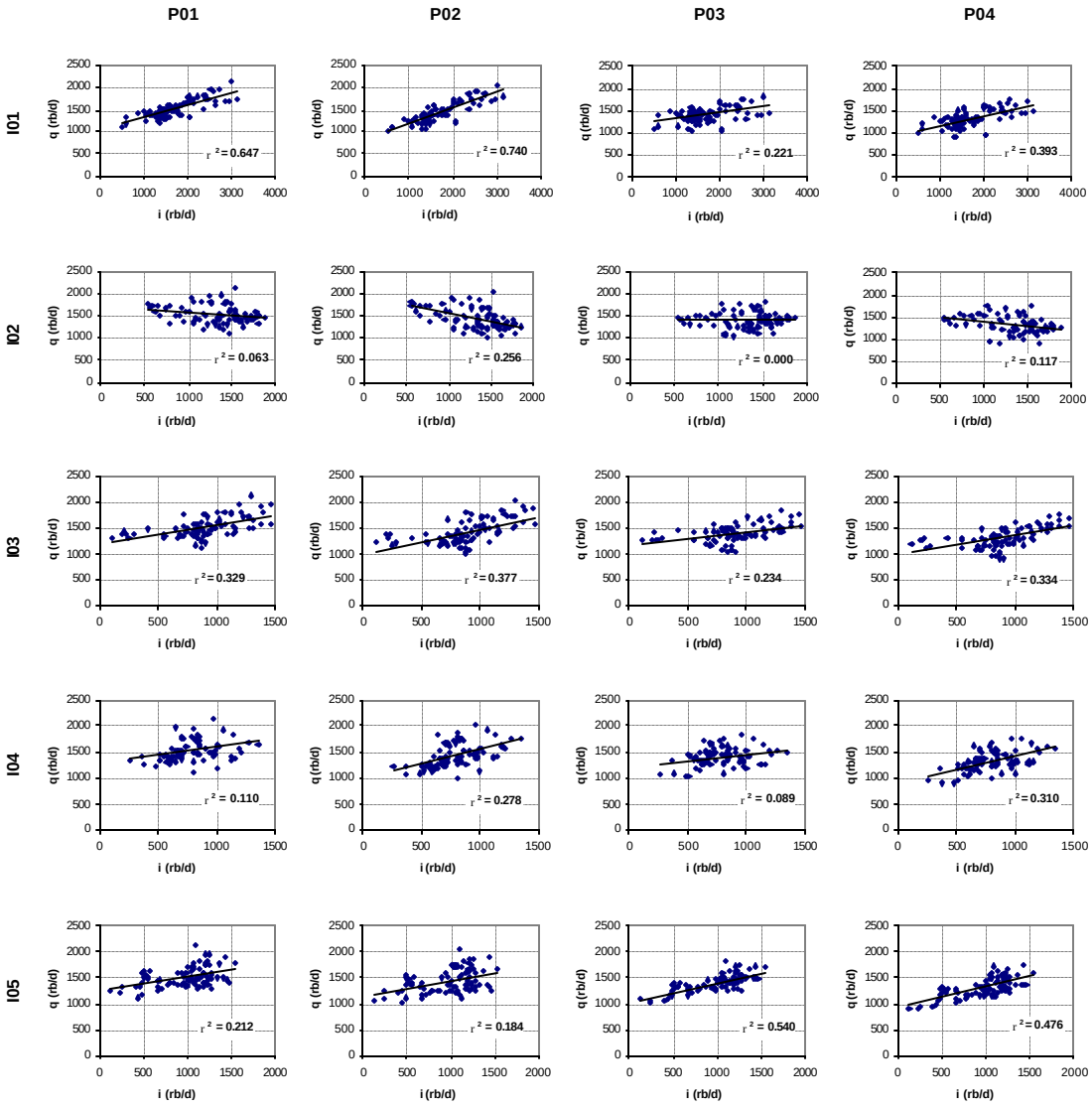

Figure 3.13 5x4 Synfield. Homogeneous reservoir. Injection rate-production rate crossplots.

d. Injection of non-reactive tracers

With the sole purpose of comparison, the injection of non-reactive tracers was also simulated in the synthetic field. Each injector was simulated to inject a different tracer. Table 3.8 and Figure 3.14 show the fraction of the non-reactive tracer injected in the i^{th} injector produced in the j^{th} producer. In the figure, the length of the arrow is proportional to the fraction.

Table 3.8 5x4 Synfield. Homogeneous reservoir. Tracer results. Fraction of the non-reactive tracer injected in the i^{th} injector produced in the j^{th} producer. See Figure 3.14.

	P01	**P02**	**P03**	**P04**	S
I01	0.47	0.53	0.00	0.00	**1.00**
I02	0.45	0.00	0.55	0.00	**1.00**
I03	0.13	0.22	0.25	0.40	**1.00**
I04	0.00	0.41	0.00	0.59	**1.00**
I05	0.00	0.00	0.45	0.55	**1.00**
S	**1.04**	**1.16**	**1.25**	**1.54**	

Unlike the ls (or bs), the tracer response is not symmetric. For example, the fraction of tracer injected in I02 and produced in P03 (0.55) is significantly different from that one injected in I04 and produced in P02 (0.41). Or, more tracer injected in I03 is produced in P04 (0.40) than in P01 (0.13). In other words, tracer response does depend on injection rate. While the l estimation is determined from the analysis of the fluctuation of injection and production rates, the tracer response is determined by rate averages. For example, the average rates of injectors I01 and I02 are

approximately 60% larger than those ones of injectors I04 and I05 (Figure 3.2). Thus, the tracer injected in I03 is more likely to be produced in P04 than in P01 (see Figure 3.14). On the one hand, tracers tell us where each barrel of injected water is being produced; on the other hand, the weighting coefficients obtained from MLR, ABMLR or IBMLR tell us what the connectivity between each injector-producer pair is. The following example illustrates this fact: none of the water injected in I04 reaches P01, but, from the *l* results in IBMLR, we know that 17 percent of its injection is influencing P01 (see Table 3.4).

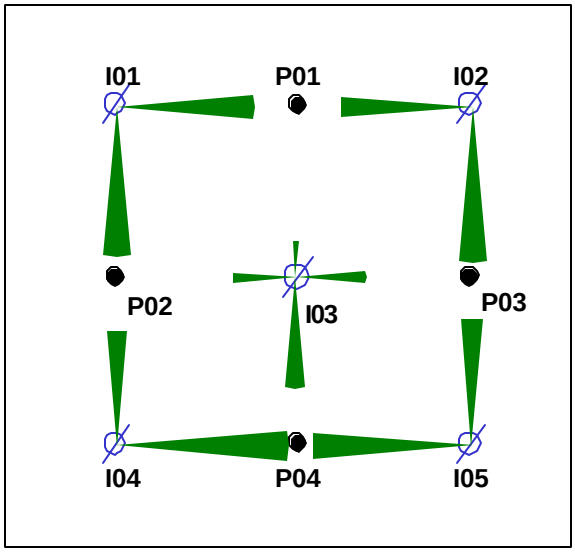

Figure 3.14 5x4 Synfield. Homogeneous reservoir. Representation of the non-reactive tracer results (Table 3.8). Fraction of the non-reactive tracer injected in the i^{th} injector produced in the j^{th} producer. The length of the arrow is proportional to the fraction.

In the simulation, a different non-reactive tracer was injected at each injector at all times. Obviously, this is not the way tracers are injected in fields. If a tracer is

injected as a pulse input, the tracer response depends not only on average injection rates, but also on the period in which the tracer is injected and produced. So, in some way, the tracers' response is dependent on even more variables and consequently less unique.

3.1.3. Anisotropic Reservoir

Two cases (case a and case b) with an anisotropic reservoir of k_y = 1/40 k_x were run in the 5x4 Synfield. The reservoir properties in both cases are exactly similar and the input injection rates are different. The input rates of case a are noisy sinusoids with different amplitudes, different frequencies, and different averages. (Figure 3.15). The input rates of case b are the same as those used in the homogeneous reservoir case (see Figure 3.2).

Figure 3.16 shows the total injection and production rates for case a. The effect of the injectors on producers is clearly more attenuated than in the homogeneous permeability cases, because the permeability in the *y* direction is forty times smaller. Furthermore, the dissipation of the injection signal causes production to be both delayed and smoothed, which makes the production rate reach the levels of the injection rate only after 300 days approximately. The same effects can be noted in case b, where with a different set of injection rates as input, the production rate is also delayed and smoothed with respect to the injection rate (Figure 3.17).

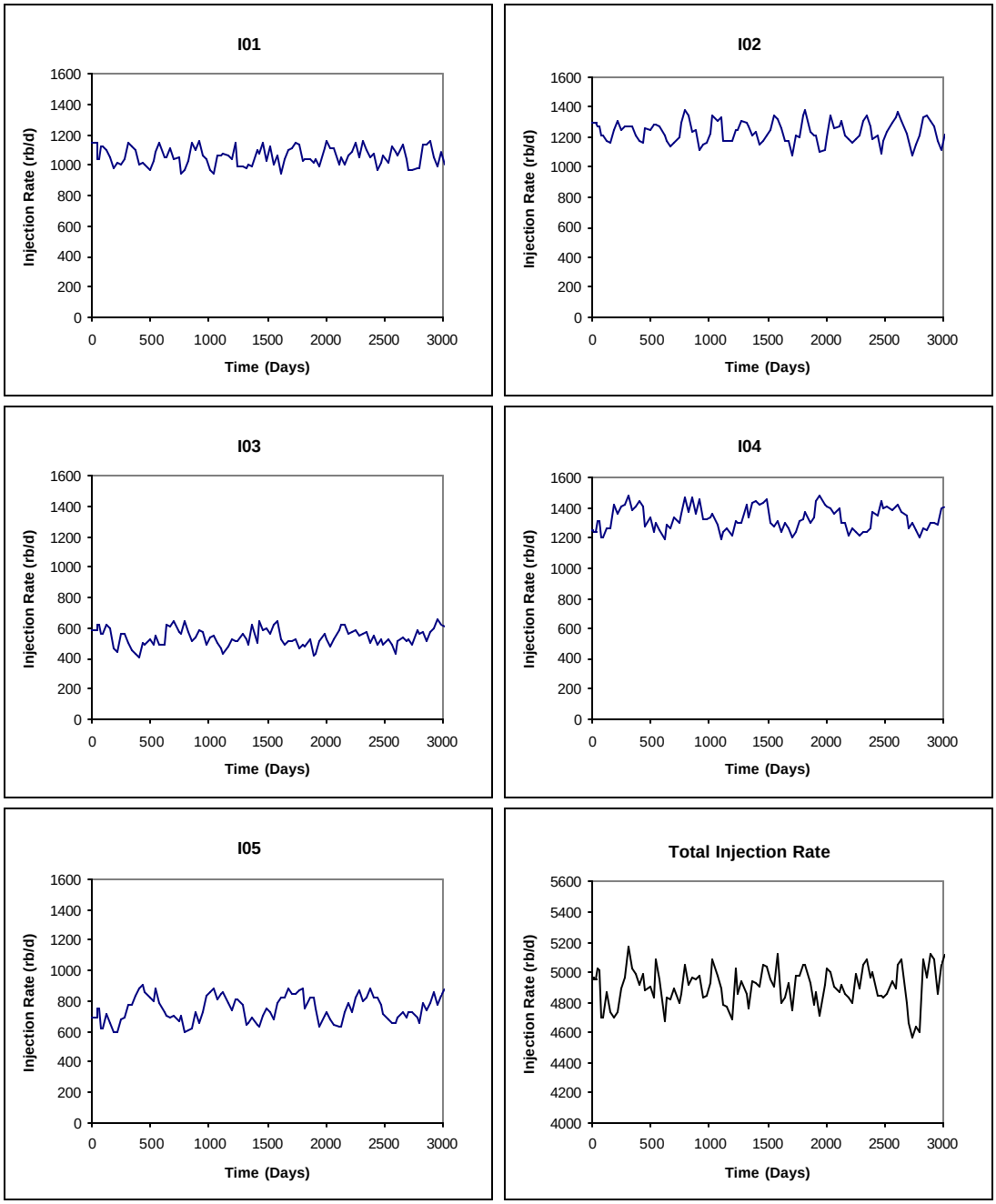

Figure 3.15 5x4 Synfield. Anisotropic reservoir. $k_y = 1/40\ k_x$, case a. Rates for the five injectors and total injection rate.

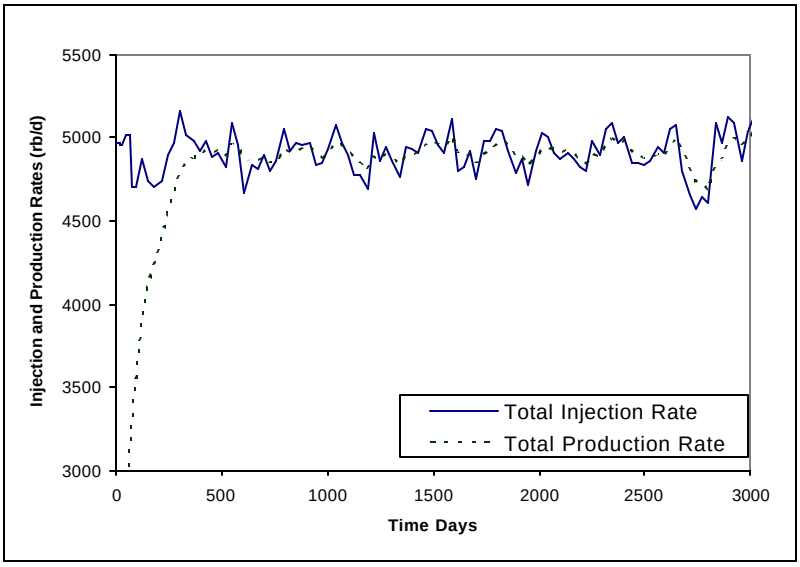

Figure 3.16 5x4 Synfield. Anisotropic reservoir. $k_y = 1/40\ k_x$, case a. Total injection and production rates. Production rate is delayed and smoothed with respect to the injection rate.

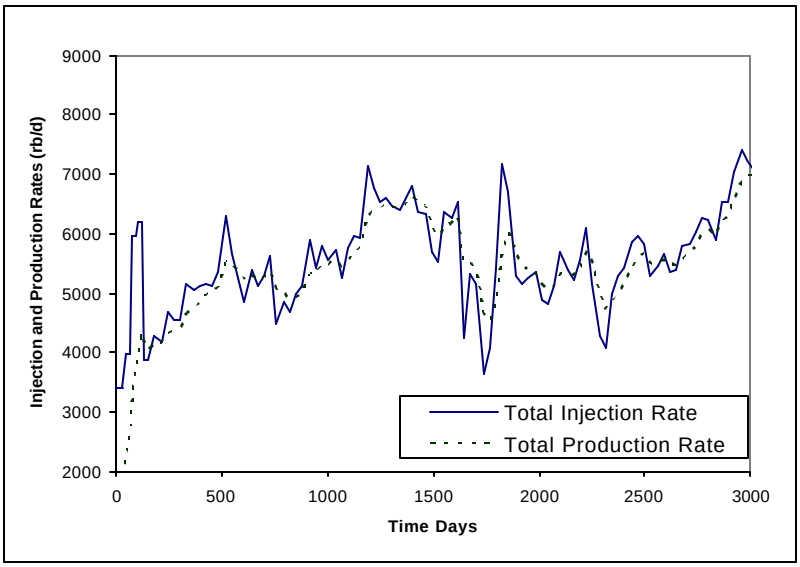

Figure 3.17 5x4 Synfield. Anisotropic reservoir. $k_y = 1/40\ k_x$, case b. Total injection and production rates.

Since total injection and production rates are balanced on average, the ABMLR approach with diffusivity filters was used to infer the weighting coefficients in both cases. Table 3.9, Table 3.10, Figure 3.18 and Figure 3.19 show that the results are similar in both cases and practically independent of injection rates. The weighting coefficients of well pairs that are connected in the x direction are much larger than those connected in the y direction, clearly showing the preferential permeability orientation. Non-adjacent injection-producer pairs connected mainly in the x direction (e.g. I01-P03, I02-P02) have even slightly larger coefficients than adjacent wells connected purely in the y direction (e.g. I01-P02, I02-P03). This anisotropic 5x4 Synfield has planes of symmetry that are different from those of the homogeneous-isotropic field, so the asymmetry coefficient can be calculated with 6 groups of well pairs. We get $A = 0.0163$ for case a, and $A = 0.0187$ for case b. These values are larger than the 0.00948 obtained in the isotropic 5x4 Synfield using the same approach (see Table 3.6), but the symmetry of the ls is still excellent.

Table 3.9 5x4 Synfield. Anisotropic reservoir. $k_y = 1/40\ k_x$, case a. ABMLR with diffusivity filters. Weighting coefficients l_{ij}. See Figure 3.18.

	P01	**P02**	**P03**	**P04**	S
I01	0.70	0.09	0.16	0.04	0.98
I02	0.72	0.15	0.11	0.03	1.01
I03	0.15	0.44	0.43	0.12	1.15
I04	0.02	0.11	0.12	0.70	0.95
I05	0.04	0.13	0.10	0.72	1.00
S	1.62	0.93	0.91	1.62	
m_j **(rb/d)**	-0.01	0.00	-0.01	0.00	

Table 3.10 5x4 Synfield. Anisotropic reservoir. k_y = 1/40 k_x, case b. ABMLR with diffusivity filters. Weighting coefficients l_{ij}. See Figure 3.19.

	P01	**P02**	**P03**	**P04**	S
I01	0.71	0.10	0.10	0.02	0.93
I02	0.71	0.13	0.13	0.02	0.98
I03	0.11	0.41	0.41	0.15	1.08
I04	0.03	0.15	0.14	0.73	1.05
I05	0.04	0.14	0.14	0.72	1.04
S	1.61	0.92	0.92	1.63	
m_j **(rb/d)**	0.58	-0.13	-0.04	-0.43	

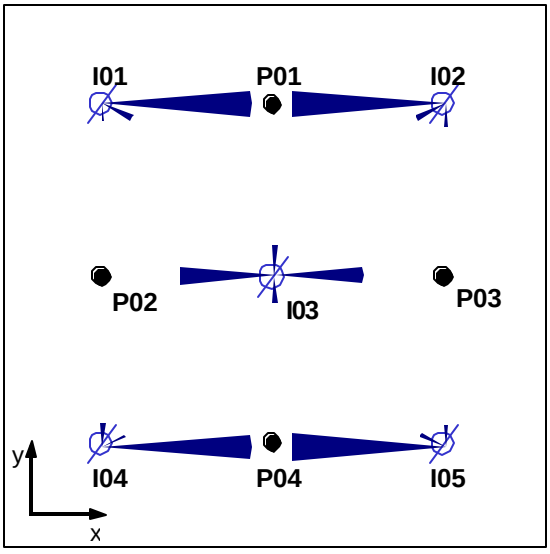

Figure 3.18 5x4 Synfield. Anisotropic reservoir. k_y = 1/40 k_x, case a. ABMLR with diffusivity filters. Representation of the weighting coefficients l_{ij} shown in Table 3.9.

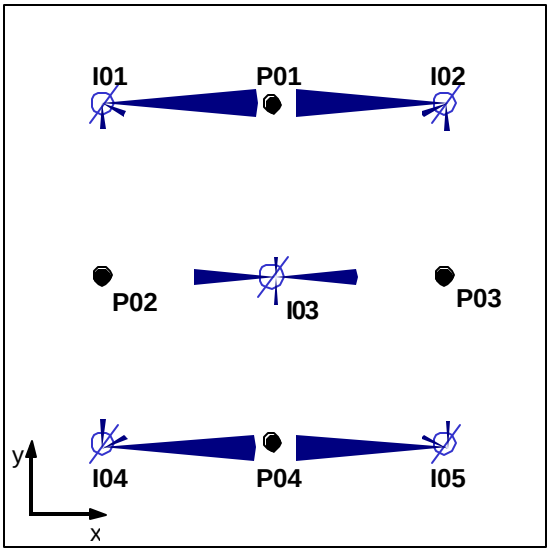

Figure 3.19 5x4 Synfield. Anisotropic reservoir. k_y = 1/40 k_x, case b. ABMLR with diffusivity filters. Representation of the weighting coefficients l_{ij} shown in Table 3.10.

Using ABMLR with diffusivity filters in case a, we get R^2 = 0.974 (Figure 3.20). Without diffusivity filters, the estimation of the coefficient of determination yields R^2 = -0.614. We get this negative value because the variability of the modeled total production rate is larger than the variability of the observed total production rate. It has no physical sense other than telling us that the correlation is very poor. Without filters we get an asymmetry coefficient A = 0.0415 which is 2.5 times larger than what we get using diffusivity filters. Similarly, the use of diffusivity filters in case b improves R^2 from 0.666 to 0.997, and A from 0.1070 to 0.0187 (Figure 3.21). In both cases, the use of diffusivity filters improves the correlation and the results significantly. In these two cases of anisotropic reservoirs, the use of diffusivity filters is more important than in isotropic ones. The lower transmissibility makes the

changes in injection rate be much more dissipated in the *y* direction before they reach the producers.

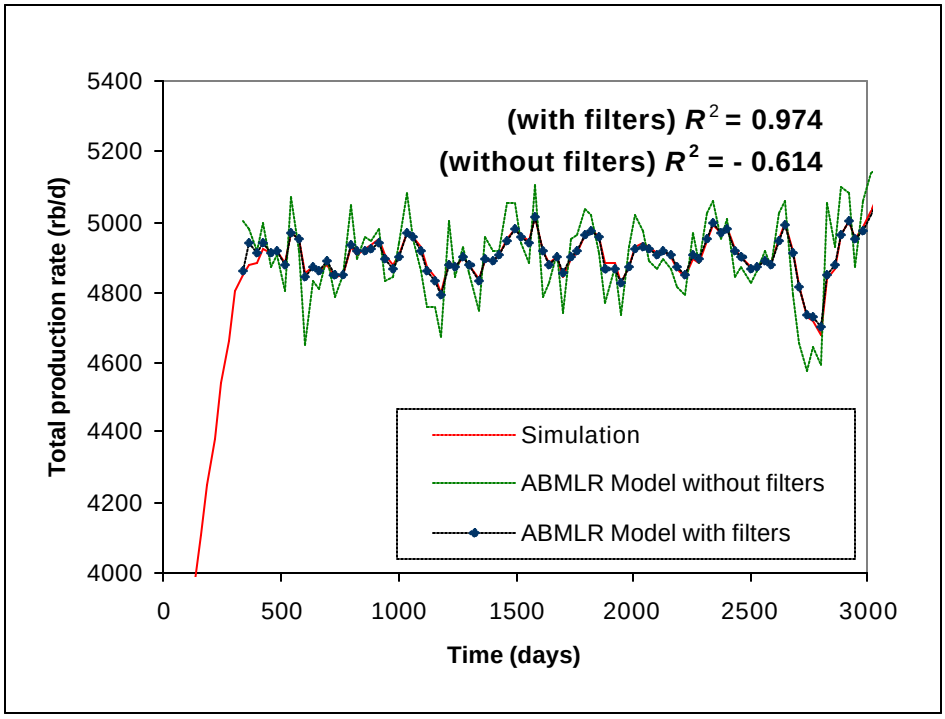

Figure 3.20 5x4 Synfield. Anisotropic reservoir. k_y = 1/40 k_x, case a. ABMLR with and without diffusivity filters. Comparison between modeled total liquid production rate and the total liquid production rate observed in simulation.

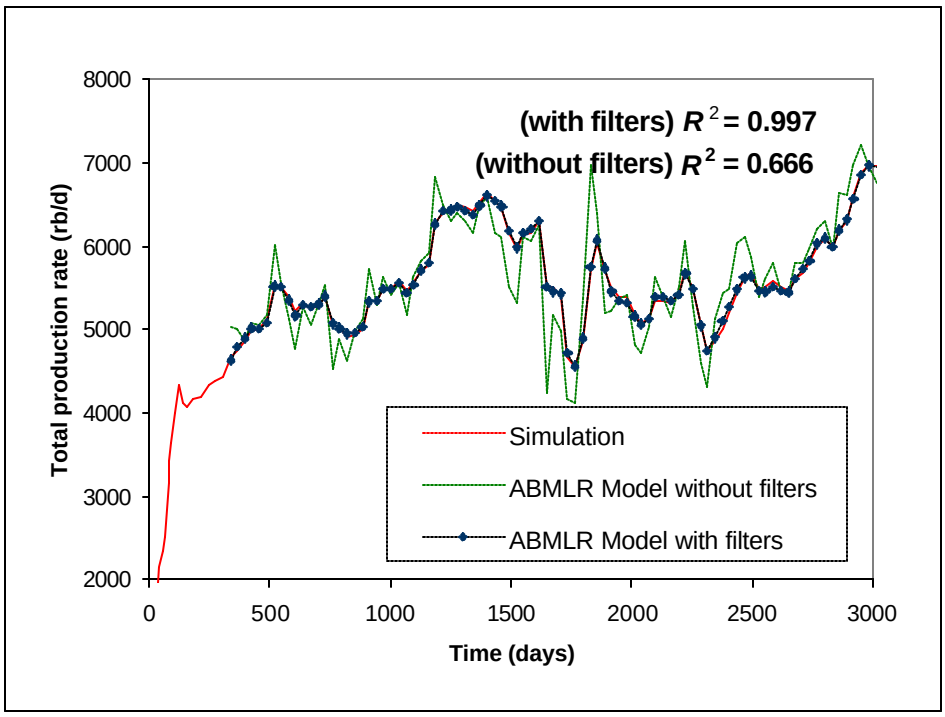

Figure 3.21 5x4 Synfield. Anisotropic reservoir. $k_y = 1/40\, k_x$, case b. ABMLR with and without diffusivity filters. Comparison between modeled total liquid production rate and the total liquid production rate observed in simulation.

Even when the reservoirs are the same in cases a and b, we get $R^2 = 0.974$ for case a and $R^2 = 0.997$ for case b. The nature of the injection rates causes this difference. In case a, the injection rates have less variability (ranging from 4,700 to 5,000 rb/d approximately) than in case b (ranging from 4,200 to 7,000 rb/d approximately). Since R^2 is inversely related to the variability of q, for results of similar quality, we expect a larger R^2 in case b than in case a. However, the weighting coefficients that describe the anisotropy do not vary significantly from one case to the other, which shows that results are consistent.

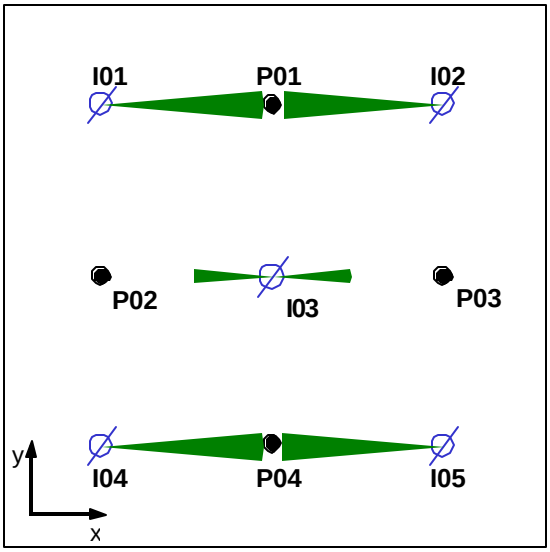

Figure 3.22 5x4 Synfield. Anisotropic reservoir. k_y = 1/40 k_x, case b. Representation of the non-reactive tracer results. Fraction of the non-reactive tracer injected in the i^{th} injector produced in the j^{th} producer. The length of the arrow is proportional to the fraction.

The injection of non-reactive tracers in the anisotropic reservoir shows that 100 percent of the tracer is produced in the *x*-oriented adjacent producers (Figure 3.22). This means that all the water injected in, for example, I02 is produced in P01. However, the weighting coefficients show that 13 percent of the water injected in I02 is supporting the production on P03 and 13 percent is supporting P02 (see Table 3.10). So, even when the anisotropy of the medium forces all of the injected water to be produced in wells connected in the *x* direction, for the case of I02, only 71 percent of its injection is supporting the production on P01.

3.1.4. Presence of a Sealing Fault

Two cases of reservoirs with sealing faults were run in the 5x4 Synfield. In the first case (case c) the sealing fault divides the entire reservoir into two hydraulically separated regions. Table 3.11 show the weighting coefficients obtained from ABMLR approach with diffusivity filters. Results are just as expected. The presence of a transmissibility barrier can be easily inferred from the weighting coefficients representation in Figure 3.23. The technique estimates the values of l corresponding to pairs of wells located on each side of the fault (e.g. l_{11}, l_{13}, l_{22}, l_{24}) to be either zero or very close to zero. This shows no communication between these wells based only on the analysis of the field injection and production rates.

Table 3.11 5x4 Synfield. Reservoir with a sealing fault, case c. ABMLR with diffusivity filters. Weighting coefficients l_{ij}. See Figure 3.23.

	P01	**P02**	**P03**	**P04**	S
I01	-0.01	0.63	-0.02	0.36	0.95
I02	0.50	-0.01	0.50	0.00	0.99
I03	0.00	0.56	0.02	0.51	1.09
I04	-0.01	0.50	-0.03	0.51	0.97
I05	0.34	-0.01	0.73	-0.01	1.05
S	0.81	1.67	1.21	1.37	
m_j **(rb/d)**	0.08	0.57	0.14	0.17	

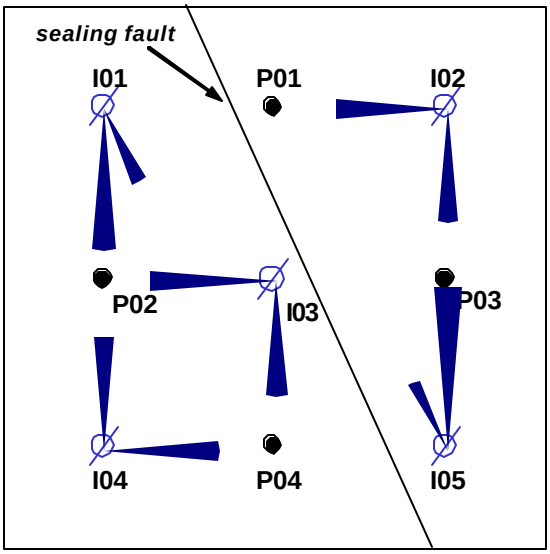

Figure 3.23 5x4 Synfield. Reservoir with a sealing fault, case c. ABMLR with diffusivity filters. Representation of the weighting coefficients l_{ij} shown in Table 3.11.

Even when very small, this is the first time we have encountered negative coefficients among the results. Negative weighting coefficients have no physical interpretation. The negative values of -0.01 to -0.03 are not considered significant; thus, they are considered as zeros for the interpretation of the connectivity between wells. Further discussion about negative coefficients is provided in section 3.2.2 and chapter 5.

Figure 3.24 presents the comparison between modeled total liquid production rate and the total liquid production rate observed in simulation. Note that, like in previous cases, the first 11 points have not been modeled because 12-month diffusivity filters are used (see section 2.5.3). R^2 = 0.991 is in the same order of

magnitude as the R^2 we obtained for the homogeneous reservoir using the same approach.

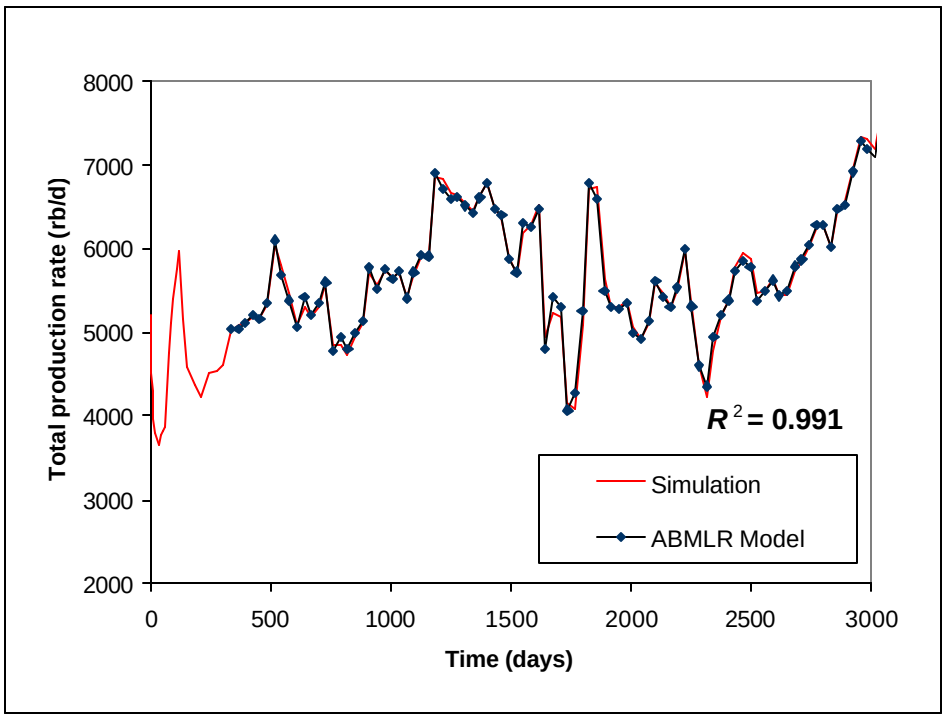

Figure 3.24 5x4 Synfield. Reservoir with a sealing fault, case c. ABMLR with diffusivity filters. Comparison between modeled total liquid production rate and the total liquid production rate observed in simulation.

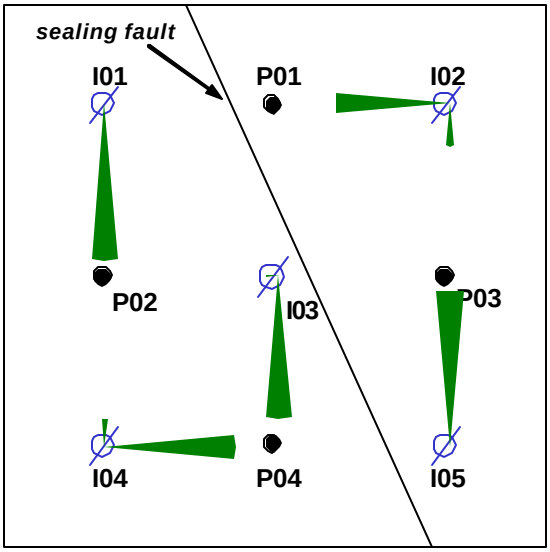

Figure 3.25 5x4 Synfield. Reservoir with a sealing fault, case c. Representation of the non-reactive tracer results.

The results of the injection of non-reactive tracer into the case c reservoir are presented in Figure 3.25. Almost no water injected in I03 is produced in P02. Similarly, almost no tracer injected in I04 is produced in P02. This could lead to an erroneous interpretation of some kind of permeability barrier between these wells. The reason for the apparent lack of communication between these wells is that all of the water injected in I01 is produced in P02, which pushes most of the water injected in I03 and in I04 towards P04. Since the ls only depend on reservoir properties and well location, the l_{32} that describes the connectivity between I03 and P02 is not affected by I01's injection rate (see Figure 3.23) while the tracer's response is. Another difference between the ls and tracers is the influence of I01 on P04 and of

I05 on P01, which are influences are shown by the weighting coefficients but not by the tracers.

The second case of a sealing fault in 5x4 Synfield (case d) has a sealing fault that crosses the reservoir partially, not completely dividing the field in two compartments. Table 3.12 and Figure 3.26 show the l values and representation respectively. Again, the fault can be inferred from the ls. I05 is not affected by the fault because the fault is approximately parallel to the direction on which the transients generated by I05 propagate. I01-P01 and I03-P01, which are adjacent wells, show virtually no connectivity. I03-P03 shows a small connectivity, because the fault does not completely separate these two wells. On the other hand, the tracer results (Figure 3.27) are very similar to those obtained in case c, which, again may lead to erroneous interpretations. The R^2 estimated for this case is also 0.991 (Figure 3.28).

Table 3.12 5x4 Synfield. Reservoir with a sealing fault, case d. ABMLR with diffusivity filters. Weighting coefficients l_{ij}. See Figure 3.26.

	P01	**P02**	**P03**	**P04**	S
I01	0.04	0.57	0.08	0.26	0.95
I02	0.44	0.06	0.38	0.11	0.99
I03	0.06	0.49	0.15	0.39	1.09
I04	0.05	0.43	0.11	0.38	0.97
I05	0.17	0.17	0.36	0.35	1.05
S	0.76	1.72	1.09	1.48	
m_j **(rb/d)**	0.01	0.70	0.09	0.29	

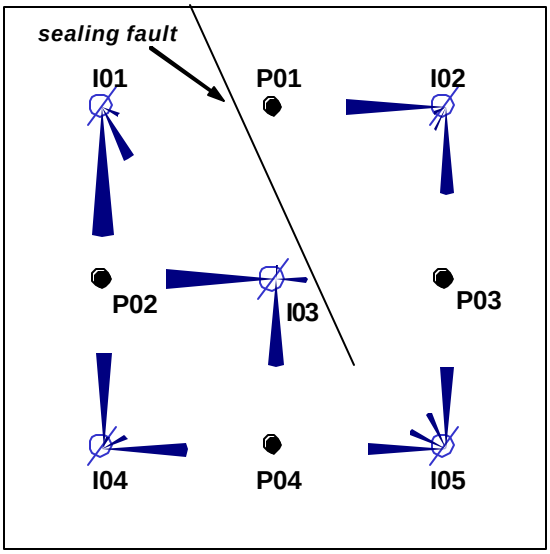

Figure 3.26 5x4 Synfield. Reservoir with a sealing fault, Case d. ABMLR with diffusivity filters. Representation of the weighting coefficients l_{ij} shown in Table 3.12.

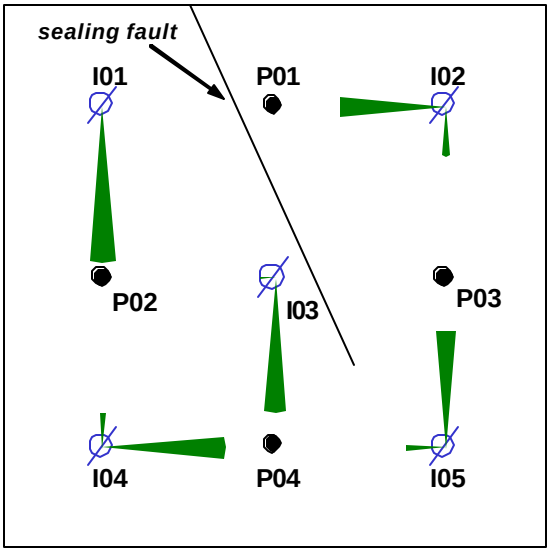

Figure 3.27 5x4 Synfield. Reservoir with a sealing fault, Case d. Representation of the non-reactive tracer results.

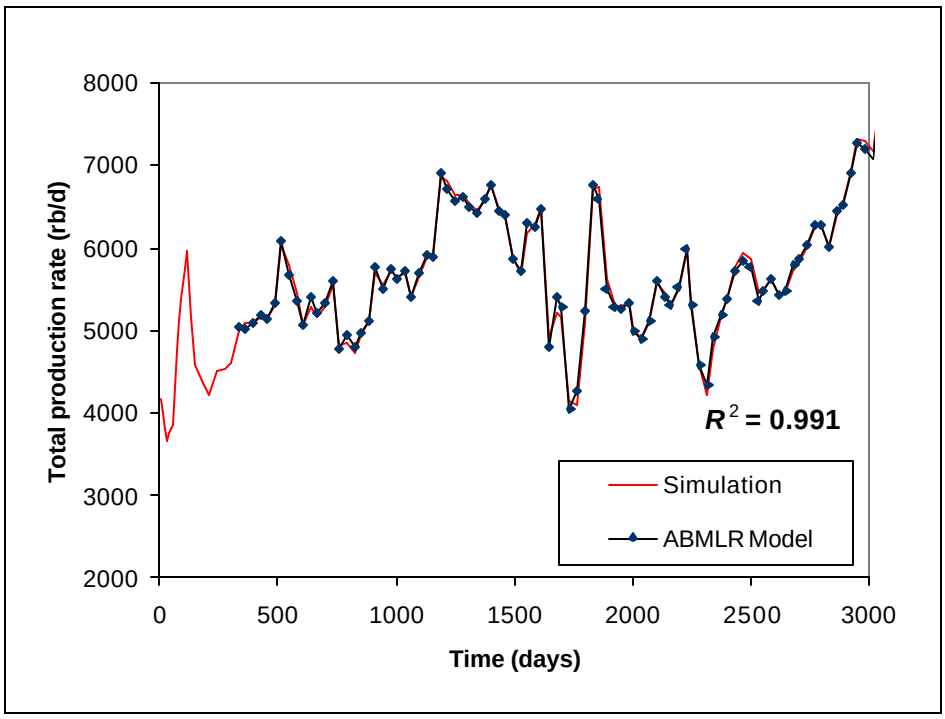

Figure 3.28 5x4 Synfield. Reservoir with a sealing fault, Case d. ABMLR with diffusivity filters. Comparison between modeled total liquid production rate and the total liquid production rate observed in simulation.

3.1.5. Vertical Heterogeneity

Two cases with vertical heterogeneity were run, again using the ABMLR approach with diffusivity filters: case e, with five continuous and isotropic layers, where the Dykstra-Parsons coefficient of heterogeneity (V) is 0.8 (Dykstra and Parsons, 1950), the minimum and maximum permeabilities are 3 and 70 md, the average permeability ($\bar{k}$) is 14.6 md and the vertical permeability (k_z) is 10 percent of the horizontal one (k_h); and case f, also with five layers, V = 0.9, permeabilities

ranging from 2 to 240 md, $\bar{k}$ = 21 md and $k_z = 0.1\ k_h$. Five layers were chosen in the vertically heterogeneous Synfields because one of the field cases has five layers.

Table 3.13 5x4 Synfield. Vertically heterogeneous reservoir. V = 0.8, case e. ABMLR with diffusivity filters. Weighting coefficients l_{ij}. See Figure 3.29.

	P01	**P02**	**P03**	**P04**	S
I01	0.32	0.32	0.15	0.15	0.95
I02	0.33	0.16	0.33	0.16	0.98
I03	0.27	0.28	0.28	0.29	1.13
I04	0.15	0.32	0.15	0.32	0.94
I05	0.18	0.17	0.36	0.35	1.06
S	1.26	1.26	1.27	1.27	
m_j **(rb/d)**	0.73	0.64	0.33	0.23	

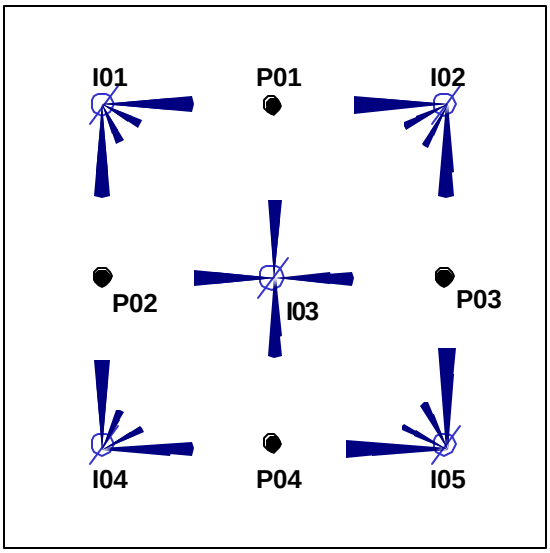

Figure 3.29 5x4 Synfield. Vertically heterogeneous reservoir. V = 0.8, case e. ABMLR with diffusivity filters. Representation of the weighting coefficients l_{ij} shown in Table 3.13.

Tables 3.13 and 3.14, and Figures 3.29 to 3.32 show the results from the use of ABMLR in these two cases. The results in both cases are very similar to those ones obtained in the homogeneous reservoir (Table 3.3 and Figure 3.9). Cases e and f show very good symmetry (A = 0.01239 and A = 0.00779, respectively) and excellent coefficients of determination (R^2 = 0.990 and R^2 = 0.996, respectively). We can conclude that vertical heterogeneity does not significantly affect the estimation and interpretation of the weighting coefficients.

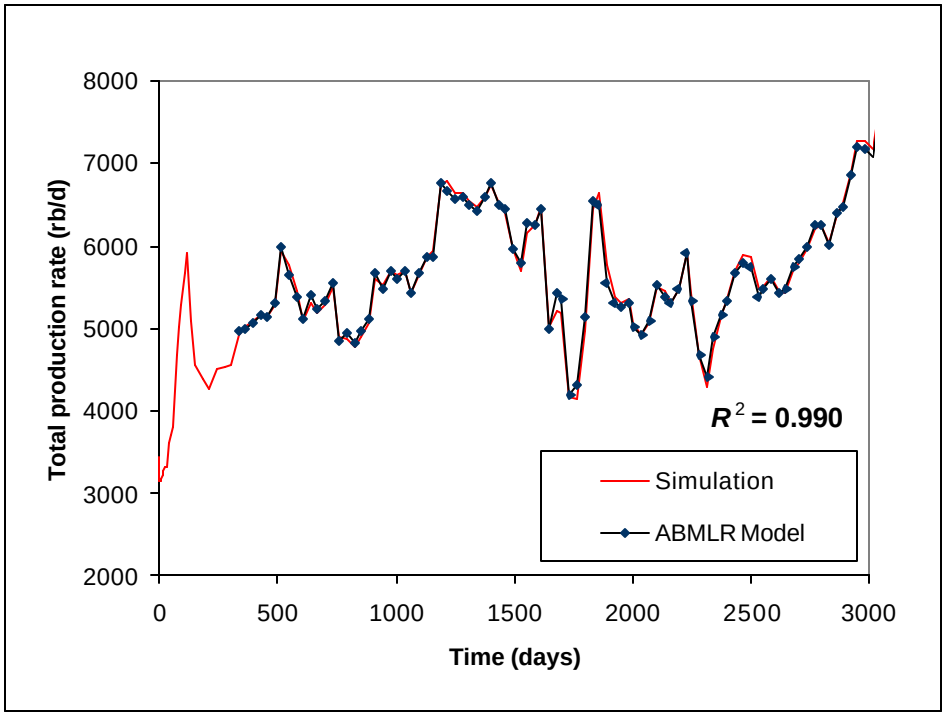

Figure 3.30 5x4 Synfield. Vertically heterogeneous reservoir. V = 0.8, case e. ABMLR with diffusivity filters. Comparison between modeled total liquid production rate and the total liquid production rate observed in simulation.

Table 3.14 5x4 Synfield. Vertically heterogeneous reservoir. $V = 0.9$, case f. ABMLR with diffusivity filters. Weighting coefficients l_{ij}. See Figure 3.31.

	P01	**P02**	**P03**	**P04**	S
I01	0.33	0.33	0.16	0.16	0.97
I02	0.33	0.17	0.33	0.17	0.99
I03	0.26	0.27	0.27	0.27	1.07
I04	0.16	0.32	0.16	0.32	0.96
I05	0.18	0.17	0.35	0.34	1.04
S	1.25	1.26	1.26	1.26	
m_j **(rb/d)**	0.48	0.42	0.24	0.18	

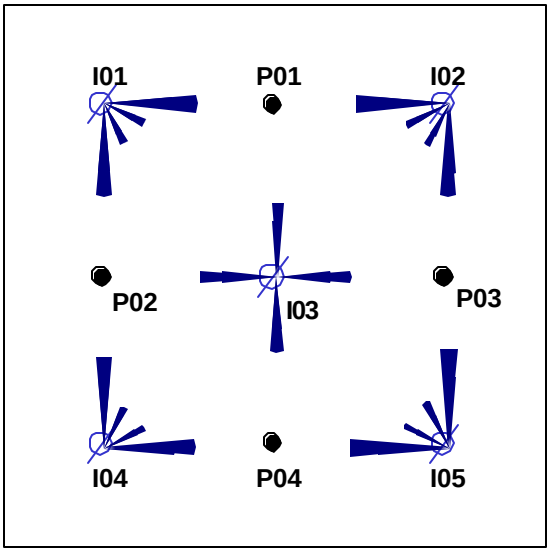

Figure 3.31 5x4 Synfield. Vertically Heterogeneous Reservoir. $V = 0.9$, case f. ABMLR With Diffusivity Filters. Representation of the weighting coefficients l_{ij} shown in Table 3.14.

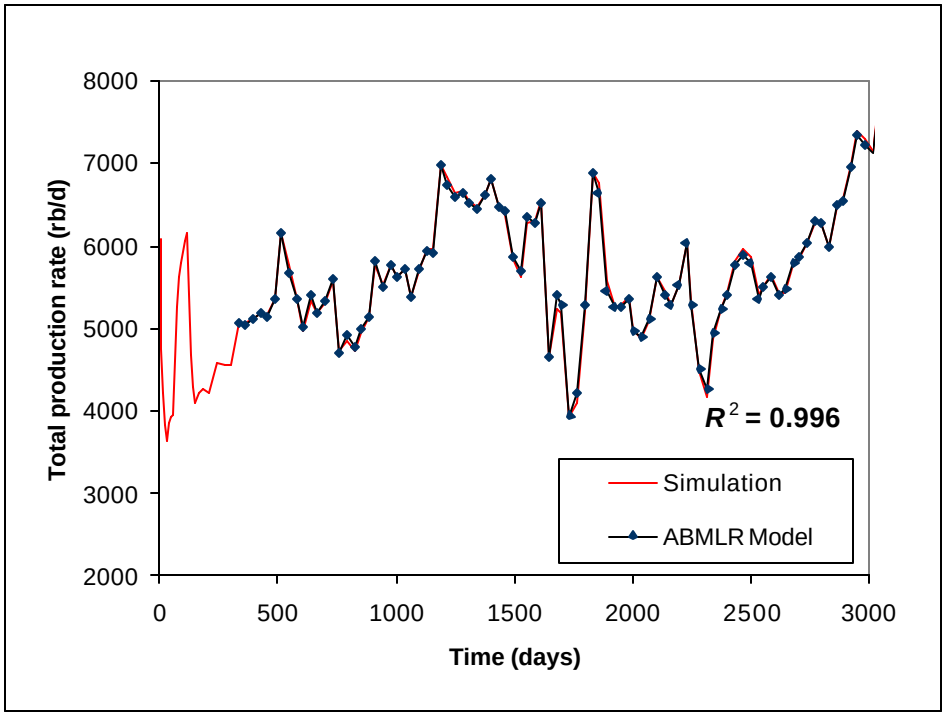

Figure 3.32 5x4 Synfield. Vertically heterogeneous reservoir. $V = 0.9$, case f. ABMLR with diffusivity filters. Comparison between modeled total liquid production rate and the total liquid production rate observed in simulation.

3.1.6. Spatial Heterogeneity

A reservoir with a channel of high permeability was simulated in the 5x4 Synfield. The results from the application of ABMLR with diffusivity filters are presented in Table 3.15 and Figure 3.33. The reservoir has a 10-md permeability. The shaded area in the figure represents a channel with a permeability of 50md.

Table 3.15 5x4 Synfield. Spatially heterogeneous reservoir. ABMLR with diffusivity filters. Weighting coefficients l_{ij}. See Figure 3.33.

	P01	P02	P03	P04	S
I01	0.19	0.23	0.09	0.41	0.92
I02	0.24	0.12	0.25	0.35	0.96
I03	0.15	0.21	0.13	0.65	1.14
I04	0.09	0.18	0.08	0.60	0.95
I05	0.10	0.11	0.21	0.69	1.11
S	0.78	0.85	0.75	2.71	
m_j **(rb/d)**	0.25	0.44	0.04	0.70	

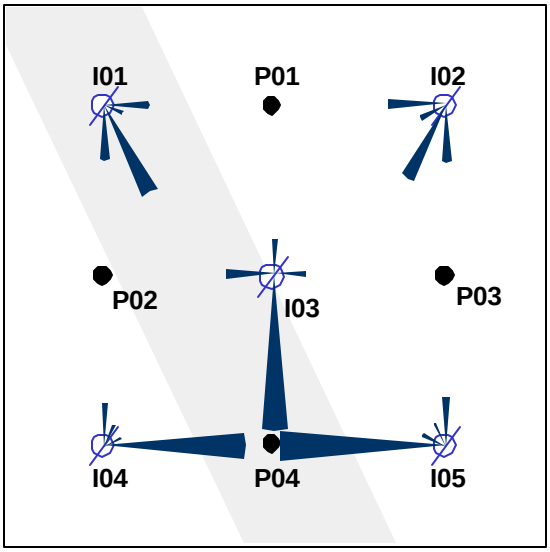

Figure 3.33 5x4 Synfield. Spatially heterogeneous reservoir. The permeability in the shaded area is 5 times the permeability in the rest of the reservoir. ABMLR with diffusivity filters. Representation of the weighting coefficients l_{ij} shown in Table 3.15.

Again, the comparison between modeled total liquid production rate and the total liquid production rate observed in simulation yields R^2 = 0.991 (Figure 3.34). In this case, the model appropriately describes the injection-production behavior and the

λs quantify the connectivity between wells accurately; but the interpretation of the presence of a channel in the position shown in the figure, only from the ls, is not so obvious. For example, the coefficients of the wells I01 and I02 are approximately symmetric, even when the channel is passing through I01 and not over I02.

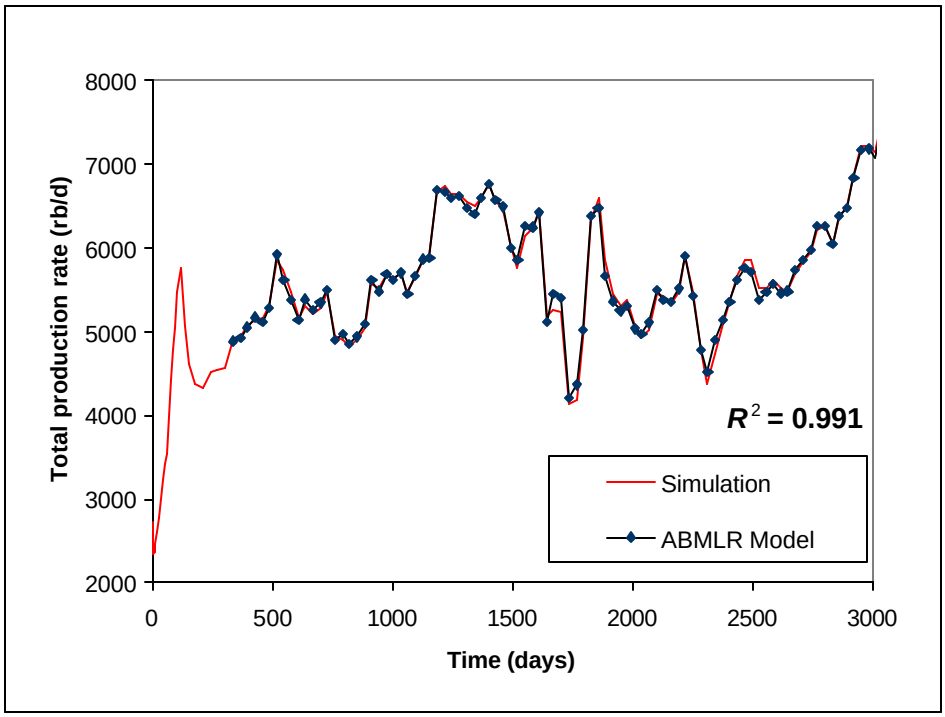

Figure 3.34 5x4 Synfield. Spatially heterogeneous reservoir. ABMLR with diffusivity filters. Comparison between modeled total liquid production rate and the total liquid production rate observed in simulation.

As in previous cases, the sum of the coefficients per injector is approximately equal to one, which is in good agreement with the instantaneously balanced condition of the field (Figure 3.35). In this case, the sum of weighting coefficients per producer

is approximately equal to 0.80 for producers P01, P02, and P03; but equal to 2.71 for P04, which is significantly different. While PO4 is the only producer that is within the high permeability channel, all of the injectors are relatively close to or within the channel, and their influence on P04 is transmitted through that high permeability medium. Indeed, for every injector, the weighting coefficient affecting P04 is larger than any of the coefficients affecting the other producers.

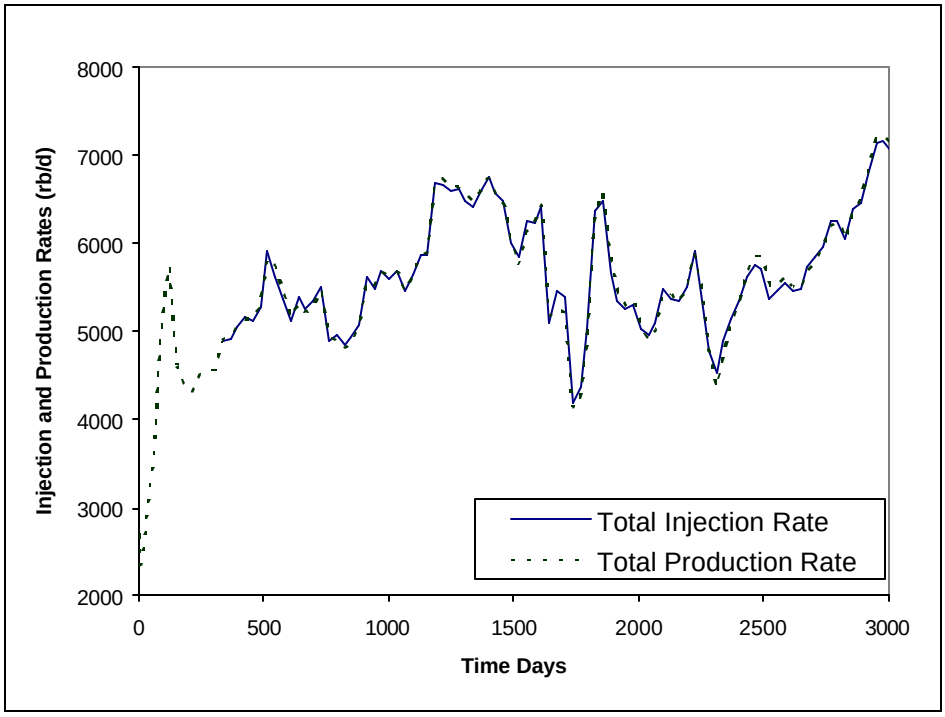

Figure 3.35 5x4 Synfield. Spatially heterogeneous reservoir. Total injection and production rates.

The interpretation of the presence of a channel from the non-reactive tracer results is also difficult (Figure 3.36). A comparison between the tracer results and the

*I*s shows that even when most of the water injected in I01 is produced in P02 (Figure 3.36), its injection is having more effect on P04 than on P02 (Figure 3.33).

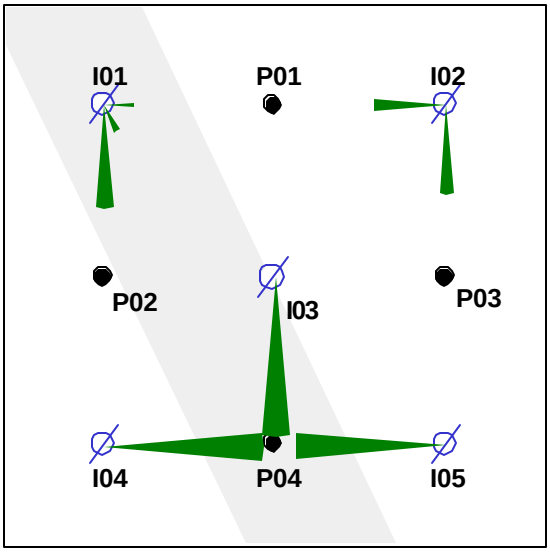

Figure 3.36 5x4 Synfield. Spatially heterogeneous reservoir. Representation of the non-reactive tracer results.

3.1.7. Other Cases

This section presents a list of other cases run using the 5x4 Synfield. The cases shown here do not add new conclusions to this work; so, a very brief discussion of each case is provided.

a. Homogeneous reservoir, set of different injection rates input (I)

Sixteen cases with different injection rate input were run on the homogeneous-isotropic 5x4 Synfield. The ABMLR approach was used. The input injection rates were generated using sinusoidal functions with random frequency and amplitude for each injector. The average injection rates were also randomly generated. The 16 cases yielded similar weighting coefficients, showing that the ls are independent of injection rates.

b. Homogeneous reservoir, large injection rate

ABMLR was tested in a homogeneous-isotropic reservoir with randomly generated sinusoidal injection rates. Two cases were run: in one case the average injection rate of I03 (center injector) was approximately two times the rate of the other injectors. In the other case, the average injection rate of I05 (corner injector) was approximately two times the rate of the other injectors. Results showed excellent symmetry and no dependence on the injection rates.

c. Homogeneous reservoir, set of different injection rates input (II)

A set of 11 cases with randomly generated injection rate input was run on the homogeneous-isotropic 5x4 Synfield. The ABMLR approach was used. In these cases, noise was incorporated to the signal so that the injection rates are not smooth. The resulting sets of weighting coefficients were similar in every case, showing that

the ls are independent of injection rates and do not require smooth functions as stimulus.

d. Anisotropic reservoir, $\mathbf{k_y = ¼\ k_x}$

ABMLR was tested in an anisotropic reservoir (k_y = ¼ k_x). Results were excellent.

e. Vertically heterogeneous reservoir, smaller permeability

ABMLR was tested in vertically heterogeneous reservoir (V = 0.8) with an average horizontal permeability of 1.46 md, ranging from 0.3 to 7 md. Results were good.

f. Homogeneous reservoir, smaller permeability

When ABMLR was tested in a homogeneous 5x4 Synfield with a horizontal permeability k_h = 1.5 md, results were poorer than the other tests in the homogeneous reservoirs. The smaller permeability (larger dissipation) affects the quality of the results and, even when the diffusivity filters improve the results, they do not solve the problem entirely. De Sant'Anna Pizarro presented a sensitivity analysis of the Spearman rank technique to total reservoir compressibility (De Sant'Anna Pizarro, 1998). Since dissipation is directly proportional to compressibility, that sensitivity analysis can be analogously used in this case to explain the poorer results.

g. IBMLR testing

IBMLR approach was run in the both anisotropic-reservoir cases (case a and case b, see section 3.1.3 for description) in the 5x4 Synfield. It was also tested in the reservoir with a sealing fault (case c, see section 3.1.4 for description). In both cases, results were excellent.

h. ABMLR and IBMLR together

A case with both the average-rate balance constraint (Eq. 2.10) and the instantaneous balance constraint (Eq. 2.14) was run in the homogeneous 5x4 Synfield. The solution matrix of this combined technique is similar to that one of the IBMLR approach (Eq. 2.18) with additional rows and columns that account for the average-rate balance condition. The entire set of l_{ij}s together with two sets of Lagrange multipliers (m_j and n_i) is solved in one step. Results were very poor. In order to satisfy both constraints, the Lagrange multipliers are significantly large and the symmetry presented by the weighting coefficients is very poor.

3.2. 25x16 SYNFIELD

The sensitivity of the technique to more wells in the field is analyzed using a homogeneous reservoir in a synthetic field of 25 injectors and 16 producers (25x16 Synfield) located following a 5-spot injection pattern (Figure 3.37).

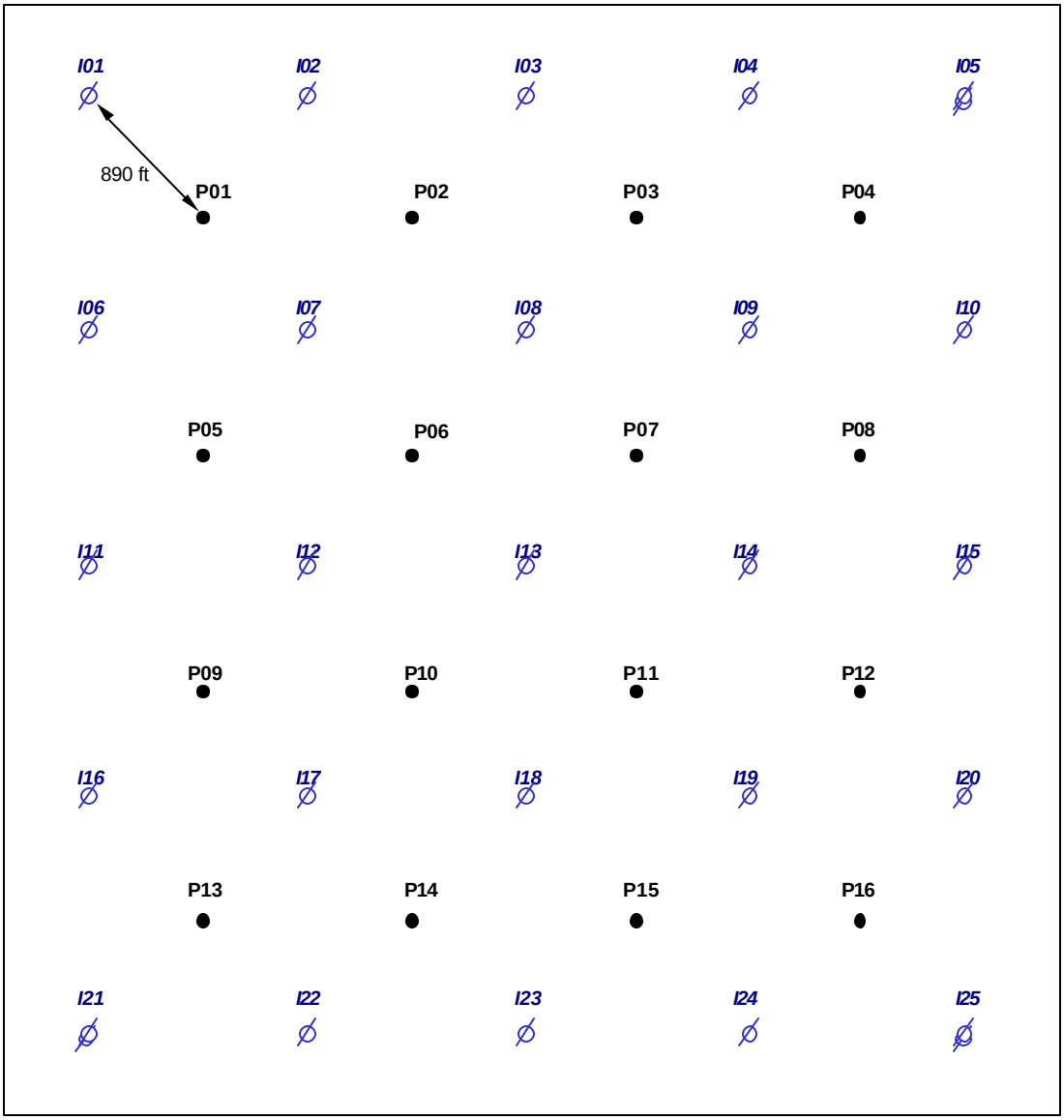

Figure 3.37 25x16 Synfield. Base map and well location.

As in the 5x4 Synfield, the input injection rates here (modified from actual data) are weakly spatially correlated; but in this case, a history of 65 data points is initially used. Likewise, the reservoir and fluid properties are similar to those used in

the 5x4 Synfield. The numerical simulator used is Eclipse 100, the gridding is 63x63x3, and the gridblocks are 90 ft in the *x* direction, by 90 ft in *y*, and 16 ft in *z*. This synthetic field is also used for comparison with the application of the technique to one of the field cases. Figure 3.38 shows that the injection and production rates are in balance.

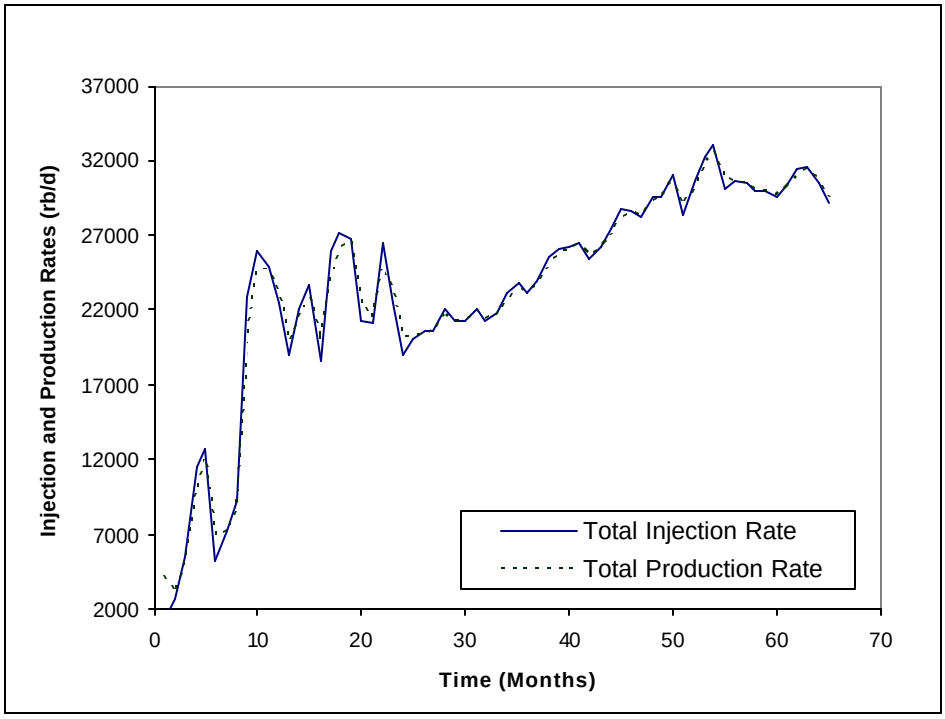

Figure 3.38 25x16 Synfield. Homogeneous reservoir. History of 65 data points. Total injection and production rates.

3.2.1. Homogeneous Reservoir

To apply ABMLR to the 25x16 Synfield, a system of 26 equations and 26 unknowns must be solved for each producer (Eq. 2.13). In the end, the solution yields 400 (25x16) weighting coefficients that quantify the connectivity between every injector-producer pair in the field. Sixteen Lagrange multipliers m_j are also estimated.

Again, since the reservoir is homogeneous, we expect the weighting coefficients to be equal across planes of symmetry. Using the major planes of symmetry, the field can be divided into 8 regions with similar characteristics (Figure 3.39). There are 6 injectors (e.g. I01, I02, I03, I08, and I13) and 3 producers (e.g. P01, P02, and P06) in each region. Some of the producers belong to two of the regions (e.g. P01 and P06) because they are exactly on the boundary of the plane of symmetry. So, injectors located in similar positions within each region should have similar weighting coefficients. For example, we expect the weighting coefficients of I02 be equal to those of I04, I06, I10, I16, I20, I22, and I24 when related to producers that are similarly located. In other words, comparing injectors I02 and I16, which are in the same relative location within a region, we expect $l_{2\text{-}1} = l_{16\text{-}13}$, $l_{2\text{-}2} = l_{16\text{-}9}$, $l_{2\text{-}6} = l_{16\text{-}10}$, $l_{2\text{-}5} = l_{16\text{-}14}$, and so on. In this homogeneous 25x16 Synfield, the combination of these 6 types of injectors and 3 types of producers gives 55 groups of similar well-pairs (Table 3.16). For example, one of the groups, named AA, is formed by the four well pairs of corner injectors and adjacent producers; the well pairs I01-P01, I05-P04,

I21-P13, and I25-P16 constitute this group. The remaining groups are determined similarly, grouping well pairs with similar relative location in the field. Using Eq. 3.1 we can estimate *A*.

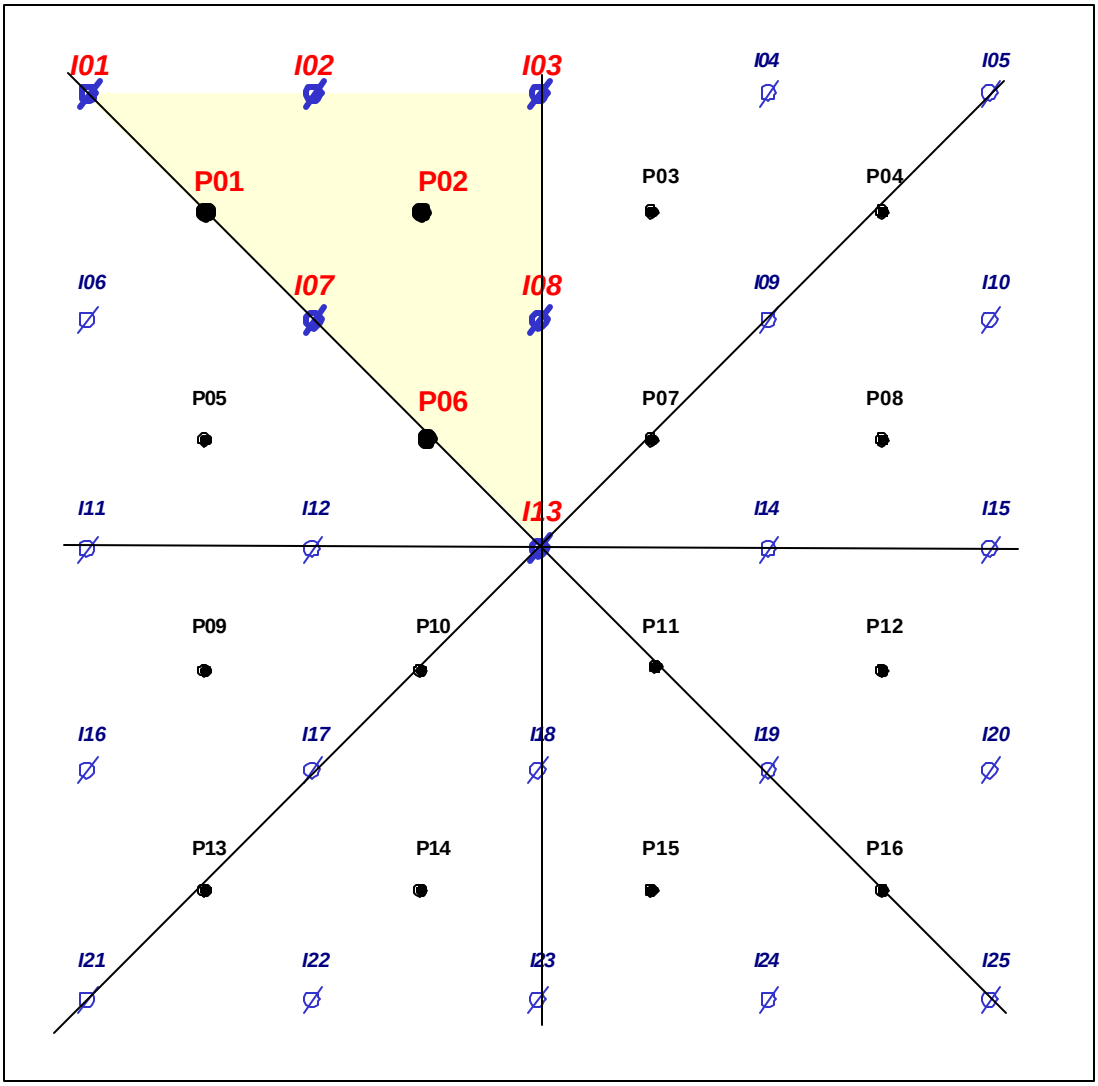

Figure 3.39 25x16 Synfield. Planes of symmetry in homogeneous reservoir. There are 6 types of injectors and 3 types of producers in the field.

Table 3.16 25x16 Synfield. Homogeneous reservoir. Well-pair groups determined by planes of symmetry. Each group is denoted by two letters. Well pairs within the same group should have similar weighting coefficients.

	P01	P02	P03	P04	P05	P06	P07	P08	P09	P10	P11	P12	P13	P14	P15	P16
I01	AA	AC	AG	AI	AC	AB	AH	AJ	AG	AH	AD	AF	AI	AJ	AF	AE
I02	FA	FG	FI	FE	FH	FB	FK	FL	FM	FN	FC	FJ	FF	FO	FP	FD
I03	BB	BA	BA	BB	BD	BC	BC	BD	BF	BE	BE	BF	BH	BG	BG	BH
I04	FE	FI	FG	FA	FL	FK	FB	FH	FJ	FC	FN	FM	FD	FP	FO	FF
I05	AI	AG	AC	AA	AJ	AH	AB	AC	AF	AD	AH	AG	AE	AF	AJ	AI
I06	FA	FH	FM	FF	FG	FB	FN	FO	FI	FK	FC	FP	FE	FL	FJ	FD
I07	CA	CC	CG	CI	CC	CB	CH	CJ	CG	CH	CD	CF	CI	CJ	CF	CE
I08	EB	EA	EA	EB	ED	EC	EC	ED	EF	EE	EE	EF	EH	EG	EG	EH
I09	CI	CG	CC	CA	CJ	CH	CB	CC	CF	CD	CH	CG	CE	CF	CJ	CI
I10	FF	FM	FH	FA	FO	FN	FB	FG	FP	FC	FK	FI	FD	FJ	FL	FE
I11	BB	BD	BF	BH	BA	BC	BE	BG	BA	BC	BE	BG	BB	BD	BF	BH
I12	EB	ED	EF	EH	EA	EC	EE	EG	EA	EC	EE	EG	EB	ED	EF	EH
I13	DA	DC	DC	DA	DC	DB	DB	DC	DC	DB	DB	DC	DA	DC	DC	DA
I14	EH	EF	ED	EB	EG	EE	EC	EA	EG	EE	EC	EA	EH	EF	ED	EB
I15	BH	BF	BD	BB	BG	BE	BC	BA	BG	BE	BC	BA	BH	BF	BD	BB
I16	FE	FL	FJ	FD	FI	FK	FC	FP	FG	FB	FN	FO	FA	FH	FM	FF
I17	CI	CJ	CF	CE	CG	CH	CD	CF	CC	CB	CH	CJ	CA	CC	CG	CI
I18	EH	EG	EG	EH	EF	EE	EE	EF	ED	EC	EC	ED	EB	EA	EA	EB
I19	CE	CF	CJ	CI	CF	CD	CH	CG	CJ	CH	CB	CC	CI	CG	CC	CA
I20	FD	FJ	FL	FE	FP	FC	FK	FI	FO	FN	FB	FG	FF	FM	FH	FA
I21	AI	AJ	AF	AE	AG	AH	AD	AF	AC	AB	AH	AJ	AA	AC	AG	AI
I22	FF	FO	FP	FD	FM	FN	FC	FJ	FH	FB	FK	FL	FA	FG	FI	FE
I23	BH	BG	BG	BH	BF	BE	BE	BF	BD	BC	BC	BD	BB	BA	BA	BB
I24	FD	FP	FO	FF	FJ	FC	FN	FM	FL	FK	FB	FH	FE	FI	FG	FA
I25	AE	AF	AJ	AI	AF	AD	AH	AG	AJ	AH	AB	AC	AI	AG	AC	AA

Table 3.17 and Figure 3.40 show the estimated l_{ij}s and m_js obtained from the application of ABMLR with diffusivity filters. The results, in general, are as expected with large ls for close pairs, smaller ls for more distant pairs, and larger weighting coefficients for injectors at the boundaries. However, results are poorer since some asymmetries can be detected.

Table 3.17 25x16 Synfield. Homogeneous reservoir. ABMLR with diffusivity filters using 65 data points, with O_d = 2.04 (see 3.2.2). Weighting coefficients l_{ij}. See Figure 3.40.

	P01	P02	P03	P04	P05	P06	P07	P08	P09	P10	P11	P12	P13	P14	P15	P16	S
I01	0.27	0.05	-0.04	-0.06	0.06	-0.01	-0.05	-0.07	-0.02	-0.05	-0.06	-0.06	-0.03	-0.05	-0.03	0.00	**-0.14**
I02	0.19	0.16	0.04	-0.01	0.04	0.02	-0.02	-0.04	-0.03	-0.03	-0.03	-0.05	-0.06	-0.05	-0.03	-0.05	**0.08**
I03	0.10	0.18	0.14	0.03	0.04	0.05	0.03	0.00	-0.01	-0.02	-0.01	-0.01	-0.02	-0.04	-0.04	-0.02	**0.40**
I04	-0.03	0.01	0.15	0.18	-0.04	-0.01	0.01	0.02	-0.02	0.00	0.00	-0.02	-0.02	0.01	-0.01	-0.03	**0.20**
I05	0.04	0.08	0.16	0.39	0.01	0.02	0.07	0.15	-0.03	0.00	0.04	0.06	-0.04	-0.01	0.03	0.02	**1.00**
I06	0.38	0.22	0.16	0.15	0.31	0.17	0.13	0.13	0.16	0.10	0.08	0.10	0.12	0.07	0.07	0.08	**2.44**
I07	0.15	0.12	0.03	0.00	0.14	0.11	0.03	0.01	0.09	0.06	0.03	0.02	0.08	0.06	0.04	0.03	**1.01**
I08	0.05	0.14	0.15	0.08	0.07	0.13	0.12	0.07	0.11	0.11	0.07	0.04	0.14	0.13	0.08	0.04	**1.51**
I09	0.03	0.06	0.15	0.17	0.02	0.04	0.13	0.14	0.00	0.01	0.03	0.04	-0.01	0.00	0.01	0.01	**0.81**
I10	0.11	0.11	0.14	0.28	0.07	0.09	0.13	0.26	0.02	0.04	0.09	0.14	0.00	0.02	0.06	0.10	**1.64**
I11	0.11	0.08	0.10	0.13	0.23	0.10	0.07	0.08	0.23	0.07	0.03	0.06	0.13	0.05	0.05	0.10	**1.63**
I12	0.09	0.07	0.05	0.03	0.15	0.14	0.06	0.03	0.14	0.13	0.05	0.03	0.05	0.04	0.03	0.01	**1.09**
I13	0.00	0.02	0.02	0.01	0.03	0.10	0.10	0.03	0.05	0.12	0.11	0.03	0.05	0.06	0.05	0.03	**0.80**
I14	0.02	0.03	0.06	0.08	0.02	0.04	0.13	0.16	0.04	0.05	0.13	0.15	0.04	0.04	0.06	0.08	**1.13**
I15	0.02	0.03	0.05	0.10	0.02	0.03	0.08	0.22	0.01	0.03	0.08	0.22	0.02	0.01	0.03	0.09	**1.03**
I16	0.05	0.03	0.02	0.01	0.11	0.06	0.04	0.02	0.22	0.08	0.05	0.04	0.25	0.09	0.06	0.06	**1.19**
I17	0.04	0.03	0.03	0.02	0.06	0.05	0.04	0.03	0.14	0.12	0.05	0.03	0.16	0.14	0.06	0.03	**1.02**
I18	0.03	0.03	0.03	0.03	0.03	0.05	0.05	0.04	0.05	0.12	0.12	0.05	0.06	0.13	0.14	0.07	**1.02**
I19	0.01	0.01	0.01	0.02	0.01	0.02	0.04	0.05	0.01	0.04	0.13	0.15	0.02	0.05	0.16	0.18	**0.91**
I20	0.04	0.05	0.06	0.07	0.03	0.04	0.06	0.11	0.04	0.05	0.08	0.24	0.03	0.05	0.11	0.28	**1.33**
I21	0.06	0.04	0.03	0.02	0.07	0.04	0.02	0.01	0.15	0.08	0.03	0.01	0.37	0.15	0.05	0.02	**1.16**
I22	0.02	0.03	0.02	0.02	0.03	0.03	0.02	0.01	0.06	0.05	0.03	0.01	0.21	0.17	0.06	0.02	**0.79**
I23	-0.01	-0.02	-0.01	0.00	0.01	0.01	0.01	0.02	0.03	0.06	0.08	0.07	0.07	0.20	0.24	0.13	**0.90**
I24	-0.01	-0.02	-0.03	-0.03	0.00	0.00	-0.01	-0.01	0.01	0.04	0.05	0.05	0.03	0.08	0.17	0.18	**0.50**
I25	0.04	0.03	0.02	0.02	0.03	0.03	0.03	0.04	0.04	0.06	0.08	0.14	0.07	0.10	0.17	0.36	**1.24**
m_j **(rb/d)**	-0.30	-0.23	-0.27	-0.34	-0.18	-0.14	-0.19	-0.28	-0.03	-0.05	-0.16	-0.26	-0.01	-0.07	-0.19	-0.31	
S	**1.78**	**1.57**	**1.54**	**1.74**	**1.56**	**1.35**	**1.32**	**1.52**	**1.51**	**1.30**	**1.34**	**1.55**	**1.70**	**1.50**	**1.58**	**1.81**	

The estimation of the asymmetry coefficient yields A = 0.0392 which is approximately 4 times larger than the asymmetry obtained using ABMLR with diffusivity filters in the 5x4 Synfield (see Table 3.6). For example, we expect the ls of I02 and I06 be similar because of their relative location in the field, but they are significantly different.

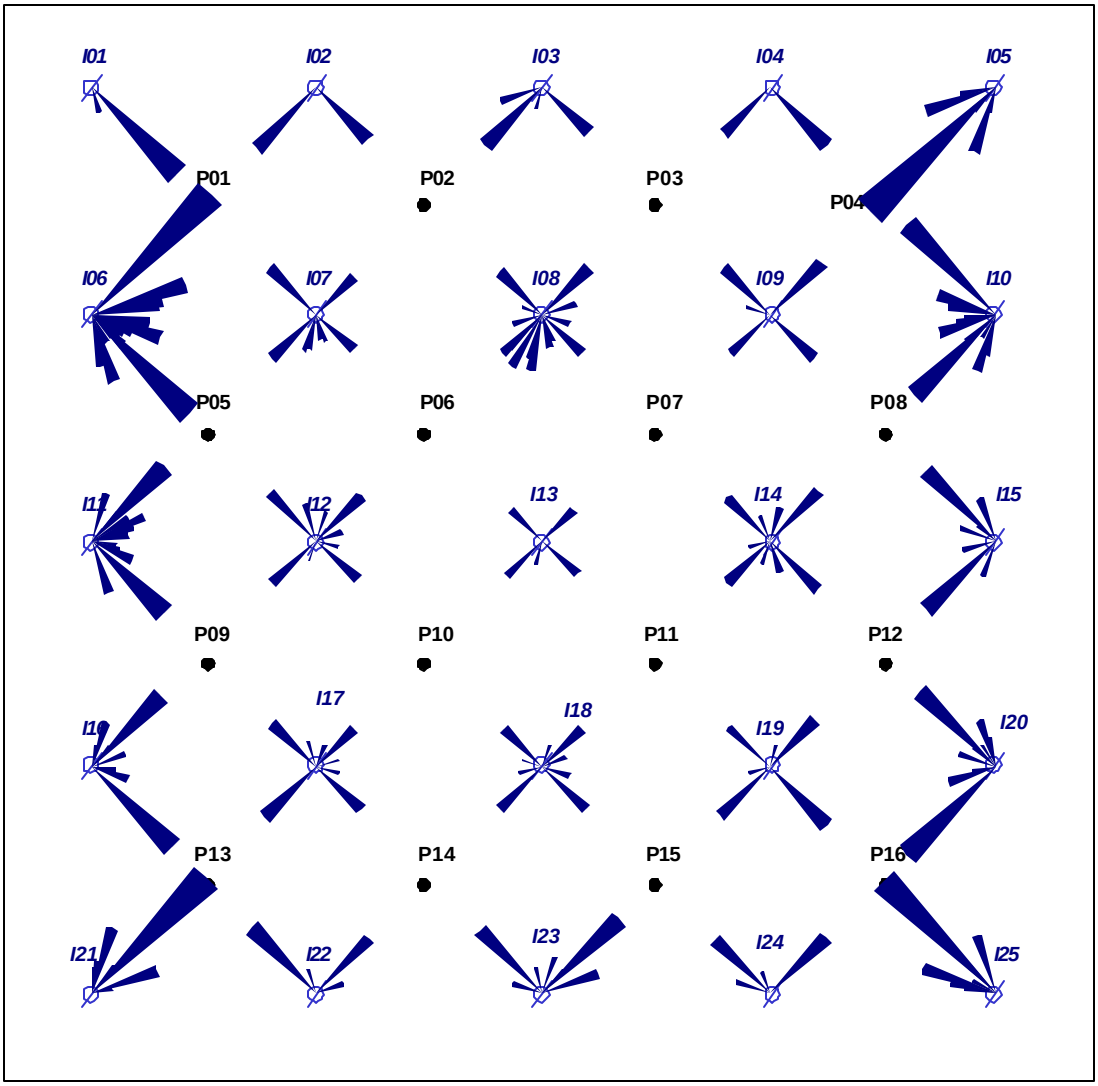

Figure 3.40 25x16 Synfield. Homogeneous reservoir. ABMLR with diffusivity filters using 65 data points, with O_d = 2.04 (see 3.2.2). Representation of the positive weighting coefficients l_{ij} shown in Table 3.17.

The same can be said about the I01 and I05, and several other pairs of similarly located wells. Moreover, in previous cases solved using ABMLR, we observed that the sum of ls per injector is approximately equal to one, in agreement

with the instantaneous balance condition. In this case, the sum of ls is significantly different from one for several injectors. In addition, we find that many weights are negative, with some of them as large as -0.07, which have no physical meaning. Negative weights are not plotted in Figure 3.40.

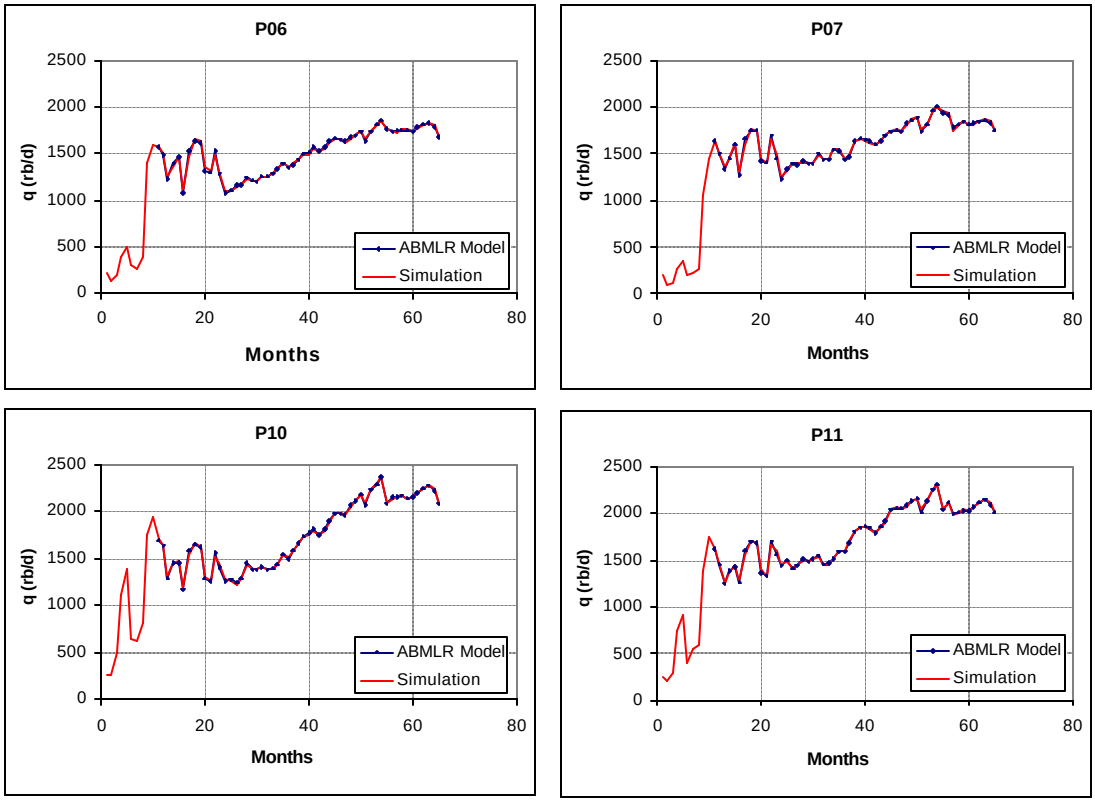

Figure 3.41 25x16 Synfield. Homogeneous reservoir. ABMLR with diffusivity filters using 65 data points, with O_d = 2.04 (see 3.2.2). Comparison between modeled liquid production rate and the liquid production rate observed in simulation in the four wells at the center of the Synfield.

In a large 5-spot injection pattern, the wells close to the center of a homogeneous field would present almost symmetric weighting coefficients.

Furthermore, in an infinitely large 5-spot pattern, all the wells in a homogeneous field would have the same weighting coefficients. When analyzing production rates, we will focus on the four wells at the center of the Synfield (P06, P07, P10, and P11), because they are the ones that are less affected by the boundaries. Besides, one of the field cases presented in this work (section 5.1) has a 5-spot injection pattern with 25 injectors, 16 producers and open boundaries, and in that case too, we focus on the center producers. So, for comparison reasons only, we will use the production rates of the four wells at the center of the Synfield.

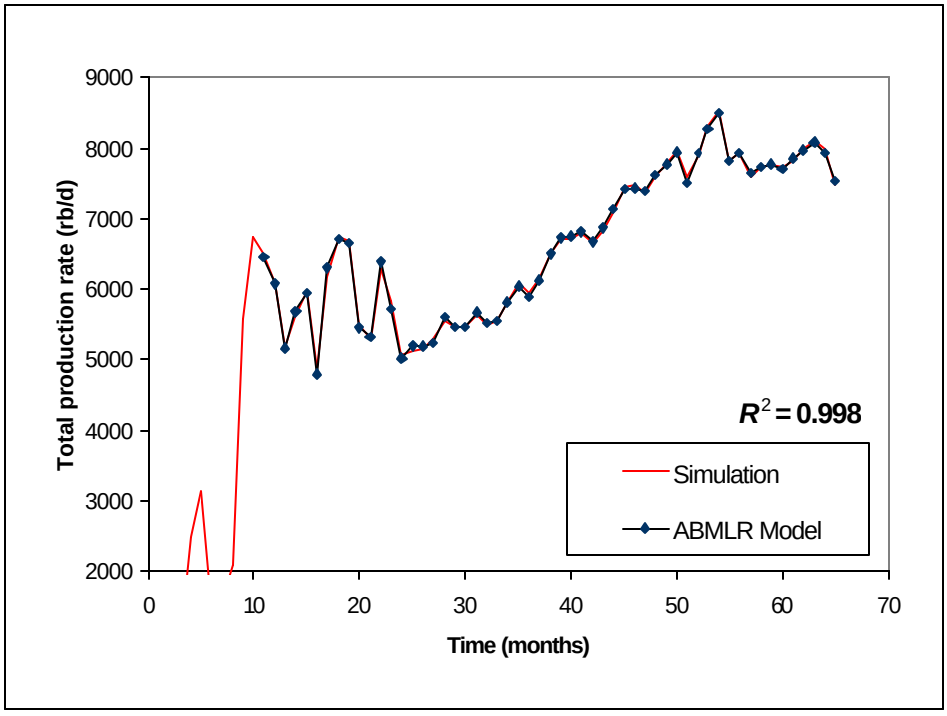

Figure 3.42 25x16 Synfield. Homogeneous reservoir. ABMLR with diffusivity filters using 65 data points, with O_d = 2.04 (see 3.2.2). Comparison between modeled total liquid production rate and the total liquid production rate observed in simulation (four center wells).

Despite the asymmetries mentioned in the previous paragraph, the model adjusts very well to the observed production rate (Figure 3.41); we get R^2 = 0.998 for the total production rate of the four wells at the center (Figure 3.42). This is a clear example were a large value of R^2 alone is not an indicator of appropriateness of the model.

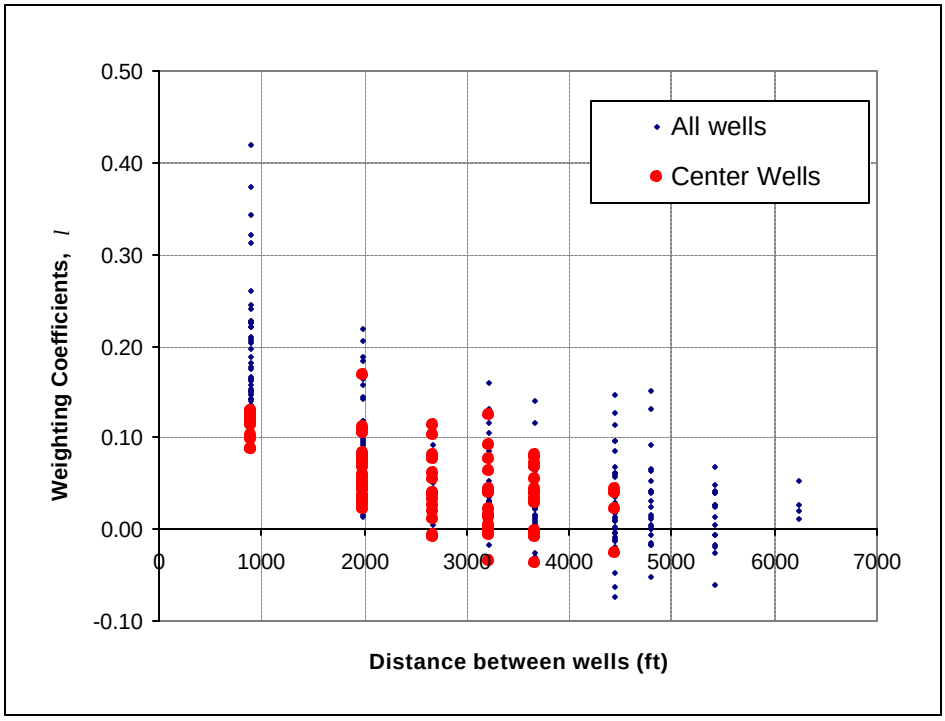

Figure 3.43 25x16 Synfield. Homogeneous reservoir. ABMLR with diffusivity filters using 65 data points, with O_d = 2.04 (see 3.2.2). Weighting coefficients l, vs distance between wells. The large dots correspond to the four wells at the center of the Synfield.

Figure 3.43 shows that the closest pairs show the highest weighting coefficients, and in general the ls are smaller for more distant wells, but some of the

coefficients are negative. Using 65 data points in the 25x16 Synfield, results are poorer than using 100 points in the 5x4 Synfield. The use of fewer data points and more injectors are the cause for the unsatisfactory results. These reasons are discussed in the following section.

3.2.2. Using a Longer Injection History

Equation 2.2 describes the variability of the slope in a bivariate linear regression model of the type $\hat{q}_j = b_{0j} + b_{1j} i_1$ where M is the total number of data points. The ratio of the two summations

$$\frac{\sum_{m=1}^{M} \left(q^{(m)} - \hat{q}^{(m)} \right)^2}{\sum_{m=1}^{M} \left(i_1^{(m)} - \bar{i}_1 \right)^2}$$

does not strongly depend on M; thus, the variability of b_{1j} is approximately inversely proportional to (M-2). Extending this analysis to the multivariate linear regression (either balanced or unbalanced), the variability of the weighting coefficients will be inversely proportional to (M-I-1). In other words, the more data points, the lower the variability of the slope and the more precise the determination of the weighting coefficients. Furthermore, since I is subtracted from M in the denominator, the precision of the results will also improve with fewer injectors.

Let's apply this concept to the 25x16 Synfield. In the MLR and the ABMLR models (Eqs. 2.5, 2.8, and 2.13), the number of unknowns per producer (b_{ij} or l_{ij}) is given by the number of injector-producer pairs plus one independent term (b_{0j} in MLR or m_j in BMLR). There are $(I+1)$ unknowns per producer. In the 25x16 Synfield, out of a total history of 65 data points, the first 12 data points were not used for the analysis because a 12-month diffusivity filter is used (see section 2.5). So, the effective number of data points is 53. Then, since we have 25 injectors, we have 26 (25 + 1) unknowns and 53 data points to solve the problem. The system is overdetermined.

We define an overdetermination coefficient (O_d) of a system as the number of effective data points divided by the number of unknowns, or

$$O_d = \frac{M_e}{(I+1)} \tag{3.2}$$

For the 25x16 Synfield, with 53 effective data points, we calculate O_d = 2.04. The application of the ABMLR model yields A = 0.03921. According to Eq. 2.2 and its extension to multivariate linear regression, an increase in the number of data points or, equivalently, an increase in O_d, should give more precise weighting coefficients or, in other words, better symmetry.

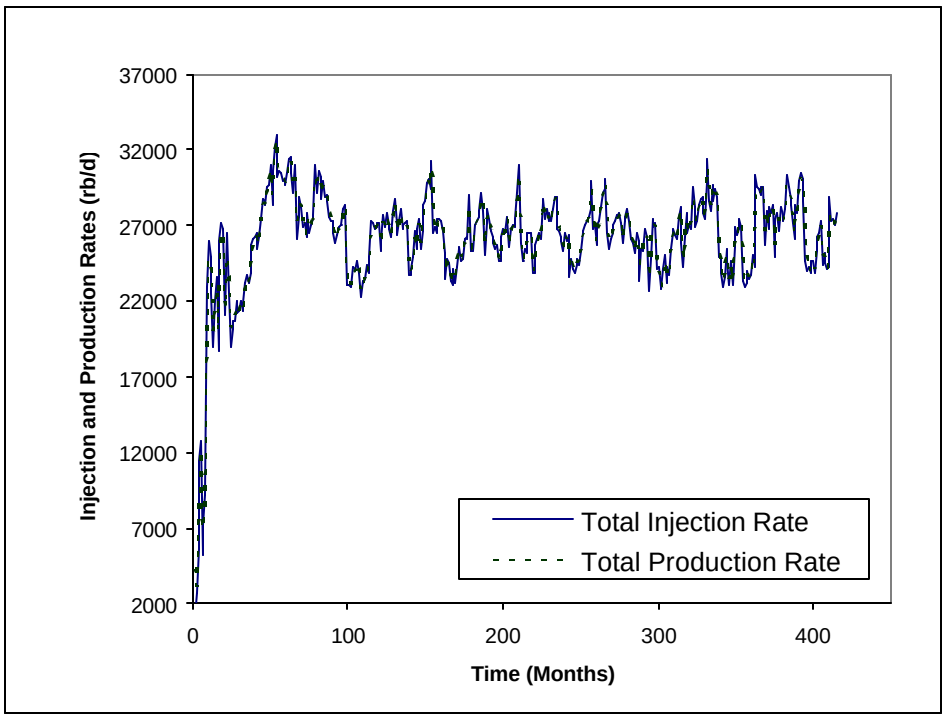

Figure 3.44 25x16 Synfield. Homogeneous reservoir. History of 415 data points. Total injection and production rates.

The increase of the number of total data points in the homogeneous 25x16 Synfield to 415 data points (Figure 3.44), with 390 effective data points after the first 25 points are omitted for the analysis, gives O_d = 15. Table 3.18 and Figure 3.45 show the weighting coefficients obtained with 390 effective data points. The figure shows excellent symmetry and the asymmetry coefficient has been lowered by almost ten times to A = 0.00492. Accordingly, the ls per injector approximately add up to one, which is in agreement with the injection-production balance shown in Figure

3.44. Likewise, there are no negative weighting coefficients and R^2 = 0.995 (Figure 3.46). Results are excellent.

Table 3.18 25x16 Synfield. Homogeneous reservoir. ABMLR with diffusivity filters using 415 data points, with O_d = 15. Weighting coefficients l_{ij}. See Figure 3.45.

	P01	P02	P03	P04	P05	P06	P07	P08	P09	P10	P11	P12	P13	P14	P15	P16	S
I01	0.36	0.13	0.04	0.01	0.13	0.07	0.02	0.01	0.04	0.03	0.02	0.01	0.03	0.02	0.02	0.01	**0.93**
I02	0.26	0.22	0.09	0.04	0.10	0.08	0.04	0.03	0.04	0.03	0.02	0.02	0.02	0.01	0.01	0.01	**1.04**
I03	0.10	0.21	0.21	0.10	0.05	0.06	0.07	0.05	0.02	0.02	0.02	0.02	0.01	0.00	0.01	0.01	**0.95**
I04	0.04	0.08	0.21	0.25	0.02	0.04	0.07	0.09	0.02	0.02	0.03	0.03	0.02	0.02	0.02	0.02	**0.98**
I05	0.02	0.04	0.13	0.35	0.01	0.02	0.06	0.13	0.01	0.01	0.02	0.05	0.01	0.01	0.01	0.02	**0.91**
I06	0.27	0.10	0.05	0.03	0.23	0.08	0.04	0.02	0.10	0.05	0.03	0.02	0.06	0.04	0.03	0.02	**1.17**
I07	0.18	0.16	0.06	0.03	0.16	0.13	0.05	0.03	0.06	0.05	0.03	0.02	0.03	0.02	0.02	0.01	**1.04**
I08	0.06	0.14	0.14	0.06	0.05	0.12	0.12	0.05	0.02	0.03	0.03	0.02	0.01	0.01	0.01	0.01	**0.89**
I09	0.03	0.06	0.15	0.17	0.02	0.04	0.13	0.15	0.01	0.02	0.04	0.05	0.01	0.01	0.02	0.02	**0.95**
I10	0.02	0.04	0.09	0.25	0.01	0.03	0.07	0.22	0.01	0.02	0.04	0.08	0.00	0.01	0.03	0.04	**0.96**
I11	0.09	0.05	0.03	0.03	0.20	0.07	0.03	0.02	0.19	0.06	0.03	0.02	0.08	0.04	0.02	0.01	**0.97**
I12	0.08	0.06	0.04	0.03	0.15	0.13	0.05	0.03	0.16	0.13	0.05	0.03	0.08	0.06	0.04	0.03	**1.14**
I13	0.04	0.05	0.05	0.03	0.05	0.12	0.12	0.05	0.05	0.12	0.12	0.05	0.04	0.05	0.05	0.03	**1.01**
I14	0.02	0.03	0.05	0.07	0.02	0.04	0.13	0.14	0.02	0.04	0.12	0.14	0.02	0.03	0.05	0.07	**1.01**
I15	0.02	0.03	0.06	0.10	0.02	0.03	0.07	0.21	0.02	0.03	0.07	0.21	0.02	0.03	0.05	0.10	**1.07**
I16	0.04	0.03	0.02	0.01	0.09	0.04	0.02	0.01	0.21	0.07	0.03	0.01	0.25	0.09	0.04	0.02	**0.98**
I17	0.03	0.02	0.02	0.01	0.06	0.05	0.03	0.02	0.16	0.13	0.05	0.02	0.18	0.16	0.06	0.03	**1.03**
I18	0.02	0.02	0.02	0.02	0.03	0.04	0.04	0.03	0.05	0.12	0.12	0.05	0.07	0.14	0.14	0.07	**0.99**
I19	0.01	0.01	0.02	0.02	0.01	0.02	0.04	0.05	0.02	0.04	0.13	0.15	0.03	0.06	0.15	0.18	**0.96**
I20	0.01	0.02	0.03	0.04	0.01	0.02	0.04	0.09	0.01	0.03	0.07	0.22	0.01	0.04	0.10	0.26	**1.00**
I21	0.03	0.02	0.01	0.01	0.05	0.03	0.02	0.01	0.13	0.07	0.03	0.02	0.36	0.13	0.05	0.02	**1.00**
I22	0.02	0.02	0.01	0.01	0.04	0.03	0.02	0.01	0.10	0.08	0.04	0.02	0.26	0.22	0.09	0.04	**1.01**
I23	0.01	0.01	0.02	0.02	0.02	0.02	0.03	0.03	0.05	0.07	0.07	0.05	0.10	0.21	0.21	0.10	**0.99**
I24	0.01	0.01	0.01	0.02	0.01	0.01	0.03	0.04	0.02	0.04	0.07	0.10	0.03	0.08	0.21	0.26	**0.94**
I25	0.01	0.02	0.02	0.03	0.01	0.02	0.03	0.06	0.02	0.03	0.07	0.14	0.03	0.05	0.13	0.36	**1.03**
m_j **(rb/d)**	-0.08	-0.08	-0.07	-0.10	-0.07	-0.06	-0.05	-0.07	-0.08	-0.06	-0.04	-0.05	-0.09	-0.07	-0.05	-0.06	
S	**1.76**	**1.57**	**1.56**	**1.77**	**1.56**	**1.36**	**1.36**	**1.56**	**1.54**	**1.35**	**1.36**	**1.57**	**1.74**	**1.55**	**1.56**	**1.77**	

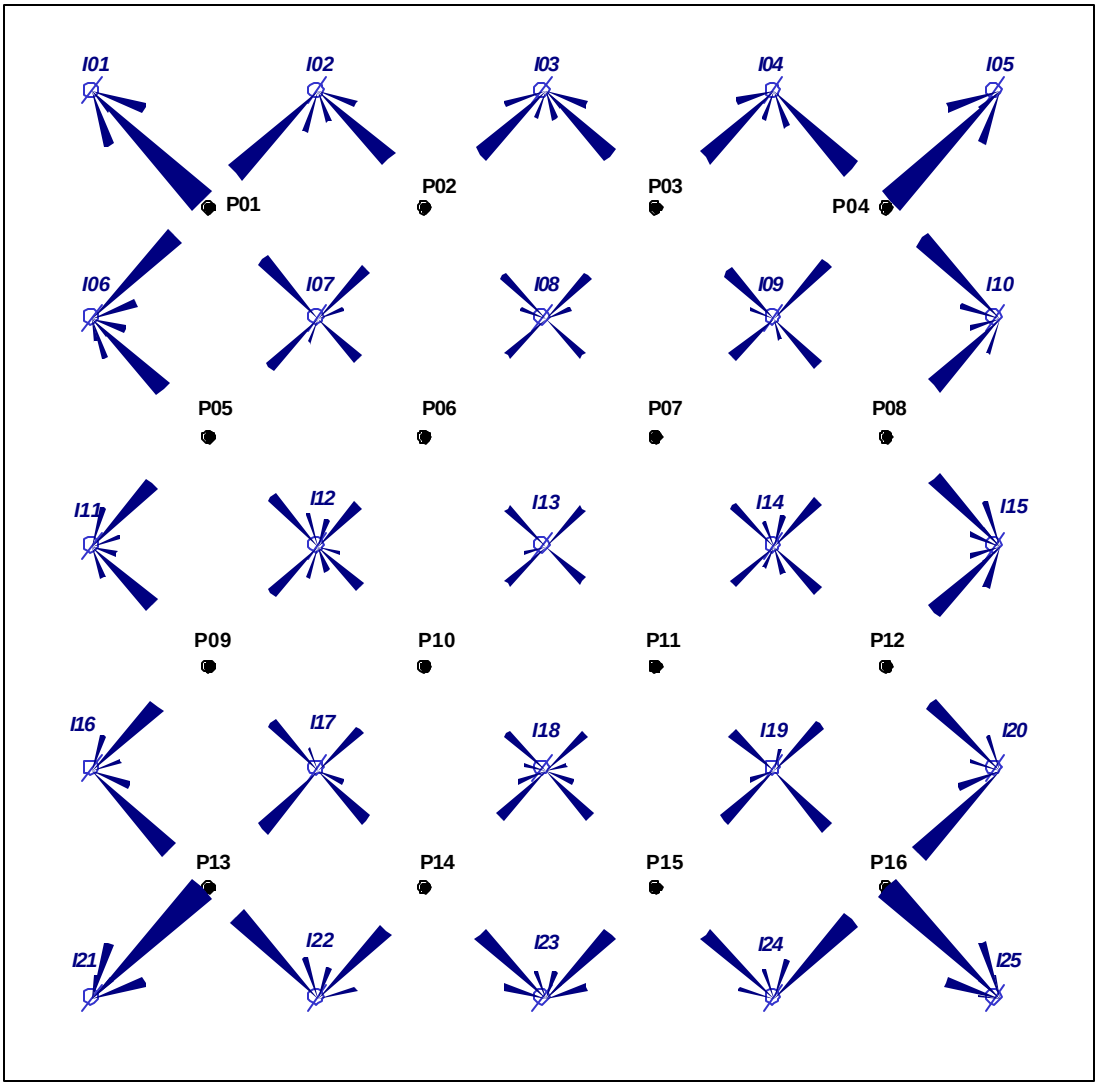

Figure 3.45 25x16 Synfield. Homogeneous reservoir. ABMLR with diffusivity filters using 415 data points, with O_d = 15. Representation of the weighting coefficients l_{ij} shown in Table 3.18.

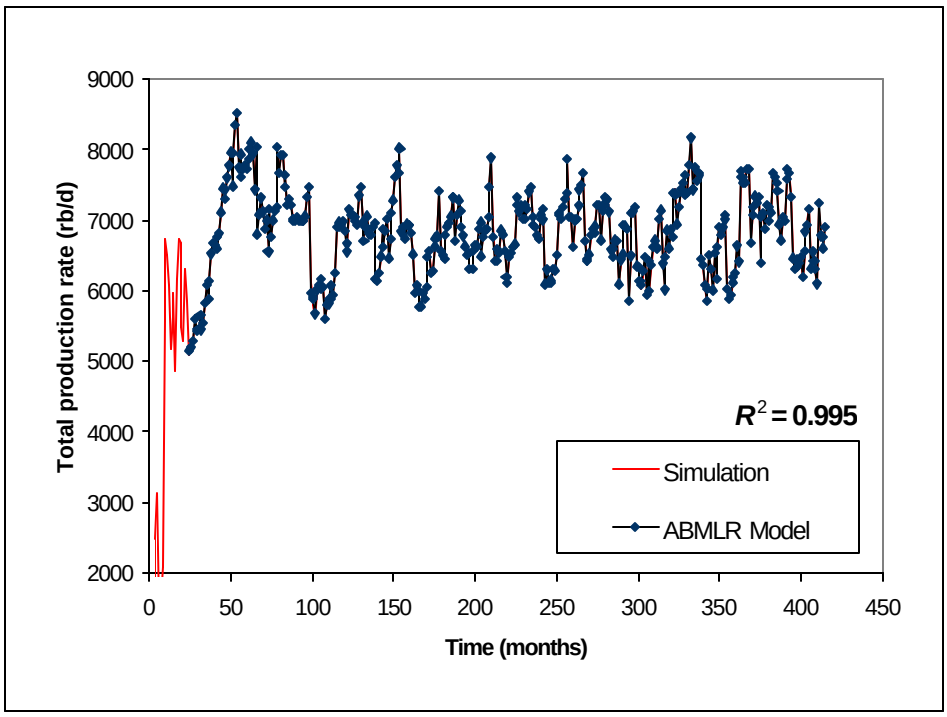

Figure 3.46 25x16 Synfield. Homogeneous reservoir. ABMLR with diffusivity filters using 415 data points, with O_d = 15. Comparison between modeled total liquid production rate and the total liquid production rate observed in simulation (four center wells).

Figure 3.47 shows that the weighting coefficients are, in general, smaller for more distant wells, and they appear in the plot grouped by well-pair similarity. For example, the four injectors at the corners of the Synfield (I01, I05, I21, and I25) have a coefficient of approximately 0.36 with their most adjacent respective producer, and 0.13 with each of the next producers in distance (e.g. I01 with P02 and P05). These groups can easily be identified in the plot. This means that around 61% (0.36 + 0.13 + 0.13) of the support provided by the injectors at the corner goes to the two most adjacent producers. Or 39% of its injection is affecting even more distant producers

of the field. Similarly, 12% of the water injected in I13 at the center of the field (see Table 3.18) is affecting each of its adjacent producers; or 52% of the water injected in I13 is supporting producers from different patterns in this 5-spot injection scheme. As shown in this simulated response, considering only adjacent producers to analyze the influence of an injector may lead to significant errors.

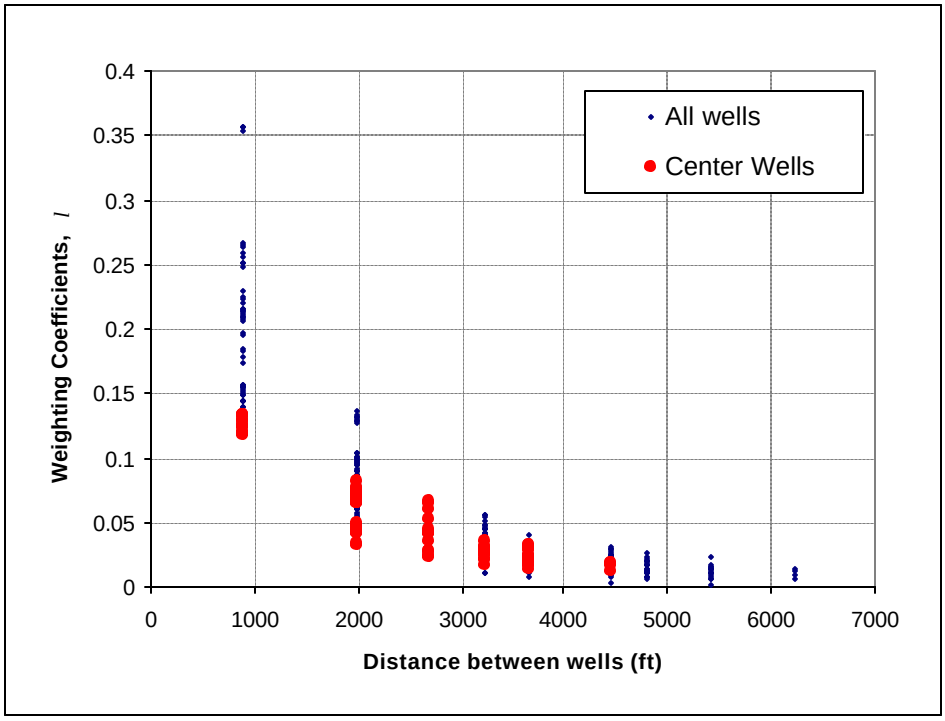

Figure 3.47 25x16 Synfield. Homogeneous reservoir. ABMLR with diffusivity filters using 415 data points, with O_d = 15. Weighting coefficients l, vs distance between wells. The large dots correspond to the four wells at the center of the Synfield.

3.2.3. Overdetermination Analysis

The effect of having different levels of overdetermination was studied for both the 5x4 and 25x16 Synfields. We can increase O_d either by changing the number of data points or by changing the number of injectors in the field.

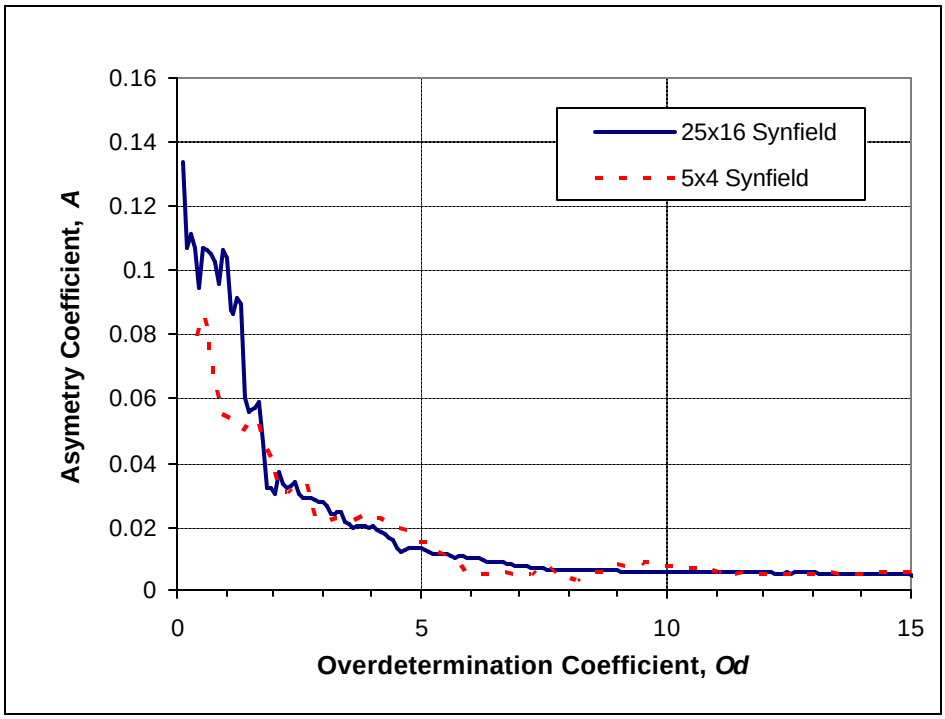

Figure 3.48 Homogeneous reservoir. ABMLR with diffusivity filters. Effect of the overdetermination on the asymmetry coefficient. Both 5x4 Synfield and 25x16 Synfield results lie on the same curve. The larger the O_d, the better the results.

A plot of A vs. O_d was built by using different number of effective data points and applying ABMLR with diffusivity filters (Figure 3.48). For example, in the 25x16 Synfield, the first 25 data points were not used for the analysis. Then, we start

using 3 effective data points (from point 26 to 28), we get O_d = 0.112 (the system is actually underdetermined) and we calculate A = 0.1338. Subsequently, we continue to increase the number of data points used, and calculate O_d and A. The quality of the results, inversely represented by A, clearly improves with large O_d (Figure 3.48). Furthermore, for $O_d > 6$, the asymmetry significantly levels-off, yielding very good results from that point on. Since both the 5x4 and 25x16 Synfield plots lie practically on the same curve, the A vs. O_d plot is independent of the number of injectors. Then, given a five-spot waterflood, Figure 3.48 can be used to quantitatively estimate the confidence one can have in the results of the application of the technique before application.

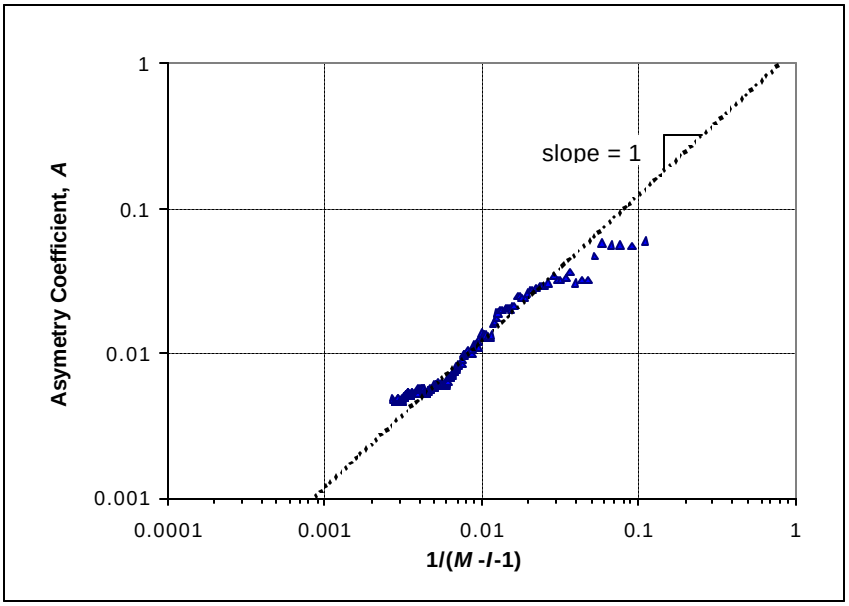

Figure 3.49 25x16 Synfield. Homogeneous reservoir. ABMLR with diffusivity filters. Log-log plot of A vs. 1/(M-I-1) with a slope of approximately 1.

In addition, the log-log plot of A vs. $1/(M\text{-}I\text{-}1)$ gives an approximate straight line of slope 1, showing that A is inversely proportional to $1/(M\text{-}I\text{-}1)$, which is in agreement with the application of Eq. 2.2 to multivariate linear regression (Figure 3.49). The log-log plot of A vs. O_d also gives a straight line of slope -1 for $O_d > 1$ (Figure 3.50).

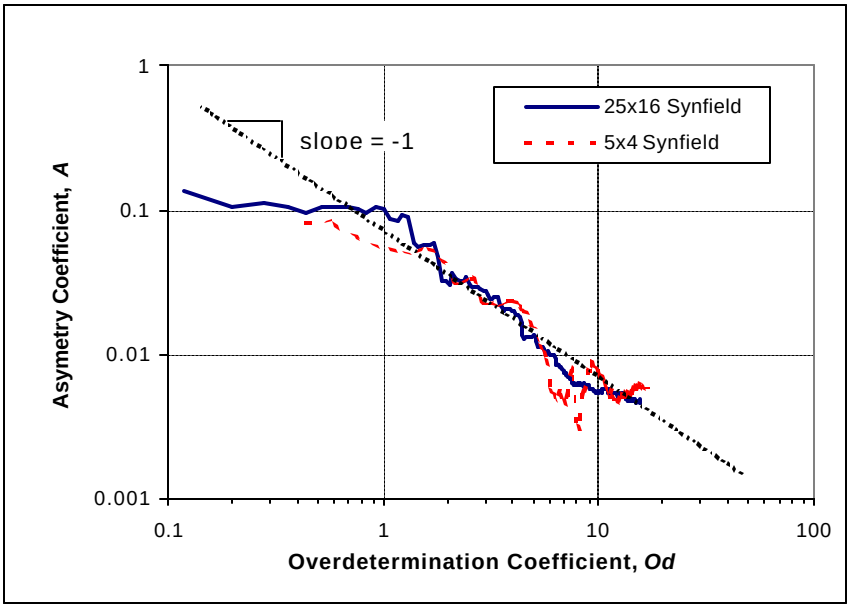

Figure 3.50 Homogeneous reservoir. ABMLR with diffusivity filters. Log-log plot of A vs. O_d. Both 5x4 and 25x16 Synfields show a slope of approximately -1 for $O_d > 1$.

In the 5x4 Filed, we also calculated the A vs. O_d plot for ABMLR without diffusivity filters, and IBMLR. In agreement with the conclusions presented in section 3.1.2.b, the IBMLR yields the best results (smallest A), and ABMLR without diffusivity filters the poorest (Figure 3.51). The three curves show the same behavior,

leveling-off at O_d = 6 approximately (note that a semi-log scale is used in the figure for easier comparison between the curves)..

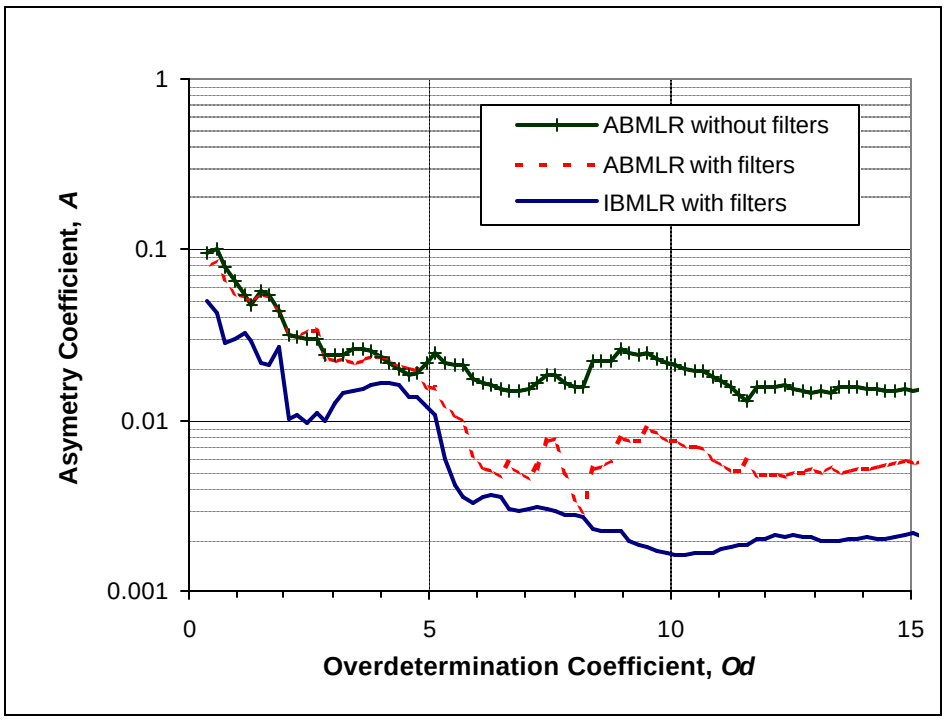

Figure 3.51 5x4 Synfield. Homogeneous reservoir. ABMLR with diffusivity filters. Plot of A vs. O_d for ABMLR with and without diffusivity filters, and IBMLR with diffusivity filters. A semi-log plot is used for easier comparison.

Another interesting thing about the plot, is the apparently irregular behavior of the ABMLR-with-diffusivity-filters curve near O_d = 8. The reason for this is that there are abrupt changes in injection rate that occur at approximately 1700 days (see Figure 3.2); at $O_d \cong 8$, the data corresponding to these sharp peaks in injection rate is included in the analysis. These changes in injection introduce periods that are highly

dominated by transients and consequently, introduce errors in the estimation of the ls. On the ABMLR-without-diffusivity-filters curve the error level is higher at O_d = 8 (A = 0.02 approximately); so, the curve seems to be less sensitive to these changes.

3.2.4. Distance Cut-off

One way of increasing the overdetermination of the problem is increasing the number of data points. Another way of increasing O_d is decreasing the number of injectors included in the regression. So we could simply include in the analysis only well pairs where the distance between wells is less than a certain distance cut-off. Unfortunately, the results of the application of distance cut-offs are not as one would like (see Figure 3.52), because the use of a distance cut-off introduces an error that is greater than the benefit we obtain from the increase of O_d. These facts are discussed in this section.

According to the planes of symmetry, in the 25x16 Synfield there are 3 types of producers (Figure 3.39). So, we can group the producers of the Synfield by similarity in three groups: GP01, GP02, and GP06. If we apply distance cut-offs, the larger the cut-off, the more injectors included in the analysis (Figure 3.53), but each of the producer groups now have a different number of injectors, depending on the position they have in the field. For example, if we use a distance cut-off of 1000 ft, only adjacent producers are included in the analysis (the injector producer distance is 891 ft), and all three groups of producers include four injectors. But if a 2200-foot

cut-off is used, producers that are closer to the boundaries (e.g. GP01) include less injectors than producers that are in the center of the field (GP06).

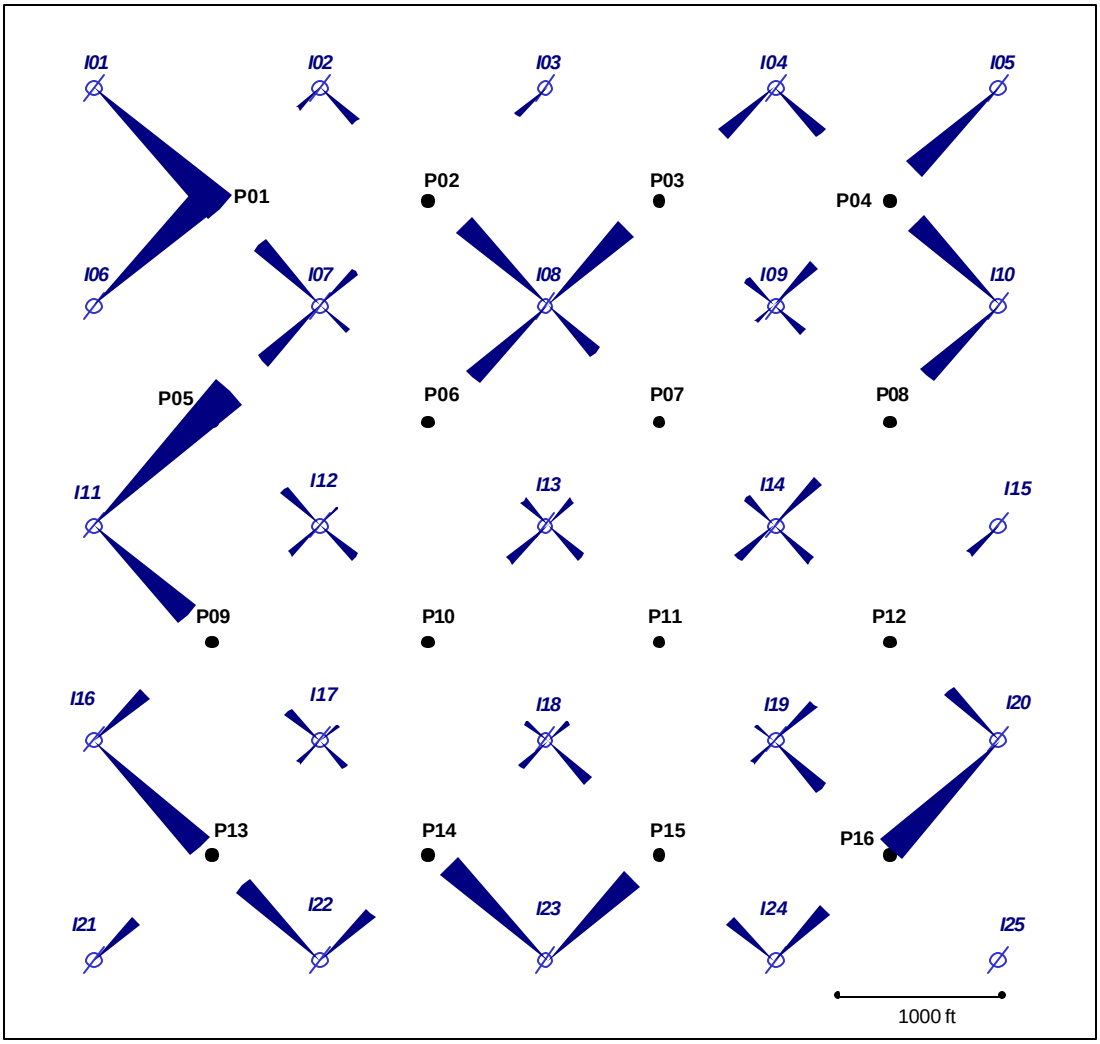

Figure 3.52 25x16 Synfield. Homogeneous reservoir. ABMLR with diffusivity filters using 41 effective data points and a distance cut-off of 1000 ft. A = 0.2290 with apparent O_d = 8.2. Representation of the weighting coefficients l_{ij}.

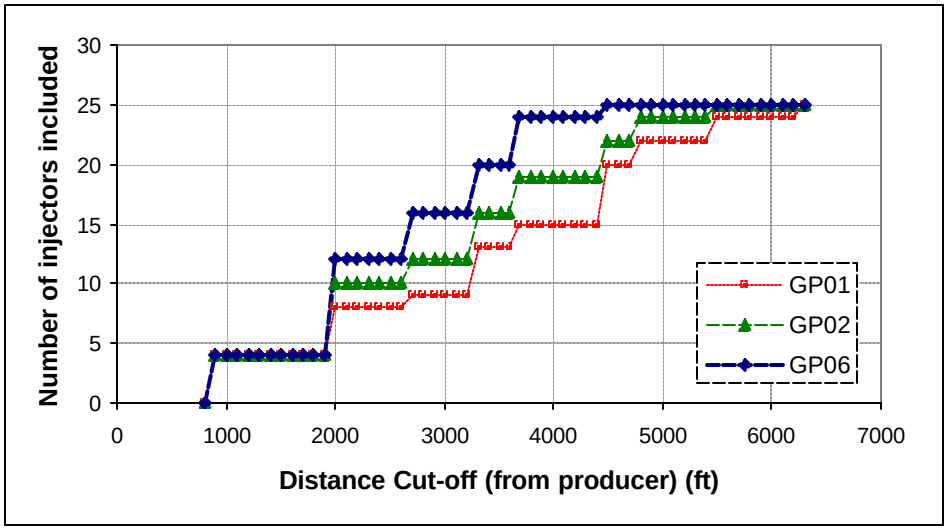

Figure 3.53 25x16 Synfield. Number of injectors included in the analysis for each producer group when applying distance cut-offs.

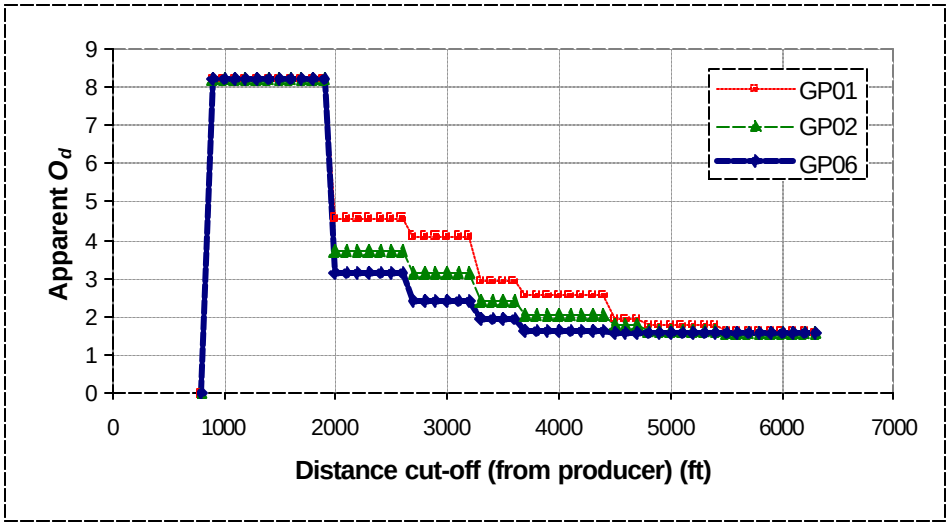

Figure 3.54 25x16 Synfield. History of 41 effective data points. Apparent O_d when applying distance cut-offs.

Taking into account the number of injectors included in the analysis when using distance cut-offs, we can estimate the apparent O_d for each cut-off. For example, for a history of 41 data points and a distance cut-off of 1000 ft, where only the adjacent injectors are included, we get an apparent $O_d = 8.2$ ($\frac{41}{(4+1)}$, see Eq. 3.2). According to Figure 3.48, we should expect very good symmetry ($O_d > 6$), but as shown in Figure 3.52, results are much poorer than expected ($A = 0.2290$). An additional error is introduced when using distance cut-offs.

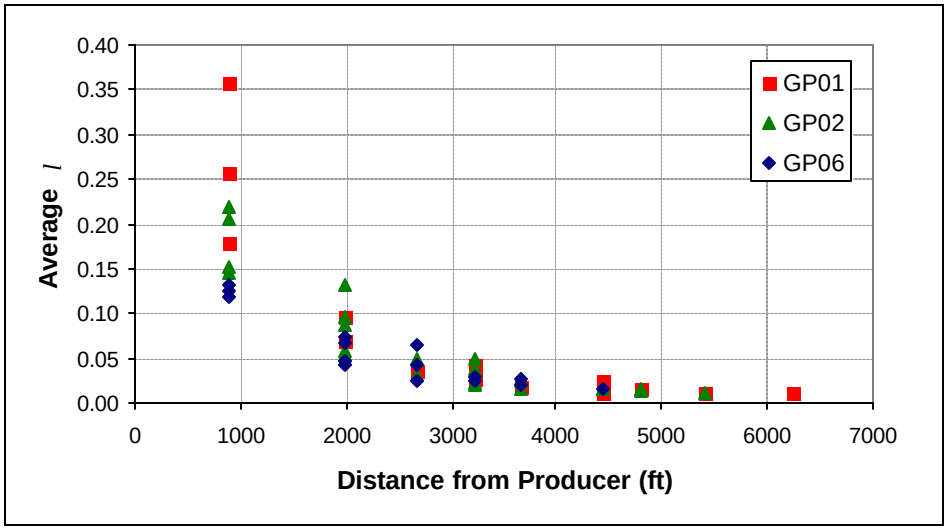

Figure 3.55 25x16 Synfield. Homogeneous reservoir. Weighting coefficients l, vs. distance between wells grouped by similar producers.

Figure 3.55 is very similar to Figure 3.47 , but it shows the average l for each well-pair group. We consider these values the best estimations for each l_{ij}, and we

use these values for the study of the error introduced when using distance cut-offs. Basically, using a distance cut-off sets some l_{ij}s to zero depending on the well-pair distance. For example, this means that if we use a distance cut-off of 1000 ft all the weights that corresponds to pairs that are more than 1000 ft away are set to zero, which is definitely not close to their true value shown in Figure 3.55, especially for closer wells (e.g. wells 1990 ft apart).

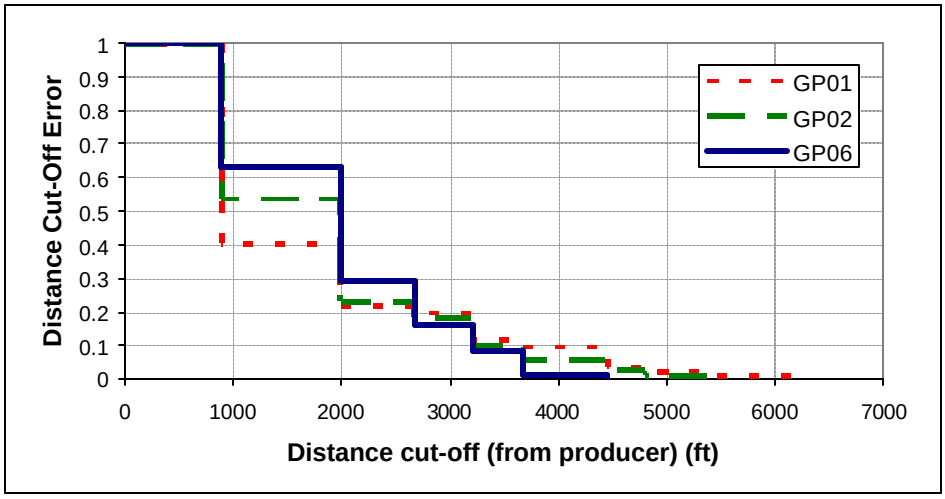

Figure 3.56 25x16 Synfield. Error introduced in the estimation of ls when applying distance cut-offs.

Figure 3.56 shows the relative error introduced in the estimation of by using distance cut-offs. Using a distance cut-off smaller than 891 ft introduces a 100% error, because all the ls are set to zero. Considering only adjacent wells for the analysis of this homogeneous 25x16 Synfield introduces errors as large as 63 percent

in the estimation of the weighting coefficients for wells close to the center of the field (GP06). This shows that considering only adjacent wells in the analysis of the influence of injectors on producers, even in synthetic cases, may lead to significant errors. Normally, the error introduced by the use of distance cut-off is larger than the benefit we obtain from having larger O_ds, so at this stage of the development of the technique, the use of distance cut-offs is not recommended.

CHAPTER 4: SCOPE OF APPLICATION

The first section of this chapter discusses the assumptions on which the multivariate linear regression (MLR), average-rate balanced multivariate linear regression (ABMLR), and instantaneously balanced multivariate linear regression (IBMLR) techniques are based, that consist on constant reservoir and injection/production conditions. Then, the possible sources of error are presented. These sources of error include deviations from assumptions, small overdetermination, poor data quality, the frequency of data sampling, the effect of boundaries, and possible injection losses. Finally, the use of the presented techniques as a predictive tool is presented.

4.1. ASSUMPTIONS

This technique is based on several assumptions. The general assumption is that within the period of time selected for the analysis, all the parameters in the field must be constant, with the obvious exception of the injection and production rates; or all the changes in production rates are caused by changes in injection rates. This assumption can be divided into two main conditions: constant injection/production conditions and constant reservoir conditions.

4.1.1. Constant Injection and Production Conditions

The production conditions are assumed to be constant within the period selected for the analysis. This means that no major changes are introduced in the wells or in the lifting/injection systems. We can subdivide these conditions into the following: no new wells, constant production bottom-hole pressure (BHP), constant well productivity, constant non-waterflooding production, and no changes in injection system.

a. No new wells

The technique presented analyzes the interaction between all the producers and injectors in the field; thus, the inclusion of a new well in the field means that a complete new analysis is required. In other words, the drilling of new injection or producing wells implies a new set of weighting coefficients. If a well interrupts its injection or production rate for a short time, it doesn't need to be removed from the analysis; moreover, the pulse generate by this interruption maybe specially useful for the determination of the weighting coefficients. But if the well interrupts its injection or production rate for long periods, then those lapses of time have to be removed from the analysis. What the length of a short time is, is yet to be determined and further research is suggested in this topic.

b. Constant production bottomhole pressure

Changes in injection rate will cause changes in pressure in the surrounding of a producer. The technique assumes that every change in the production rate is exclusively caused by changes in injection rates, so the production conditions must remain constant. This means that the bottomhole pressure (BHP) must be constant during the period selected for analysis. The change of the lifting system of a producer often produces significant changes on its production conditions; if that is the case, the waterflood cannot be analyzed in one single period.

At the same time, many artificial lift systems work on the basis of constant production rate and not constant BHP. For example, the production rate of a rod-pumping unit can be calculated from the pump size, strokes per minute, the length of each stroke, and the efficiency. So, changes in pressure in the surroundings of a producer with a rod-pumping unit may not produce changes in production rate, but an increase of the BHP, which is not captured by the proposed technique.

It is important to make a comment about the model at this point. Overall, one would think that all the wells in the field have an impact on their neighbors, no matter they are injecting or producing. So, producers could also be included in the model (Eqs. 2.3 and 2.9). But this is not practical. To include other producers in the model we should be able to distinguish between two types of production-rate changes: (1) production-rate changes caused by injection-rate changes, and (2) production rate changes caused by changes in the production conditions (changes in the BHP, shut-

ins, etc.). The changes in production rate that one should include in the model would be those caused by changes in BHP. But since most of the times we are not able to separate these two types of production rate changes, we assume that BHP is constant, we exclude from the analysis the periods where the producers are shut-in, and we don't include other producers in the model.

c. Constant well productivity

The productivity of a well is assumed to be constant during the period selected for analysis. Opening new layers for production changes productivity of a well and also changes the drainage conditions. So, no new layers should be completed during the analyzed period. Besides, no major changes in skin or in other well properties should occur in the producers within the analyzed period of time.

d. Constant non-waterflloding production

In the MLR approach, the production accounted for by non-waterflooding reasons (mainly primary production) is assumed to be constant. Similarly, if some water is being injected in layers that are not productive, these injection losses are assumed to be constant within the analyzed period. On the other hand, ABMLR and IBMLR approaches do not consider non-waterflooding injection/production.

e. No changes in injection system

In many waterfloods, water is selectively injected in the reservoir. This means that a set of mandrels and valves control the injection rate on each layer. The technique assumes that injection conditions do not change within the period selected for analysis; so no major changes in selective injection system must occur.

4.1.2. Constant Reservoir Conditions

The constant reservoir condition assumption states that reservoir and fluid properties must remain constant during the period selected for analysis. This condition is rarely strictly attained in a waterflood, because some reservoir and fluid properties depend on pressure and saturations. But in most waterfloods a proper selection of the period for analysis allows these conditions to be satisfactorily met. The constant reservoir conditions include the following: constant reservoir and fluid properties, constant total compressibility, and constant effective permeabilities.

a. Constant major reservoir and fluid properties

The main reservoir properties, such as absolute directional permeabilities, porosity, layer thickness, fractures position and orientation, fluid viscosity are assumed to be constant. A very strong dependence of reservoir permeability or fluid viscosity on reservoir pressure may lead to less precise results of the technique if large changes in reservoir pressure occur within the analyzed period. Likewise,

injection pressures above the parting-pressure provoke fractures that alter the reservoir conditions during injection. Since these fractures are not stable, they open, close and change their length and conditions with relatively small changes in injection pressure; thus, the reservoir properties are not constant.

b. Constant total compressibility

The technique assumes that the reservoir properties are constant; consequently, the diffusivity factor is assumed to be constant. Thus, the total compressibility (c_t) must be constant. c_t is defined by the rock, water, oil, and gas compressibilities, together with the oil, water, and gas saturations; so, changes in any of these factors cause changes in c_t. Since oil and water compressibilities are typically small and can be considered constant, changes in oil and water saturation do not significantly affect the value of c_t. Of course, the latter is not true if oil compressibility is high. However, gas compressibility is not only high but also not constant. So, changes in gas saturation (S_g) and pressure significantly change the total compressibility or, in other words, change the overall reservoir properties.

At the same time, changes in S_g cause changes in the production gas-oil ratio (GOR). Indeed, we can indirectly monitor the changes in S_g by looking at the GOR. Therefore, if we select for analysis periods where the GOR is constant, then S_g will be constant. Furthermore, in waterfloods, the GOR is constant usually when all the free gas has been produced or redissolved in the oil, so that S_g is equal to the residual gas

saturation. At this stage, with relatively small and constant S_g, the waterflood has reached a state were the pressure changes are usually small. So, the selection of periods with constant and minimum GOR in waterfloods (equal to the dissolved gas-oil ratio) is equivalent to the selection of periods where c_t is approximately constant. An example of the selection of data points is presented in section 5.1.2.

c. Constant effective permeabilities

The effective permeabilities to oil and water are assumed to be constant during the period selected for analysis. It is impossible to strictly meet this condition, because water and oil saturation change during the waterflood, with the consequent change in relative permeabilities and effective permeabilities. However, it is possible to be close to these conditions. In mature waterfloods, the changes in oil and water saturation are relatively small; consequently, the changes in the relative permeabilities are also small. On the other hand, in early stages of the waterflood the changes in relative permeabilities are large. However, if the mobility ratio is close to one, the effect of the saturation changes is less significant.

4.2. SOURCES OF ERROR

The possible sources of error in the application of the proposed techniques are discussed in this section. Deviations from assumptions, small overdetermination, and data quality are first discussed because they are the most relevant and frequent causes

that may lead to errors in the weighting coefficients estimation. Particularly, the sensitivity of the technique to the data quality is analyzed. Besides, a brief discussion about data sampling and boundary effects is also included.

4.2.1. Deviations From Assumptions

The previous section discussed the assumptions on which MLR, ABMLR, and IBMLR are based. These assumptions are divided into two main conditions: constant injection/production conditions and constant reservoir conditions. Deviations from these assumptions introduce errors into the estimation of the weighting coefficients. Of course, it is practically impossible to meet all the conditions described in the previous section, but the selection of the period for the analysis must be oriented to minimize the deviation from the stated assumptions. On the other hand, knowing how many of those assumptions are met and how many are not is an indicator of the confidence one must have on the results.

4.2.2. Small Overdetermination

Section 3.2.3 discusses the effect that the overdetermination has on the results. Figure 3.48 can be used to determine the quality of the results before the application of the technique, from the number of data points and the number of injectors used in the analysis. As in any statistical analysis, the more data points, the more confident one can be on the results. In the case of a five-spot waterflood, an overdetermination

smaller than 6 may lead to a source of error in the estimation of the weighting coefficients.

4.2.3. Data Quality

Production and injection rates can be measured in the field in different ways and with a wide range of accuracy; so, a sensitivity study of the technique to data quality was performed and is presented in this section. Different levels of normally distributed relative error with zero mean were introduced to the simulated injection and production rate data in the homogeneous 5x4 Synfield, representing random errors in the rate measurements. The errors introduced range from no-error to a relative error with a standard deviation of 0.3 (relative error). This means that, for example, in the realizations where the maximum error was used, the standard deviation of the relative error was equal to 0.30. For each level of error introduced, 100 realizations were run and, for each realization, the coefficient of determination R^2 and the asymmetry coefficient A were calculated.

The average and standard deviation of R^2 and A over the 100 realizations were calculated for each level of error and are shown in Figure 4.1. The technique is sensitive to data quality: R^2 decreases from 0.994 for the case with no error (using ABMLR and diffusivity filters) to R^2 = 0.8 on average for a relative error with a standard deviation of 10 percent. Similarly, the asymmetry, which is an inverse

measure of the quality of the results in a homogeneous reservoir, increases 5.7 times from $A = 0.0095$ to $A = 0.0542$ for a relative error of 0.10 standard deviation.

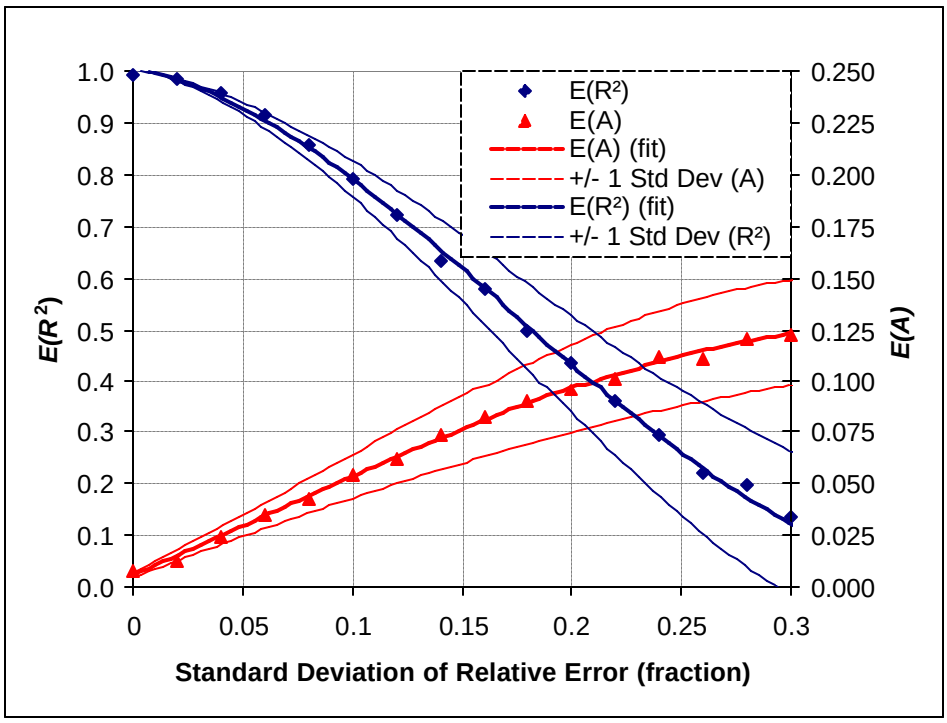

Figure 4.1 5x4 Synfield. Homogeneous reservoir. ABMLR with diffusivity filters. Sensitivity of the technique to data quality. Expected values of R^2 and A over 100 realizations for different levels of random relative error in the rate measurement.

4.2.4. Data Sampling

Injection and production rates are typically reported monthly. Depending on the importance of the well and rate measurement policies, the rate of a well can be tested once or twice within a month. Then, the monthly report is typically an average

of these tests and sometimes modified by an allocation factor. This type of measurement and reporting may lead to errors in the representativity of the reported rate over the whole month. The rate fluctuations that occur within a month are not captured by monthly reports and, consequently, cannot be analyzed by the regression technique. On the other hand, in some exceptional fields, rates are measured daily. Excessively frequent data may include variations in production that are not caused by changes in injection and, besides, the rate information maybe highly dominated by transients. So, some averaging may be needed. Indeed, the optimum data sampling frequency may be dictated by the reservoir properties and, in some way, related to the relation between the reservoir diffusivity (which determines the radius of investigation of an impulse at a certain time) and the minimum distance between injectors and producers. Further research is suggested in this topic.

4.2.5. Boundaries

Boundaries have an effect on the determination of the weighting coefficients. Closed boundaries (like those of the 5x4 and the 25x16 Synfield) make the weighting coefficients of the injectors closer to the boundaries be larger than those of injectors that are far from the boundaries in a reservoir with homogeneous properties and regular injection pattern, because the injected water is forced to flow only in one direction. There is no error at all in this type of estimation, but care must be taken in the interpretation of the weighting coefficients of wells close to sealed boundaries.

On the other hand, open boundaries do introduce error. A producer close to a boundary may be receiving support for an injector not included in the analysis. In that case, were MLR must to be used, the influx coming from outside the boundaries is captured by b_0. Since the term b_0 is constant, the fluctuations of injectors out of boundaries influencing inner producers are not analyzed. Furthermore, the fluctuations in producers caused by outer injectors are attributed through the regression technique to other inner injectors, which obviously constitutes an error.

4.3. USE AS A PREDICTIVE TOOL

Until now, we have discussed the use of multivariate linear regression (MLR), average-rate balanced MLR (ABMLR) and instantaneously balanced MLR (IBMLR) techniques as diagnosis tools. They have been used to determine the weighting coefficients, which describe injector-producer connectivity in a waterflood. Furthermore, the weighting coefficients have been used to describe the reservoir properties and permeability trends. But these techniques can also be used as a prediction tool.

This section shows the use of ABMLR as a predictive tool. MLR and IBMLR can be analogously used. For comparison purposes, two of the Synfields presented in chapter 3 are used in this section. The predictive capacity of the proposed technique is tested in the homogeneous 5x4 Synfield and the anisotropic 5x4 Synfield, case b.

4.3.1. Prediction of the Homogeneous 5x4 Synfield

The first case to be analyzed is the prediction in the homogeneous 5x4 Synfield (see section 3.1.1). This Synfield has a history of 100 data points in where the first 12 data points are not used in the analysis because 12-month diffusivity filters are used (see section 2.5). So, of the remaining 88 data points, the first 44 data points were used for estimating the weighting coefficients (training period) and the last 44 to compare the predicted results with the production observed in the simulation (prediction period). Using 44 effective data points for the analysis with 5 injectors in the Synfield gives O_d = 7.33, which is greater than 6, so one should be confident in the results and a good prediction is expected (see Figure 3.48).

Table 4.1 5x4 Synfield. Homogeneous reservoir. ABMLR with diffusivity filters. Weighting coefficients l_{ij} obtained using 44 effective data points and used for prediction in Figure 4.2.

	P01	**P02**	**P03**	**P04**
I01	0.31	0.32	0.14	0.15
I02	0.32	0.16	0.32	0.16
I03	0.28	0.27	0.29	0.29
I04	0.16	0.33	0.16	0.33
I05	0.19	0.18	0.36	0.35
m_j **(rb/d)**	0.12	0.25	-0.17	-0.04

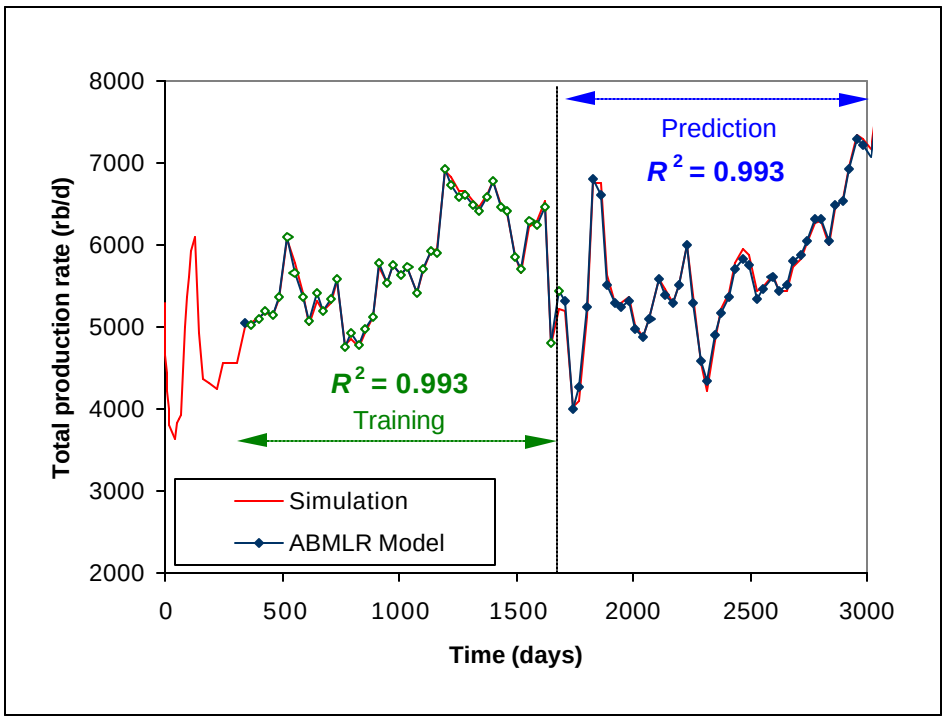

Figure 4.2 5x4 Synfield. Homogeneous reservoir. ABMLR with diffusivity filters. Comparison between modeled total liquid production rate and the total liquid production rate observed in simulation. The first portion of the data is used as training period to estimate ls (see Table 4.1) and the last portion used to test the prediction.

The ls obtained using 44 data points (see Table 4.1) give A = 0.0152 which is slightly higher than A = 0.0095 obtained using 100 data points, but the symmetry is still very good. R^2 for the training period is 0.993. When these weighting coefficients are used to model the production rate of the last 44 data points, the prediction period also gives R^2 = 0.993. This large R^2 shows that the prediction is excellent. See Figure 4.2.

4.3.2. Prediction of the Anisotropic 5x4 Synfield, Case b.

Prediction was also tested in the anisotropic 5x4 Synfield, case b (see section 3.1.3). Again, the first 44 effective data points were used to determine the weighting coefficients (training period) and the last 44 were used to test the prediction (training period). Table 4.2 shows the weighting coefficients obtained from the training period, which gives R^2 = 0.997 and A = 0.0630. R^2 is equal to the value obtained before using the whole history of 100 data points, but A is 3.3 times larger, which means that the quality of the results, though still good, is poorer than before. Consequently, we should expect a good prediction, but not as good as that one obtained for the homogeneous case. Figure 4.3 shows that, as expected, the prediction is very good (R^2 = 0.980), but slightly off the total production rate observed in the simulation.

Table 4.2 5x4 Synfield. Anisotropic reservoir, case b. ABMLR with diffusivity filters. Weighting coefficients l_{ij} obtained using 44 effective data points and used for prediction in Figure 4.3.

	P01	**P02**	**P03**	**P04**
I01	0.62	0.07	0.07	0.03
I02	0.65	0.10	0.10	0.04
I03	0.26	0.48	0.47	0.12
I04	0.11	0.21	0.19	0.70
I05	0.10	0.13	0.14	0.72
m_j **(rb/d)**	-0.42	-0.14	-0.07	-0.13

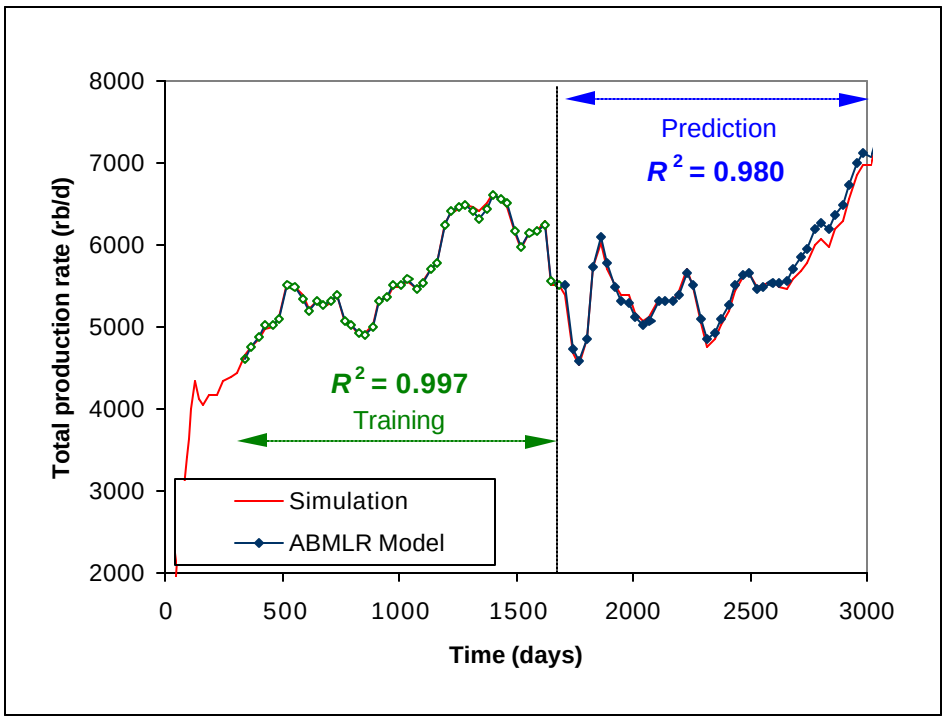

Figure 4.3 5x4 Synfield. Anisotropic reservoir, case b. ABMLR with diffusivity filters. Comparison between modeled total liquid production rate and the total liquid production rate observed in simulation. The first portion of the data is used as training period to estimate ls (see Table 4.2) and the last portion used to test the prediction.

CHAPTER 5: APPLICATION TO FIELD DATA

The technique presented in this thesis was applied to two waterflooded fields in Argentina: the Chihuido de la Sierra Negra Field and the Bloque I Field. This chapter presents a brief description of the fields and shows the application results. In addition, a heuristic method to improve the results is also presented and discussed. The last section of this chapter provides a brief discussion about a general procedure that should be followed to use the proposed statistical techniques.

5.1. CHIHUIDO DE LA SIERRA NEGRA FIELD

5.1.1. Field Description

The Chihuido de la Sierra Negra (ChSN) Field is located in Western Argentina. Having more than 1000 wells, only a portion of the field, with 25 injectors and 16 producers, was selected for the analysis (Figure 5.1). From this point on the selected portion of the field will be referred as ChSN Field. Since only a portion of the field is being analyzed and the boundaries are open, the multivariate linear regression (MLR) approach is used.

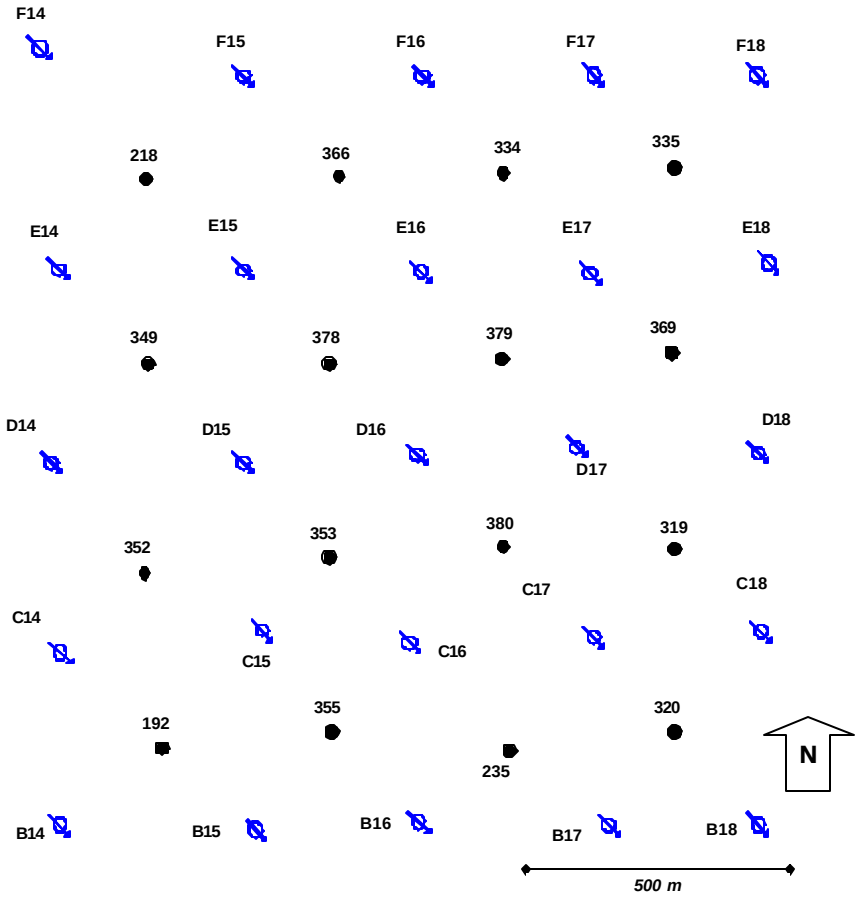

Figure 5.1 Chihuido de la Sierra Negra Field. Base map.

The ChSN field is undergoing a waterflood on a five-spot pattern. Fairly continuous eolian and river-channel sandstones constitute the reservoir, which has five main productive layers. The average depth is 1000 meters, the average net thickness is 20 meters, porosity ranges from 0.15 to 0.25, and the average permeability is 40 md. Oil and water compressibilities are moderate and the water-oil mobility ratio is approximately equal to one. The injectors have selective injection

systems, where the injection rate per layer (or group of layers) is controlled by a set of downhole mandrels and valves. The rate distribution in the injectors suffered changes during the waterflood. Most of the producers have undergone changes in the artificial lift system, during the waterflood, from rod-pump units to electro-submergible pumps.

5.1.2. Selection of Data Points

Figure 5.2 shows a plot of injection rate, liquid production rate, and gas-oil ratio (GOR) in the ChSN Field. The GOR has a peak at approximately month 60 that sharply decreases after the water injection starts. By month 74, the GOR is at a minimum and approximately constant because only dissolved gas is being produced. Approximately constant compressibility (reservoir conditions) can be assumed starting on month 74. Likewise, starting on month 74, the injection and liquid production rates are in approximate balance. So, months 74 through 126 (53 data points) are selected for the analysis. With 53 data points and 25 injectors in the field, the coefficient of overdetermination, O_d = 2.04, is rather small. The average injection rate per well in the period selected for analysis is 193 rm^3/d (m^3/d in reservoir volumes) and the average production rate per well is 185 rm^3/d.

From Figure 3.48 we know in advance that we will obtain less than optimal results and the estimated weighting coefficients will be imprecise. Besides, the open boundaries introduce errors in the estimation of the weighting coefficients and some

of the assumptions are not completely met (not constant BHP, changes in production and injection conditions). However, some general features can be inferred from the application of MLR to the ChSN Field.

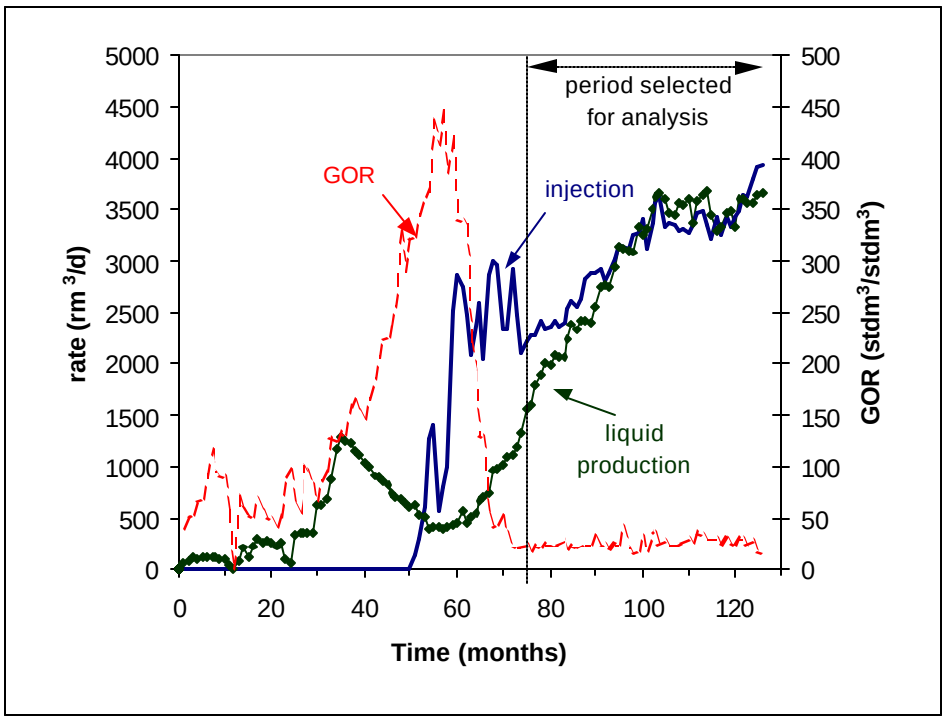

Figure 5.2 Chihuido de la Sierra Negra Field. Injection rate, production rate and gas-oil ratio (GOR) of the selected portion of the field. The period selected for the analysis starts on month 75 where injection and production rates are in approximate balance and only dissolved gas is produced.

5.1.3. Results

The application of MLR with diffusivity filters to the ChSN Field gives the weighting coefficients shown in Table 5.1 and represented in Figure 5.3.

Table 5.1 Chihuido de la Sierra Negra Field. MLR with diffusivity filters, with O_d = 2.04. Weighting coefficients b_{ij}. See Figure 5.3.

	192	218	235	319	320	334	335	349	352	353	355	366	369	378	379	380
B14	0.15	0.05	0.08	0.02	-0.01	0.34	0.34	0.12	-0.08	0.11	0.02	0.23	0.22	0.25	-0.14	0.54
B15	0.12	-0.06	-0.02	-0.04	0.00	0.29	-0.12	-0.26	-0.26	0.10	0.01	0.24	0.64	0.09	0.21	0.10
B16	0.07	-0.37	0.11	0.17	0.11	0.14	0.43	0.42	-0.01	0.74	0.08	0.15	-0.05	-0.06	0.55	0.07
B17	0.01	0.05	-0.17	0.23	-0.06	-0.31	0.04	-0.22	0.04	0.88	-0.03	-0.21	-0.20	-0.22	-0.26	-0.47
B18	-0.03	-0.12	0.10	0.12	-0.07	0.40	-0.09	0.17	-0.10	-0.01	-0.05	0.42	0.16	0.06	0.06	-0.49
C14	-0.02	-0.05	-0.11	0.08	0.33	0.00	0.29	-0.31	-0.15	0.64	-0.03	-0.03	-0.39	0.25	-0.07	0.37
C15	0.15	-0.02	0.12	0.09	0.07	0.44	0.50	-0.06	0.19	0.11	-0.03	0.55	0.51	1.27	0.26	0.22
C16	-0.03	0.07	0.07	0.18	0.13	-0.08	0.07	0.06	0.31	-0.16	0.02	-0.14	0.40	-0.05	0.02	0.24
C17	0.18	0.08	0.02	-0.05	0.17	0.21	0.25	0.11	0.04	0.29	0.00	0.06	0.03	-0.25	0.10	-0.10
C18	-0.19	-0.05	-0.01	-0.07	-0.12	-0.22	-0.07	-0.23	0.11	0.00	0.03	-0.15	-0.32	0.24	-0.11	0.57
D14	0.11	-0.04	-0.10	0.25	-0.06	0.31	0.03	0.44	0.21	-0.38	0.10	-0.04	-0.30	-0.08	0.12	0.23
D15	0.04	-0.04	0.02	0.05	-0.06	-0.27	0.26	0.10	-0.32	-0.03	-0.05	0.15	-0.09	0.14	0.28	-0.03
D16	0.11	0.15	-0.03	0.12	0.13	0.28	0.25	0.02	0.27	0.42	0.04	0.46	0.17	0.04	0.23	0.18
D17	0.02	-0.02	0.04	-0.08	0.04	0.29	-0.22	0.05	-0.11	-0.16	0.03	0.55	0.41	0.34	-0.13	0.21
D18	0.05	0.12	-0.01	0.37	0.23	-0.29	0.58	0.02	-0.06	0.14	0.06	-0.24	-0.04	0.17	-0.11	0.45
E14	0.10	-0.01	0.08	-0.10	-0.11	0.17	0.32	0.02	0.15	0.06	0.05	0.18	-0.14	0.12	0.22	0.10
E15	0.03	0.18	0.04	0.08	0.13	0.23	0.17	0.08	0.19	0.17	0.04	0.17	0.01	-0.01	0.14	0.13
E16	-0.05	0.06	0.00	-0.08	0.00	0.15	0.05	0.07	-0.04	-0.05	0.00	0.15	-0.01	0.10	-0.02	0.17
E17	-0.01	-0.13	-0.14	-0.32	-0.04	0.20	-0.15	-0.34	-0.35	0.18	-0.09	0.30	0.23	-0.06	0.07	-0.41
E18	-0.09	0.02	-0.11	-0.13	-0.08	-0.14	-0.01	-0.29	-0.05	0.03	0.00	0.24	0.04	-0.11	-0.08	-0.08
F14	-0.01	0.00	0.01	-0.06	-0.03	0.05	-0.04	-0.03	0.05	-0.01	-0.01	0.00	0.04	-0.06	-0.07	-0.03
F15	0.02	0.05	0.09	0.00	0.08	0.05	0.24	0.15	0.01	-0.14	-0.01	0.11	-0.26	0.13	-0.08	0.28
F16	0.17	-0.19	-0.08	-0.23	0.21	0.18	0.67	0.17	0.10	0.21	-0.03	0.25	-0.18	-0.46	0.07	0.03
F17	0.09	0.04	0.13	0.62	0.29	0.20	0.33	0.19	0.10	0.68	0.06	0.18	0.36	0.36	0.16	0.33
F18	-0.05	0.06	-0.12	-0.03	-0.07	0.04	-0.12	-0.02	0.12	-0.09	-0.02	0.10	-0.10	-0.01	0.01	-0.21
b_{oj} **(rb/d)**	-66.0	90.4	74.6	-13.3	-79.1	-243.9	-337.7	48.1	60.5	-381.2	22.0	-453.1	-11.0	-33.6	44.1	-86.7

In Figure 5.3, like before, the weighting coefficients b_{ij} are represented by inverted arrows that start from the i^{th} injector and point to the j^{th} producer, where the size of the arrow is proportional to the value of b_{ij}. Since the reservoir is not homogeneous, we do not expect symmetry in the results. At first glance, we can note that there are many negative weighting coefficients. This was expected because of the small overdetermination, the open boundaries, and the changing production/injection conditions, which do not satisfy the assumptions on which the

technique is based. But the analysis of these negative weighting coefficients will be discussed later in this section.

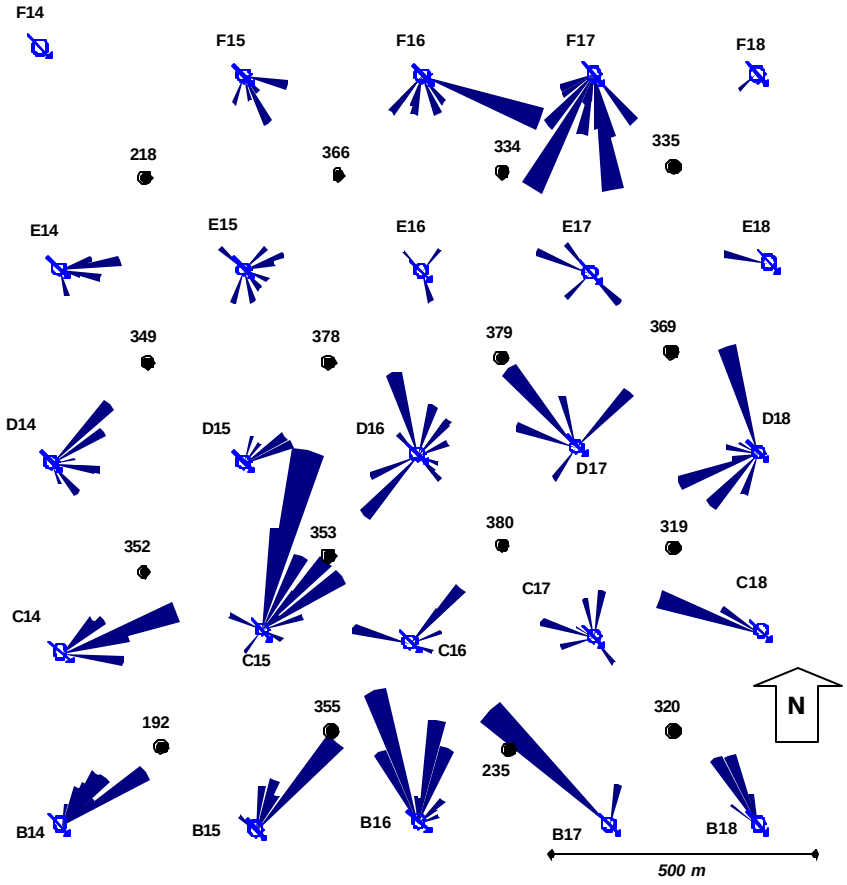

Figure 5.3 Chihuido de la Sierra Negra Field. MLR with diffusivity filters, with O_d = 2.04. Representation of the positive weighting coefficients b_{ij} shown in Table 5.1. The size of the arrows is proportional to the value of the weighting coefficient.

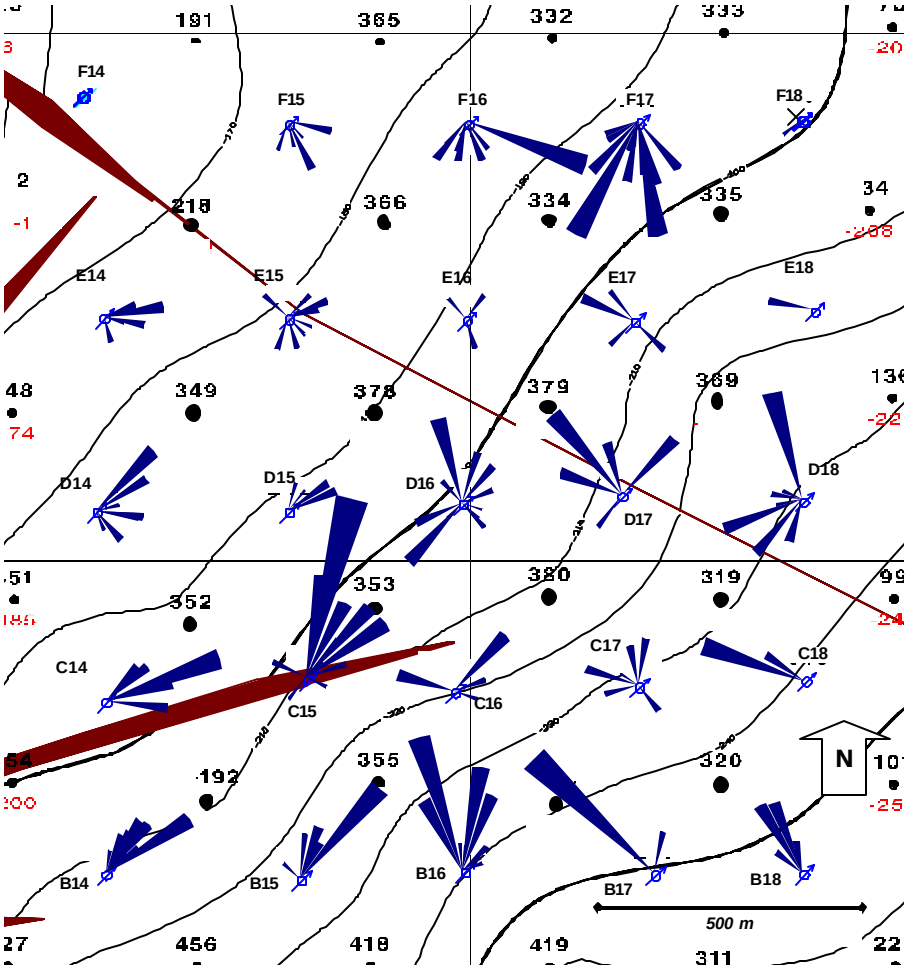

Figure 5.4 Chihuido de la Sierra Negra Field. MLR with diffusivity filters, with O_d = 2.04. Representation of the positive weighting coefficients b_{ij} and comparison with known geological features. A structural map is overlain.

A structural map obtained from the operator is overlain on the results in Figure 5.4. In general, injectors in the north of the field show smaller weighting coefficients than those in the south. Three injectors (F14, F18, and E18), particularly, seem to have little influence on inner producers. The orientation of the coefficients in wells C14 and C15 (and even C16 and partly C17) seem to be in agreement with the

presence of an inferred fault that is slightly south of C14 and C15. However, some coefficients relate injectors B14, B15, and B16 to inner producers, which is in disagreement with the presence of this fault. This error could be attributed to boundary effects or the small O_d. Another explanation is that the fault may not be completely sealing.

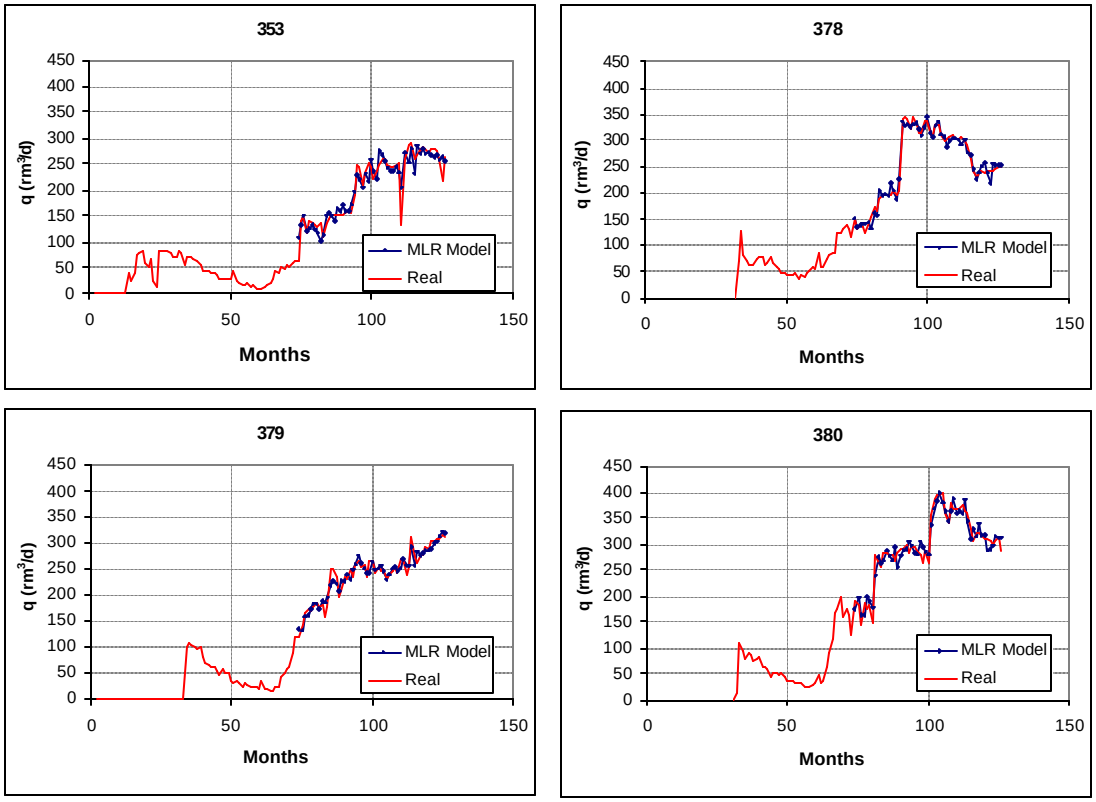

Figure 5.5 Chihuido de la Sierra Negra Field. MLR with diffusivity filters, with O_d = 2.04. Comparison between modeled liquid production rate and the observed liquid production rate in the four wells at the center of the field.

The estimation of the liquid production rate using the MLR model in the four wells at the center of the field (those less affected by boundary effects) shows that the correlations are very good (Figure 5.5). Likewise, the model total liquid production rate of the four wells at the center of the field gives a coefficient of determination R^2 = 0.971 (Figure 5.6).

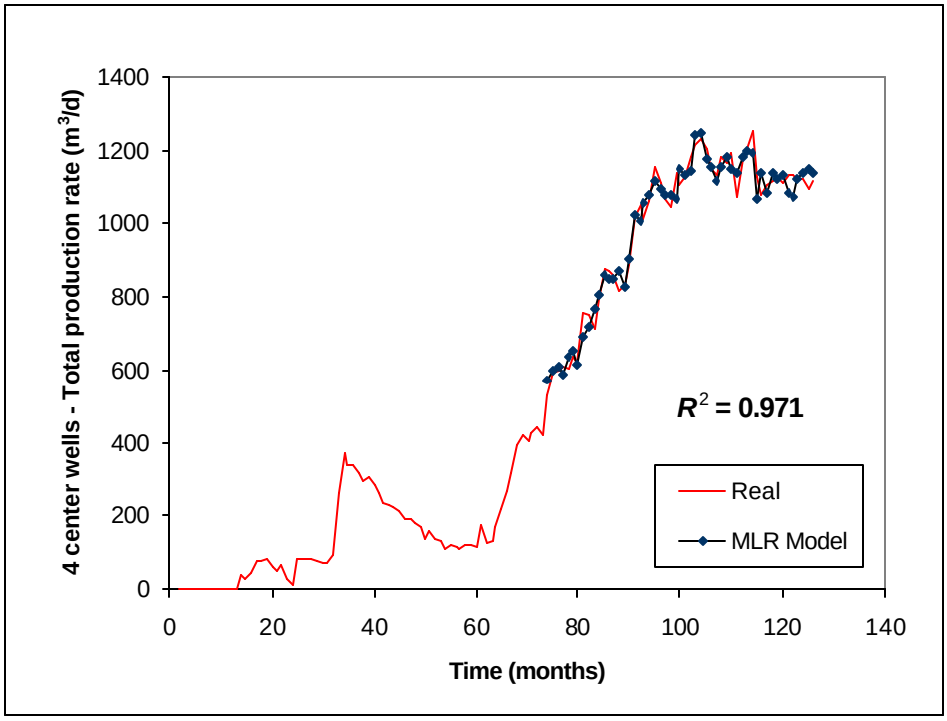

Figure 5.6 Chihuido de la Sierra Negra Field. MLR with diffusivity filters, with O_d = 2.04. Comparison between modeled total liquid production rate and the total observed liquid production rate (four center wells).

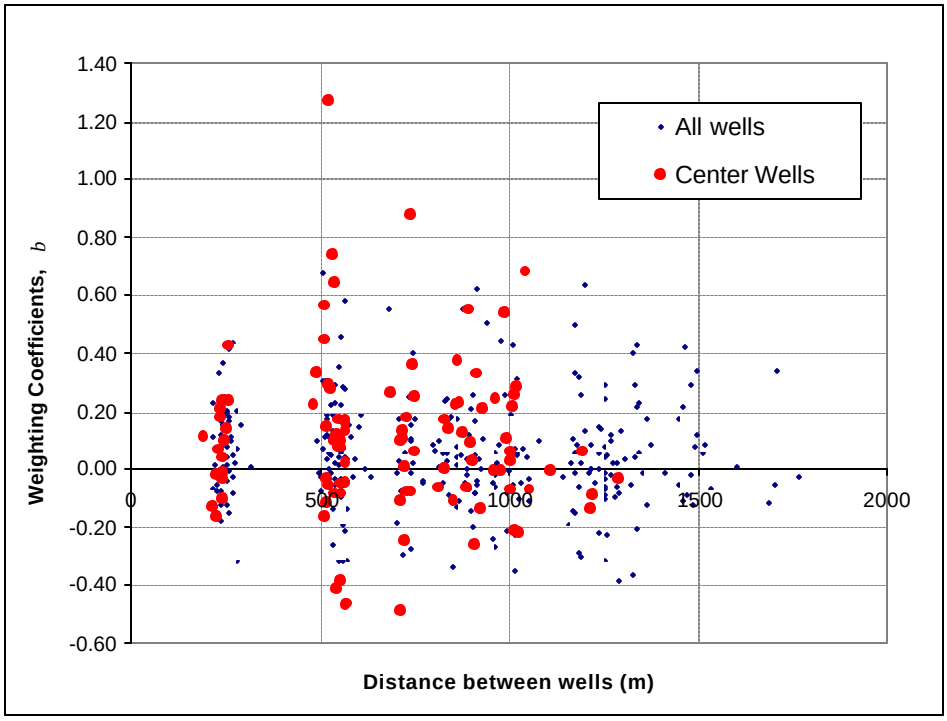

Figure 5.7 Chihuido de la Sierra Negra Field. MLR with diffusivity filters, with O_d = 2.04. Weighting coefficients b_{ij} vs injector-producer distance. The large dots correspond to the four wells at the center of the field.

Since O_d is relatively small and some of the assumptions are not completely met, we expect imprecise results, or in other words, the occurrence of negative weighting coefficients. Figure 5.7 shows the values of b_{ij} versus distance. Reasonable weighting coefficients are obtained for the closest well pairs, but unrealistically large (greater than one) and even negative coefficients are obtained for more distant pairs. Negative weighting coefficients are just statistical results that minimize the error, but they have no physical meaning. Similarly, large positive b_{ij}s are also unrealistic. A weighting coefficient b_{ij} greater than one would indicate that

the rate of the j^{th} producer associated to the i^{th} injector is larger than the i^{th} injection rate itself, which is physically impossible.

5.1.4. Further Improvement of Results

Since negative weighting coefficients have no physical meaning, a simple procedure to eliminate the negative weighting coefficients is presented here. First, the most negative b_{ij} (in the ChSN case, it is $b_{B18,380}$ = -0.49) is set to zero. Second, the regression is performed again recalculating the entire set of weighting coefficients with one fewer well-pair. Then, the new most negative weighting coefficient is set to zero, and the weighting coefficients recalculated. This procedure is repeated until no negative coefficients remain. We call this procedure the successive elimination of negative weighting coefficients (SE-N procedure).

The results of the application of MLR, with filters, after the SE-N procedure are presented in Table 5.2. Before the SE-N procedure, 160 weights out of 400 (40 percent) were negative (see Table 5.1). After the SE-N procedure, not 160 but 180 weights has been set to zero (45 percent) because some of the b_{ij}s that were small positive weighting coefficients before the SE-N became negative within the procedure and were set to zero too. 220 weights (55 percent) remain positive.

Table 5.2 Chihuido de la Sierra Negra Field. MLR with diffusivity filters, with O_d = 2.04. Weighting coefficients b_{ij} after the successive elimination of the negative weighting coefficients. See Figure 5.9.

	192	218	235	319	320	334	335	349	352	353	355	366	369	378	379	380
B14	0.18	0.06	0.15	0.00	0.00	0.44	0.45	0.37	0.12	0.22	0.08	0.28	0.20	0.11	0.00	0.72
B15	0.08	0.09	0.00	0.06	0.12	0.22	0.02	0.00	0.00	0.27	0.10	0.10	0.70	0.25	0.13	0.42
B16	0.04	0.00	0.00	0.00	0.00	0.23	0.20	0.13	0.00	0.51	0.00	0.25	0.00	0.00	0.28	0.00
B17	0.00	0.00	0.00	0.02	0.00	0.00	0.00	0.00	0.02	0.80	0.00	0.00	0.00	0.00	0.00	0.00
B18	0.00	0.00	0.13	0.05	0.00	0.37	0.00	0.17	0.00	0.00	0.00	0.38	0.16	0.13	0.03	0.00
C14	0.00	0.00	0.00	0.16	0.30	0.36	0.13	0.00	0.03	0.44	0.00	0.21	0.00	0.45	0.07	0.50
C15	0.05	0.00	0.00	0.02	0.00	0.23	0.45	0.00	0.00	0.09	0.00	0.50	0.16	1.19	0.12	0.01
C16	0.00	0.00	0.00	0.00	0.05	0.00	0.01	0.06	0.13	0.00	0.00	0.00	0.23	0.00	0.07	0.07
C17	0.19	0.24	0.10	0.13	0.23	0.12	0.37	0.20	0.16	0.27	0.04	0.00	0.14	0.00	0.12	0.19
C18	0.00	0.00	0.00	0.00	0.00	0.00	0.00	0.00	0.10	0.00	0.00	0.00	0.00	0.14	0.00	0.43
D14	0.06	0.00	0.00	0.52	0.00	0.32	0.17	0.58	0.46	0.00	0.17	0.00	0.00	0.00	0.19	0.00
D15	0.01	0.00	0.09	0.00	0.00	0.00	0.28	0.17	0.00	0.00	0.00	0.15	0.15	0.00	0.30	0.04
D16	0.04	0.06	0.00	0.00	0.07	0.26	0.20	0.00	0.23	0.39	0.01	0.46	0.00	0.00	0.24	0.13
D17	0.00	0.00	0.02	0.02	0.01	0.17	0.00	0.02	0.00	0.00	0.04	0.46	0.41	0.28	0.00	0.11
D18	0.03	0.15	0.00	0.22	0.19	0.00	0.43	0.00	0.00	0.05	0.07	0.00	0.00	0.22	0.00	0.46
E14	0.09	0.00	0.00	0.00	0.00	0.05	0.28	0.04	0.09	0.01	0.01	0.12	0.00	0.00	0.08	0.00
E15	0.00	0.20	0.00	0.06	0.09	0.19	0.07	0.00	0.15	0.05	0.01	0.16	0.00	0.00	0.01	0.08
E16	0.00	0.00	0.00	0.00	0.00	0.17	0.01	0.02	0.00	0.00	0.00	0.14	0.04	0.05	0.00	0.02
E17	0.00	0.00	0.00	0.00	0.00	0.16	0.00	0.00	0.00	0.18	0.00	0.27	0.24	0.00	0.13	0.00
E18	0.00	0.00	0.00	0.00	0.00	0.00	0.07	0.00	0.00	0.11	0.01	0.22	0.16	0.00	0.00	0.00
F14	0.01	0.00	0.01	0.00	0.00	0.05	0.00	0.00	0.05	0.00	0.00	0.00	0.00	0.00	0.00	0.00
F15	0.05	0.00	0.15	0.00	0.10	0.09	0.32	0.16	0.06	0.00	0.01	0.09	0.00	0.10	0.00	0.34
F16	0.10	0.00	0.00	0.00	0.19	0.06	0.66	0.07	0.02	0.19	0.00	0.18	0.00	0.00	0.00	0.00
F17	0.08	0.07	0.09	0.19	0.22	0.45	0.29	0.07	0.01	0.56	0.00	0.39	0.20	0.36	0.31	0.63
F18	0.00	0.10	0.00	0.00	0.00	0.00	0.00	0.00	0.15	0.00	0.01	0.04	0.00	0.00	0.00	0.00
b_{oj} **(rb/d)**	-94.4	-49.3	-61.9	-65.8	-151.2	-443.1	-444.9	-182.5	-166.6	-467.0	-33.2	-545.3	-276.1	-193.0	-105.4	-392.7

Figure 5.8 shows that he elimination of the negative weighting coefficients has caused R^2 to decrease from 0.971 to 0.952, which is not a significant decrease.

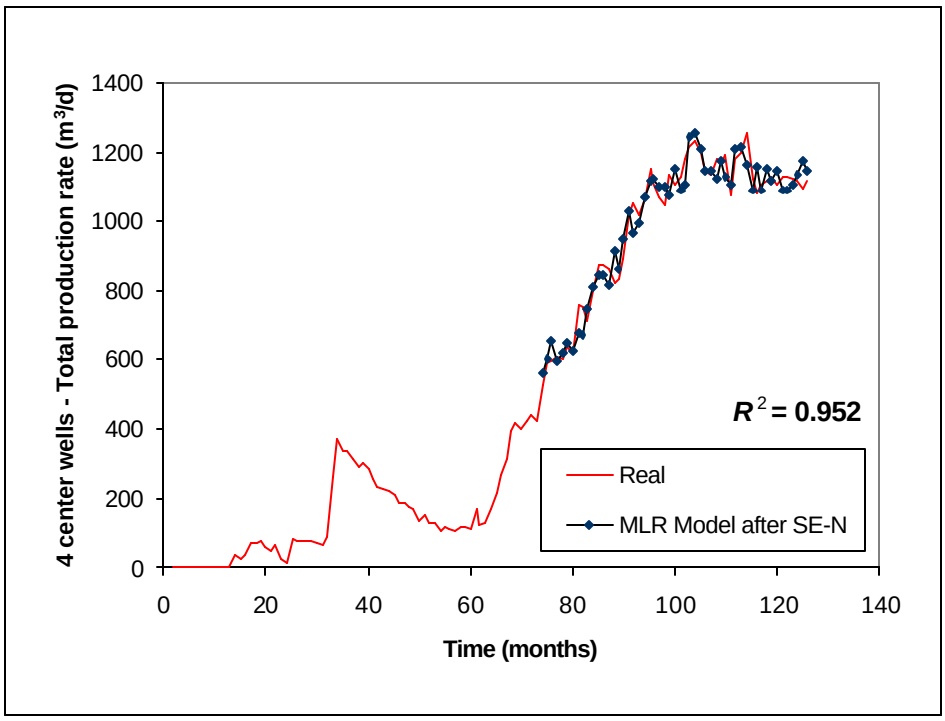

Figure 5.8 Chihuido de la Sierra Negra Field. MLR with diffusivity filters, with O_d = 2.04. Comparison between modeled total liquid production rate and the total observed liquid production rate (four center wells), after the successive elimination of the negative weighting coefficients.

The representation of the weighting coefficients (Figure 5.9) shows that the interpretation of the weighting coefficients suffered some qualitative changes, but it basically follows the results for the case before the SE-N procedure.

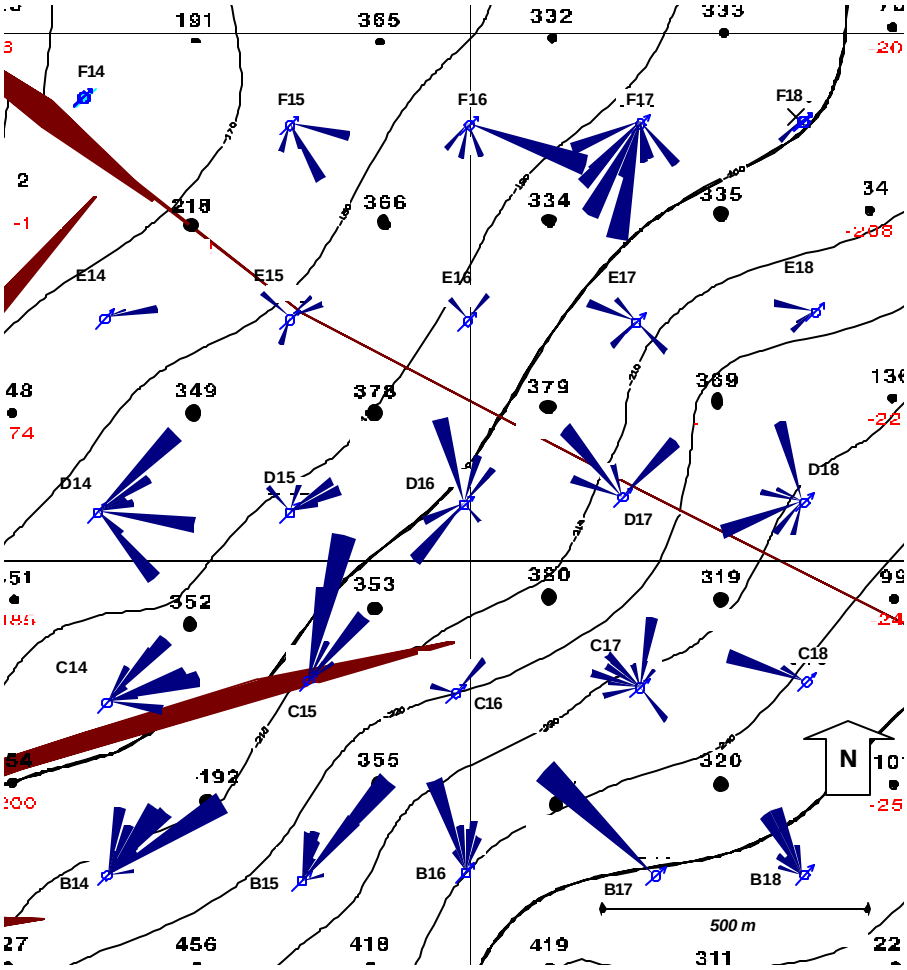

Figure 5.9 Chihuido de la Sierra Negra Field. MLR with diffusivity filters, with O_d = 2.04. Representation of the weighting coefficients b_{ij} (after the successive elimination of the negative weighting coefficients) shown in Table 5.2 and comparison with known geological features. A structural map is overlain.

Figure 5.10 shows a plot of R^2 (calculated using the total liquid rate of the four wells at the center of the field) vs. the number of well pairs eliminated during the SE-N procedure. The maximum and minimum weighting coefficient at each step of elimination are also plotted. At the steps where a well pair not corresponding to any

of the four center wells is eliminated, R^2 suffer no changes; but in general, the elimination of the minimum b_{ij} at each step causes a decrease in R^2. At certain specific steps the new minimum weight (recalculated after the elimination, with one fewer well pair) is larger in absolute value than that one of the previous step; but in general, the minimum weighting coefficient converges to 0 as more weighting coefficients are eliminated. Once the 120th coefficient has been eliminated, the successive elimination do not cause significant changes to R^2. The maximum weighting coefficient also shows a decreasing trend with the SE-N procedure, even when no positive weighting coefficients are eliminated.

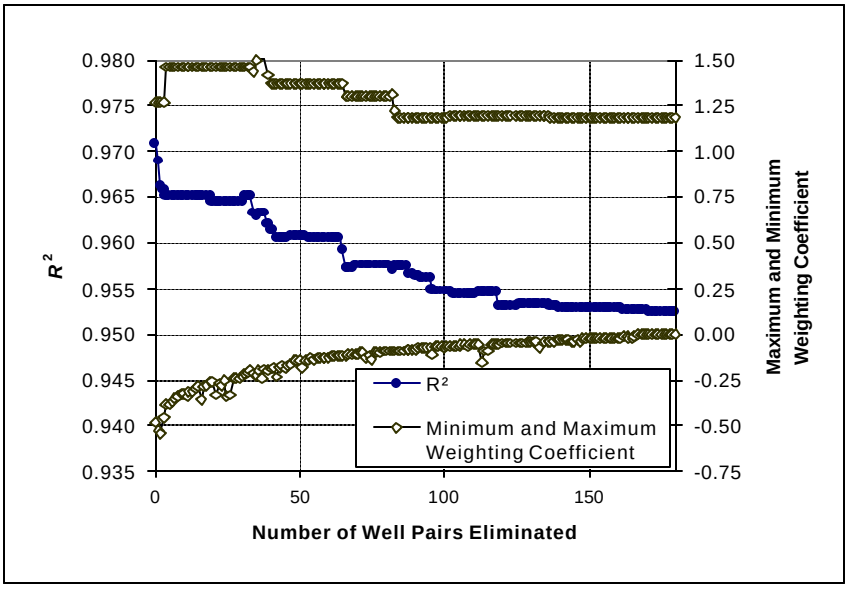

Figure 5.10 Chihuido de la Sierra Negra Field. MLR with diffusivity filters, with O_d = 2.04. Effect of the successive elimination of the negative weighting coefficients on the R^2 corresponding to the 4 wells at the center of the field. The maximum and minimum weighting coefficient at each step of elimination are also plotted.

Figure 5.11 shows that after the SE-N procedure not only the negative coefficients have been set to zero, but also, some of the large positive weighting coefficients have become smaller. However, there are still large positive coefficients (e.g. $b_{C15,378}$ = 1.19) that must be considered as incorrect.

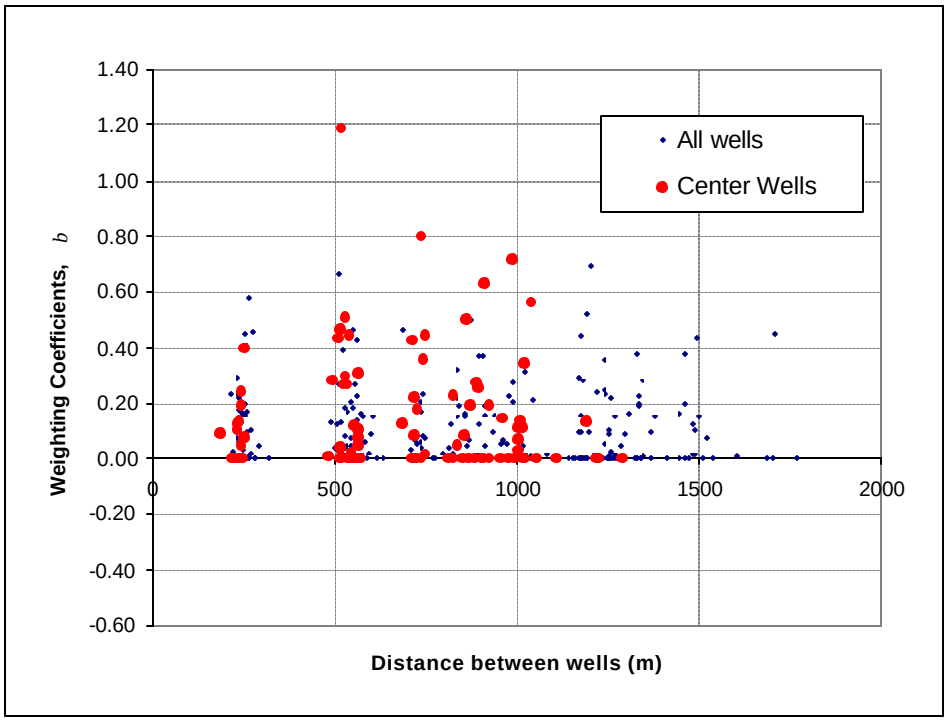

Figure 5.11 Chihuido de la Sierra Negra. MLR with diffusivity filters, with O_d = 2.04. Weighting coefficients b_{ij} vs injector-producer distance, after the successive elimination of the negative weighting coefficients. The large dots correspond to the four wells at the center of the field.

The results of the application of MLR to the ChSN Field before and after the SE-N procedure, show that even with a small overdetermination and without meeting

all the assumptions, the proposed technique can be effectively used and the interpretation of the weighting coefficients seem to agree with geological features.

5.2. BLOQUE I FIELD

5.2.1. Field Description

The technique was applied to the Bloque I Field, located in southern Argentina. The waterflooded field has 6 injectors and 21 producers (see Figure 5.12). There are 10 productive layers with irregular spatial continuity in the field. The reservoirs are constituted by river channel sandstones with moderate permeability and compressibilities. The injectors have selective injection systems where the injection rate per layer (or group of layers) is controlled by a set of downhole mandrels and valves.

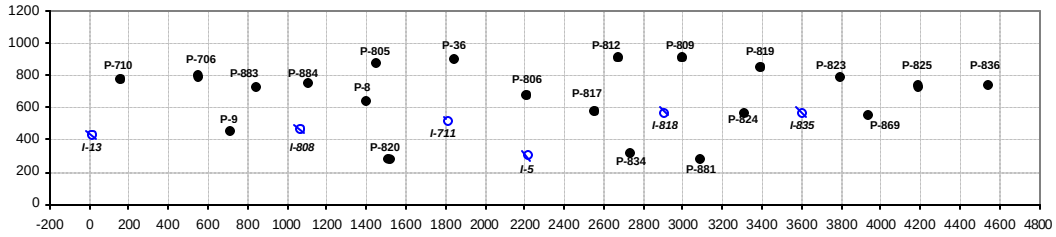

Figure 5.12 Bloque I Field. Base map. The horizontal and vertical axes show the coordinates, in meters.

5.2.2. Selection of Data Points

Figure 5.13 presents the injection and production rates in the Bloque I Field. After a declining primary production period, water injection starts in month 48.

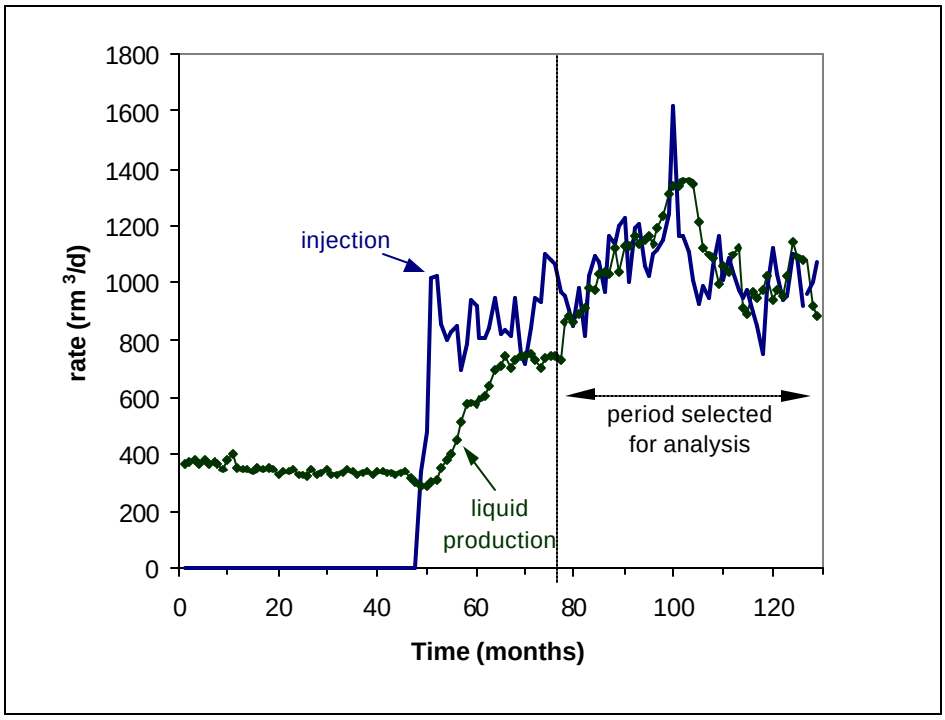

Figure 5.13 Bloque I Field. Injection and production rates. Period selected for the analysis.

The gas rate measurements are inaccurate, and consequently are not reported. If we select the period for analysis starting at month 76, 28 months after the beginning of injection, all the gas produced in the field in that period is probably dissolved gas. This is in agreement with the balance shown by injection and production rates, also starting on month 76 approximately. So, from month 76 to

month 129, 54 data points are included in the analysis. With 6 injectors in the field, we get O_d = 7.71. In terms of overdetermination, results are expected to be good (see Figure 3.48). The average injection rate per well and production rate per well within the period selected for the analysis are 174 rm^3/d is 48 rm^3/d respectively.

Both the MLR and the ABMLR approaches will be applied to the Bloque I Field. On the one hand, the MLR model allows injection to non-productive layers and constant primary production. On the other hand, since the field is in good balance, ABMLR can also be applied. The results of both applications are compared in the following sections.

5.2.3. Results of MLR

The application of MLR with diffusivity filters on Bloque I Field gives the results shown in Table 5.3 and Figures 5.14 to 5.16. With R^2 = 0.892, there are 59 negative weighting coefficients (47 percent) out of a total of 126 well pairs. The minimum weighting coefficient is $b_{I5,P883}$ = -4.09 and the maximum is $b_{I13,P823}$ = 1.50. It can be noted that many of the negative coefficients correspond to the injector I-5. A further improvement of the results is suggested and performed in the following section.

Table 5.3 Bloque I Field. MLR with diffusivity filters, with O_d = 7.71. Weighting coefficients b_{ij}. See Figure 5.15.

	P-8	P-9	P-36	P-706	P-710	P-805	P-806	P-809	P-812	P-817	P-819	P-820	P-823	P-824	P-825	P-834	P-836	P-869	P-881	P-883	P-884
I-5	-0.58	0.45	-0.33	-0.11	-0.15	-0.81	-0.98	0.03	0.22	-1.71	0.03	-0.25	-2.76	-0.70	0.13	-0.09	-0.44	0.02	-1.19	-4.09	-2.16
I-13	-0.12	-0.59	0.47	-0.22	0.14	0.11	-1.78	0.01	-0.26	0.11	-0.05	0.18	1.50	-0.23	0.09	0.16	0.00	0.14	-0.05	0.74	1.11
I-711	-0.10	-0.22	0.05	0.07	-0.01	0.00	0.22	0.00	0.00	-0.06	0.08	0.02	0.01	0.04	0.02	-0.06	0.02	0.00	-0.08	-0.51	0.37
I-808	0.02	0.00	-0.04	-0.02	0.00	-0.06	-0.05	0.00	0.01	-0.02	0.04	-0.03	0.00	0.06	-0.01	0.05	0.00	0.01	0.04	0.57	0.36
I-818	-0.09	-0.23	0.04	0.06	-0.01	0.01	-0.40	0.00	-0.02	0.09	-0.02	0.03	-0.07	-0.05	0.00	0.02	-0.05	-0.02	0.09	0.37	0.33
I-835	0.31	0.27	0.09	0.11	0.07	0.18	-0.20	0.00	-0.02	-0.03	0.02	0.03	0.32	0.16	0.01	-0.12	-0.02	0.04	0.23	0.07	-0.36
b_{oj} **(rb/d)**	49.5	111.4	-4.1	19.8	-3.5	28.1	263.4	-0.3	17.9	100.5	2.4	5.6	30.7	24.9	5.5	52.8	41.3	7.1	26.7	-6.5	-148.7

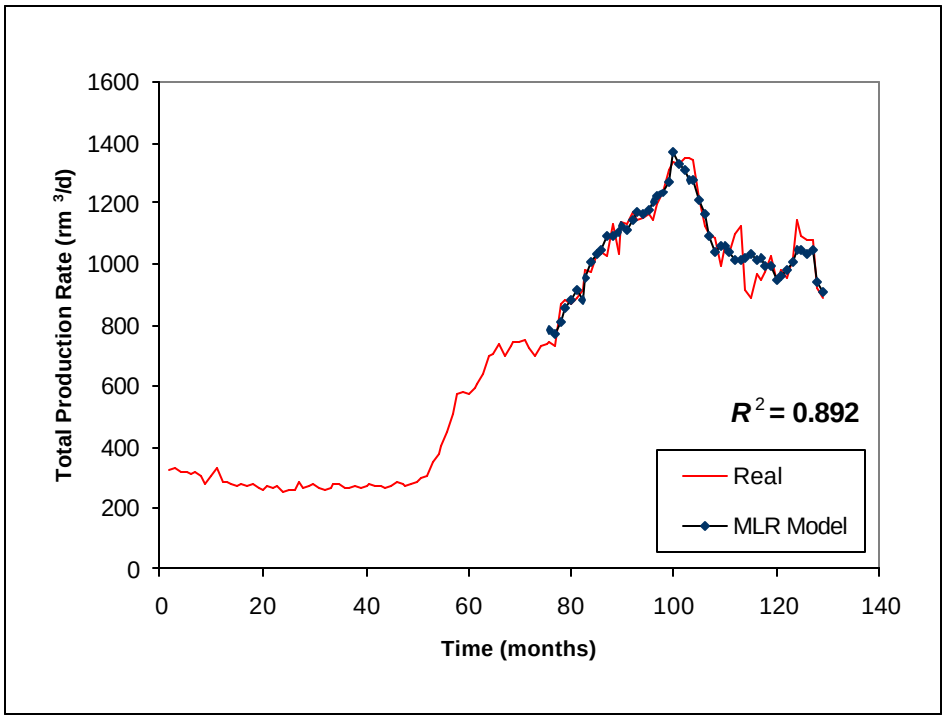

Figure 5.14 Bloque I Field. MLR with diffusivity filters, with O_d = 7.71. Comparison between modeled total liquid production rate and the total observed liquid production rate.

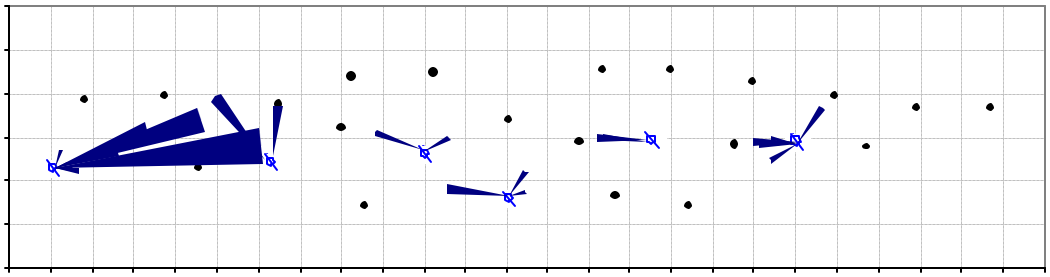

Figure 5.15 Bloque I Field. MLR with diffusivity filters, with O_d = 7.71. Representation of the positive weighting coefficients b_{ij} shown in Table 5.3.

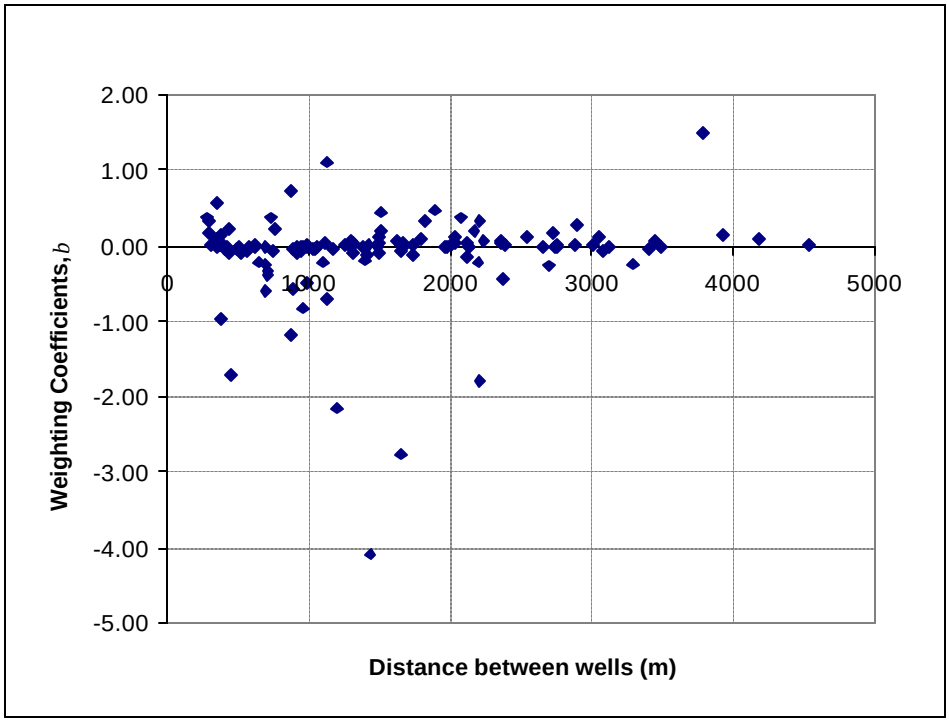

Figure 5.16 Bloque I Field. MLR with diffusivity filters, with O_d = 7.71. Weighting coefficients b_{ij} vs injector-producer distance.

5.2.4. Further Improvement of Results (MLR)

Section 5.1.4 describes and shows the results of the successive elimination of negative weighting coefficients (SE-N) in the ChSN MLR case. The elimination of negative weighting coefficients made some of the large positive weighting coefficients become smaller. However, after eliminating all the negative b_{ij}s, which have no physical meaning, some weighting coefficients remain large and positive (see Table 5.2 and Figure 5.11). Positive weighting coefficients greater than one have no physical meaning either. So, we will extend the SE-N procedure and also eliminate the large positive weighting coefficients without physical meaning. We call this procedure the successive elimination of physically non-significant weighting coefficients (SE-P).

During the elimination procedure, one of the weighting coefficients remained greater than one ($b_{I5,P9}$ = 1.17) and was set to zero. At the same time, one of the weighting coefficients that was significantly large corresponded to an injector-producer pair with a distance of 3800 meters ($b_{I13,P823}$ = 0.59). A weighting coefficient of 0.59 is very unlikely to correspond to a well-pair with a 3800-meter distance in this field, so it was also considered physically non-significant and, consequently, eliminated. Elimination based on previous knowledge of the field and general criteria is also included in the SE-P procedure. This type of elimination makes the outcome of the SE-P procedure non-unique, but physically more significant.

Table 5.4 Bloque I Field. MLR with diffusivity filters, with O_d = 7.71. Weighting coefficients b_{ij} after the successive elimination of physically non-significant weighting coefficients. See Figure 5.17.

	P-8	P-9	P-36	P-706	P-710	P-805	P-806	P-809	P-812	P-817	P-819	P-820	P-823	P-824	P-825	P-834	P-836	P-869	P-881	P-883	P-884	S
I-5	0.00	0.00	0.00	0.00	0.00	0.00	0.00	0.04	0.00	0.00	0.00	0.00	0.00	0.00	0.26	0.25	0.00	0.12	0.00	0.00	0.00	**0.30**
I-13	0.00	0.00	0.30	0.00	0.13	0.00	0.00	0.01	0.00	0.00	0.00	0.05	0.00	0.00	0.03	0.00	0.00	0.14	0.00	0.31	0.69	**0.52**
I-711	0.00	0.00	0.06	0.09	0.00	0.01	0.27	0.00	0.00	0.00	0.07	0.02	0.10	0.06	0.03	0.00	0.04	0.00	0.00	0.00	0.29	**0.70**
I-808	0.02	0.00	0.00	0.00	0.00	0.00	0.00	0.00	0.00	0.04	0.03	0.00	0.18	0.06	0.00	0.06	0.01	0.01	0.09	0.71	0.35	**0.35**
I-818	0.00	0.00	0.03	0.05	0.00	0.04	0.00	0.00	0.00	0.24	0.00	0.01	0.00	0.06	0.00	0.12	0.00	0.00	0.20	0.79	0.79	**0.44**
I-835	0.33	0.41	0.08	0.07	0.08	0.18	0.00	0.00	0.00	0.00	0.03	0.02	0.39	0.16	0.01	0.00	0.00	0.05	0.22	0.11	0.00	**1.75**
b_{oj} **(rb/d)**	-9.0	-34.6	-12.5	10.8	-13.4	-6.7	41.1	-1.3	3.4	15.8	-1.2	0.3	-51.5	-21.6	0.0	-8.4	14.2	-1.1	-45.2	-300	-297	
S	**0.35**	**0.41**	**0.47**	**0.22**	**0.21**	**0.23**	**0.27**	**0.05**	**0.00**	**0.28**	**0.13**	**0.11**	**0.66**	**0.35**	**0.33**	**0.44**	**0.05**	**0.33**	**0.51**	**1.93**	**2.12**	

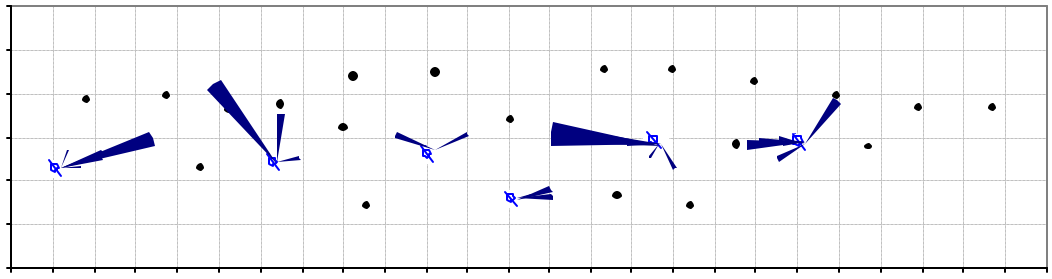

Figure 5.17 Bloque I Field. MLR with diffusivity filters, with O_d = 7.71. Representation of the positive weighting coefficients b_{ij} (after the successive elimination of physically non-significant weighting coefficients) shown in Table 5.4.

Table 5.4 and Figure 5.17 show the b_{ij}s using MLR with diffusivity filters after the SE-P procedure. The injectors have influence on most of the producers, but some of the producers (P812, P809, P836, P820, and P819) receive very little influence from injection, suggesting that the injection patterns may be changed to improve the performance of the waterflood.

After the SE-P procedure R^2 decreased from 0.892 to 0.763 (Figure 5.18), which means that we have obtained better physical results at the expense of poorer statistical results. In general, the weighting coefficients are larger for closer well pairs, but there are large weighting coefficients ($b_{ij} \cong 0.8$) for well pairs that are approximately 2000 meters away (Figure 5.19).

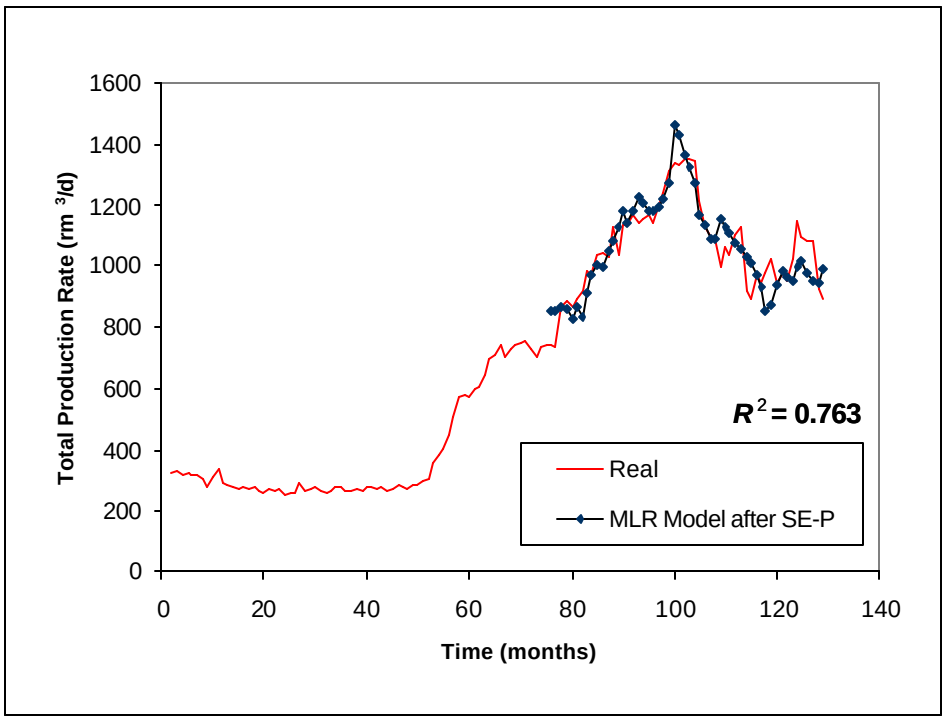

Figure 5.18 Bloque I Field. MLR with diffusivity filters, with O_d = 7.71. Comparison between modeled total liquid production rate and the total observed liquid production rate, after the successive elimination of the physically non-significant weighting coefficients.

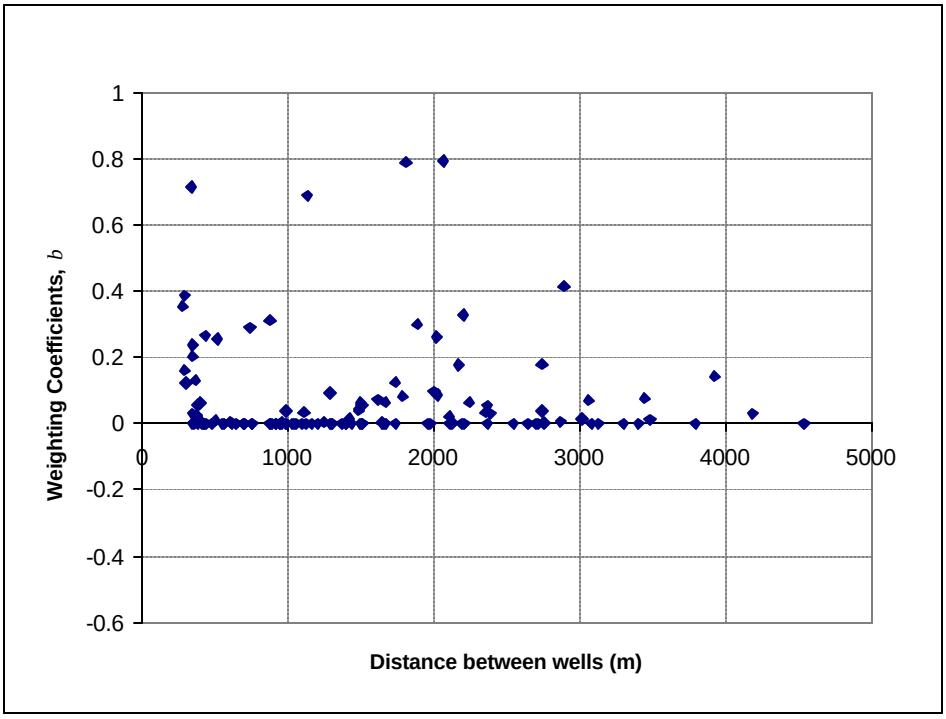

Figure 5.19 Bloque I Field. MLR with diffusivity filters, with O_d = 7.71. Weighting coefficients b_{ij} vs injector-producer distance after the successive elimination of the physically non-significant weighting coefficients.

Figure 5.20 shows the effect of the SE-P procedure on R^2 and the maximum and minimum weighting coefficient at each step of elimination. The trends are the same as those observed in the ChSN case (see Figure 5.10); as more well pairs are eliminated, R^2 decreases, the minimum weight converges to zero, and there is a decrease of the maximum weighting coefficient. In this case, the unrealistic positive weighting coefficients ($b_{I5,P9}$ and $b_{I13,P823}$) were eliminated at steps 23 and 24. This causes an unexpected increase in R^2. Actually, the correlation coefficient R^2 of the liquid production rate of producers P9 and P823 decreased with the elimination of

$b_{I5,P9}$ and $b_{I13,P823}$, as expected, because less weighting coefficients are used in the q_9 and q_{823} estimation. However, the R^2 corresponding to the total liquid production rate of the field shows an increase at steps 23 and 24.

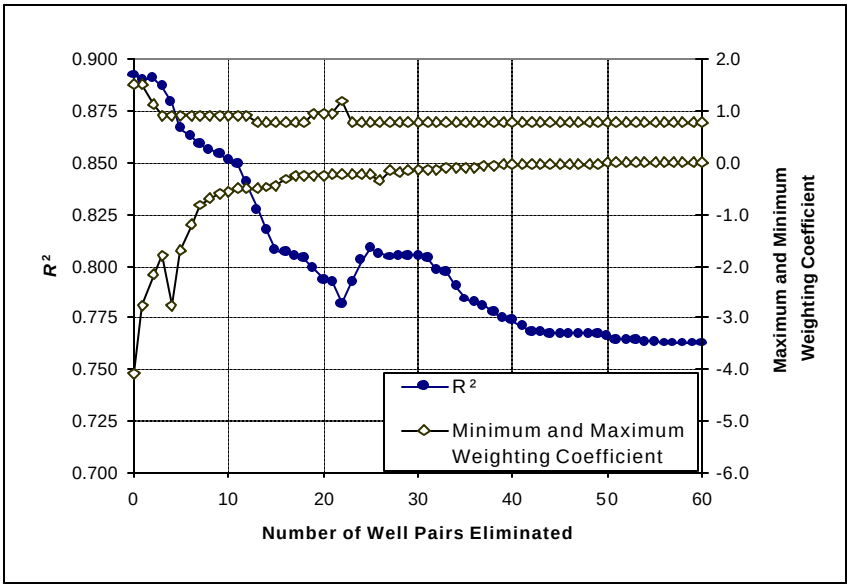

Figure 5.20 Bloque I Field. MLR with diffusivity filters, with Od = 7.71. Effect of the successive elimination of the physically non-significant weighting coefficients on R^2. The maximum and minimum weighting coefficient at each step of elimination are also plotted.

5.2.5. Results of ABMLR

Since the Bloque I is in approximate balance during the period selected for analysis, the average-rate balance MLR (ABMLR) approach can be used. First, the ABMLR approach with diffusivity filters is applied without any further improvement of results (Table 5.5).

Table 5.5 Bloque I Field. ABMLR with diffusivity filters, with O_d = 7.71. Weighting coefficients l_{ij}.

	P-8	P-9	P-36	P-706	P-710	P-805	P-806	P-809	P-812	P-817	P-819	P-820	P-823	P-824	P-825	P-834	P-836	P-869	P-881	P-883	P-884	s
I-5	0.08	1.95	-0.38	0.16	-0.20	-0.44	1.67	0.02	0.40	-0.82	0.06	-0.18	-2.35	-0.42	0.20	0.38	0.16	0.12	-0.92	-4.18	-4.17	**-0.24**
I-13	-0.20	-0.69	0.47	-0.23	0.14	0.06	-1.92	0.01	-0.28	0.07	-0.05	0.17	1.43	-0.27	0.08	0.13	-0.12	0.12	-0.09	0.74	1.30	**-1.21**
I-711	-0.09	-0.18	0.05	0.08	-0.02	0.00	0.26	0.00	0.01	0.00	0.08	0.02	0.04	0.07	0.03	-0.02	0.07	0.01	-0.06	-0.51	0.34	**0.35**
I-808	0.02	0.02	-0.04	-0.01	0.00	-0.06	-0.02	0.00	0.02	0.02	0.04	-0.03	0.02	0.07	-0.01	0.07	0.03	0.01	0.06	0.57	0.34	**0.04**
I-818	0.04	0.04	0.03	0.11	-0.02	0.08	0.25	0.00	0.01	0.28	-0.02	0.04	-0.03	-0.01	0.01	0.11	0.01	-0.01	0.13	0.36	-0.05	**0.81**
I-835	0.40	0.42	0.08	0.13	0.07	0.23	0.25	0.00	0.00	0.09	0.02	0.04	0.33	0.17	0.01	-0.06	0.01	0.05	0.25	0.06	-0.60	**2.26**
m_j **(rb/d)**	-0.08	-0.14	0.01	-0.02	0.00	-0.04	-0.66	0.00	-0.05	-0.30	0.00	-0.01	-0.05	-0.05	-0.01	-0.16	-0.04	-0.01	-0.07	0.01	0.20	
s	**0.24**	**1.57**	**0.21**	**0.24**	**-0.02**	**-0.13**	**0.50**	**0.03**	**0.16**	**-0.35**	**0.14**	**0.06**	**-0.56**	**-0.38**	**0.31**	**0.62**	**0.17**	**0.29**	**-0.62**	**-2.96**	**-2.83**	

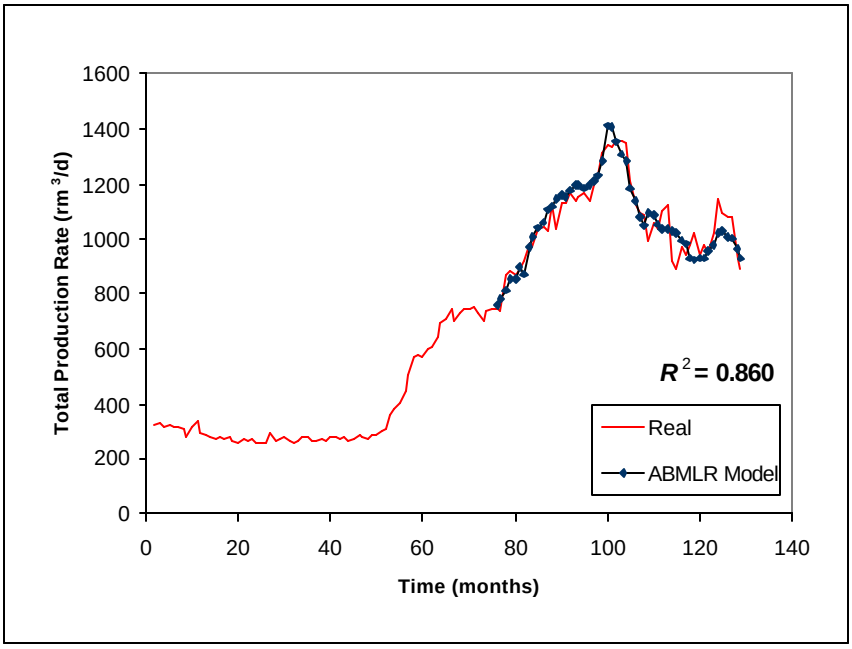

Figure 5.21 Bloque I Field. ABMLR with diffusivity filters, with O_d = 7.71. Comparison between modeled total liquid production rate and the total observed liquid production rate.

The rate constraint make the R^2 = 0.860 slightly lower than R^2 = 0.892 obtained using MLR (Figure 5.21). 34 percent of the weighting coefficients are

negative and there are 4 weighting coefficients that are larger than one. A further improvement of the results must be performed.

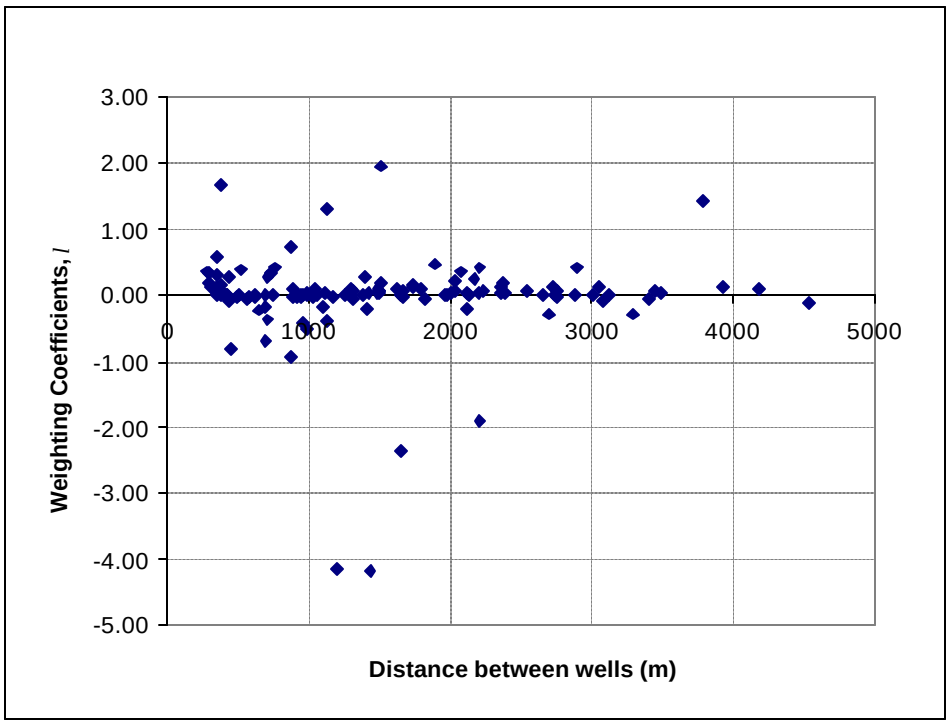

Figure 5.22 Bloque I Field. ABMLR with diffusivity filters, with O_d = 7.71. Weighting coefficients l_{ij} vs injector-producer distance.

5.2.6. Further Improvement of Results (ABMLR)

The SE-P procedure was applied using the ABMLR with diffusivity filters. In this case, 62 negative weighting coefficients were successively eliminated and only one large positive weighting coefficient ($l_{I5,P9}$ = 1.00) was eliminated during the procedure. Table 5.6 and Figure 5.23 show the results. There are 5 producers that

receive little influence from the injectors (P809, P710, P812, P820, and P836). The R^2 = 0.605 is the lowest of all cases studied for the Bloque I Field, but results seem to be the most significant from a physical standpoint (Figure 5.24). Figure 5.25 shows a plot of the weighting coefficients vs. injector-producer distance. All the l_{ij}s present physically reasonable values and, in general, the weights are smaller for more distant well pairs. As a general rule, the weighting coefficients corresponding to closer well pairs (probably up to 1700 m) should be considered as more significant than those of more distant well pairs.

Table 5.6 Bloque I Field. ABMLR with diffusivity filters, with O_d = 7.71. Weighting coefficients l_{ij} after the successive elimination of the physically non-significant coefficients. See Figure 5.23.

	P-8	P-9	P-36	P-706	P-710	P-805	P-806	P-809	P-812	P-817	P-819	P-820	P-823	P-824	P-825	P-834	P-836	P-869	P-881	P-883	P-884	s
I-5	0.00	0.00	0.00	0.10	0.00	0.00	0.00	0.02	0.09	0.00	0.02	0.00	0.00	0.00	0.26	0.10	0.03	0.10	0.00	0.00	0.00	**0.49**
I-13	0.00	0.00	0.26	0.00	0.01	0.00	0.00	0.00	0.00	0.00	0.00	0.05	0.34	0.00	0.03	0.00	0.00	0.15	0.00	0.00	0.00	**0.69**
I-711	0.00	0.00	0.05	0.10	0.00	0.00	0.39	0.00	0.00	0.00	0.07	0.02	0.00	0.02	0.03	0.00	0.06	0.00	0.00	0.00	0.00	**0.68**
I-808	0.01	0.00	0.00	0.00	0.00	0.00	0.00	0.00	0.00	0.04	0.03	0.00	0.11	0.06	0.00	0.06	0.02	0.00	0.08	0.27	0.04	**0.25**
I-818	0.00	0.00	0.01	0.08	0.00	0.03	0.05	0.00	0.01	0.28	0.00	0.01	0.00	0.03	0.00	0.10	0.02	0.00	0.10	0.29	0.37	**0.50**
I-835	0.31	0.22	0.06	0.09	0.03	0.16	0.00	0.00	0.00	0.04	0.03	0.02	0.30	0.14	0.01	0.00	0.01	0.05	0.11	0.00	0.00	**1.40**
m_j **(rb/d)**	0.18	2.07	0.05	-0.02	0.56	0.03	-0.48	0.18	-0.01	-0.10	0.01	0.00	0.44	0.09	0.00	0.07	-0.05	0.01	0.27	8.10	6.03	
s	**0.32**	**0.22**	**0.37**	**0.37**	**0.04**	**0.19**	**0.44**	**0.02**	**0.10**	**0.36**	**0.15**	**0.11**	**0.75**	**0.25**	**0.33**	**0.26**	**0.14**	**0.31**	**0.29**	**0.55**	**0.41**	

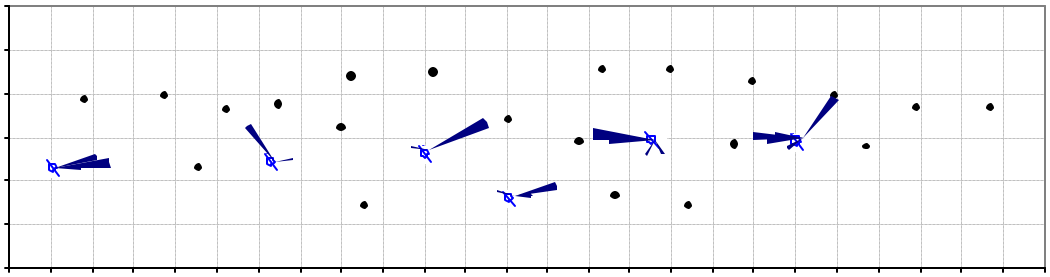

Figure 5.23 Bloque I Field. ABMLR with diffusivity filters, with O_d = 7.71. Representation of the positive weighting coefficients l_{ij} (after the successive elimination of physically non-significant weighting coefficients) shown in Table 5.6.

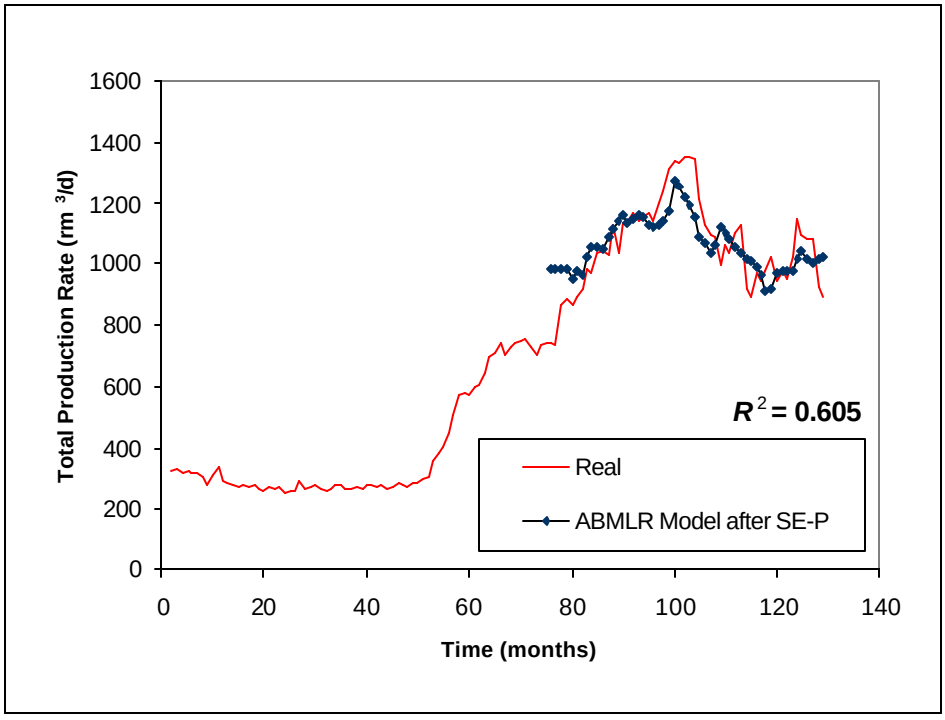

Figure 5.24 Bloque I Field. ABMLR with diffusivity filters, with O_d = 7.71. Comparison between modeled total liquid production rate and the total observed liquid production rate, after the successive elimination of the physically non-significant weighting coefficients.

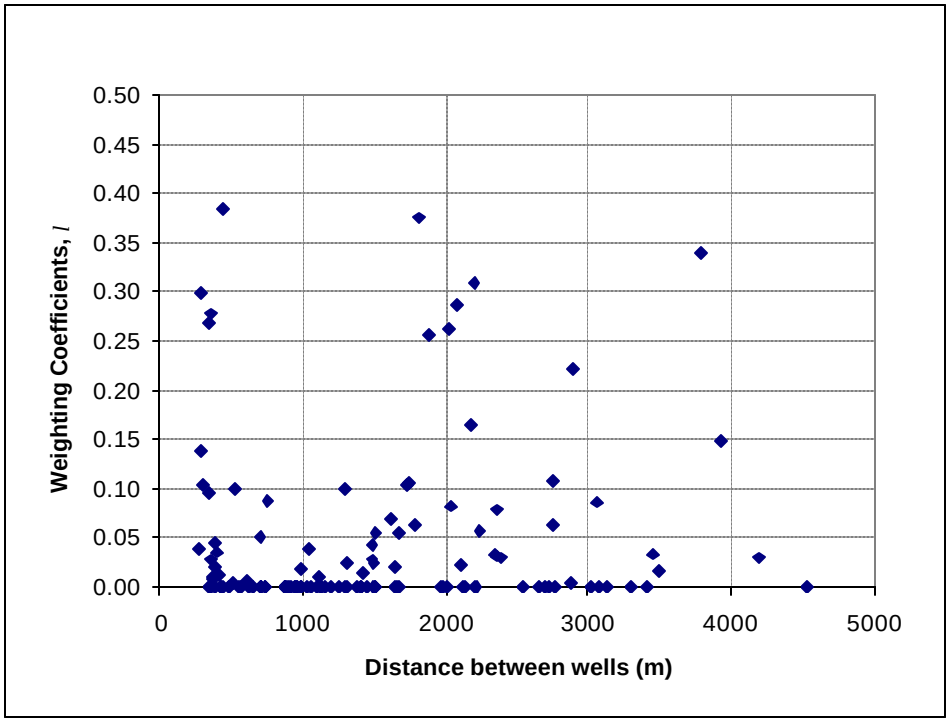

Figure 5.25 Bloque I Field. ABMLR with diffusivity filters, with O_d = 7.71. Weighting coefficients l_{ij} vs injector-producer distance after the successive elimination of the physically non-significant weighting coefficients.

5.3. GENERAL PROCEDURE

The previous sections of this chapter showed different ways of applying the proposed statistical techniques to two waterflooded fields. This section serves as a summary and provides an enumeration of the general steps that should be followed when applying this technique. More detail about these steps is found throughout this thesis.

The general procedure include four main steps: (1) selection of period for the analysis, (2) selection of regression approach, (3) determination of the diffusivity filters, and (4) successive elimination of physically non-significant weighting coefficients.

1. Selection of period for the analysis.
    - Check Assumptions: All the assumptions and possible sources of error must be checked for the determination of the period selected for the analysis. The most important factors to take into account are the absence of free gas production, data quality, no changes in production conditions, and no changes in injection conditions (especially in selective injection systems).
    - In general, look for periods in production/injection balance or periods where the unbalance (production/injection difference) is approximately constant.
    - Check the over determination factor, based on the number of data points and the number of injectors in the field.
    - Perform elimination of highly transient dominated periods if necessary. See step number 3.
2. Selection of regression approach.
    - Multivariate linear regression (MLR), average-rate balanced MLR (ABMLR) or instantaneously balanced MLR (IBMLR) must be selected according to the conditions of the field and the period selected for the analysis.

- Two approaches may be selected and the results compared (remember that IBMLR needs further research).

3. Determination of diffusivity filters
   - Perform the regression with a uniform initial guess for all the diffusivity factors h_{ij} and calculate R^2.
   - Iteratively change the uniform h_{ij}s until R^2 is maximized.
   - Iteratively change the local h_{ij}s (change their well-pair values one by one) until R^2 is maximized again. The determination of the h_{ij}s may be done following previously known geological features.
   - If the dissipation is relatively large, erase the data points that correspond to periods that are highly dominated by transients (sharp injection peaks). See step number 1.
4. Successive elimination of physically non-significant weighting coefficients
   - Start with the most negative weighting coefficient and proceed.
   - Successively eliminate the negative weighting coefficients and the large positive weighting coefficients without physical meaning.

The general procedure described here involves steps that are both clearly defined and have unique results, and steps that require the user criteria for their application, based on the knowledge of the technique and the field. These second

types of steps give non-unique results making the overall procedure one whose results depend in some degree on the criteria applied by the reservoir engineer.

The use of diffusivity filters in reservoirs with moderate and large dissipation improves the results. Initial guesses of uniform diffusivity factors (the same h_{ij} for every well pair in the field) rarely result in an R^2 smaller than that one without diffusivity filters. The further maximization of R^2 using uniform h_{ij}s is fairly simple. On the other hand, we must not forget that the local refinement of diffusivity filters, in many cases, is a second-order correction of the regression technique. This means that results may be satisfactory using only uniform diffusivity factors to maximize R^2. For example, using uniform h_{ij}s in a strongly anisotropic medium still yields weighting coefficients that show the anisotropy of the reservoir. Adjusting the h_{ij}s to match the anisotropy will further improve the results, but it may not be strictly necessary to obtain satisfactory results.

CHAPTER 6: CONCLUSIONS AND FUTURE WORK

This research work was performed on the basis of three main hypotheses:

- It is possible to quantitatively determine the communication between wells in a waterflood using only production and injection rate data.
- Production rate in every producer can be predicted from given the injection rate.
- The information about inter-well connectivity can be used to map reservoir heterogeneities, preferential permeability trends, and transmissibility barriers.

Following these hypotheses, different statistical approaches based on constrained multivariate linear regression were developed. These techniques were tested in several numerically simulated fields and then applied to two waterfloods in Argentina.

The conclusions drawn from this thesis are presented in this chapter. The last section of this chapter presents recommendations for future work including further research on topics that remain unresolved and research on topics that were not studied in this work but may give satisfactory solutions to the problems encountered.

6.1. CONCLUSIONS

A practical technique to quantify communication between wells in a waterflooded reservoir using only production and injection rate data has been developed. From this research work, the following conclusions were drawn:

1. The connectivity between wells is described by coefficients that only depend on geology and relative position between wells. The so-called weighting coefficients are independent of injection rates.
2. The technique is useful for determining permeability trends and the presence of permeability barriers. In addition, it can be used to predict total production from given injection rate.
3. The technique works in anisotropic media and media with vertical and spatial heterogeneity.
4. The determination of the influence of an injector on a certain producer simply using the injection-production rate correlation coefficient r may lead to significant errors. The rates between an injector-producer pair may be uncorrelated (or even negatively correlated) just because of the effect of other injectors on the same producer. r^2 alone is not an indicator of the connectivity between wells.
5. Considering only adjacent producers to analyze the influence of an injector may lead to significant errors. An injector may significantly support a producer that belongs to a different injection pattern.

6. The use of diffusivity filters improves the results and extends its range of application. The diffusivity filters account for the time lag and attenuation that occurs between the stimulus (injection) and the response (production). The filters transform the injection rates affecting a certain producer so that they take the form of an equivalent injection rate acting in an incompressible medium, which results in a convoluted or effective injection rate at a certain time.
7. Diffusivity filters become more important for large distances between injectors and producers and for large dissipation in the medium.
8. Three different statistical were developed: multivariate linear regression (MLR), average-rate balanced multivariate linear regression (ABMLR), and instantaneously balanced multivariate linear regression (IBMLR). ABMLR and IBMLR are constrained multivariate linear regressions.
9. The MLR approach must be used when the waterflood is not in balance (total injection rate is different from total liquid production rate) and in the case of areas with open boundaries. The ABMLR approach must be used when average total injection rate over time is approximately equal to the average total production rate over time. The IBMLR approach must be used when injection and liquid production rates are in balance at every time.
10. The quality of the expected results can be determined before the application of this method to a five-spot waterflooding, by a simple calculation based on the number of available data points and the number of injectors (overdetermination).

The use of a small number of data points and a large number of injectors lead to large inaccuracy in the determination of the weighting coefficients.

11. The response of the injection of non-reactive tracers in a synthetic field and weighting coefficients obtained from this technique the do not necessarily agree. On the one hand, tracers tell where each barrel of injected water is being produced, but they depend on injection rates. On the other hand, the weighting coefficients describe the connectivity between injector-producer pairs and the effective influence of each barrel of injected water on each producer.
12. The technique was applied to the Chihuido de la Sierra Negra waterflood in Argentina, and even when the overdetermination of the problem is smaller than that recommended, some features could be inferred. The validation of these results is very difficult; however, the results do seem to agree with the presence of known geological features.
13. A heuristic procedure to eliminate physically non-significant results was developed and presented. The application of this procedure improves the results of the technique.
14. The technique was also applied to the Bloque I waterflooded field. Results after the successive elimination of the physically non-significant weighting coefficients suggest that some of the producers are not receiving influence from the injectors. Changes in injection patterns are recommended.
15. A general procedure for the application of the technique is presented.

6.2. FUTURE WORK

The recommendations for future work on topics that remain unresolved or need further research are the following:

1. Study in more detail the relation between the weighting coefficients and the response of the non-reactive tracers.
2. Test the instantaneously balanced multivariate linear regression (IBMLR) on the 25x16 Synfield and actual fields.
3. Perform tests in the 25x16 Synfield with more complex reservoirs, combining spatial heterogeneities, faults, anisotropy, and study the interpretation of the weighting coefficients in these cases.
4. Analyze the effect of open boundaries in more depth.
5. Perform sensitivity analysis to: (1) different mobility ratios, (2) changes in bottomhole pressure, (3) changes in well productivity (increasing skin factor), (4) declining primary production, (5) the use of selective injection system where the injection rate is controlled by layer, (6) different levels of reservoir dissipation, and (7) gas saturation in the reservoir.

On the other hand, there are topics that were not studied in this research work but may give satisfactory solutions to the encountered problems, improve the technique, and extend its the range of application. The recommendations for future research on these topics are the following:

6. One way of improving the quality of the results is with a larger overdetermination. Based on injection and production rate data (typically monthly data) it may be possible to statistically generate in-fill data to increase the overdetermination of the system.
7. The use of filters to remove the error in the injection and production rate measurements may decrease the sensitivity of the technique to data quality.
8. The rate fluctuations that occur within a month are not captured by monthly reports and, consequently, cannot be analyzed by the regression technique. On the other hand, excessively frequent data sampling may include variations in production that are not caused by changes in injection and, besides, the rate information may be highly dominated by transients. Based on reservoir properties and distance between wells, the optimum range of data sampling frequency should be determined.
9. One of the assumptions of this technique is that no wells must be drilled within the analyzed period. A short shut-in is particularly useful information to compare the well rate fluctuations in injectors and producers. But a long shut-in is, to some extent, equivalent to the absence of a well. So, long shut-ins must not be included in the period selected for analysis. The maximum length of a shut-in so that it can be included in the analysis should be determined.
10. Changes in injection rate will cause changes in pressure in the surrounding of a producer. However, changes in pressure in the surroundings of a producer with a

some type of artificial lift systems (e.g. rod-pumping units) may not necessarily cause changes in production rate, but an increase of the bottomhole pressure (BHP). If the monthly BHP information is available, total potentials (combination of rate and BHP) can be calculated. It is suggested to develop an alternative technique that uses potentials instead of rates to determine the connectivity between wells.

11. The diffusivity filters developed in this work only partially solve the transient problem, probably because the superposition effect is addressed only from the injector and not from the producer standpoint. In reservoirs with large dissipation, the transient effects of the producers may be significant. The development of diffusivity filters that include the effect of the producers in transients is recommended.
12. In MLR the constant term b_0 accounts for unbalances. These unbalances may be caused by primary production. The use of a declining term in the MLR, based on previous primary decline analysis, instead of a constant term may improve the results of the technique.
13. A small overdetermination introduces errors to the estimation of the weighting coefficients. Moreover, in the analysis of areas with open boundaries, the estimation of the weighting coefficients corresponding to wells that are close to the boundaries are less precise. It may be possible to develop a compound

technique that analyzes different portions of a field by parts and then combines the results for the whole field.

14. The technique presented in this work uses the maximization of R^2 to determine the diffusivity factors h_{ij} that define the diffusivity filters. Instead of the maximization of R^2, the determination of the h_{ij}s could be performed seeking the minimization of the coefficient of variability of the weighting coefficients. It is recommended to study this possibility.
15. The determination of the diffusivity factors is an inverse-problem solution. Following the determination of the h_{ij}s, if the porosity f, the viscosity m, and the total compressibility c_t of the medium are known, then the effective permeability that connects two wells can be easily determined. But some further development to the diffusivity filters technique is required to obtain reliable results in the determination of the permeability of the medium.
16. The proposed technique analyzes existing injection and production-rate natural fluctuations to determine connectivity between wells. It is suggested to study the benefits of deliberately perturbing the injection rates in the field with different signals to perform the analysis. This means that each injector may follow known sinusoidal or square-wave's injection-rate patterns, with different frequencies that characterize the injector. Another possibility is to perturb each injector with a known injection pattern at different times. In any case, the characteristics of the signal (perturbation of the injection rate) should satisfy two main restrictions: (1)

the frequency must be such that it is captured by discrete rate measurements in the producer and is not averaged by the reservoir dissipation, and (2) the amplitude should be large enough to be captured by the producers (some artificial lift systems tend to produce on the constant-rate basis, rather than the constant bottomhole pressure basis).

NOMENCLATURE

A = asymmetry coefficient, dimensionless

C_1 = proportionality constant, psi

C_2 = proportionality constant, dimensionless

C_3 = proportionality constant, rb/d or rm^3/d

$Cov()$ = covariance

c_t = total compressibility, psi^{-1} or mips

d = dissipation constant, cp/md-psi

$E()$ = expected value

F_n = normalized filter function, $days^{-1}$

GOR = gas oil ratio, scf/bbl or sm^3/sm^3

I = total number of injection wells

I_d = identity matrix

i_i = observed injection rate, rb/d or rm^3/d

$\bar{i}_j$ = average injection rate, rb/d or rm^3/d

i^c_{ij} = convoluted injection rate, rb/d or rm^3/d

$\overline{II}$ = injector-injector average rate matrix, $(rb/d)^2$ or $(rm^3/d)^2$

$\overline{IP}_j$ = injector-producer average rate matrix, $(rb/d)^2$ or $(rm^3/d)^2$

J = productivity index, (rb/d)/psi or (rm^3/d)/MPa

k = permeability, md

$\bar{k}$ = average permeability, md

K = total number of independent variables in the linear model

k_h = horizontal permeability, md

k_z = vertical permeability, md

M = total number of data points

M_e = effective number of data points

N = total number of production wells

O_d = overdetermination coefficient, dimensionless

$\overline{P}$ = average pressure, psi or MPa

P_{wf} = bottom-hole flowing pressure, psi or MPa

q_j = observed liquid production rate, rb/d or rm^3/d

$\hat{q}_j$ = modeled liquid production rate, rb/d or rm^3/d

$\overline{q}_j$ = average liquid production rate, rb/d or rm^3/d

r = injector-producer distance, ft or m

R^2 = coefficient of determination

S_g = gas saturation, fraction

$s^2_{b\,1j}$ = variability of regression parameter b_{1j}

t = time (days or months)

U = unit column vector

V = Dykstra-Parsons coefficient

$Var()$ = variance

x = independent variable in the linear model

x = principal direction in simulation model

y = dependent variable in the linear model

y = principal direction in simulation model

z = principal direction in simulation model

$\alpha_{ij}^{(n)}$ = diffusivity filter coefficient, dimensionless

b_{ij} = weighting coefficient in MLR, dimensionless

b_{0j} = additive constant term in MLR, rb/d or rm^3/d

Di = change in injection rate, rb/d or rm^3/d

DP = pressure change, psi or MPa

Dq = production rate change, rb/d or rm^3/d

e = random error

f = porosity, fraction

h = diffusivity constant, md-psi/cp

h_{ij} = diffusivity constant of injector-producer pair, md-psi/cp

L_j = weighting coefficient column vector, dimensionless

l_{ij} = weighting coefficient in ABMLR and IBMLR, dimensionless

m = fluid viscosity, cp

m_j = Lagrange multiplier, rb/d or rm^3/d

n_i = Lagrange multiplier, $(rb/d)^2$ or $(rm^3/d)^2$

N = Lagrange multipliers column vector, $(rb/d)^2$ or $(rm^3/d)^2$

r = correlation coefficient

s^2 = variance, $(rb/d)^2$ or $(rm^3/d)^2$

s^2_{ii} = injector-injector covariance, $(rb/d)^2$ or $(rm^3/d)^2$

s^2_{ij} = injector-producer covariance, $(rb/d)^2$ or $(rm^3/d)^2$

S_j = injector-producer covariance column vector, $(rb/d)^2$ or $(rm^3/d)^2$

S_{inj} = injector-injector covariance matrix, $(rb/d)^2$ or $(rm^3/d)^2$

Subscripts

i = injector index

h = injector index

k = parameter index in the linear model

j = producer index

Superscripts

m = observed data point

n = time

REFERENCES

Alabert, F.G and Modot, V.: “Stochastic Models of Reservoir Heterogeneity: Impact on Connectivity and Average Permeabilities,” paper SPE 24893 presented at the SPE ATCE, Washington, October 4-7, 1992.

Araque-Martinez, A.N.: "Estimation of autocorrelation and its use in sweep efficiency calculation," M.S. Thesis, The University of Texas at Austin, 1993.

Bertsekas, D.P.: *Constrained optimization and Lagrange multiplier methods*, Academic Press, New York, 1982.

Canas, J.A. and Wu, C.H.: “Use of Hydraulic Interwell Connectivity Concepts in Reservoir Characterization,” paper SPE 27698 presented at the SPE Permian Basin Oil and Gas Recovery Conference, Midland, March 16-18, 1994.

De Sant'Anna Pizarro, J.O.: "Estimating injectivity and lateral autocorrelation in heterogeneous media," Ph.D. Thesis, The University of Texas at Austin, 1998.

Dykstra, H. and Prsons, R.L.: "The prediction of oil recovery by waterflood," *Secondary recovery of oil in the United States*, API (1950) 160-74.

Griffiths Barros, I.: "The extreme Spearman rank correlation coefficient in the characterization of the North Buck Draw field," M.S. Thesis, The University of Texas at Austin, 1998.

Heffer, K.J., Fox, R.J., and McGill, C.A.: "Novel techniques show links between reservoir flow directionality, earth stress, fault structure and geomechanical changes in mature waterfloods," paper SPE 30711 presented at the SPE ATCE, Dallas, October 22-25, 1995.

Hird, K. B. and Dubrule, O.: "Quantification of Reservoir Connectivity for Reservoir Description Applications," paper SPE 30571 presented at the SPE ATCE, Dallas, October 22-25, 1995.

Jansen, F.E. and Kelkar, M.G. (A): "Application of Wavelets to Production Data in Describing Inter-Well Relationships," paper SPE 38876 presented at SPE ATCE, San Antonio, October 5-8, 1997

Jansen, F.E. and Kelkar, M.G. (B): "Non-Stationary Estimation of Reservoir Properties Using Production Data," paper SPE 38729 presented at SPE ATCE, San Antonio, October 5-8, 1997

Jensen, J.L., Lake, L.W., Corbett, P.W.M., and Goggin, D.J.: *Statistics for petroleum engineers and geoscientists*, Prentice-Hall Inc., Upper Saddle River, New Jersey (1997).

Malik, Z.A., Silva, B.A., Brimhall, R.M., and Wu, C.H.: "An Integrated Approach To Characterize Low-Permeability Reservoir Connectivity for Optimal Waterflood Infill Drilling," paper SPE 25853 presented at SPE Rocky Mountain Regional/Low Permeability Reservoirs Symposium, Denver, April 12-14, 1993.

Miller, R.G.: *Beyond ANOVA, basics of applied statistics*, John Wiley & Sons, New York, 1986.

Panda, M.N. and Chopra, A.K.: "An integrated approach to estimate well interactions," paper SPE 39563 presented at SPE India Oil and Gas Conference and Exhibition, New Delhi, India, February 17-19, 1998.

Refunjol, B.T.: "Reservoir characterization of North Buck Draw field based on tracer response and production/injection analysis," MSc. Thesis, The University of Texas at Austin, 1996.

Sabet, M.A.: *Well test analysis*, Gulf Publishing Company, Houston, Texas (1991) 40.

Soeriawinata, T. and Kelkar, M.: "Reservoir management using production data," paper SPE 52224 presented at the SPE Mid-Continent Operation Symposium, Oklahoma City, Oklahoma, March 28-31, 1999.

VITA

Alejandro Albertoni, son of Alcira María del Carmen Batlle and Juan Carlos Bartolomé Albertoni, was born in Buenos Aires, Argentina, on January 13, 1972. After receiving the degree of Bachelor of Science in Petroleum Engineering from the Instituto Tecnológico de Buenos Aires in 1994, he joined Repsol-YPF S.A. He worked as drilling engineer during 1995. During 1996-2000, he worked as reservoir engineer in different fields and locations in Argentina, mainly in the areas of secondary recovery and reservoir simulation. He is a member of the Society of Petroleum Engineers (SPE) and of the Instituto Argentino del Petróleo y Gas (IAPG).

Permanent address: Viamonte 1881 10A
(C1056ABA) Buenos Aires
Argentina

aalbertoni@yahoo.com

This thesis was typed by the author.

The Dissertation Committee for Yuan Qiu Certifies that this is the approved version of the following dissertation:

NATURAL FRACTURE MODELING AND CHARACTERIZATION

Committee:

Jon. E. Olson, Supervisor

Larry W. Lake

Stephen E. Laubach

William R. Rossen

Joe Vogt

NATURAL FRACTURE MODELING AND CHARACTERIZATION

by

Yuan Qiu, B.S.; M.S.

DISSERTATION

Presented to the Faculty of the Graduate School of

The University of Texas at Austin

in Partial Fulfillment

of the Requirements

for the Degree of

DOCTOR OF PHILOSOPHY

The University of Texas at Austin

May, 2002

Dedication

To my father, BangLiang Qiu and mother, Yunyan Sun

for their support and patience through my long education

To all my friends

for their encouragement and support

Acknowledgements

First of all, I would like to express my immeasurable gratitude to my supervisor, Dr. Jon E. Olson for his support and guidance in all my years at The University of Texas at Austin. His patience, encouragement and rigorous scientific approach are something I deeply appreciate and admire. I also own many thanks to all my dissertation committee members, Dr. Larry W. Lake, Dr. Stephen E. Laubach, Dr. William R. Rossen and Dr. Joe Vogt for their help and valuable suggestions.

I would like to extend my thanks to my student colleagues and friends, Jing Du, Zeno Philip, Peggy Rijken, Xiuping Wang, Jing Xie, Shashank Raizada, Rajarajan Narayanasamy, Dan Shan, Liang Cheng and Oliver Ohsu for their help and encouragement.

I owe special thanks to Anping Yang, for the useful discussion over the phone; and my gratitude to Delores Holubec and Cliffh Holubec for their moral support, and spiritual encouragement throughout my study at The University of Texas at Austin.

This work was supported by Department of Energy (DOE) and the Reservoir Engineering Research Program (RERP) of the Center for Petroleum and Geosystems Engineering of The University of Texas at Austin.

Yuan Qiu

Department of Petroleum and Geosystem Engineering

The University of Texas at Austin

Austin, TX 78712

May 2002

NATURAL FRACTURE MODELING AND CHARACTERIZATION

Publication No._____

Yuan Qiu, Ph. D.

The University of Texas at Austin, 2002

Supervisor: Jon E. Olson

The production of oil and gas from a naturally fractured reservoir requires an understanding of fracture connectivity and fracture pattern geometry. To study fracture connectivity, it is important to know fracture path. Pseudo-three-dimensional numerical simulations in linear elastic materials show that fracture growth geometry is affected by not only the ratio of remote differential stress to driving stress but also by bed thickness and fracture propagation environment. Fractures will propagate straight if either the remote differential stress ratio or fracture spacing to bed thickness ratio is above one. Fractures are more planar if the propagation condition is subcritical.

A cumulative fracture length distribution is derived based on mechanical principles. The mechanical interaction between two mode-I cracks is a function of fracture length, spacing, overlap and bed thickness. Crack propagation is

enhanced when the en echelon cracks slightly underlap, but it is impeded when the cracks overlap. If a small crack is close enough to a large crack, it can suppress the large crack's propagation and capture it. The probability of a large crack passing close to a small crack depends on the large crack's length and the density of small cracks. Putting the mechanics together with the probability analysis results in a negative exponential distribution for two-dimensional map view sampling.

A semi-analytical geomechanical model is developed to simulate a single set of parallel fracture network. In this model, only a few cracks are modeled explicitly and other cracks are treated as a continuum through an effective elastic modulus controlled by crack density. The semi-analytical model simulates fracture patterns similar to a more rigorous displacement-discontinuity boundary-element model. Compared to the boundary element numerical model, the semi-analytical model computes faster and can deal with thousands fractures. A sensitivity study of fracture pattern development shows that the initial flaw density, subcritical index, bed thickness and elastic modulus affect fracture length, spacing and the degree of fracture clustering. The systematic relationship between the model inputs (boundary conditions and rock properties) and final fracture geometry indicates that this high-speed semi-analytical model can be used for the further investigation of fracture pattern inversion from observed data.

Table of Contents

Acknowledgments v

Abstract vii

List of Figures xii

List of Tables xxvii

CHAPTER 1: OVERVIEW 1

REFERENCES 4

CHAPTER 2: FRACTURE PATH INTERPRETATION FROM PSEUDO-THREE-DIMENSIONAL LINEAR ELASTIC NUMERICAL SIMULATION 5

ABSTRACT 5

INTRODUCTION 5

THEORY OF SIMULATION MODEL 8

VERIFICATION: FRACTURE PROPAGATION PATHS IN TWO DIMENSIONAL PLANE STRAIN 10

Critical Fracture Growth 10

Subcritical Fracture Growth 13

PROPAGATION PATHS FOR FINITE HEIGHT FRACTURES 14

Critical Fracture Growth 14

Subcritical Fracture Growth 15

CONCLUSIONS 17

REFERENCES 19

CHAPTER 3: MECHANICAL INTERACTION BETWEEN FRACTURES 37

ABSTRACT 37

INTRODUCTION 38

THEORETICAL BACKGROUND 40

FRACTURE CONFIGURATION AND MODEL VERIFICATION 41

Fracture Configuration 41
Model Verification 42
MECHANICAL INTERACTION BETWEEN TWO FRACTURES 44
In Igneous Rock (2d Plain Strain) 45
In Sedimentary Rock (Pseudo-3d Case) 48
DISCUSSION 50
REFERENCES 52

CHAPTER 4: EFFECT OF MECHANICAL INTERACTION ON FRACTURE LENGTH DISTRIBUTION 65
ABSTRACT 65
INTRODUCTION 65
FRACTURE CAPTURE MODEL 70
ANALYTICAL MODEL OF FRACTURE LENGTH DISTRIBUTION 75
FIELD DATA ANALYSIS 83
CONCLUSIONS 87
REFERENCES 89

CHAPTER 5: A SEMI-ANALYTICAL FRACTURE PATTERN GROWTH SIMULATOR 108
ABSTRACT 108
INTRODUCTION 108
CONDITIONS FOR CRACK PROPAGATION 110
MODEL ALGORITHM 112
Local Interaction Factor, k_I 113
Effective Elastic Modulus, $\tilde{E}$ 116
THE RANGE OF MODEL INPUT PARAMETERS 118
VERIFICATION 118
Base Case Comparison 119
2D case comparison 119

3D case comparison..... 121
SENSITIVITY ANALYSIS..... 122
Base Case..... 123
Sensitivity to Initial Flaw Density..... 124
Sensitivity to Subcritial Growth Index..... 126
Sensitivity to Bed Thickness..... 128
Sensitivity to Elastic Modulus and Strain Rate..... 130
CONCLUSIONS..... 131
REFERENCES..... 132
REFERENCES… 159
Vita… 169

List of Figures

Figure 2.1 Maximum circumferential stress criterion of Erdogan and Sih (1963). Fractures propagate radially from the crack tip at an angle q, the direction of maximum circumferential tension, s_{qq}, which coincides with the direction of zero shear stress, $s_{rq}=0$..... 23

Figure 2.2 Three fundamental modes of fracture. A: mode I, opening mode; B: mode II, in-plane shear or sliding mode; C: mode III, anti-plane shear or tearing mode. 24

Figure 2.3 Boundary conditions used for critical fracture growth simulation. The constant stress components s_{11}^{r} and s_{22}^{r} act perpendicular and parallel to crack plane, respectively. 25

Figure 2.4 Boundary conditions used for subcritical fracture growth simulation. A constant strain rate is imposed perpendicular to the crack plane, with a constant stress ($DS=s_{22}^{r}-s_{11}^{r}$) parallel to it. ……..25

Figure 2.5 Magnitude of crack perpendicular stress (s_{yy}) around two interacting fractures. The crack-induced stress in front of the fracture tips is tensile stress (negative), and the stress at both side of the fractures are compressive (positive). The unit of the stress is MPa. 26

Figure 2.6a Theoretical fracture paths driven by internal fluid pressure for bed thickness of 100m (fracture is under critical growth). The three sets of curves represent the results for various differential stress (0, 1 and 4 MPa). The initial fracture spacing is 3m. Fractures are propagated simultaneously towards each other. 27

Figure 2.6b Driving pressure required to propagate one fracture to a specified length keeping $K_I=K_{IC}$. Each curve represents a specific differential stress. Fracture configuration is illustrated as Figure 2.6a. 27

Figure 2.7 Two parallel fractures each with length L are tip-to-tip. The distance perpendicular to the two fractures is S. Fracture height is H, and the bed thickness is T. In this case fracture height equals bed thickness (H=T). 28

Figure 2.8a Theoretical fracture paths driven by internal fluid pressure for bed thickness of 100m. (This is a mapview. The bed thickness is in the direction perpendicular to the paper). The three sets of curves represent different initial spacing to length ratios. Remote differential stress is zero and the fracture is under critical growth... 29

Figure 2.8b Driving pressure required to propagate one fracture to a specified length. Each curve represents different spacing to length ratio. The fracture configuration is illustrated in Figure 2.8a. Remote differential stress is zero. 29

Figure 2.9 Distribution of crack perpendicular stress, s_{11}, induced by internal fluid pressure for 2D plane strain, DS=0. On both sides of the fracture, the induced stress is compressive (positive). In front of the fracture tips the induced stress is tensile (negative). The size of compressive stress range is proportional to fracture length. 30

Figure 2.10 Theoretical fracture paths driven by remote constant stain rate for a bed thickness of 100m for subcritical growth. The three sets of curves represent various differential stresses. The initial fracture spacing is 3m. The two fractures propagate simultaneously towards each other. 31

Figure 2.11 Distribution of crack perpendicular stress, s_{11}, induced by internal fluid pressure for a bed thickness of 5m and DS=0. On both sides of the fracture, induced stress is compressive, and in front of the fracture tips induced stress is tensile. The size of compressive stress range is proportional to bed thickness. 32

Figure 2.12a Theoretical fracture paths for different bed thickness given critical growth. Initial crack spacing is 5m and ΔS=0. 33

Figure 2.12b Driving pressure required to propagate one fracture to a specified length. Each curve represents a specific bed thickness. Fracture configuration and propagation condition are shown in Figure 2.12a. 33

Figure 2.13a Theoretical fracture paths for different bed thickness given critical growth. Initial crack spacing is 2m and ΔS=0. 34

Figure 2.13b Driving pressure required to propagate one fracture to a specified length. Each curve represents a specific bed thickness. Fracture configuration and propagation condition are shown in Figure 2.13a. 34

Figure 2.14a Theoretical fracture paths for different bed thickness given subcritical growth. Initial crack spacing is 5m and ΔS=0. 35

Figure 2.14b Stress intensity factors required propagating one fracture to a specified length. Fracture configuration and propagation condition are shown in Figure 2.14a. 35

Figure 2.15a Theoretical fracture paths for different bed thickness given subcritical growth. Initial crack spacing is 2m and ΔS=0. 36

Figure 3.1 Non-dimensioned normal stress, s_{11}/s_{11}^r, along the plane perpendicular to the crack through the crack middle. The normal stress s_{11}/s_{11}^r along the symmetry plane x_2=0 calculated from Olson's pseudo-3d model is similar to the stress predicted by the true 3d (calculated by equation 3.1). 55

Figure 3.2 Fracture configuration illustrates main crack with length of 2a and field crack with length of 2b, and their relative position, which is quantified as Overlap (2o), the crack-parallel distance between the two cracks' inner tips, and Spacing (2s), the crack-perpendicular distance between the two cracks. 2d is the crack-parallel distance between the two cracks' centers. 56

Figure 3.3 The dimensionless crack extension force verse joint length ratio for different spacing of two-dimensional case, comparing with Figure 2.11 of Segall and Pollard, 1983. 57

Figure 3.4 The dimensionless crack extension force for the middle crack of a three-crack array. 57

Figure 3.5 Distribution of crack perpendicular stress, s_{11}, for 2D plane strain. On both sides of the fracture, the induced stress is compressive. In front of the fracture tips induced stress is tensile. The size of compressive stress range is proportional to fracture length. 58

Figure 3.6 Distribution of crack perpendicular stress, s_{11}, for bed thickness of 5m. On both sides of the fracture, induced stress is compressive, and in front of the fracture tips induced stress is tensile. The size of compressive stress range is proportional to bed thickness. 59

Figure 3.7 The influence of the crack length ratio (a/b) on the crack interaction factor, plotted versus dimensionless overlap for the inner tip of the main crack. (2d plane strain and *s/b*=0.25). 60

Figure 3.8 The influence of crack length ratio (a/b) on crack interaction factor, plotted versus dimensionless overlap for the outer tip of the main crack. (2d plane strain case and *s/b*=0.25). 60

Figure 3.9 The influence of dimensionless spacing on crack interaction factor, plotted versus dimensionless overlap for the inner tip of the main crack (2d plane strain case and *a/b*=20). 61

Figure 3.10 The influence of the crack length ratio (a/b) on the crack interaction factor, plotted versus dimensionless overlap for the inner tip of the main crack. (Pseudo-3d with *T/b*=2.5 and *s/b*=0.25). 61

Figure 3.11 The influence of the crack length ratio (a/b) on the crack interaction factor, plotted versus dimensionless overlap for the outer tip of the main crack. (Pseudo-3d with *T/b*=2.5 and *s/b*=0.25). 62

Figure 3.12 The influence of dimensionless spacing on crack interaction factor, plotted versus dimensionless overlap for the inner tip of the main crack (Pseudo-3d with *T/b*=2.5 and *a/b*=20). 62

Figure 3.13 The influence of the crack length ratio (a/b) on the crack interaction factor, plotted versus dimensionless overlap for the inner tip of the main crack. (Pseudo-3d with *T/b*=0.5 and *s/b*=0.25). 63

Figure 3.14 The influence of the crack length ratio (a/b) on the crack interaction factor, plotted versus dimensionless overlap for the outer tip of the main crack. (Pseudo-3d with *T/b*=0.5 and *s/b*=0.25). 63

Figure 3.15 The influence of dimensionless spacing on crack interaction factor, plotted versus dimensionless overlap for the inner tip of the main crack (Pseudo-3d with *T/b*=0.5 and *a/b*=20). 64

Figure 4.1 The different types of distribution laws used in this paper to describe fracture length distribution. The probability distribution functions, f(x) are shown as above. m, mean; s, standard deviation, $1/l = m = s$, C_1, D_1 are constant. 95

Figure 4.2 Fracture configuration illustrates main crack with length of 2a and field crack with length of 2b, and their relative position, which is quantified as Overlap (2o), the crack-parallel distance between the two cracks' inner tips, and Spacing (2s), the crack-perpendicular distance between the two cracks. 2d is the crack-parallel distance between the two cracks' centers. 96

Figure 4.3a The influence of dimensionless spacing on crack interaction factor, plotted versus dimensionless overlap for the inner tip of the main crack (2d plane strain case and *a/b*=20). 97

Figure 4.3b The influence of dimensionless bed thickness on crack interaction factor, plotted versus dimensionless overlap for the inner tip of the main crack (*a/b*=20 and *s/b*=0.5). 97

Figure 4.4a Capture ratio versus dimensionless overlap for different main crack to field crack's length ratios (*s/b*=0.25, and 2D Plane strain case). 98

Figure 4.4b Capture ratio versus dimensionless overlap for different main crack to field crack's length ratios (*s/b*=0.5, and 2D Plane strain case). 98

Figure 4.4c Capture ratio versus dimensionless overlap for different dimensionless spacing (*a/b*=50, and 2D Plane strain case). 99

Figure 4.4d Capture ratio versus dimensionless overlap for different bed thickness (*a/b*=50, and *s/b*=0.25). 99

Figure 4.5 A main crack of length 2a propagating through a region of field cracks of lengths 2b. The capture zone increases in size as the main crack growth. If a field crack is encountered in the capture zone of the main crack, propagation is arrested. 100

Figure 4.6 Complementary cumulative distribution function for fracture length (constant fracture height model), an illustration of the effect of exponential constant, D, i.e. the product of field crack area intensity and size. 100

Figure 4.7 Idealization of natural fracture growth in sedimentary rock of variable fracture height model (after Olson, 1993) 101

Figure 4.8 A main crack of initial length L and height L propagating through a region of field cracks of with radius of b. The capture zone increases in size as the main crack growth. T is the bed thickness. If *n* field crack are encountered in the capture zone of the main crack, propagation is arrested. 102

Figure 4.9 The probabilities for an exact number of cracks in the capture zone. 102

Figure 4.10 Complementary cumulative distribution function for fracture length (true 3D analysis), an illustration of the effect of exponential constant, D, i.e. the product of field crack volume intensity and size. 103

Figure 4.11 The fracture growth from a penny shape crack to a lateral propagation of blade-like (fixed height) fracture. The corresponding complementary cumulative distribution function for fracture length distribution changes from a concave curve to a straight line. 103

Figure 4.12 Fracture lengths collected in granitic rock of Ward Lake, Sierra Nevada show a negative exponential distribution. 104

Figure 4.13 Field fracture lengths collected in granitic rock of Florence, Sierra Nevada fit the constant fracture model with a negative exponential distribution. Variable fracture height model fits the synthetic 3d data up to 10m. 104

Figure 4.14 Synthesized 3d fracture lengths distribution from the 2d planar fracture trace-length data. For a specific fracture length 2a there are totally *Nv* fractures in the defined volume. Randomly select a depth of *Z*, and count the fracture numbers (*N*) cut by the horizontal plane perpendicular to *Z*. 105

Figure 4.15a Fracture lengths collected in Frontier Formation Sandstones, Southwestern Wyoming shows a negative exponential distribution (a semi-log plot). 106

Figure 4.15b Fracture lengths fit negative exponential distribution better than power law distribution in Frontier Formation Sandstones, Southwestern Wyoming (a log-log plot). 106

Figure 4.16 Micro-fracture lengths in calcite cemented Frontier Formation sandstone, Oil Mountain fit negative exponential distribution. 107

Figure 4.17 Fracture lengths collected in siltstone of Culpeper Quarry fit negative exponential distribution up to 1.2m. 107

Figure 5.1 A single set of parallel fractures subject to uniaxial extension at a constant strain rate, *de/dt*. Cracks outside contours *S* are treated as a continuum with effective modulus $\tilde{E}$. Cracks inside *S* are modeled explicitly. Δs is the average stress transmitted across *S* (Segall, 1984) 137

Figure 5.2 Fracture interacting factor versus dimensionless overlap for dimensionless spacing of 0.1 (*s/b*=0.1) and crack length ratios of 0.1 and 0.2. (*a/b*=0.1, *a/b*=0.2). Note if dimensionless overlap is in between 0 and 1 (0<*o/b*<1), the interacting factor (*K/K*$_i$) is near zero. 138

Figure 5.3a Initial fracture pattern with 100 cracks and initial fracture density of 0.01. 139

Figure 5.3b Fracture patterns generated by the boundary element model (right) and analytical mode (left). Fractures growth started from the pattern shown as Figure 5.3a, 2D plane strain case, with $n = 40, \dot{e} = 1.67 \times 10^{-13} / s, e = 5 \times 10^{-3}, r_f = 1.1.$ 139

Figure 5.3c Fracture length column chart illustrates comparison between fracture lengths generated by the numerical model and the semi-analytical model (2D plane strain). 140

Figure 5.3d Complementary cumulative distribution of the fracture length for the numerical model and the semi-analytical model (2D plane strain). 140

Figure 5.3e Fracture spacing column chart illustrates comparison between fracture spacing generated by the numerical model and the semi-analytical model (2D plane strain). 141

Figure 5.3f Complementary cumulative distribution of the fracture spacing for the numerical model and the semi-analytical model (2D plane strain). 141

Figure 5.4a Initial fracture pattern with an initial fracture density of 0.01 and a bed thickness of 2m. This map view is exactly the same as Figure 5.3a. 142

Figure 5.4b Fracture patterns generated by the boundary element model (left) and the analytical model (right). Fractures propagation started from the pattern shown as Figure 5.4a, a bed thickness (H) of 2m, with $n = 40, \dot{e} = 1.67 \times 10^{-13} / s, e = 5 \times 10^{-3}, r_f = 1.1.$) 142

Figure 5.4c Fracture length column chart illustrates comparison between fracture lengths generated by the numerical model and the semi-analytical model (H=2). 143

Figure 5.4d Complementary cumulative distribution of the fracture length for the numerical model and the semi-analytical model (H=2m)... 143

Figure 5.4e Fracture spacing column chart illustrates comparison between fracture spacing generated by the numerical model and the semi-analytical model (H=2m). 144

Figure 5.4f Complementary cumulative distribution of the fracture spacing for the numerical model and the semi-analytical model (H=2m)... 144

Figure 5.5a Fracture trace maps (map view), fractures simulations start with initial flaw length of 0.02m and flaw intensities, N/A, of 10, 20, 50 and 100 per square meter. This corresponds to flaw densities of 1×10^{-3}, 2×10^{-3}, 5×10^{-3}, 1×10^{-2}..... 145

Figure 5.5b Final fracture length distributions started with initial flaw length of 0.02m and flaw intensities, N/A, of 10, 20, 50 and 100 per square meter. This corresponds to flaw densities of 1×10^{-3}, 2×10^{-3}, 5×10^{-3}, 1×10^{-2}..... 146

Figure 5.6a Fracture trace maps (map view) for fracture spacing study (Figure 5.6b) with flaw intensities, N/A of 20, 35 and 50 per square meter, corresponding to flaw densities of 2×10^{-3}, 3.5×10^{-3}, 5×10^{-3}, respectively. 147

Figure 5.6b Fracture spacing distributions from the simulations used for Figure 5.6a. 147

Figure 5.7a Fracture trace maps (map view), simulated for fracture length study (Figure 5.7b) with subcritical growth indices of, 2, 10, 20 and 80, using $N/A = 50, \dot{e} = 1\times10^{-13}/s, e = 5\times10^{-3}$ (total crack numbers, N=2000). 148

Figure 5.7b Fracture length distributions for subcritical growth indices of, 2, 10, 20 and 80, using $N/A = 50, \dot{e} = 1\times10^{-13}/s, e = 5\times10^{-3}$ (total crack numbers, N=2000). 149

Figure 5.8a Fracture trace maps (map view) for fracture spacing study (Figure 5.8b) with subcritical indices n, of 2, 20, 40 and 80. 150

Figure 5.8b Fracture spacing distributions for subcritical growth indices, 2, 10, 20 and 80, using $N/A = 50, \dot{e} = 1\times10^{-13}/s, e = 5\times10^{-3}$ (total crack numbers, N=2000). 150

Figure 5.9a Fracture trace maps (map view) simulated for fracture length study (Figure 5.9b) with bed thickness of 2, 4, and 8 meters, using N/A=20/m^2, n=20, $\dot{e} = 1\times10^{-13}/s$, e=5×10^{-3}. 151

Figure 5.9b Fracture length distributions for bed thicknesses of 2, 4, and 8 meters, using N/A=20/m^2, n=20, $\dot{e} = 1\times10^{-13}/s$, e=5×10^{-3}. 152

Figure 5.10a Fracture trace maps (map view) for fracture spacing investigation (Figure 5.10b) with bed thicknesses of 2, 4 and 8 meters 153

Figure 5.10b Fracture spacing distributions for bed thicknesses of, 2, 4 and 8 m, using N/A=20/m^2, n=20, $\dot{e} = 1\times10^{-13}/s$, e=5×10^{-3}. 153

Figure 5.11a Fracture trace maps (map view) generated for fracture length study (Figure 5.11b) with elastic moduli of 4×10^3 MPa, 2×10^4 Mpa, and 1×10^5 Mpa, using N/A=50/m^2, n=20, $\dot{e} = 1\times10^{-13}/s$, and e=5×10^{-3} 154

Figure 5.11b Fracture length distribution for elastic moduli of 4×10^3 MPa, 2×10^4 Mpa, and 1×10^5 Mpa, using N/A=50/m^2, n=20, $\dot{e} = 1\times10^{-13}/s$, and ε=5×10^{-3} 155

Figure 5.12a Fracture trace maps (map view) for fracture spacing study (Figure 5.12b) with elastic moduli of 4×10^3 MPa, 2×10^4 Mpa, and 1×10^5 Mpa. 156

Figure 5.12b Fracture spacing distribution for elastic moduli of 4×10^3 MPa, 2×10^4 Mpa, and 1×10^5 Mpa, using *N/A=50/m²*, n=20, $\dot{e} = 1\times10^{-13}/s$, $e = 5\times10^{-3}$ 156

List of Tables

Table 5.1: Interaction factors and associated errors for a five-crack array of s/b = 0.5 and o/b = -0.5 157

Table 5.2: Interaction factors and associated errors for a five-crack array of s/b = 0.5 and o/b = 0 157

Table 5.3: Interaction factors and associated errors for a five-crack array of s/b=0.5 and o/b=1 158

Table 5.4: Interaction factors and associated errors for three randomly generated cracks 158

CHAPTER 1: OVERVIEW

In reservoirs with natural fractures, the opening fractures control fluid flow paths. The production of oil and gas from naturally fractured reservoirs is significantly different from that of conventional reservoirs. The presence of natural fractures causes dramatic production changes due to closing of these fractures as the reservoir pressure drops and also influences the growth and final geometry of hydraulic fractures used to enhance production (Lorenz, et al., 1988; Teufel and Clark, 1984). Natural fracture networks can have a significant influence on the secondary or tertiary oil recovery. Opening fractures cause early water breakthrough and reduce tertiary recovery efficiency due to channeling of injected gas or fluids. It is reported that in at least two hundred oil and gas fields, natural fractures control reservoir performance (Nelson, 1985). Because of the unique characteristics of a naturally fractured reservoir, it is essential to know fracture location and fracture geometric characteristics (orientation, spatial intensity, length, spacing and connectivity). Detailed fracture network information allows a producer to design optimal recovery processes utilizing the opening fractures to direct oil and gas toward wells more efficiently.

Opening fractures are normally below seismic resolution. Direct detections of subsurface fractures are limited to core or image logs. Most natural fractures are vertical and are unlikely intersected by a vertical or deviated wellbore (Lorenz and Warpinski, 1996). Due to the sparseness of the available data, geostatistical (La Pointe and Hudson, 1985; Dershowitz and Einstein, 1988;

Kulatilake, et al., 1993) and geomechanical methods (Rives et al., 1992; Olson, 1997) are used to extrapolate the subsurface fracture attributes. A geomechanical model has its advantage over geostatistical methods in that it emphasizes fracturing processes, such as fracture propagation, interaction and termination, and it requires less direct fracture sampling than statistical method. By dividing a reservoir into multiple grid blocks and applying appropriate initial and boundary conditions for each grid block, geomechanical models can potentially generate reasonable fracture patterns (Olson, 1997). The initial and boundary conditions as well as the rock properties in each grid block can be determined from laboratory testing, numerical experiments and field observations.

The objective of this study is to build a geomechanical model which has a high computation speed, can deal with large numbers of fractures and the initial fractures start at small scale. A simplified geomechanical forward model with such features would be used in the future for the purpose of fracture pattern inversion from observed data. This dissertation includes four sections. Chapter 2 focuses on the shape of fracture paths, i.e. under what conditions do fractures propagate straight, and when do they curve. Our study shows that beside the ratio of remote differential stress to fracture driving stress identified by Olson and Pollard (1989), bed thickness and fracture propagation mode also have a major influence on fracture paths. Although non-planar fractures are commonly observed in the field, straight fracture paths are the more dominant geometry (Pollard and Segall, 1987; Renshaw, 1994). Based on these observations and for

computational simplicity, straight fracture paths are assumed in subsequent chapters (3, 4 and 5).

Chapter 3 quantifies mechanical interaction between two straight finite height fractures using a displacement-discontinuity boundary element model (Crouch and Starfield 1983; Olson, 1997). The interaction factor (the magnitude of the fracture interaction) is expressed as a function of the two fracture's length ratio and their relative position on a map view (a look-up table is built). Based on this fracture interaction study, by assuming straight fracture path we propose a fracture capture model, which predicts that a fracture will stop propagating due to the mechanical interaction with its neighbor crack. Using this premise, in chapter 4 we derive a negative exponential fracture length distribution, which compares favorably with length data from the field. The systematical fracture interaction study in chapter 3 also enables us to define a fracture's direct influence region ("local" group), which provides a base for the simplified geomechanical fracture pattern growth simulator described in chapter 5. In this semi-analytical fracture pattern growth simulator, only a few fractures (local group fractures) are explicitly modeled, and the surrounding area is treated as a continuum with an effective modulus controlled by fracture density (Segall, 1984). The semi-analytical model generates fracture patterns that are similar to the more rigorous boundary element model. A sensitivity study based on the simplified fracture growth model shows that initial flaw density, subcritical index, bed thickness and elastic modulus influence the final fracture geometry.

REFERENCES

Crouch, S. L. and Starfield, A. M., 1983, *Boundary Element Methods in Solid Mechanics*. George Allen and Unwin, London, U. K.

Dershowitz W.S. and Einstein H.H., 1988, Characterizing rock joint geometry with joint system models, *Rock Mechanics and Rock Engineering*, Springer-Verlag: Redmond/Cambridge, 21-51.

Kulatilake, P.H.S.W., Wathugala, D.N., and Stephansson, O., 1993, Joint network modeling with a validation exercise in Stripa mine, Sweden, *Int. J. Rock Mech. Min. Sci. and Geomech. Abstr.*, 30(5), 503-526.

La Pointe, P.R. and Hudson, J.A., 1985, Characterization and interpretation of rock mass joint patterns, *Geological Society of America Special Paper* 199, 37.

Lorenz, J.C., Warpinski, N.R., and et al., 1988, Results of the Mulitwill experiment: In situ stresses, natural fractures and other geologic controls on reservoirs, *EOS*, Aug. 30, 817-826.

Lorenz, J.C., Warpinski, N.R, 1996, Natural fracture characteristics and effects, *Leading Edge*, 15(8), 909-911.

Nelson, R.A., 1985, *Geologic Analysis of Naturally Fractured Reservoirs*, Gulf Publishing Co., Houston, Texas, 1985.

Olson, J. E., 1997, Natural fracture pattern characterization using a mechanical-based model constrained by geologic data – moving closer to a predictive tool. *Int. J. Rock Mech. & Min. Sci.*, 34(3/4), 391, Paper No. 237.

Rives, T., Razack, M., Petit, J. P. and Rawnsley, K.D., 1992, Joint spacing: analogue and numerical simulations, *Journal of Structural Geology*, 14(8/9), 925-937.

Segall, P., 1984, Formation and Growth of extensional fracture sets, *Geological Society of America Bulletin*, 95, 454-462.

Teufel, L.W. and Clark, J.A., 1984, Hydraulic fracture propagation in layered rock: Experimental studies of fracture containment, *Soc. Petrl. Engrs.J.*, 24, 19-32.

CHAPTER 2: FRACTURE PATH INTERPRETATION FROM PSEUDO-THREE-DIMENSIONAL LINEAR ELASTIC NUMERICAL SIMULATION

ABSTRACT

Fracture paths are important because they determine fracture connectivity and a reservoir grid block's effective permeability. Two-dimensional, plane strain numerical simulations of critical fracture propagation have shown that fracture growth geometries are sensitive to the ratio of remote differential stress to driving stress. Pseudo-three-dimensional numerical investigations suggest that bed thickness and fracture propagation mode also have a major influence on the fracture path. Numerical calculations predict that fractures will be more planar in thin beds for a given spacing. Subcritical fracture growth paths tend to be straighter than critical fracture propagation path because mechanical interaction between fractures is weaker when cracks propagate subcritically.

INTRODUCTION

Fracture propagation direction depends on the stress field around the fracture tip. If the stresses along the fracture length have both normal and shearing components (i.e., mixed-mode loading), the fracture will curve. In linear elastic fracture mechanics there are several mixed-mode propagation criteria. To understand these criteria, several terms need to be defined. The stress intensity factor, K_i controls the near tip stress field as (Lawn and Wilshaw, 1975)

$$s_{ij} = \frac{K_i}{\sqrt{2pr}} f_{ij}(q) \qquad (2.1)$$

where K_i is defined as (Pollard and Segall, 1984)

$$K_i = \Delta s_i \sqrt{pa} \qquad \text{for } i = I, II \text{ or } III \qquad (2.2)$$

r is the radial distance, q is the angle (Figure 2.1) and $f_{ij}(q)$ is a well defined function of q depending upon the loading mode. The symbols I, II and III refer to the different modes of fracture propagation (Lawn and Wilshaw, 1975). Mode I is the opening mode, the crack surface displacements are perpendicular to the plane of the crack. Mode II is the sliding mode, the crack surface displacements occur in the plane of the crack and perpendicular to the leading edge of the crack. Mode III is the tearing mode, the crack surface displacements are also in the plane of the crack but parallel to the leading edge (Figure 2.2). For non planar propagation of vertical fractures as seen in map view (after Olson and Pollard, 1989), we are concerned only with mode I and mixed I-II. The driving stress for mode I is the tensile stress normal to the crack surface. The driving stress for mode II is the shear stress along the fracture plane.

The mixed-mode fracture propagation criteria are: (1) fractures propagate perpendicular to the direction of the maximum circumferential stress (Erdogan and Sih, 1963), (2) fractures propagate in the direction of minimum strain energy density (Sih, 1974), (3) fractures propagate in the direction of maximum energy release rate (Strifors, 1974; Nuismer, 1975; Wu, 1978), and (4) fractures propagate in the direction of pure opening mode (mode I) (Kalthoff, 1973; Cotterell and Rice, 1980). The various criteria have the common feature that $K_{II}=0$ at an extending fracture tip, though the maximum circumferential stress,

minimum strain energy density, and maximum energy release rate criteria do not necessarily coincide with $K_{II}=0$, when the fracture initially deviate from the straight propagation path (Cotterell and Rice, 1980). Bergkvist and Guex (1979) concluded from their finite element calculations that the entire fracture path predicted by the local Mode I criterion and other methods are similar. Mixed mode (I+II) fracture experiments verify the theoretical predictions (Ingraffea, 1981; Maccagno and Knott, 1989; Mahajan and Ravi-Chandar, 1989; Maji and Wang, 1992; Thomas and Pollard, 1993).

We follow Olson and Pollard (1989) in using the maximum circumferential stress criterion (Erdogan and Sih, 1963), which states that fracture extension starts in a plane normal to the direction of the maximum circumferential tension, s_{qq}, at an angle of zero shear stress, s_{rq} =0 (Figure 2.1). Two-dimensional, linear elastic numerical simulations of homogenous, isotropic materials for critical fracture growth have shown that fracture growth geometries are sensitive to the ratio of remote differential stress to driving stress (Olson and Pollard, 1989; Cruikshank, et al., 1991; Thomas and Pollard, 1993; Renshaw, 1994). For a fixed driving stress, larger remote differential results in a straighter fracture path. Besides the differential stress, Renshaw (1994) further states that material anisotropy, fracture surface roughness, and inelastic behavior will affect the curvature of the fracture path. However, Thomas and Pollard (1993) state that grain-scale heterogeneities of rock will not significantly change the propagation pattern from the homogenous numerical model. All these studies are restricted to two-dimensional fracture propagation, but to investigate the degree of crack path

curvature developed between two interacting fractures in sedimentary rock, we can't neglect the fracture height. An analytical analysis from Kachanov (1987) shows that the crack interactions are generally weaker in three-dimensional analysis than in two-dimensional plane strain.

THEORY OF SIMULATION MODEL

To investigate the in-plane (mixed mode I+II) growth paths for a fracture confined in a finite bed thickness, we simplified the problem by assuming a homogeneous and isotropic elastic material with smooth fracture surfaces. The displacement-discontinuity, boundary element method (Crouch and Starfield, 1983) with a correction factor incorporated for fracture height effects (Olson, 1997) is used as the pseudo-three-dimensional fracture growth model. We follow the experimental design of Olson and Pollard (1989) except that we take account for three-dimensional effects.

Fractures start from pre-existing flaws throughout the earth's crust (Atkinson, 1982). Fractures either propagate critically when the stress intensity factor (K_I) equals or exceeds the fracture toughness of the material (K_{IC}), or subcritically at a value substantially lower than K_{IC} (Atkinson and Meredith, 1987). The critical fracture propagation (dynamic fracture) speed can approach the elastic wave speed in a rock (Irwin, 1958) on the order of 10^1 to 10^3 m/s (Olson, 1993). Subcritical crack growth can be attributed to chemical effects of pore fluid in the crust environment (Atkinson, 1982; Kirby, 1984; Rice, 1978;

Atkinson and Meredith, 1987) and long-term loading of tectonically strained rocks. Subcritical growth occurs when

$$K_{Ic}^{*} \le K_I \le K_{Ic}, \tag{2.3}$$

where K_{IC}^{*} represents the lower threshold stress intensity. We assume a lower threshold stress intensity of $K_{IC}^{*}=K_{IC}/10$ (Segall 1984a; Atkinson and Meredith 1987b; Olson, 1993) in the following subcritical fracture growth path simulation. Subcritical propagation velocities may vary from 10^{-10} to 10^{-1} m/s, and can be described by the subcritical growth law (Atkinson, 1984; Swanson, 1984; Atkinson and Meredith, 1987b; Olson, 1993),

$$V = V_{\max}\left(\frac{K_I}{K_{Ic}}\right)^{n}, \tag{2.4}$$

where n is a rock property referred to as the subcritical fracture growth index. $V_{\max}$ is a constant, representing the maximum possible fracture propagation speed.

We use constant stresses parallel (σ_{22}^{r}) and perpendicular (σ_{11}^{r}) to the initial crack planes (compression is positive) for our modeling of critical fracture growth simulation, following Olson and Pollard (1989). Natural fractures caused by earthquakes or by flow of ground water into the fracture (i.e. natural hydraulic fracture) are considered to be critical growth (Olson, 1989). The differential stress is defined as $\Delta\sigma=(\sigma_{22}^{r}-\sigma_{11}^{r})$. The fluid pressure inside the fracture is P (Figure 2.3), and $(\Delta\sigma_I=P-\sigma_{11}^{r})$ is the mode I driving stress. The internal fluid pressure was adjusted at each growth increment so that $K_I=K_{IC}$ (Olson and Pollard, 1989). For the subcritical fracture growth simulation, we include an initial differential stress (ΔS), i.e. $\Delta\sigma=\Delta S$ parallel to the initial cracks and zero normal stress perpendicular to the cracks. On top of the initial differential stress

state, a constant strain rate perpendicular to the crack plane is imposed (Figure 2.4).

In an isotropic, homogenous material, the isolated crack depicted in Figure 2.3 would propagate straight. This can be explained by looking at the stress trajectories around the fracture tip (Figure 3 of Olson and Pollard, 1989). When two fractures are close enough, they will interact with each other, and the stress field around the fracture tips will be altered (Figure 2.5), potentially causing the fracture path to curve. The degree of curvature depends on the magnitude of the mechanical interaction relative to the in situ differential stress between the two fractures (Dey and Wang, 1981; Pollard et al., 1982; Olson and Pollard, 1989; Olson and Pollard, 1991). Fracture interactions are generally weaker in 3D configurations than in 2D configurations. This conclusion is based on an analytical method of stress analysis in elastic solids with many cracks (Kachanov, 1987). Based on this analytical prediction, we expect that fractures confined by finite bed thickness to be more planar than fractures simulated in 2D plane strain case.

VERIFICATION: FRACTURE PROPAGATION PATHS IN TWO DIMENSIONAL PLANE STRAIN

Critical Fracture Growth

The first set of simulations were run to compare against the results of Olson and Pollard (1989). Using the pseudo-3d code of Olson (1997), plane strain is approximated by a bed thickness that is many times larger than fracture

length and spacing ($T=100$m). An initial fracture spacing of 3 meters was used, and differential stress was varied from 0 to 1 Mpa to 4 Mpa. Fracture growth curves (Figure 2.6a) show that larger differential stress results in straighter crack paths, in agreement with Olson and Pollard (1989). Driving stress decreases as the two fractures move toward each other, reaching a minimum value when the two cracks are about tip-to-tip (fracture length is about 10 meters, Figure 2.6b). There are two reasons for this drop in driving stress. (1) For an isolated plane strain crack under critical growth, the driving stress required for crack propagation is,

$$\Delta s_I = \frac{K_{Ic}}{\sqrt{pa}} \tag{2.5}$$

As the cracks propagate, fracture length increases, and the driving stress correspondingly decreases. (2) Mechanical interaction between fractures enhances the fracture's propagation when the two fractures underlap (underlap is defined as opposite to overlap, i.e. the two fractures haven't reached each other), and thus less driving force is needed to maintain K_I at K_{IC}. When the two fractures overlap (fracture length is larger than 10 meters, Figure 2.6b), the mechanical interaction impedes fracture's growth, so that the driving stress has to rise to maintain the crack's propagation. For our configuration, the required driving stress drops again after about 15 meters of growth because the propagating inner tip of one crack approaches the non-propagating outer tip of the other crack. This is an artificial effect, as in a real case these outer tips would be expected to propagate as well, preventing the inner tips of the two-crack array from approaching them. The fracture growth path (Figure 2.6a) and driving stress

curve (Figure 2.6b) match Olson and Pollard (1989) exactly after correcting an error with respect to the driving stress calculation in Olson and Pollard (1989) (A constant of $\sqrt{p}$ is missing in their driving stress calculation. Their calculated driving stress should be $\sqrt{p}$ times lower).

The fracture path can be predicted by the ratio of remote differential stress to crack driving stress, R (Cruikshank, et al., 1991; Thomas and Pollard, 1993; Renshaw, 1994):

$$R = \frac{(s^r_{22} - s^r_{11})}{(p - s^r_{11})} \tag{2.6}$$

where the driving stress $(p - s^r_{11})$ is constant. For our cases, driving stress changes, and the peak driving stress (p-$s_{11}{}^r$) value, which occurs when the two fractures overlap (shown in Figure 2.6b) is chosen for our remote differential stress (R) calculation. When the differential stress ratio is less than 1 ($R<1$), fractures are more curved. As the differential stress ratio increases above 1 ($R>1$), cracks tend to be straight. This is the same result observed by other researchers (Cottrell and Rice, 1980; Cruikshank, et al., 1991; Thomas and Pollard, 1993; Renshaw, 1994).

Fracture propagation path is also determined by fracture spacing-to-length ratio (S/L), where the fracture length ($L=2a$) is the fracture segment length when the two fractures are tip to tip horizontally (Figure 2.7). Similar to Olson and Pollard (1989), fractures are observed to be more planar (Figure 2.8a) with increasing S/L. The distribution of crack perpendicular stress (s_{11}) around a fracture in 2D plane strain (Figure 2.9) shows an induced compressive stress on both sides of a fracture (stress shadow region) and an induced tensile stress ahead

of the fracture tips. Figure 2.9 shows the width of a 2D plane strain fracture's influence area is nearly equal to the fracture length on each side of the crack. Thus, for two fractures with a spacing-to-length ratio greater than one ($S/L>1$), the fractures are out of each other's influence region. Even for isotropic remote stress (Figure 2.8a, $S/L=2$) the fractures do not interact strongly enough to cause fracture path curving leading to intersection. For isotropic stress and a spacing-to-length ratio equal to or less than one ($S/L=1$), the two fractures interact strongly enough to cause intersection. The driving stress upon overlap decreases as S/L increases (Figure 2.8b), because the impedance effect imposed by its neighbor crack diminishes with increase of S/L. For spacing-to-length ratio of two ($S/L=2$), the driving stress curve is almost identical to that of an isolated crack (Figure 2.8b), because there is very little mechanical interaction between wide spaced cracks.

Subcritical Fracture Growth

Crack interaction is diminished for subcritical crack growth compared to critical growth. Subcritical growth occurs at a lower stress intensity values than critical propagation, thus less driving stress is required (Olson and Pollard, 1989). According to Renshaw (1994), for a fixed flaw length and remote differential stress, small K_{IC} causes a high R, thus resulting in more planar fractures. A constant displacement boundary condition and the subcritical crack growth law are used to numerically simulate slow natural fracture propagation in deformed

porous rock. The results confirm that fractures propagating subcritically are straighter than those propagating critically (compare Figure 2.10 to Figure 2.6a).

PROPAGATION PATHS FOR FINITE HEIGHT FRACTURES

Critical Fracture Growth

It is important to consider finite height cracks because sedimentary rocks tend to have fractures confined to beds. The crack perpendicular stress (σ_{11}) around a fluid-pressurized fracture shows that the stress perturbation extends out from the crack about the same distance as fracture height (Figure 2.11) when the smaller dimension of a fracture plane is the height. Under these conditions, *S/H* instead of *S/L* controls fracture path curving. *H=T* refers to sedimentary rock in which fracture height is restricted by the layer boundary. In our pseudo-3d model a simplification of *H=T* is made for fracture height based on field observations in sedimentary rocks.

Crack paths and the driving pressure behavior are investigated for bed thickness effects for the case of isotropic remote stress ($\Delta S = 0$) (Figures 2.12a, 2.12b, 2.13a and 2.13b). The pseudo-three-dimensional simulations show that the fractures have the highest degree of convergence in the 2D plane strain case (*T*=100m and *S/T*=0.05 in Figure 2.12a; and *S/T*=0.02 in Figure 2.13a). Increasing the spacing to bed thickness ratio (*S/T*) results in straighter cracks, because the crack interaction decreases with an increase in *S/T*. Eventually, when S/T is greater than one, the fractures become nearly planar (Figure 2.12a and 2.13a) indicating a strongly diminished mechanical interaction.

When *S/T* is less than one and the adjacent cracks overlap, mechanical interaction inhibits the fracture's propagation. Consequently, the driving stress has to increase to continue the fracture growth (Figures 2.12b and 2.13b). As S/T increases, the mechanical interaction decreases, and the driving stress curves get flatter (Figures 2.12b and 2.13b). When *S/T* is above 1 (*S/T=2.5*), one fracture is nearly out of the other crack's stress perturbation region. Therefore, the fracture behaves like an isolated crack, which has a straight growth path and a characteristic driving stress curve (comparing curves of *S/T=2.5* and isolated fracture for bed thickness of 2m in Figure 2.12b). As predicted by equation 2.5, for an isolated finite-height fracture, the driving stress decreases with an increase of fracture length, until the length exceeds the height. Once fracture length exceeds the height, the driving stress approaches a constant value. Equation 2.5 also indicates a higher driving stress is required in a thinner bed, because the fracture height constrained by the thinner bed is smaller.

Subcritical Fracture Growth

Using the same methodology as for the 3d critical fracture growth path, two sets of differently spaced en echelon cracks (spacing of 5m, Figure 2.14; and 2m, Figure 2.15) are studied for subcritical fracture growth paths. Compared to the critical growth path given isotropic remote stress, the subcritical growth path for a finite height fracture is always straighter (compare Figures 2.12a and 2.14a for spacing of 5m; and Figures 2.13a and 2.15a for spacing of 2m). Subcritical fracture growth requires a lower driving stress and causes less stress perturbation

than critical fracture growth. This results in less mechanical interaction and a smaller degree of fracture curving for a given *S/T*.

As with the critical propagation case, fractures become more planar as *S/T* increases (comparing Figure 2.12a to Figure 2.13a). For an isolated crack, the stress intensity factor first increases with fracture length, and then slightly decreases (Figures 2.14b and 2.15b). When $S/T>1$, the stress intensity factor follows a similar trend as that of an isolated crack in 2D plane strain, but has a smaller magnitude ($S/T=2.5$ in Figure 2.14b; and $S/T=2$ in Figure 2.15b). There are two reasons for this. (1) If the spacing between the two cracks is greater than one bed thickness, mechanical interaction effects are almost zero, thus the stress intensity factor shares a similar trend as that of an isolated crack. (2) The stress intensity factor depends not only on driving stress, but also on crack dimension. The limited fracture height results in a lower stress intensity factor. The stress intensity factor of a crack under the influence of its neighbor fracture shares the similar changing trend of an isolated crack prior to overlap ($L<8m$). The rapid decrease of the stress intensity factor for $L>8m$ (compared to the slight decrease of an isolated crack) indicates the degree of mechanical interaction between the fractures. Figures 2.14b and 2.15b show that for an interacted crack with $L>8m$, the smaller the *S/T* the faster the stress intensity factor decreases with the increasing fracture length. The higher mechanical interaction for a smaller *S/T* results in a highly curved fracture path (Figures 2.14a and 2.15a).

In general, with reference to 3d effects, the same conclusions are made for critical and subcritical crack propagation. (1) Fracture paths become straight

when $S/T>1$. (2) If $S/T<1$, the degree of fracture curvature is determined by both S/T and R. Reducing either S/L or R results in highly curved fractures.

CONCLUSIONS

The degree of crack path curvature developed between mechanically interacting fractures in sedimentary rock depends on the differential stress ratio (R) and fracture spacing-to-length ratio (S/L). It is also controlled by the spacing-to-bed thickness ratio (S/T) and the fracture propagation mechanism. In a 2D plane strain case, S/L has dominant influence on fracture propagation paths. S/T is more important than S/L in sedimentary rock if fracture height is confined by bed thickness. If $S/T>1$, the fractures do not interact with each other, and the growth paths are straight regardless of R. When $S/T<1$ and $R>1$, fractures also remain straight. If both $S/T<1$ and $R<1$, fractures will curve and likely intersect. The smaller S/T and R, the higher the degree of fracture curvature is.

Because subcritical fracture growth requires less driving stress for propagation, there is less crack-induced stress perturbation and consequently less mechanical interaction, resulting in straighter fracture paths.

The highly curved fractures indicate small fracture spacing and a lower differential stress compared to the driving stress when fractures are formed. Although highly curved fractures have been reported in the field, straight crack patterns are more common (Segall, 1984, Rives et al., 1992; Olson, 1993; Becker and Gross, 1996). By limiting our study to straight cracks for the subsequent

chapters, we are able to take advantage of simpler formulations for fracture network simulation and can limit the geometric possibilities.

REFERENCES

Anderson, O.L., and Grew, P.C., 1977, Stress corrosion theory of crack propagation with applications to geophysics. *Rev. Geophys. Space Phys.* 15, 77-104.

Atkinson, B. K., 1982, Subcritical crack propagation in rocks: theory, experimental results and application, *Journal of Strucural Geology*, 4, 41-56.

Atkinson, B. K., 1984, Subcritical crack growth in geological materials. *Journal of Geophysical Research,* 89, 4077-4114.

Atkinson, B. K. and Meredith, P. G., 1987, The theory of subcritical crack growth with applications to minerals and rocks. Atkinson, B. K., ed., *Fracture Mechanics of Rock*, Academic Press, San Diego, USA

Cotterell, B. and Rice, J. R., 1980, Slightly curved or kinked cracks, *International Journal of Fracture,* 16, 155-169.

Crouch, S. L. and Starfield, A. M., 1983, *Boundary Element Methods in Solid Mechanics*. George Allen and Unwin, London, U. K.

Cruikshank, K.M., Zhao, G., and Johnson, A. M., 1991, Analysis of minor fractures associated with joints and faulted joints, *Journal of Structural Geology,* 13, 865-886.

Cruikshank, Kenneth M. and Aydin, Atilla, 1994, Role of fracture localization in arch formation, Arches National Park, Utah, *Geological Society of America Bulletin*, 106, 879-891.

Dershowitz, W. S. and Einstein, H. H., 1988, Characterizing rock joint geometry with joint system models. *Rock Mech. Rock Eng.*, 21, 21-51.

Dey, T. N. and Wang, C. Y., 1981, Some mechanisms of microcrack growth and interaction in compressive rock failure: *International Journal of Rock Mechanics and Mining Science*, 18, 199-209.

Engelder, T., and Geiser, P., 1980, On the use of regional joint sets as trajectories of plaeostress fields during the development of the Appalachian Plateau, New York, *Journal of Geophysical Research,* 85, 6319-6341.

Erdogan, F. and Sih, G. C., 1963, On the crack extension in plates under plane loading and transverse shear. *ASME Transactions*, 85, 519-527.

Ingraffea, Anthony R., 1987, Theory of crack initiation and propagation in rock. In: Atkinson, B.K. (Ed.), *Fracture Mechanics of Rock*. Academic Press, London, 277-349.

Irwin, G. R., 1958, Fracture. In: *Encyclopedia of Physics*, edited by S. Flugge, Springer-Verlag, Berlin, 551-590.

Kachanov, M., 1987, Elastic solids with many cracks: A simple method of analysis, *International Journal of Solids and Structures, 23(1), 23-43.*

Kalthoff, J. F., in *Dynamic Crack Propagation*, Noordhoff International Publishing, Leyden, 449-458.

Kirby, S. H., 1984, Introduction and digest to the special issue on chemical effects of water on the deformation and strengths of rocks, *Journal of Geophysical Research*, 89, 3991-3995.

Lawn, B. R., and Wilshaw, T. R., 1975, *Fracture of brittle solids*, Cambridge, England, Cambridge University Press, 204.

Muller, O. H., and Pollard, D. D., 1977, The stress state near Spanish Peaks, Colorado, determined from a dike pattern, *Pure Appl. Geophys.*, 115, 69-86.

Nuismer, R. J., 1975, An energy release rate criterion for mixed mode fracture, *International Journal of Fracture*, 11, 245-250.

Ode, H., 1957, Mechanical analysis of the dike pattern of the Spanish Peaks area, Colorado, *Geological Society of America Bulletin*, 68, 567-576.

Olson, J. E., 1991, Fracture mechanics analysis of joints and veins, *Dissertation*, Stanford University.

Olson, J. E., 1993, Effects of subcritical crack growth and mechanical crack interaction. *Journal of Geophysical Research*, 98(B7), 12251-12265.

Olson, J. E., 1997, Natural fracture pattern characterization using a mechanical-based model constrained by geologic data – moving closer to a predictive tool. *International Journal of Rock Mechanics and Mining Science*, 34(3/4), 391, Paper No. 237.

Olson, J. E. and Pollard, D. D., 1989, Inferring paleostresses from natural fracture patterns: A new method, *Geology*, 17, 345-348.

Olson, J. E. and Pollard, D. D., 1991, The initiation and growth of en echelon veins, *Journal of Structural Geology*, 13(5), 595-608.

Pollard and Muller, 1976, The effect of gradients in regional stress and magma pressure on the form of sheet intrusions on cross section, *Journal of Geophysical Research*, 81, 975-988.

Pollard, D. D., Segall, P., and Delaney, P.T., 1982, Formation and interpretation of dilatant echelon cracks: *Geological Society of America Bulletin*, 93, 1291-1303.

Pollard, D. D. and Segall, P., 1987, Theoretical displacements and stresses near fractures in rocks: with applications to faults, joints, veins, dikes and solution surfaces. In: Atkinson, B.K. (Ed.), *Fracture Mechanics of Rock*. Academic Press, London, 277-349.

Renshaw, C. E., 1993, Modeling fluid migration through physically-based fracture networks, *Dissertation*, Stanford University.

Renshaw, C. E., 1994, Are large differential stresses required for straight fracture propagation paths? *Journal of Structural Geology*, 16 (6), 817-822.

Rice, J. R., 1978, Thermodynamics of the quasi-static growth of Griffith cracks: *Journal of Mechanics and Physics of Solids*, 26, 61-78.

Secor, D.T., 1969, Mechanics of natural extension fracturing at depth in the earth's crust, in Baer, A.J., and Norris, D.K., eds., *Research in tectonics: Geological Survey of Canada Special Paper* 68-52, 3-47.

Segall, P., 1984a, Formation and growth of extensional fracture sets. *Geological Society of America Bulletin*, 95, 454-462.

Segall, P., 1984b, Rate-dependent extensional deformation resulting from crack growth in rock. *Journal of Geophysical Research*, 89, 4185-4195.

Sih, G. C. 1974, Strain-energy-density factor applied to mixed mode crack problems, *International Journal of Fracture*, 10, 305-321.

Strifors, H. C., 1974, A generalized force measure of conditions at crack tip, *International Journal of Solids and Structures*, 10, 1389-1404.

Thomas, A. L., and Pollard, D. D., 1993, The geometry of echelon fractures in rock: Implications from laboratory and numerical experiments, *Journal of Structural Geology*, 15(3-5), 323-334.

Wu, C. H., 1978, Fracture under combined loads by maximum energy release rate criterion, *Journal of Applied Mechanics*, 45, 553-558.

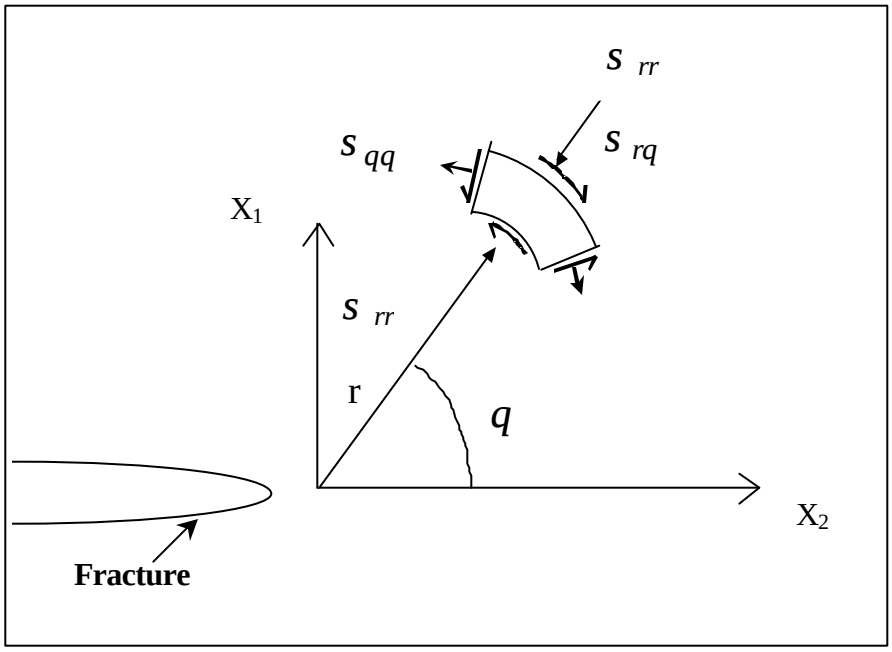

Figure 2.1 Maximum circumferential stress criterion of Erdogan and Sih (1963). Fractures propagate radially from the crack tip at an angle θ, the direction of maximum circumferential tension, $\sigma_{\theta\theta}$, which coincides with the direction of zero shear stress, $\sigma_{r\theta}=0$.

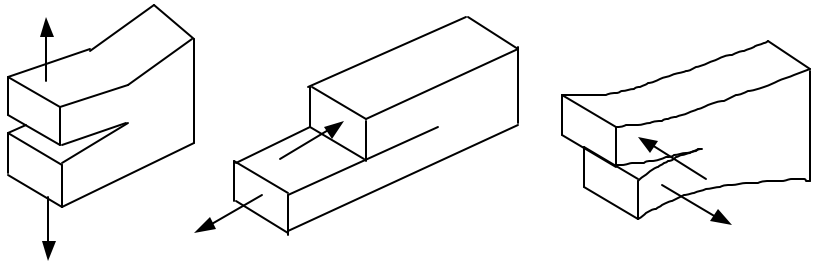

Figure 2.2 Three fundamental modes of fracture. A: mode I, opening mode; B: mode II, in-plane shear or sliding mode; C: mode III, anti-plane shear or tearing mode.

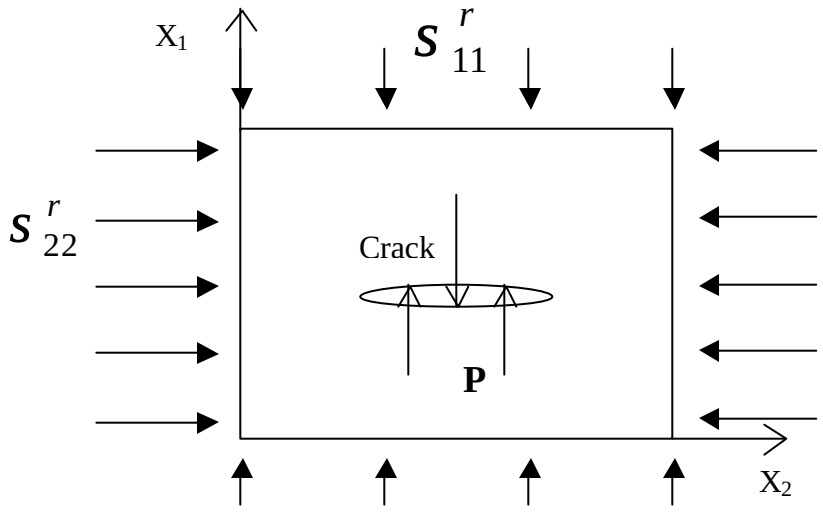

Figure 2.3 Boundary conditions used for critical fracture growth simulation. The constant stress components s_{11}^r and s_{22}^r act perpendicular and parallel to crack plane, respectively.

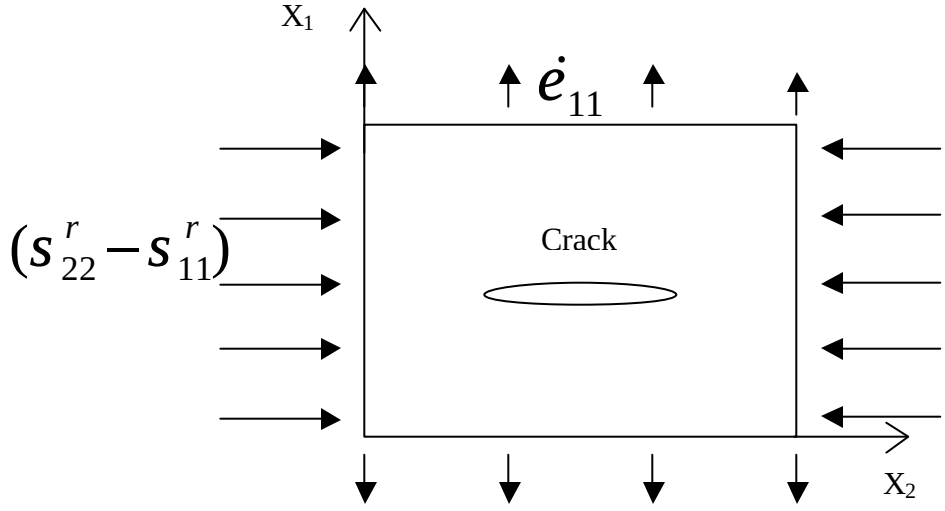

Figure 2.4 Boundary conditions used for subcritical fracture growth simulation. A constant strain rate is imposed perpendicular to the crack plane, with a constant stress ($DS = s_{22}^r - s_{11}^r$) parallel to it.

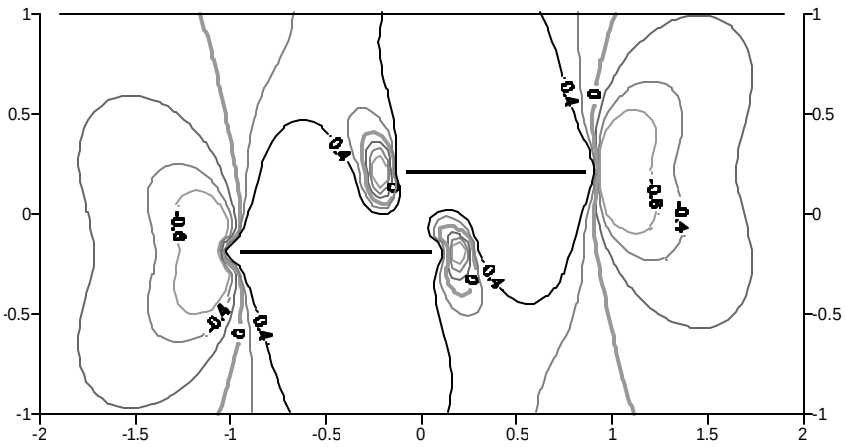

Figure 2.5 Magnitude of crack perpendicular stress (s_{yy}) around two interacting fractures. The crack-induced stress in front of the fracture tips is tensile stress (negative), and the stress at both side of the fractures are compressive (positive). The unit of the stress is MPa.

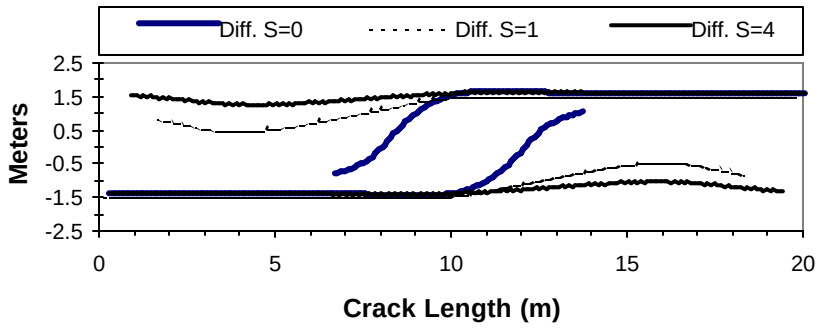

Figure 2.6a Theoretical fracture paths driven by internal fluid pressure for bed thickness of 100m (fracture is under critical growth). The three sets of curves represent the results for various differential stress (0, 1 and 4 MPa). The initial fracture spacing is 3m. Fractures are propagated simultaneously towards each other.

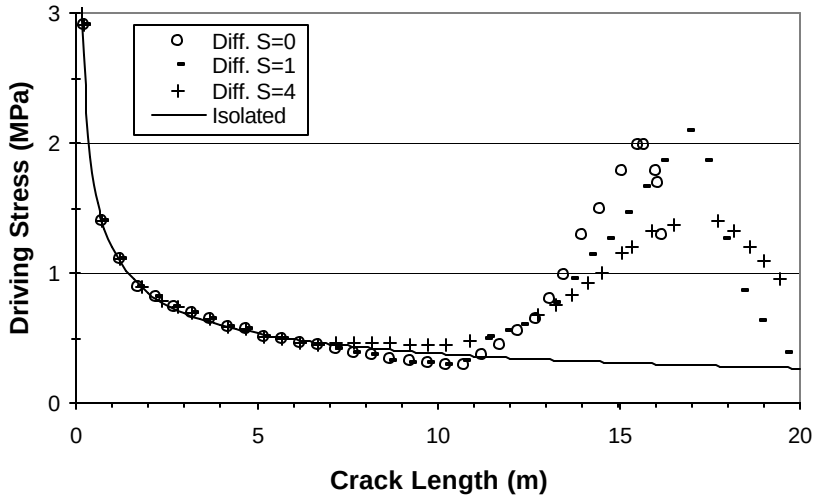

Figure 2.6b Driving pressure required to propagate one fracture to a specified length keeping $K_I=K_{IC}$. Each curve represents a specific differential stress. Fracture configuration is illustrated as Figure 2.6a.

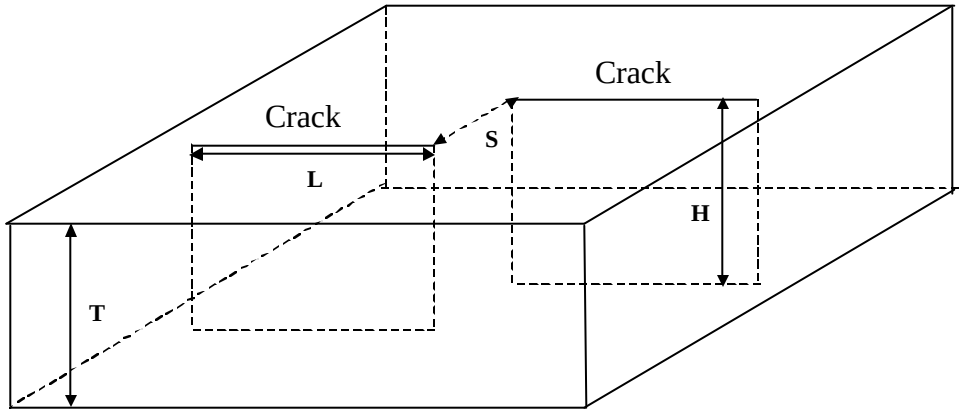

Figure 2.7 Two parallel fractures each with length L are tip-to-tip. The distance perpendicular to the two fractures is S. Fracture height is H, and the bed thickness is T. In this case fracture height equals bed thickness (H=T).

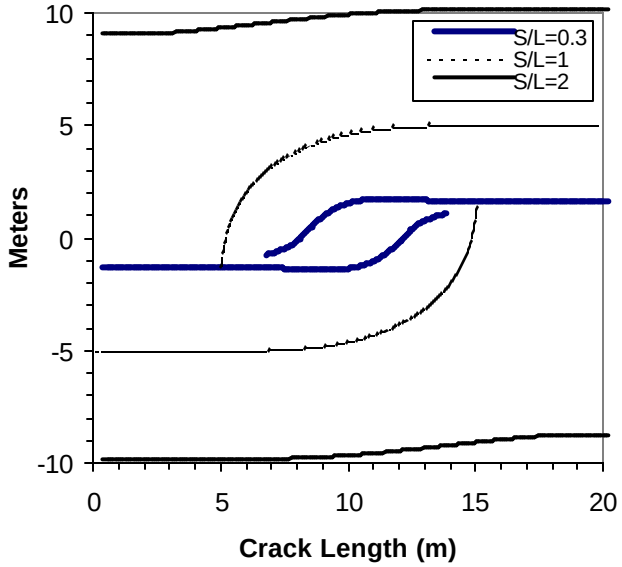

Figure 2.8a Theoretical fracture paths driven by internal fluid pressure for bed thickness of 100m. (This is a mapview. The bed thickness is in the direction perpendicular to the paper). The three sets of curves represent different initial spacing to length ratios. Remote differential stress is zero and the fracture is under critical growth.

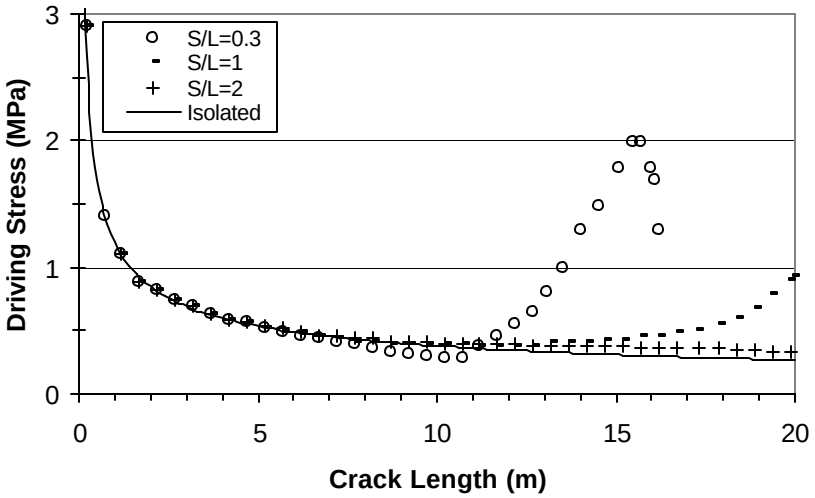

Figure 2.8b Driving pressure required to propagate one fracture to a specified length. Each curve represents different spacing to length ratio. The fracture configuration is illustrated in Figure 2.8a. Remote differential stress is zero.

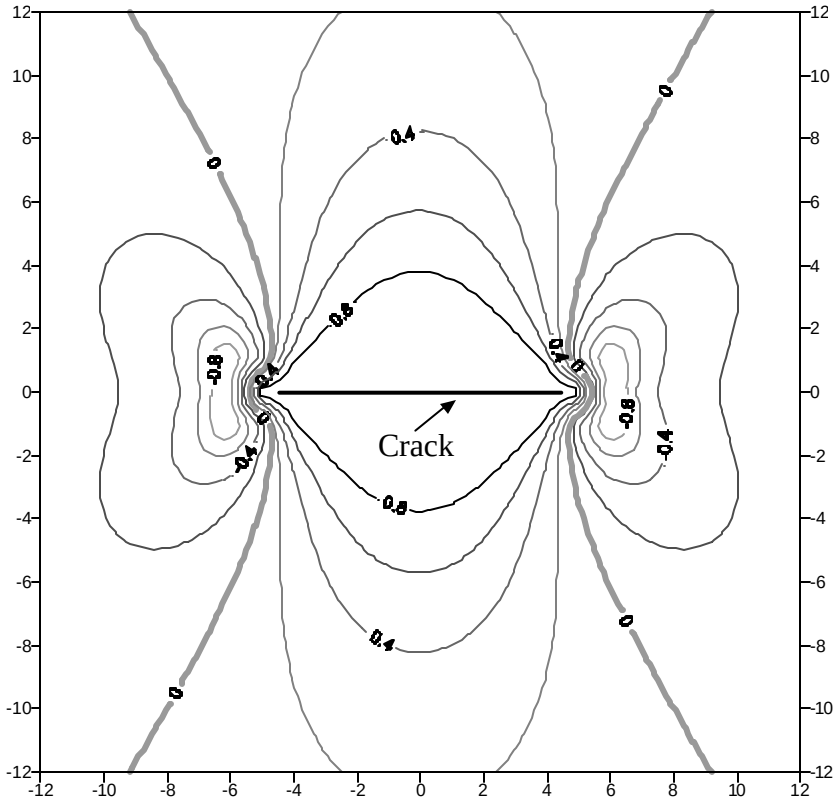

Figure 2.9 Distribution of crack perpendicular stress, s_{11}, induced by internal fluid pressure for 2D plane strain, DS=0. On both sides of the fracture, the induced stress is compressive (positive). In front of the fracture tips the induced stress is tensile (negative). The size of compressive stress range is proportional to fracture length.

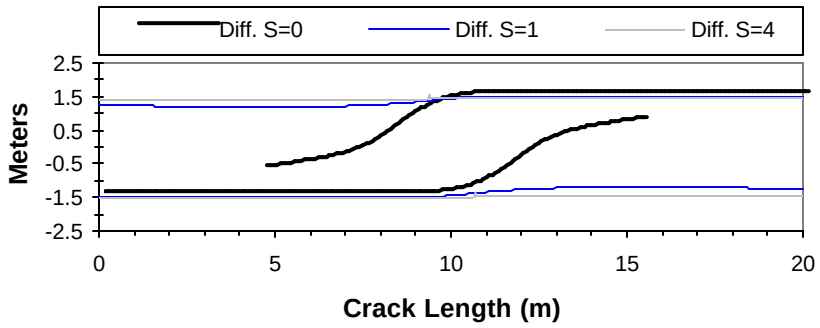

Figure 2.10 Theoretical fracture paths driven by remote constant stain rate for a bed thickness of 100m for subcritical growth. The three sets of curves represent various differential stresses. The initial fracture spacing is 3m. The two fractures propagate simultaneously towards each other.

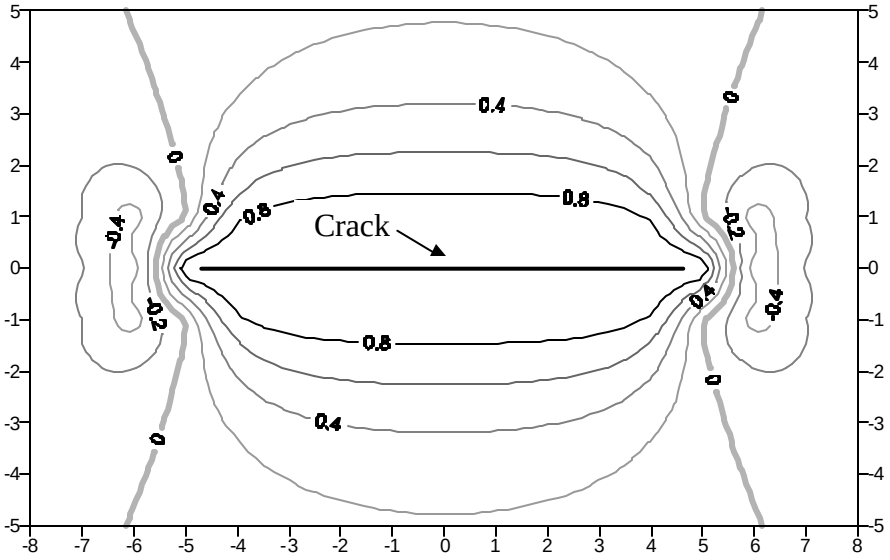

Figure 2.11 Distribution of crack perpendicular stress, s_{11}, induced by internal fluid pressure for a bed thickness of 5m and DS=0. On both sides of the fracture, induced stress is compressive, and in front of the fracture tips induced stress is tensile. The size of compressive stress range is proportional to bed thickness.

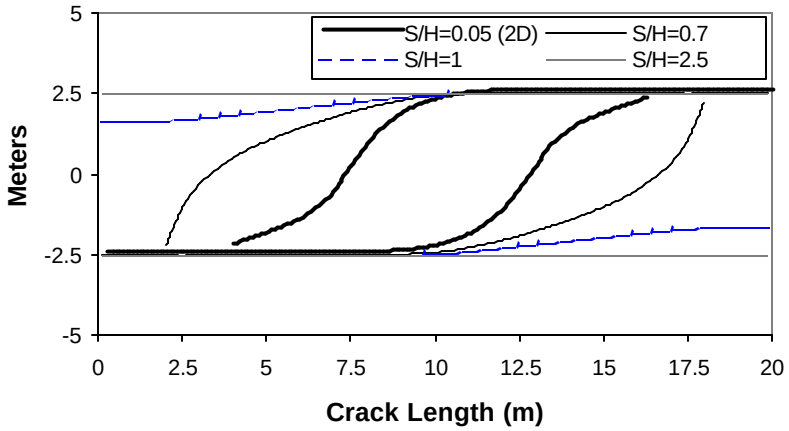

Figure 2.12a Theoretical fracture paths for different bed thickness given critical growth. Initial crack spacing is 5m and ΔS=0.

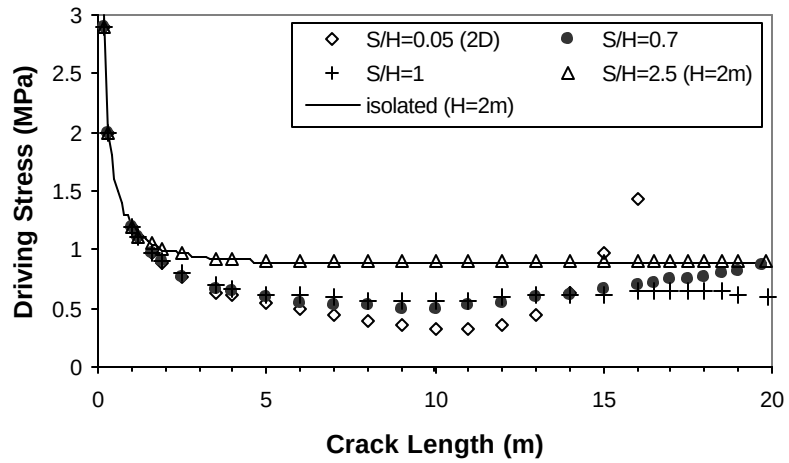

Figure 2.12b Driving pressure required to propagate one fracture to a specified length. Each curve represents a specific bed thickness. Fracture configuration and propagation condition are shown in Figure 2.12a.

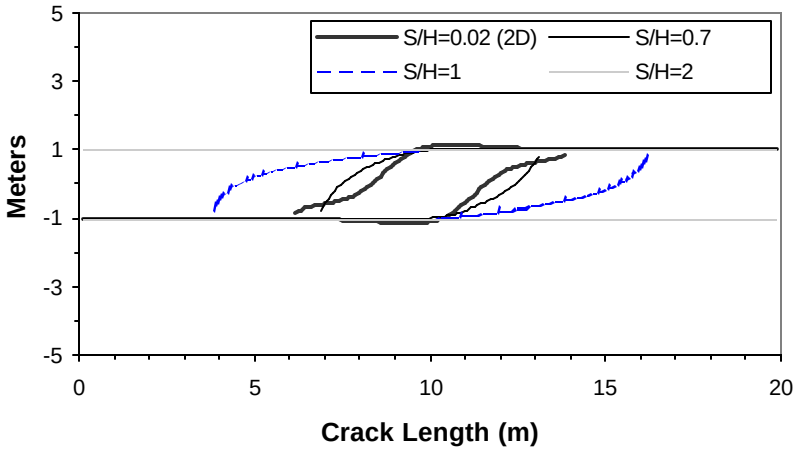

Figure 2.13a Theoretical fracture paths for different bed thickness given critical growth. Initial crack spacing is 2m and ΔS=0.

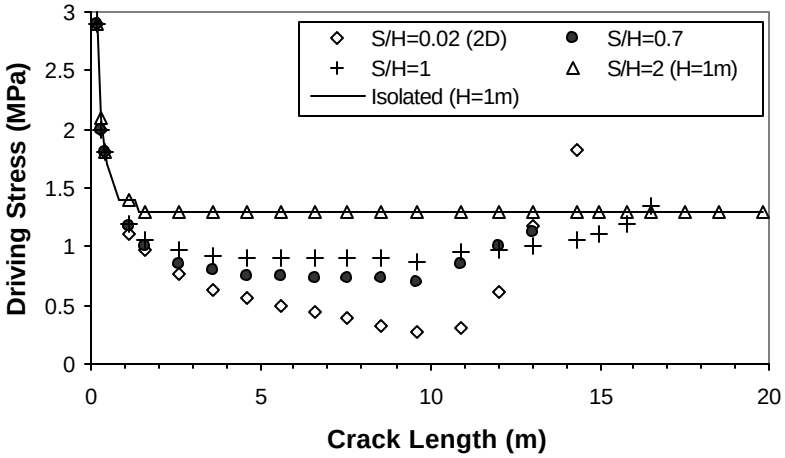

Figure 2.13b Driving pressure required to propagate one fracture to a specified length. Each curve represents a specific bed thickness. Fracture configuration and propagation condition are shown in Figure 2.13a.

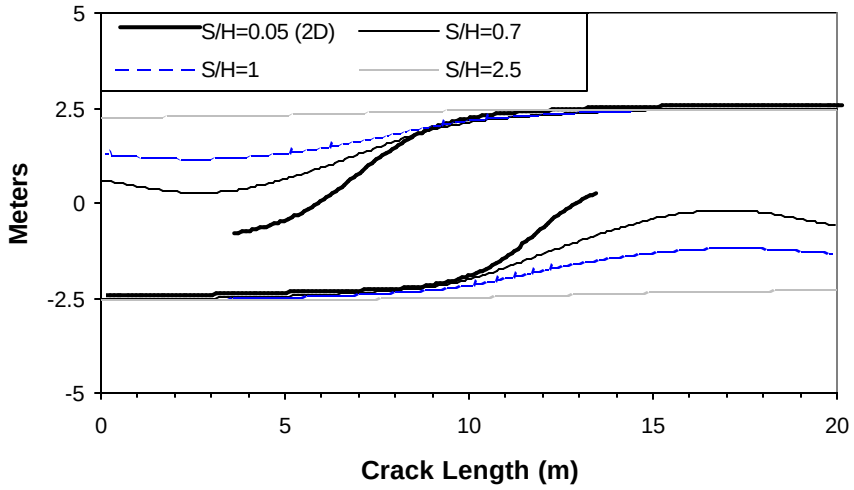

Figure 2.14a Theoretical fracture paths for different bed thickness given subcritical growth. Initial crack spacing is 5m and ΔS=0.

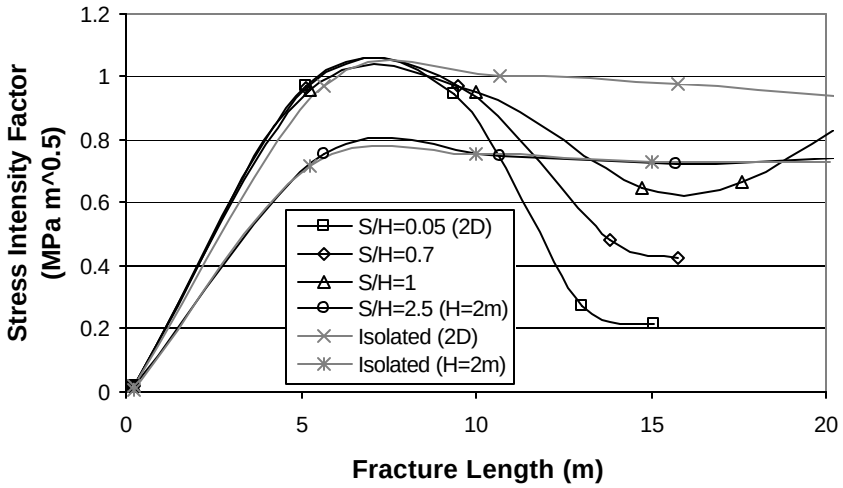

Figure 2.14b Stress intensity factors required propagating one fracture to a specified length. Fracture configuration and propagation condition are shown in Figure 2.14a.

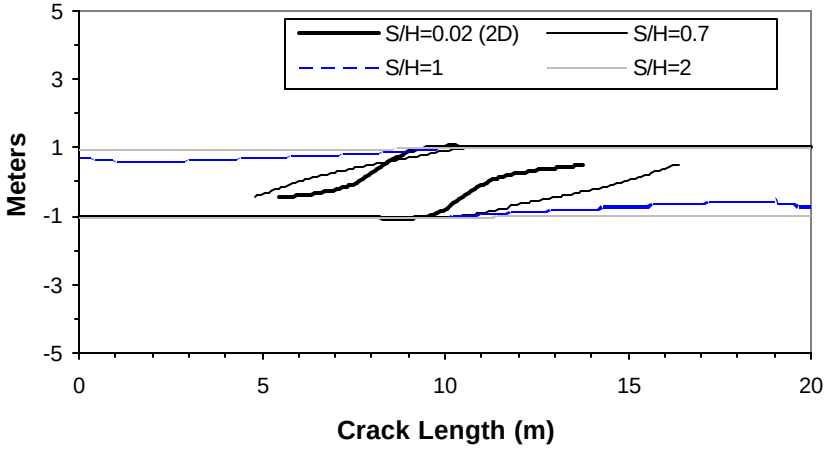

Figure 2.15a Theoretical fracture paths for different bed thickness given subcritical growth. Initial crack spacing is 2m and ΔS=0.

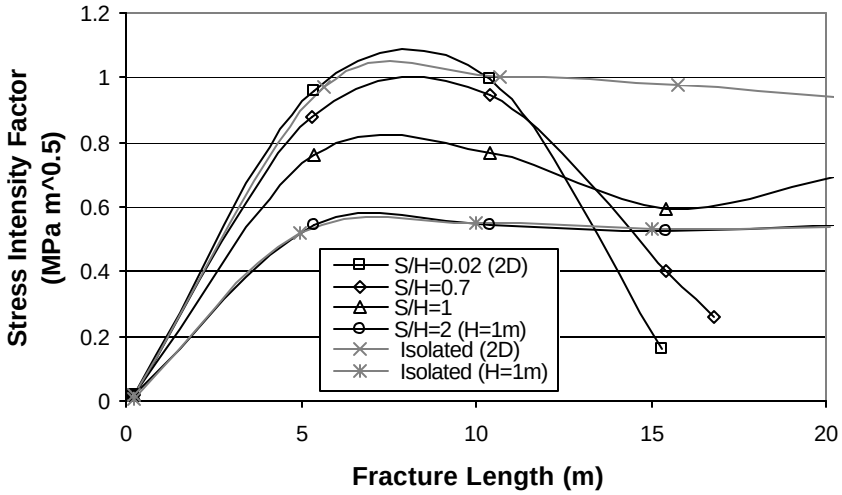

Figure 2.15b Stress intensity factor to propagate one fracture to a specified length. Each curve stands for a specific bed thickness. Fracture configuration and propagation condition are shown in Figure2.15a.

CHAPTER 3: MECHANICAL INTERACTION BETWEEN FRACTURES

ABSTRACT

Mechanical interaction between fractures directly affects a fracture's propagation and termination, and controls final fracture pattern. Using a displacement discontinuity boundary element model, we investigated the elastic mechanical interaction between two mode-I cracks in two-dimensional plane strain and pseudo-three dimensions. A fracture directly interacts with its neighbor cracks, if both the vertical distance and the horizontal distance between the two fractures' inner tips (the fracture tips that toward each other) are less than three times of the fracture's length. When the bed thickness is larger than the crack length, the fracture spacing to length ratio has more influence on the crack interaction. Otherwise, the spacing to bed thickness ratio dominates the magnitude of fracture interaction. En echelon crack propagation is enhanced when two cracks underlap slightly, but is impeded when the cracks overlap. The mechanical interaction between fractures decreases with declining bed thickness for fixed fracture spacing. If cracks of unequal size are close enough to one another relative to the dimension of the smaller crack, the propagation of the inner (overlapping) tips of the both cracks can be arrested and the outer tip of small crack will carry on the propagation.

INTRODUCTION

En echelon arrays indicate the prevalence of mechanical interaction (Kranz, 1979; Dey and Wang, 1981; Pollard e al, 1982; Olson and Pollard, 1989; Olson and Pollard, 1991). Mechanical interaction between fractures is caused by the stress perturbation around the crack induced by nearby fractures. This stress perturbation influences both fracture propagation direction and fracture termination, and therefore determines the fracture pattern geometry (Pollard et al., 1982; Nur, 1982; Segall and Pollard, 1983; Pollard and Aydin, 1984; Pollard and Aydin, 1988; Olson and Pollard, 1991).

Stress intensity factor (K) and crack extension force or strain energy release rate (G) are two terms in fracture mechanics used to predict a fracture's initiation, propagation and termination. In order to calculate the crack extension force, G, and predict the growth direction for a particular crack, we must consider the mechanical effects of all the other fractures in a defined area (Segall, 1984). Since the mechanical effect from every single fracture is hard to account for explicitly without using a numerical model, Segall (1984) proposed a separation of the fractures into two groups: 1) a "local group," near the particular crack that interacts directly with this crack, and 2) a much larger "remote group," which influences the crack only through a change in elastic modulus. One purpose of this chapter is to quantify the "local" and "remote" group by studying the mechanical interaction.

The crack extension force, G, for each crack depends on the remote stress or strain, mechanical interaction from other cracks and fracture length. Those

cracks with the greatest extension force propagate at the expense of others (Segall and Pollard, 1983). Numerous calculations have been done to investigate the effect of fracture interaction (Segall and Pollard, 1980; Pollard et al., 1982; Segall and Pollard, 1983; Pollard and Aydin, 1984; Olson and Pollard, 1991). For two center-aligned cracks, a longer fracture impedes the shorter one's growth (Segall and Pollard, 1983). If fracture spacing is small and cracks are about tip-to-tip in horizontal direction, a fracture's propagation enhancement is at a maximum (Pollard, Segall and Delaney, 1982; Olson and Pollard, 1991). Pollard and Aydin (1984) concluded that en echelon arrays with small horizontal separations enhance a fracture's propagation until an over-lapped configuration is achieved, beyond which fracture interaction hinders crack growth. All of these studies are two-dimensional analyses. An exception is from Kachanov (1987), who concluded from an analytical stress analysis of an elastic solid with many cracks that crack interaction is weaker in 3D configurations than in 2D configurations.

Based on a displacement discontinuity boundary element model (Crouch and Starfield, 1983; Olson, 1991; Olson, 1997), we systematically calculate the mechanical interaction between cracks of different length, spacing and overlap, and also account for the three-dimensional effects of bed-contained fractures. By studying the interaction curves, we propose that when a small crack is close to a large crack, it can significantly suppress the large crack's propagation.

THEORETICAL BACKGROUND

We focus on the elastic interaction between two mode I cracks in infinite (two-dimensional, plane strain) and finite bed thickness (three-dimensional) cases. We restrict ourselves to straight crack propagation, which implies the presence of a large crack-parallel differential compression. When the ratio of remote differential stress to crack driving stress (the remote differential stress ratio) is above one, the fracture tends to be straight (Cottrell and Rice, 1980; Olson and Pollard, 1989; Cruikshank, et al., 1991; Thomas and Pollard, 1993; Renshaw, 1993). Theoretical analyses have shown that a remote compressive stress acting parallel to a crack may produce a straight crack path even in the presence of a mode II stress intensity (Cotterell and Rice, 1980; Karihaloo and others, 1980; Pollard et al., 1982; Olson and Pollard, 1989).

Two-dimensional, plane strain, linear elasticity is initially utilized to calculate fracture interaction. The two-dimensional plane strain case is one end member of our three-dimension model, in which the bed thickness is much greater than fracture length. The two-dimensional analysis is an approximation, which applies to three idealized types of fracturing in nature (Olson, 1993): (1) the vertical propagation of horizontally elongated, blade-like fractures in an infinite body, as in joints propagating across a sedimentary layer from one bed boundary to another, (2) the horizontal propagation of slot-like fractures of fixed height that can freely open at top and bottom, as in the lateral growth of a joint confined to a bed that has freely slipping interlayer boundaries, and (3) the propagation of penny-shaped fractures in an unlayered intrusive body.

The fracture propagation model we used to calculate fracture interaction is based on a displacement-discontinuity boundary element numerical technique (Crouch and Starfield, 1983). Olson modified Crouch and Starfields' model and applied it to fracture network simulation for both two-dimensional plane strain (Olson, 1989; Olson, 1991; Olson, 1993) and pseudo-three dimensional cases (Olson, 1997). In Olson's pseudo-3d model, a correction factor has been incorporated to account for fracture height by assuming fracture height equals bed thickness. The correction factor modeled after equation 8.67 in Pollard and Segall (1987),

$$\frac{\sigma_{11}(\frac{x_1}{T}, x_2 = 0)}{\sigma_{11}^{r}} = 8|\frac{x_1}{T}|^3 [4(\frac{x_1}{T})^2 + 1]^{-\frac{3}{2}} \qquad (3.1)$$

where σ_{11} is the normal stress at a distance x_1 from the joint on the symmetry plane $x_2=0$, σ_{11}^{r} is remote stress, and T is bed thickness. This correction results in a stress perturbation that dies off at a length scale proportional to layer thickness. The normal stress σ_{11} along the symmetry plane $x_2=0$ calculated from Olson's pseudo 3d model is similar to the stress predicted by the true 3d (Figure 3.1). The following fracture mechanical interaction is directly calculated from Olson's numerical model (1997).

FRACTURE CONFIGURATION AND MODEL VERIFICATION

Fracture Configuration

To calculate the fracture interaction between two cracks, we use the fracture geometric configuration as shown in Figure 3.2. The lengths of the main

and field cracks are *2a* and *2b*, respectively. The crack-parallel distance between the two crack centers is *2d*, and the crack-perpendicular spacing between the two cracks is $2s$. The tips that will initially overlap are called the inner tips and exterior tips are outer tips. Crack overlap is defined as the distance between the inner tips of the upper and lower cracks (*2o*). The two cracks underlap if $o/b<0$; and overlap if $o/b>0$. Because of the symmetry of the crack configuration, we only investigate cases for $d=0$. The crack geometry (fracture length, spacing and overlap) is non-dimensionalized by the field crack length, *2b*. By assuming straight fracture path, we are concerned only with mode I cracks. Stress intensity factor of mode I crack, K_I, is normalized by the stress intensity factor of an isolated mode I crack with the same fracture length and applied stress, K_I^i. We define a dimensionless stress intensity factor, K_I / K_I^i, also called the fracture interaction factor.

Model Verification

Historically, the dimensionless crack extension force (G/G_i) has been used to quantify facture interaction (Pollard et al., 1982; Segall and Pollard, 1983; Pollard and Aydin, 1984; Pollard and Aydin, 1988; Olson and Pollard, 1991). G is the crack extension force of a main crack under mechanical interaction of a field crack. G_i is the crack extension force of the isolated main crack. For two-dimensional analysis, the crack extension force relates to the two stress intensity factors (K_I and K_{II}) as,

$$G = (K_I^2 + K_{II}^2)(1-u)/2m \qquad (3.2)$$

where K_I is the mode I stress intensity factor, and K_{II} is the mode II stress intensity factor. The various mixed-mode propagation criteria (the maximum circumferential stress, minimum strain energy density, maximum energy release rate, and the local Mode I criteria) have the common feature that $K_{II} = 0$ at an extending fracture tip, though they do not necessarily coincide with $K_{II} = 0$ at the early kink (Cotterell and Rice, 1980). The entire fracture path predicted by the local Mode I criterion and other methods are similar (Bergkvist and Guex, 1979; Cotterell and Rice, 1980). So for our straight fracture growth study, G/G_i can be approximated by,

$$G/G_i \approx (K_I / K_I^i)^2 \tag{3.3}$$

In the displacement discontinuity boundary element model (Olson, 1991; Olson, 1997), the mode I stress intensity factor (K_I) can be directly calculated. We used equation 3.3 to convert the fracture interaction factor (K_I / K_I^i) to the dimensionless crack extension force (G/G_i), so that our results are comparable to published results (Pollard et al.,1982; Segall and Pollard, 1983; Tamuzs and Petrova, 1999).

For two center-aligned (o/b=1) cracks with different spacing and length ratio, our numerical results are almost identical to those calculated by Segall and Pollard (Figure 11 of Segall and Pollard, 1983) using the Schwarz-Neumann alternating technique (Muskhelishvili, 1954; Sokolnikoff, 1956) (Figure 3.3).

To compare with the result of Pollard et al. (1982), we calculated the G/G_i of the middle crack in a three-crack en echelon array using the displacement discontinuity boundary element method. Besides directly calculating G/G_i from

the three-crack en echelon array, we also use an approximation method. In the approximation method, the three-crack array ($array_{123}$ made of crack 1, 2 and 3) is divided into two independent two-crack arrays ($array_{12}$ made of cracks 1 and 2, and $array_{23}$ made of crack 2 and 3). By multiplying the dimensionless crack extension force calculated from $array_{12}$ (G_{12}^2/G_i^2) and $array_{23}$ (G_{23}^2/G_i^2), G_{123}^2/G_i^2 of the middle crack (crack 2) in a three-crack en echelon array, $array_{123}$ can be approximated by

$$\frac{G_{123}^2}{G_i^2} = \frac{G_{12}^2}{G_i^2} \times \frac{G_{23}^2}{G_i^2} \tag{3.4}$$

The results from direct calculation and approximation methods are remarkably similar. Both of them are consistent with the results shown in Figure 12A of Pollard, et al. (1982) (Figure 3.4). This demonstrates that we can reasonably model the mechanical interaction of a three-crack echelon array by multiplying the results of two-crack arrays.

MECHANICAL INTERACTION BETWEEN TWO FRACTURES

One interesting phenomena observed in the field is that fractures tend to the long and straight in sedimentary rocks (Dyer, 1988), and are short and contain many en echelon array cracks in igneous rock (Segall, 1983). This can be quantitatively explained by the different mechanical interactions between cracks in 2d plane strain and pseudo 3d. The mechanical interaction imposed on a main crack (Figure 3.2 for the fractures' configuration) is caused by the stress perturbation induced by its nearby field fracture. The width of the stress perturbation area is proportional to the field fracture height or length, depending

on which one is smaller (Olson, 1993; Olson, 1997). If the main crack lies within the field crack-perturbed stress region, the main crack is directly affected by the field crack, and the interaction factor will not be equal to one (i.e. $K_I/K_I^i \neq 1$). In 2d plane strain, the width of stress perturbation region is about the same size as fracture length (*2b*), where the fracture length is much smaller than the fracture height (Figure 3.5). In sedimentary rocks, fracture height (*H*) is constrained by bed thickness (*T*), and the bed thickness is typically smaller than its length. Thus, the region of fracture-perturbed stress in sedimentary rocks is normally controlled by *T* (Figure 3.6). The crack-induced stresses in sedimentary rock and igneous rock are quite different, so do the caused mechanical interaction. These difference results in diverse fracture patterns.

In Igneous Rock (2d Plain Strain)

We systemically investigate the fracture interaction factor (K_I/K_I^i) as a function of dimensionless overlap, length and spacing (*s/b*, *o/b* and *a/b*) (Figures 3.7, 3.8 and 3.9). The interaction factor (K_I/K_I^i) changes dramatically with dimensionless overlap (*o/b*) (Figures 3.7 and 3.8). The stress intensity factor for significantly under-lapped and over-lapped cracks (quantitatively, this can be defined as $|o/b|>3$) is essentially the same as that for an isolated crack ($K_I/K_I^i=1$), i.e., if the two cracks are far apart, they don't affect each other. As the main crack moves close to the field crack (increasing of *o/b* in the region of $o/b<0$), K_I/K_I^i of the main crack's inner tip increases significantly and reaches its peak value when o/b is close to zero, i.e., the main and field cracks' inner tips are

nearly tip-to-tip (Figures 3.7). In the fracture under-lap region of $-3<o/b<0$, $K_I/K_I^i>1$, i.e. the mechanical interaction from the field crack enhances the main crack's propagation. The interaction factor of crack's inner tip (K_I/K_I^i) decreases sharply once the two cracks start to overlap ($o/b>0$), and soon drops below one ($K_I/K_I^i<1$), i.e. the mechanical interaction from the field crack impedes the main crack's propagation. The maximum impedance of the fracture's inner tip occurs at $o/b\approx0.5$ (Figure 3.7). The normalized overlap determines whether the propagation of a main fracture is enhanced or impeded by its neighbor field crack.

Overall, the relative length of the field crack doesn't have much impact on the main crack's inner tip, but it has a big influence on the main crack's outer tip (Figure 3.8). To investigate the effect of fracture length ratio (a/b), K_I/K_I^i is plotted versus o/b at different a/b (Figure 3.7). Figure 3.7 shows that the results are virtually identical for all crack length ratios for $-3<o/b<\sim0.2$. Then the peak impedance occurs at $o/b\approx0.5$, depending on a/b. As a/b gets smaller, the minimum value becomes smaller (from 0.5 to 0.1) and it occurs at lesser overlap (~0.8 down to 0.5). When $a/b>5$ the impedance is independent of a/b.

The interaction factor of the main crack's outer tip is sensitive to the fracture length ratio when it is plotted versus overlap (Figures 3.8, 3.11 and 3.14). This is because that overlap is defined as the distance between the inner tip of the field crack and the inner tip of the main crack. When the main crack is small (such as a/b=0.2 in Figures 3.8, 3.11 and 3.14), its two tips (inner and outer tips) are so close, that when the main crack's inner tip is close to the field crack inner tip, the main crack's outer tip also approaches it. Thus, for a/b=0.2 the interaction

factor versus overlap for both the inner and outer tips of the main crack look similar (comparing Figures 3.7 to 3.8; Figures 3.10 to 3.11; and Figures 3.13 to 3.14 for a/b=0.2). When the main crack is much larger than the field crack (such as a/b=20), Even if the inner tip of the main crack is close to the field crack, the outer tip of the main crack is still far away from it. So the outer tip of the main crack is unlikely affected by the field crack ($K_I/K_I^i \approx 1$), even if the main crack's inner tip is in the field crack's influence region ($-3 \le o/b \le 3$) (Figures 3.8, 3.11 and 3.14 for a/b=20). Because the effect of crack length ratio on the interaction factor of a main crack's outer tip is not essential, we will focus our study on the main crack's inner tip.

The dimensionless fracture spacing (*s/b*) has a controlling effect on the magnitude of interacting factor (K_I/K_I^i), over the fracture length ratio (*a/b*). When *s/b*=3, $K_I / K_I^i = 1$, indicates that the field crack doesn't directly interact with the main crack (Figure 3.9). $K_I / K_I^i > 1$ suggests that the field crack enhance the main crack's propagation. While $K_I / K_I^i < 1$ means that the field crack inhibit the main crack's propagation. As *s/b* decreases, the mechanical interaction between the field and main cracks increases dramatically. For 2d plane strain fracture, as *s/b* decreases from 3 for 0.1, the maximum K_I / K_I^i increases from 1 to 2 (the main crack's propagation is more enhanced) and the minimum K_I/K_I^i decreases from 1 to 0.2 (for $K_I / K_I^i < 1$, the smaller the K_I/K_I^i, the greater main crack is impeded, shown in Figure 3.9). The field crack further enhances or impedes the main crack propagation, when the spacing between the two cracks is small.

In Sedimentary Rock (Pseudo-3d Case)

Cracks are prevalent in sedimentary rocks, so it is important to consider the bed thickness effect. The stress field induced by a finite height field crack is different from that caused by a 2D, plane strain field crack (Figures 3.5 and 3.6), so the resulting mechanical interaction on the main crack is different. The magnitude of the main crack's interaction factor is determined by its relative position in the field crack's perturbed stress region. The relative position can be measured by *2s/2b*, when the field crack length (*2b*) controls the perturbed stress region size (i.e. when *H/2b*>1) and is calculated by *2s/H*, while the field crack height (*H*) determines the dimension of the stress perturbation area (i.e. when *H/2b*<1). In our pseudo-3d model fracture height always equals bed thickness (*H*=*T*), so the relative position of a main fracture towards a field crack is determined by 2s/min(2b, T).

To investigate the bed thickness effect, I explored two typical cases, one for *T/2b*>1 (Figures 3.10, 3.11 and 3.12) and the other for *T/2b*<1 (Figures 3.13, 3.14 and 3.15). The dimensionless spacing is determined by *s/b* for the case of *T/2b*=2.5 (*T/2b*>1) and by *2s/T* for the case of *T/2b*=0.5 (*T/2b*<1). Similar to the mechanical interaction study in 2d plane strain (Figure 3.7), the crack length ratio effect is investigated for the crack's inner and outer tips under the bed thickness of *T/2b*=2.5 and *T/2b*=0.5. For the main crack's inner tip, seen from left to right (Figures 3.7, 3.10 and 3.13), when the two cracks are far apart (*o/b*<-3) the main crack is not affected by the field crack ($K_I / K_I^i = 1$). As the main crack moves

towards the field crack, the field crack enhances the main crack's propagation ($K_I / K_I^i > 1$). Once the two cracks overlap, the field crack impedes the main crack's propagation ($K_I / K_I^i < 1$). When the main crack completely passes the field crack (*a/b*>3), the main crack will again behave like an isolated crack ($K_I / K_I^i = 1$). Figure 3.13 shows when *a/b*>0.6, the interaction factor (K_I / K_I^i) is virtually independent of a*/b* for a small bed thickness of *T/2b*=0.5. The influence of crack length ratio on K_I / K_I^i is further reduced in the thin bed. Overall, the magnitudes of interaction factors in 2d plane strain are slightly larger those in *T/2b*=2.5, and the interaction factors for *T/2b*=2.5 are slightly greater than those in *T/2b*=0.5 (Comparison of Figures 3.7, 3.10 and 3.13 for main crack's inner tip; Figures 3.8, 3.11 and 3.14 for main crack's outer tip), but in the dimensionless form the difference is small.

With the increase of dimensionless spacing (*2s/2b* or *2s/T*), the interaction factor decreases rapidly for both *T/2b*=2.5 and *T/2b*=0.5. The overall influences of dimensionless spacing on the crack interaction factor for 2d plane strain, *T/2b*=2.5 and *T/2b*=0.5 are nearly the same (Figures 3.9, 3.12 and 3.15). For the same equivalent dimensionless spacing (*2s/2b* or *2s/T*), decreasing bed thickness decreases the interaction factor of the main crack's inner tip. For a dimensionless spacing of 0.1, the maximum interaction factors (maximum enhancement) are 1.95, 1.8 and 1.6 for 2d plane strain, *T/2b*=2.5 and *T/2b*=0.5, respectively. The minimum interaction factors (maximum impedance) are 0.2, 0.2 and 0.1, respectively (Figures 3.9, 3.12 and 3.15). Although for a specific observed spacing (*2s*), the mechanical interaction between two cracks is weaker in a thinner

bed, especially when $T/2b<1$. After the bed thickness is incorporated into the dimensionless spacing, However, the interaction factor is nearly the same for a given normalized spacing ($2s/2b$ or $2s/T$) regardless of the absolute T value.

The study of dimensionless spacing effect (Figures 3.9, 3.12 and 3.15) shows that even though a field crack is much smaller than a main crack (here, $a/b=20$), the mechanical interaction from the field crack can significantly suppress the propagation of the main crack, if they are close enough to each other. For example, at $s/b=0.25$ and $o/b=0.5$ (the peak impedance), the stress intensity factor of the main crack's inner tip reduces to about 0.5 of its original value for 2d plane strain case (Figure 3.9), and to 0.5 and 0.3 of its original values for $T/2b=2.5$ and $T/2b=0.5$, respectively (Figures 3.12 and 3.15).

DISCUSSION

To understand the influence of a field crack on a main crack, we quantify mechanical interaction between two fractures, such that the interacting factor (K_I / K_I^i) is calculated as a function of dimensionless spacing (s/b or $2s/T$), dimensionless overlap (o/b) and crack length ratio (a/b). A field crack has influence on its neighbor main crack, when both dimensionless spacing, and dimensionless overlap are less than 3. Thus a crack's "local group" region (Segall, 1984), in which the crack has direct influence on others, is quantified. The field crack enhances the main crack's propagation, when the two cracks under-lap and are close to each other ($-3<o/b<0$). Once the two cracks overlap, the field crack impedes the main crack's growth.

The influence of a field crack on a main crack decreases rapidly when the dimensionless spacing (s/b or $2s/T$) increases. For a fixed spacing ($2s$), the magnitude of interaction factor decreases promptly with bed thickness, if the fracture length exceeds bed thickness ($T/2b<1$). This is because the interaction factor is directly related to the perturbed stress field, which is controlled by the smallest dimension of the fracture. When the dimensionless bed thickness is greater than one ($T/2b>1$), the length of the field crack has a dominant influence on the main crack, which is the same as the 2D case. When the dimensionless bed height is less than one ($T/2b<1$), the fracture height, which equals the bed thickness, is the smallest dimension. The difference of mechanical interaction in 2d and pseudo-3d can be used to explain the different fracture patterns in sedimentary and igneous rocks. In practice, the bed thickness can be included into the dimensionless spacing to quantify the mechanical interaction.

REFERENCES

Atkinson, B. K. and Meredith, P. G., 1987, The theory of subcritical crack growth with applications to minerals and rocks. Atkinson, B. K., ed., *Fracture Mechanics of Rock*, Academic Press, San Diego, USA

Bai, T., and Pollard, D. D., 2000, Fracture spacing in layered rocks: a new explanation based on the stress transition, *Journal of Structural Geology*, 22, 43-57.

Becker, A., and Gross, M. R., 1996, Mechanism for joint saturation in mechanically layered rocks: an example from southern Israel, *Tectonophysics*, 257, 223-237.

Cotterell, B., and Rice, J. R., 1980, Slightly curved or kinked cracks: *International Journal of Fracture*, 16, 155-169.

Crouch, S. L. and Starfield, A. M., 1983, *Boundary Element Methods in Solid Mechanics*. George Allen and Unwin, London, U. K.

Cruikshank, K.M., Zhao, G., and Johnson, A. M., 1991, Analysis of minor fractures associated with joints and faulted joints, *Journal of Structural Geology*, 13, 865-886.

Dershowitz, W. S. and Einstein, H. H., 1988, Characterizing rock joint geometry with joint system models. *Rock Mech. Rock Eng*., 21, 21-51.

Dey, T.N. and Wang, C.Y., 1981, Some mechanisms of microcrack growth and interaction in compressive rock failure, *International Journal of Rock Mechanics and Mining Science*, 18, 199-209.

Dyer, R., 1988, Using joint interactions to estimate paleostress ratios, *Journal of Structural Geology*, 10 (7), 685-699.

Erdogan, F. and Sih, G. C., 1963, On the crack extension in plates under plane loading and transverse shear. *ASME Transactions*, 85, 519-527.

Karihaloo, B. L., Keer, L. M., and Nemat-Nasser, S., 1980, Crack kinking under nonsymmetric loading: *Engineering Fracture Mechanics*, 13, 879-888.

Kranz, R.L., 1979, Crack-crack and crack-pore interactions in stressed granite, *International Journal of Rock Mechanics and Mining Science*, 16, 37-47.

Lawn, B. R., and Wilshaw, T. R., 1975, *Fracture of brittle solids*, Cambridge, England, Cambridge University Press, 204.

Muskhelishvili, N. I., 1954, *Some Basic Problems of Mathematical Theory of Elasticity*, P. Noordhoff Ltd., Groningen, The Netherlands.

Nur, A., 1982, The origin of tensile fracture lineaments, *Journal of Structural Geology*, 4, 31-40.

Olson, J. E., 1991, Fracture mechanics analysis of joints and veins, Dissertation, Stanford University.

Olson, J. E., 1993, Effects of subcritical crack growth and mechanical crack interaction, *Journal of Geophysical Research*, 98(B7), 12251-12265.

Olson, J. E., 1997, Natural fracture pattern characterization using a mechanical-based model constrained by geologic data – moving closer to a predictive tool. *Int. J. Rock Mech. & Min. Sci.*, 34(3/4), 391, Paper No. 237.

Olson, J. E. and Pollard, D. D., 1989, Inferring paleostresses from natural fracture patterns: A new method, *Geology*, 17, 345-348.

Olson, J. E. and Pollard, D. D., 1991, The initiation and growth of en echelon veins, *Journal of Structural Geology*, 13(5), 595-608.

Pollard, D. D., Segall, P., and Delaney, P. T., 1982, Formation and interpretation of dilatant echelon cracks, *Geological Society of America Bulletin*, 93, 1291-1303.

Pollard, David D. and Aydin, A., 1984, Propagation and linkage of oceanic ridge segments, *Journal of Geophysical Research*, 89(B12), 10,017-10,028.

Pollard, D. D. and Segall, P., 1987, Theoretical displacements and stresses near fractures in rocks: with applications to faults, joints, veins, dikes and solution surfaces. In: Atkinson, B.K. ed., *Fracture Mechanics of Rock*. Academic Press, London, 277-349.

Pollard, D. D. and Aydin, A., 1988, Progress in understanding jointing over the past century, *Geological Society of America Bulletin*, 100, 1181-1204.

Renshaw, C. E., 1993, Modeling fluid migration through physically-based fracture networks, *Dissertation*, Stanford University.

Rives, T., Razack, M., Petit, J. P. and Rawnsley, K.D., 1992, Joint spacing: analogue and numerical simulations, *Journal of Structural Geology*, 14(8/9), 925-937.

Segall, P., 1984, Formation and Growth of extensional fracture sets, *Geological Society of America Bulletin*, 95, 454-462.

Segall, P., and Pollard, D. D., 1980, Mechanics of discontinuous faults, *Journal of Geophysical Research*, 85(B8), 4337-4350.

Segall, P., and Pollard, D. D., 1983, Joint formation in granitic rock of the Sierra Nevada, *Geological Society of America Bulletin*, 94, 563-575.

Sokolnikoff, I. S., 1956, *Mathematical Theory of Elasticity*, 2nd ed., 475, McGraw-Hill, New York.

Tamuzs V. and Petrovab V., 1999, Modified model of macro-microcrack interaction, *Theoretical and Applied Fracture Mechanics*, 32(2), 111-117.

Thomas, A. L., and Pollard, D. D., 1993, The geometry of echelon fractures in rock: Implications from laboratory and numerical experiments, *Journal of Structural Geology*, 15(3-5), 323-334.

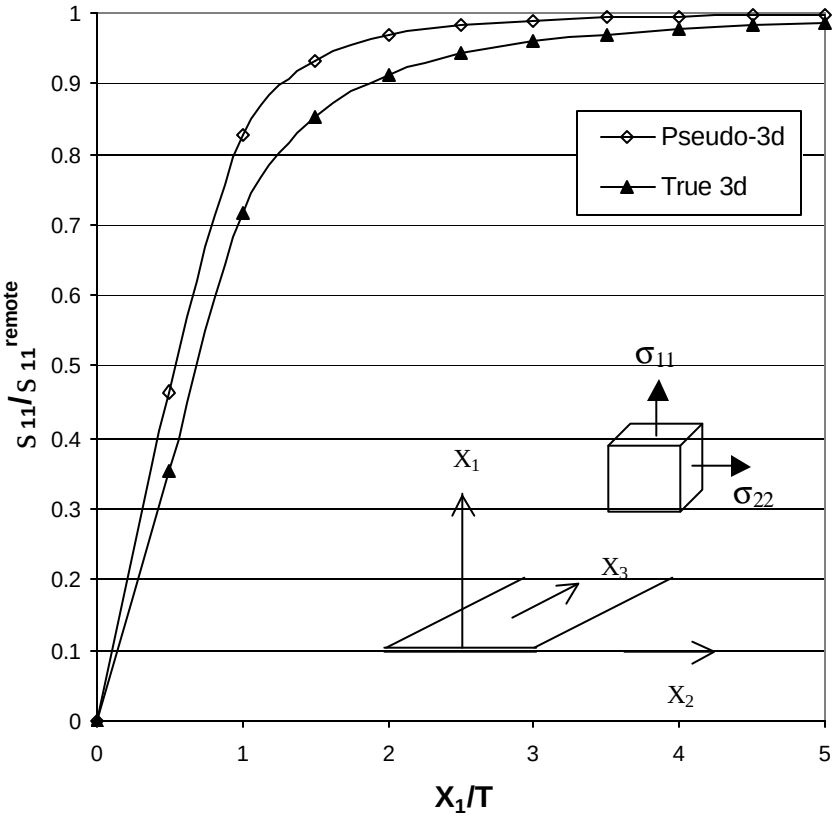

Figure 3.1 Non-dimensioned normal stress, s_{11}/s_{11}^{r}, along the plane perpendicular to the crack through the crack middle. The normal stress s_{11}/s_{11}^{r} along the symmetry plane $x_2=0$ calculated from Olson's pseudo-3d model is similar to the stress predicted by the true 3d (calculated by equation 3.1).

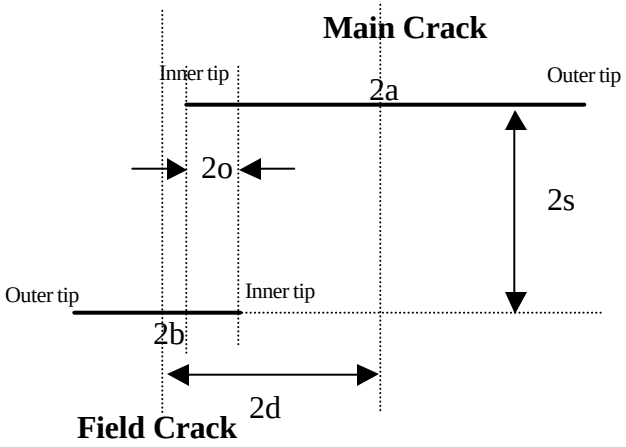

Figure 3.2 Fracture configuration illustrates main crack with length of 2a and field crack with length of 2b, and their relative position, which is quantified as Overlap (2o), the crack-parallel distance between the two cracks' inner tips, and Spacing (2s), the crack-perpendicular distance between the two cracks. 2d is the crack-parallel distance between the two cracks' centers.

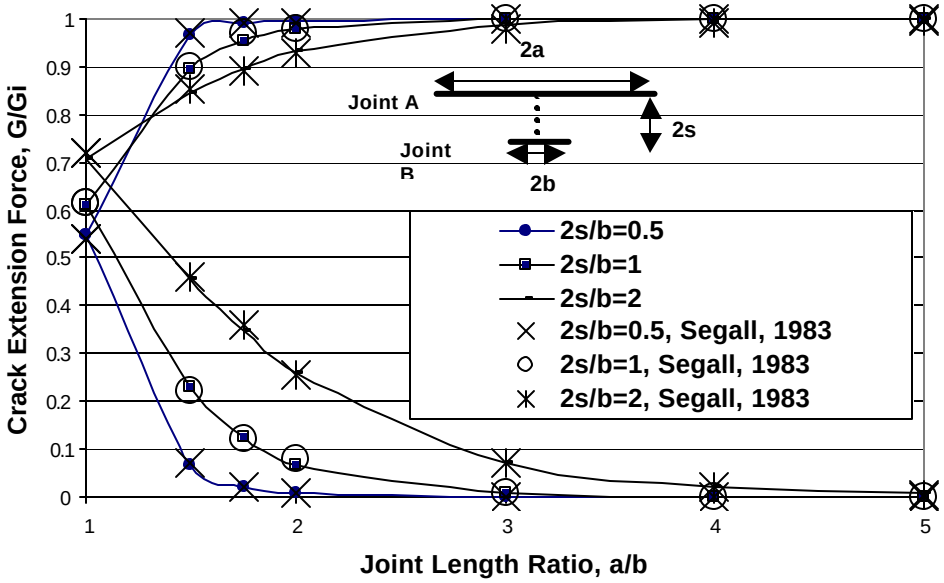

Figure 3.3 The dimensionless crack extension force verse joint length ratio for different spacing of two-dimensional case, comparing with Figure 2.11 of Segall and Pollard, 1983.

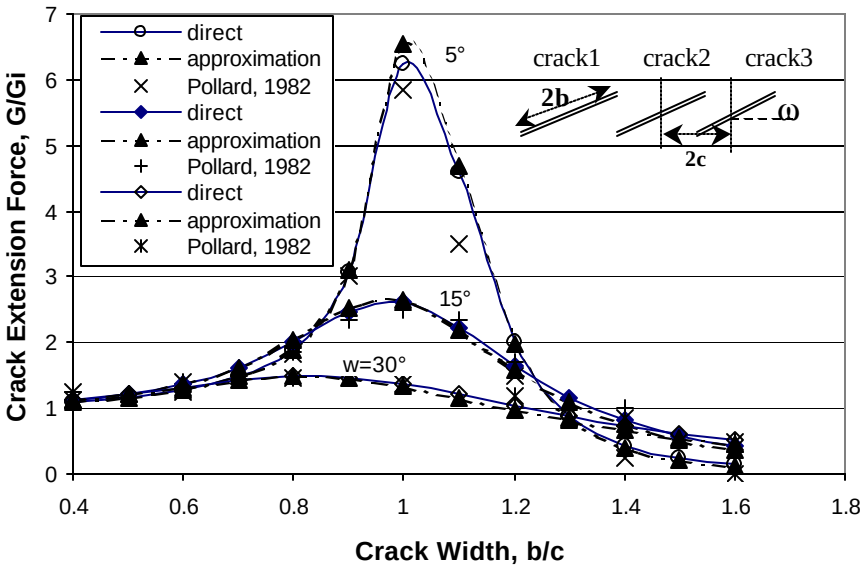

Figure 3.4 The dimensionless crack extension force for the middle crack of a three-crack array.

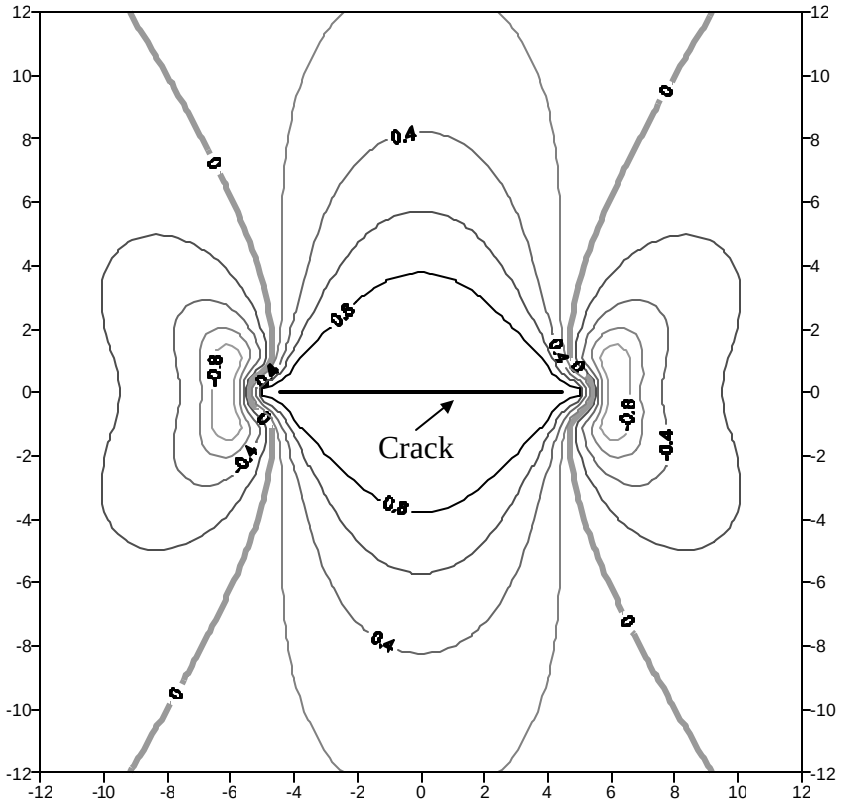

Figure 3.5 Distribution of crack perpendicular stress, s_{11}, for 2D plane strain. On both sides of the fracture, the induced stress is compressive. In front of the fracture tips induced stress is tensile. The size of compressive stress range is proportional to fracture length.

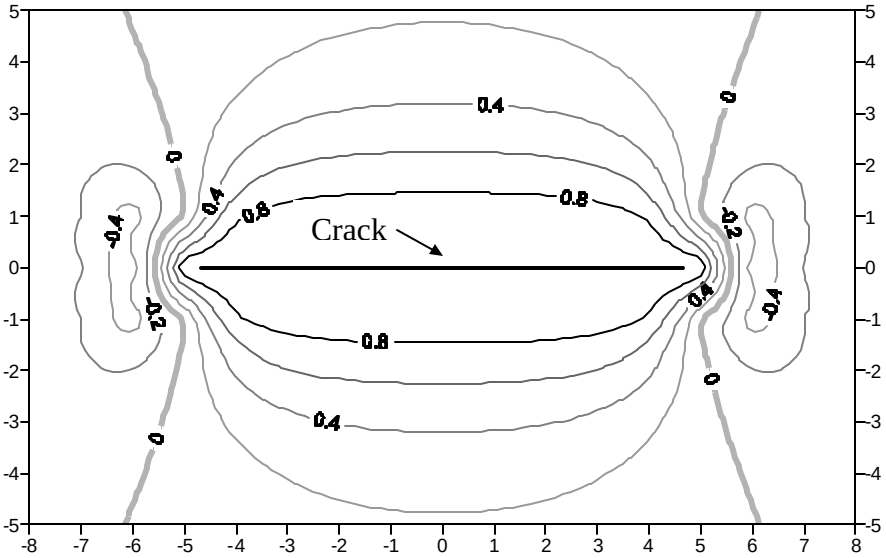

Figure 3.6 Distribution of crack perpendicular stress, s_{11}, for bed thickness of 5m. On both sides of the fracture, induced stress is compressive, and in front of the fracture tips induced stress is tensile. The size of compressive stress range is proportional to bed thickness.

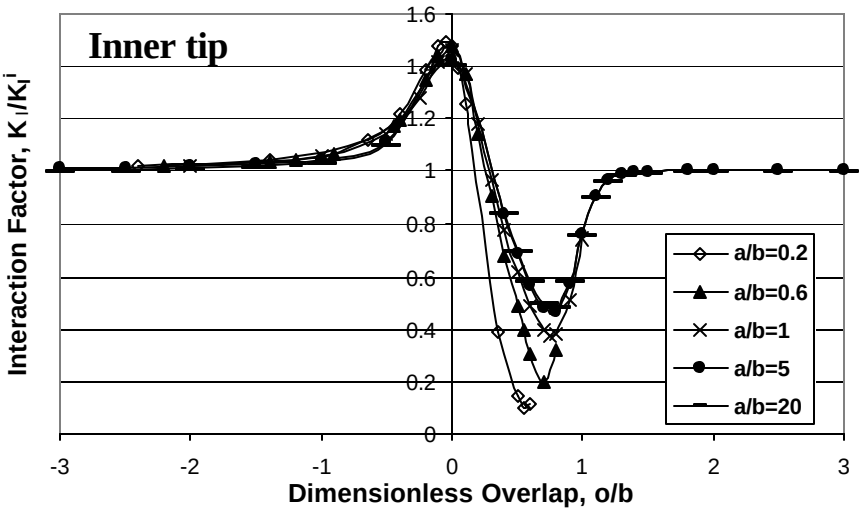

Figure 3.7 The influence of the crack length ratio (a/b) on the crack interaction factor, plotted versus dimensionless overlap for the inner tip of the main crack. (2d plane strain and s/b=0.25).

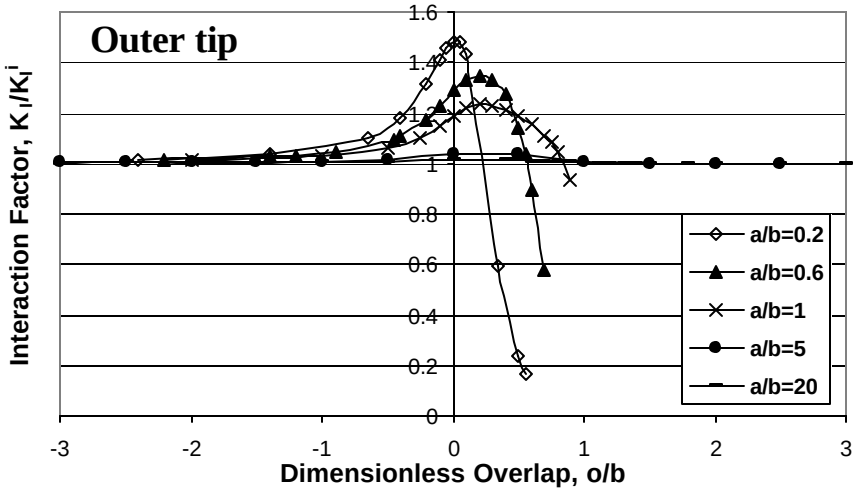

Figure 3.8 The influence of crack length ratio (a/b) on crack interaction factor, plotted versus dimensionless overlap for the outer tip of the main crack. (2d plane strain case and s/b=0.25).

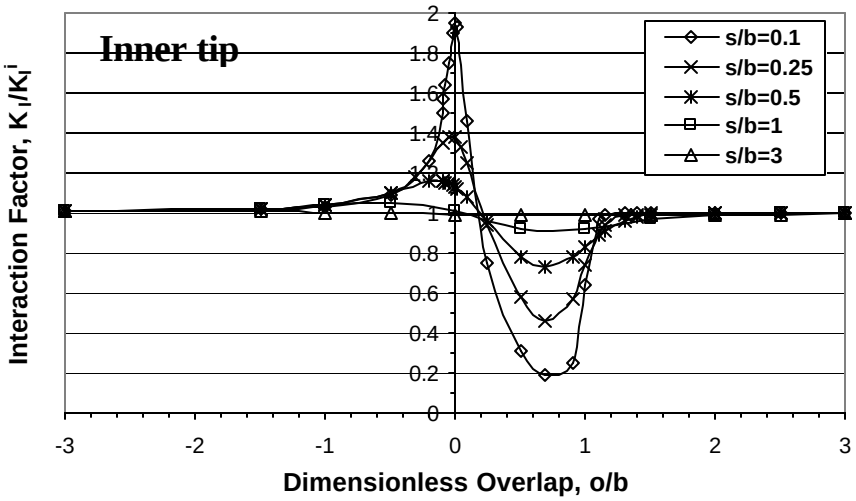

Figure 3.9 The influence of dimensionless spacing on crack interaction factor, plotted versus dimensionless overlap for the inner tip of the main crack (2d plane strain case and a/b=20).

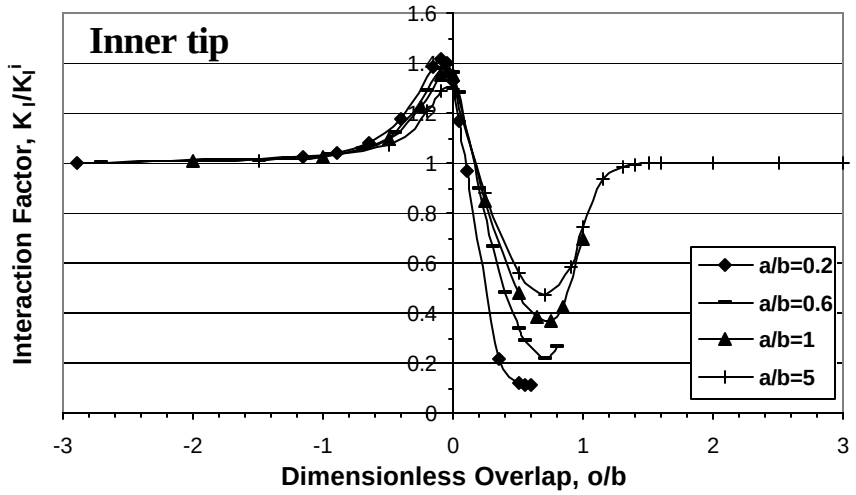

Figure 3.10 The influence of the crack length ratio (a/b) on the crack interaction factor, plotted versus dimensionless overlap for the inner tip of the main crack. (Pseudo-3d with T/b=2.5 and s/b=0.25).

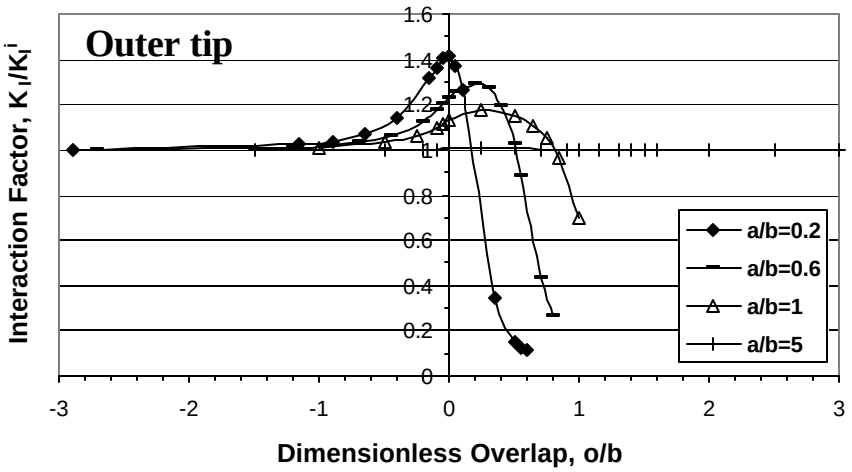

Figure 3.11 The influence of the crack length ratio (a/b) on the crack interaction factor, plotted versus dimensionless overlap for the outer tip of the main crack. (Pseudo-3d with T/b=2.5 and s/b=0.25).

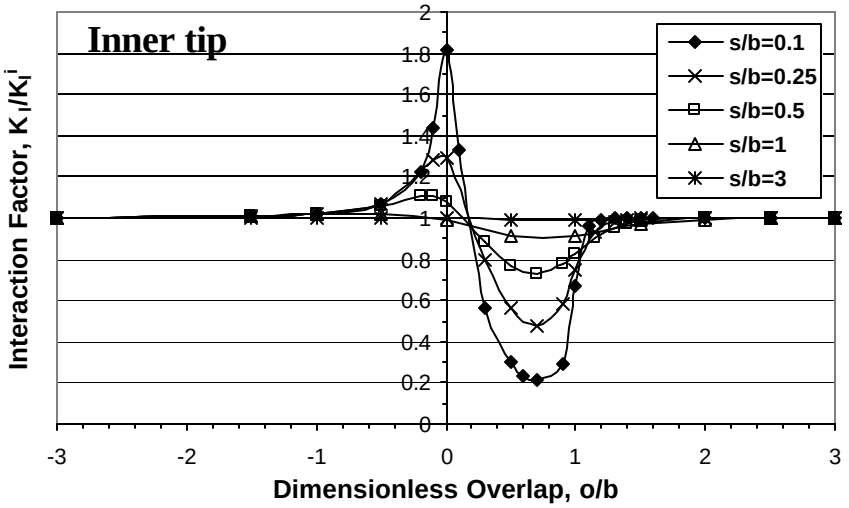

Figure 3.12 The influence of dimensionless spacing on crack interaction factor, plotted versus dimensionless overlap for the inner tip of the main crack (Pseudo-3d with T/b=2.5 and a/b=20).

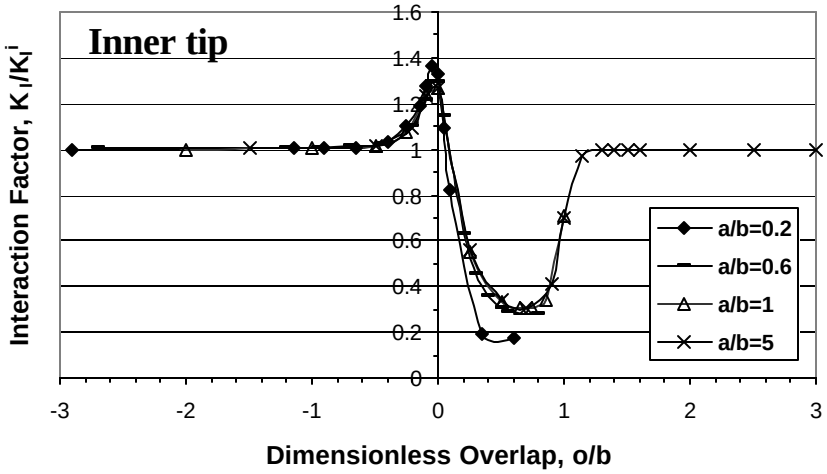

Figure 3.13 The influence of the crack length ratio (a/b) on the crack interaction factor, plotted versus dimensionless overlap for the inner tip of the main crack. (Pseudo-3d with *T/b*=0.5 and *s/b*=0.25).

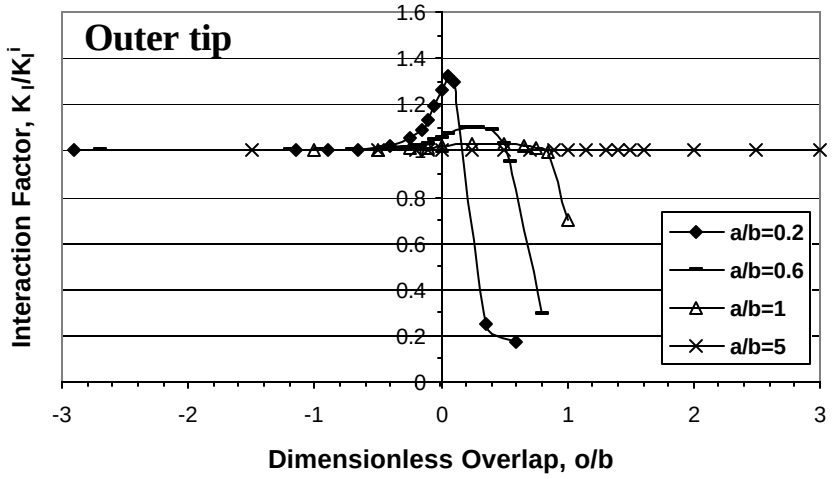

Figure 3.14 The influence of the crack length ratio (a/b) on the crack interaction factor, plotted versus dimensionless overlap for the outer tip of the main crack. (Pseudo-3d with *T/b*=0.5 and *s/b*=0.25).

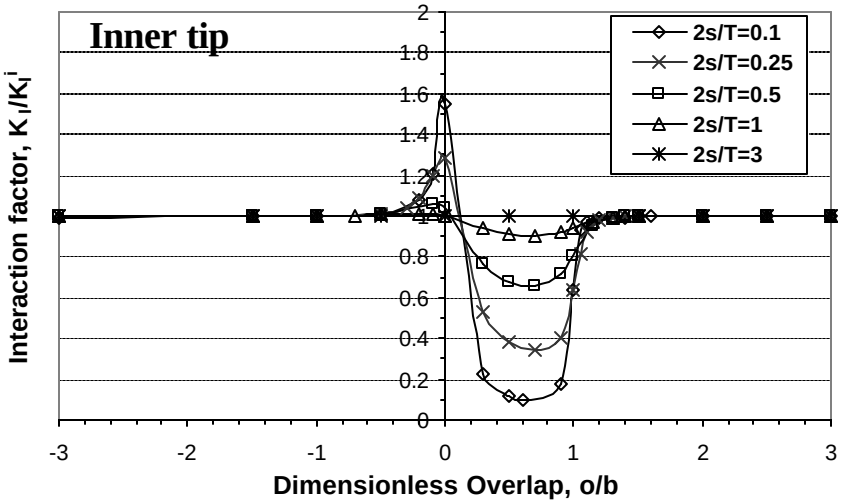

Figure 3.15 The influence of dimensionless spacing on crack interaction factor, plotted versus dimensionless overlap for the inner tip of the main crack (Pseudo-3d with $T/b=0.5$ and $a/b=20$).

CHAPTER 4: EFFECT OF MECHANICAL INTERACTION ON FRACTURE LENGTH DISTRIBUTION

ABSTRACT

The underlying mechanisms of fracture propagation and interaction provide indications to the expected shape of fracture length distributions. When a small fracture is close enough to a large fracture, it can trap the large fracture and cause it to stop propagating due to mechanical interaction effects. According to this criterion, an analytical equation is derived for the probability distribution function of fracture length showing fracture lengths follow a negative exponential distribution for two-dimensional map view sampling.

INTRODUCTION

Fractures can vary from mineral-grain size up to several kilometers long. Fracture length is generally assumed to be the result of random processes, and distributions are determined from the best-fit function to the collected field data (Dershowitz and Einstein, 1988; Barton and Zoback, 1992). There are various published distribution functions for fracture lengths, each depending limited observations (Figure 4.1). The distribution of fracture lengths observed in many studies appears to be lognormal (MacMahon, 1974; Bridges, 1976; Priest and Hudson, 1976; Baecher et al., 1977; Barton, 1977; 1981; Cruden, 1977; Baecher and Lanney, 1978; Einstein et al., 1980; Warburton, 1980; Einstein and Baecher,

1983; Hudson and Priest, 1983; Dershowitz and Einstein, 1988; Renshaw, C.E., 1993). Historically, the lognormal distribution has been used to describe fracture length data primarily for mathematical simplicity with no inherent physical significance (Barton and Zoback, 1992). A lognormal distribution can result from a common distribution where there is inadequate sampling of small-scale features (Einstein and Baecher, 1983).

Another hypothesis about fracture and fault length populations is that they obey fractal or power law distributions (e. g. Segall and Pollard, 1983; Gudmundsson, 1987; Okubo and Aki, 1987; LaPointe, 1988; Hirata, 1989; Heffer and Bevan, 1990; Laubach, 1992; Hatton et al., 1994; Johnston and McCaffrey, 1996; Cladouhos and Marrett, 1996; Marrett, 1997; Odling, 1997; Marrett et al., 1999; Ortega and Marrett, 2000; Stowell, 2000). A power-law relationship is defined as (Cladouhos and Marrett, 1996):

$$N = C\, x^{-D}, \tag{4.1}$$

where N is the numerical rank of a fracture of length x when sorted in ascendant order, D is the power law exponent, and C is a constant of proportionality. For fracture populations that follow fractal distributions, a plot of $\log(N)$ vs. $\log(x)$ will follow a straight line with slope of $-D$.

Data are required over a wide range of scales to verify that fracture length follows a power law distribution. A subset of the data can often look log-normal, but many argue that the parent population covering all scales is most likely governed by a universal fractal distribution (Marrett, 1997; Odling, 1997; Marrett et al., 1999; Ortega and Marrett, 2000). Odling (1997) systemically gathered

fracture trace-length data in Devonian sandstones in western Norway in the seven different scales, in which fractures are mapped from 7 different observation heights from 1.5m to 368m. Although the analysis of the collected data from the 7 maps suggests a power-law distribution of fracture trace lengths with a constant exponent of –2.1, the power-law distribution has its upper and lower limits. Reducing the observation height to less than 1.5m, very few cracks are detected between the fractures, which is observed from a height of 1.5m (Odling, 1997). Odling (1997) concluded the lower cut-off of the power law distribution in Devonian sandstones in western Norway is around 1m, and the micro-fractures on the scale of the rock grains may not belong to the same power law distribution. At the longer end, fracture length data are fit to a power law distribution with a higher constant, *D*, which implies that long fractures are less abundant than in a strictly self-similar system (Odling, 1997).

Self-similar distributions are scale invariant; that is, objects appear the same when viewed at different scales. Self-similarity is a common explanation for the power law distribution of fracture length, which suggests that many phenomena evident at one scale are evident at other scales (e.g., Tchalenko, 1970; King, 1984; Barton and Larson, 1985; Okubo and Aki, 1987; LaPointe, 1988; Barton and Hsieh, 1989). Self-similarity in a fracture process suggests the existence of a universal fracturing mechanism. Castaing et al. (1997) argued that joint and fault systems individually could be scale independent, but combined throughout the scales they render the organization hierarchical in nature, i.e. scale dependent. Overall, the applicability of universal scaling to field observations

and rock mechanics measurements remains the subject of debate (Johnston, 1996; Odling, 1997; Lyakhovsky, 2001).

Based on fracture mechanics, Lyakhovsky (2001) explained that opening fracture growth, governed by the subcritical growth law, produces a self-similar shape, but the power law distribution breaks down if the fractures propagated dynamically. However, Lyakhovsky's mechanical model (of mode I crack growth) is not suitable to explain field observations of natural fractures. First, constant stress is not a good boundary condition for natural fracture simulation in a geological time frame. According to Griffith's energy-balance theory (Griffith, 1924), if a crack is loaded in uniform tension, the cracked system's energy is a maximum at equilibrium, which causes the fracture to be unstable, and to propagate without limit (i.e. dynamic growth) (Lawn and Wilshaw, 1975). Another potential shortcoming in Lyakhovsky (2001) is that the mechanical interaction between fractures is ignored. Numerical analyses by Pollard et al. (1982) and Olson and Pollard (1989) suggest mechanical interaction will have an impact on fracture length.

Faults as natural shear fractures have different growth mechanisms than opening fractures. Fault growth is considered a self-similar process (Scholz, 1997). The fault growth model and the fault linkage model were used to explain the power law distribution of fault length distribution (Cladouhos and Marrett, 1996). In the fault growth model, the total geological slip scales linearly with fault length (Cowie and Scholz, 1992; Cladouhos and Marrett, 1996; Scholz, 1997). Under the assumption of an initial power-law distribution of fault lengths

and a constant number of faults (no fault birth or death), fault length is simulated to be a power law distribution (Cladouhos and Marrett, 1996). Cladouhos and Marrett's (1996) fault growth model still is a single-fault growth model. The fault linkage model refers to fault lengthening by coalescence with other faults. The fault linkage model specifies the amount of fault growth. If a nearby fault is encountered, the two faults or fractures link. With the fault linkage model, it is possible to produce a power-law fracture length distribution from an initial fault or flaw distribution that is other than fractal.

In contrast, Nicol (1996) stated that fault size populations do not follow a power law distribution but conform to a negative exponential distribution (Robertson, 1970; Call et al., 1976; Dershowitz and Einstein, 1988). The probability distribution function, f(x), for a negative exponential law can be expressed as:

$$f(x) = l e^{-lx}. \qquad (4.2)$$

As shown, there are multiple hypotheses for the nature of fracture length distributions based on empirical evidence. However, no published study proposes a physical mechanism for fracture initiation, propagation, interaction and termination, or uses those basic assumptions to predict the nature of fracture length distributions. We propose a mechanical model to predict fracture length distribution based on fracture mechanics and independently determined by initial and boundary conditions.

FRACTURE CAPTURE MODEL

When a fracture propagates, it disturbs the nearby stress field. This causes a mechanical interaction between the propagating fracture and its neighbors. The interaction influences a fracture's growth and arrest, and therefore affects the fracture's length. Fracture interaction has been quantitatively studied using fracture mechanics (Pollard et al. 1982; Segall and Pollard, 1983; Pollard and Aydin, 1984; Pollard and Aydin, 1988; Olson and Pollard, 1991, Tamuzs and Petrovab, 1999). Based on these two-dimensional analyses, we systemically investigate the interaction between fractures of different lengths and center locations, and also account for the three dimensional effects of fractures contained within finite thickness sedimentary beds. We propose that small flaws, if close enough to a larger crack, can significantly suppress or arrest the larger crack's propagation. This fracture interaction, combined with the number of flaws in a given area, exerts a controlling influence on fracture length distributions.

The fracture capture model proposed herein is built on several characteristics. Firstly, the model focuses on the elastic interaction between two mode-I cracks under 2d plane strain and 3d cases. These conditions correspond to the lateral propagation of slot-like (2d) through blade-like (3d) cracks (Olson, 1993). For simplicity, the model is restricted to straight crack propagation, which implies the presence of a large crack-parallel differential compression (Cotterell and Rice, 1980; Olson and Pollard, 1989; Cruikshank, et al., 1991; Thomas and Pollard, 1993). Theoretical analyses have shown that a remote compressive stress acting parallel to a crack may produce a straight crack path even in the presence

of a mode II stress intensity (Cotterell and Rice, 1980; Karihaloo et al., 1980; Olson and Pollard, 1989). Straight crack patterns are common in outcrops (Segall, 1984, Rives et al, 1992; Olson, 1993; Becker and Gross, 1996). The assumption of straight cracks allows the use of simpler analytical models for our fracture length distribution study and also limits the geometric possibilities. The geometric fracture configuration applied in this model is shown in Figure 4.2. For convenience, we defined "field cracks" as the small cracks dispersed throughout a body that may be encountered by a "main crack" as it propagates through that body. The lengths of the main and field cracks are 2a and 2b, respectively. The crack-parallel distance between the two crack centers is 2d, and the crack-perpendicular spacing between the two cracks is 2s. Crack overlap is defined as the distance between the inner tips of the main and the field cracks, which is represented as 2o.

Two-dimensional, plane strain, linear elasticity is utilized to calculate the interaction factor between cracks. The model is based on a displacement discontinuity boundary element numerical technique (Olson, 1993). An approximate correction factor has been incorporated into the model accounting for constrained fracture height (Olson, 1997). These interaction factors are described in detail in chapter 2. A subcritical crack propagation law (Atkinson, 1987) is used to represent fracture growth under geologic conditions (i.e., long term and low strain rate loading). In the subcritical crack propagation law, propagation velocity can be defined as (Atkinson, 1987; Olson, 1993)

$$V = V_{\max}\left(\frac{K_I}{K_{Ic}}\right)^n, \tag{4.3}$$

where K_I is the mode I stress intensity factor, K_{Ic} is the fracture toughness of the material, n is the subcritical growth index of the material, and V_{max} is the maximum possible propagation velocity at critical growth ($K_{I=} K_{Ic}$).

The interaction factor, $K_I / K_I^{\,i}$, is defined as the ratio of main crack, mode I stress intensity factor to the stress intensity of an isolated crack of the same length loaded by the same uniform stress. The interaction factor quantifies the magnitude of mechanical interaction imposed by a field crack on to the main crack and varies with fracture spacing. For a dimensionless spacing of 3 (s/b=3), the interaction factor is equal to 1 ($K_I / K_I^{\,i}$=1) for all overlaps investigated (-2=o/b=2, Figure 4.3a). Decreasing the spacing (crack-perpendicular distance) between the main and field crack increases mechanical interaction (Figure 4.3a). Different overlaps (crack-parallel distance) determine whether the main crack's propagation is enhanced or impeded. When the crack tips have not yet met (o/b<0), the interaction factor increases as the main crack passes closer to the field crack (Seen from left to right with o/b increased from –2 to 0 in Figure 4.3a), representing propagation enhancement for the main crack. The maximum increase occurs when the two cracks are about tip-to-tip (o/b=0). Once the two cracks overlap (o/b>0, seen from left to right with o/b increased from 0 to 2 in Figure 4.3a), the interaction factor decreases rapidly and finally drops below one ($K_I/K_I^{\,i}$<1, when 0.2=o/b=1.5), representing propagation impedance of the main crack. When the main crack right tip completely passes the field crack (o/b>1.5), the main crack is no longer influenced. The magnitude of mechanical interaction increases rapidly, as dimensionless spacing decreases. As s/b decrease from 3 to

1, the peak interaction factor (enhancement) increases from 1 to 1.95, and the lowest value (peak impedance) changes from 1 to 0.2. The mechanical interaction between cracks reduces with decrease of bed thickness (Figure 4.3b), because the finite bed thickness diminishes stress perturbation and restricts crack opening.

To quantify propagation tendency, we define a capture ratio, R_c, which is defined as the ratio of the stress intensity factor of the outer tip of a field crack, $K_I^{outer-field}$, to that of the inner tip of a main crack, $K_I^{inner-main}$.

$$R_c = \frac{K_I^{outer-field}}{K_I^{inner-main}}. \tag{4.4}$$

Propagation velocity can be related to stress intensity factor through subcritical growth law (equation 4.3). Combining equation 4.3 and 4.4, the velocity ratio of the outer tip of the field crack to that of the inner tip of the main crack can be expressed as

$$\frac{V^{outer-field}}{V^{inner-main}} = \frac{V_{\max}\left(\frac{K_I^{outer-field}}{K_{IC}}\right)^n}{V_{\max}\left(\frac{K_I^{inner-main}}{K_{IC}}\right)^n} = \left(\frac{K_I^{outer-field}}{K_I^{inner-main}}\right)^n = {R_c}^n. \tag{4.5}$$

When the capture ratio is larger than one, the field crack's propagation velocity exceeds that of the main crack (equation 4.5). Thus the propagation is transferred to the field crack, while the main crack stops or propagates more slowly. When the capture ratio is less than one, the main crack continues to propagate past the field crack. The experimentally determined subcritical crack growth index for oil field rocks have been measured in the range of ~ 20 to 200 (Holder et al. 2001).

According to equation 4.5, the velocity contrast between these two cracks can be substantial, depending on the magnitude of the subcritical index.

The capture ratio is a function of crack length ratio, overlap, spacing and bed thickness (Figures 4.4a, 4.4b, 4.4c and 4.4d). There is a weak dependence on length ratio for a given spacing (s/b), where the smaller the length ratio of a main crack to a field crack, the higher the capture ratio (Figures 4.4a and 4.4b). For a small spacing ratio of s/b=0.25 and equal length cracks (a/b=1), the maximum capture ratio occurs at o/b»0.6 with a value of R_c»2.8. It drops to R_c=2.0 for a/b=10, but doesn't change much for even smaller field cracks (a/b=25, 50) (Figure 4.4a). Similar results can be seen at larger spacing, s/b=0.5 (Figure 4.4b). However, the capture ratio increases dramatically with a decrease in s/b (Figure 4.4c). The maximum R_c occurs at o/b»0.7 (Figure 4.4c). For s/b=0.1, the maximum R_c»5.4. The peak R_c drops to 1.8 for s/b=0.25, and drops to 1 for s/b=0.5. When s/b>0.5, the capture ratios are less than one (R_c<1) and the main crack will not be captured at all. Thus, we define 0.5 field crack length as our critical spacing, and the area within is our capture zone. For a fixed spacing of s/b=0.25, the smaller the bed thickness, the lower the maximum capture ratio is (Figure 4.4d). The maximum R_c occurs at o/b»0.7. For T/b=0.5, the maximum capture ratio is about 1.5 (R_c»1.5). For T/b=2.5 and 2d plane strain, the maximum R_c»1.8.

ANALYTICAL MODEL OF FRACTURE LENGTH DISTRIBUTION

Based on the numerical results, the critical spacing for capture is one half the field crack length. Assuming the propagation of any main crack passing within this critical distance of a field crack is arrested, we calculated the probability that a main crack propagating through a material with randomly distributed parallel flaws (field cracks) will reach a particular length. This probability is the same as the probability that the propagating main crack will be captured by a smaller field crack. By quantifying fracture capture probability, we can further calculate the expected cumulative and probability distribution function for fracture length.

The probability that a main crack with length 2a will be captured is equal to the probability that at least one field crack of length 2b will lie within its capture zone (Figure 4.5). The capture zone is a rectangular region around the main crack of length (2a+2b) and a width of 2 times the critical spacing (because the capture zone lies on both sides of the main crack), or $(2a+2b)\times 2b$. Since the field crack length $2b$ is much smaller than the main crack's length $2a$, area size can be simplified as $2a\times 2b$. The area outside the capture zone has a size of $A-2a\times 2b$. Assuming N field cracks are uniformly randomly distributed in a total area A, the probability, P', that at least one field crack will lie within the capture zone of a propagating main crack is equal to one minus the probability, P_{N_out}, that no cracks reside in the capture zone (i.e. all field cracks locate outside the capture zone) or

$$P'(2a)=1-P_{N\_out}(2a). \tag{4.6}$$

Since we assume the field cracks are uniformly randomly distributed, the probability, P_{1_out}, of one field crack being outside the capture zone can be expressed as

$$P_{1\_out}(2a) = \frac{A - 2a \times 2b}{A}. \tag{4.7}$$

The probability that all N cracks are located outside the capture zone is

$$P_{N\_out}(2a) = P_{1\_out}(2a)^N = \left(\frac{A - 2a \times 2b}{A}\right)^N. \tag{4.8}$$

The probability, P, of a main crack of length $x=2a$ not being captured is

$$P(X > x) = \left(\frac{A - 2bx}{A}\right)^N = \left(1 - \frac{2b}{A}x\right)^N. \tag{4.9}$$

This is the probability that the crack will propagate to a length of at least x. Taking the logarithm of equation 4.9, we get

$$\ln P(X > x) = N \ln\left(1 - \frac{2b}{A}x\right). \tag{4.10}$$

Assuming area A is a square and the main crack of length x is prohibited from propagating out of the area of interest, the maximum dimension possible for x is $\sqrt{A}$ (or $A=x^2$). Given also that field cracks are equivalent to flaws or micro-cracks and will always be much smaller than the propagating main crack ($2b<<x$), we have

$$\frac{2bx}{A} \le \frac{2b}{x} << 1. \tag{4.11}$$

Under these constraints, we can consequently conclude, by 1st order Taylor expansion (Kreyszig, 1993, p803)

$$\ln\left(1 - \frac{2b}{A}x\right) \approx -\frac{2b}{A}x. \tag{4.12}$$

Inserting equation 4.12 into equation 4.10, we get

$$\ln P(X > x) = N \ln(1 - \frac{2b}{A} x) \approx -\frac{2bN}{A} x . \quad (4.13)$$

Therefore, the probability of the main crack not being captured, i.e. the probability for a fracture having a length larger than x (complementary cumulative distribution function) can be simplified as

$$P(X > x) = e^{-Dx}, \quad (4.14)$$

where the exponential constant, D, is given by

$$D = 2b \frac{N}{A} . \quad (4.15)$$

Consequently, the probability of the main crack being captured can be expressed as

$$P(X \le x) = 1 - e^{-Dx} . \quad (4.16)$$

This is the same as the cumulative distribution function for a crack's length being less than or equal to x, i.e.,

$$F(X \le x) = 1 - e^{-Dx} . \quad (4.17)$$

The probability distribution function, *f(x)*, can be converted from the cumulative distribution function, *F(x)* by

$$f(x) = \frac{dF(x)}{dx} = D\, e^{-Dx} . \quad (4.18)$$

Therefore, mechanical crack interaction for a main crack propagating through a population of smaller field cracks predicts a negative exponential fracture length distribution (equation 4.18), where the mean (m) and standard deviation (s) of fracture length equals

$$m = s = \frac{1}{D} = 1 \Big/ \left(2b \frac{N}{A}\right) . \quad (4.19)$$

Equations 4.18 and 4.15 represent a theoretically derived expression for fracture length prediction based on independent fracture mechanics principles for mode I crack growth. The independent variables required for the equation are measurable rock characteristics, field crack density (N/A) and field crack length ($2b$).

Varying the exponent D changes the shape of the complementary fracture length distribution (Figure 4.6). If we increase D by increasing field crack density, the main crack has a higher probability of being arrested at a shorter length because of more potential flaws that could be inside the capture zone. If D increases by increasing the field crack length, 2b, a main crack is more likely to be arrested at a shorter length because the capture zone $(2a+2b)\times 2b$ is larger in size. For higher values of D, shorter fractures make up a larger relative portion of the population than longer fractures. For lower values of D, the longer fractures dominate the population.

In the above 2d constant height fracture analysis, the fracture height is assumed to be infinite or to grow equally with length. This is a simplification of reality. In inter-bedded sedimentary sequences, fracture length and height equally develop (penny-shape cracks) until the fracture height reaches bed thickness (3d variable fracture height analysis). After the fracture has propagated completely through the thickness of the bed, fracture propagation can be viewed as lateral propagation of blade-like fractures (Figure 4.7). In our 2d constant fracture height analysis, we assume initial flaw height equals the bed thickness. As a result of this assumption, a single flaw is capable of capturing the propagation crack. In reality, the flaw height is much smaller than bed thickness, and can be assumed to

be equal to its length. Under these conditions, it may take multiple flaws to capture the main crack. Based on these assumptions for variable height fractures, a fracture length distribution is derived for a three-dimensional sampling problem.

In the 3d variable fracture height analysis, we assume cracks are penny-shaped until the fractures propagate across bed of thickness, T. Under this condition, the capture zone is a rectangular parallelepiped around the main crack with dimensions of $L \times 2b \times \min(L,H)$ (where L is crack length; $2b$ is 2 times the critical spacing; and $\min(L,H)$ is crack length or crack height depending on which is smaller) (Figure 4.8). Assuming N_v field cracks are uniformly randomly distributed in a total volume $A \times T$, the probability that *at least n* field cracks lie within the capture zone of a propagating main crack of length L is equal to 1 minus the probability of having *exactly* 0, 1, 2, 3……and n-1 cracks within the capture zone.

To better visualize the difference between the probabilities of *exactly n* cracks in the capture zone versus *at least* n, Figure 4.9 shows a histogram of the probabilities for an exact number of cracks in the capture zone. All of these probabilities will sum to 1. The probability that at least 1 crack exists in the capture zone (the same as having 1 or more cracks) is the sum $P_1+P_2+P_3+\ldots\ldots+P_n+\ldots\ldots+P_{Nv}$. This is the same as $1-P_0$. The probability of at least 2 cracks in the capture zone is $P_2+P_3+\ldots\ldots+P_n+\ldots\ldots+P_{Nv}$, or $1-P_0-P_1$. Therefore, the probability of at least n cracks in the capture zone is $1-P_0-P_1-P_2-\ldots\ldots P_{n-1}$, or

$$P_{\geq n} = 1 - \sum_{i=0}^{n-1} P_i \,. \tag{4.20}$$

Similar to the 2d constant fracture height analysis, based on the assumption that field cracks are uniformly randomly distributed, the probability of 1 field crack being outside the capture zone, P_{1_out}, can be expressed as the volume outside the capture zone (*AT-2bLM*) divided by the total volume (*AT*), or

$$P_{1\_out}(L) = \frac{AT - 2bLM}{AT}, \tag{4.21}$$

where M is defined as the smaller of the fracture length (L) or height (H). Initially, the cracks are penny-shaped ($L=H$). This is true as long as the length is less than bed thickness, i.e.,

$$M = L = H \qquad for \qquad L \le T. \tag{4.22}$$

We further assume that fracture height cannot exceed bed thickness ($H=T$). Therefore, when the fracture length exceeds the bed thickness, the fracture will propagate with a fixed height, i.e.,

$$M = H = T \qquad for \qquad L > T. \tag{4.23}$$

The probability of no crack lying within the capture rectangular parallelepiped zone equals the probability of having all field cracks located outside the capture zone, i.e.,

$$P(0) = \left(\frac{AT - 2bLM}{AT} \right)^{N_V}. \tag{4.24}$$

The probability of having exactly 1 crack within the capture zone, P_1, can be expressed as

$$P_1(L) = \frac{2bLM}{AT}. \tag{4.25}$$

The probability of having exactly n cracks within the capture zone, P_n can be expressed as

$$P_n(L) = \left(\frac{2bLM}{AT}\right)^n . \tag{4.26}$$

Using equations 4.20, 4.24, 4.25 and 4.26, we can express the probability of at least *n* cracks in the capture zone as

$$P_{\geq N} = 1 - \left(\frac{AT - 2bLM}{AT}\right)^{N_V} - \sum_{i=1}^{n-1}\left(\frac{2bLM}{AT}\right)^i . \tag{4.27}$$

The summation can be simplified as

$$\sum_{i=1}^{n-1}\left(\frac{2bLM}{AT}\right)^i = \frac{\frac{2bLM}{AT} - (\frac{2bLM}{AT})^n}{1 - \frac{2bLM}{AT}} . \tag{4.28}$$

Consequently, the probability of the main crack being captured, i.e. the cumulative fracture length distribution, which is defined as the probability of a fracture having a length less than or equal to $L=x$ is

$$F_{3D}(X \leq L) = 1 - \left(1 - \frac{2bLM}{AT}\right)^{N_V} - \frac{\frac{2bLM}{AT} - (\frac{2bLM}{AT})^n}{1 - \frac{2bLM}{AT}} . \tag{4.29}$$

Assuming area A is a square and the main crack of length L is prohibited from propagating out of the area of interest, the maximum dimension possible for L is $\sqrt{A}$ (or $A=L^2$). Given also that field cracks are equivalent to flaws or microcracks and will always be much smaller than the propagating main crack ($2b<<L$), we have

$$\frac{2bL}{A} \leq \frac{2b}{\sqrt{A}} << 1. \tag{4.30}$$

M is the smaller of main crack length or bed thickness ($M=min(L,H)=T$), i.e.,

$$\frac{M}{T} \leq 1. \tag{4.31}$$

Combining equations 4.30 and 4.31, we get

$$\frac{2bLM}{AT} << 1. \tag{4.32}$$

Under these constraints, similar to equation 4.14, $\left(1-\frac{2bLM}{AT}\right)^{N_V}$ can be simplified as

$$\left(1-\frac{2bLM}{AT}\right)^{N_V} \approx e^{-\frac{N_V}{AT}2bLM}. \tag{4.33}$$

By the constraints of equation 4.32, and also given that the number of field cracks, *n*, required to capture the main crack is larger than one, we obtain,

$$\frac{\frac{2bLM}{AT}-(\frac{2bLM}{AT})^n}{1-\frac{2bLM}{AT}} \approx \frac{2bLM}{AT}. \tag{4.34}$$

In the penny-shaped case, fracture height is less than bed thickness, so that

$$M = \min(L, H) = L. \tag{4.35}$$

Consequently, the cumulative fracture length distribution can be simplified as

$$F_{3D}(X \le L) = 1 - e^{-\frac{N_V}{AT}2bL^2} - \frac{2bL^2}{AT}. \tag{4.36}$$

Where the constant *D* is

$$D = \frac{N_V}{AT}2b. \tag{4.37}$$

Thus, the corresponding complementary cumulative fracture length distribution is

$$P_{3D}(X > L) = e^{-\frac{N_V}{AT}2bL^2} + \frac{2bL^2}{AT}. \tag{4.38}$$

Similar to 2d constant fracture height analysis, increasing the exponential constant *D* (i.e. flaw intensity, $\frac{N_V}{AT}$, and flaw length 2b) reduces the portion of large fractures (Figure 4.10). Instead of a straight line in a semi-log plot (Figure

4.6, 2d constant fracture height analysis), the 3d variable crack height analysis shows a concave curve, which gives a higher percentage of smaller cracks compared to the 2d constant fracture height case. When the fracture height reaches the bed thickness (M equals T), equation 4.41 reduces to equation 4.16; i.e. the penny-shaped case is reduced to the constant fracture height case. The corresponding complementary cumulative fracture length distribution changes from a concave curve to a straight line on a semi-log plot (Figure 4.11).

FIELD DATA ANALYSIS

Our exponential model fits fracture length data for opening mode cracks at different scales. Published examples come from joints mapped in granite in the Sierra Nevada of California (Segall and Pollard 1983; Segall, 1984), micro-cracks (Olson, 1998; Hennings et al., 2000) imaged with SEM cathode-luminescence and macro-cracks (Laubach, 1992) from the Frontier sandstone of Oil Mountain, Wyoming and vein segments mapped at Culpeper Quarry, Virginia (Vermilye and Scholz, 1995). In all cases, the length distributions have a negative exponential shape (Figures 4.12, 4.13, 4.15, 4.16 and 4.17).

Detailed mapping of the cracks in granitic rock of the Ward Lake outcrop, Sierra Nevada (mapped area size of 35m×60m) reveals approximately 25±10 cracks per square meter, or $N/A = 25 \pm 10$ (Segall and Pollard, 1983, Figure 4.9). The initial flaw sizes are estimated to be somewhat larger than the average grain size of the granodiorite, or approximately 1.5±1cm (Segall and Pollard, 1983). These flaws are considered to be equivalent to our field cracks. We obtain an

empirical exponent (*D*) of 0.0715 by fitting our analytical fracture length model to the real data (Figure 4.12). Setting the flaw size to 0.5 cm based on the field data, according to equation 4.15, we can reasonably estimate the crack intensity of *N/A=15* cracks/m^2 (well within Segall's field estimate). In the Florence Lake outcrop, for the mapped area of 70×130 m^2, using a field crack length of 1 cm based on Segall and Pollards' field observations, we were able to match the measured length distribution using a *N/A=17* per square meter (Figure 4.13).

The 2d model tacitly assumes that fractures have a fixed height. In a granite, it may be more approximate to assume the fractures are penny-shaped. Using our 3d variable fracture height model, we can test this hypothesis. Fitting the 3d variable height model to the fracture trace-length data from Florence, Sierra Nevada (Segall and Pollard, 1983), we find that the 3d variable height model doesn't work as well as the 2d constant height model (Figure 4.13). This is because the collected fracture length data are from 2d map view of the outcrop. Cracks that appear in a planar outcrop may not be representative of the total population. For the case of penny-shaped cracks, not all the joints extend from top to bottom in the bed. A longer crack with a large fracture height has a greater chance to reveal itself on a planar outcrop than a short crack with small height. If the field data is collected using a three-dimensional sampling in a cubic volume, we expect to see many more smaller cracks and roughly the same number of large cracks compared to the observation from the 2d sample, which corresponds to a higher percentage of smaller cracks and a lower percentage of larger ones shown

in the complementary cumulative frequency plot (Figure 4.13). To validate our 3d variable height model, we need to fit the 3d model to 3d sampling data.

In reality, it is not feasible to do 3d fracture sampling. Consequently, 3d fracture length distribution need to be estimated from the 2d planar fracture trace-length data. Therefore, a numerical sampling converter was designed. In the numerical converter, a total of N_V penny-shaped cracks with a specific length are uniformly randomly located in a defined volume (Figure 4.14). At a randomly chosen depth (Z), the fracture numbers (N) revealed on the horizontal plane perpendicular to Z can be counted from our converter. Therefore, the inputs of the converter are N_V and L. At each run the converter will automatically pick up a random Z and output the fracture numbers (N) revealed at this depth. At fixed N_V and L, N is collected after each run. After multiple runs, we could statistically correlate the 3d fracture numbers Nv to the mean 2d fracture numbers N. In Florence, Sierra Nevada (Segall and Pollard, 1983), the discrete probability distribution of fracture length is given. For each specific fracture length, using the published 2d crack frequency number N as a model constraint, we can obtain Nv by doing a forward numerical conversion. The 3d variable fracture length model fits the synthetic fracture lengths less than 8 meters, but underestimates longer ones (Figure 4.13). Similar to the theoretical prediction of fracture length in sedimentary rock (Figure 4.11), in igneous rock the negative exponential model also fits the longer fractures ($>8m$ in Florence, Sierra Nevada) better than the penny-shaped model (Figure 4.13). This may be due to the fact that the penny

shape model no longer holds, when a fracture is long, even if it's in an igneous rock.

Another example comparing model results versus field observations was conducted to show that the constant fracture height model fits the fracture trace-length in Frontier Formation sandstones, southwestern Wyoming (Laubach and Lorenz, 1992). The observed fracture lengths are from millimeter to ~100 meter. The Frontier Formation is a deposit of alternating sandstone and shale, and its porosity is 5% to 15% (Laubach and Lorenz, 1992). Using a grain size of ~60 micrometers for the sandstone (Peters, 2001) and an average porosity of 10%, we approximate the initial flaw length to be 1 mm (See Figure 10 of Hatzor and Palchik, 1997). Fitting the model to the field data, we are able to match the measured length distribution using $N/A=28$ cracks/m^2, which is reasonable (Figure 4.15a). The exponential model fits the field data better than the power law model without restricting analysis to a small subset of data (Figure 4.15b).

The exponential model also displays a good agreement with micro-fracture lengths. Micro-fracture data from Oil Mountain (Olson, 1998) has an extremely high magnitude exponent of negative 136 (Figure 4.16). If we directly use this exponential model to predict macro-fractures number, we may make a substantial under-estimation. Because of the grain boundaries effect, the material is highly heterogeneous when examined microscopically. At macroscopic scale, fractures are much larger than grain sizes, and thus the material can be viewed as a homogenous body. The fact that the constant (D) of our exponential model is much larger at the microscopic scale than for other macroscopic observations may

indicate that for microscopic crack growth not only the main fracture's neighbor cracks but also grain boundaries impede the main fracture's propagation.

We also examined vein data from Culpeper Quarry (Figure 4.12, Vermilye and Scholz, 1995), which was formed in the calcareously cemented Balls Bluff Siltstone (Upper Triassic, from the Bull Run Formation of the Culperper Group). If we base our fit on the fractures with a length of less than 1 meter, the number of longer fractures predicted is less than that observed (Figure 4.12). This may be explained by the observation that the longer fractures in this outcrop are made up of multiple segments (Vermilye and Scholz, 1995). In the context of our model, the individual segments would represent captured fractures, and the segment lengths are what should be fit with the exponential model. Using the array lengths over-predicts the number of longer fractures.

CONCLUSIONS

The fracture capture model reliably predicts fracture length distribution in both igneous and sedimentary rocks. The model is based on a mechanism for fracture propagation, interaction, and termination, when small cracks or flaws in the near tip region of a large crack capture the large crack's propagation and cause it to stop.

Based on this mechanism, assuming constant fracture height, we derive an exponential fracture length distribution for 2d sampling given by equation 4.14,

$$P(X > x) = e^{-DL},$$

where P is the complementary cumulative frequency, and the constant D can relate to the flaw size and the flaw density (the number of fractures per area) through equation 4.15,

$$D = b\frac{N}{A}.$$

Assuming fractures are penny-shaped rather than constant height gives a different complementary fracture length distribution for 3d sampling expressed as equation 4.38,

$$P_{3D}(X > x) = e^{-\frac{N}{AT}2bLM} + \frac{2bLM}{AT},$$

where M is the minimum number between fracture length and height. When fracture height is equal to the bed thickness, the variable fracture height model reduces to the constant height model. The constant fracture height model is more appropriate and applicable to two-dimensional sampling of planar outcrops.

REFERENCES

Atkinson, B. K. and Meredith, P. G., 1987, The theory of subcritical crack growth with applications to minerals and rocks. Atkinson, B. K., ed., *Fracture Mechanics of Rock*, Academic Press, San Diego, USA.

Baecher, G.B., Lanney, N.A. and Einstein, H.H., 1977, Statistical description of rock properties and sampling, *18th US Symposium on Rock Mechanics* 5C1, 1–8.

Baecher, G.B. and Lanney, N.A., 1978, Trace length biases in joint surveys. *Proceedings, Symposium on Rock Mechanics* 19, 56–65.

Barton, C. A. and Zoback, M. D., 1992, Self-similar distribution and properties of macroscopic fractures at depth in crystalline rock in the Cajon Pass scientific drill hole, *Journal of Geophysical Research*, 97(B4), 5181-5200.

Barton, C. C. and Larson, E., 1985, Fractal geometry of two-dimensional fracture networks at Yucca Mountain, Southwestern Nevada, *Fundamentals of Rock Joints: Proceedings of International Symposium on Fundamental of Rock Joints, Bjorkliden, Sweden,* edited by O. Stephannson, International Society for Rock Mechanics, 77-84.

Barton, C. C. and Hsieh, P.A., 1989, *Physical and Hydrologic-Flow Properties of Fractures, Field Trip Guideb.*, T385, AGU, Washington, D. C..

Barton, C. M., 1978, Analysis of joint traces, *Proceedings of the 19th U. S. Symposium on Rock Mechanics*, American Institute of Mining Engineers, 39-40.

Bridges, M. C., 1976, Presentation of fracture data for rock mechanics, *Proceedings 2nd Australian – New Zealand Conference on Geomechanics*, Brisbane, 144-148.

Becker, A., and Gross, M. R., 1996, Mechanism for joint saturation in mechanically layered rocks: an example from southern Israel, *Tectonophysics* 257, 223-237.

Call, R. D., Savely, J., and Nicholas, D. E., 1976, Estimation of joint set characteristics from surface mapping data. *Proceedings 17th U. S. Symposium on Rock Mec*hanics, 2B2-1 – 2B2-9.

Cladouhos, T. T., and Marrett, R, 1996, Are fault growth and linkage models consistent with power-law distributions of fault lengths?, *Journal of Structural Geology*, 18, 281-293.

Clark, M.B., Brantley, S.L. and Fisher, D.M., 1995, Power-law vein thickness distributions and positive feedback in vein growth, *Geology* 23, 975–978.

Cotterell, B., and Rice, J. R., 1980, Slightly curved or kinked cracks: *International Journal of Fracture*, 16, 155-169.

Cowie, P. A. and Scholz, C. H., 1992, Growth of faults by accumulation of seismic slip, *Journal of Geophysical Research*, 97, 11085-11095.

Crouch, S. L. and Starfield, A. M., 1983, *Boundary Element Methods in Solid Mechanics*, George Allen and Unwin, London, U. K..

Dershowitz, W. S. and Einstein, H. H., 1988, Characterizing rock joint geometry with joint system models, *Rock Mech. Rock Eng.*, 21, 21-51.

Einstein, H. H., Baecher, G. B., Verneziano, D. et al, 1980, Risk analysis for rock slopes in open pit mines, *Final Technical Report. Publication No. R80-17, Order No. 669,* Department of Civil Engineering, Massachusetts Institute of Technology, Cambridge, Massachusetts.

Einstein, H. H., and Baecher, G. B., 1983, Probabilistic and statistical methods in engineering geology, *Rock Mech. Rock Eng.*, 16, 39-72.

Erdogan, F. and Sih, G. C., 1963, On the crack extension in plates under plane loading and transverse shear, *ASME Transactions*, 85, 519-527.

Griffith, A. A., 1924, The theory of rupture, *In Proc. First Internat. Congr. Appl. Mech. (ed. C. B. Biezeno and J. M. Burgers),* J. Waltman Jr. Delft, 55-63.

Gross, M.R., 1993, The origin and spacing of cross joints: Examples from the Monterrey Formation, Santa Barbara coastline, California, *Journal of Structural Geology* 15, 737–751.

Gudmundsson, 1987, Geometry, formation and development of tectonic fractures on the Reykjanes Peninsula, southwest Iceland, *Tectonophysics* 139, 295–308

Hatton, C.G., Main, I.G. and Meredith, P.G., 1994, Non universal scaling of fracture length and opening displacement, *Nature* 367, 160–162.

Hatzor, Y.H. and Palchik, V., 1997, The influence of grain size and porosity on crack initiation stress and critical flaw length in Dolomites, *Int. J. Rock Mech. Min. Sci.*, 34(5), 805-816.

Heffer, K.J. and Bevan, T.G., 1990, Scaling relationships and natural fractures: data, theory and applications, *Society of Petroleum Engineers*, 20981, 367–376.

Hennings, P., Olson, J. and Thompson, L., 2000, Combining outcrop and 3-d structural modeling to characterize fractured reservoirs, *American Association of Petroleum Geologists Bulletin*, 84(6), 830-849.

Hirata, T., 1989, Fractal dimension of fault systems in Japan: Fractal structure in rock fracture geometry at various scales, *Pure Appl. Geophys.*, 131, 157-170.

Holder, Jon, Olson, Jon E., and Philip, Zeno, 2001, Experimental determination of subcritical crack growth parameters in sedimentary rock, *Geophysical Research Letters*, 28 (4), 599-602.

Hudson, J. A. and Priest, S. D., 1983, Discontinuity frequency in rock masses, *Int. J., Rock Mech. Min. Sci. Geomech. Abstr.*, 20, 73-89.

Jensen, J. L., Lake, L. W., Corbett, P. W.M. and Goggin, D. J., 1997, *Statistics for Petroleum Engineers and Geoscientists*, Prentice Hall PTR, USA.

Johnston, J.D. and McCaffrey, K.J.W., 1996, Fractal geometries of vein systems and the variation of scaling relationships with mechanism, *Journal of Structural Geology*, 18, 349–358.

Karihaloo, B. L., Keer, L. M., and Nemat-Nasser, S., 1980, Crack kinking under nonsymmetric loading: *Engineering Fracture Mechanics*, 13, 879-888.

Kreyszig, Erwin, 1993, *Advanced Engineering Mathematics*, John Wiley & Sons, Inc., USA.

LaPointe, P.R., 1988, A method to characterize fracture density and connectivity through fractal geometry, *Int. J. Rock Mech. Min. Sci. Geomech.*, 25, 421-429.

Laubach, S. E., 1992, Fracture networks in selected Cretaceous Sandstones of the Green River and San Juan Basins, Wyoming, New Mexico, and Colorado.

Geological studies relevant to horizontal Drilling in Western North America, Rocky Mountain Association of Geologists, 115-127.

Laubach, S. E. and Lorenz, J. C., 1992, Preliminary assessment of natural fracture patterns in Frontier Formation Sandstones, Southwestern Wyoming. *Forty-third field Conference, Wyoming geological association guidebook*, 87-96.

Lawn, B. R., and Wilshaw, T. R., 1975, *Fracture of brittle solids*, Cambridge, England, Cambridge University Press, 204.

Lyakhovsky, V., 2001, Scaling of fracture length and distributed damage, *Geophys. J. Int*, 144, 114-122.

MacMahon, B., 1974, Design of rock slopes against sliding on preexisting surface. *3rd International Symp. On Rock Mechanics*, II-B, 803-808.

Mandelbrot, B. B., 1982, The fractal geometry of nature, Freeman, San Francisco.

Marrett, R., 1997. Permeability, porosity, and shear-wave anisotropy from scaling of open fracture populations. In: Hoak, T.E., Klawitter, A.L. and Blomquist, P.K. Editors, 1997. *Fractured Reservoirs: Characterization and Modeling Guidebook* Rocky Mountain Association of Geologists, 217–226.

Marrett, R., Ortega, O.J. and Kelsey, C.M., 1999. Extent of power-law scaling for natural fractures in rock. *Geology* 27, 799–802

Nicol, A., Walsh, J. J., Watterson, J., and Gillespie, P.A., 1996, Fault size distributions – are they really power-law?, *Journal of Structural Geology*, 18, 191–197.

King, G. C. P., 1984, The accommodation of large strains in the upper lithosphere of the earth and other solids by self-similar fault systems: The geometric origin of the b values, *Pure Apply. Geophys.*, 121, 761-815.

LaPointe, P. R., 1988, A method to characterize fracture density and connectivity through fractal geometry, *Int. J. Rock Mech. Min. Sci. Geomech.*, 25, 421-429.

Odling, N., 1997, Scaling and connectivity of joint systems in sandstones from western Norway, *Journal Structural Geology*, 19, 1257-1271.

Okubo, P. G., and Aki, K., 1987, Fractal geometry in the San Andreas fault system, *Journal of Geophysical Research,* 92, 345-355.

Olson, J. E., 1993, Effects of subcritical crack growth and mechanical crack interaction, *Journal of Geophysical Research*, 98(B7), 12251-12265.

Olson, J. E., 1997, Natural fracture pattern characterization using a mechanical-based model constrained by geologic data – moving closer to a predictive tool, *Int. J. Rock Mech. & Min. Sci.*, 34(3/4), 391, Paper No. 237.

Olson, J. E. and Pollard, D. D., 1989, Inferring paleostresses from natural fracture patterns: A new method. *Geology*, 17, 345-348.

Olson, J. E. and Pollard, D. D., 1991, The initiation and growth of en echelon veins, *Journal of Structural Geology*, 13(5), 595-608.

Olson, J. E., Hennings, P. H., and Laubach, S. E., 1998, Integrating wellbore data and geomechanical modeling for effective characterization of naturally fractured reservoirs. *SPE* 47352.

Ortega, O. and Marrett, R., 2000, Prediction of macrofracture properties using microfracture information, Mesaverde Group sandstones, San Juan basin, New Mexico, *Journal of Structural Geology*, 22, 571-588.

Pickering, G., Bull, J.M. and Sanderson, D.J., 1995, Sampling power-law distributions, *Tectonophysics* 248, 1–20.

Pollard, D. D., Segall, P., and Delaney, P. T., 1982, Formation and interpretation of dilatant echelon cracks. *Geological Society of America Bulletin*, 93, 1291-1303.

Pollard, D. D. and Aydin, A., 1984, Propagation and linkage of oceanic ridge segments, *Journal of Geophysical Research*, 89(B12), 10,017-10,028.

Pollard, D. D. and Segall, P., 1987, Theoretical displacements and stresses near fractures in rocks: with applications to faults, joints, veins, dikes and solution surfaces. In: Atkinson, B.K. (Ed.), *Fracture Mechanics of Rock*, Academic Press, London, 277-349.

Pollard, D. D. and Aydin, A., 1988, Progress in understanding jointing over the past century, *Geological Society of America Bulletin*, 100, 1181-1204.

Priest, S. D., and Hudson, J. A., 1976, Discontinuity spacing in rock, *Int. J. Rock Mech. Min. Sci. Geomech. Abstr.*, 13, 135-148.

Priest, S. D., and Hudson, J. A., 1981, Estimation of discontinuity spacing and trace length using scanline surveys, *Int. J. Rock Mech. Min. Sci. Geomech. Abstr*., 18, 183-197.

Peters, E.J., 1997, Petrophysics course note, *The University of Texas at Austin*.

Renshaw, C. E. and Park, J. C., 1997, Effect of mechanical interactions on the scaling of fracture length and aperture, *Nature*, 386, 482-484.

Renshaw, C. E., 1993, Modeling fluid migration through physically-based fracture networks, *Dissertation*, Stanford University.

Rives, T., Razack, M., Petit, J. P. and Rawnsley, K.D., 1992, Joint spacing: analogue and numerical simulations, *Journal of Structural Geology*, 14(8/9), 925-937.

Robertson, A., 1970, The interpretation of geological factors for use in slope stability, *Proc. Symp. On the Theo. Background to the Planning of Open Pit Mines with Special Ref. To Slope Stability*, 55-71

Scholz, C. H., 1997, Scaling properties of faults and their populations, *Int. J. Rock Mech. Min. Sci.*, 34(3/4), 348.

Segall, P., 1984, Formation and growth of extensional fracture sets, *Geological Society of America Bulletin*, 95, 454-462.

Segall, P., and Pollard, D. D., 1983, Joint formation in granitic rock of the Sierra Nevada, *Geological Society of America Bulletin*, 94, 563-575.

Stowell, J.F.W., 2000, Specifying lengths of horizontal wells in fractured reservoirs: *Society of Petroleum Engineers*, SPE 65458.

Tamuzs V. and Petrovab V., 1999, Modified model of macro-microcrack interaction, *Theoretical and Applied Fracture Mechanics*, 32(2), 111-117.

Tchalenko, J. S., 1970, Similarities between shear zones of different magnitudes, *Geol. Soc. Am. Bull.*, 81, 1625-1640.

Warburton, P. M., 1980, A stereological interpretation of joint trace data, *Int. J. Rock Mech. Min. Sci. Geomech. Abstr.*, 17, 181-190.

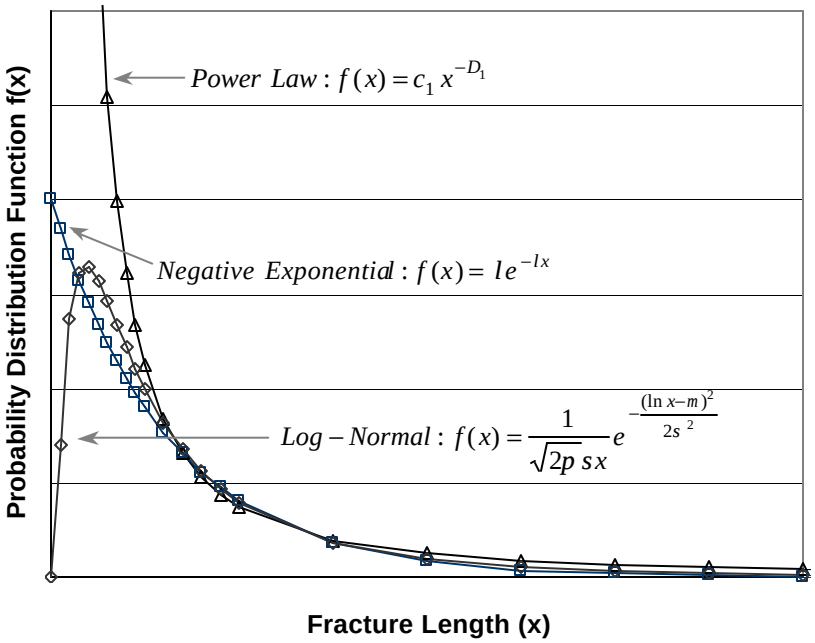

Figure 4.1 The different types of distribution laws used in this paper to describe fracture length distribution. The probability distribution functions, f(x) are shown as above. μ, mean; σ, standard deviation, $1/\lambda = \mu = \sigma$, C_1, D_1 are constant.

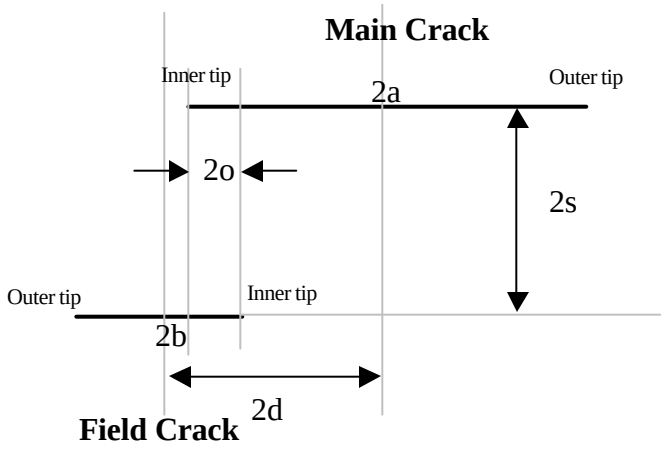

Figure 4.2 Fracture configuration illustrates main crack with length of 2a and field crack with length of 2b, and their relative position, which is quantified as Overlap (2o), the crack-parallel distance between the two cracks' inner tips, and Spacing (2s), the crack-perpendicular distance between the two cracks. 2d is the crack-parallel distance between the two cracks' centers.

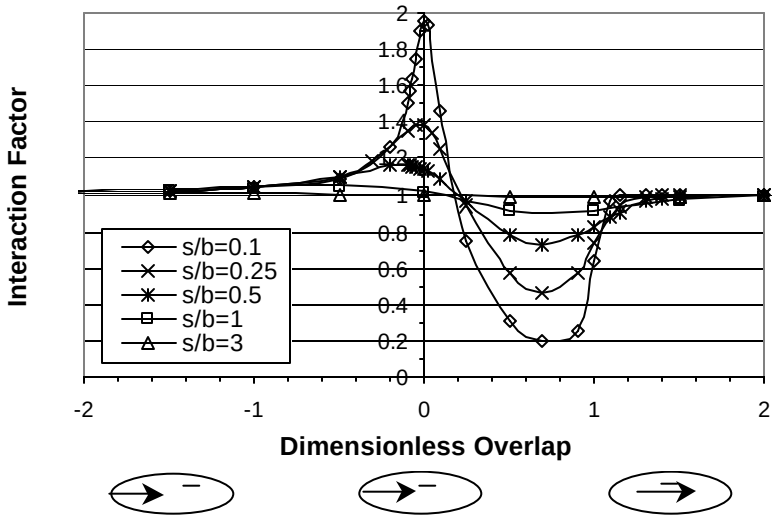

Figure 4.3a The influence of dimensionless spacing on crack interaction factor, plotted versus dimensionless overlap for the inner tip of the main crack (2d plane strain case and a/b=20).

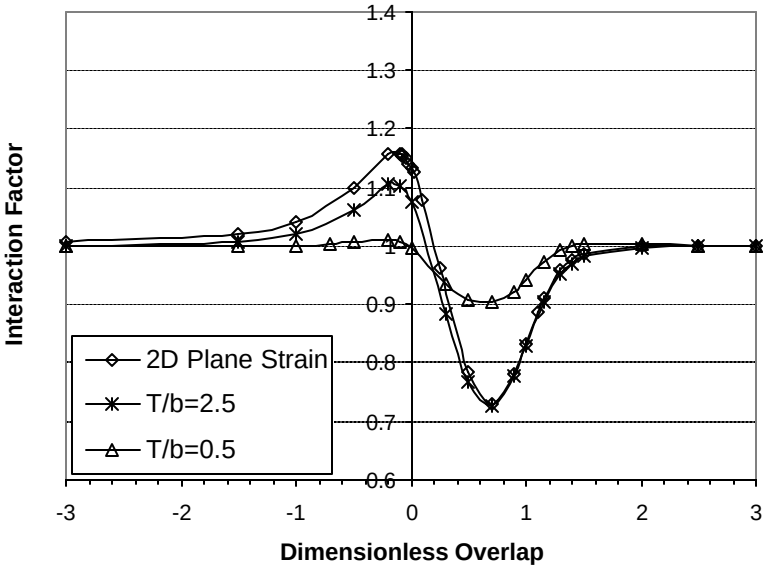

Figure 4.3b The influence of dimensionless bed thickness on crack interaction factor, plotted versus dimensionless overlap for the inner tip of the main crack (a/b=20 and s/b=0.5).

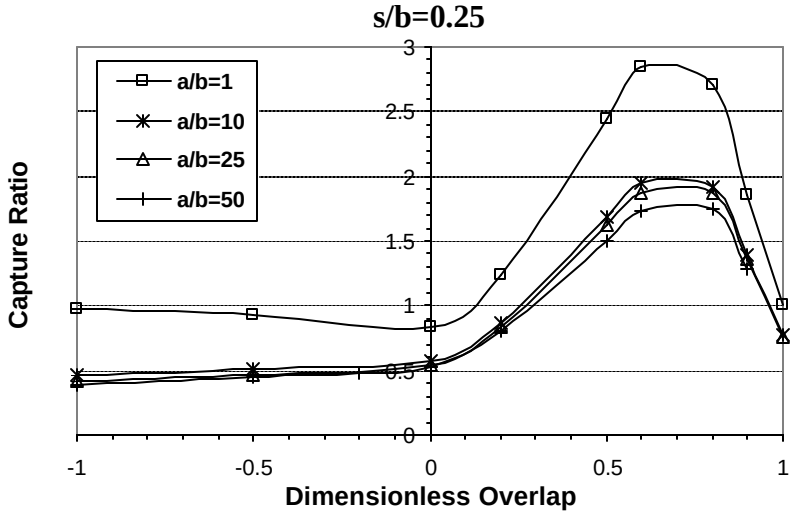

Figure 4.4a Capture ratio versus dimensionless overlap for different main crack to field crack's length ratios (*s/b*=0.25, and 2D Plane strain case).

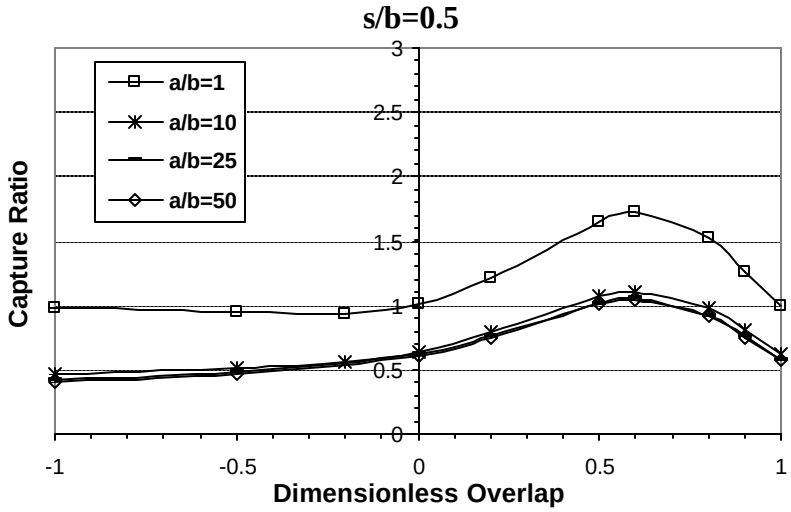

Figure 4.4b Capture ratio versus dimensionless overlap for different main crack to field crack's length ratios (*s/b*=0.5, and 2D Plane strain case).

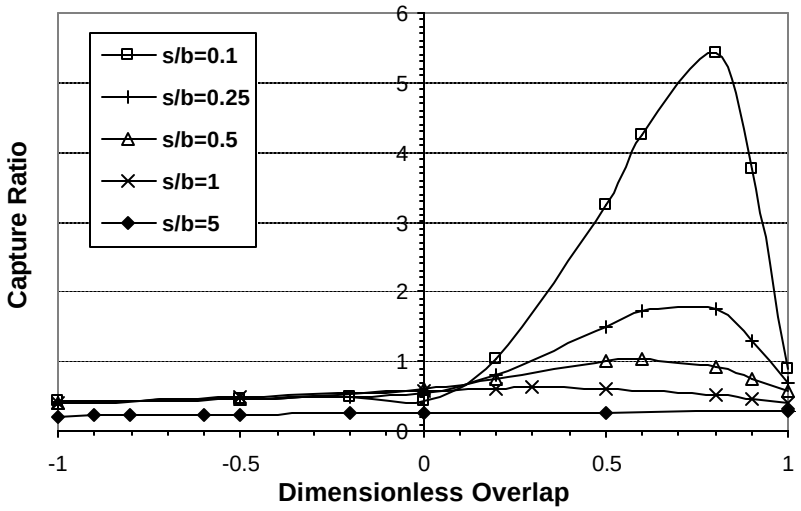

Figure 4.4c Capture ratio versus dimensionless overlap for different dimensionless spacing (*a/b*=50, and 2D Plane strain case).

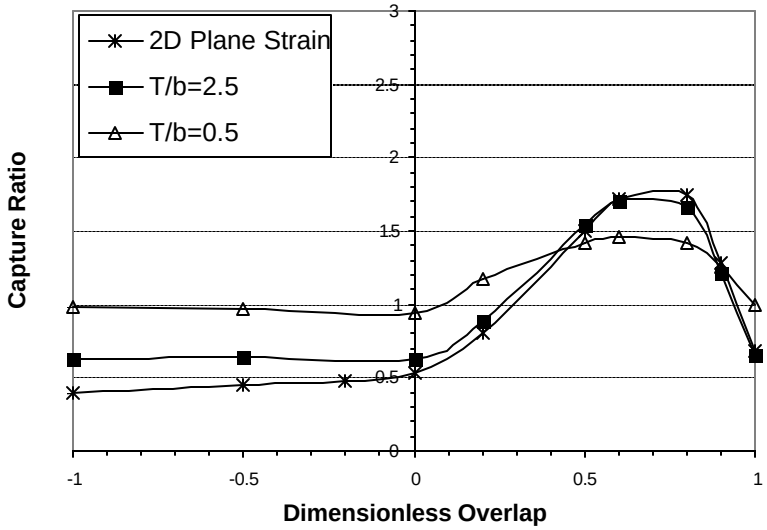

Figure 4.4d Capture ratio versus dimensionless overlap for different bed thickness (*a/b*=50, and *s/b*=0.25).

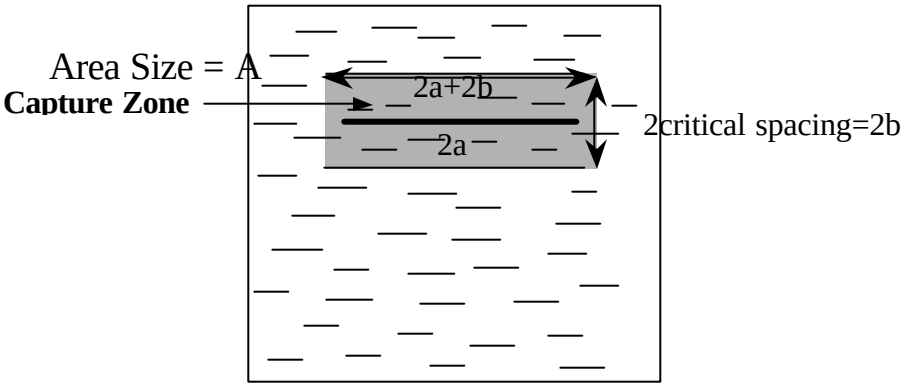

Figure 4.5 A main crack of length 2a propagating through a region of field cracks of lengths 2b. The capture zone increases in size as the main crack growth. If a field crack is encountered in the capture zone of the main crack, propagation is arrested.

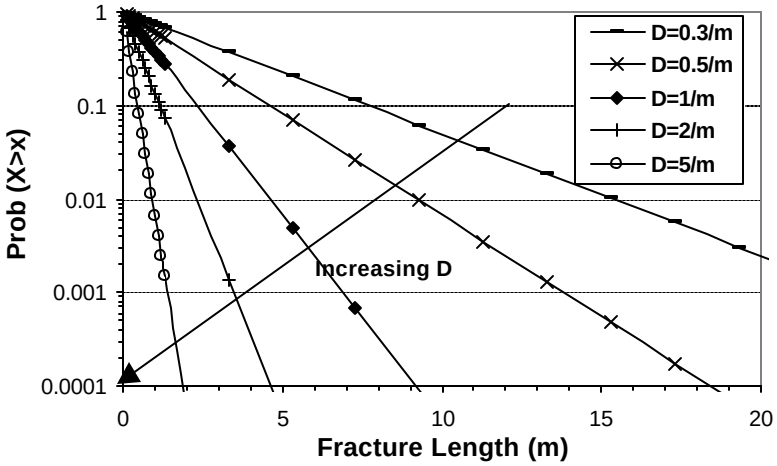

Figure 4.6 Complementary cumulative distribution function for fracture length (constant fracture height model), an illustration of the effect of exponential constant, D, i.e. the product of field crack area intensity and size.

a

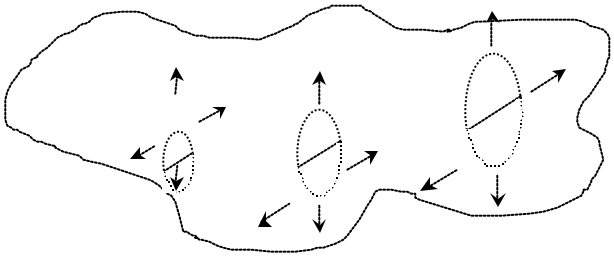

b

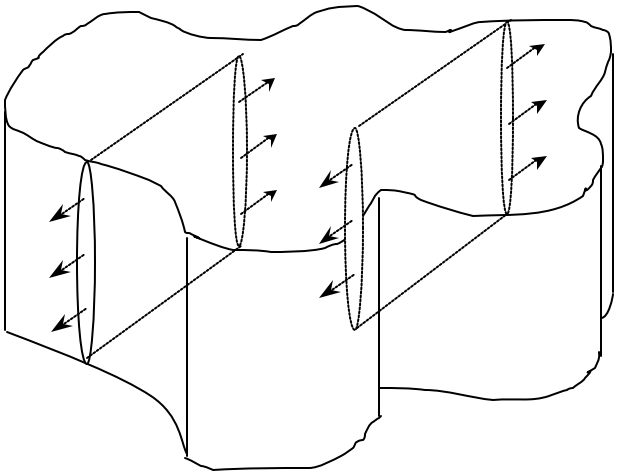

Figure 4.7 Idealization of natural fracture growth in sedimentary rock of variable fracture height model (after Olson, 1993)

a. Under inter-bedded sedimentary sequences, fracture length and height equally develop (penny-shape cracks) until the fracture height reaches bed thickness.

b. After the fracture has propagated completely through the thickness of the bed, fracture propagation can be viewed as lateral propagation of blade-like fractures.

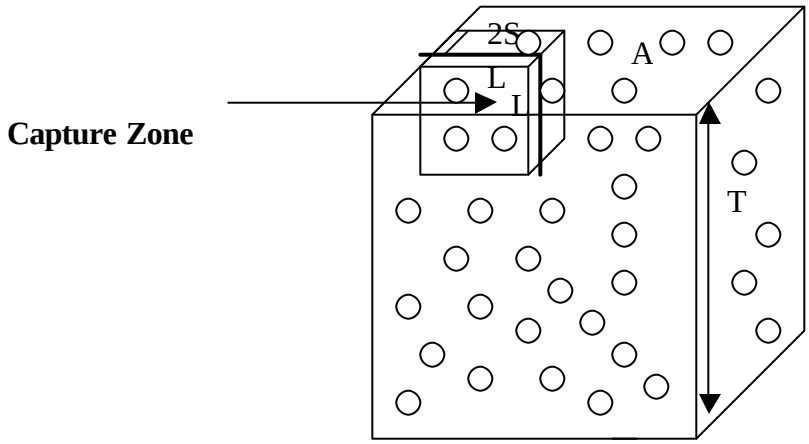

Figure 4.8 A main crack of initial length L and height L propagating through a region of field cracks of with radius of b. The capture zone increases in size as the main crack growth. T is the bed thickness. If *n* field crack are encountered in the capture zone of the main crack, propagation is arrested.

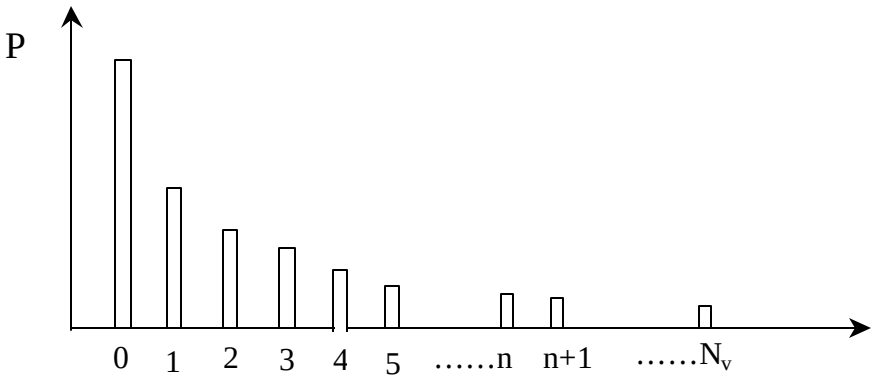

Figure 4.9 The probabilities for an exact number of cracks in the capture zone.

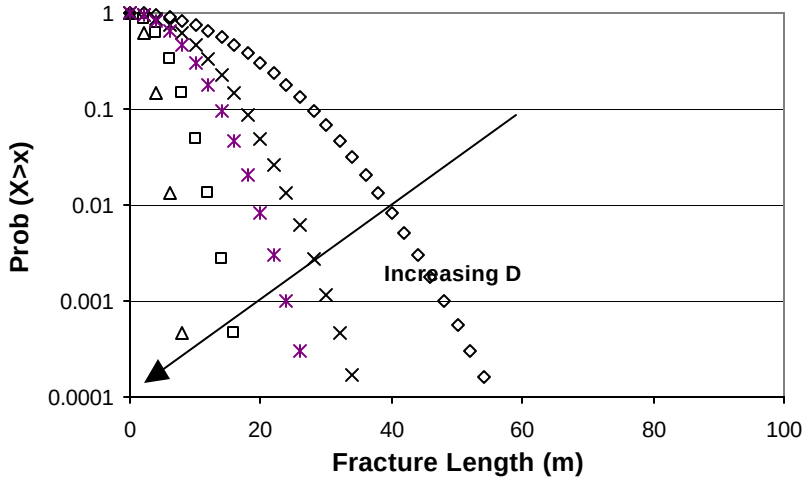

Figure 4.10 Complementary cumulative distribution function for fracture length (true 3D analysis), an illustration of the effect of exponential constant, D, i.e. the product of field crack volume intensity and size.

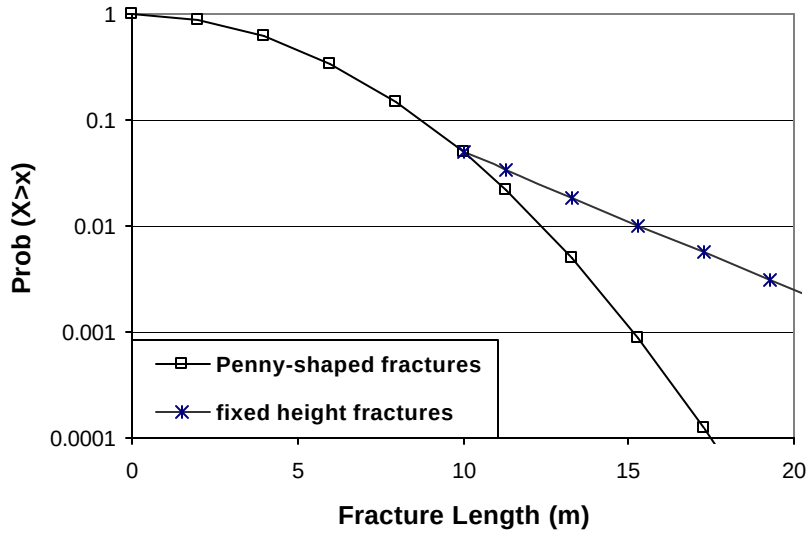

Figure 4.11 The fracture growth from a penny shape crack to a lateral propagation of blade-like (fixed height) fracture. The corresponding complementary cumulative distribution function for fracture length distribution changes from a concave curve to a straight line.

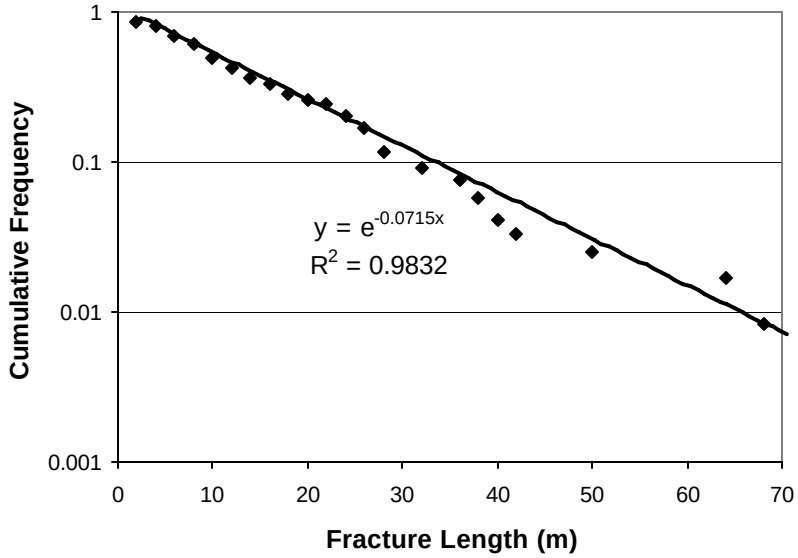

Figure 4.12 Fracture lengths collected in granitic rock of Ward Lake, Sierra Nevada show a negative exponential distribution.

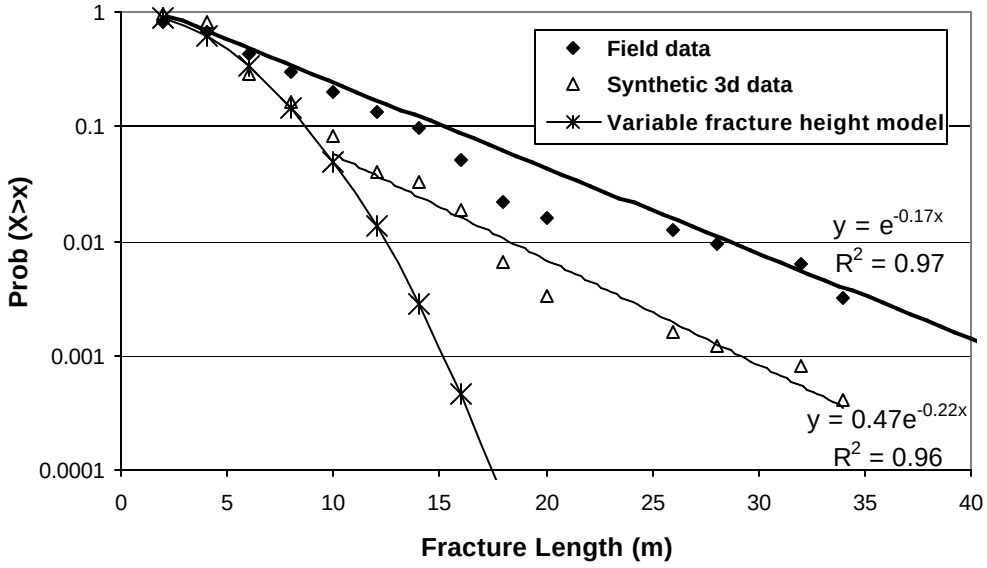

Figure 4.13 Field fracture lengths collected in granitic rock of Florence, Sierra Nevada fit the constant fracture model with a negative exponential distribution. Variable fracture height model fits the synthetic 3d data up to 10m.

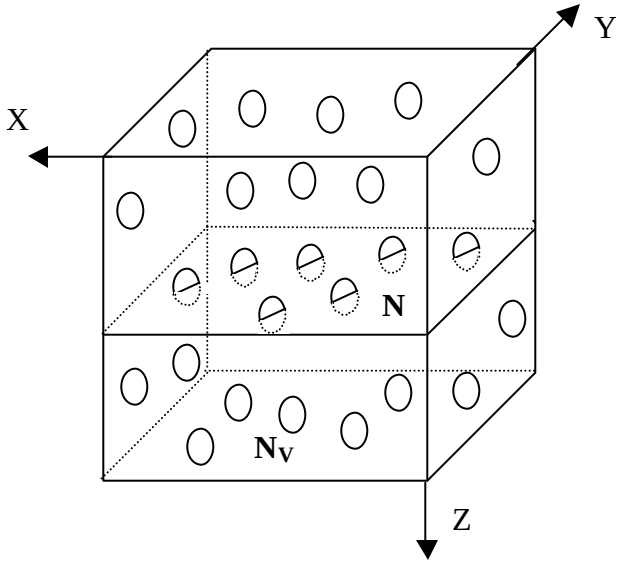

Figure 4.14 Synthesized 3d fracture lengths distribution from the 2d planar fracture trace-length data. For a specific fracture length 2a there are totally *Nv* fractures in the defined volume. Randomly select a depth of *Z*, and count the fracture numbers (*N*) cut by the horizontal plane perpendicular to *Z*.

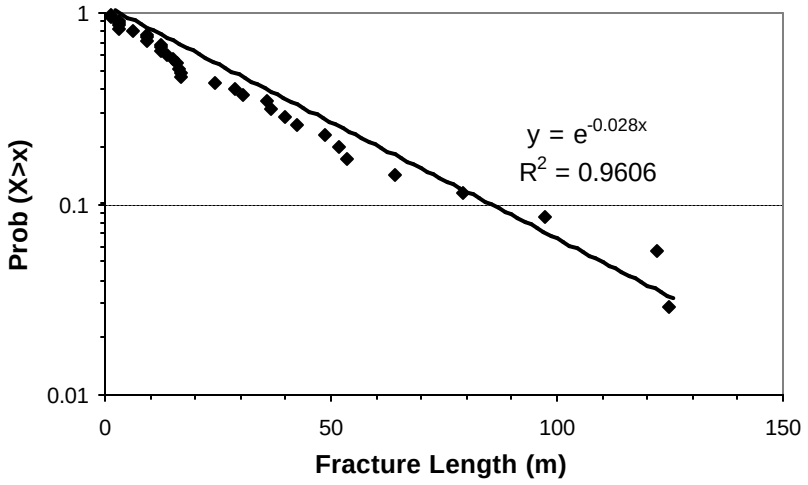

Figure 4.15a Fracture lengths collected in Frontier Formation Sandstones, Southwestern Wyoming shows a negative exponential distribution (a semi-log plot).

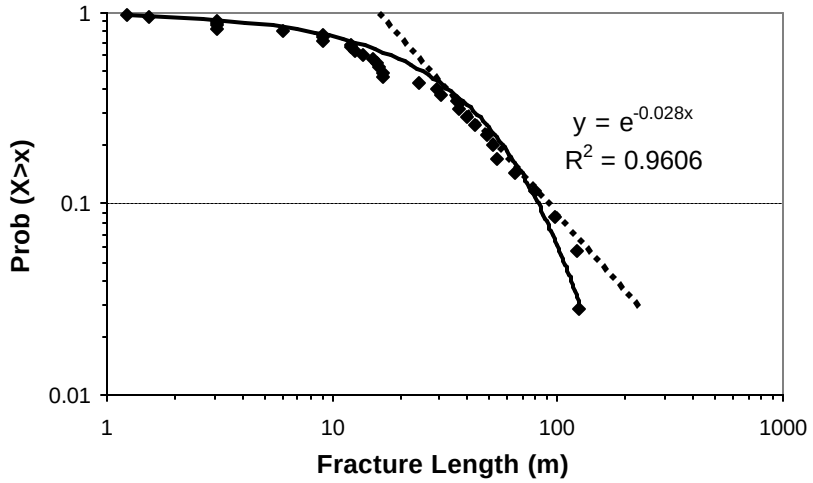

Figure 4.15b Fracture lengths fit negative exponential distribution better than power law distribution in Frontier Formation Sandstones, Southwestern Wyoming (a log-log plot).

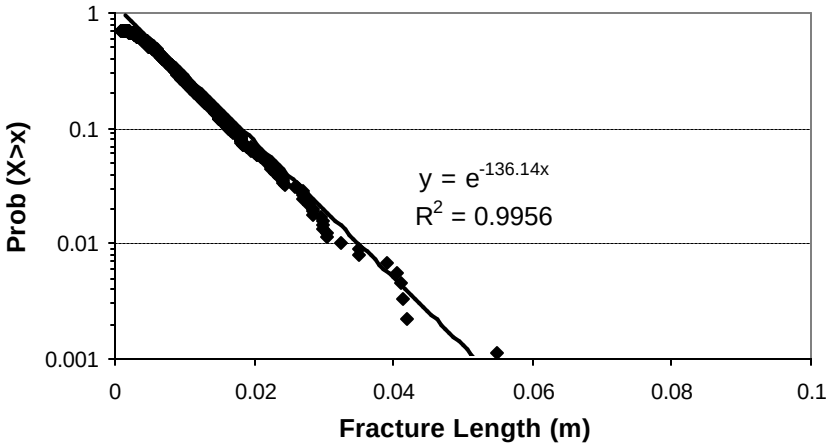

Figure 4.16 Micro-fracture lengths in calcite cemented Frontier Formation sandstone, Oil Mountain fit negative exponential distribution.

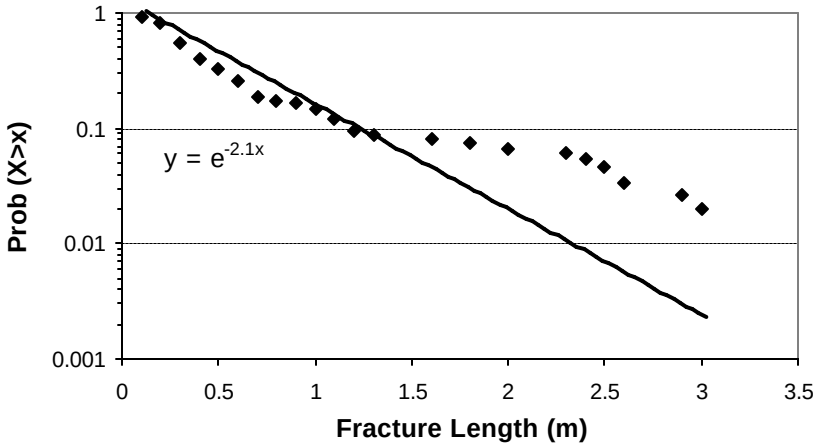

Figure 4.17 Fracture lengths collected in siltstone of Culpeper Quarry fit negative exponential distribution up to 1.2m.

CHAPTER 5: A SEMI-ANALYTICAL FRACTURE PATTERN GROWTH SIMULATOR

ABSTRACT

A semi-analytical geomechanical model is proposed for the development of a single set of parallel fractures. This simplified approach explicitly models a few cracks and treats the surrounding area as a continuum with the effective elastic modulus controlled by crack density. Type curves are developed for the mechanical interactions between the explicitly modeled cracks using a displacement discontinuity boundary element code. A comparison between a complete numerical solution and the semi-analytical approach shows consistency. The semi-analytical model can accurately simulate the development of fracture sets. Compared to the boundary element code, the semi-analytical model is fast and can handle thousands of cracks started at the centimeter or millimeter scale as initial flaws. The simplified model is also used to better understand how parameters such as initial flaw density, subcritical index, bed thickness and elastic modulus influence the geometry of fracture sets. This forward model provides a basis for solving optimization or inverse problems based on available fracture spacing data observed from core or image logs.

INTRODUCTION

Natural opening fractures act as permeability heterogeneities and control the flow of hydrocarbons. The simulation of naturally fractured reservoirs requires an understanding of fracture spatial distribution (i.e., orientation,

aperture, length, spacing and connectivity). Opening mode fractures are normally below seismic resolution. Direct detection of these fractures is limited to cores and wellbore images. The fracture orientation, aperture, and spacing data observed from an one-dimensional wellbore scan line are very sparse, because the chance of a vertical or deviated wellbore intersecting vertical fractures is very low (Lorenz and Warpinski, 1996).

To compensate for the inadequacy of available data and to generate a complete fracture network, statistical (La Pointe and Hudson, 1985; Dershowitz et al., 1988; Kulatilake et al., 1993) and geomechanical models (Olson, 1993; Renshaw, 1993 and Olson, 1997) are used to characterize subsurface fractures. Due to the sparseness of subsurface data, statistical models normally assume fracture attributes in the subsurface follow the data distribution of the surface outcrop (Olson et al., 2001). Instead of directly extrapolating the surface data, mechanical models emphasize the fracturing process (i.e. fracture's initiation, propagation, interaction and termination). By specifying the boundary condition and rock properties, geomechanical models generate physically reasonable fracture networks (Olson et al., 2001).

Olson (1997) modified the displacement discontinuity boundary element numerical technique (Crouch and Starfield, 1983), and simulated fracture network development in sedimentary rock by incorporating a three-dimensional factor. Renshaw (1993) developed a two-dimensional analytical model based on a superposition and self-consistency technique (Kachanov, 1987), and verified his result by physical experimental data. Following Segall's conceptual model

(1984), and incorporating fracture interaction effect from Olson's numerical model, we developed a pseudo-three-dimensional, semi-analytical model to simulate a single fracture set. Compared to Olson's numerical model, this simplified model computes quickly and can deal with thousands of fractures grown from initial flaws that range in size from the millimeter to centimeter scales. The computational efficiency of the semi-analytical model allows us to do a more complete study as to how the boundary conditions and rock properties affect the final fracture pattern. This provides a basis for future fracture pattern inversion from observed data.

CONDITIONS FOR CRACK PROPAGATION

Multiple sets of fractures, with one intersected by the other (i.e. they formed at different time), are common on outcrops. To simplify the problem, we focus on a single set of fractures, assuming fractures in each set are parallel. Multiple fracture sets can be solved by superposition, assuming non-interaction between different fracture sets. In this study we assume that the fractures are straight, which indicates the presence of a large crack-parallel differential compression (Olson and Pollard, 1989; Renshaw, 1993). Theoretical analyses have shown that a remote compressive stress acting parallel to a crack may produce a straight crack path even in the presence of a mode II stress intensity (Cotterell and Rice, 1980; Karihaloo and others, 1980). This suggests that our model is widely applicable despite the restriction of a single parallel straight fracture path.

For a geological body that has been deformed by long-term loading, uniaxial extension at a constant strain rate is used as the boundary condition. The uniaxial extension is in the direction of the minimum principal compression, which is perpendicular to the initial fracture planes (Figure 5.1). This is the commonly accepted orientation of opening mode fractures relative to the in-situ stresses (Pollard and Aydin, 1988). The opening mode stress intensity factor, K_I, for an isolated fracture equals

$$K_I = \Delta s_I \sqrt{p\ a}\ , \tag{5.1}$$

where a is the fracture's half-length, and $\Delta\sigma_I$ is the driving stress. Driving stress can be expressed as (Olson, 1993)

$$\Delta s_I = (p + \Delta p) + (s_3 + s_{tectonic}) \tag{5.2}$$

where tensile stress is defined as positive stress for sign convention. For a fracture to propagate, the fluid pressure within the crack, $p+Dp$, must exceed the remote stress normal to the crack plane, $s_3+s_{tectonic}$. Under the assumption of reference state of stress, $p+\sigma_3=0$, equation 5.2 can be simplified as (Segall, 1984; Olson, 1993),

$$\Delta s_I = \Delta p + s_{tectonic}\ . \tag{5.3}$$

Consequently, either the decrease of tectonic stress ($s_{tectonic}$) or the increase of the fluid pressure inside the crack (p) can cause the fracture to propagate. Here, we assume fluid pressure inside the fracture remains constant. Thus driving force for fracture propagation comes only from the tectonic stress, $s_{tectonic}$, which in our model is caused by the constant strain rate boundary condition. The model also

assumes that the fracture growth occurs at subcritical stress conditions, where the propagation velocity is governed by (Atkinson, 1987; Olson, 1993),

$$V = V_{\max}\left(\frac{K_I}{K_{Ic}}\right)^n \tag{5.4}$$

where K_{Ic} is the fracture toughness of the material, n is the subcritical growth index of the material, and V_{max} is the maximum possible propagation velocity at critical growth ($K_I = K_{Ic}$).

In our linear elastic semi-analytical model, the initial flaw length at which a fracture starts to propagate is estimated from the mean grain size and porosity (Hatzor and Palchik, 1997). According to Hatzor and Palchik (1997), in low porosity textures the individual grains function as stress concentrators, and the initial flaw length roughly equals the mean grain size. In porous rocks, the flaw length rises rapidly with increase in porosity. Depending upon the magnitude of the porosity, the initial flaw length may be up to two orders of magnitude higher than the mean grain size. This suggests that in highly porous rock the union of several individual grain boundaries may serve as the initial stress concentrator (Hatzor and Palchik, 1997). Hatzor and Palchiks' statements are based on experiments of dolomite. Here we assume other type of rocks behave similarly.

MODEL ALGORITHM

We follow the algorithm of Segall (1984) to compute the stress intensity factor of each individual crack in the fracture set. The fractures are divided into a local group and a remote group. The local group is the group of fractures near a particular crack and directly interacting with this crack. The remote group

consists of fractures far from the crack and influence the fracture stress field through an effective elastic modulus, $\tilde{E}$ (Figure 5.1) (Segall, 1984). Thus, according to Segall (1984), the opening mode stress intensity factor for an isolated fracture can be modified as

$$K_I = k_I(\Delta s_I)\sqrt{pc} \tag{5.5}$$

where k_I is the local interaction factor, representing the mechanical influence of nearby (local) cracks. For our constant strain rate boundary condition, the driving force can be expressed as (Dieter, 1976; Segall, 1984),

$$\Delta s = \frac{\tilde{E}}{(1-\tilde{E}u^2/E)}\dot{e}t \tag{5.6}$$

where E is the elastic modulus of the un-fractured matrix, $\tilde{E}$ is the effective elastic modulus affected by remote fractures, u is the Poisson ratio and $\dot{e}$ is the strain rate imposed on the model boundary.

Local Interaction Factor, k_I

A type curve table of the interaction factor between two fractures as a function of dimensionless spacing, dimensionless overlap and fracture length ratio for two-dimensional plane strain case was built. The two-crack interaction factor is numerically calculated by using the boundary element fracture code (Olson, 1993). A field crack directly interacts with a main crack if the dimensionless overlap (overlap divided by field crack length) or dimensionless spacing (spacing divided by field crack length) between them is less than three (Figure 2.12). In a layered bed, if the dimensionless spacing between the field crack and the main

crack is larger than the bed thickness, there is small interaction between these two cracks (Figure 2.15). Based on these we can define each fracture's local influence region. By using the look-up table, we obtain the interaction factor of one particular crack to all other cracks. The local interaction factor imposed on a specific crack is the combined interaction effect from all its neighbor cracks. An empirical equation of this joint interaction is expressed by,

$$k_I(i) = \prod_{j=1}^{N} k_I(i, j) \tag{5.7}$$

where $k_I(i)$ is the local interaction factor of crack i and N is the total number of fractures. $k_I(i, j)$ is the mechanical interaction factor from crack i to crack j. If a crack i does not interact with all other cracks, $k_I(i)$ equals 1.

To test the accuracy of equation 5.7, we compared the local interaction factor calculated from equation 5.7, $k_I(i)$, to the one directly calculated from a boundary element model (Olson, 1997). In general, for en echelon array the interaction factor calculated from equation 5.7 is lower than that obtained from the numerical simulation, but the error is tolerable (typically about 10%. See Tables 5.1 and 5.2. Note that the cracks are of equal length.). The biggest error, 36% comes from the top and bottom cracks in a parallel center-aligned equal-length crack array, i.e. stacked array (Table 5.3). The stacked fracture array is one extreme case of the equal-length en echelon array, and the associated error for $k_I(i)$ in a stacked array is higher than any other equal-length en echelon array.

Fractures initiate from flaws above a critical length. We assume the initial flaws are of the same size. Normally, flaws are too sparse to have much direct interaction with each other, as evidenced in a detailed outcrop study discussed in

chapter 3. In this study, Segall and Pollard (1983) showed the flaw intensity in granite was approximately 25±1 cracks per square meter, $N/A=25\pm10$, and the flaw size is about 1.5±1 cm. The crack with highest K_I (i.e., largest k_I in this equal flaw size case) will propagate first. The longer a fracture propagates, the more influence it will have on other cracks. Thus, in equation 5.7 the weight of the interaction factor from a long crack will be prominent. The cracks presented in Tables 5.1, 5.2 and 5.3 are close-spaced and of equal length, the weight of the interaction factor from each crack is similar. Therefore, the equal length close-spaced cracks (Table 5.1, 5.2 and 5.3) result in larger errors from using equation 5.7, compared to a case with different length more widely-spaced cracks (Table 5.4).

Our fracture interaction study also shows that if a small fracture is close enough to a large fracture ($a/b<0.2$ and $s/b<0.1$), and the small fracture's tip is in between the large fractures' inner and outer tips ($0.2<o/b<0.8$), the small crack will not propagate due to the stress shielding caused by the large crack (Figure 5.2). Once, the two tips of the small crack are both in the large stress shield region, the small crack will close, and it will have no influence on other cracks.

In sedimentary rock, we assume fracture arrest at mechanical layer boundaries. In our pseudo-3d model, the fracture height equals the mechanical layer thickness. Therefore, the stress shielding effect of fracture height can be expressed as (Pollard and Segall, 1987),

$$\frac{s}{s^r} = 8\left|\frac{x_1}{T}\right|^3 \left[4\left(\frac{x_1}{T}\right)^2 + 1\right]^{-\frac{3}{2}} \qquad (5.8)$$

where T is the bed thickness, s^r is the remote stress, and s is the stress at the distance of x_1 from the crack center. Equation 5.8 is used as a correction factor in the numerical model (Olson, 1997) to diminish fracture interaction distance compared to the 2d case. Therefore, the size of a crack's local influence region will decrease and fewer fractures will directly interact with it.

By using equation 5.7 and applying other fracture interaction and termination rules proposed above, we are able to reasonably simulate the mechanical interaction in the local region.

Effective Elastic Modulus, $\tilde{E}$

Remote cracks affect the modeled crack through the effective elastic modulus. Many approximate methods for determining the effective modulus of cracked solids have been proposed in literature. Bristow (1960) was the first to obtain a solution (mean-field method) for micro-cracked solids, in which crack interaction is ignored. O'Connell and Budiansky (1974) proposed a model for the effect of cracks on the macroscopic elastic properties of solids based on a self-consistent approximation. In their model, the effect of interactions between cracks is included by assuming that each crack behaves as though it were embedded in a material having the average elastic properties of the cracked body. Bruner (1976) proposed a modified (differential) self-consistent method by considering a process, in which the crack density is gradually increased from zero to its final value. In both the 2d and 3d cases, the effective modulus of the cracked isotropic matrix material can be found analytically by a non-interacting

solution. Among all these methods, the non-interacting method provides the simplest solution, and also has a wider than expected applicability range due to the cancellation of the competing effects of stress shielding and amplification in arrays of interacting cracks (Kachanov, 1992). Davis and Knopoff (1995) computed the effective elastic modulus of cracked solids with a boundary element model, and compared their results with the effective elastic modulus derived from the non-interacting method, the self-consistent method, and the differential self-consistent method. Davis and Knopoff (1995) concluded that the non-interacting model gives a better approximation to the calculation of the elastic modulus than either the self-consistent or the differential self-consistent methods.

The two dimensional effective modulus for the non-interacting, parallel cracks is expressed as (Jaeger and Cook, 1976)

$$\frac{\tilde{E}}{E} \cong \frac{1}{1+2p(1-u^2)r} \quad , \tag{5.9}$$

and for three dimensions it is (Walsh, 1965)

$$\frac{\tilde{E}}{E} \cong \frac{1}{1+4p(1-u^2)r} \quad , \tag{5.10}$$

where u is the Poisson's ratio and r is the spatial crack density. The spatial crack density for the 2d and 3d cases are expressed as

$$r_{2d} = \frac{1}{A}\sum_{n=1}^{N} C_n^2 \tag{5.11}$$

and

$$r_{3d} = \frac{1}{V}\sum_{n=1}^{N} C_n^3 \tag{5.12}$$

where N is the number of cracks of half-length C_n in an area A for the 2d case, or in a volume V for the 3d case. In the 2d case, if the initial flaws have the same half-length, C_o, the flaw density (r_{2d}) is related to the flaw intensity (N/A) as

$$r_{2d} = \frac{N}{A} C_0^2 \tag{5.13}$$

THE RANGE OF MODEL INPUT PARAMETERS

The critical flaw length, as predicted by Hatzor (1997), is affected by the mean grain size and porosity. Granitic rock has low porosity, and the initial critical flaw length is expected to be equal to the average grain size of the granodiorite. This implies that the initial crack length is 1.5±1 cm (Segall, 1984). For dolomite, the grain size ranges from 0.05 to 1mm, and porosity varies from 3% to 21%. The correspondent critical flaw sizes range from 2.3mm to several centimeters (Hatzor, 1997).

Strain rates in typical tectonic settings are generally estimated to be in the range of 1×10^{-15} to 1×10^{-13} per second (Pfiffner and Ramsay, 1982). Strain rates for elastic-brittle deformation range from 1×10^{-9} to 1×10^{-14} per second. Physical experimental rock deformation is restricted to very fast strain rates of 1×10^{-7} or higher (Twiss and Moores, 1992). In our model, we chose the strain rate of 1×10^{-13} per second.

VERIFICATION

The displacement discontinuity boundary element model (Olson, 1991 and Olson, 1997) successfully simulates the development of a fracture network.

Olson's numerical model is used to verify our semi-analytical model results. For both the semi-analytical model and the numerical model, the initial flaws are distributed in a finite-size body dimensioned 10×10 square meters. Fractures are limited to a larger area of 12×12 square meters. Simulations terminate when a final strain is reached. Due to the computational limitation of Olson's numerical model, for the purpose of comparison we used 100 randomly seeded cracks with larger initial cracks length of 0.2 meters.

Base Case Comparison

2D case comparison

Both the numerical model and the analytical model start with the same initial flaws (all having an initial flaw length of 0.2m, a flaw density of r_{2d} =0.01, Figure 5.3a), and stop with the same final strain of 5×10^{-3} (Figure 5.3b). Simulations are based on the same input parameters: Young's modulus of 2×10^{4} MPa, strain rate of 1.67×10^{-13} per second, a subcritical growth index of 40, and a bed thickness of 1000 meters is used to simulate 2D plane strain case. The fracture trace maps (Figure 5.3b) show that the final fracture patterns generated by numerical model and semi-analytical model are similar, with major fractures propagated at the same places.

The fracture length column chart shows that overall fractures simulated by the semi-analytical model are longer than those generated by the numerical model (Figure 5.3c). The semi-analytical model predicts more fracture growth than the

numerical model, especially for fractures less than 1m (in the semi-analytical model, there are 20 fractures less than 1m, i.e., 51% of the population; while in the numerical simulation there are only 3, which counts for 17% of the entire population) (Figures 5.3c and 5.3d). The semi-log complementary cumulative fracture length distribution suggests a lower a median fracture length (the length at which its complementary cumulative frequency equals 50%) in the semi-analytical model (~1m) than that in the numerical model (~3m) (Figure 5.3d). This is caused by the high percentage of short fractures in the semi-analytical model. The coefficient of variance (C_V), which is defined as the ratio of standard deviation ($\sqrt{Var(k)}$) to sample mean (m),

$$C_V = \frac{\sqrt{Var(k)}}{m} \tag{5.14}$$

is a dimensionless measurement of sample variability or dispersion (Jensen et al., 1997). The C_V of fracture length generated in the semi-analytical model is 1.15, but it is 0.63 in the numerical model. The large C_V in the semi-analytical model suggests a wide spread of fracture lengths.

The fracture spacing column chart (Figure 5.3e) shows that the fracture spacing distributions between ~1m to ~3m are nearly the same in the numerical model as that in the semi-analytical model, but the semi-analytical model generated more small spacings (10 out of 22 fracture spacings i.e. 45% are less than 0.5m) than the numerical model (3 out of 13, i.e. 23% fracture spacing is less than 0.5m). The larger percentage of small fracture spacing (45% comparing to 23%) causes a much lower median spacing in the semi-analytical model (~0.7m) than that in the numerical model (~2.2m) (Figure 5.3f). The fracture spacing

coefficient of variance analysis shows that the spacing is widely spread in the semi-analytical model than that in the numerical model (C_V=0.9 in the semi-analytical model versus C_v=0.64 in numerical model). Large fractures propagated at similar places in the semi-analytical model as in the numerical model, but the semi-analytical model generated more close-spaced short cracks, which suggest fractures are more clustered in the simplified analytical model than those in the numerical model. The fracture clustering also can be directly observed in the fracture trace maps (Figure 5.3b).

3D case comparison

The effect of the bed thickness is included in the analytical model. A bed thickness of 2 meters is used for the 3d base case study. Except for the bed thickness, all the other parameters are the same as those in the 2d case. Simulations were run starting with initial fractures shown in Figure 5.4a, and ending at a final strain of 5×10^{-3}. The final fracture patterns simulated from the numerical model and the semi-analytical model are almost the same (Figure 5.4b).

The fracture length column chart shows that nearly equal number of fractures propagated in the semi-analytical model and the numerical model (Figure 5.4c). The overall fractures simulated by the semi-analytical model (median spacing of ~4m) are slightly longer than those generated by the numerical model (median spacing of ~3m), but the entire fracture length distributions are alike (Figures 5.4c and 5.4d). For fracture length, C_V is 0.61 in

the semi-analytical model, while C_V equals 0.59 in the numerical model, which indicates the spread of data is very similar.

The fracture spacing distribution is nearly the same in the semi-analytical model as in the numerical model, except for a few more closely spaced fractures simulated by our simplified model (Figures 5.4e and 5.4f). For fracture spacing, the coefficient of variance is nearly the same in the semi-analytical model (C_V=0.69) as in the numerical model (C_V=0.66). For 3d case,

In summary, the semi-analytical model produces a very similar fracture pattern, length and spacing distribution as the numerical model for 3d case, but gives a higher degree of clustering than the numerical model for the 2d case.

SENSITIVITY ANALYSIS

The sensitivity of fracture pattern to initial flaw density, subcritical growth index, bed thickness, elastic modulus and the strain rate is tested here. Three or four sets of numerical experiments for each of the test parameters are performed. For each experiment, we keep all other input parameters the same as those in the base case, and only vary the one that is being tested. For each simulation, fracture length distribution, spacing distribution, fracture clustering and final spatial density are determined. Clustering can be quantified by intensity and variance (distance from the centroid). Intensity is a property of a cluster that is defined as a relatively thick swarm of data points in a space as compared to other areas of that space which may have comparatively few or no points (Aldenderfer and Blashfield, 1984). Variance is the degree of dispersion of the

points in this space from the center of the cluster. Therefore, clusters can be said to be "tight" when all data points are near the centroid, or "loose" when the data points are dispersed from the center. To quantify the intensity of a fracture cluster, besides fracture numbers in the clustered zone, we also need to consider the different fracture sizes. The area of the cluster zone is used as an equivalent to the variance. For calculation convenience, we combined the fracture intensity and variance into one dimensionless term of fracture density (r_c) to describe the "thickness" or "tightness" of the cluster, such as

$$r_c = \frac{1}{A_c}\sum_{i=1}^{N_c} C_i^2 \tag{5.15}$$

Here N_c is the fracture number in the clustered zone, C_i is fracture's half-length and A_c is the size of the clustered zone. The clustered zone can be identified from the fracture trace map. In the following discussion, the average spacing is defined as the mean spacing between the clustered zones. The complementary cumulative spacing distribution is used as assistance to the fracture trace map to identify fracture cluster.

Base Case

An initial critical flaw size of 2 cm, strain rate of 1×10^{-13} per second, final strain of 5×10^{-3}, a subcritical growth index of 20, an elastic modulus of 2×10^{4} MPa, and a bed thickness of 2 m are selected for our base case input parameters. For computational efficiency, an elongated rectangle area (▭) is selected to calculate fracture length distribution, and a short but wide region (▯) is chosen

for fracture spacing calculation. The simulation area size is varied from case to case to optimize the computation time. Fractures are designed to propagate horizontally in one direction, and they are physically limited inside the simulated region. To eliminate the boundary edge effect, a border of 20% of the area length is added at each side of the y-frame in the x direction ( ). The initial flaws are randomly located inside the solid simulation region, and fractures are forced to stop at the extended edges.

Sensitivity to Initial Flaw Density

An elongated rectangle area with a width of 4m (y-direction), length of 10m (x-direction) and border of 2m in the horizontal x direction is used to test the sensitivity of fracture length to initial flaw density (r). With the increase of initial flaw intensity (*N/A*), there are more fractures to propagate, and the overall individual fracture length becomes shorter (Figures 5.5a and 5.5b). This is because that for low flaw intensity, there are less mechanical interactions between fractures. Fractures which propagate first tend to grow until reaching the boundary. Fractures that are longer than 5cm are included in the complementary cumulative distribution plots (initial flaws that do not grow are excluded). Fracture length distributions for a flaw intensity, *N/A*, of 10, 20, 50 and 100 cracks per square meter, corresponding to a flaw density $r3d = 1\times10^{-3}$, 2×10^{-3}, 5×10^{-3} and 1×10^{-2}, are shown in Figure 5.5b. As predicted by our fracture length model (equations 4.16 and 4.17), the exponential curve-fits calculated by the semi-analytical model show an increase in the exponent value (equivalent to

$\frac{2bN}{A}$) as the number of initial flaws increases (Figure 5.5b), which is also consistent with the simulation from the numerical model (Olson et al., 2001). The complementary cumulative frequency of fracture length distribution shows that the constant fracture height model (equation 4.17) predicts that the exponent magnitude should change as 1:2:5:10, but the semi-analytical simulation results in 1:2:5:7. The results are as expected except for fractures developed from a high initial flaw intensity, 100 cracks per square meter. This is because our semi-analytical fracture length derivation is based on mechanical interaction between two cracks. In the derivation we assume every other fracture would have the same influence over the crack we modeled. In low fracture density case, this is a good assumption. However, for high fracture intensity, the mechanical interactions are much more complicated, and the influence on a specific fracture comes from a combined effect from its large number of neighbor cracks (Olson et al., 2001).

As with fracture length, fracture spacing is also significantly affected by flaw intensity. An area with a width of 10m (y-direction), length of 4m (x-direction) and border of 1m in the horizontal x direction is used to test the sensitivity of fracture spacing to initial flaw density. Simulations are run for flaw intensities (N/A) of 20, 35 and 50 per square meters, corresponding to flaw densities (r) of 2×10^{-3}, 3.5×10^{-3} and 5×10^{-3}. The total flaw numbers (N) are 800, 1440 and 2000, respectively. We exclude flaws that have not propagated from our spacing analysis. The complementary cumulative spacing distribution shows that the spacing distributions are similar for $N/A=20$ and $N/A=35$, but quite

different from *N/A=50* (Figures 5.6b). For *N/A=50* the median spacing is 0.5m, but for *N/A=20* and *N/A=35* the median spacing is ~1.5m. The fracture trace map shows that fractures are relatively regular-spaced for *N/A=20* and *N/A=35*, but highly clustered for *N/A=50* (Figure 5.6a). The larger percentage of small spacing in *N/A=50* comes from the cluster zone. According to equation 5.14, the density of the clustered zone (r_c) for *N/A=50* is 10.4.

Sensitivity to Subcritial Growth Index

An elongated rectangle area with a width of 4m (y-direction), length of 10m (x-direction) and border of 2m in the horizontal x direction is used to test the sensitivity of fracture length to subcritical growth index (n). The influence of subcritical index on the length distribution is investigated using a flaw intensity of $50/m^2$ and a flaw length of 0.02 m, which corresponds to a flaw density of 5×10^{-3}. Increasing the subcritical index from n=2 to n=20 causes a decrease in the exponent magnitude for the length complementary cumulative frequency curve from 0.92 to 0.46, resulting in a larger number of long fractures and a smaller number of short fractures for higher n values (Figure 5.7b). According the subcritical growth law (equation 5.4), when the subcritical growth index, n, is low, the velocity contrast between the fractures is small, which enables more fractures to develop simultaneously at different locations.

Increasing the subcritical growth index from n=20 to n=40 reverses the slope change of the length distribution. When n=40, the exponent magnitude of the complementary cumulative frequency curve rise to 0.71. A subcritical index

of 80 causes a further increase to 1.17. This is because according to equation 5.4, if subcritical growth index is high, any stress intensity factor less than 1 will cause nearly zero velocity. Thus, fractures will only propagate at nearly critical stress intensity level. The stress in these "critical" propagation fractures near tip region can be expressed as (Lawn and Wilshaw, 1975)

$$s_{ij} = \frac{K_I}{\sqrt{2pr}} f_{ij}(q) \qquad (5.16)$$

where r is the radial distance, and q is the angle (Figure 2.1). As show in equation 5.16, given a large stress intensity factor, the stress in the fracture near tip region can be large enough to cause the flaws in the near fracture tip region to propagate. Although the fracture length distribution for low and high subcritical index may look similar, they have a quite different spatial distribution in the mapview. For n=2, short fractures are located throughout the body, while for n=80 short fractures are centralized around the long fractures (Figure 5.7a). Similar results, such that the fracture length exponential constant first decreases with increase of subcritical growth index then reverses trend are also found by the numerical simulation (Olson et al., 2001).

The subcritical index also affects fracture spacing and clustering. The results are from 2000 cracks, which have the same initial spatial distribution in an area with a width of 10m (y-direction), length of 4m (x-direction) and border of 1m in the horizontal x direction. We exclude flaws that have not propagated from the spacing analysis. Both a high subcritical index of 80 and an exceptionally low subcritical index of 2 show a high degree of fracture clustering (Figure 5.8a). For *n=2* there are 5 major cluster zones, while for *n=20, n=40* and *n=80* there are 4

(Figure 5.8a). The average spacing between the clustered zoned is 2.4, 2.6, 2.8 and 2.7, for *n=2, n=20, n=40* and *n=80* respectively. The correspondent clustered zone densities (r_c) are 12.0, 10.2, 10.4 and 11.2. Increasing the subcritical index from 2 to 20, the propagated crack numbers decrease from 297 to 59, median spacing increases from 0.2m to 0.9m (Figure 5.8b) and fractures become more regularly spaced and less clustered (Figure 5.8a). As the subcritical index increases from 20, 40 to 80, the number of propagated fractures increases from 59, 110 to 282, median spacing decreases from 0.9m, 0.4m to 0.1m (Figure 5.8b) and fractures become more clustered. Subcritical index alters fracture spacing and controls the degree of cluster. A high subcritical index results in far spaced highly clustered zones.

Sensitivity to Bed Thickness

The effects of bed thickness (*T*) on fracture length and spacing are simulated by using a flaw intensity of $N/A=10/m^2$, a flaw length of 0.02 m (which corresponds to a flaw density of 1×10^{-3}), and a subcritical index of 20. An elongated rectangle area with a width of 6m (y-direction), length of 20m (x-direction) and border of 2m on each side is used to generate the length distribution for *T=2*. An area with width of 8m, length of 40m and border of 2m is used for *T=4*. For *T=8* the simulation area has a width of 8m, a length of 50m and a border of 5m. The purpose of varying the area size is to save computation time. Increasing the bed thickness from 2 m to 8 m causes an increase of the exponential constant from 0.093 to 0.136, resulting in a larger percentage of short

fractures and a smaller percentage of long fractures for the thick bed (Figures 5.9a and 5.9b). Finite bed thickness diminishes stress perturbation and reduces the mechanical interaction. Thus, a thin bed tends to have longer fractures.

To study the influence of bed thickness on fracture spacing, three simulations were run on areas of different sizes to eliminate the boundary effect. For *T=2*, the simulation area has a width of 10m, length of 2m and border of 2m at each side; For *T=4*, it has a width of 20m, length of 4m and border of 4m at each side; For *T=8*, the width is 40m, length is 8m and border is 8m at each side. Fractures are more clustered in a thick bed than in a thin bed (Figure 5.10a). In a thick bed, there are a larger number of short cracks that have propagated around a long fracture due to a larger stress perturbation. For a bed thickness of 8 m, 50% of the fracture spacing is less than 0.4 m. For a bed thickness of 4 m, 35% of the spacing is less than 0.4 m. When the bed thickness reduces to 2m, the spacing less than 0.4 m only counts for 20% of the total spacings (Figure 5.10b). The average fracture spacing for a bed thickness of 2m is 2.6m. For bed thicknesses of 4m and 8m, the fracture spacing is 5.6 m and 9.0 m, respectively (Figure 5.10a). Our simulation shows that the fracture spacing is proportional to bed thickness. The classical explanation for this is that the lateral extent of the stress reduction shadow around a fracture increases with increasing fracture height, which corresponds to the bed thickness for many sedimentary rock (Lachenbruch, 1961, Bur, 1982, Pollard and Segall, 1987 and Gross et al., 1995).

Sensitivity to Elastic Modulus and Strain Rate

The influence of the elastic modulus on the length distribution is investigated using a flaw intensity of $50/m^2$ and a flaw length of 0.02 m (corresponding to a flaw density of 5×10^{-3}). An area with a width of 4m, length 10m and border of 2m of each side are used for the fracture length study. Increasing the elastic modulus from 4×10^3 MPa to 2×10^4 MPa and 1×10^5 MPa causes a decrease in the exponent constant in the complementary cumulative frequency curve from 0.30 to 0.23 and finally to 0.20 (Figure 5.11b). After reaching the same final strain of 5×10^{-3}, the final fracture densities (r) are 1.2, 1.7 and 2.2 for elastic moduli of 4×10^3 MPa, 2×10^4 MPa and 1×10^5 MPa, respectively. Crack propagation depends on stress (equations 5.1 and 5.3), increased elastic modulus enhances stress for a given strain, and fracture propagation is likewise affected. More fractures tend to propagate in a high modulus bed, and their lengths also tend to be longer.

Fracture spacing is smaller in a bed with a high elastic modulus (Figures 5.12a and 5.12b) because stresses are higher in a stiffer bed at lower strain levels. Further, smaller strain increments are required for infilling fracturing events (Gross et al., 1995). In stiff beds, fractures are also more clustered. The high elastic modulus causes a high fracture stress intensity factor. These higher stress intensity values increase the tensile stress perturbation around the crack tip, and the propagation of flaws in the crack tip region is enhanced.

The strain rate has a similar overall influence on fracture propagation as the elastic modulus. Like the elastic modulus, a higher strain rate increases the

stress applied to the crack, and produces longer fractures, smaller fracture spacing, more fracture clustering and a larger fracture density.

CONCLUSIONS

Following Segall's (1984) conceptual model and identifying local and remote interacting groups, I present an analytically based model for fracture propagation. The simplified model produces fracture sets that are similar to those generated by a complete numerical calculation.

Sensitivity analysis studies (for the initial flaw density, the subcritical index, bed thickness and elastic modulus) show that a high initial flaw density results in a larger number of short fractures and smaller number of long fractures. Fractures are more clustered, and the fractures are more closely spaced for a high initial flaw density. The subcritical index determines whether the fractures are clustered or more uniformly distributed. A large subcritical index causes widely spaced fracture cluster zones. A small bed thickness results in longer fractures, and more uniform fracture spacing. Fractures tend to be more clustered in thicker beds. The overall fracture spacing is proportional to bed thickness only under special circumstances. A large elastic modulus causes more fractures to propagate and results in a higher final fracture density. In a bed with high elastic modulus, fractures tend to be longer and more closely spaced.

REFERENCES

Aldenderfer, Mark S. and Blashfield, Roger K., 1984, *Cluster Analysis*, Sage Publications.

Atkinson, B. K., 1979, A fracture mechanics study of subcritical tensile cracking of quartz in wet environments, *Pure Appl. Geophys.*, 117, 1011-1024.

Atkinson, B. K. and Meredith, P. G., 1987, The theory of subcritical crack growth with applications to minerals and rocks. Atkinson, B. K., ed., *Fracture Mechanics of Rock*, Academic Press, San Diego, USA.

Atkinson, B. K., 1980, Stress corrosion and the rate-dependent tensile failure of a fine-grained quartz rock, *Tectonophys.*, 65, 281-290.

Bai, T. and Pollard, D.D., 2000, Fracture spacing in layered rocks: a new explanation based on the stress transition, *Journal of Structural Geology*, 22, 43-57.

Bristow, J.R., 1960, Microcracks and the static and dynamic elastic constants of annealed and heavily conventional-worked metals. *British J. Appl. Phys.* 11, 81-85.

Bruner, W.M., 1976, Comment on 'Seismic Velocities in Dry and Saturated Cracked Solids' by Richard J. O'Connell and Bernard Budiansky, *Journal of Geophysical Research*, 81(14), 2573-2576.

Budiansky, B., O'Connell, R.J., 1976, Elastic moduli of a cracked solid. *Int. J. Solids Struc.*, 12, 81-97.

Childs, E.C., 1957, The anisotropic hydraulic conductivity of soil, *Journal of Soil Science* 8(1), 42-47.

Crouch, S. L. and Starfield, A. M., 1983, *Boundary Element Methods in Solid Mechanics*. George Allen and Unwin, London, U. K.

Dieter, G. E. 1976, *Mechanical metallurgy*, New York, McGraw-Hill, 774.

Dershowitz, W. S. and Einstein, H. H., 1988, Characterizing rock joint geometry with joint system models. *Rock Mech. Rock Eng.*, 21, 21-51.

Gross, M. R., 1993. The origin and spacing of cross joints: Examples from the Monterrey Formation, Santa Barbara coastline, California, *Journal of Structural Geology*, 15, 737–751.

Gross, M. R., Fischer, M. P., Engelder, T and Greenfield, R, 1995, Factors controlling joint spacing in interbedded sedimentary rocks: integrating numerical models with field observations from the Monterey Formation, USA, *Fracture topography as a tool in fracture mechanics and stress analysis*, Geological Society Special Publication No. 92, 215-233.

Hatzor, Y.H. and Palchik, V., 1997, The influence of grain size and porosity on crack initiation stress and critical flaw length in Dolormites, *Int. J. Rock. Mech. Min. Sci.*, 34(5), 805-816.

Jaeger, J.C. and Cook, N.G.W., 1976, *Fundamentals of Rock Mechanics*, Chapman and Hall, London.

Jensen, J.L., Lake, L.W., Corbett, P.W.M., and Goggin, D.J., 1997, *Statistics for Petroleum Engineers and Geoscientists*, Prentice Hall PTR, USA

Kachanov, M., 1992, Effective elastic properties of cracked solids: critical review of some basic concepts, *Appl. Mech. Rev.*, 45(8), 304-335.

Kulatilake, P.H.S.W., Wathugala, D.N., and Stephansson, O., 1993, Joint network modeling with a validation exercise in Stripa Mine, Sweden, *Int. J. Rock Mech. Min. Sci. and Geomech. Abstr.*, 30(5), 503-526.

Lachenbruch, A. H., 1961, Depth and spacing of tension cracks, *Journal of Geophysical Research 66*, 4273-4292.

Laubach, S., 1997, A method to detect natural fracture strike in sandstones, *AAPG Bulletin*, 81(4), 604-623.

Laubach, S., Marrett, R. and Olson, J. E., 2000, New directions in fracture characterization, *The Leading Edge*, 704-711.

La Pointe, P. R. and Hudson, J. A., 1985, Characterization and interpretation of rock mass joint patterns, Geological Society of America Speical Paper, 199, 37.

Lawn, B. R., and Wilshaw, T. R., 1975, *Fracture of Brittle Solids*, Cambridge, England, Cambridge University Press, pp. 204.

Lorenz, J. C. and Warpinski, N. R., 1996, Natural fracture characteristics and effects, *Leading Edge*, 15(8), 909-911.

Love, A. E. H., 1927, A *Treatise on the Mathematical Theory of Elasticity*, Cambridge University Press, pp. 643.

Nur, A, 1982, The origin of tensile fracture lineaments, *Journal of Structural Geology* 4, 31-40.

O'Connell, J. R., and Budiansky, B., 1974, Seismic velocities in dry and saturated cracked solids, Journal of Geophysical Research, 79, 5412-5426.

Olson, J. E, 1991, Fracture mechanics analysis of joints and veins. *Dissertation*, UMI.

Olson, J. E., 1993, Effects of subcritical crack growth and mechanical crack interaction. *Journal of Geophysical Research*, 98(B7), 12251-12265.

Olson, J. E., 1997, Natural fracture pattern characterization using a mechanical-based model constrained by geologic data – moving closer to a predictive tool. *Int. J. Rock Mech. & Min. Sci.*, 34(3/4), 391, Paper No. 237.

Olson, J. E. and Pollard, D. D., 1989, Inferring paleostresses from natural fracture patterns: A new method. *Geology*, 17, 345-348.

Olson, J. E. and Pollard, D. D., 1991, The initiation and growth of en echelon veins, *Journal of Structural Geology*, 13(5), 595-608.

Olson, J. E., Qiu, Y., Holder, J. and Rijken, P., 2001, Constraining the spatial distribution of fracture networks in naturally fractured reservoirs using fracture mechanics and core measurements. *SPE Annual Technical Conference and Exhibition: New Orleans, L.A., SPE 71342*.

Pollard, D. D., Segall, P., and Delaney, P. T., 1982, Formation and interpretation of dilatant echelon cracks, *Geological Society of America Bulletin*, 93, 1291-1303.

Pollard, D. D. and Aydin, A., 1984, Propagation and linkage of oceanic ridge segments, *Journal of Geophysical Research*, 89(B12), 10,017-10,028.

Pollard, D. D. and Segall, P., 1987, Theoretical displacements and stresses near fractures in rocks: with applications to faults, joints, veins, dikes and

solution surfaces. In: Atkinson, B.K. (Ed.), *Fracture Mechanics of Rock*. Academic Press, London, 277-349.

Pollard, D. D. and Aydin, A., 1988, Progress in understanding jointing over the past century, *Geological Society of America Bulletin*, 100, 1181-1204.

Pfiffner, O.A. and Ramsay, J.G., 1982, Constraints on geological strain rates: arguments from finite-strain states of naturally deformed rocks, *Journal of Geophysical Research*, 87(B1), 311-321.

Renshaw, C. E., 1993, Modeling fluid migration through physically-based fracture networks, *Dissertation*, Stanford University.

Renshaw, C. E. and Park, J. C., 1997, Effect of mechanical interactions on the scaling of fracture length and aperture, *Nature*, 386, 482-484.

Rives, T., Razack, M., Petit, J. P. and Rawnsley, K.D., 1992, Joint spacing: analogue and numerical simulations, *Journal of Structural Geology*, 14(8/9), 925-937.

Robertson, A., 1970, The interpretation of geological factors for use in slope stability. *Proc. Symp. On the Theo. Background to the Planning of Open Pit Mines with Special Ref. To Slope Stability*, 55-71.

Secor, D.T., 1965, Role of fluid pressure in jointing, *Amer. J. Sci.*, 263, 633-646.

Secor, D.T., 1969, Mechanics of natural extension fracturing at depth in the earth's crust, in Baer, A.J., and Norris, D.K., eds., *Research in tectonics: Geological Survey of Canada Special Paper* 68-52, 3-47.

Segall, P., and Pollard, D. D., 1983, Joint formation in granitic rock of the Sierra Nevada. *Geological Society of America Bulletin*, 94, 563-575.

Segall, Paul, 1984, Formation and growth of extensional fracture sets, *Geological Society of America Bulletin*, 95, 454-462.

Swanson, P.L., 1984, Subcritical crack growth and other time- and environment behavior in crustal rocks, *Journal of Geophysical Research*, 89(B6), 4137-4152.

Tamuzs V. and Petrovab V., 1999, Modified model of macro-microcrack interaction, *Theoretical and Applied Fracture Mechanics*, 32(2), 111-117.

Walsh J. B., 1965, The effect of cracks on the uniaxial elastic compression of rocks, *Journal of Geophysical Research*, 70(2), 399-411.

Warren, J. E. and Root, P.J., 1963, The behavior of naturally fractured reservoirs, *SPE Journal*, 245-255.

Wilkins, B.J., 1980, Slow crack growth and delayed failure of granite, *Int. J. Rock Mech. Min. Sci. Geomech. Abstr.*, 17, 365-369.

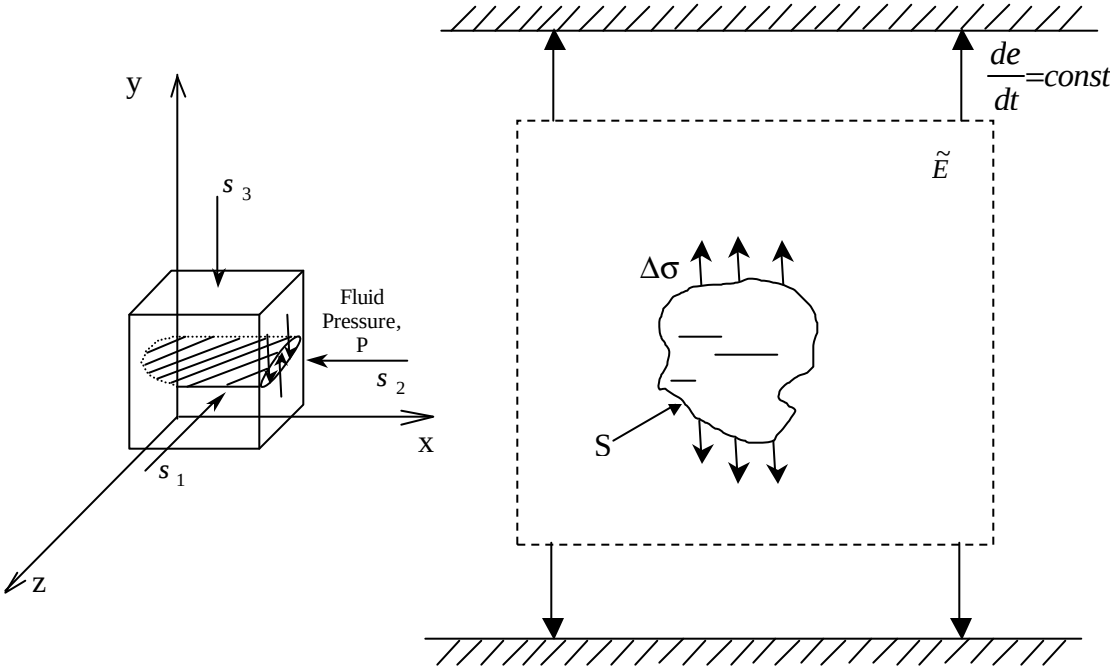

Figure 5.1 A single set of parallel fractures subject to uniaxial extension at a constant strain rate, *de/dt*. Cracks outside contours *S* are treated as a continuum with effective modulus $\tilde{E}$. Cracks inside *S* are modeled explicitly. Δs is the average stress transmitted across *S* (Segall, 1984)

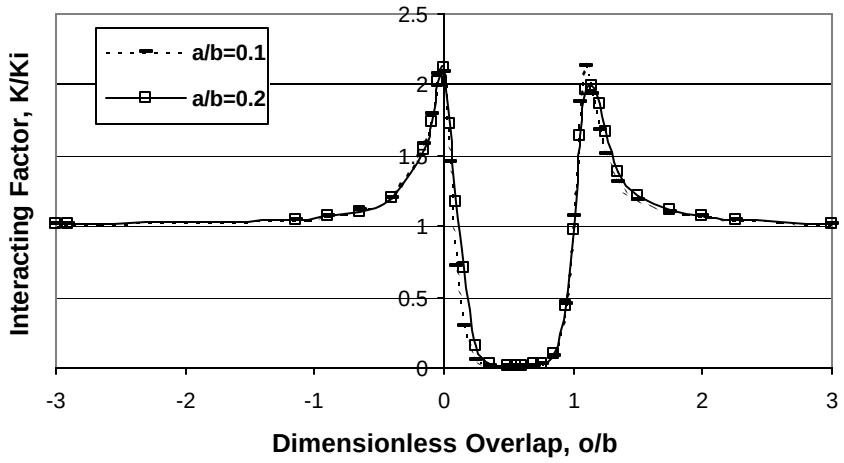

Figure 5.2 Fracture interacting factor versus dimensionless overlap for dimensionless spacing of 0.1 (s/b=0.1) and crack length ratios of 0.1 and 0.2. (a/b=0.1, a/b=0.2). Note if dimensionless overlap is in between 0 and 1 ($0<o/b<1$), the interacting factor (K/K_i) is near zero.

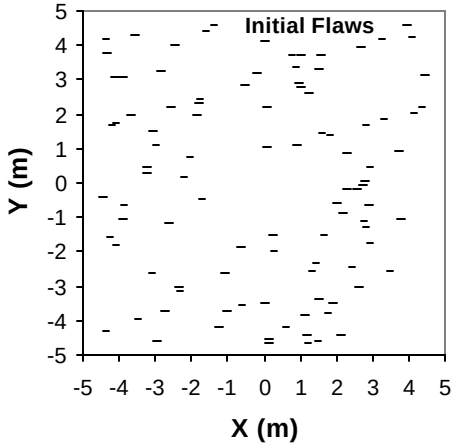

Figure 5.3a Initial fracture pattern with 100 cracks and initial fracture density of 0.01.

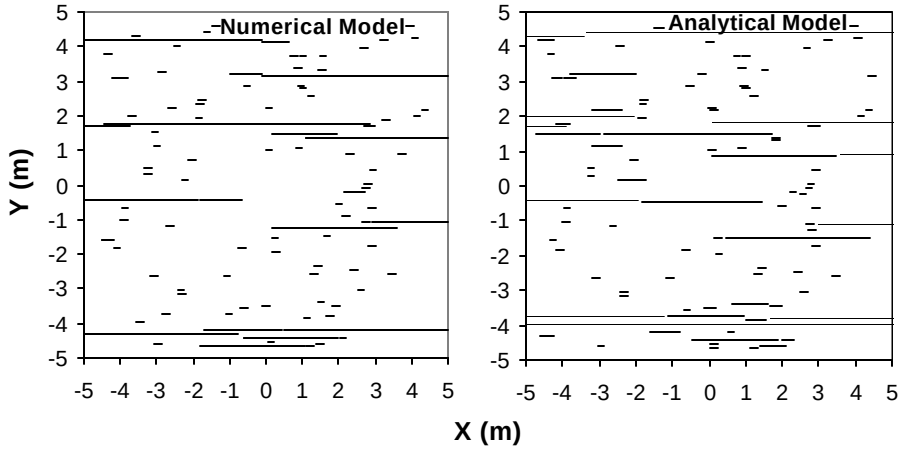

Figure 5.3b Fracture patterns generated by the boundary element model (right) and analytical mode (left). Fractures growth started from the pattern shown as Figure 5.3a, 2D plane strain case, with $n = 40, \dot{e} = 1.67 \times 10^{-13} / s, e = 5 \times 10^{-3}, r_f = 1.1.$

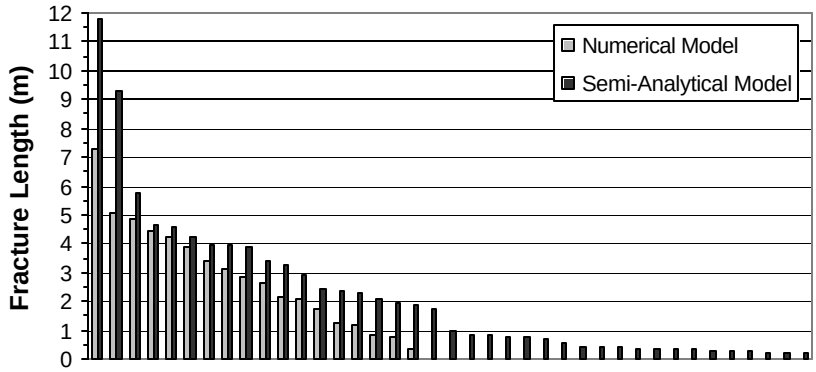

Figure 5.3c Fracture length column chart illustrates comparison between fracture lengths generated by the numerical model and the semi-analytical model (2D plane strain).

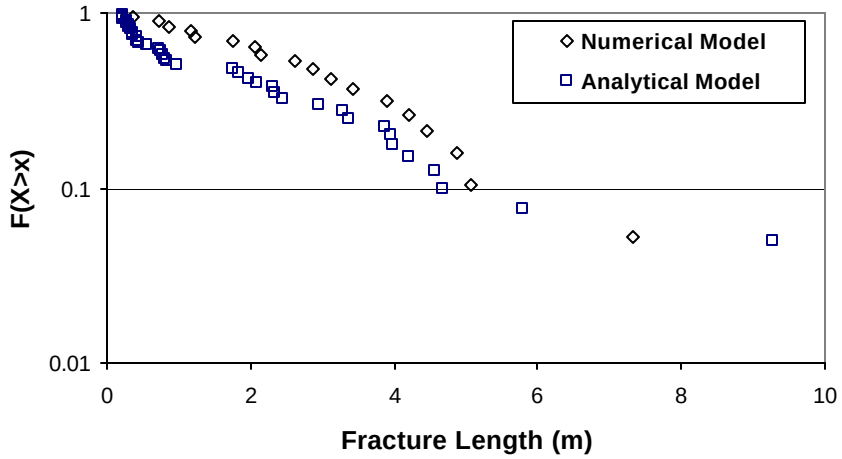

Figure 5.3d Complementary cumulative distribution of the fracture length for the numerical model and the semi-analytical model (2D plane strain).

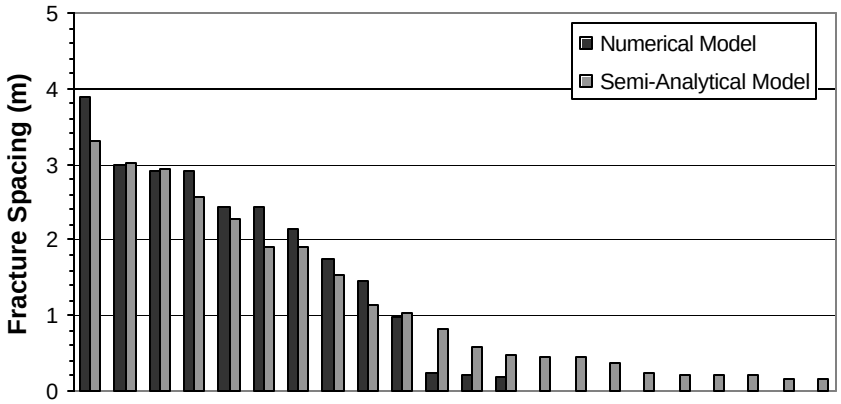

Figure 5.3e Fracture spacing column chart illustrates comparison between fracture spacing generated by the numerical model and the semi-analytical model (2D plane strain).

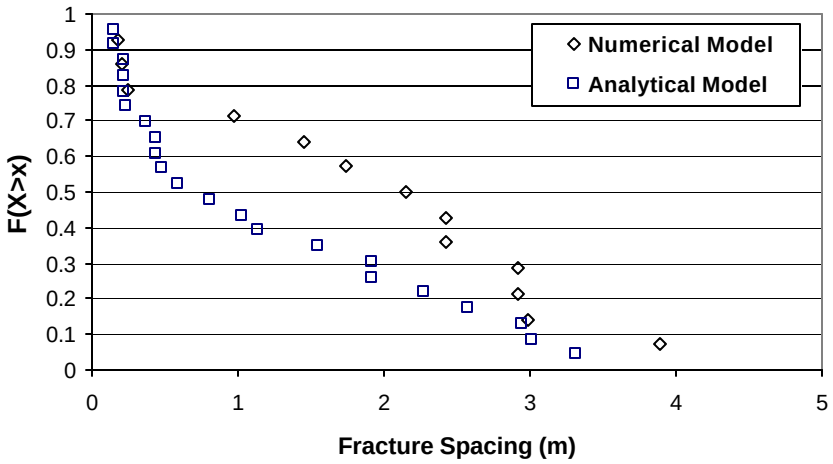

Figure 5.3f Complementary cumulative distribution of the fracture spacing for the numerical model and the semi-analytical model (2D plane strain).

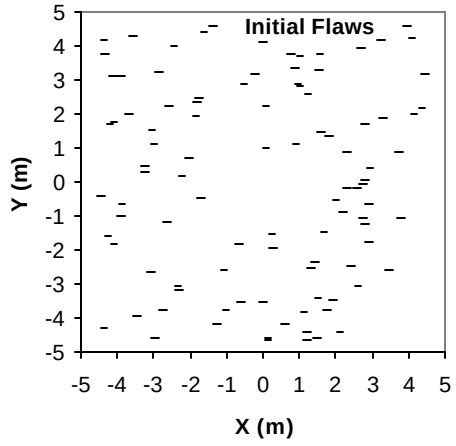

Figure 5.4a Initial fracture pattern with an initial fracture density of 0.01 and a bed thickness of 2m. This map view is exactly the same as Figure 5.3a.

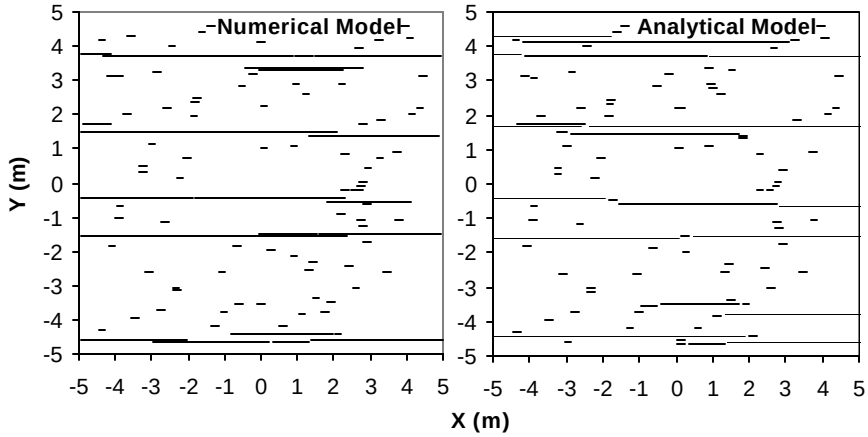

Figure 5.4b Fracture patterns generated by the boundary element model (left) and the analytical model (right). Fractures propagation started from the pattern shown as Figure 5.4a, a bed thickness (H) of 2m, with $n = 40, \dot{e} = 1.67 \times 10^{-13} / s, e = 5 \times 10^{-3}, r_f = 1.1.$)

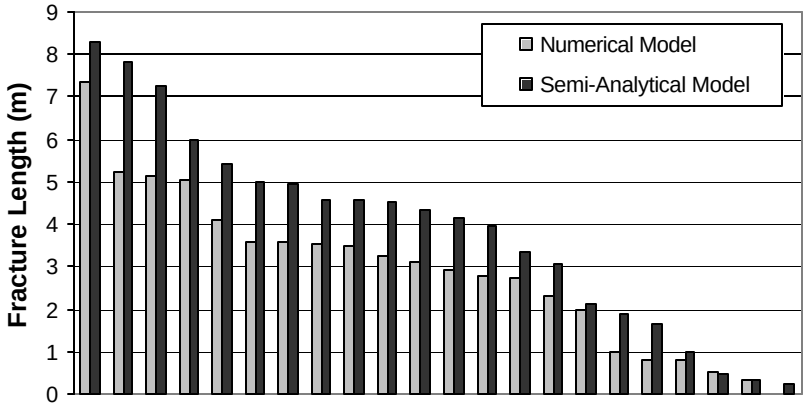

Figure 5.4c Fracture length column chart illustrates comparison between fracture lengths generated by the numerical model and the semi-analytical model (H=2).

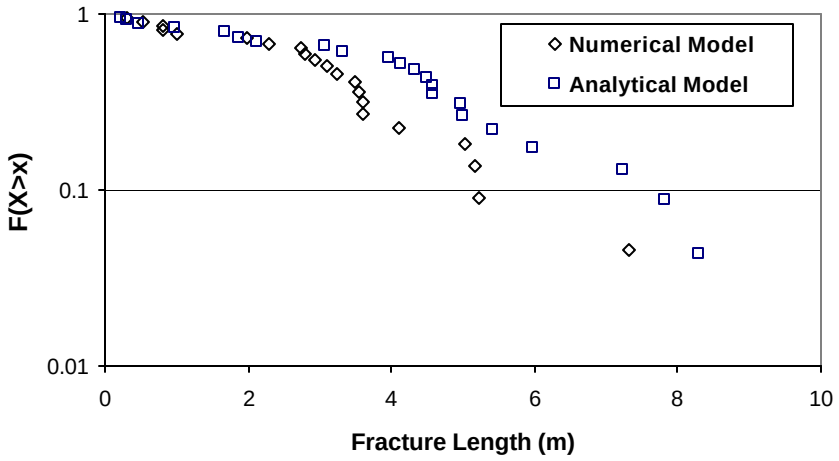

Figure 5.4d Complementary cumulative distribution of the fracture length for the numerical model and the semi-analytical model (H=2m).

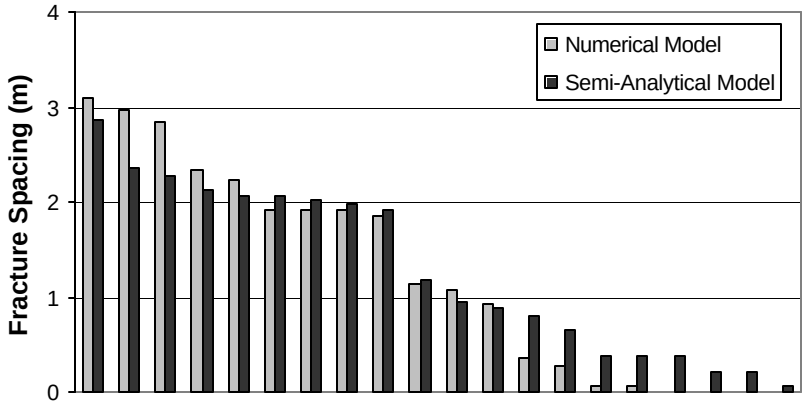

Figure 5.4e Fracture spacing column chart illustrates comparison between fracture spacing generated by the numerical model and the semi-analytical model (H=2m).

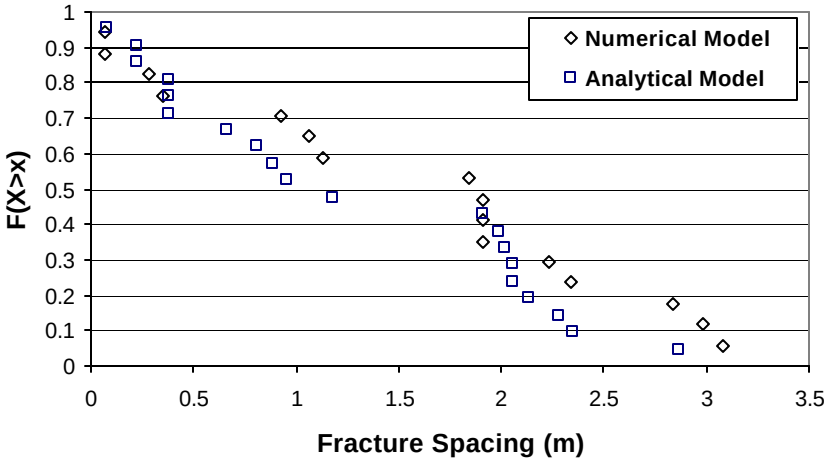

Figure 5.4f Complementary cumulative distribution of the fracture spacing for the numerical model and the semi-analytical model (H=2m).

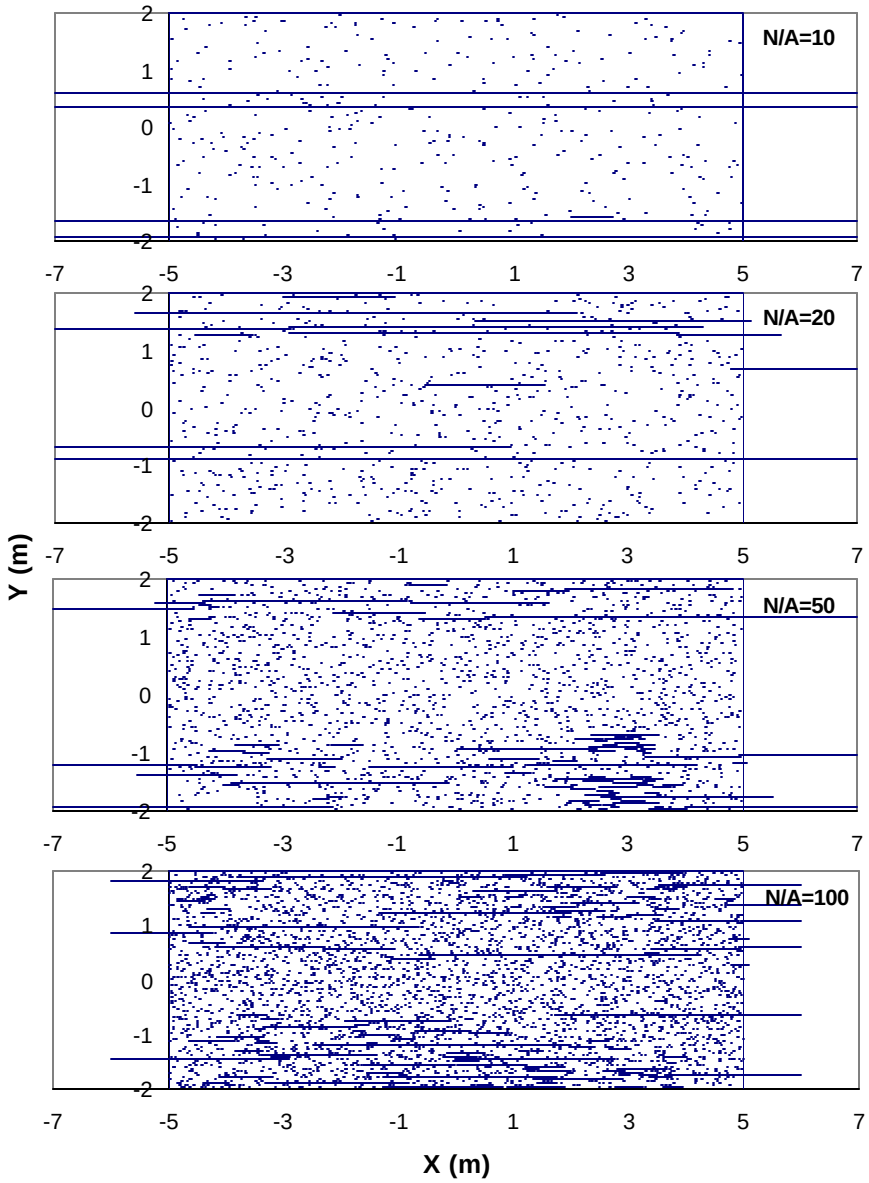

Figure 5.5a Fracture trace maps (map view), fractures simulations start with initial flaw length of 0.02m and flaw intensities, N/A, of 10, 20, 50 and 100 per square meter. This corresponds to flaw densities of 1×10^{-3}, 2×10^{-3}, 5×10^{-3}, 1×10^{-2}.

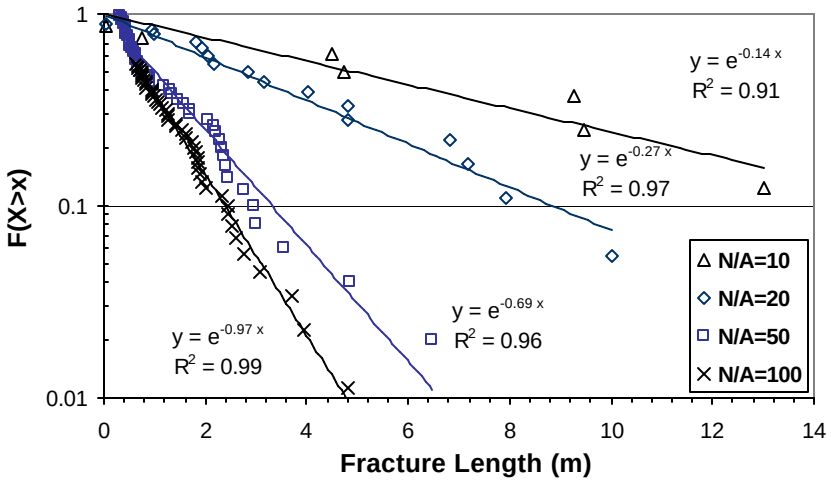

Figure 5.5b Final fracture length distributions started with initial flaw length of 0.02m and flaw intensities, N/A, of 10, 20, 50 and 100 per square meter. This corresponds to flaw densities of 1×10^{-3}, 2×10^{-3}, 5×10^{-3}, 1×10^{-2}.

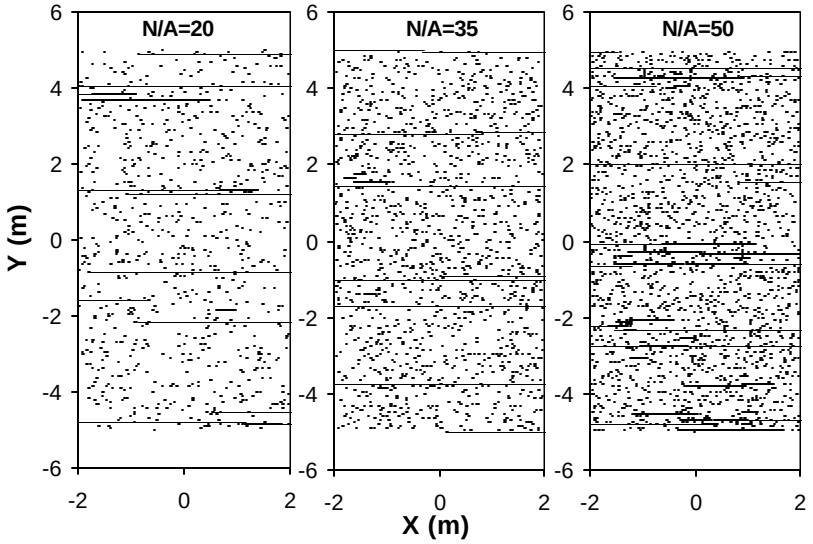

Figure 5.6a Fracture trace maps (map view) for fracture spacing study (Figure 5.6b) with flaw intensities, N/A of 20, 35 and 50 per square meter, corresponding to flaw densities of 2×10^{-3}, 3.5×10^{-3}, 5×10^{-3}, respectively.

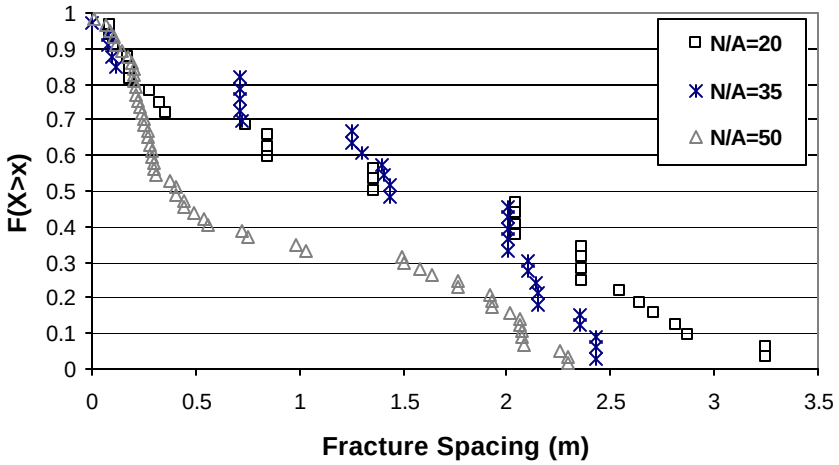

Figure 5.6b Fracture spacing distributions from the simulations used for Figure 5.6a.

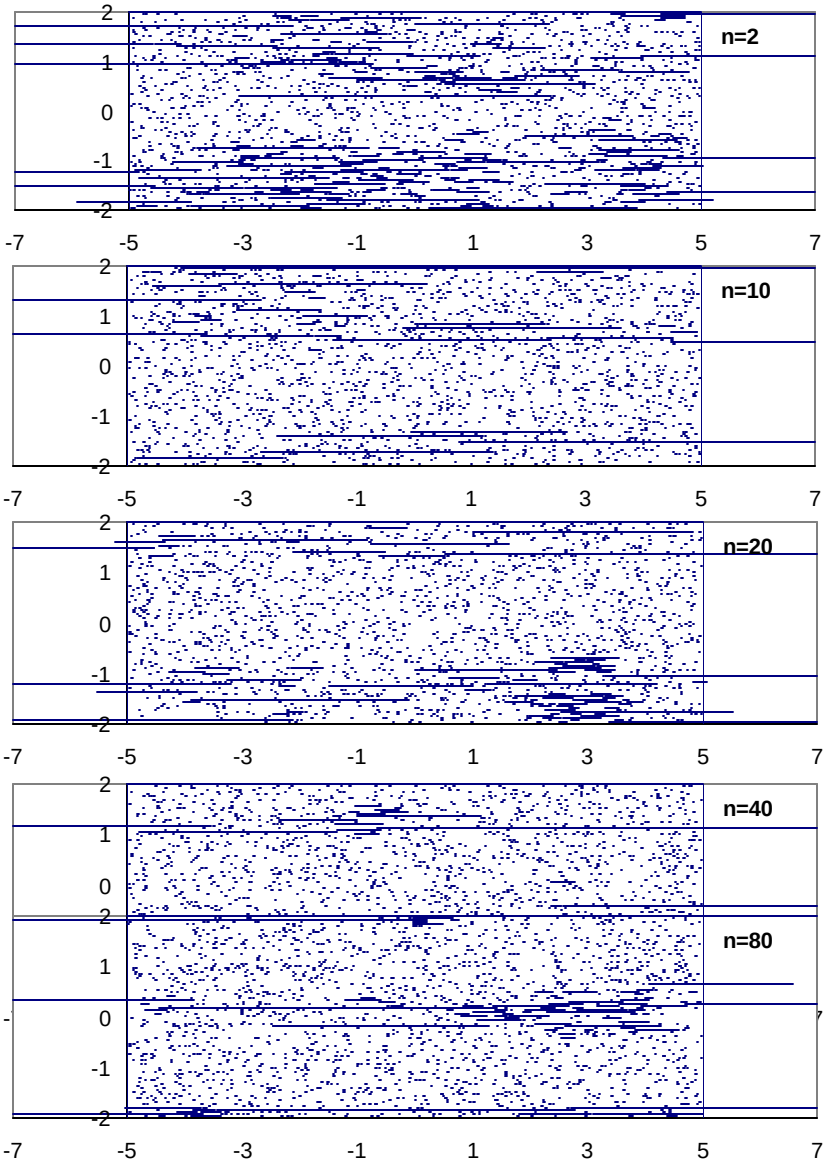

Figure 5.7a Fracture trace maps (map view), simulated for fracture length study (Figure 5.7b) with subcritical growth indices of, 2, 10, 20 and 80, using $N/A = 50, \dot{e} = 1\times10^{-13}/s, e = 5\times10^{-3}$ (total crack numbers, N=2000).

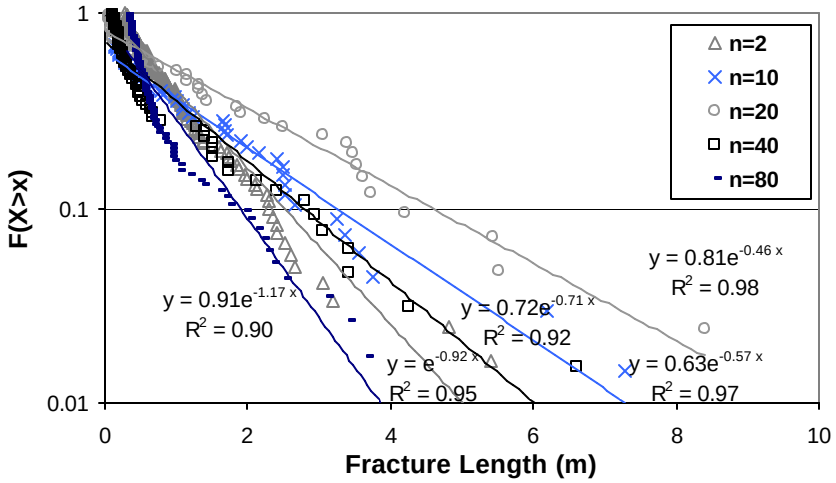

Figure 5.7b Fracture length distributions for subcritical growth indices of, 2, 10, 20 and 80, using $N/A = 50, \dot{e} = 1\times10^{-13}/s, e = 5\times10^{-3}$ (total crack numbers, N=2000).

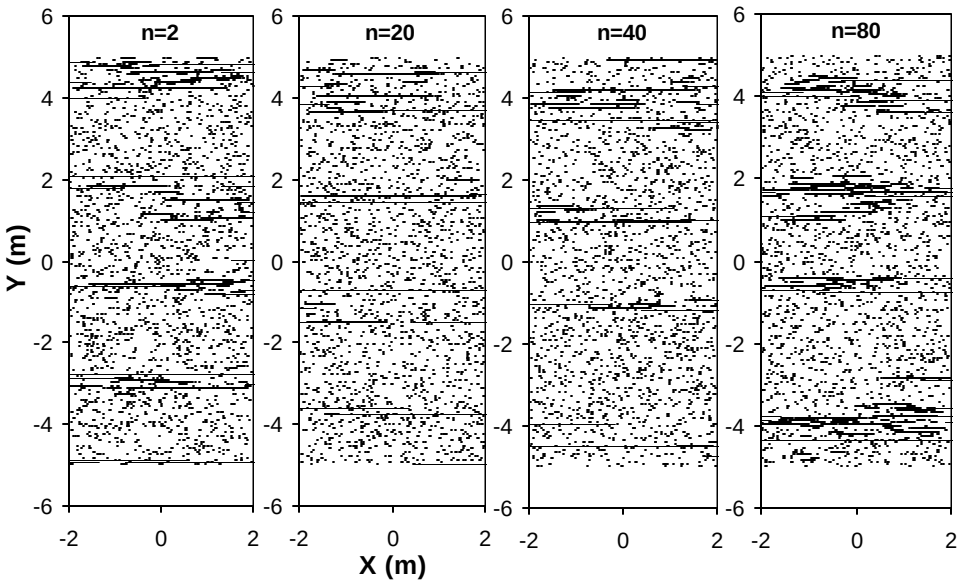

Figure 5.8a Fracture trace maps (map view) for fracture spacing study (Figure 5.8b) with subcritical indices n, of 2, 20, 40 and 80.

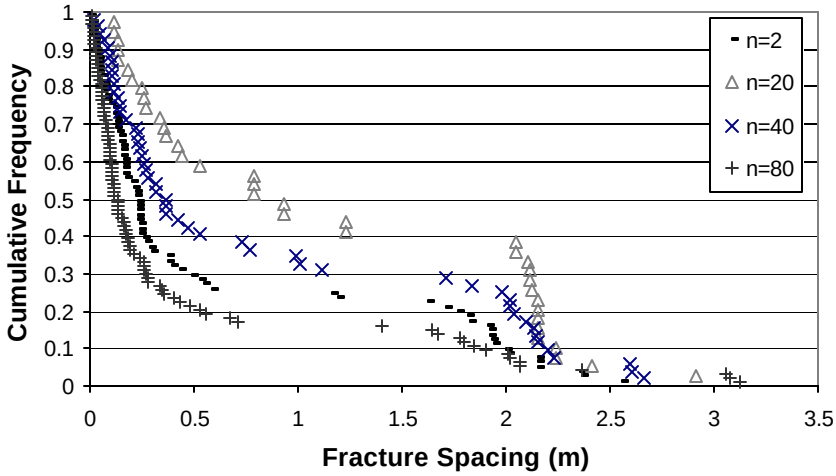

Figure 5.8b Fracture spacing distributions for subcritical growth indices, 2, 10, 20 and 80, using $N/A = 50, \dot{e} = 1\times10^{-13}/s, e = 5\times10^{-3}$ (total crack numbers, N=2000).

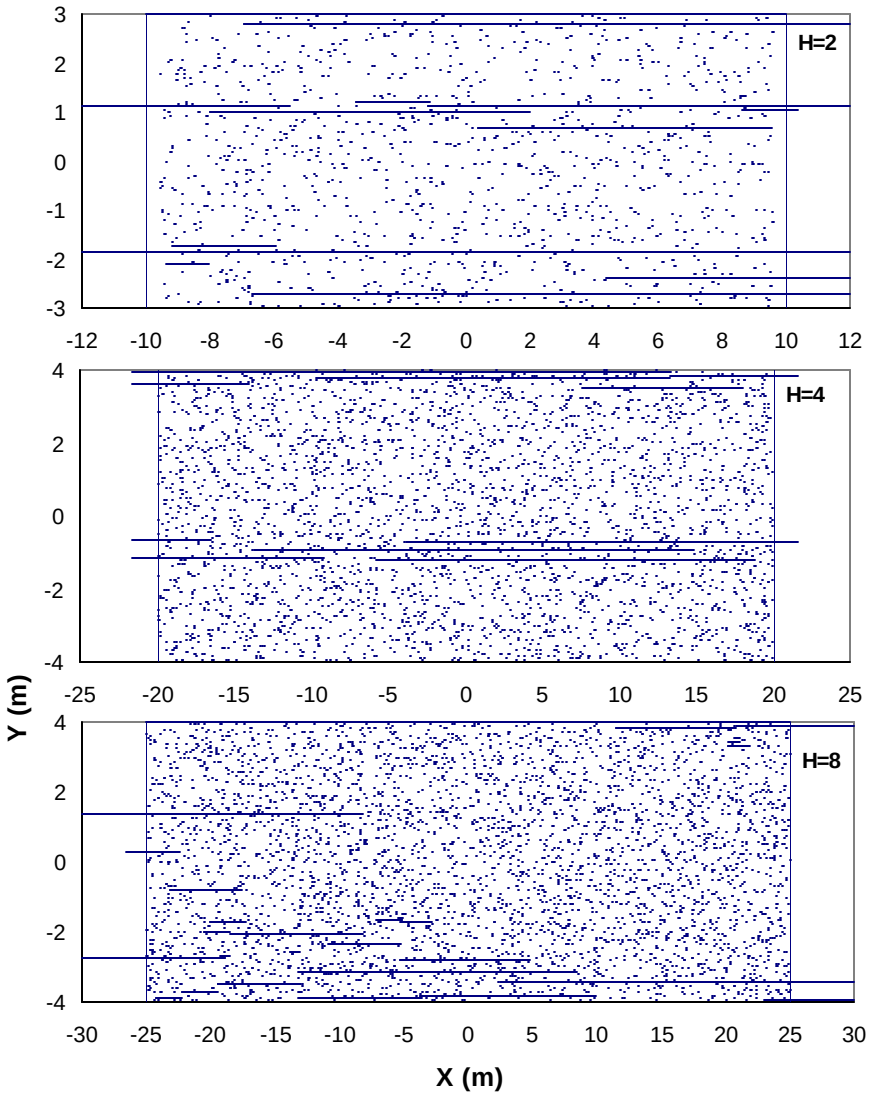

Figure 5.9a Fracture trace maps (map view) simulated for fracture length study (Figure 5.9b) with bed thickness of 2, 4, and 8 meters, using N/A=20/m^2, n=20, $\dot{e} = 1\times10^{-13}/s$, e=5×10^{-3}.

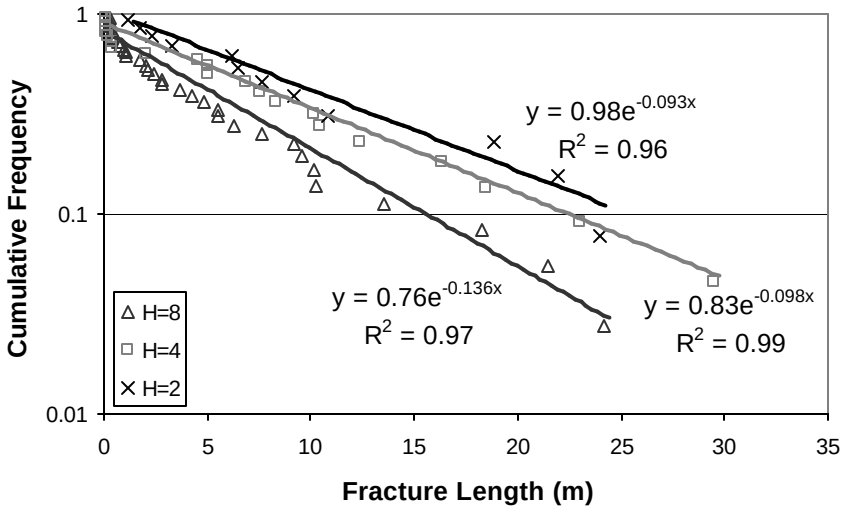

Figure 5.9b Fracture length distributions for bed thicknesses of 2, 4, and 8 meters, using N/A=20/m^2, n=20, $\dot{e} = 1\times10^{-13}/s$, e=5×10^{-3}.

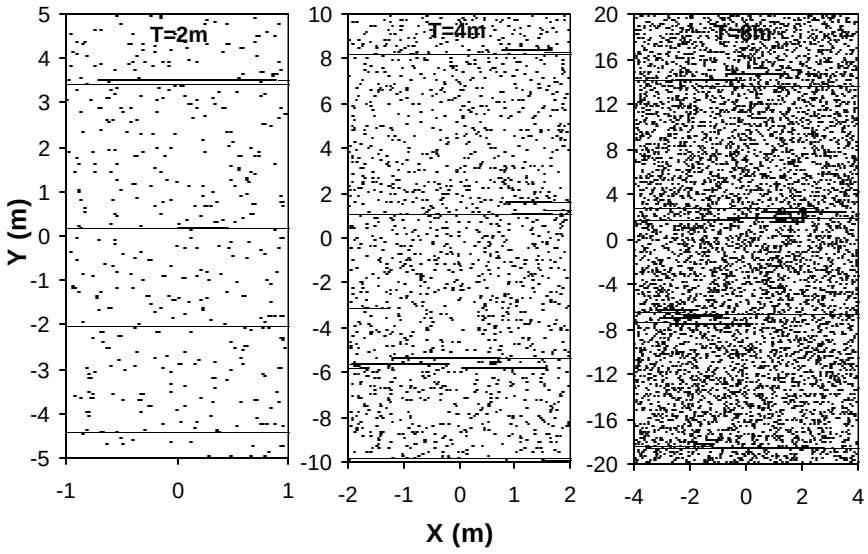

Figure 5.10a Fracture trace maps (map view) for fracture spacing investigation (Figure 5.10b) with bed thicknesses of 2, 4 and 8 meters

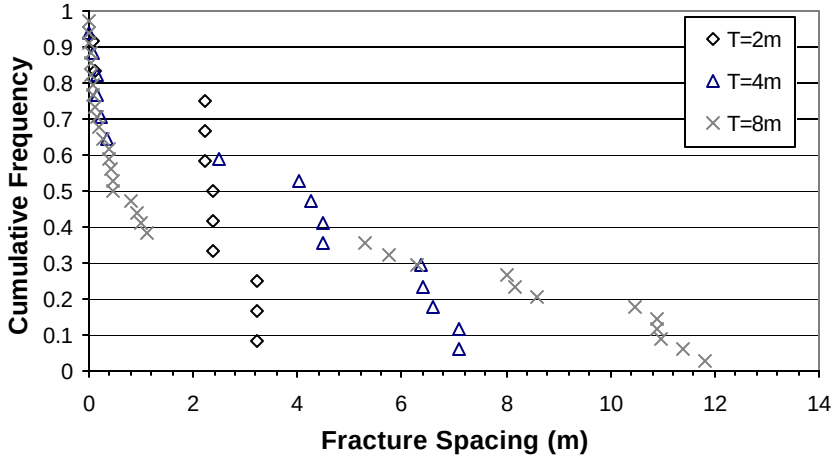

Figure 5.10b Fracture spacing distributions for bed thicknesses of, 2, 4 and 8 m, using N/A=20/m^2, n=20, $\dot{e} = 1\times10^{-13}/s$, e=5×10^{-3}.

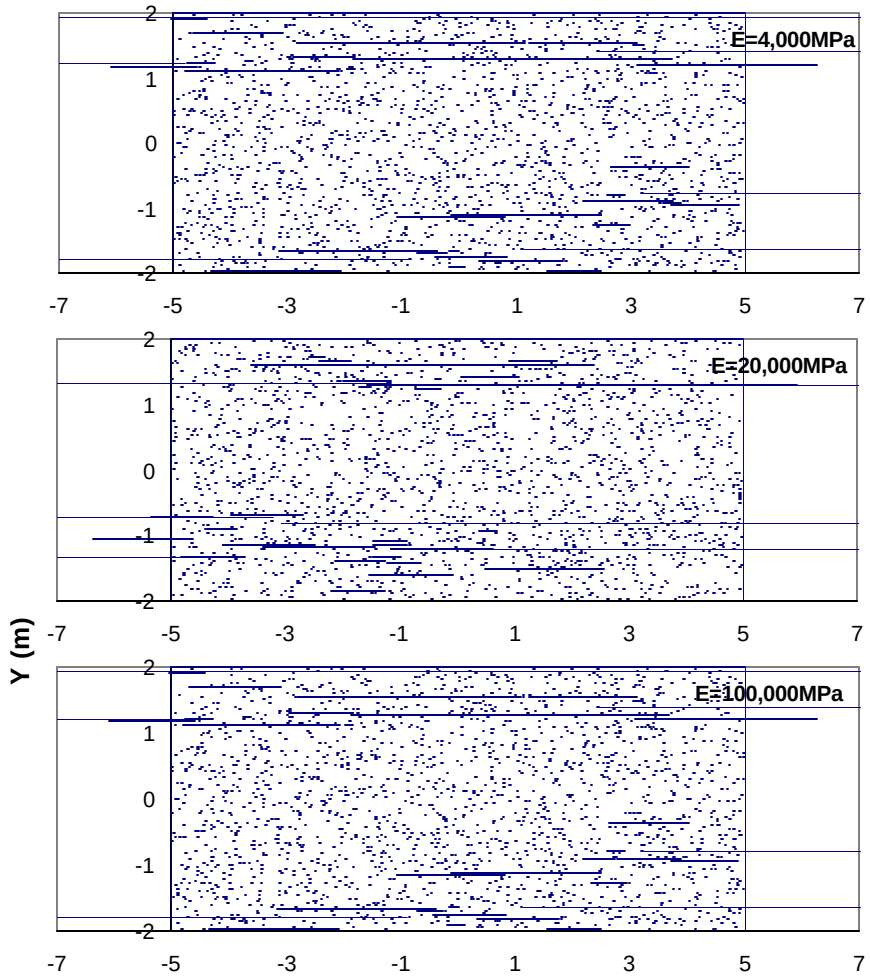

Figure 5.11a Fracture trace maps (map view) generated for fracture length study (Figure 5.11b) with elastic moduli of 4×10^3 MPa, 2×10^4 Mpa, and 1×10^5 Mpa, using $N/A=50/m^2$, $n=20$, $\dot{e}=1\times10^{-13}/s$, and $e=5\times10^{-3}$.

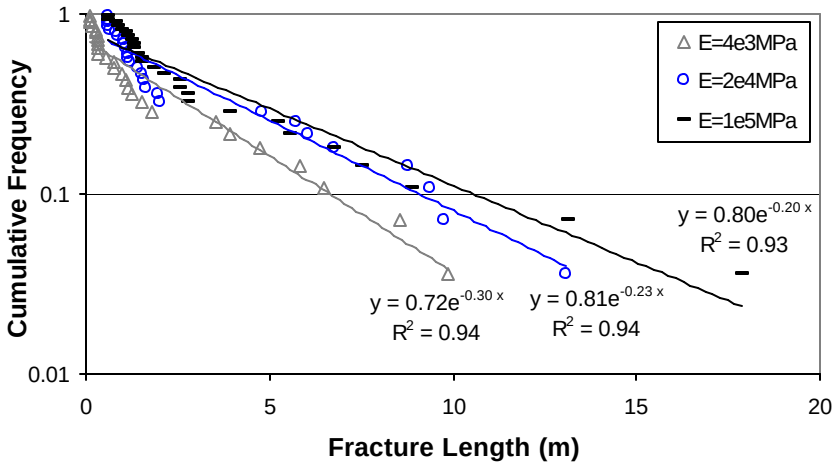

Figure 5.11b Fracture length distribution for elastic moduli of 4×10^3 MPa, 2×10^4 Mpa, and 1×10^5 Mpa, using $N/A=50/m^2$, $n=20, \dot{e}=1\times10^{-13}/s$, and $\varepsilon=5\times10^{-3}$.

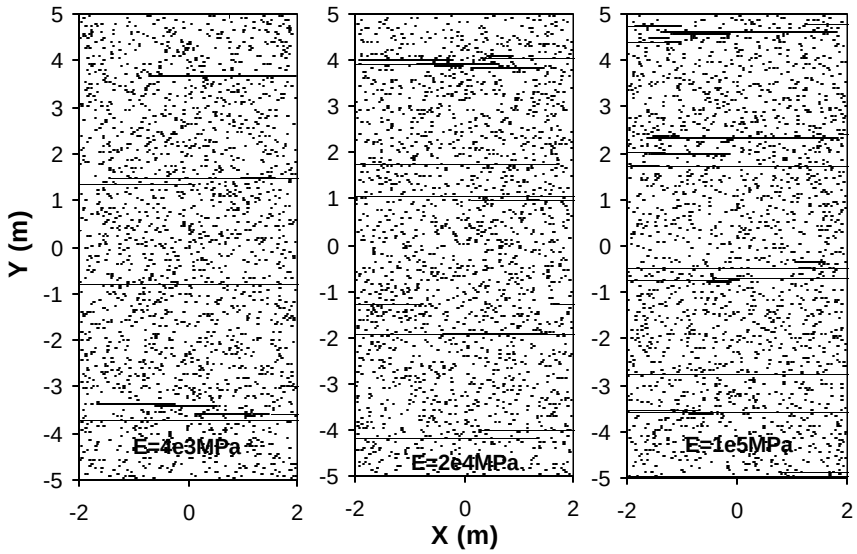

Figure 5.12a Fracture trace maps (map view) for fracture spacing study (Figure 5.12b) with elastic moduli of 4×10^3 MPa, 2×10^4 Mpa, and 1×10^5 Mpa.

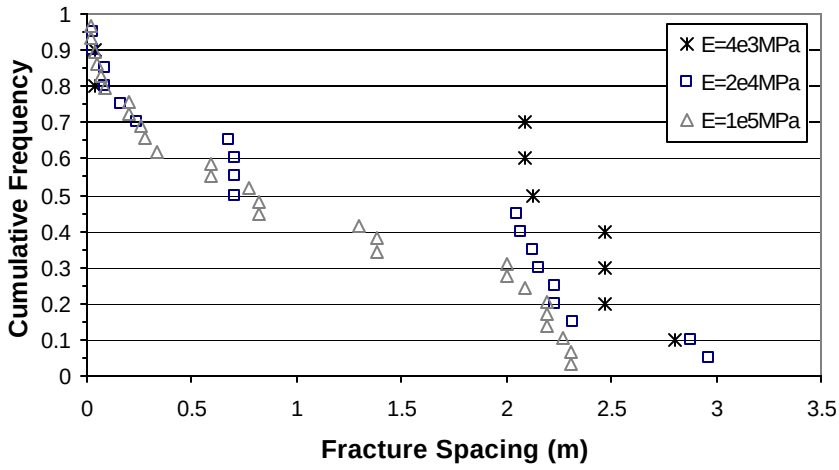

Figure 5.12b Fracture spacing distribution for elastic moduli of 4×10^3 MPa, 2×10^4 Mpa, and 1×10^5 Mpa, using $N/A=50/m^2$, n=20, $\dot{e}=1\times10^{-13}/s$, $e=5\times10^{-3}$.

Table 5.1: Interaction factors and associated errors for a five-crack array of s/b = 0.5 and o/b = -0.5

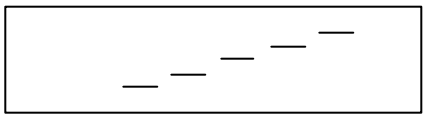

	BEM Calculation		Results from Multiply		Associated Error	
	Left-tip	Right-tip	Left-tip	Right-tip	Left-tip	Right-tip
Crack 1	0.774	1.271	0.704	1.213	-9%	-5%
Crack 2	0.860	0.908	0.757	0.825	-12%	-9%
Crack 3	0.910	0.910	0.790	0.790	-13%	-13%
Crack 4	0.908	0.860	0.825	0.757	-9%	-12%
Crack 5	1.271	0.774	1.214	0.704	-5%	-9%

Table 5.2: Interaction factors and associated errors for a five-crack array of s/b = 0.5 and o/b = 0

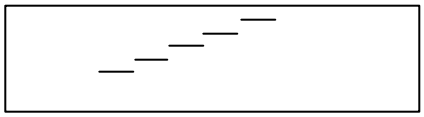

	BEM Calculation		Results from Multiply		Associated Error	
	Left-tip	Right-tip	Left-tip	Right-tip	Left-tip	Right-tip
Crack 1	1.397	1.335	1.299	1.255	-7%	-6%
Crack 2	1.581	1.539	1.500	1.471	-5%	-4%
Crack 3	1.615	1.615	1.528	1.528	-5%	-5%
Crack 4	1.539	1.581	1.471	1.500	-4%	-5%
Crack 5	1.335	1.397	1.255	1.299	-6%	-7%

Table 5.3: Interaction factors and associated errors for a five-crack array of s/b=0.5 and o/b=1

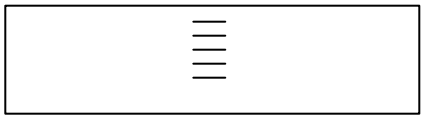

	BEM Calculation		Results from Multiply		Associated Error	
	Left-tip	Right-tip	Left-tip	Right-tip	Left-tip	Right-tip
Crack 1	0.528	0.528	0.340	0.340	-36%	-36%
Crack 2	0.296	0.296	0.314	0.314	6%	6%
Crack 3	0.292	0.292	0.289	0.289	-1%	-1%
Crack 4	0.296	0.296	0.314	0.314	6%	6%
Crack 5	0.528	0.528	0.340	0.340	-36%	-36%

Table 5.4: Interaction factors and associated errors for three randomly generated cracks

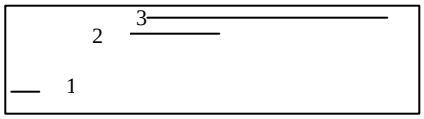

	BEM Calculation		Results from Multiply		Associated Error	
	Left-tip	Right-tip	Left-tip	Right-tip	Left-tip	Right-tip
Crack 1	1.926	1.962	2.100	2.141	-8%	-8%
Crack 2	1.474	0.150	1.474	0.150	0%	0%
Crack 3	0.292	0.292	0.289	0.289	1%	1%

REFERENCES

Aldenderfer, Mark S. and Blashfield, Roger K., 1984, *Cluster Analysis*, Sage Publications.

Anderson, O.L., and Grew, P.C., 1977, Stress corrosion theory of crack propagation with applications to geophysics. *Rev. Geophys. Space Phys.* 15, 77-104.

Atkinson, B. K., 1979, A fracture mechanics study of subcritical tensile cracking of quartz in wet environments, *Pure Appl. Geophys.*, 117, 1011-1024.

Atkinson, B. K., 1980, Stress corrosion and the rate-dependent tensile failure of a fine-grained quartz rock, *Tectonophys.*, 65, 281-290.

Atkinson, B. K., 1982, Subcritical crack propagation in rocks: theory, experimental results and application, *Journal of Strucural Geology*, 4, 41-56.

Atkinson, B. K., 1984, Subcritical crack growth in geological materials. *Journal of Geophysical Research*, 89, 4077-4114.

Atkinson, B. K. and Meredith, P. G., 1987, The theory of subcritical crack growth with applications to minerals and rocks. Atkinson, B. K., ed., *Fracture Mechanics of Rock*, Academic Press, San Diego, USA

Baecher, G.B., Lanney, N.A. and Einstein, H.H., 1977, Statistical description of rock properties and sampling, *18th US Symposium on Rock Mechanics* 5C1, 1–8.

Baecher, G.B. and Lanney, N.A., 1978, Trace length biases in joint surveys. *Proceedings, Symposium on Rock Mechanics* 19, 56–65.

Bai, T., and Pollard, D. D., 2000, Fracture spacing in layered rocks: a new explanation based on the stress transition, *Journal of Structural Geology*, 22, 43-57.

Becker, A., and Gross, M. R., 1996, Mechanism for joint saturation in mechanically layered rocks: an example from southern Israel, *Tectonophysics*, 257, 223-237.

Barton, C. A. and Zoback, M. D., 1992, Self-similar distribution and properties of macroscopic fractures at depth in crystalline rock in the Cajon Pass scientific drill hole, *Journal of Geophysical Research*, 97(B4), 5181-5200.

Barton, C. C. and Larson, E., 1985, Fractal geometry of two-dimensional fracture networks at Yucca Mountain, Southwestern Nevada, *Fundamentals of Rock Joints: Proceedings of International Symposium on Fundamental of Rock Joints, Bjorkliden, Sweden,* edited by O. Stephannson, International Society for Rock Mechanics, 77-84.

Barton, C. C. and Hsieh, P.A., 1989, *Physical and Hydrologic-Flow Properties of Fractures, Field Trip Guideb.*, T385, AGU, Washington, D. C..

Bridges, M. C., 1976, Presentation of fracture data for rock mechanics, *Proceedings 2nd Australian – New Zealand Conference on Geomechanics*, Brisbane, 144-148.

Bristow, J.R., 1960, Microcracks and the static and dynamic elastic constants of annealed and heavily conventional-worked metals. *British J. Appl. Phys.* 11, 81-85.

Bruner, W.M., 1976, Comment on 'Seismic Velocities in Dry and Saturated Cracked Solids' by Richard J. O'Connell and Bernard Budiansky, *Journal of Geophysical Research*, 81(14), 2573-2576.

Budiansky, B., O'Connell, R.J., 1976, Elastic moduli of a cracked solid. *Int. J. Solids Struc.*, 12, 81-97.

Call, R. D., Savely, J., and Nicholas, D. E., 1976, Estimation of joint set characteristics from surface mapping data. *Proceedings 17th U. S. Symposium on Rock Mec*hanics, 2B2-1 – 2B2-9.

Childs, E.C., 1957, The anisotropic hydraulic conductivity of soil, *Journal of Soil Science* 8(1), 42-47.

Cladouhos, T. T., and Marrett, R., 1996, Are fault growth and linkage models consistent with power-law distributions of fault lengths?, *Journal of Structural Geology*, 18, 281-293.

Clark, M.B., Brantley, S.L. and Fisher, D.M., 1995, Power-law vein thickness distributions and positive feedback in vein growth, *Geology* 23, 975–978.

Cotterell, B., and Rice, J. R., 1980, Slightly curved or kinked cracks: *International Journal of Fracture*, 16, 155-169.

Cowie, P. A. and Scholz, C. H., 1992, Growth of faults by accumulation of seismic slip, *Journal of Geophysical Research*, 97, 11085-11095.

Crouch, S. L. and Starfield, A. M., 1983, *Boundary Element Methods in Solid Mechanics*, George Allen and Unwin, London, U. K..

Cruikshank, K.M., Zhao, G., and Johnson, A. M., 1991, Analysis of minor fractures associated with joints and faulted joints, *Journal of Structural Geology*, 13, 865-886.

Cruikshank, Kenneth M. and Aydin, Atilla, 1994, Role of fracture localization in arch formation, Arches National Park, Utah, *Geological Society of America Bulletin*, 106, 879-891.

Dieter, G. E. 1976, *Mechanical metallurgy*, New York, McGraw-Hill, 774.

Dershowitz, W. S. and Einstein, H. H., 1988, Characterizing rock joint geometry with joint system models. *Rock Mech. Rock Eng*., 21, 21-51.

Dey, T.N. and Wang, C.Y., 1981, Some mechanisms of microcrack growth and interaction in compressive rock failure, *International Journal of Rock Mechanics and Mining Science*, 18, 199-209.

Dyer, R., 1988, Using joint interactions to estimate paleostress ratios, *Journal of Structural Geology*, 10 (7), 685-699.

Einstein, H. H., Baecher, G. B., Verneziano, D. et al, 1980, Risk analysis for rock slopes in open pit mines, *Final Technical Report. Publication No. R80-17, Order No. 669*, Department of Civil Engineering, Massachusetts Institute of Technology, Cambridge, Massachusetts.

Einstein, H. H., and Baecher, G. B., 1983, Probabilistic and statistical methods in engineering geology, *Rock Mech. Rock Eng.*, 16, 39-72.

Engelder, T., and Geiser, P., 1980, On the use of regional joint sets as trajectories of plaeostress fields during the development of the Appalachian Plateau, New York, *Journal of Geophysical Research*, 85, 6319-6341.

Erdogan, F. and Sih, G. C., 1963, On the crack extension in plates under plane loading and transverse shear. *ASME Transactions*, 85, 519-527.

Griffith, A. A., 1924, The theory of rupture, *In Proc. First Internat. Congr. Appl. Mech. (ed. C. B. Biezeno and J. M. Burgers),* J. Waltman Jr. Delft, 55-63.

Gross, M. R., 1993. The origin and spacing of cross joints: Examples from the Monterrey Formation, Santa Barbara coastline, California, *Journal of Structural Geology*, 15, 737–751.

Gross, M. R., Fischer, M. P., Engelder, T and Greenfield, R, 1995, Factors controlling joint spacing in interbedded sedimentary rocks: integrating numerical models with field observations from the Monterey Formation, USA, *Fracture topography as a tool in fracture mechanics and stress analysis*, Geological Society Special Publication No. 92, 215-233.

Gudmundsson, 1987, Geometry, formation and development of tectonic fractures on the Reykjanes Peninsula, southwest Iceland, *Tectonophysics* 139, 295–308

Hatton, C.G., Main, I.G. and Meredith, P.G., 1994, Non universal scaling of fracture length and opening displacement, *Nature* 367, 160–162.

Hatzor, Y.H. and Palchik, V., 1997, The influence of grain size and porosity on crack initiation stress and critical flaw length in Dolomites, *Int. J. Rock Mech. Min. Sci.*, 34(5), 805-816.

Heffer, K.J. and Bevan, T.G., 1990, Scaling relationships and natural fractures: data, theory and applications, *Society of Petroleum Engineers*, 20981, 367–376.

Hennings, P., Olson, J. and Thompson, L., 2000, Combining outcrop and 3-d structural modeling to characterize fractured reservoirs, *American Association of Petroleum Geologists Bulletin*, 84(6), 830-849.

Hirata, T., 1989, Fractal dimension of fault systems in Japan: Fractal structure in rock fracture geometry at various scales, *Pure Appl. Geophys.*, 131, 157-170.

Holder, Jon, Olson, Jon E., and Philip, Zeno, 2001, Experimental determination of subcritical crack growth parameters in sedimentary rock, *Geophysical Research Letters*, 28 (4), 599-602.

Hudson, J. A. and Priest, S. D., 1983, Discontinuity frequency in rock masses, *Int. J., Rock Mech. Min. Sci. Geomech. Abstr.*, 20, 73-89.

Ingraffea, Anthony R., 1987, Theory of crack initiation and propagation in rock. In: Atkinson, B.K. (Ed.), *Fracture Mechanics of Rock*. Academic Press, London, 277-349.

Irwin, G. R., 1958, Fracture. In: *Encyclopedia of Physics*, edited by S. Flugge, Springer-Verlag, Berlin, 551-590.

Jaeger, J.C. and Cook, N.G.W., 1976, *Fundamentals of Rock Mechanics*, Chapman and Hall, London.

Jensen, J. L., Lake, L. W., Corbett, P. W.M. and Goggin, D. J., 1997, *Statistics for Petroleum Engineers and Geoscientists*, Prentice Hall PTR, USA.

Johnston, J.D. and McCaffrey, K.J.W., 1996, Fractal geometries of vein systems and the variation of scaling relationships with mechanism, *Journal of Structural Geology*, 18, 349–358.

Kachanov, M., 1987, Elastic solids with many cracks: A simple method of analysis, *International Journal of Solids and Structures, 23(1), 23-43.*

Kachanov, M., 1992, Effective elastic properties of cracked solids: critical review of some basic concepts, *Appl. Mech. Rev.*, 45(8), 304-335.

Kalthoff, J. F., in *Dynamic Crack Propagation*, Noordhoff International Publishing, Leyden, 449-458.

Karihaloo, B. L., Keer, L. M., and Nemat-Nasser, S., 1980, Crack kinking under nonsymmetric loading: *Engineering Fracture Mechanics*, 13, 879-888.

Kirby, S. H., 1984, Introduction and digest to the special issue on chemical effects of water on the deformation and strengths of rocks, *Journal of Geophysical Research*, 89, 3991-3995.

Kranz, R.L., 1979, Crack-crack and crack-pore interactions in stressed granite, *International Journal of Rock Mechanics and Mining Science*, 16, 37-47.

Kreyszig, Erwin, 1993, *Advanced Engineering Mathematics*, John Wiley & Sons, Inc., USA.

Kulatilake, P.H.S.W., Wathugala, D.N., and Stephansson, O., 1993, Joint network modeling with a validation exercise in Stripa mine, Sweden, *Int. J. Rock Mech. Min. Sci. and Geomech. Abstr.*, 30(5), 503-526.

LaPointe, P.R. and Hudson, J.A., 1985, Characterization and interpretation of rock mass joint patterns, *Geological Society of America Special Paper* 199, 37.

LaPointe, P.R., 1988, A method to characterize fracture density and connectivity through fractal geometry, *Int. J. Rock Mech. Min. Sci. Geomech.,* 25, 421-429.

Lachenbruch, A. H., 1961, Depth and spacing of tension cracks, *Journal of Geophysical Research 66,* 4273-4292.

Laubach, S., 1997, A method to detect natural fracture strike in sandstones, *AAPG Bulletin,* 81(4), 604-623.

Laubach, S., Marrett, R. and Olson, J. E., 2000, New directions in fracture characterization, *The Leading Edge*, 704-711.

Lawn, B. R., and Wilshaw, T. R., 1975, *Fracture of Brittle Solids*, Cambridge, England, Cambridge University Press, 204.

Lorenz, J.C., Warpinski, N.R., and et al., 1988, Results of the Mulitwill experiment: In situ stresses, natural fractures and other geologic controls on reservoirs, *EOS*, Aug. 30, 817-826.

Lorenz, J. C. and Warpinski, N. R., 1996, Natural fracture characteristics and effects, *Leading Edge,* 15(8), 909-911.

Love, A. E. H., 1927, A *Treatise on the Mathematical Theory of Elasticity*, Cambridge University Press, pp. 643.

MacMahon, B., 1974, Design of rock slopes against sliding on preexisting surface. *3rd International Symp. On Rock Mechanics*, II-B, 803-808.

Mandelbrot, B. B., 1982, The fractal geometry of nature, Freeman, San Francisco.

Marrett, R., 1997. Permeability, porosity, and shear-wave anisotropy from scaling of open fracture populations. In: Hoak, T.E., Klawitter, A.L. and Blomquist, P.K. Editors, 1997. *Fractured Reservoirs: Characterization and Modeling Guidebook* Rocky Mountain Association of Geologists, 217–226.

Marrett, R., Ortega, O.J. and Kelsey, C.M., 1999. Extent of power-law scaling for natural fractures in rock. *Geology* 27, 799–802

Muller, O. H., and Pollard, D. D., 1977, The stress state near Spanish Peaks, Colorado, determined from a dike pattern, *Pure Appl. Geophys.*, 115, 69-86.

Muskhelishvili, N. I., 1954, *Some Basic Problems of Mathematical Theory of Elasticity,* P. Noordhoff Ltd., Groningen, The Netherlands.

Nelson, R.A., 1985, *Geologic Analysis of Naturally Fractured Reservoirs*, Gulf Publishing Co., Houston, Texas, 1985.

Nicol, A., Walsh, J. J., Watterson, J., and Gillespie, P.A., 1996, Fault size distributions – are they really power-law?, *Journal of Structural Geology*, 18, 191–197.

Nuismer, R. J., 1975, An energy release rate criterion for mixed mode fracture, *International Journal of Fracture*, 11, 245-250.

Nur, A., 1982, The origin of tensile fracture lineaments, *Journal of Structural Geology*, 4, 31-40.

O'Connell, J. R., and Budiansky, B., 1974, Seismic velocities in dry and saturated cracked solids, Journal of Geophysical Research, 79, 5412-5426.

Ode, H., 1957, Mechanical analysis of the dike pattern of the Spanish Peaks area, Colorado, *Geological Society of America Bulletin*, 68, 567-576.

Olson, J. E., 1991, Fracture mechanics analysis of joints and veins, *Dissertation*, Stanford University.

Olson, J. E., 1993, Effects of subcritical crack growth and mechanical crack interaction. *Journal of Geophysical Research*, 98(B7), 12251-12265.

Olson, J. E., 1997, Natural fracture pattern characterization using a mechanical-based model constrained by geologic data – moving closer to a predictive tool. *International Journal of Rock Mechanics and Mining Science*, 34(3/4), 391, Paper No. 237.

Olson, J. E. and Pollard, D. D., 1989, Inferring paleostresses from natural fracture patterns: A new method, *Geology*, 17, 345-348.

Olson, J. E. and Pollard, D. D., 1991, The initiation and growth of en echelon veins, *Journal of Structural Geology*, 13(5), 595-608.

Olson, J. E., Hennings, P. H., and Laubach, S. E., 1998, Integrating wellbore data and geomechanical modeling for effective characterization of naturally fractured reservoirs. *SPE* 47352.

Olson, J. E., Qiu, Y., Holder, J. and Rijken, P., 2001, Constraining the spatial distribution of fracture networks in naturally fractured reservoirs using fracture mechanics and core measurements. *SPE Annual Technical Conference and Exhibition: New Orleans, L.A., SPE 71342*.

Ortega, O. and Marrett, R., 2000, Prediction of macrofracture properties using microfracture information, Mesaverde Group sandstones, San Juan basin, New Mexico, *Journal of Structural Geology*, 22, 571-588.

Pollard and Muller, 1976, The effect of gradients in regional stress and magma pressure on the form of sheet intrusions on cross section, *Journal of Geophysical Research*, 81, 975-988.

Pollard, D. D., Segall, P., and Delaney, P.T., 1982, Formation and interpretation of dilatant echelon cracks: *Geological Society of America Bulletin*, 93, 1291-1303.

Pollard, D. D. and Aydin, A., 1984, Propagation and linkage of oceanic ridge segments, *Journal of Geophysical Research*, 89(B12), 10,017-10,028.

Pollard, D. D. and Segall, P., 1987, Theoretical displacements and stresses near fractures in rocks: with applications to faults, joints, veins, dikes and solution surfaces. In: Atkinson, B.K. (Ed.), *Fracture Mechanics of Rock*. Academic Press, London, 277-349.

Pollard, D. D. and Aydin, A., 1988, Progress in understanding jointing over the past century, *Geological Society of America Bulletin*, 100, 1181-1204.

Pfiffner, O.A. and Ramsay, J.G., 1982, Constraints on geological strain rates: arguments from finite-strain states of naturally deformed rocks, *Journal of Geophysical Research*, 87(B1), 311-321.

Renshaw, C. E., 1993, Modeling fluid migration through physically-based fracture networks, *Dissertation*, Stanford University.

Renshaw, C. E., 1994, Are large differential stresses required for straight fracture propagation paths? *Journal of Structural Geology*, 16 (6), 817-822.

Renshaw, C. E. and Park, J. C., 1997, Effect of mechanical interactions on the scaling of fracture length and aperture, *Nature*, 386, 482-484.

Rice, J. R., 1978, Thermodynamics of the quasi-static growth of Griffith cracks: *Journal of Mechanics and Physics of Solids*, 26, 61-78.

Rives, T., Razack, M., Petit, J. P. and Rawnsley, K.D., 1992, Joint spacing: analogue and numerical simulations, *Journal of Structural Geology*, 14(8/9), 925-937.

Robertson, A., 1970, The interpretation of geological factors for use in slope stability. *Proc. Symp. On the Theo. Background to the Planning of Open Pit Mines with Special Ref. To Slope Stability*, 55-71.

Scholz, C. H., 1997, Scaling properties of faults and their populations, *Int. J. Rock Mech. Min. Sci.*, 34(3/4), 348.

Secor, D.T., 1965, Role of fluid pressure in jointing, *Amer. J. Sci.*, 263, 633-646.

Secor, D.T., 1969, Mechanics of natural extension fracturing at depth in the earth's crust, in Baer, A.J., and Norris, D.K., eds., *Research in tectonics: Geological Survey of Canada Special Paper* 68-52, 3-47.

Segall, P., 1984a, Formation and growth of extensional fracture sets. *Geological Society of America Bulletin*, 95, 454-462.

Segall, P., 1984b, Rate-dependent extensional deformation resulting from crack growth in rock. *Journal of Geophysical Research*, 89, 4185-4195.

Segall, P., and Pollard, D. D., 1983, Joint formation in granitic rock of the Sierra Nevada, *Geological Society of America Bulletin*, 94, 563-575.

Sih, G. C. 1974, Strain-energy-density factor applied to mixed mode crack problems, *International Journal of Fracture*, 10, 305-321.

Stowell, J.F.W., 2000, Specifying lengths of horizontal wells in fractured reservoirs: *Society of Petroleum Engineers*, SPE 65458.

Strifors, H. C., 1974, A generalized force measure of conditions at crack tip, *International Journal of Solids and Structures*, 10, 1389-1404.

Swanson, P.L., 1984, Subcritical crack growth and other time- and environment behavior in crustal rocks, *Journal of Geophysical Research*, 89(B6), 4137-4152.

Tamuzs V. and Petrovab V., 1999, Modified model of macro-microcrack interaction, *Theoretical and Applied Fracture Mechanics*, 32(2), 111-117.

Tchalenko, J. S., 1970, Similarities between shear zones of different magnitudes, *Geol. Soc. Am. Bull.*, 81, 1625-1640.

Teufel, L.W. and Clark, J.A., 1984, Hydraulic fracture propagation in layered rock: Experimental studies of fracture containment, *Soc. Petrl. Engrs.J.*, 24, 19-32.

Thomas, A. L., and Pollard, D. D., 1993, The geometry of echelon fractures in rock: Implications from laboratory and numerical experiments, *Journal of Structural Geology*, 15(3-5), 323-334.

Walsh J. B., 1965, The effect of cracks on the uniaxial elastic compression of rocks, *Journal of Geophysical Research*, 70(2), 399-411.

Warburton, P. M., 1980, A stereological interpretation of joint trace data, *Int. J. Rock Mech. Min. Sci. Geomech. Abstr.*, 17, 181-190.

Warren, J. E. and Root, P.J., 1963, The behavior of naturally fractured reservoirs, *SPE Journal*, 245-255.

Wilkins, B.J., 1980, Slow crack growth and delayed failure of granite, *Int. J. Rock Mech. Min. Sci. Geomech. Abstr.*, 17, 365-369.

Wu, C. H., 1978, Fracture under combined loads by maximum energy release rate criterion, *Journal of Applied Mechanics*, 45, 553-558.

Vita

Yuan Qiu was born on May 16, 1969 in Jining, Inner Mongolia, P. R. China. Her father is Bangliang Qiu and mother is Yunyan Sun. She received her B.S. in geology in 1990 from Peking (Beijing) University (PKU), and her M.S. in applied geophysics in 1993 form Beijing Graduate School, China University of Mining & Technology (CUMT). She worked there as a lecturer and researcher in Data Processing Center for three and a half years. In August 1996, she was admitted to the Ph.D. program in the Department of Petroleum and Geosystems Engineering, The University of Texas at Austin. Her supervisor is Dr. Jon E. Olson. In 1997 and 1998, she worked for Exploration & Production Department, Texaco as a summer intern.

Permanent address: Yuan Qiu c/o Delores Holubec
6000 Sun Vista
Austin, TX 78749
USA

This dissertation was typed by Yuan Qiu.

8. Appendix 2: FRAC Technology Transfer Meeting

The Fracture Research and Application Consortium is an industrial sponsors group the funds much of our research related to fractured reservoirs and provides much of the cost-sharing for the DOE contract. This group consists of 8 to 10 member companies (membership varies from year to year). This appendix includes the handouts for the presentations made at two review meetings: one in Monterey, Mexico in February 2002 and another in Jackson Hole, Wyoming in June 2002. Representatives from the following companies attended at least one of these meetings: PEMEX, Schlumberger, Chevron, Marathon, Devon, YPF-Reposl, PDVSA, Shell, Tom Brown, Inc., Williams Petroleum and Petrobras.

The purpose of the meeting in Mexico was to review the fracture mechanics aspects of the research and then present a field seminar on fracturing related to folding. The outcrops in the Sierra Madre Oriental in the vicinity of Monterrey are an excellent opportunity to view these relationships. The summer meeting in Jackson Hole, Wyoming reviewed the entire program for the year, with the highlight of a field trip in western Wyoming looking at the Frontier Formation in the Fold and Thrust Belt. The Frontier is of particular interest because it is a major tight gas play in the Rocky Mountatins.

Fracture Research and Application Consortium

Agenda, Day 1 Sunday February 24

Background Review for Application Meeting

2.00pm – 5.00pm, 24th February 2002

Conference Room, Chipinque Hotel
Monterrey, Mexico

2.00–4.00pm **Review** (1st van group from airport)

- New methods and technologies for reservoir characterization (in Spanish)
    - Issues in fracture characterization
    - Structural diagenesis, microfractures, and surrogates
    - Quantifying fracture intensity using scaling principles
    - Measuring fracture quality. Where are the open fractures?
    - Predicting fractures.
        - Subcritical crack index tests and geomechanical models
- Discussion
- Fracture intensity quantification and scaling exercise (in English)
- Introduction to structural diagenesis
- Example case study (optional if time allows)

Concurrent posters

5.00–5:45pm **Sum up background review** (2nd van group from airport)

Concurrent posters

6.00–7:00pm Informal discussion and posters (3rd van group from airport)

Fracture Research and Application Consortium

Agenda, Day 2 Monday February 25

Application Meeting
8.00am – 1.00pm, 25th February 2002

Conference Room, Chipinque Hotel
Monterrey, Mexico

8.15am Welcome and overview

1. Objectives of morning presentations and application exercise
2. Relation of morning presentations and exercises to Tuesday field trip
3. Plans for discussion and setting research agenda in context of presentations, exercises and field example

8.30am– 12.45pm Morning presentations (Olson, Holder)
Fracture Prediction. Fracture size and spatial distribution modeling and incorporation of fractures in flow simulation. Two coffee breaks planned for am.

Introduction to fracture mechanics and applications to
-fracture aperture and relation to length
-fracture connectivity
-fracture length distribution shape
-fracture spacing

Subcritical crack growth and geomechanical modeling
-look at fracture spacing and clustering
-generate fracture aperture distributions
-constrain modeling with in situ measurements

Applications to flow modeling
-what do analytical models say
-use geomechanical patterns in ECLIPSE simulation
-what fracture parameters are important for flow
-influence of mineral infilling of fractures

Case studies

12:45 – 1.00pm Sum up morning session; plan for evening session and field trip

1.00 – 2.45pm Buffet in hotel (comida Mexican style) and posters

2.45 – 4:45pm Discussion and setting of research agenda

4.45 – 6.00pm Fracture intensity exercise and discussion (Gale, Laubach, Marrett)

6.00 – 7.30pm Open (dinner in hotel)

7.30 – 9.00pm Introduction to field area (Marrett, Monroy)

- Structure and stratigraphy of SMO, and fold-related fracturing
- Structural diagenesis of Cupido Formation

Fracture Research and Application Consortium

Agenda, Day 3 Tuesday February 26

Field Trip

7.00am – 7.00pm, 26th February 2002

Sierra Madre Oriental
Vicinity of Monterrey, Mexico

6:30-7:00 Continental Breakfast

7:00-8:45 **Depart Hotel and Travel to First Stop**
Not described in Guidebook

8:45-10:15 **Stops 1 and 2**
Guidebook Pages 6-11

10:15-10:30 **Break with refreshments**

10:30-11:00 **Travel to Main Stops**
Guidebook Page 23

11:00-6:00 **Stops 8-10, lunch on outcrop**
Guidebook Pages 23-27, 57-123

6:00-8:00 **Return to Hotel (with optional transport to Airport if needed)**

Dinner in Monterrey after field trip.

Vans will travel to airport early am on February 27th.

Fracture Research and Application Consortium

The University of Texas at Austin

Introduction

Applications Meeting

Denver
February 2002

About FRAC

The University of Texas at Austin

Fracture Research and Application Consortium

- **Cooperative research program**
  - **Department of Petroleum & Geosystems Engineering**
  - **Department of Geological Sciences**
  - **Bureau of Economic Geology**
  - **Industry Members**

Objectives

What are the attributes of fractures in my prospect or reservoir?

- **Accurate pre-drill prediction**
- **Reliable bed-by-bed evaluation**

Conceptual Approach of FRAC

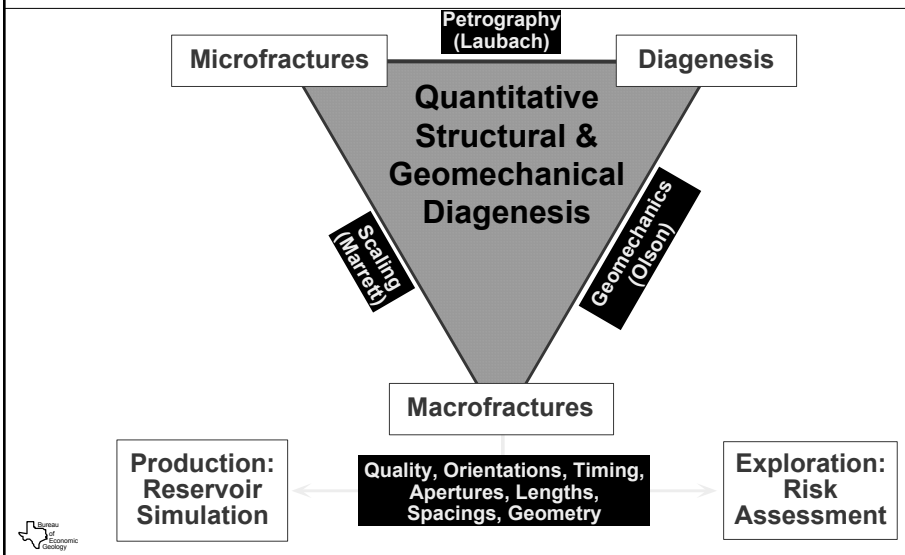

Convergence: An Example
Two Routes to Fracture Pattern Prediction

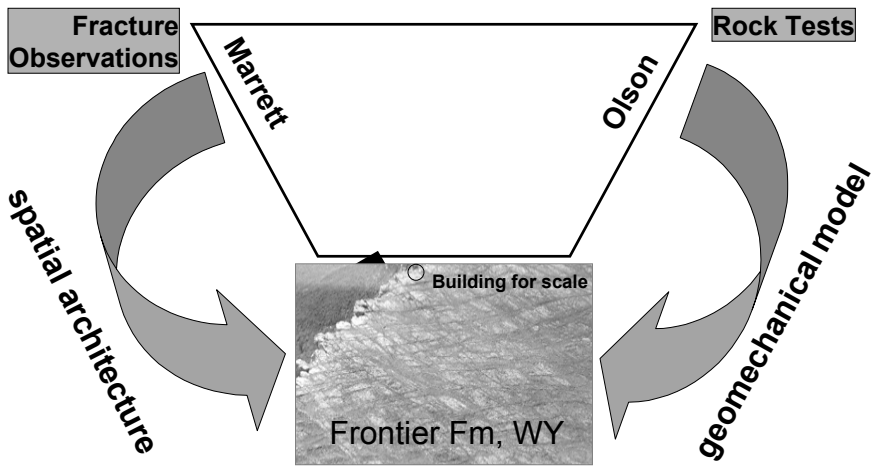

Convergence: An Example
Two Routes to Fracture Pattern Prediction

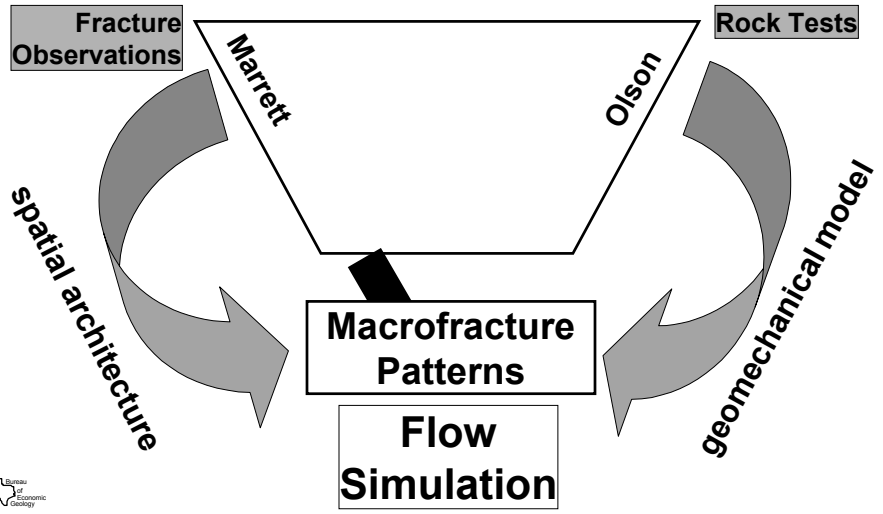

Fracture Prediction & Evaluation System

Prediction

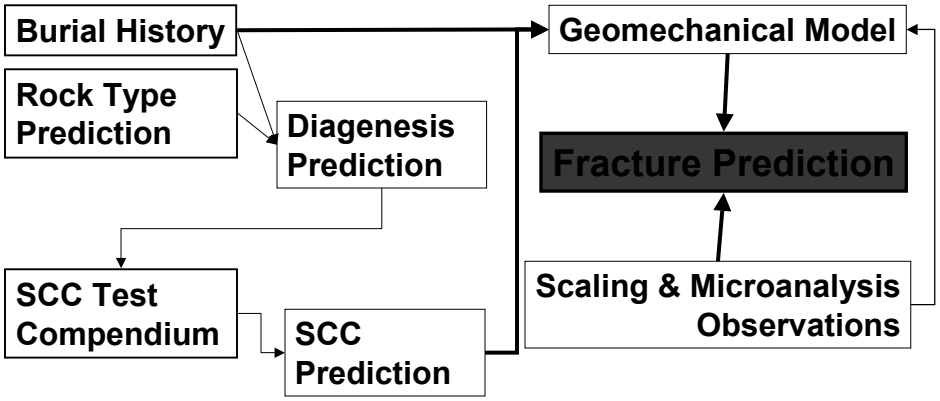

Pre-Drill Prediction **Evaluation**

Fracture Prediction & Evaluation System
Staff

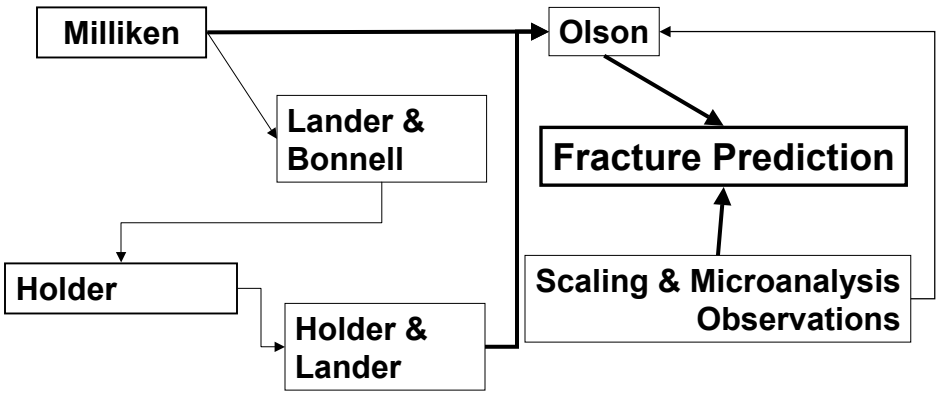

Pre-Drill Prediction **Evaluation**

Fracture Prediction & Evaluation System

Evaluation

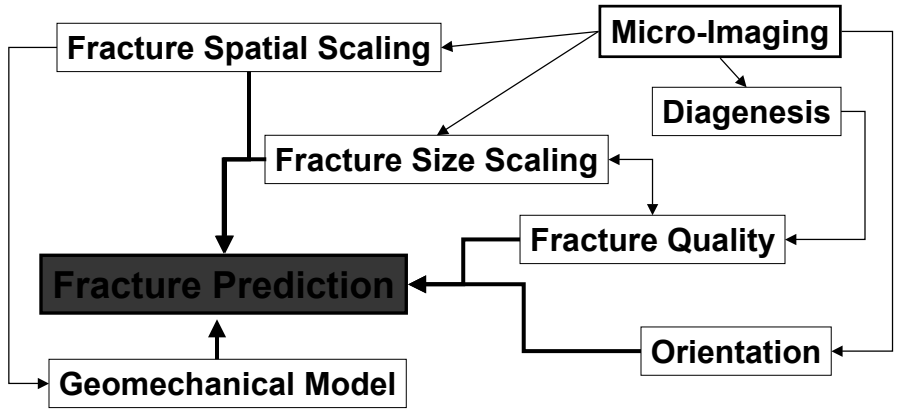

Pre-Drill Prediction **Evaluation**

Fracture Prediction & Evaluation System
Staff

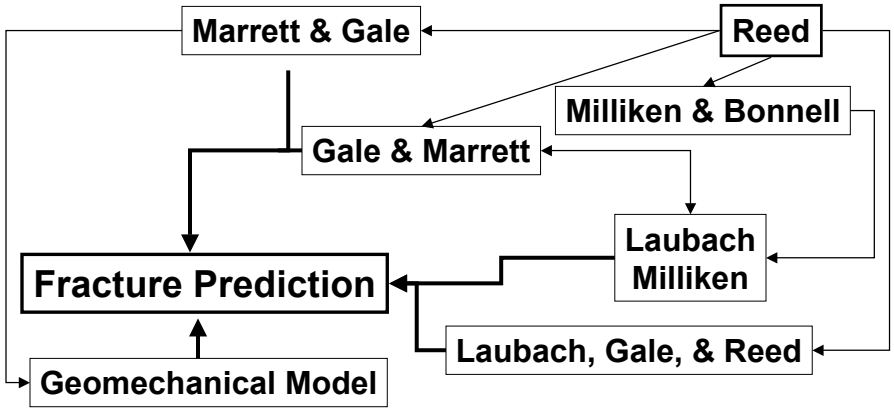

Pre-Drill Prediction **Evaluation**

Objectives

What are the attributes of fractures in my prospect or reservoir?

- **Accurate pre-drill prediction**
  - **Verifiable**
- **Reliable bed-by-bed evaluation**
  - **Solves sampling dilemma**
  - **Time/effort/cost allow for widespread deployment**
- **In addition, for both:**
  - **Suitable for calibration of seismic fracture detection**
  - **Can be incorporated in flow simulator**

Making Effective Use of Research Results

Fracture Research & Application Consortium

- **Information Transfer**
  - **Member Private Web Site**
  - **Applications Meetings**
  - **Research Meetings**
  - **Site Visits and Training for Members**
- **Effective Technology Deployment**
  - **Member Case Studies**
  - **Other**

Project Website

http://www.beg.utexas.edu/indassoc/fraccity/private/index.htm

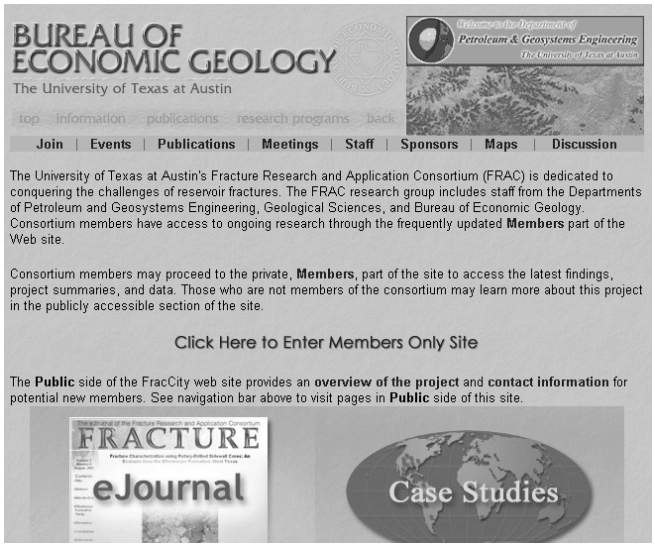

Private FRAC Project Website

http://www.beg.utexas.edu/indassoc/fraccity/private/index.htm

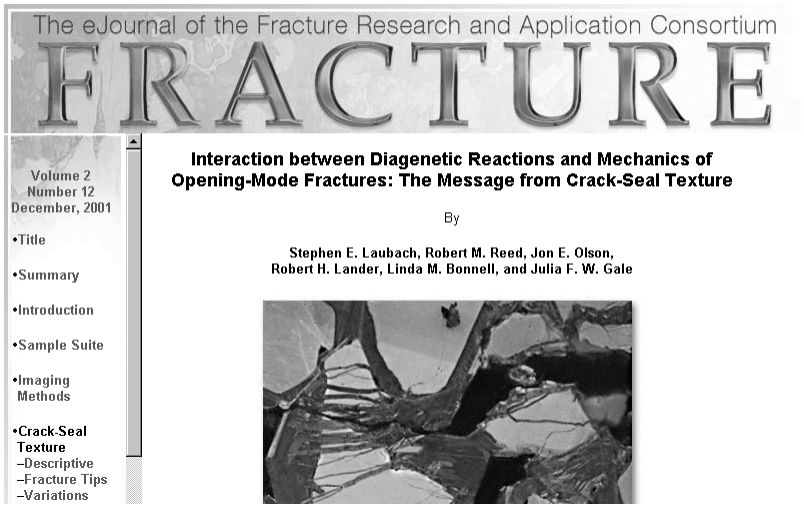

Multidisciplinary FRAC Research

- **Essential program components**
  - **Quantitative analysis of fracture populations**
  - **Geomechanical modeling**
  - **Experiments on Subcritical Crack Index**
  - **Diagenesis, microstructure, & fracture porosity**
    - **High-resolution microstructure imaging**
- **Case studies**
  - **Verify applications of research**
  - **Collaborate with Members**

Basic Fracture Questions
FRAC Solutions

• **What orientation are the fractures?**	• **Microfracture strike using oriented sidewall cores**
• **Are fractures open, closed?**	• **Microanalysis of fracture timing, degradation, emergent threshold, geochemical fingerprinting of late cements, evaluation of stress controls**
• **How large & abundant are fractures? Spacing? Swarms?**	• **Spatial scaling & geomechanical modeling linked to SCC testing, diagenetic modeling, rock property catalog**
• **Where are fractures?**	• **Geomechanical models, SCC tests, mechanical & fracture stratigraphy, calibration of seismic**

Improved Microstructure Imaging

SEM-Based Cathodoluminescence

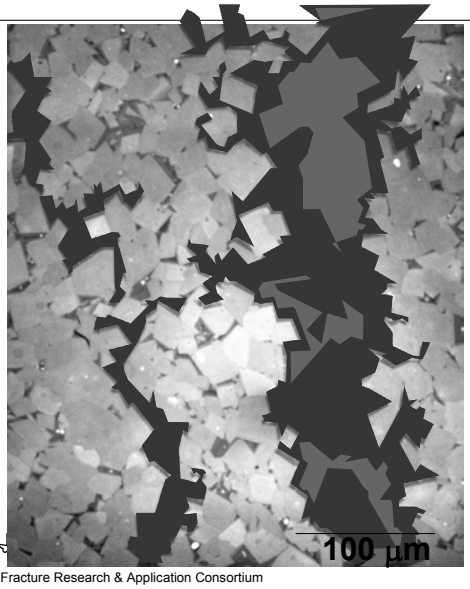

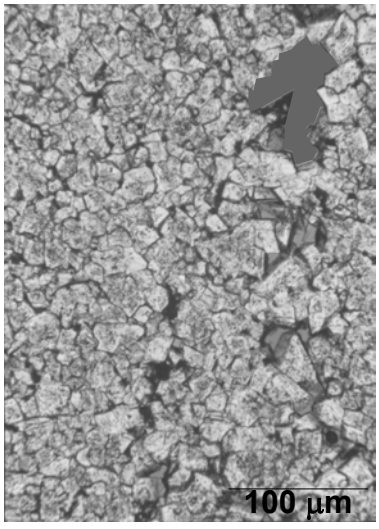

Predicting Attributes of Large Fractures

Insights from Linked Mechanics & Diagenesis Research

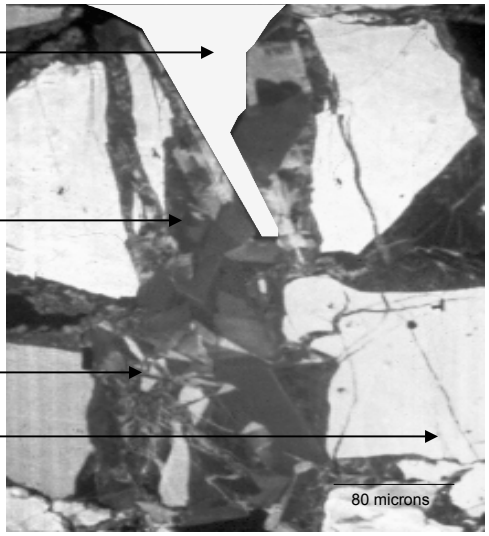

Fracture

- **Swarms ?**
- **Connectivity ?**
- **Strike ?**
- **Intensity ?**
- **Quality (Open?)**

S. Laubach, 2001, in preparation

Example: Cretaceous Lance Fm, Green River Basin, WY

Microfractures Defined

- **Engineering Usage**
  - Smaller than flow model grid block size
  - Length dimensions of meters to decimeters

- **Geological Usage**
  - Smaller than can be seen with unaided eye
    - Need a microscope
  - Length dimensions of microns to millimeters

Guides to Attributes of Large Fractures

Transgranular Microfractures Imaged Using Scanned CL

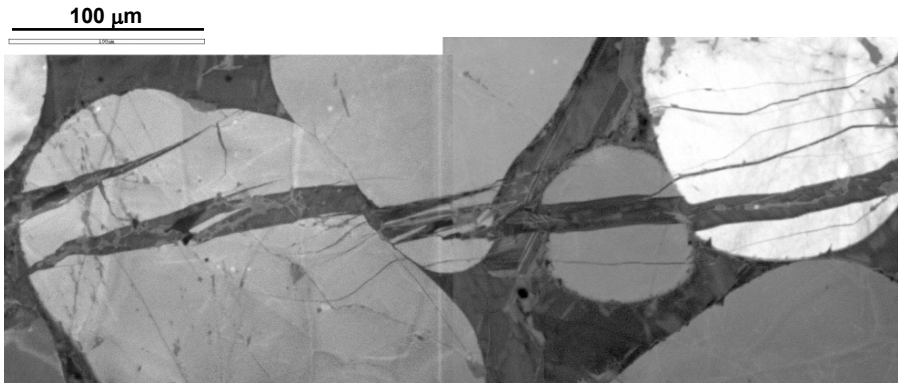

Oil Reservoir, Paleozoic, Oklahoma

Samples: Lariat Petroleum
Image: Rob Reed
LBL13404

What are Surrogates?

Microfractures

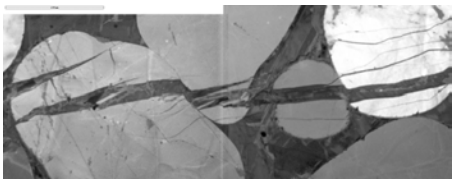

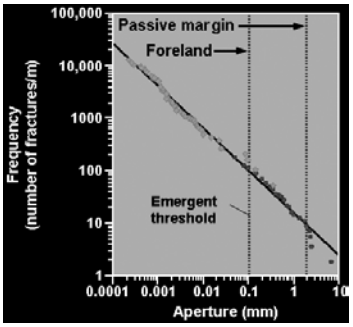

Microfracture Population Statistics

What are Surrogates?

Microfractures

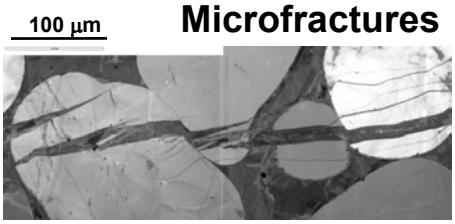

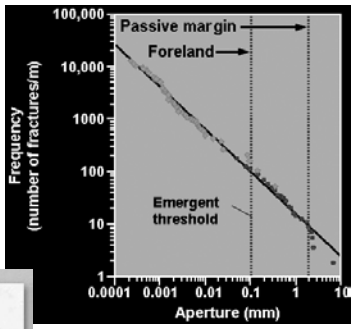

Microfracture Population Statistics

Fracture & Diagenesis Patterns

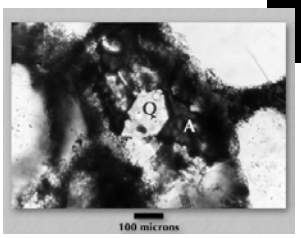

What do Surrogates Provide?

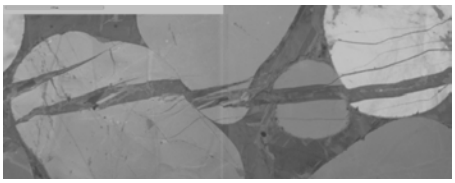

Strike

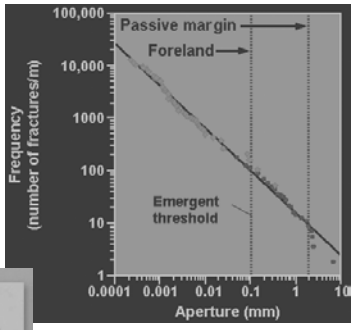

Are Fractures Open?

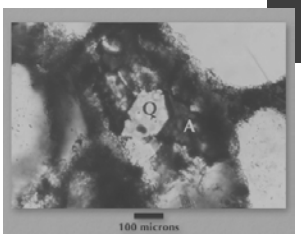

Fracture Intensity

Fracture Strike Mapping

Consistent Fracture Strike From Sidewall Cores

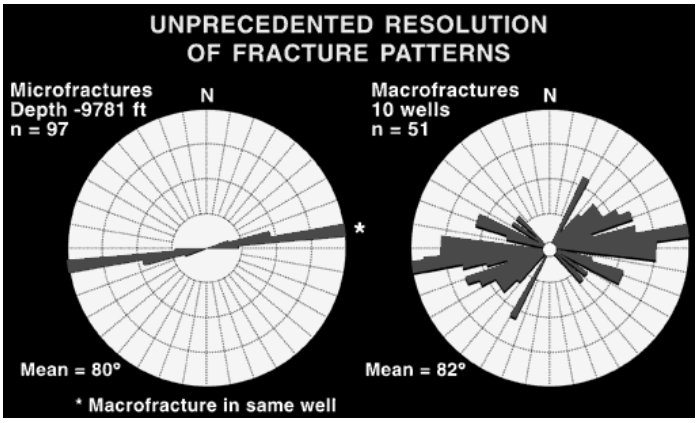

Fracture Strike

Laubach et al, 2000, The Leading Edge
Laubach, 1997, AAPG Bulletin

Where are the Open Fractures?
Fracture Quality Maps

- **Low degradation areas are fairways for open fractures**
- **Fairways predict location of exceptionally productive wells**
- **Measured rapidly from inexpensive samples**

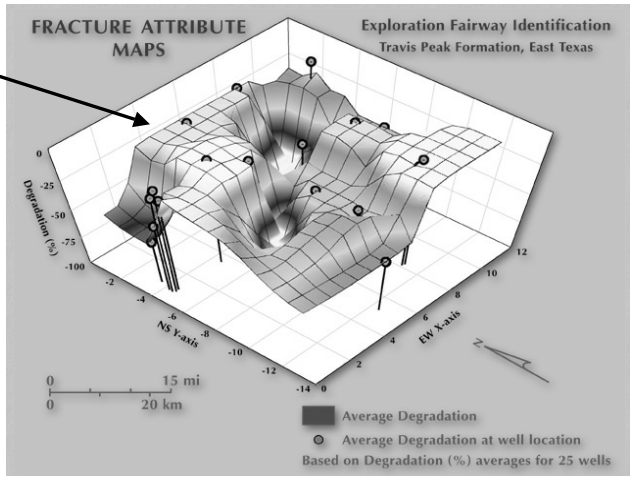

Laubach, 2001, Case Study

Measure Fracture Intensity in Any Sample
Design horizontal well length?

Microfractures & Large Fractures Follow Same Power Law

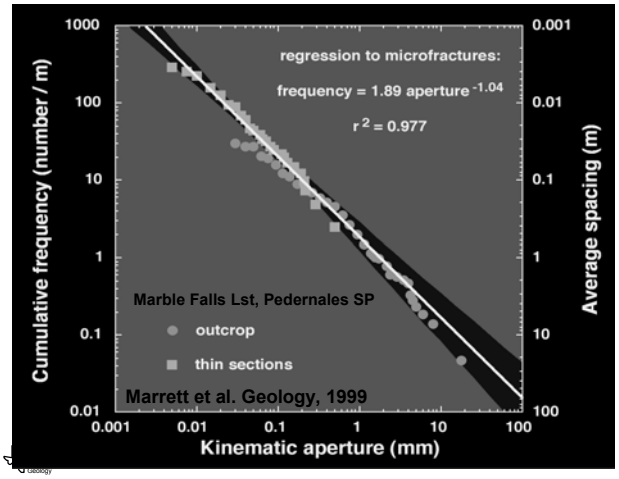

Scanned CL Image
Microfracture Detection

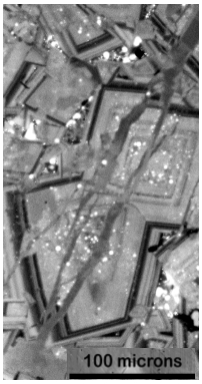

Estimate Permeability Enhancement

Threshold Frequency Prediction

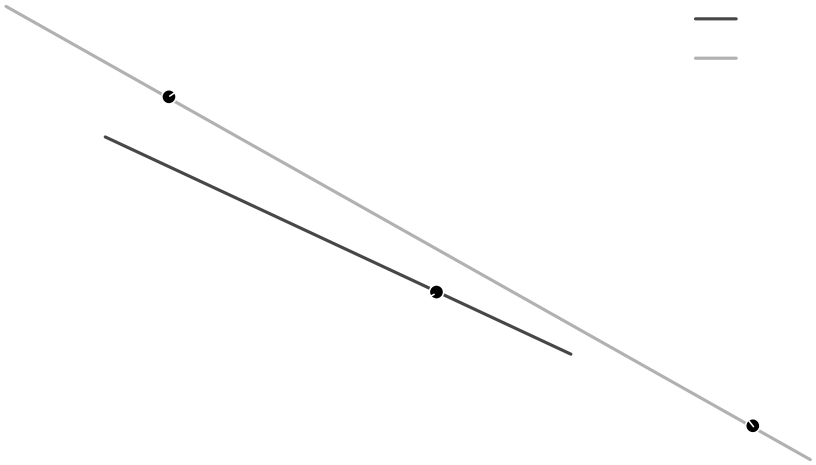

Spatial Scaling

Normalized Correlation Integral

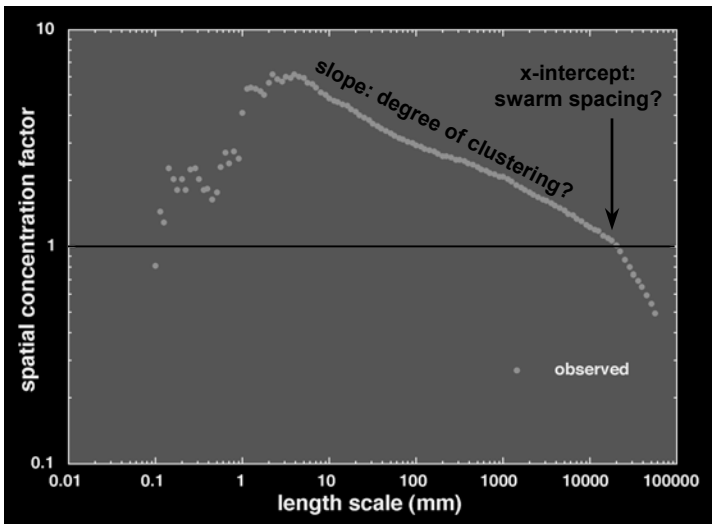

Seismic-Based Fracture Evaluation
Ground Truth is Essential

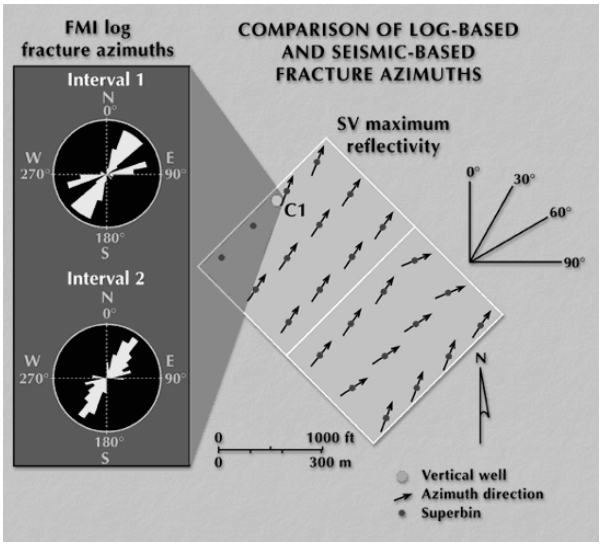

Approaches to Fracture Characterization
Solving Sampling Challenges Using Surrogates

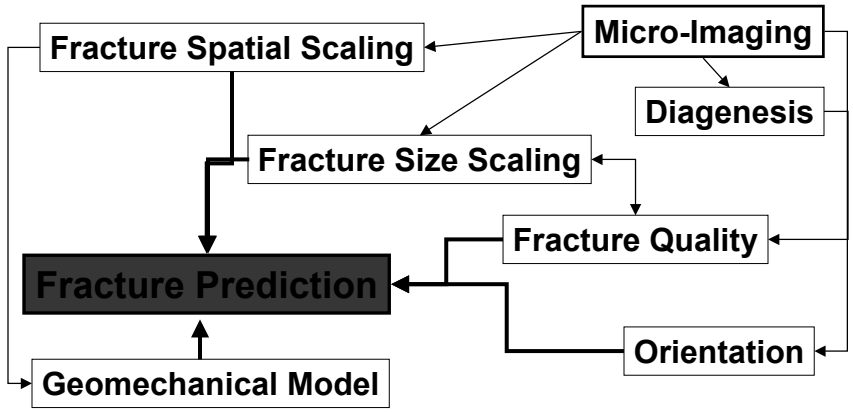

Laubach et al., The Leading Edge, July 2000

Fracture Research & Application Consortium
2002 Application Meeting, Monterrey, Mexico

Naturally Fractured Reservoirs: Characterization to Flow Modeling

Jon E. Olson
Center for Petroleum and Geosystems Engineering

The University of Texas at Austin

About FRAC

The University of Texas at Austin
Fracture Research and Application Consortium

- Cooperative research program
  - Department of Petroleum & Geosystems Engineering
  - Department of Geological Sciences
  - Bureau of Economic Geology
  - Industry Members
- Leveraged funds
  - DOE, National Petroleum Technology Office, ~$840k

Multidisciplinary FRAC Research

- Essential program components
  - Quantitative analysis of fracture populations
  - Geomechanical modeling
  - Experiments on Subcritical Crack Index
  - Reservoir Simulation of Fractured Reservoirs
  - Diagenesis, microstructure, & fracture porosity
- Case studies
  - Verify applications of research
  - Collaborate with Members

Conceptual Approach of FRAC

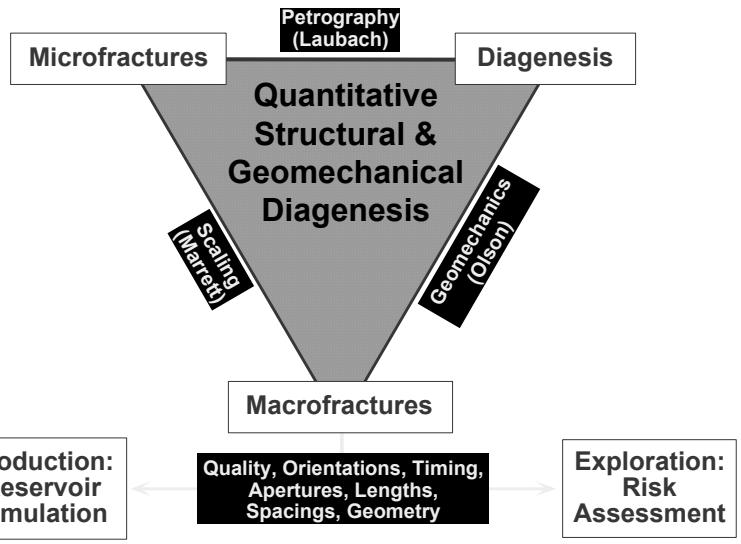

Outline for the Morning

- introduction to fracture mechanics and applications to
  - fracture aperture and relation to length
  - fracture connectivity
  - fracture length distribution shape
  - fracture spacing
- subcritical crack growth and geomechanical modeling
  - look at fracture spacing and clustering
  - generate fracture aperture distributions
  - constrain modeling with in situ measurements
- applications to flow modeling
  - what do analytical models say
  - use geomechanical patterns in ECLIPSE simulation
  - what fracture parameters are important for flow
  - case studies

Introduction to Fracture Mechanics

- fracture mechanics can be used to predict fracture attributes of interest for fluid flow
  - aperture depends on driving stress
  - spacing controlled by stress shadow
  - mechanical interaction controls fracture length
  - subcritical crack index captures dynamics of process

Kinematic Terminology

- fractures can be idealized as planar discontinuities
- modes of fracture depend on the *displacement discontinuity* at the crack tip

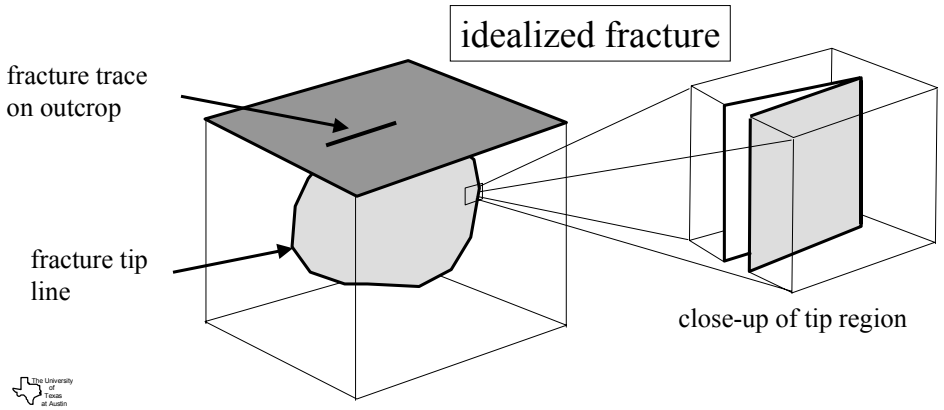

Crack Tip Displacement Modes

- look at relative motion of opposing fracture faces

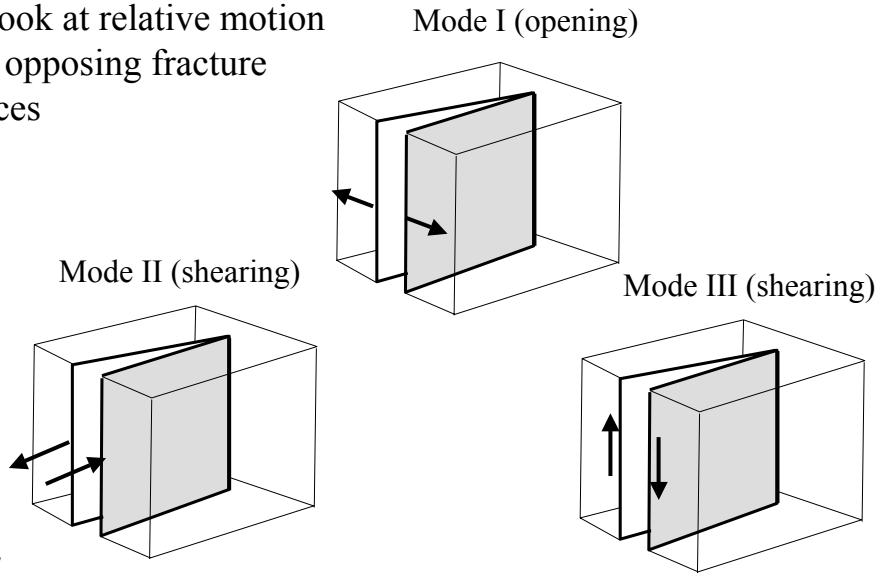

Fracture Types – Joints, Veins and Faults

- joints, veins and cracks (tensile failure)
  - a fracture with relative displacement perpendicular to fracture face = *opening mode* fractures, includes dikes and veins (~mineralized joints)
- faults (shear failure)
  - relative displacement is parallel to fracture face
  - detect displacement by shear offset of markers

Theory – Stress Concentration

- stress concentration around elliptical hole

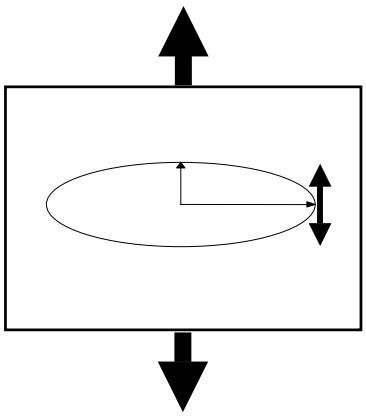

$$\sigma_{yy} = \sigma_{yy}^{remote}\left(1 + 2\frac{a}{b}\right)$$

- for a>>b,

$$\sigma_{yy} \propto \sigma_{yy}^{remote}\sqrt{a}$$

Griffith's Energy Balance

- constant stress loading (dead weight) example

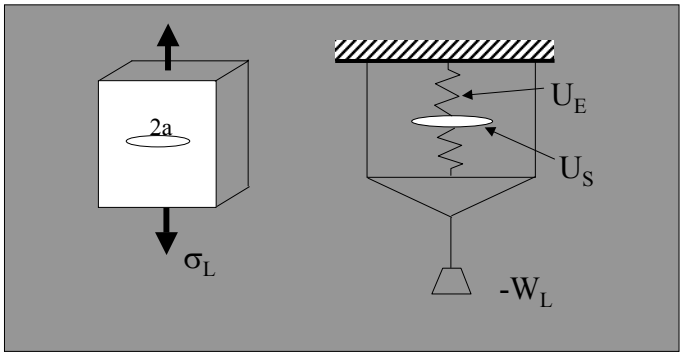

$$U_T = U_S + (U_E - W_L) + U_O$$

- Crack surface energy

$$U_S/\text{width} = 2 * 2a * \gamma$$

- Strain energy for cracked body for plane strain, uniaxial loading

$$U_E/\text{width} = \pi * a^2 * \sigma_L^2 * (1-\nu^2)/E$$

Theory – Energy Balance

- assume total energy of system is constant $\dfrac{\partial U}{\partial a} = 0$
- critical stress required for increment of crack growth (note fundamental instability)

$$\sigma_L^{crit} = \sqrt{\frac{2\gamma E}{\pi(1-\nu^2)a}}$$

- rearrange to resemble conclusion from Griffith's experiments (i.e., failure at constant $\sigma_L\sqrt{a}$)

$$\sigma_L^{crit}\sqrt{\pi a} = \sqrt{\frac{2\gamma E}{1-\nu^2}}$$

- fracture mechanics terminology
  - KI is stress intensity factor, represents loading and crack geometry
  - KIc is the fracture toughness or "strength" of material

$$K_I = K_{Ic}$$

Important Fracture Mechanics Equations

- driving stress

$$\Delta\sigma_I = P_{frac} - \sigma_n^{remote}$$

- stress intensity

$$K_I = \Delta\sigma_I\sqrt{\pi a}$$

- fracture toughness

$$K_{Ic} \cong 1-10\ \text{MPa}\text{-}\sqrt{\text{m}}$$

- crack opening equation (aperture)

$$\Delta u_I = \frac{4(1-\nu^2)}{E}\Delta\sigma_I\sqrt{a^2-x^2}$$

- aspect ratio

$$\frac{\Delta u_I}{a} = \frac{4(1-\nu^2)\Delta\sigma_I}{E}$$

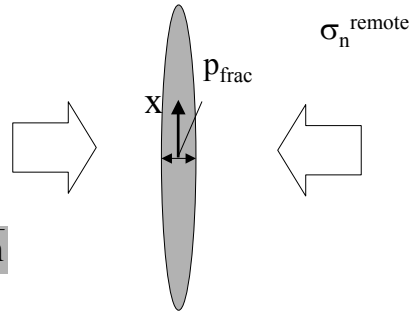

What is the mechanism for natural fracture propagation?

Natural Hydraulic Fracturing

- mode I cracks propagate ⊥ S_{hmin} (defined for extenstional tectonics)

$$S_{h\,min} = \frac{\nu}{1-\nu}(\sigma_{vert} - \alpha_p P) + \alpha_p P + \frac{E}{1-\nu^2}\varepsilon_{tect} + \frac{E\alpha_t \Delta T}{1-\nu}$$

- what defines crack propagation?

$$K_I = \Delta\sigma_I \sqrt{\pi a} = K_{Ic}$$

- define in terms of P and S_{hmin}:

$$(P - S_{h\,min})\sqrt{\pi a} = K_{Ic}$$

- pore pressure required for fracture

$$P = S_{h\,min} + \frac{K_{Ic}}{\sqrt{\pi a}}$$

Natural Hydraulic Fracturing

- for discussion sake, let's simplify the expression
  - ignore thermal & tectonic strains
  - ignore K_{Ic} (significant for initiation from microcracks, but can be counteracted by extension)

$$P = \frac{\nu\sigma_{vert}}{1 - \nu - \alpha_p(1-2\nu)}$$

- plot P required for fracture propagation as a fraction of overburden
- in most situations, conditions highly favorable for NHF

Natural Hydraulic Fracturing

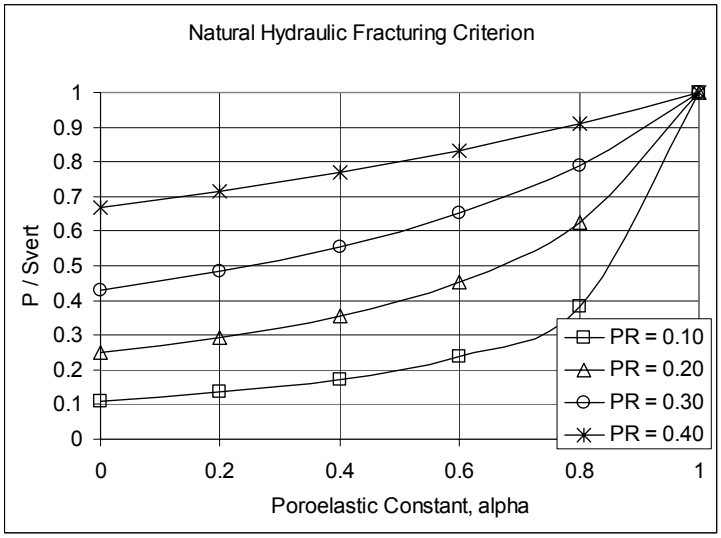

Can we predict fracture attributes?

Aperture and Length

- often observe apertures
  - from scanlines in field
  - from core or logs in wellbore
- rarely observe length
- can we predict length from aperture?
- do large aperture fractures imply deep penetration into the reservoir?

Aperture vs. Length Scaling

- Analytical opening equation (*constant stress*)

$$w = \Delta\sigma_I \frac{(1-\nu^2)}{E}(2a)$$

- Propagation criteria

$$K_{Ic} = \Delta\sigma_I \sqrt{\pi a}$$

- Combine for equilibrium crack growth (*constant K_I*)

$$w = \frac{K_{Ic}(1-\nu^2)}{E\sqrt{\pi}} 2\sqrt{a}$$

Aperture vs. Length

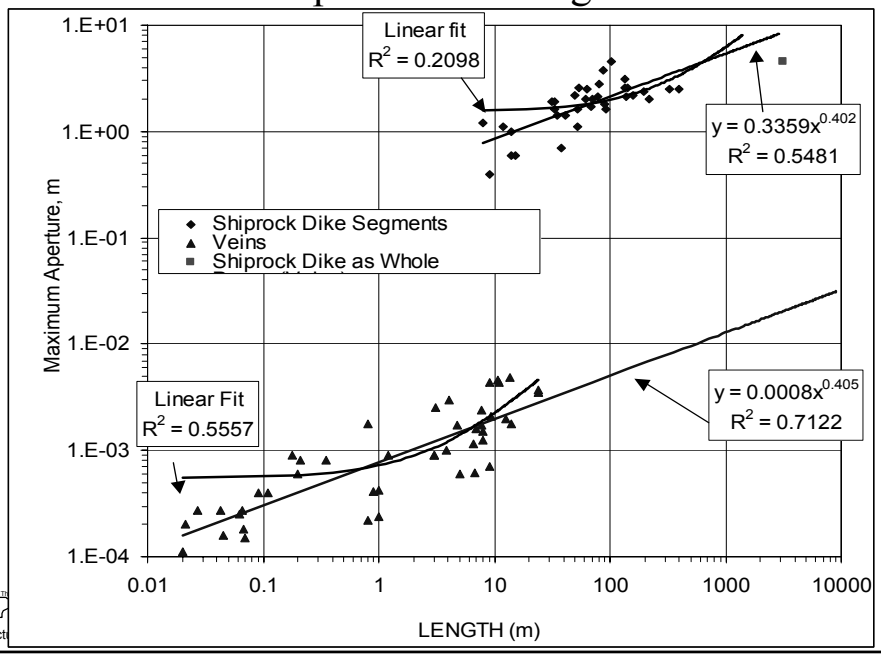

Aspect Ratio

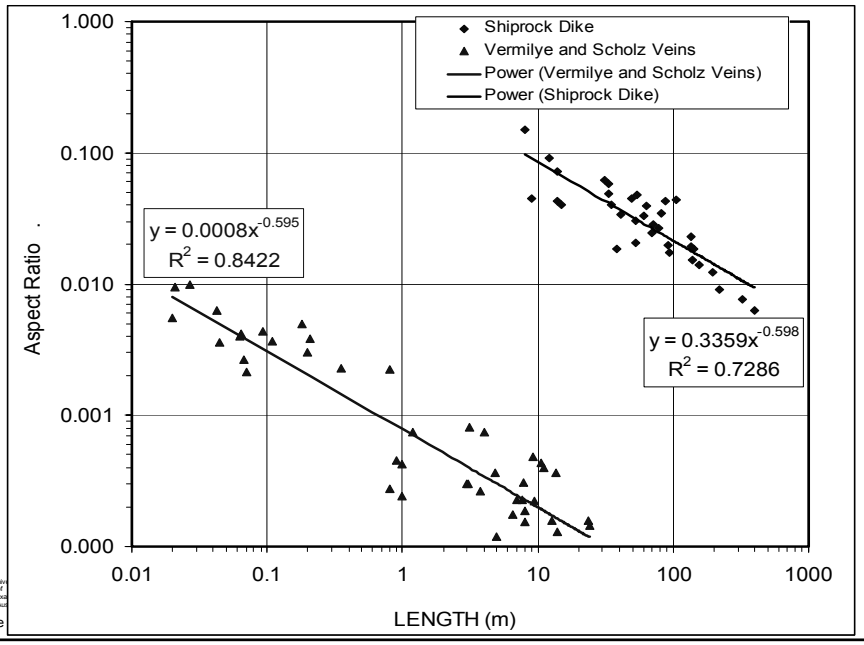

Multi-segment Array Data

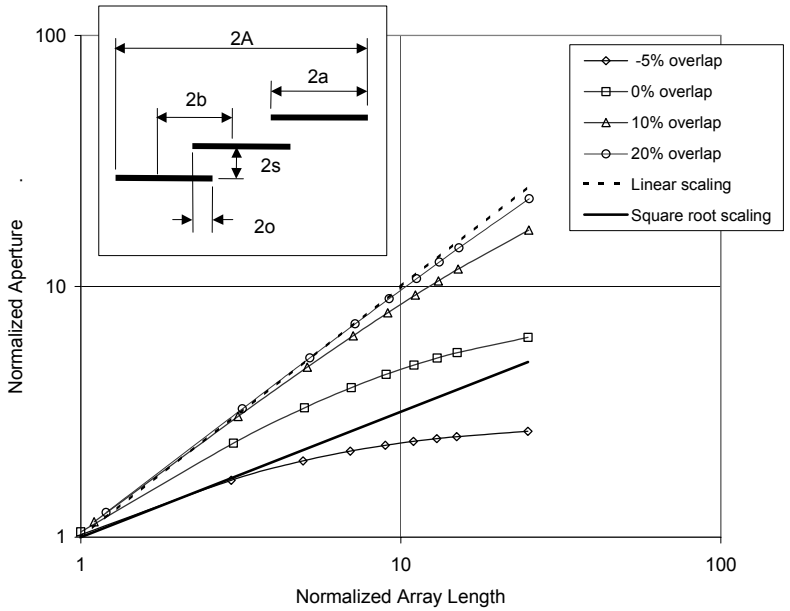

3d Effects

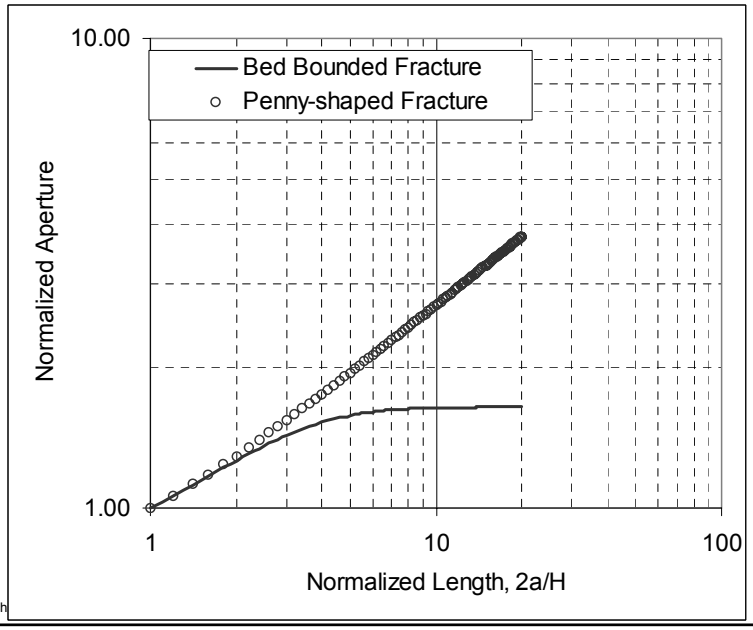

Aperture and Length Discussion

- what is the state of the fracture when cementation occurs?
  - cementation occurs simultaneously with equilibrium propagation ($K_I=K_{Ic}$), giving square root scaling
  - cementation occurs under constant stress boundary conditions, giving linear aperture to length
    - catastrophic growth during earthquakes
    - relaxed growth when no cracks are propagating
- fracture segmentation implies sub-linear aperture to length
- 3d effects predict sub-linear aperture to length

Predicting Propagation Paths and Connectivity

- natural fractures tend to occur in en echelon arrays
- array segments overlap
  - sometimes intersect
  - sometimes propagate straight

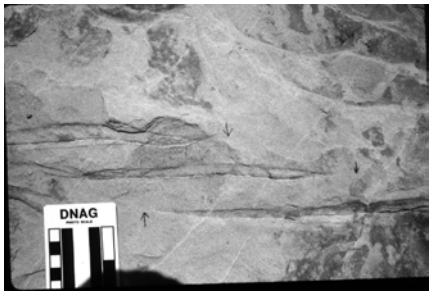

Predicting Propagation Paths and Connectivity

- look at elastic stress field around crack tip (only valid in neartip region & doesn't include remote stress contribution)
- singular stresses as r => 0

$$\sigma_{ij} = \frac{K_m}{\sqrt{2\pi r}} f_{ij}(\theta)$$

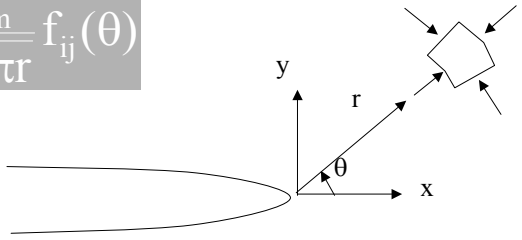

Simulation Boundary Conditions

- biaxial stress state
- pressurized crack

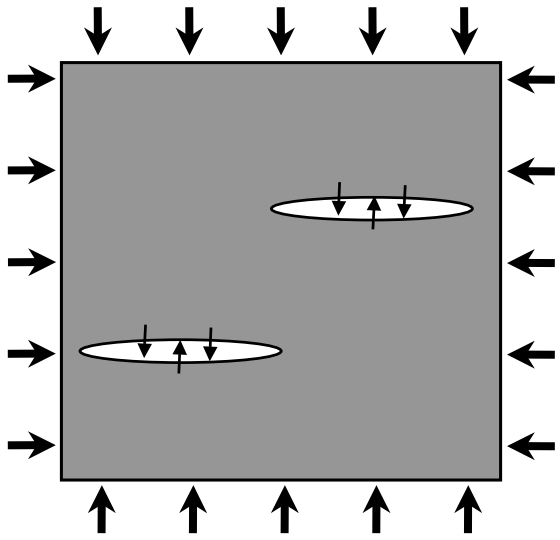

Numerical Method

- Base code => 2-d displacement discontinuity (with 3d extension)
- Propagation accomplished by adding elements at crack tip (according to propagation criterion)

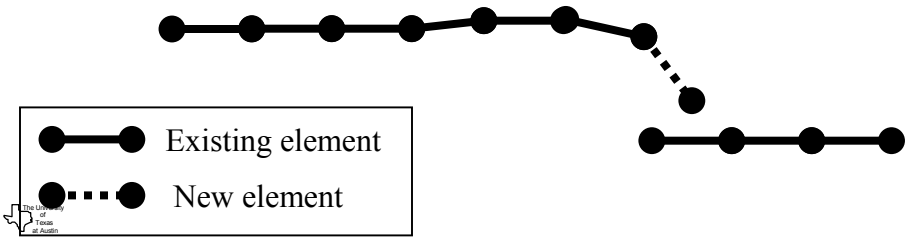

Predicting Propagation Paths and Connectivity

Simulation

Mechanical Crack Interaction

- differential stress level controls crack path hooking and intersection
- interaction initially enhances then hinders propagation => dictates length

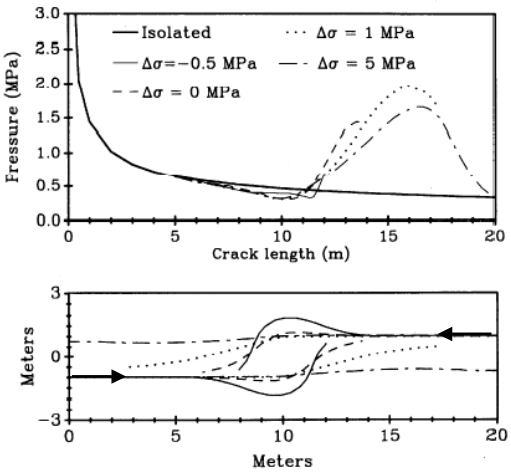

Olson and Pollard, 1989, Geology

Predicting Fracture Length Distributions Based on Mechanical Interaction

- natural fractures propagate in rocks full of flaws
- fracture interaction between propagating crack and flaws can *capture* propagating tip
- when field crack captures main crack, field crack continues propagation

Crack Tip Stress Shielding

•main crack encounters field crack
•interaction stops main crack

•field crack propagates at outer tip

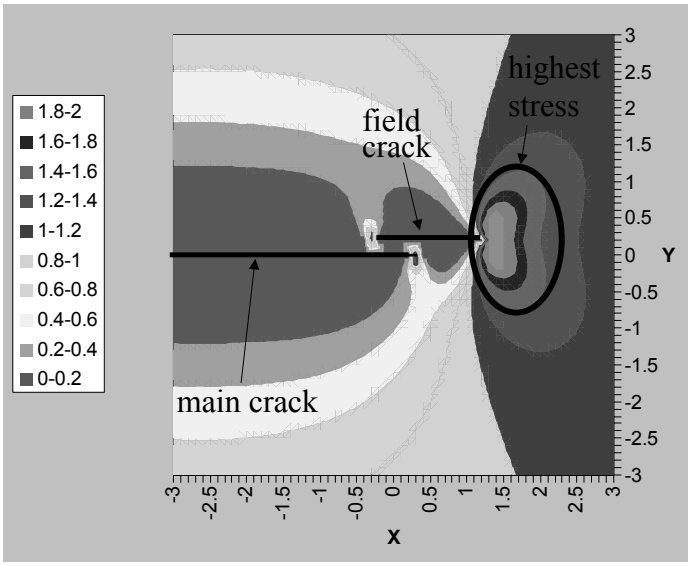

Main Crack Propagating Through Field Cracks

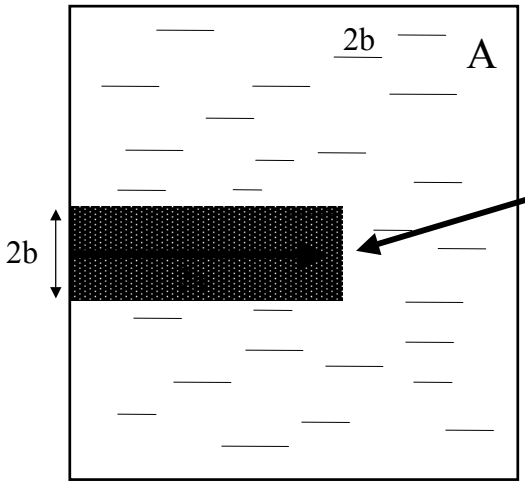

- Expect capture when spacing ≤ b
- Capture zone area

$$A_{cz} \cong (2a)(2b)$$

- Capture if *at least* one crack in A_{cz}

Theoretical Length Distribution

Probability of capture given random field cracks

$$P = 1 - \left(\frac{A - 2a \times 2b}{A}\right)^N$$

Cumulative frequency

$$F(x) = 1 - P(x) = \left(1 - \frac{2bx}{A}\right)^N$$

$$F(x) \cong e^{-x\left(2bN/A\right)}$$

when $0 < \frac{2bx}{A} << 1$

2b is flaw size, N/A is flaw density

Granite Field Case (Segall and Pollard)

b=0.5 cm
N/A = 25 ±10

predicted
exponent = .075-.125

measured
exponent = .072

(semi-log plot)

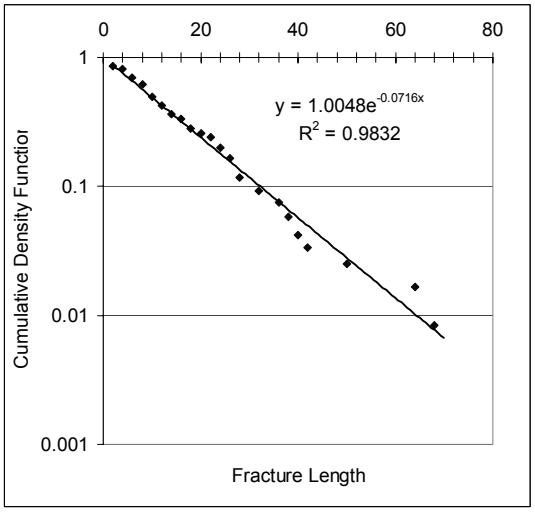

Fracture Length from Frontier Ss

- apparent power-law fit implies censor-bias starting at **80 ft**
- exponential predicts less fractures at extremes

b=1.2 mm
N/A=22/m^2

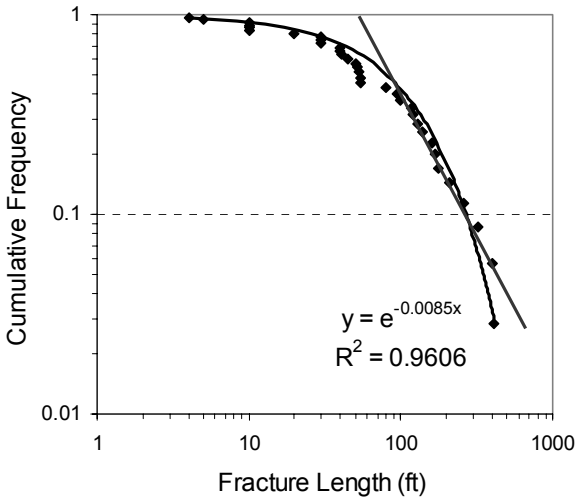

Fracture Length

- can build analytical model based on two crack interaction
- mechanical interaction can stop propagation
- simple 2d model predicts negative exponential scaling
- 3d model derived, but interaction assumptions more problematic

Geomechanical Analysis of the Spatial Organization of Fractures

Fracture Networks

- systematic fractures, with parallel sets of common morphology
- regional and local tectonic

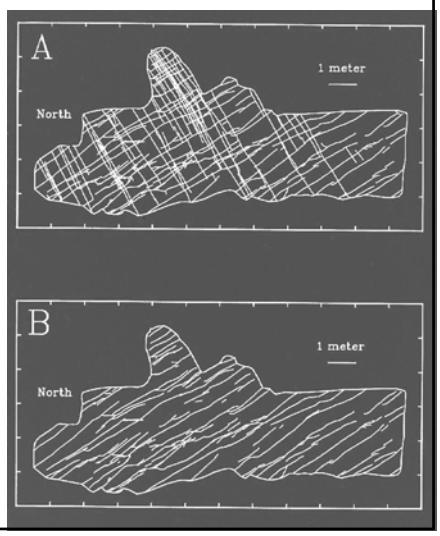

Systematic and Non-systematic Fracture Sets – Oil Mountain, Wyoming

Note:
- planarity
- spacing
- orientation
- cross-cutting relationships

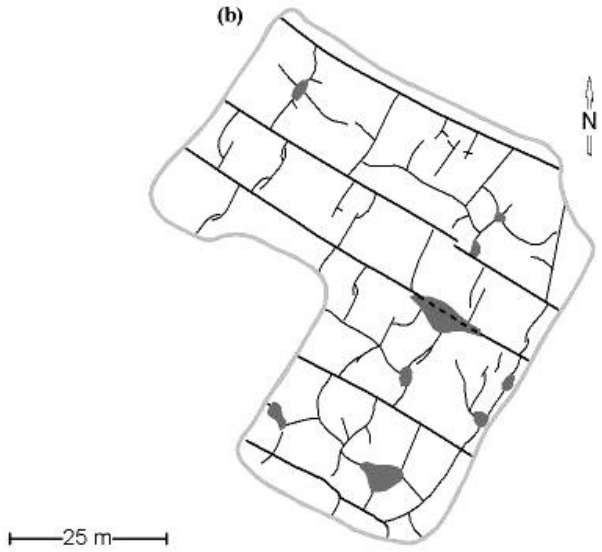

Fracture Clustering & Spacing

Clustered (irregular)

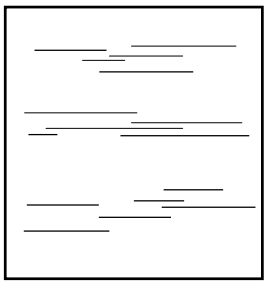

Non-clustered (regular)

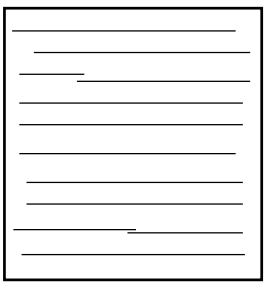

Multi-segment Fracture (typical of long fractures)

Mechanical Fracture Interaction = Stress Shadow

- stress relief from existing fractures removes energy available for other cracks to grow
- fracture spacing should be proportional to size of stress shadow

Fracture Stress Perturbation Calculation

- body loaded in uniaxial tension
- one opening mode crack perpendicular to tension
- result symmetrical about crack (only show half)

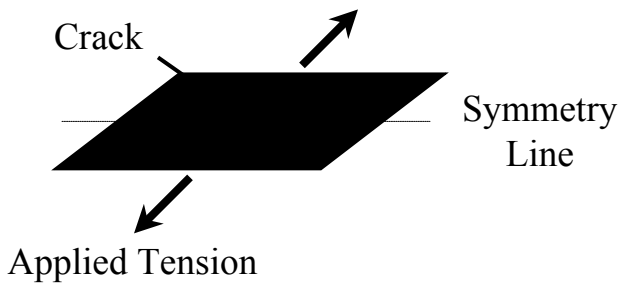

Example - 2d, Plane Strain Crack

- stress shadow grows in size with increasing crack length (from 1 m to 6 m)
- plots show normal stress perpendicular to crack

Stress Shadow Growth - L=1

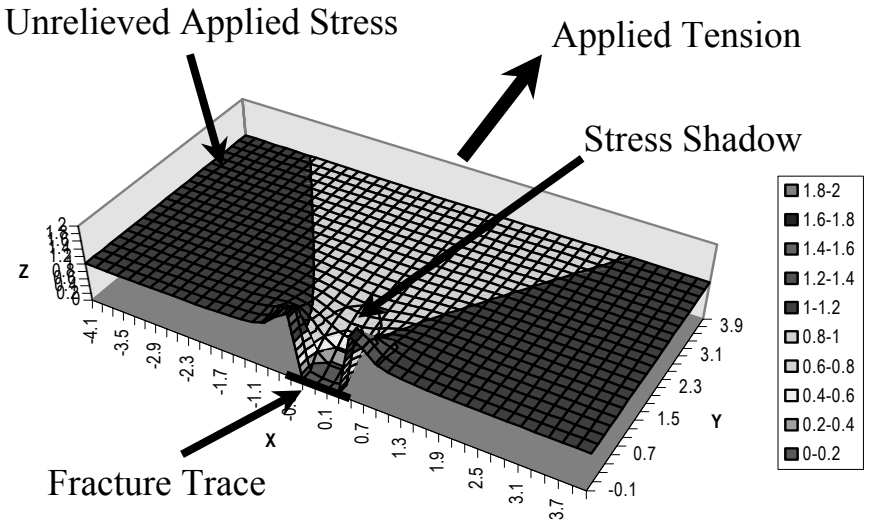

2d, Plane Strain Fracture

Stress Shadow Growth - L=3

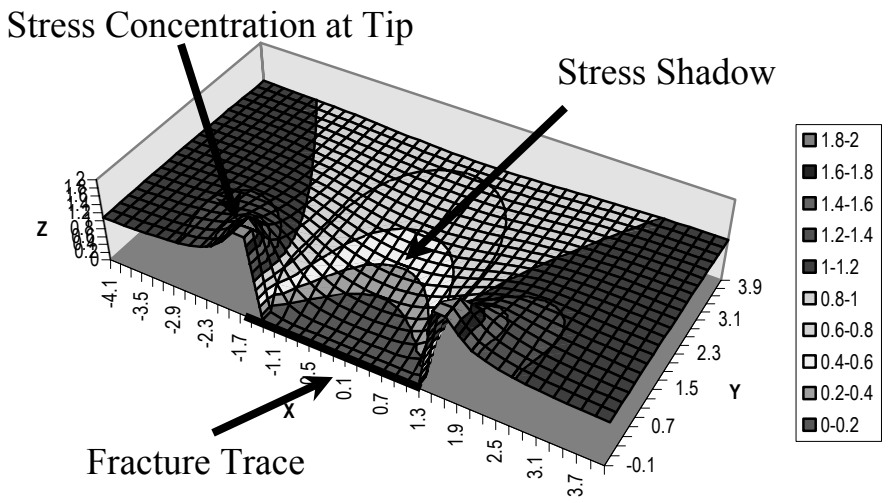

Stress Shadow Growth - L=6

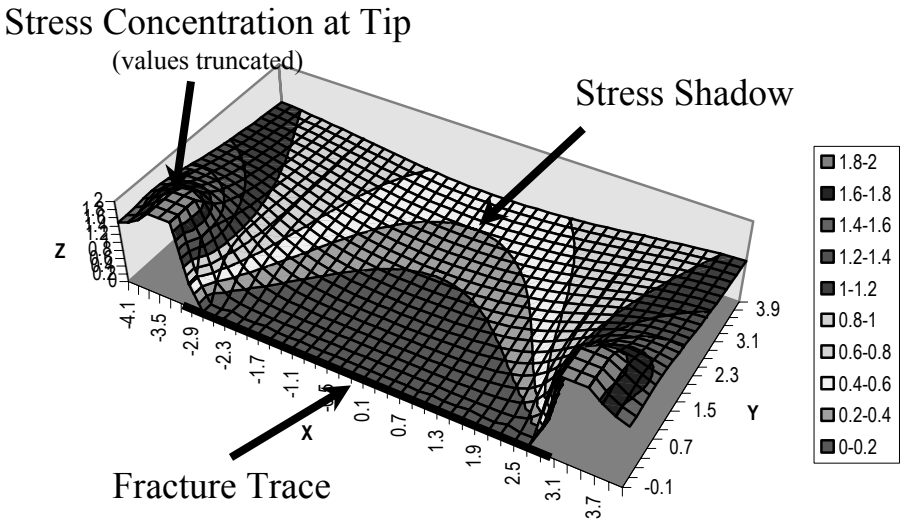

Plumose show fracture propagation disrupted by bedding planes

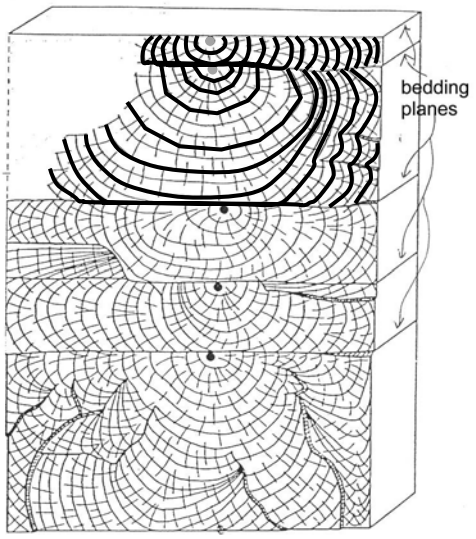

Plumose Structure – joints in thin beds

Plumose structure – joint in Weber sandstone, Dinosaur National Monument

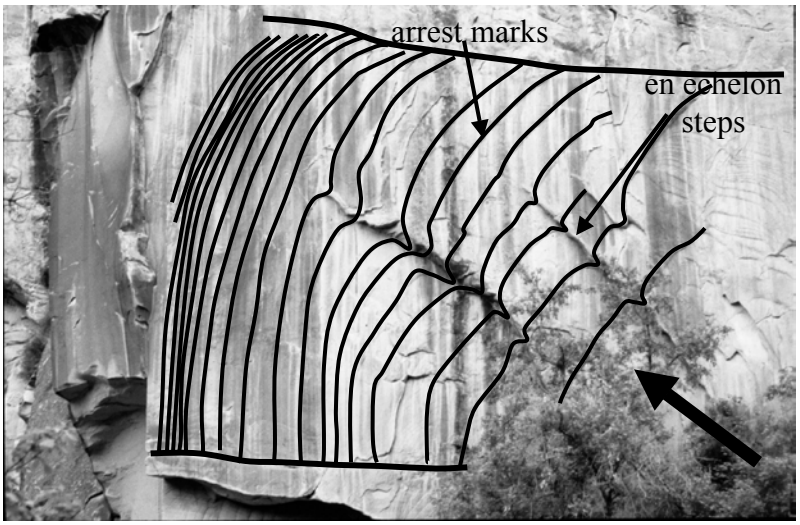

Example - Finite Height Crack

- 3d fracture geometry
- width of stress shadow scaled to fracture height, unaffected by increasing length
- suggests closer fracture spacing than plane strain model

Stress Shadow Growth - L=1

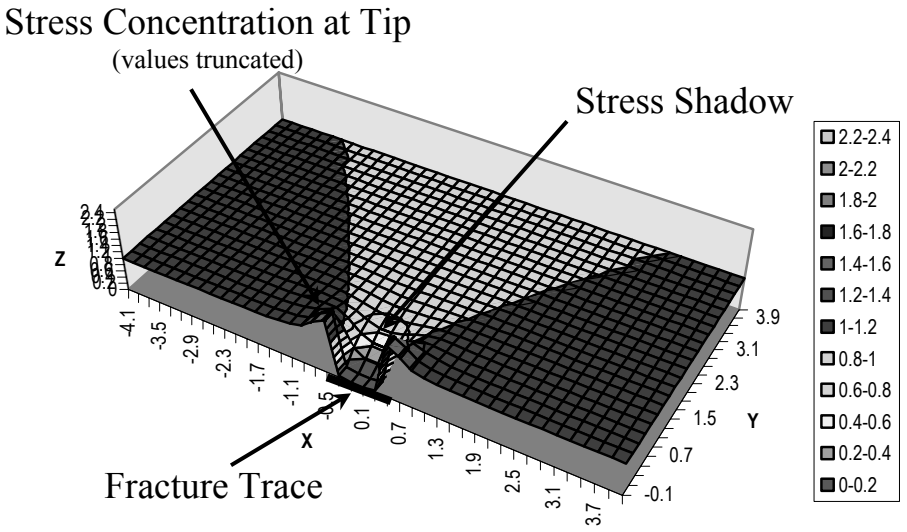

Finite Height Fracture, H=2

Stress Shadow Growth - L=3

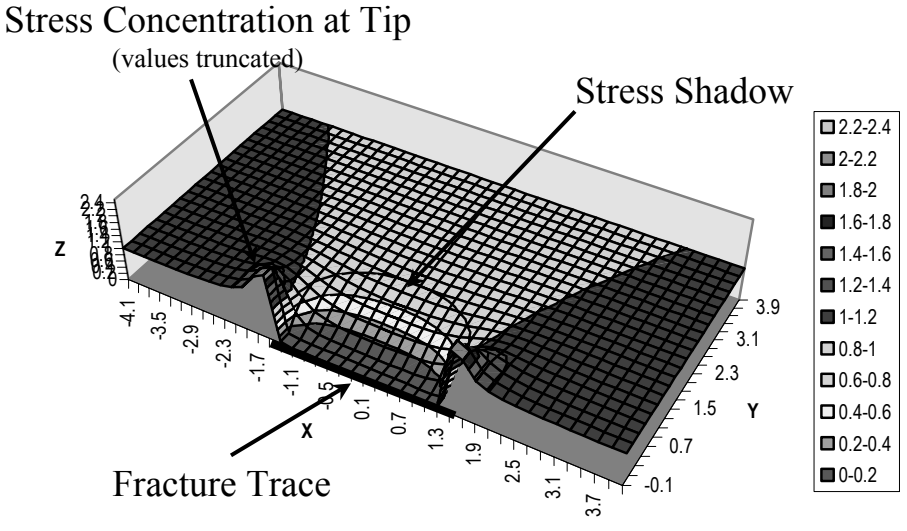

Finite Height Fracture, H=2

Stress Shadow Growth - L=6

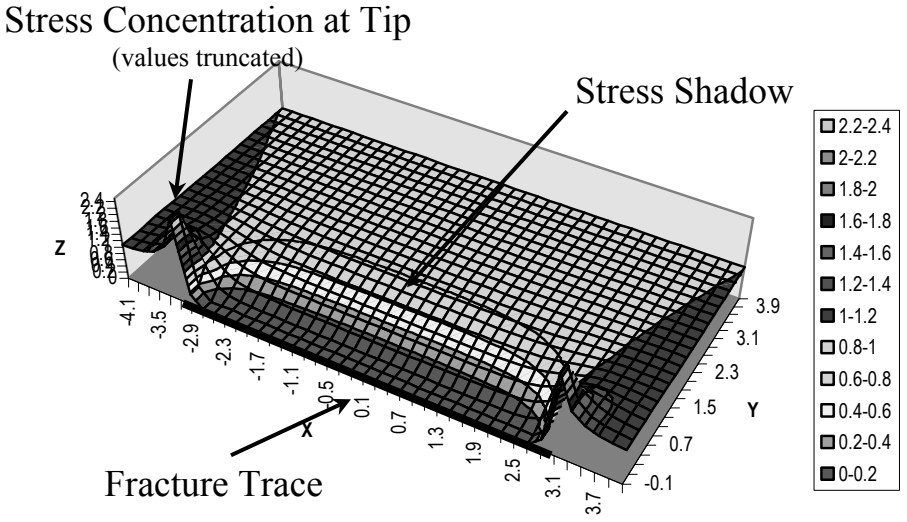

Finite Height Fracture, H=2

Static Analysis - Stress Shadow

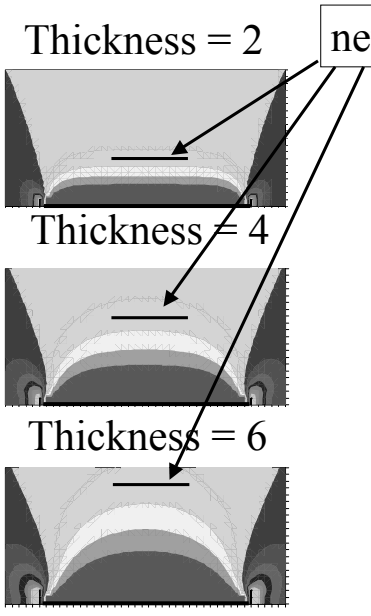

Spacing vs. Bed Thickness

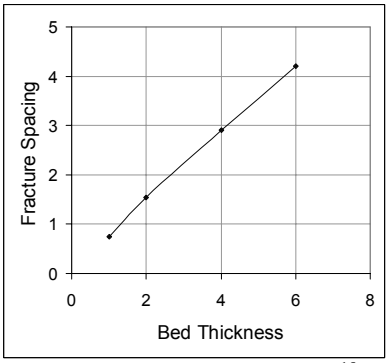

For Bedded Sedimentary Rocks

- fractures confined to mechanical layers
- field data shows spacing depends on bed thickness

=> 3d stress shadow more appropriate

What does "static" analysis lack?

- need to look at propagation dynamics
- how fast do cracks grow?
- how many cracks grow at a time?

Subcritical Propagation Law

- Stress Intensity Criterion (pure mode I)
  - $K_I^* < K_I < K_{Ic}$
- Velocity Rule
  - $v \alpha (K_I / K_{Ic})^n$

    v = propagation velocity

    n = subcritical index

Why Subcritical Crack Growth in Rock?

- indicative of rock weakening due to
  - long term, low-level loading
  - corrosive pore fluids (water)
- lack of dynamic propagation indications in rock (such as crack tip branching)
- modeling gives compelling results

Propagation Velocity vs. Stress Intensity Factor

$v \alpha (K_I / K_{Ic})^n$

<u>lower n</u>
- less velocity contrast
- more growth at low stress intensity

<u>higher n</u>
- more velocity contrast
- growth only at high stress intensity
- approaching critical

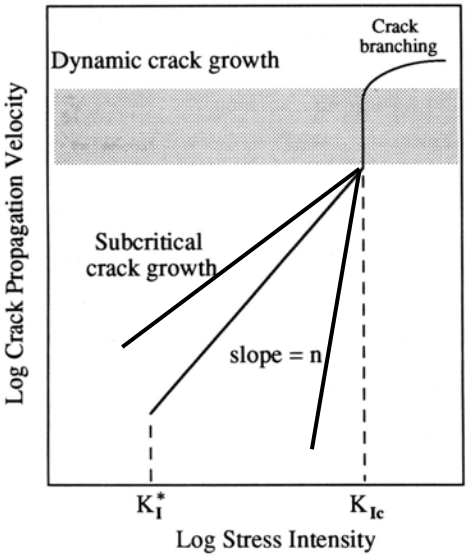

(after Atkinson, 1987)

Simulation Boundary Conditions

- Displacement control, uniaxial extension
- Lateral boundaries - zero normal disp, zero shear stress
- Randomly located starter cracks
- All fractures are vertical

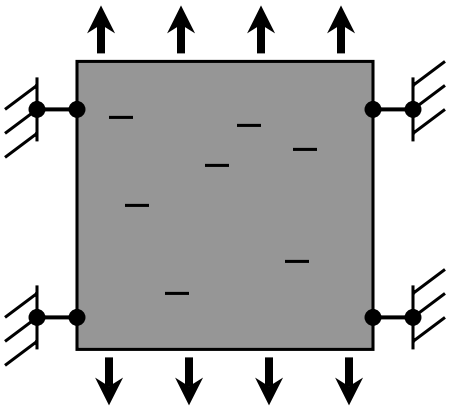

Fracture Clustering & Spacing

Clustered (irregular)

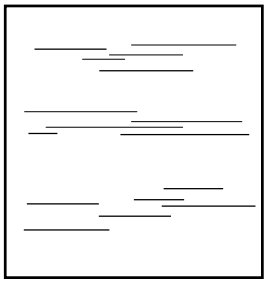

Non-clustered (regular)

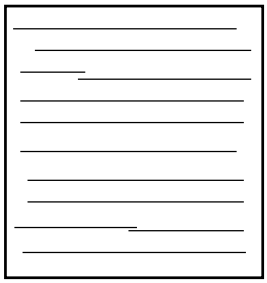

Multi-segment Fracture (typical of long fractures)

Subcritical index & network geometry

- low n, spacing < bed thickness, early subcritical growth
- high n, widely spaced clusters, late critical growth

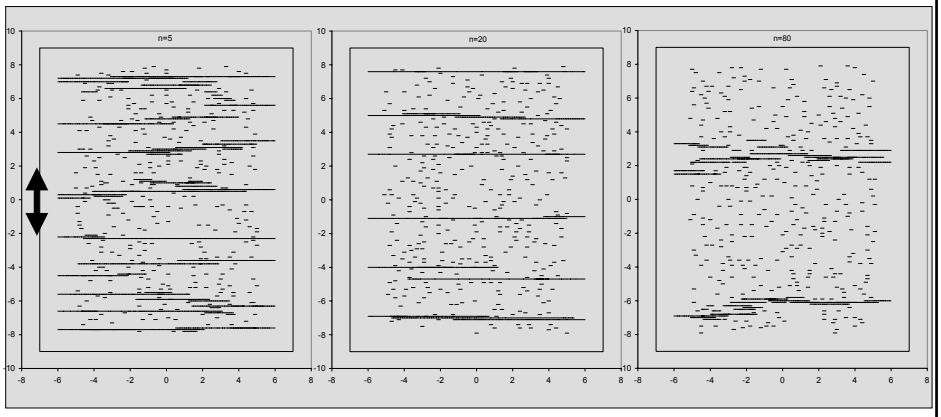

n=5 n=20 n=80

Discussion

- does localized loading cause clusters, or do fractures self-organize?
- can you predict the presence of clustering?
- can you predict the location of a cluster?
- what mechanism controls length distributions – does it have a distinctive, predictable shape?

Fracture spacing and clustering

- increase n from 5 to 20, median spacing increases
- n=40 and 80, median spacing goes down because of clustering
- maximum spacing increases smoothly from n=5 to 80

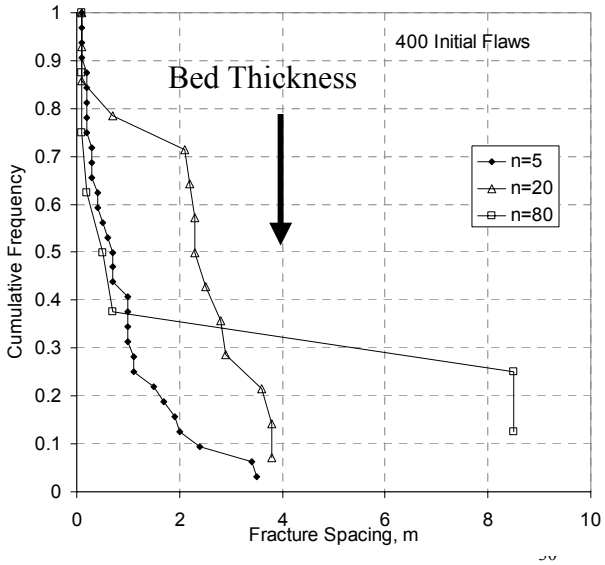

Effect of SCC index on length distribution

- 400 flaws
- same BC's
- vary n from 5 to 80

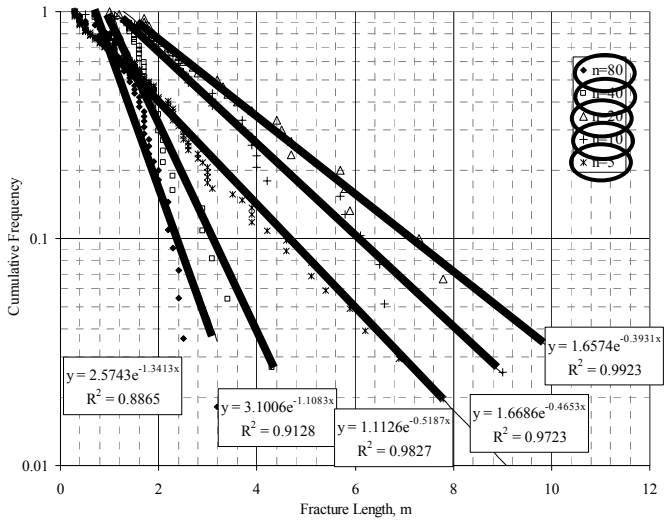

31

Effect of flaw number on length distribution

- n=20
- 100, 200, and 400 flaws
- same BC's
- more flaws reduce max length

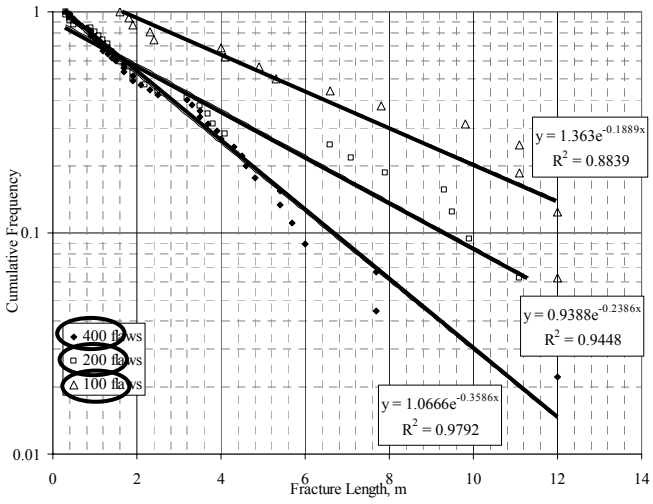

32

Fracture Zones or Clusters

Comb Ridge, Utah

Santa Barbara, CA

Fracture Clustering, n=80

- high subcritical index simulation
  - stress relief seen through crack tip stress intensity factor
  - bubble plot shows aperture and stress intensity
- note high K_1 around propagating tips

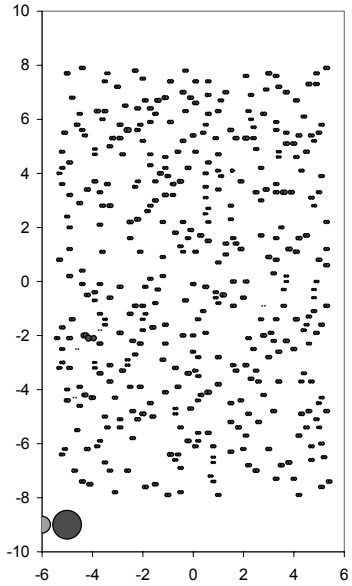
10
8
6
4
2
0
-2
-4
-6
-8
-10
-6
-4
-2
0
2
4
6

35

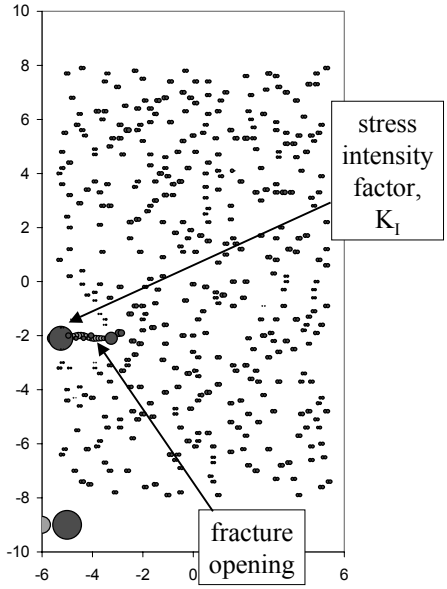
10
8
6
4
2
0
-2
-4
-6
-8
-10
-6
-4
-2
0
6
stress intensity factor, K_I
fracture opening

36

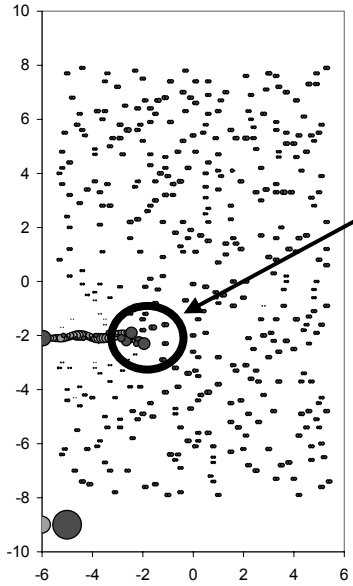

•elevated stress intensity at head of cluster
•like a process zone

37

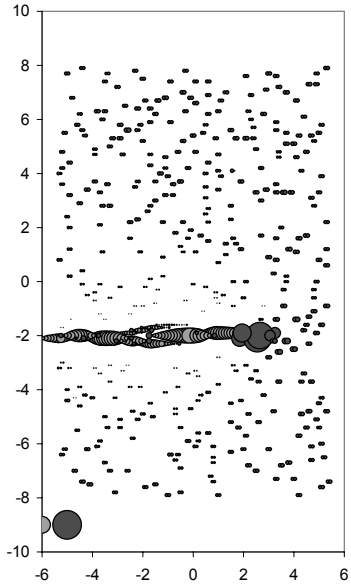

42

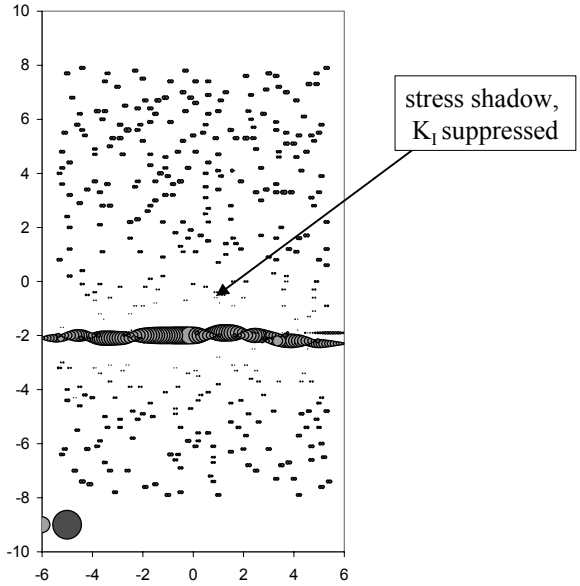

47

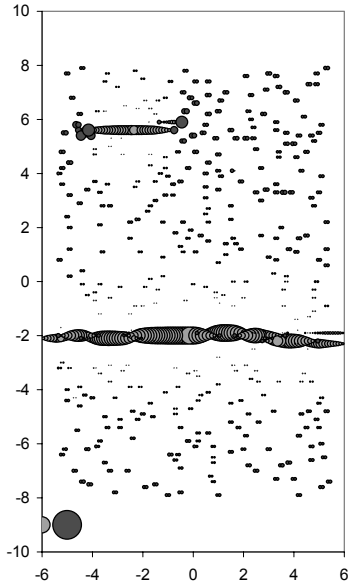

49

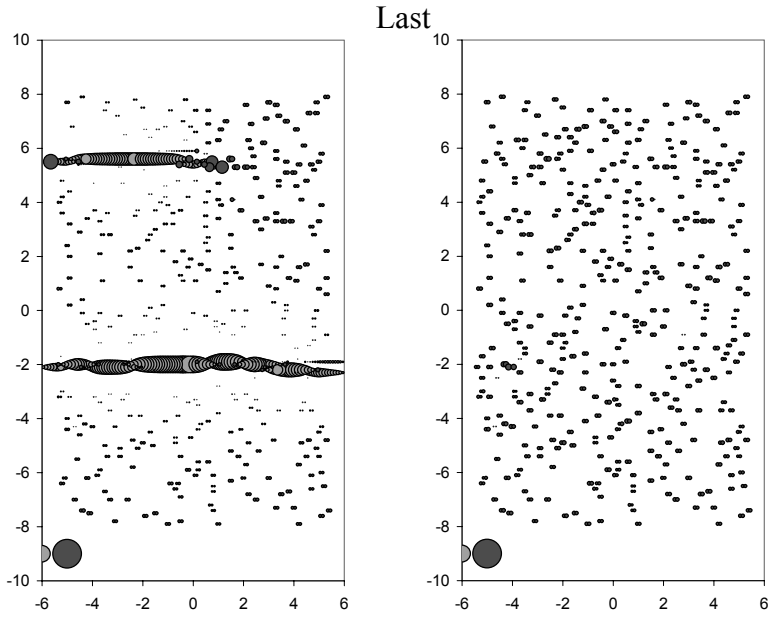

51

Summary

- Size of stress shadow exerts basic control on spacing
- Propagation modeling suggests subcritical growth index, n, controls clustering and modifies spacing from simple bed thickness proportionality
- Fracture length distribution controlled by subcritical index (initial flaw density also important)
- Fracture model predicts exponential length distributions, consistent with field data

52

Conclusions

- low subcritical index
  - earlier fracturing (more likely to be filled)
  - closer spacing of fractures & clusters
- moderate subcritical index
  - intermediate time
  - regular spacing, non-clustered
  - greater length
- high subcritical index
  - very late fracturing (less likely to be filled)
  - highly clustered (bimodal spacing, shorter lengths)

Site-Specific Constraints

- perform subcritical crack tests on core
  - require thin section size sample
  - can test layer by layer
  - can assess reservoir fluid influence
- correlate subcritical index with petrography or petrophysics
  - grain size
  - diagenesis

More Complex Simulation

- development of "orthogonal," well connected network
- constant strain rate, uniaxial extension
- fracture propagation direction flips back and forth through time
- apertures open and close through time

1

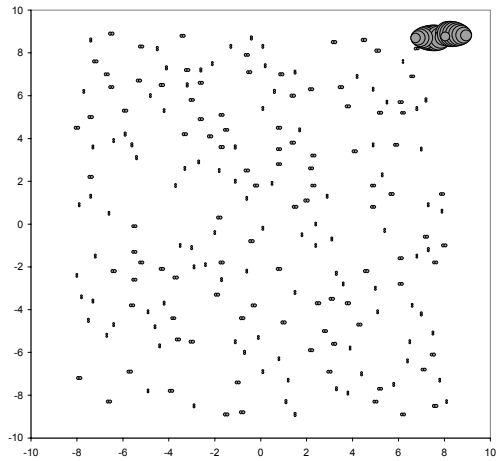

2

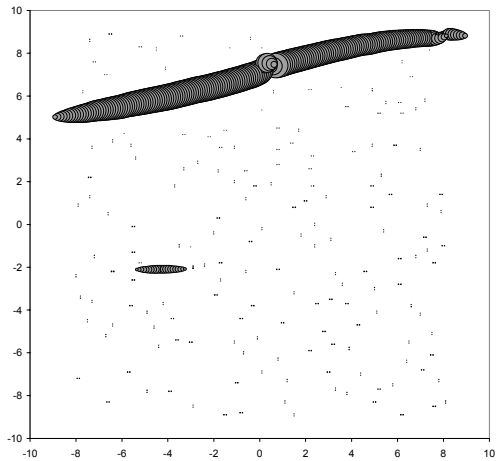

3

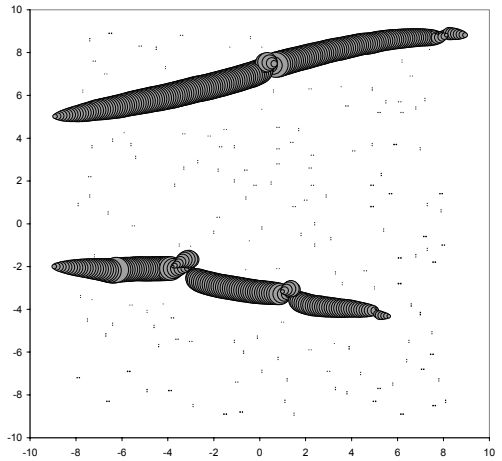

4

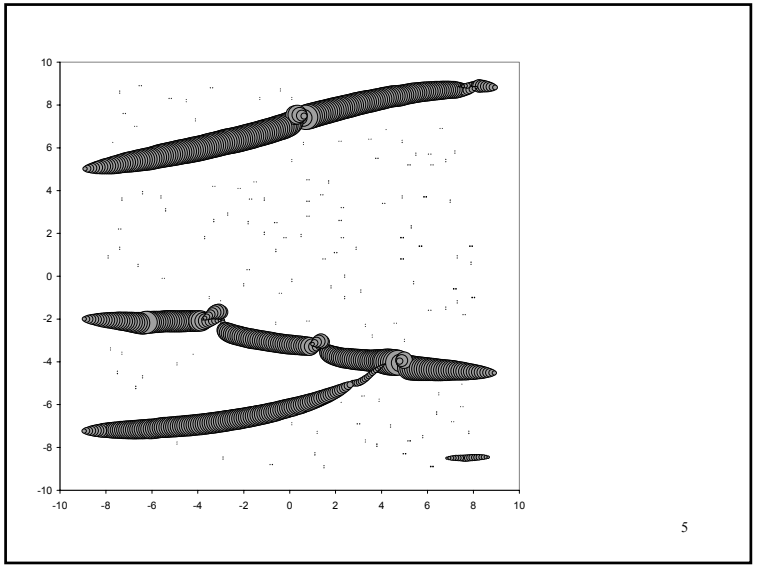
10
8
6
4
2
0
-2
-4
-6
-8
-10
-10 -8 -6 -4 -2 0 2 4 6 8 10

5

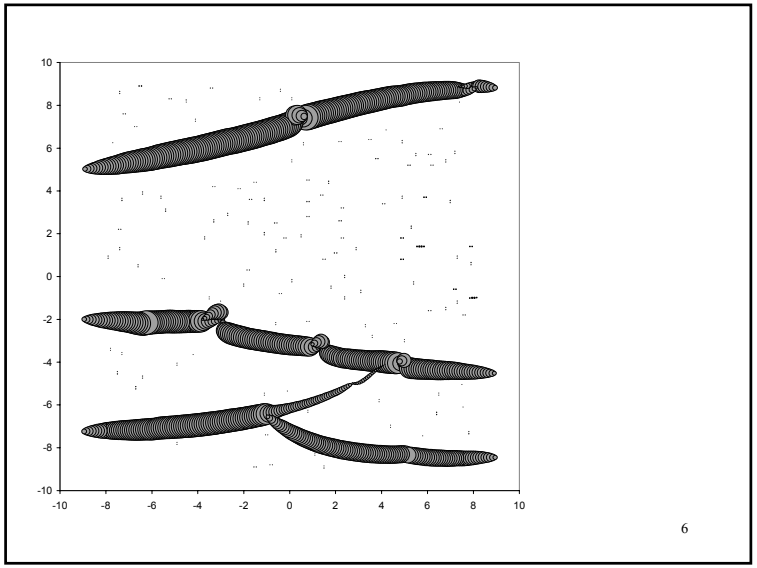
10
8
6
4
2
0
-2
-4
-6
-8
-10
-10 -8 -6 -4 -2 0 2 4 6 8 10

6

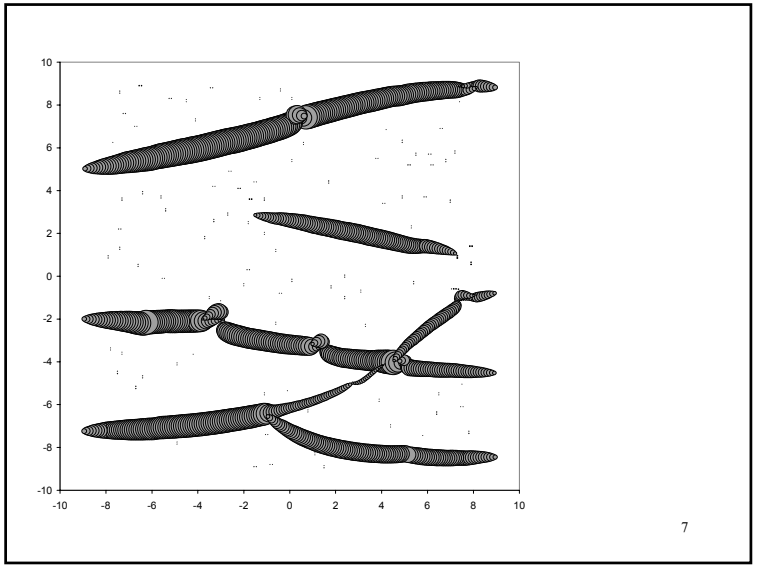
10
8
6
4
2
0
-2
-4
-6
-8
-10
-10 -8 -6 -4 -2 0 2 4 6 8 10

7

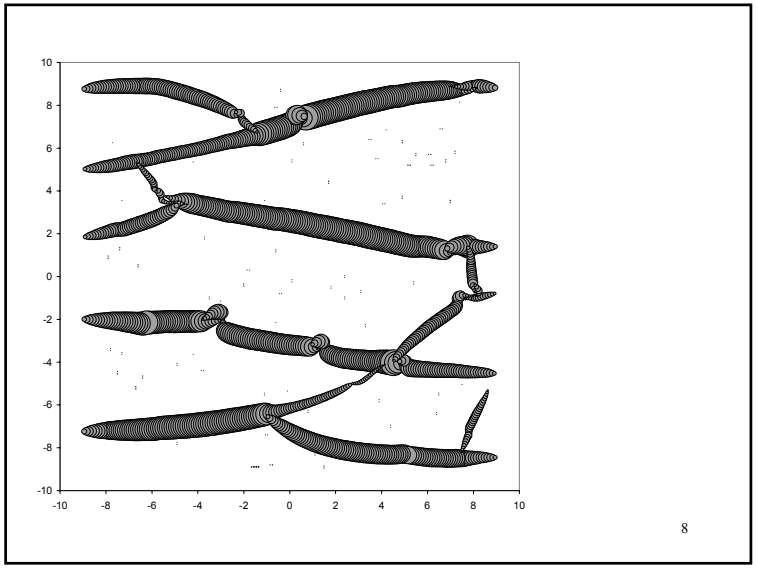
10
8
6
4
2
0
-2
-4
-6
-8
-10
-10 -8 -6 -4 -2 0 2 4 6 8 10

8

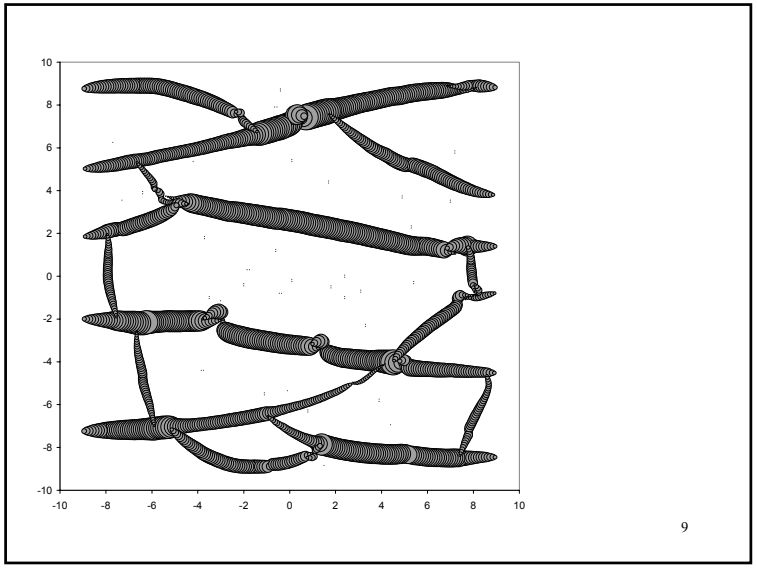

9

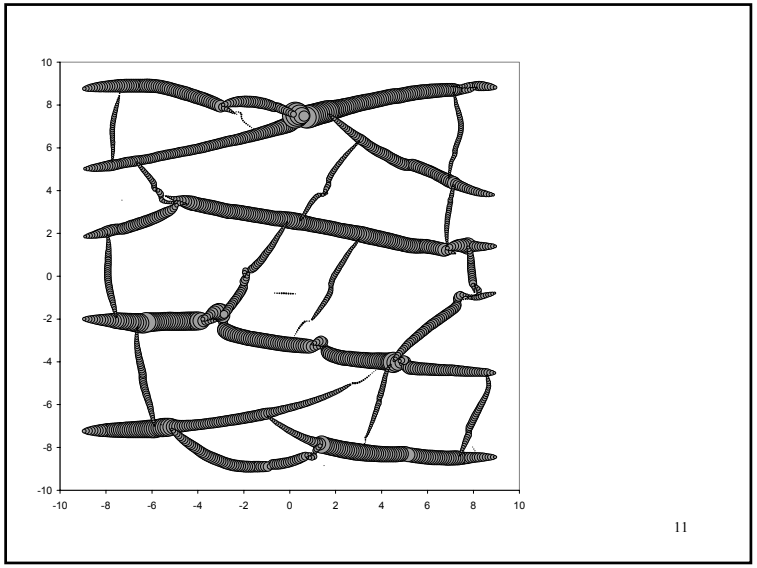

11

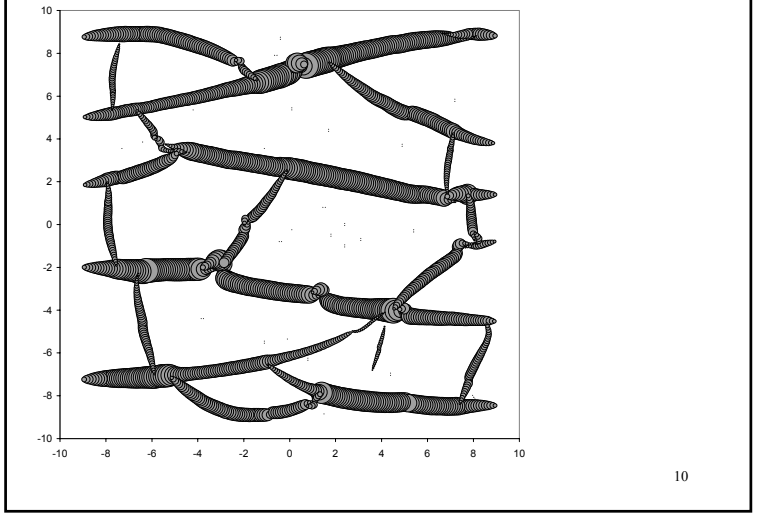

10

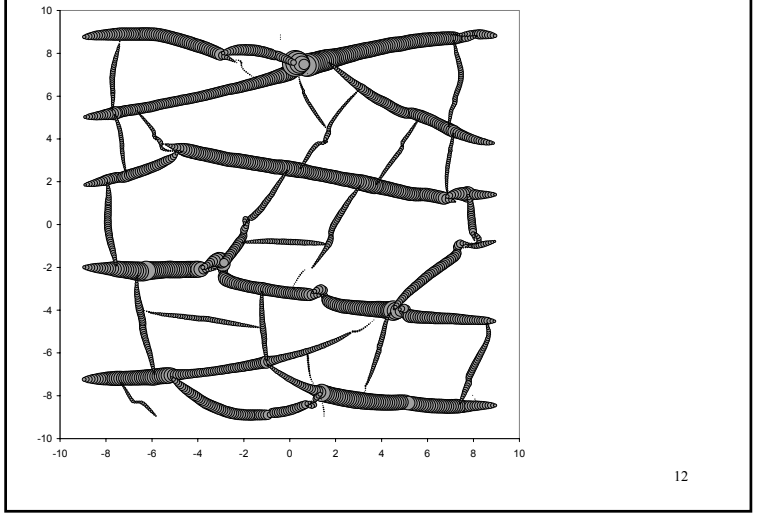

12

Orthogonal 3

Other Orthogonal Simulations

- included to demonstrate variety of fracture patterns possible
- trace patterns only
- varying
  - crack number
  - subcritical index
  - bed thickness
  - initial pattern

13

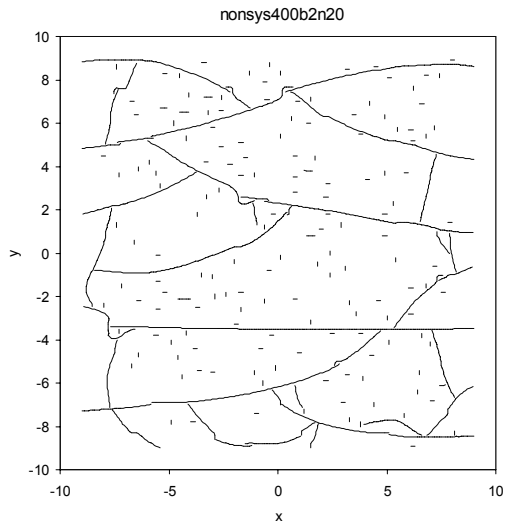

14

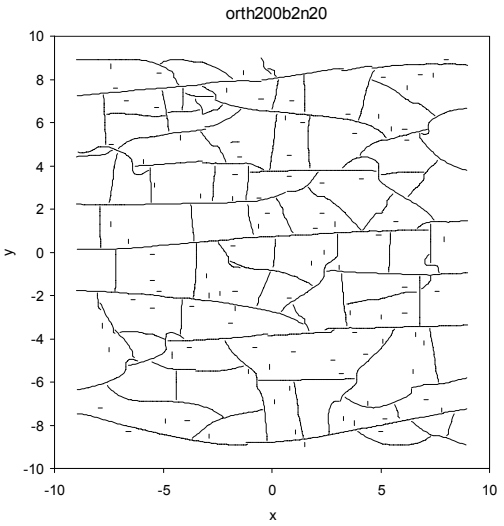

15

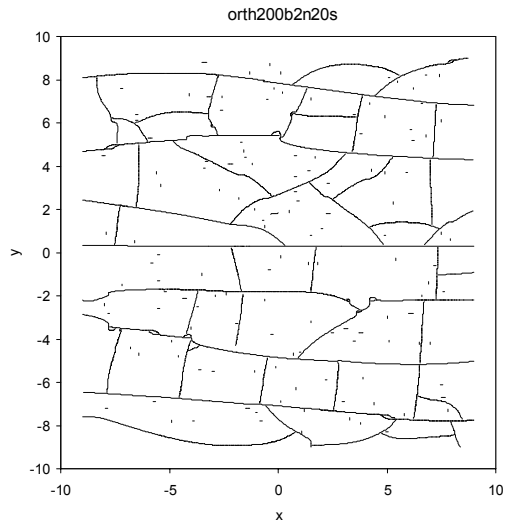

16

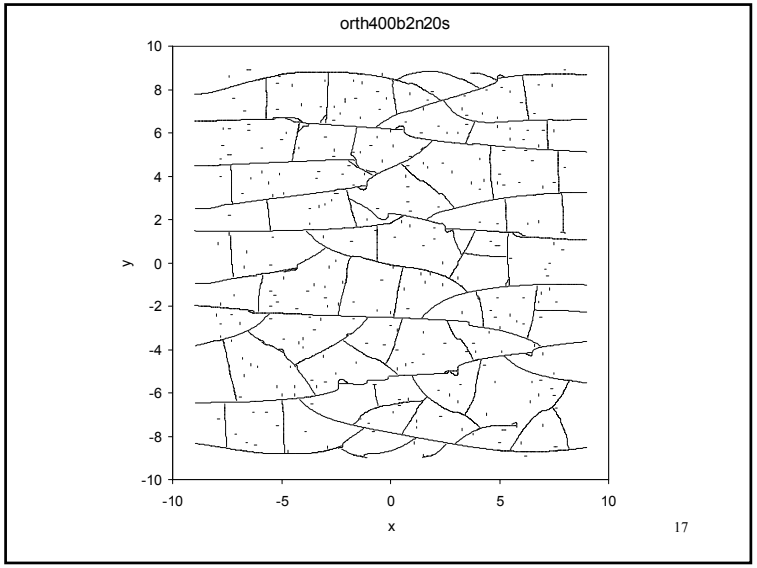
orth400b2n20s
10
8
6
4
2
0
-2
-4
-6
-8
-10
y
-10
-5
0
5
10
x
17

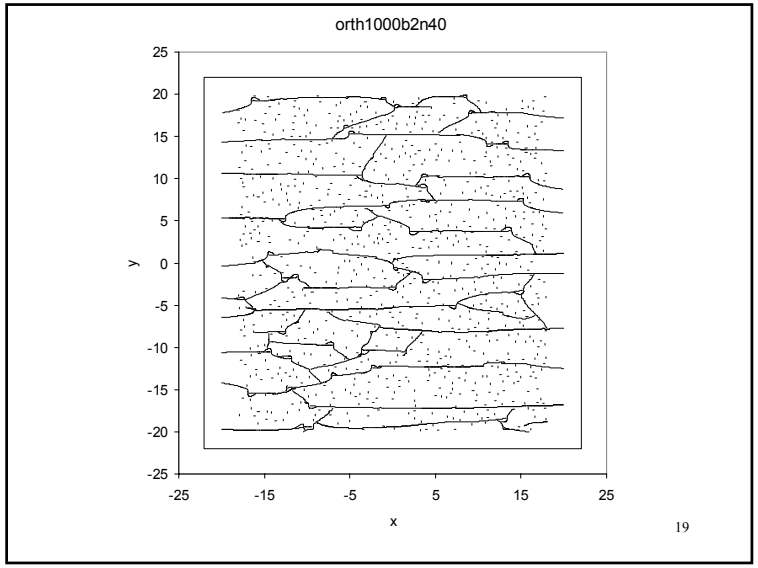
orth1000b2n40
25
20
15
10
5
0
-5
-10
-15
-20
-25
y
-25
-15
-5
5
15
25
x
19

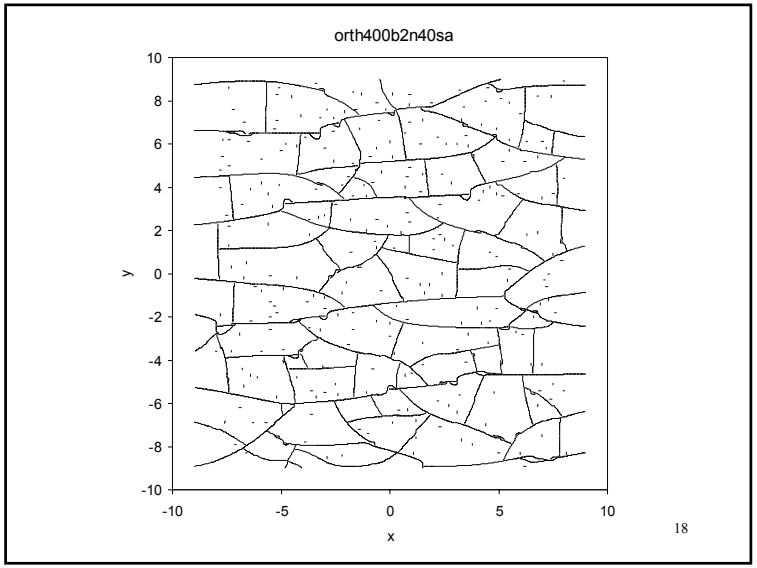
orth400b2n40sa
10
8
6
4
2
0
-2
-4
-6
-8
-10
y
-10
-5
0
5
10
x
18

Subcritical Crack Measurements in Tight Sandstones

Peggy Rijken, Jon Olson, Jon Holder

1

Outline

1. Objective
2. Experimental theory and setup
3. Literature analysis
4. Results
5. Difficulties
6. Conclusions and recommendations

2

Objective

Correlation of subcritical crack index with rock properties

Why?

Subcritical fracture index has been shown to influence fracture length, spacing and clustering

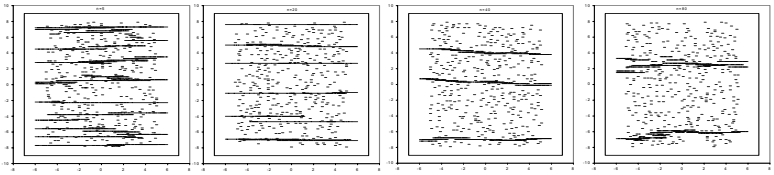

Increase in subcritical index

3

Empirical Subcritical Behavior

v = Velocity

K_I = Stress intensity factor

K_{Ic} = Fracture toughness

n = Sub-critical index

4

Why Double-torsion?

- Simple setup
- Stress intensity independent of crack length
- Robust

Double-torsion Apparatus

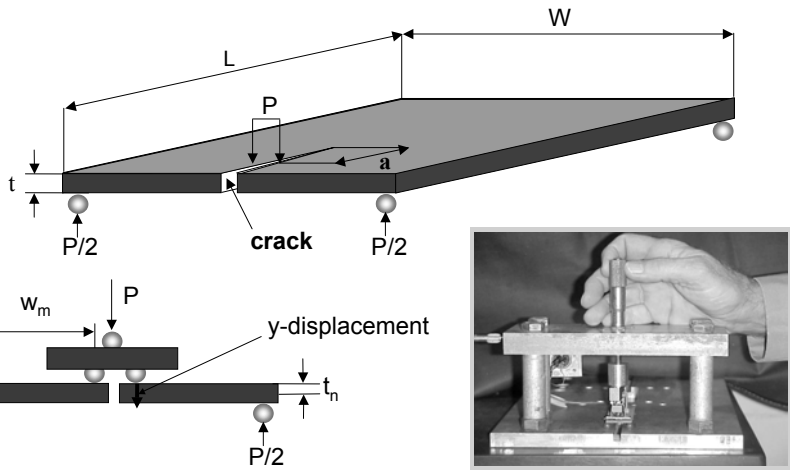

Test Methodology

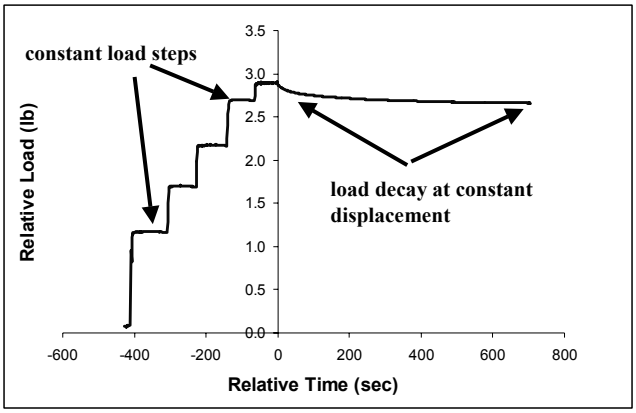

To eliminate transient load variations, sample is preloaded in incremental steps during which load is held constant by displacement adjustment (Holder et al., 2001).

9

Literature (Atkinson and Meredith, 1989)

- Subcritical Index depends on:
  - Microstructure: grainsize, degree of heterogeneity, etc.
  - Chemical environment: weakening of bonds due to water presence
  - Driving force for crack extension
  - Temperature
  - Pressure
  - Residual strain

10

Literature:
Polycrystalline Material (Gesing and Bradt, 1983)

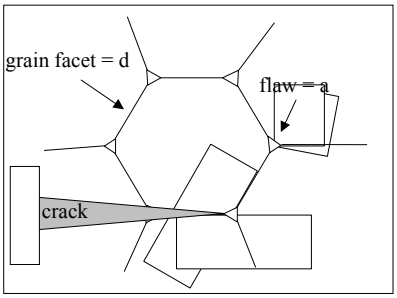

- **Assumptions:**
  - **Propagation only if fracture extension force exceeds energy required to propagate all fractures**
  - **Propagation is a linking of flaws along the grainboundaries (Intergranular growth)**
  - **Crack extends with subcritical velocity until local fracture toughness is exceeded**

Literature:
Polycrystalline Material (Gesing and Bradt, 1983)

n	=	subcritical index
c	=	constant
a	=	flaw size
d	=	grain or facet size
G	=	applied crack extension force
G_0	=	critical crack extension force (surface energy; material property)

Theory: Prediction

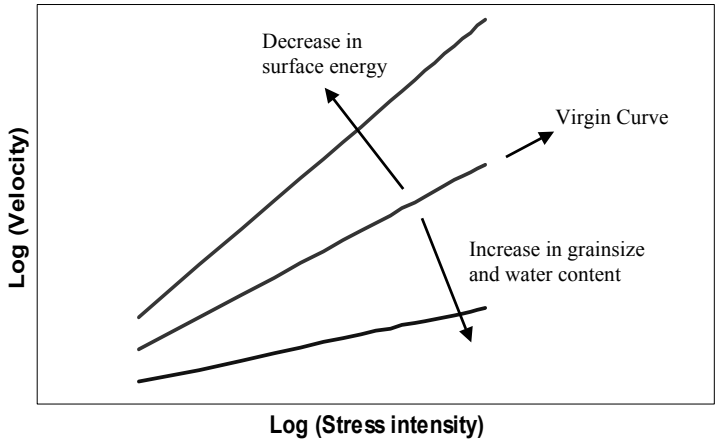

13

Travis Peak formation

- Sand rich channel deposition
- Lower cretaceous
- West flank of Sabine uplift, gentle north-trending structural dome
- Depth: 6000-11,000 ft

14

Travis Peak: Location

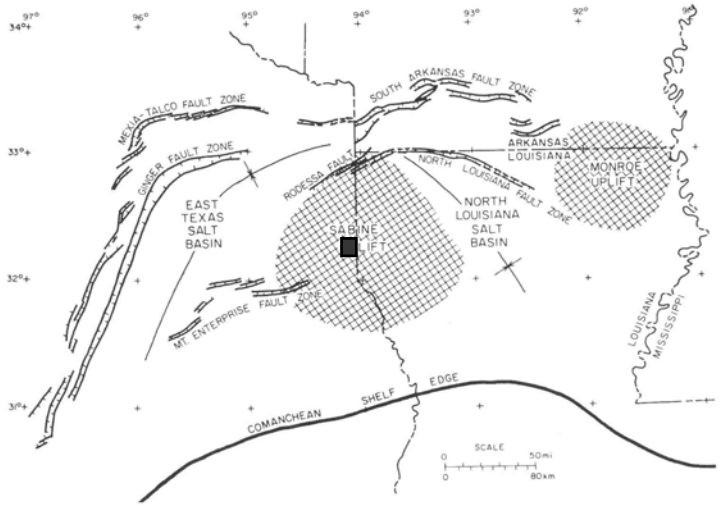

Test Methodology

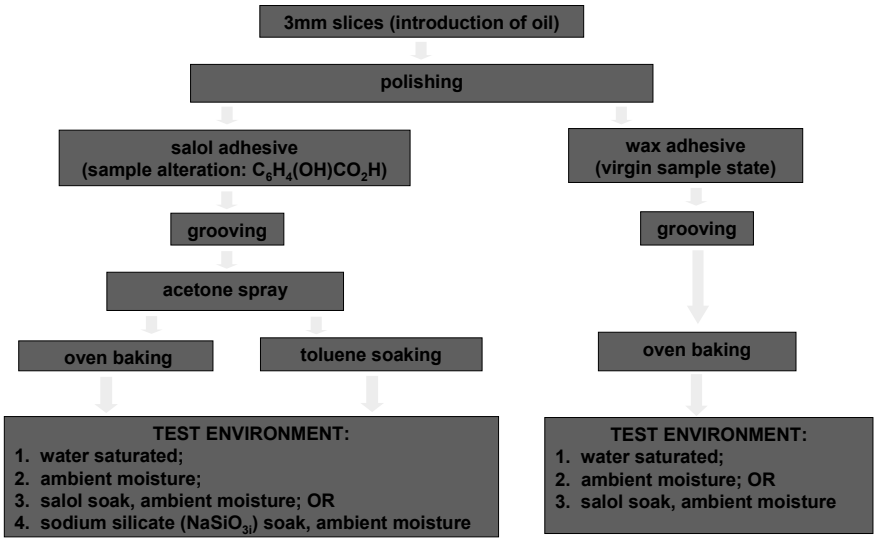

Results: Travis Peak

Well	Depth (ft)	Qtz matrix (%)	Qtz cement (%)	Carb cement (%)	Grain size (mm)	index dry	index wet
26	5962	59	20	10	0.105	50±12	--
26	6206	60.5	16.5	2.5	0.97	65±4	66±5
26	6270	72	10.25	14.5	0.102	61±14	54±16
26	6295	52	19	18	0.097	51±12	--
26	7457	76.25	14.25	0	0.150	56±16	56±9
26	7506	72.75	18.75	0	0.155	58±15	70±8
24	5952	68.5	12	1.5	0.208	61±8	70±7
24	6244	68.25	13.75	0.75	0.129	54±7	52
18	6633	67	10.5	11.5	0.108	81±17	--
17	7737	70.3	17.3	1	0.058	42±6	63±9
15	10141	74.75	11.75	3.25	0.094	73±22	54±16
14	9817	73.7	17.3	0	0.186	53±11	60±15
14	9837	73.5	9.5	12.5	0.222	69±8	--
14	9880	7475	18	0	0.262	52±10	--

17

Thin-sections

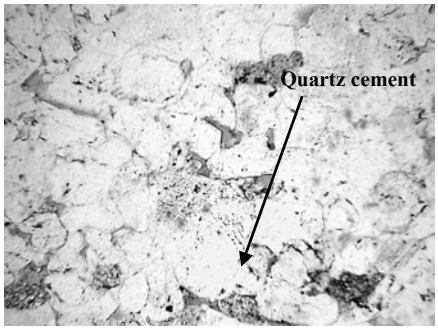

Quartz cemented sandstone

~ 7506 ft

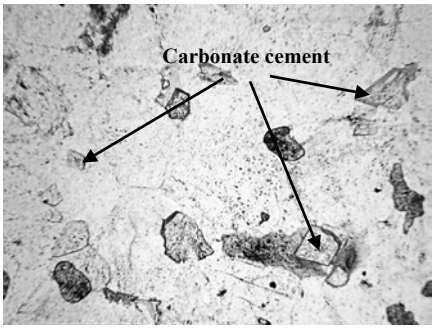

Carbonate cemented sandstone

~ 9330 ft

18

Results: Travis Peak by Location

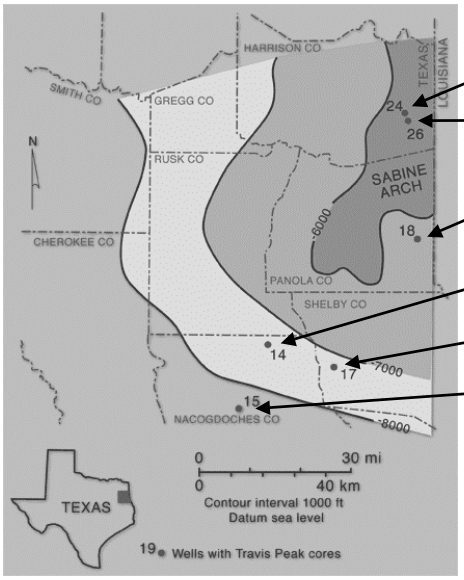

Subcritical Index values

n = 61; 54

n = 65; 61; 58; 56; 51;50

n = 81

n = 69; 53; 52

n = 42

n = 73

Well locations and structure contours, Top of the Travis Peak formation.

(after Laubach, restricted data) 19

Grain size dependence

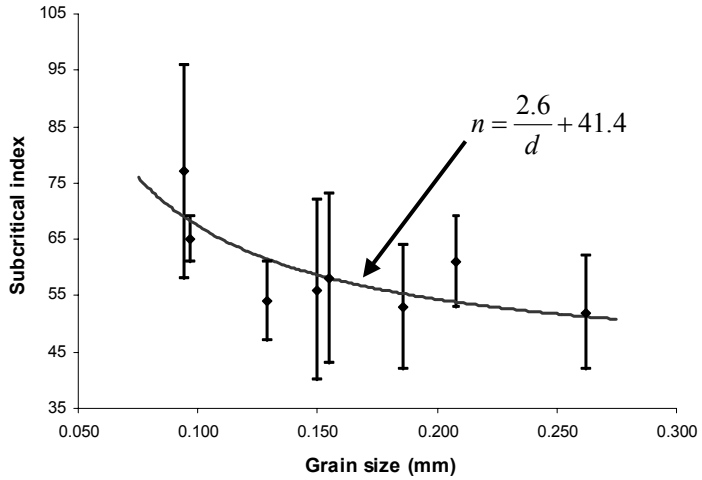

20

Carbonate Cement

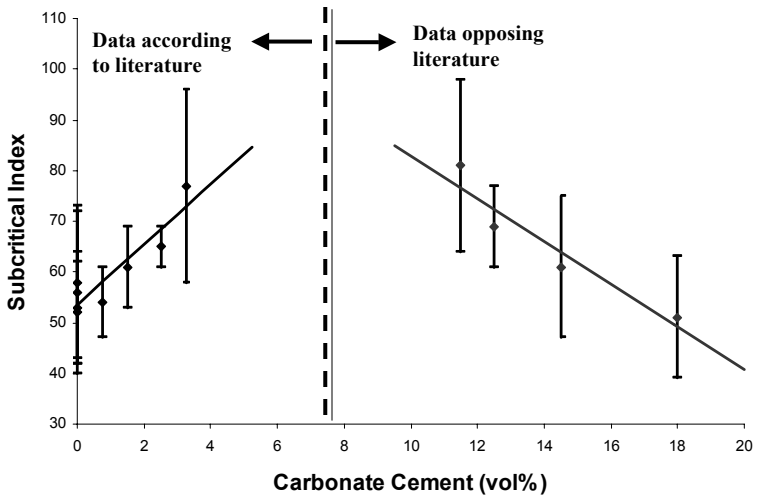

21

Water Saturation

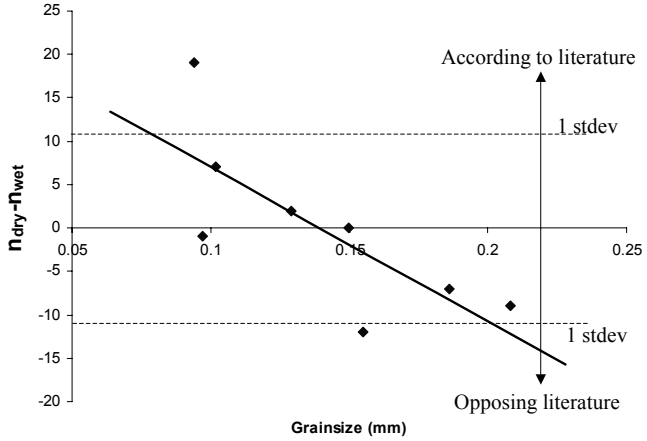

22

Artificial Cement:

Isolate Single Variable

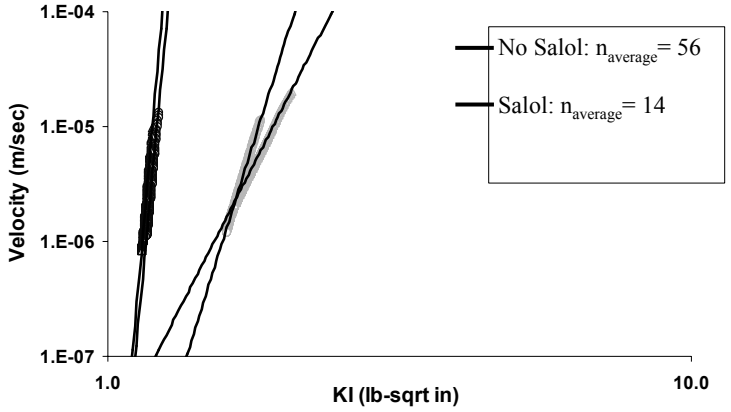

Additional SS Results: San Juan Formation

WELL	DEPTH	SPECIMEN CONDITION	n	
			dry	sat.
0RC-26	14,327'	Oil-wet (native)	53 ± 11	
		Water-wet (toluene bath)	46 ± 12	59 ± 8
0RC-26	14,547'	Oil-wet (native)	58 ± 12	
		Water-wet (toluene bath)	59 ± 17	50*

* single measurement

Additional SS Results: Cozzette Formation

WELL	DEPTH	TEST CONDITIONS	INDEX	
			DRY	WATER
MWX-1	7,892'	toluene - cleaned	66±**17**	-
		acetone - cleaned	68±25	39±4
		salol (residue from polishing)	44±4	32±11
MWX-2	7,892'	toluene - cleaned	64±16	67±18

25

Summary:

- Grainsize dependence as predicted in polycrystalline materials: n ~ 1/grainsize
- SC index increases with cement concentration for small amounts of carbonate cement, but decreases with concentration for large amounts
- SC index decreases with introduction of artificial (salol and sodium silicate) cement
- Water saturation relationship depends on grainsize
- Average subcritical index for TP sandstone between 50 and 60

26

Data analysis: Difficulties

- Multi-variable problem: heterogeneity of samples scatters data and obscures relationships (minerals present, grainsize)
- Effects of moisture content obscure other variations
- Although different rock samples can be selected, constituents are not determined until after testing, complicating determination of systematics.

27

Data interpretation

Inhomogeneity or RH?

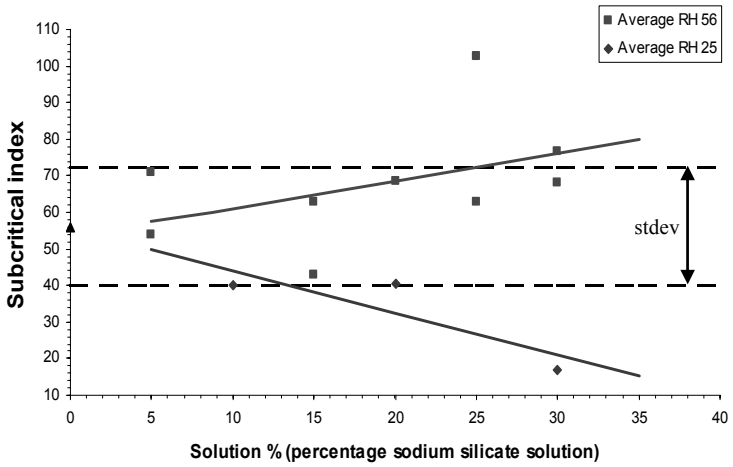

28

Conclusions

- **General:**
  - Subcritical index of fine-grained sandstone = 50–70
  - Subcritical index ~ 1/grainsize
  - Subcritical index dependends on cement type and content
  - Subcritical index dependends on water content
- **Implications:**
  - Subcritical index will vary within a sedimentary structure and even within one bed as grain size and cement content changes
  - Diagenetic history of the reservoir may significantly impact the natural fracture pattern
  - Fluids present during fracturing alter fracture pattern geometry

Suggestions

- Further testing (build database), expand to other formations and rock-types
- Creating artificial samples to have control over sample variables

Fluid Flow in Fractured Reservoirs

- leveraged funds from DOE $850k contract (Olson, Lake and Laubach)
- collaboration with Dr. Jim Jennings, UT-BEG (DOE Clear Fork project)
- Chevron discrete fracture code
- Waseda University discrete fracture code (Sato and Arihara)

1

DOE Project

- Task 1 – Observational verification of emergent threshold (Laubach, Doherty, … - carbonates vs. clastics)
- Task 2 – Geochemical modeling to predict emergent threshold (Lake, Noh - carbonates vs. clastics)
- Task 3 – Relate subcritical index to diagenesis (Holder, Rijken, Olson)
- Task 4 – Reservoir simulation of "realistic" fracture patterns (Lake, Olson, Jennings – use geomechanics codes ➔ CVBEM or ECLIPSE)

2

Aperture Development – Combine Geomechanics & Diagenesis

- subsurface, paleo-subcritical index correction based on diagenetic history
- generate fracture patterns with basin history and rock properties
- modify fracture simulation with mineral in-filling during growth

3

Aperture Development – Preliminary Work with Geomechanics & Diagenesis

- low subcritical index
- 700 starter cracks
- no diagenesis during growth

4

Final

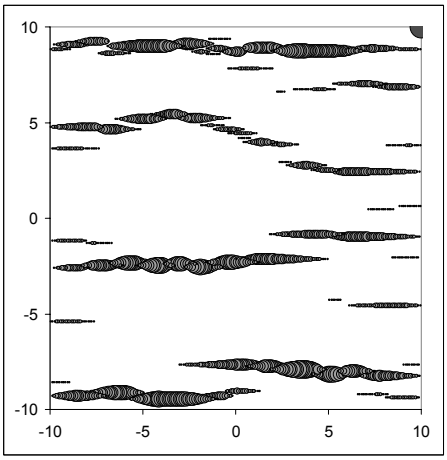

21

Aperture Development

- low subcritical index
- 700 starter cracks
- diagenesis during growth (cracks cannot completely close once opened)

22

Final

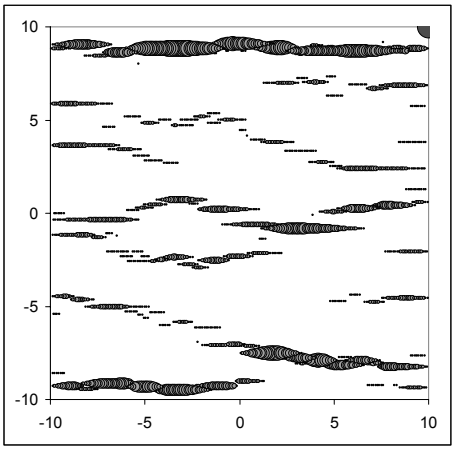

35

Without diagenesis

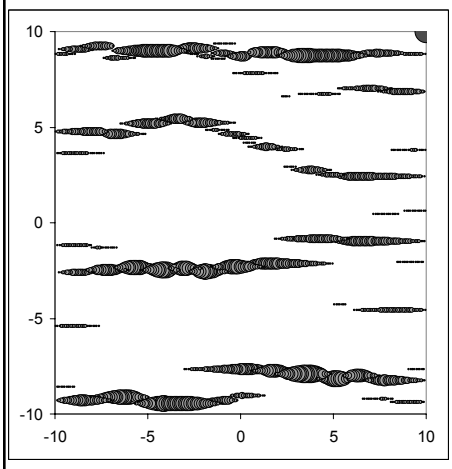

With "pseudo-"diagenesis

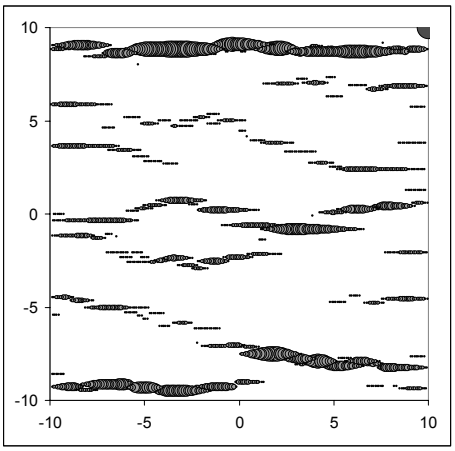

36

The effect of subcritical index on fracture spacing

n=20

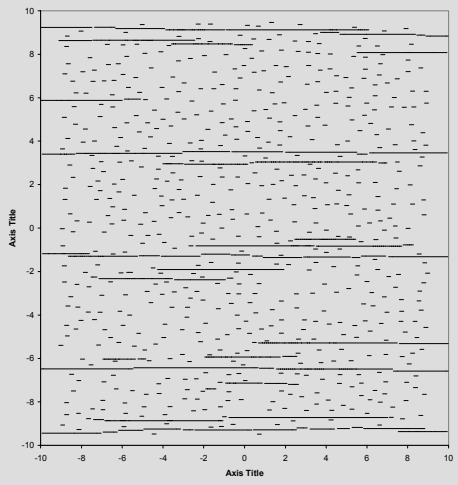

n=5

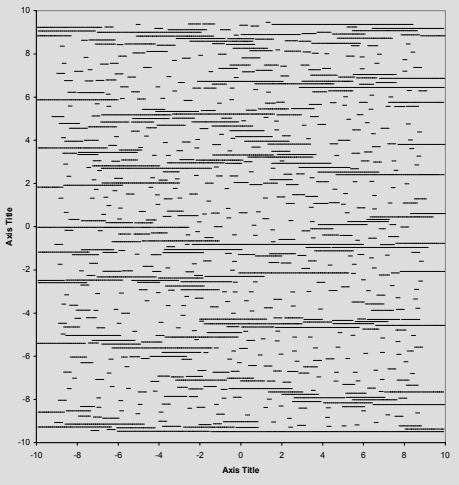

Permeability map – is smaller spacing better?

n=20

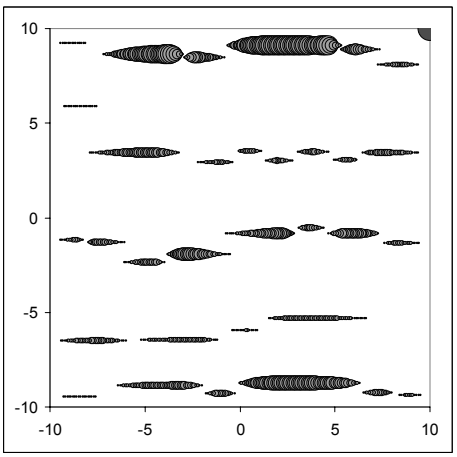

n=5

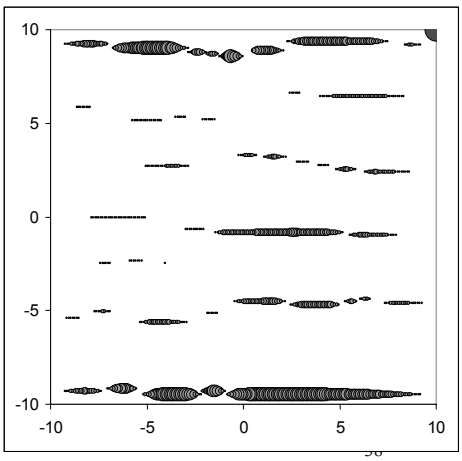

Preliminary Reservoir Simulation Work (Philip, Jennings & Olson)

- revisit Chirlin analytical solution
- utilize ECLIPSE for discrete fractures (everybody has it?! = tech transfer)
- methodology
  - non-neighbor connections
  - explicitly grid fractures

39

ECLIPSE Non-neighbor Connections

- allow flow between non-adjacent reservoir blocks
- specify transmissibilities between blocks

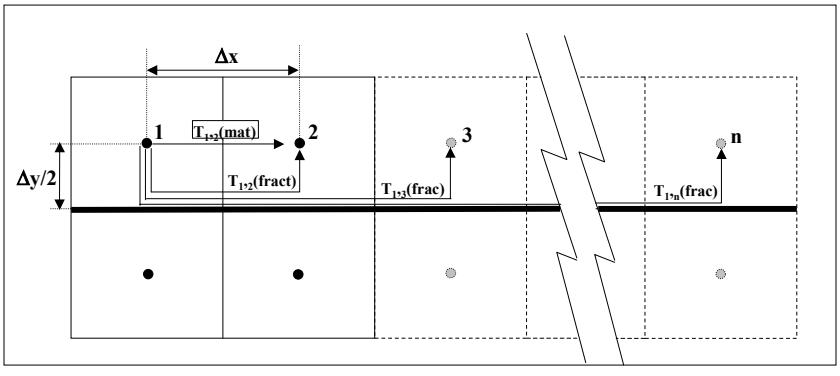

Comparison with Analytical

- periodic array of non-interconnected fractures
- matrix gap between tips is αW
- spacing is h

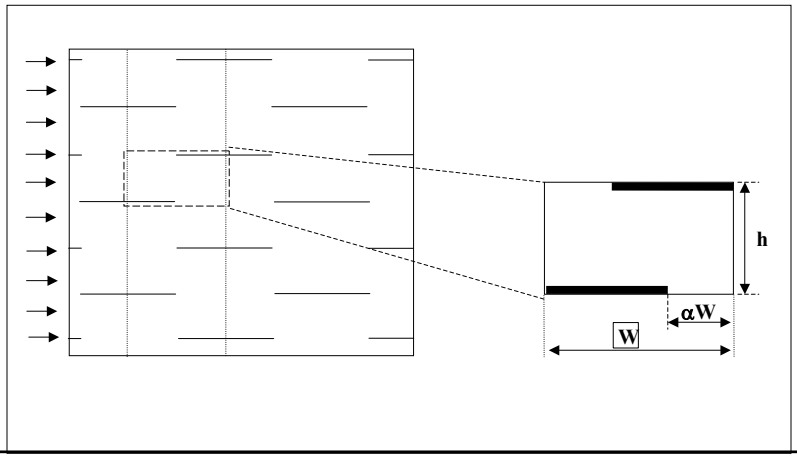

Chirlin's Solution for Effective Permeability Ratio for Flow Parallel to Fractures

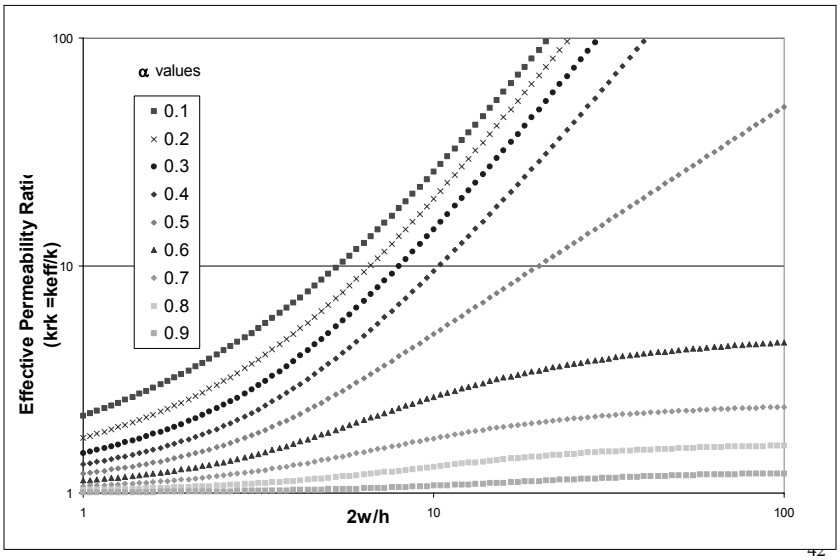

Preliminary Results

- non-neighbor connections feasible approach
- agreement with analytical solution for permeability with 4 reservoir blocks between fractures
- geomechanical model can provide input fracture patterns (utilize layer by layer experimental data on subcritical index)

Reunión Anual 2002 – Consorcio FRAC

Nuevas Metodologías y Tecnologías Para la Caracterización de Yacimientos Naturalmente Fracturados :

Un Enfoque Multidisciplinario

Faustino Monroy & Leonel Gómez

Jackson School of Geosciences

Fracture Research and Application Consortium, Bureau of Economic Geology
Department of Geological Sciences

The University of Texas at Austin

INTRODUCCION

Figure courtesy of Brian Russell

INTRODUCCION

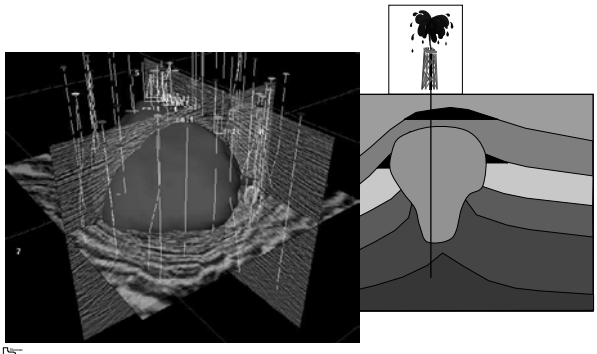

Figures courtesy of Phillips Petroleum Co.

INTRODUCCION

Contenido

[redacted]

Contenido

[redacted]

Enfoque Conceptual de FRAC

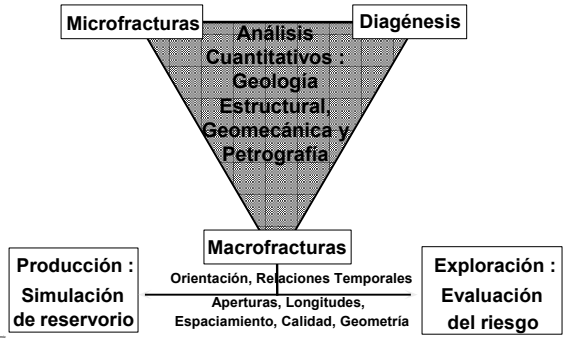

Compañías socias en Fracture Research & Application Consortium

BG Group
Chevron
conoco
devon ENERGY CORPORATION
Ashland
MARATHON
PEMEX
LARIAT PETROLEUM, INC.
PDVSA
JNOC
Japan National Oil Corporation
Williams
BR PETROBRAS
eog resources
REPSOL YPF
Enron Global
Geocosm
TOTAL FINA ELF

Petroleum & Geosystems Engineering – Geological Sciences – Bureau of Economic Geology
The University of Texas at Austin

Porqué Estudios Empíricos ?

Sólo cuando se conozca muy bien :

- Cómo se encuentran las fracturas en la naturaleza
- Cómo medir y representar en forma cuantitativa las propiedades de un sistema fracturado

Porqué Modelar las Fracturas ?

Sólo cuando se conozca muy bien :

- Cómo se encuentran las fracturas en la naturaleza
- Cómo medir y representar en forma cuantitativa las propiedades de un sistema fracturado

Se podrá generar modelos matemáticos que representen adecuadamente un sistema fracturado

- Modelos que puedan predecir correctamente el flujo de hidrocarburos

Contenido

- Enfoque Conceptual de FRAC
- Clasificación de Fracturas Subsuelo
  - Diaclasas vs. Venas o Vetas
  - Subsuelo vs. Superficie

Clasificación de Fracturas

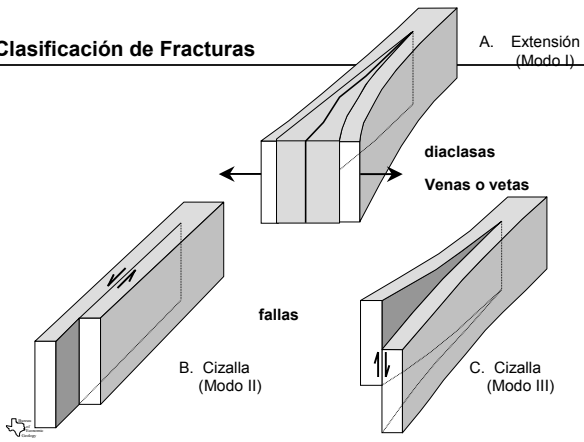

Twiss and Moores, 1997

Diaclasas Vs. Venas

Diaclasa	Vena o veta
• Desplazamiento pequeño	• Desplazamiento variable
• Apertura limitada	• Rango amplio (μ – cm)
• Sin cemento cristalino	• Total o parcialmente rellena
• Originada en la superficie	• Formada en el subsuelo

Porque estudiar venas?

• Venas son abundantes en las rocas.

• <u>El relleno mineral de las venas preservan su historia geológica.</u>

El estudio de los cementos minerales puede revelar información importante acerca del origen, tiempo y condiciones en las cuales el fracturamiento fue originado.

• <u>Las venas pueden estar partialmente abiertas y por lo tanto ser conductoras de fluidos en el subsuelo.</u>

Aplicaciones importantes en almacenamiento de material peligroso (radioactivo), caracterización de yacimentos de petróleo, evaluación de riesgo en zonas sísmicas, etc.

Fuentes de Información Acerca del Fracturamiento

Subsuelo	Superficie
<u>Yacimientos de aceite y gas</u>	<u>Afloramientos</u>

Información de Fracturas

Distribución espacial, orientación, apertura, longitud, densidad, relleno mineral, textura, porosidad, e interpretación del origen

Problemas en la Colección de Datos de Fracturamiento

Subsuelo	Superficie
• procesos repetitivos (sobreimpuestos)	• procesos repetitivos (sobreimpuestos)
• problema de muestreo	• No existen problemas de muestreo
• problema de escala	• No existen problemas de escala
• Resolución sísmica	• Colección de datos restringido al tiempo.

Los estudios diagenéticos pueden en parte resolver el problema de procesos sobreimpuestos relacionados con el sepultamiento, levantamiento, exhumación y erosión. Por lo tanto podemos estudiar los principales procesos que gobiernan el fracturamiento en la superficie y aplicar el aprendizaje en el subsuelo donde los datos son escasos.

Fracturas en Afloramientos

Consideraciones:

- Los afloramientos proveen abundante información sobre la historia diagenética y tectónica de las rocas en estudio.
- Pero esta historia diagenética y tectónica puede ser diferente en las roca en subsuelo, sin embargo las metodologías y los resutados obtenidos en estudios de rocas en afloramientos tienen aplicabilidad en el subuelo.

Aplicación de los Estudios de Afloramientos

- Permiten calibrar las técnicas de detección y medición del fracturamiento.
- Permiten proponer postulados sobre el origen y evolución de los sistemas fracturados.

Contenido

- Enfoque conceptual de FRAC
- Clasificación de Fracturas
- Muestreo de Fracturas en el Subsuelo
  - Nuevo enfoque y nuevas metodologías
  - Microfracturas como guía de Macrofracturas

Muestreo de Fracturas en Subsuelo

Cantidad de fracturas en muestras del subsuelo es baja

- Pozos y fracturas usualmente verticales
- Características de fracturas puede cambiar entre capas
- Espaciamiento entre fracturas es en general >> Diámetro de pozo

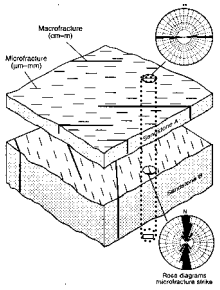

Muestreo de Fracturas en Subsuelo

- Aún si las fracturas son muestreadas, los datos pueden ser incompletos o inadecuados
  - Gran cantidad de datos son requeridos para predecir propiedades del sistema de fracturas mas allá del pozo

- **Detección sísmica de fracturas**
  - **Muestreo inadecuado hace difícil verificar resultados de métodos indirectos de detección de fracturas**

Problema de Muestrear Fracturas en Subsuelo

Puede ser resuelto con un nuevo enfoque :

- Microfracturas como guía de las Macrofracturas
- Meticulosa observación y medición de características de micro y macrofracturas

Y nuevas metodologías y tecnologías como :

- Orientación de sidewall cores
- Catodoluminiscencia (CL) en microscopio electrónico (SEM)

MICROfracturas y MACROfracturas

Microfractura :

Se necesita de algún instrumento para observarla y medirla

- Lupa
- Microscopio Petrográfico
- Microscopio Electrónico

Macrofractura :

Se puede observar a simple vista

Microfracturas : Abundantes y Selladas

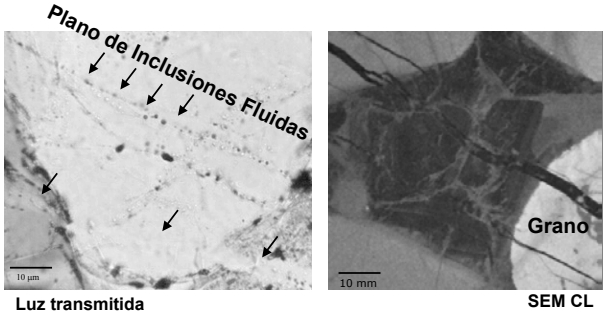

Luz transmitida **SEM CL**

Arenisca Flathead , WY

SEM/CL Revela MICROfracturas en Dolomitas

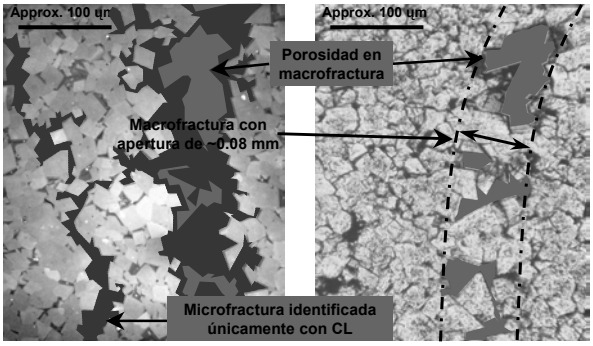

Catodoluminiscencia Petrografía Convencional

Fracture Research & Application Consortium **Sección delgada vertical - Sidewall core – Fm. Ellenburger – West Texas**

Microfracturas y Macrofracturas

Pozo: Caparroso 35 **Corazon: No. 2**

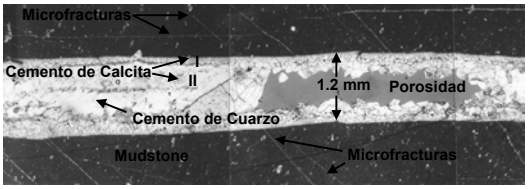

top

Fracture Research & Application Consortium

Microfracturas vs. Macrofracturas

	Microfracturas	Macrofracturas
• Abundancia relativa	Mayor	Menor
• Probabilidad de muestreo	Alta	Baja
• Calidad (porosidad de fractura)	Baja – nula	Alta - Moderada
• Permeabilidad	Baja – nula	Alta

Las microfracturas colaboran en poco o nada a la permeabilidad del yacimiento

Fracture Research & Application Consortium

MICROfracturas como Guía de MACROfracturas

Si microfracturas y macrofracturas comparten :
- Historia diagenetica (tipo de cementos, etc.)
- Orientación
- Relaciones temporales con otro tipo de estructuras (fracturas, estilolitas, etc.)

Se puede asumir que ambos tipos de fracturas forman parte de un mismo juego de fracturas

La orientación no es criterio suficiente debido a la dificultad de medir la orientación 3D de las microfracturas

Fracture Research & Application Consortium

Limitaciones en el uso de Orientación de Fracturas

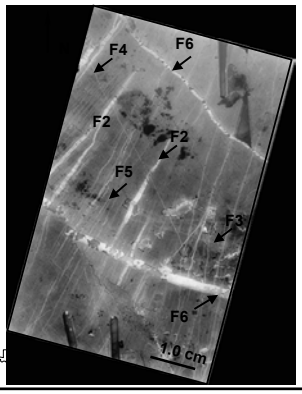

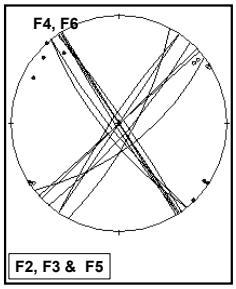

Cañon Las Palmas

MICROfracturas como Guía de MACROfracturas

El consorcio FRAC ha podido probar que las microfracturas :

- Son más abundantes que las macrofracturas
- Pueden predecir de las macrofracturas :
  - Orientación (Laubach, 1997)
  - Abundancia (Marrett et al., 1999)
  - Calidad (fractura abierta)
  - Historia Diagenética (Monroy et al. 2001)

Micro y macrofracturas están ligadas cuantitativamente

MACROfracturas continúan siendo Valiosas !

Si están presentes, las macrofracturas pueden aportar importante información :

- Orientación
- Historia de cementación
- Presencia de hidrocarburos
- Tamaño mínimo de fractura abierta

Contenido

- Enfoque conceptual de FRAC
- Clasificación de Fracturas
- Muestreo de Fracturas en el Subsuelo
- Orientación de Fracturas

Micro y Macrofracturas de un mismo Sistema

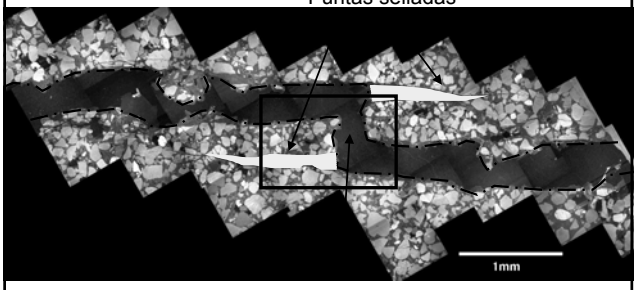

Collage de imágenes obtenidas en SEM / CL

Fracture Research & Application Consortium

Micro y Macrofracturas de un mismo Sistema

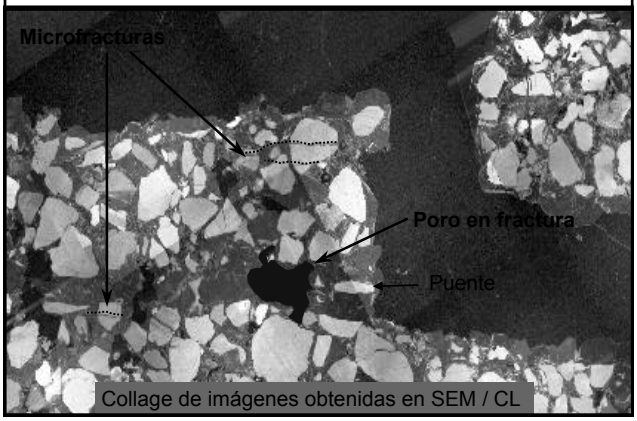

Qué Microfracturas deben usarse ?

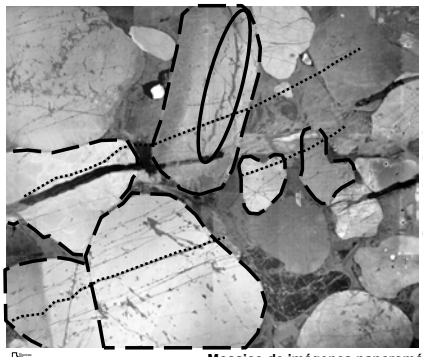

Solamente las microfracturas que crucen grano(s) y cemento(s) deben ser usadas para predecir la orientación de Macrofracturas (Laubach, 1997)

Fracture Research & Application Consortium

Mosaico de imágenes pancromática SEM/CL

Fm. Cambrian Bliss, Texas

Orientación Final de Micro y Macrofracturas

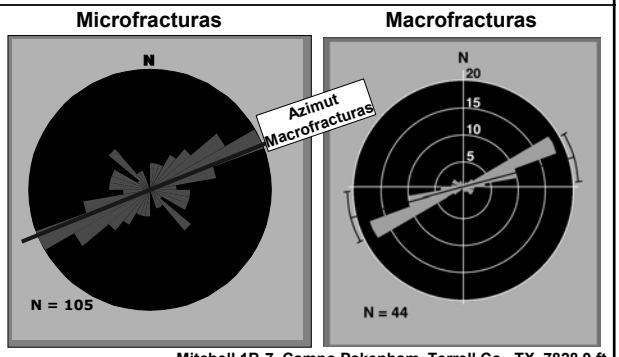

Fracture Research & Application Consortium

Mitchell 1B-7, Campo Pakenham, Terrell Co., TX, 7828.9 ft

Fm. Wolfcamp, Cuenca Val Verde, West Texas

Contenido

- Enfoque conceptual de FRAC
- Clasificación de Fracturas
- Muestreo de Fracturas en el Subsuelo
- Orientación de Fracturas
- Escalamiento
  - Intensidad de Fracturamiento

Poblaciones de Fracturas Sintéticas

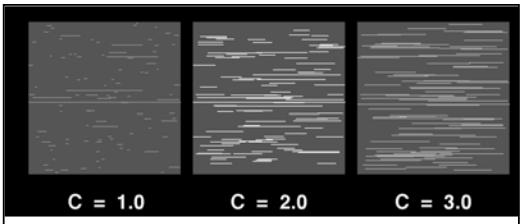

- La fractura mas larga en cada mapa tiene la misma longitud
- 100 fracturas en cada mapa
- La distribución de longitudes de fracturas en cada mapa es diferente

Poblaciones de Longitud de Fracturas

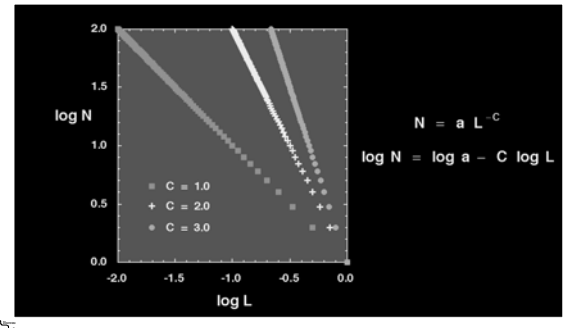

Estimar Intensidad de Fracturamiento

Medir apertura de microfracturas :

- Cruzan grano(s) y cemento
- A lo largo de una línea
- Perpendicular a la orientación de sistema de fracturas

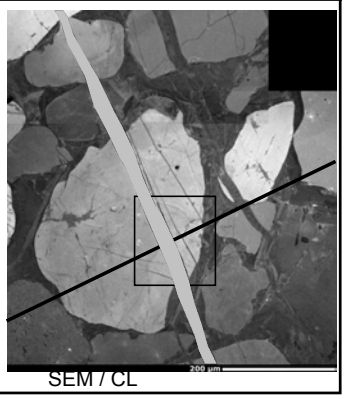

SEM / CL

Estimar Intensidad de Fracturamiento

~ 3 µm

~ 27 µm

Normaliza el número de fracturas por la longitud de la línea de medición :

Ej.: 10 microfracturas >≥ 20 µm en 1mm

$$\frac{10\ mf}{mm} \times \frac{1000\ mm}{1\ m} = \frac{10000\ mf}{1\ m}$$

Fractura con diferente orientación

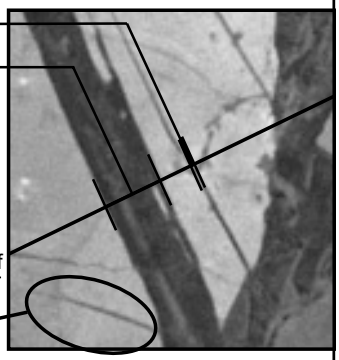

SEM / CL — 25 µm

Fracture Research & Application Consortium

Escalamiento de Fallas en Yucca Mountain ESF y Mapas Regionales

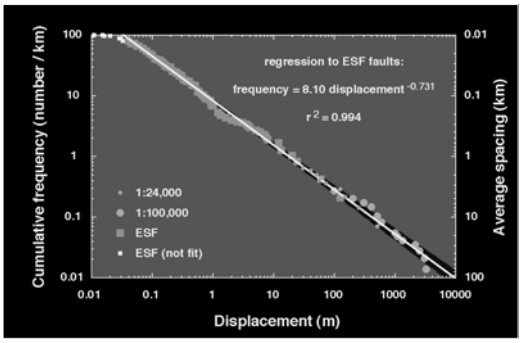

Fracture Research & Application Consortium

Fallas en la Rampa Norte ESF, Yucca Mountain Nevada

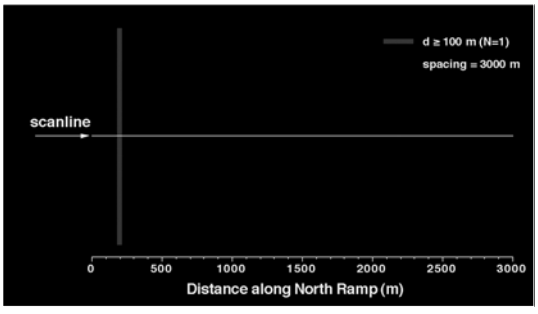

Fracture Research & Application Consortium

Escalamiento de Fallas en Yucca Mountain ESF y Mapas Regionales

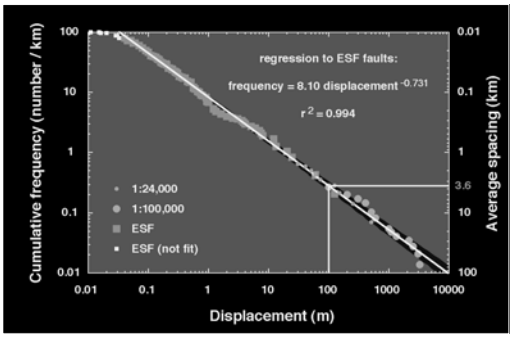

Fracture Research & Application Consortium

Escalamiento de Fallas en Yucca Mountain ESF y Mapas Regionales

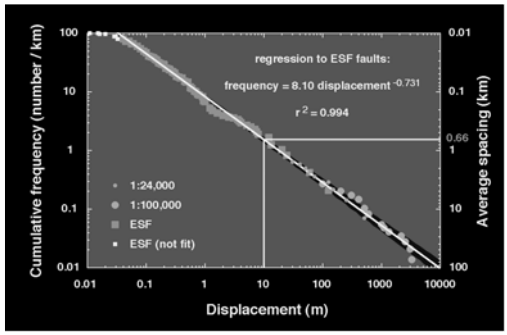

Fallas en la Rampa Norte ESF, Yucca Mountain Nevada

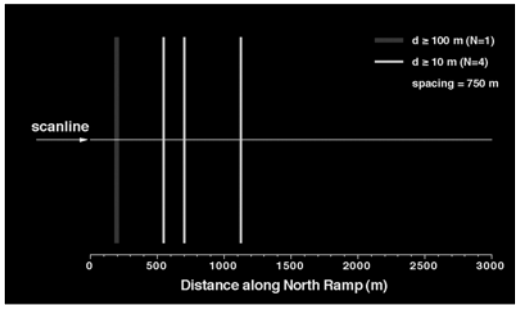

Escalamiento de Fallas en Yucca Mountain ESF y Mapas Regionales

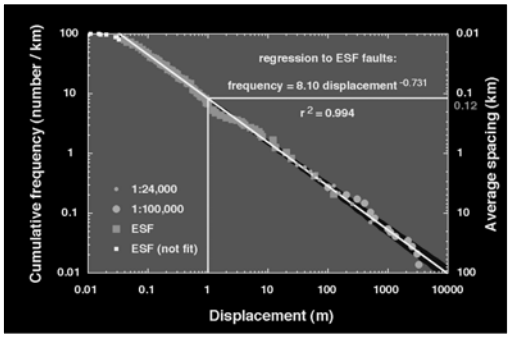

Fallas en la Rampa Norte ESF, Yucca Mountain Nevada

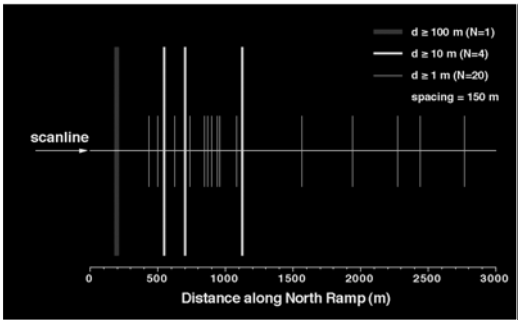

Escalamiento de Fallas en Yucca Mountain ESF y Mapas Regionales

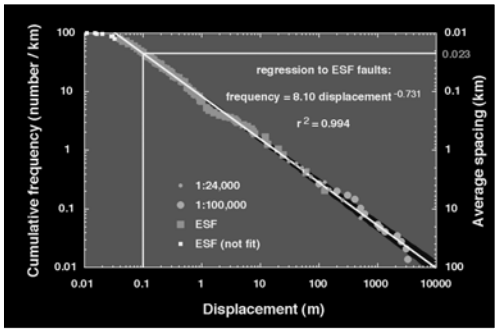

Fallas en la Rampa Norte ESF, Yucca Mountain Nevada

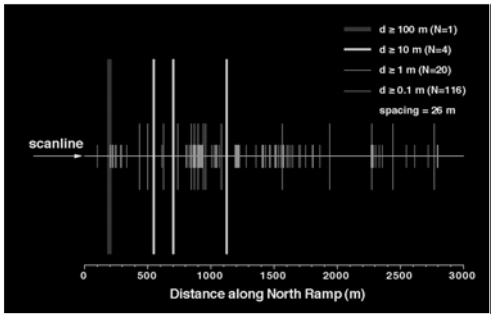

Arenisca Ozona, Texas Pozo Blakeney-Krueger #1

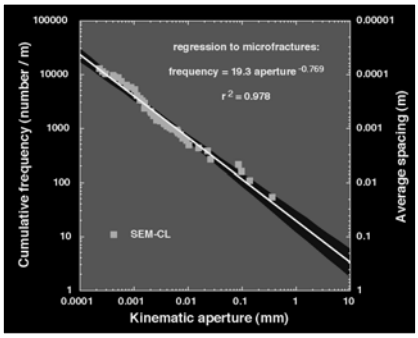

Arenisca Ozona, Texas Pozo Blakeney-Krueger #1

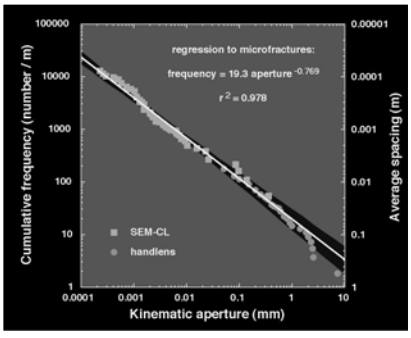

Caliza Marble Falls
Pedernales Falls State Park, Texas

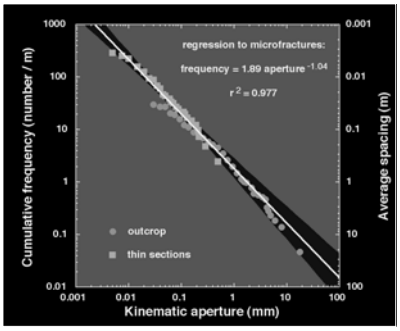

Escalamiento de Aperturas y Predición de Macro- a partir de Microfracturas

- Pedernales (Caliza Marble Falls)
- NE de México (Formación Cupido)
- NE de Texas (Austin Chalk)
- W de Venezuela (Formación Apon)
- SE de México (Campo Citam)

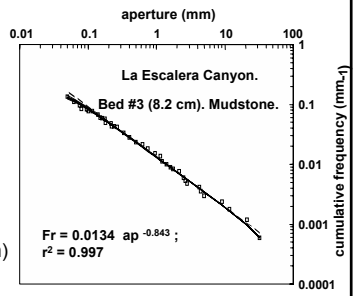

Comparando Intensidades de Fracturamiento

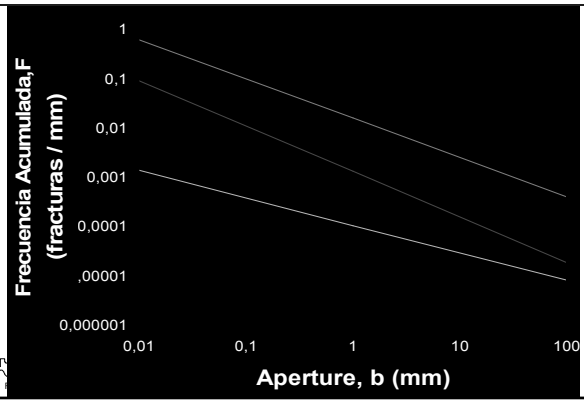

Escalamiento

Pozo: Caparroso 35 **Núcleo: 2**

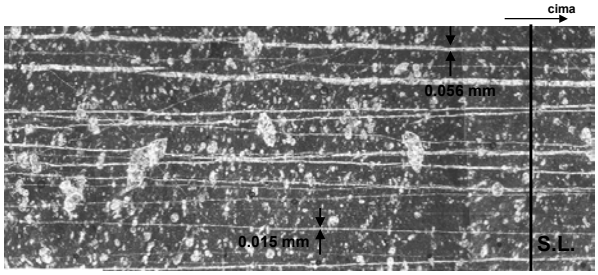

Escalamiento

Pozo: Caparroso 35 **Núcleo: 2**

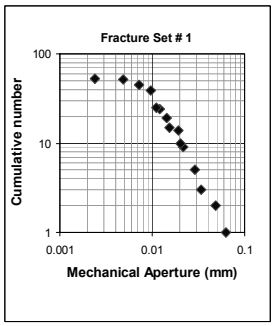

Contenido

- Enfoque conceptual de FRAC
- Clasificación de Fracturas
- Muestreo de Fracturas en el Subsuelo
- Orientación de Fracturas
- Escalamiento
- Calidad de Fractura
  - Fracturamiento y Tipos de Cemento
  - Predicción de Fracturas Abiertas (Indice de Degradación)

Diagénesis y su importancia

La mayoría de libros de texto definen diagenésis como <u>todos los procesos</u> (químicos, físicos y biológicos) que afectan los sedimentos despues de ser depositados hasta antes de entrar en condiciones de metamorfismo a elevadas presiones y temperaturas.

MICRITIZATION, NEOMORFISMO, DISOLUCION, COMPACTACION, DOLOMITIZATION Y CEMENTACION

Y el Fracturamiento?

diagénesis ⟺ **fracturamiento**

Interrelacionados?

Posibles interrelaciones

diagénesis

- **afecta porosidad, y permeabilidad**
- **afecta las propiedades mecánicas de las rocas**
- **afecta el fracturamiento**

⟺

fracturamiento

- **afecta las propiedades mecánicas de las rocas**
- **afecta el flujo de fluidos**
- **afecta otros procesos diagenéticos**

Importancia de las fractures

Aplicación en yacimientos de hidrocarburos, geohidrología, minería, etc.

Fracturamiento y Tipos de Cement

- Cemento Syn-cinemático
  - Precipita durante el desarrollo del sistema de fracturas
  - Usualmente no sella fracturas grandes pero genera “puentes” y textura “crack-seal”

Cemento de Cuarzo Syn-cinemático

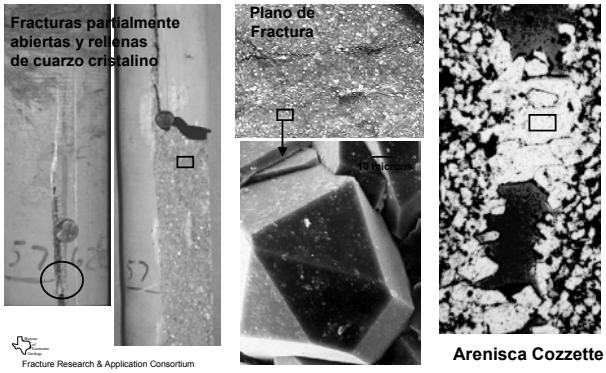

Textura “Crack Seal” en Areniscas

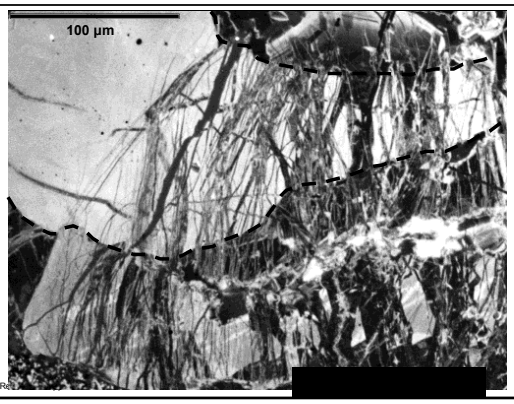

Fracturamiento y Tipos de Cemento

- Cemento Syn-cinemático
  - Precipita durante el desarrollo del sistema de fracturas
  - Usualmente no sella fracturas grandes pero genera “puentes” y textura “crack-seal”
- Cemento(s) Post-cinemático
  - Precipita después del desarrollo del sistema de fracturas
  - Principal culpable de sellar fracturas grandes

Tipo de Cementos

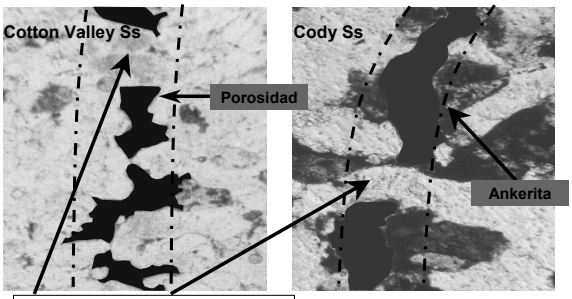

Cementos tempranos vs Cements tardíos

El cemento Syn-cinemático precipita ~ cuando las fracturas se están abriendo

El cemento Post-cinemático precipita ~ cuando las fracturas están estáticas

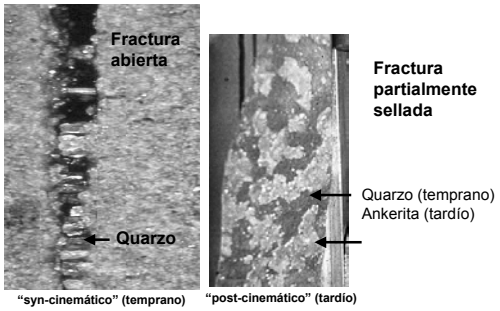

Que Substitutos hay Disponibles ?

Se puede diferenciar esos cementos sin muestrear las fracturas grandes ?

- Propiedad de la roca que se pueda medir y que proven información local sobre las fracturas sin necesidad de muestrearlas :
  - Porosidad y porcentaje del(os) cemento(s) en las roca – análisis petrográfico convencional
  - Relación temporal del(os) cemento(s) con las fracturas (paragenesis)

Referencia: **"New Directions in Fracture Characterization"**
The Leading Edge July 2000 Laubach, Marrett, & Olson

Indice de Degradación

- Fracturas grandes están abiertas o selladas
  - Si las fracturas grandes están selladas, cemento post-cinemático (PK) es usualmente el culpable (Indice de Degradación alto = fracturas selladas)

$$\text{Degradación (Dg) \%} = \left(\frac{\text{\% cemento Post-K}}{\Phi + \text{\% cemento(s) Post-K}} \right) \times 100$$

Relación de cemento post-cinemático con respecto al volumen intergranular

- Si están presentes, macrofracturas se pueden usar para calibración

Probando el Indice de Degradación

- Prueba a ciegas de dos pozos en la misma arenisc
  - Uno productor, uno secc
  - Núcleos disponibles
  - Porosidad matriz similar
  - Observó número similar de fracturas en ambos pozos
- Procedimientos de perforación idénticos

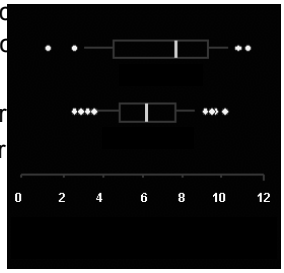

Campo Pakenham - Chevron

Probando el Indice de Degradación

- Indice de Degradación identificó áreas de fracturas abiertas y cerradas
- Se pudo diferenciar el pozo seco del pozo productor

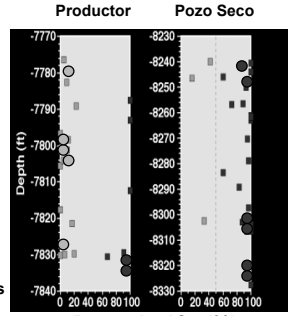

Macrofracturas
Selladas
Abiertas

Alto Indice de Degradación = Fracturas selladas

Contenido

- Enfoque conceptual de FRAC
- Clasificación de Fracturas
- Muestreo de Fracturas en el Subsuelo
- Orientación de Fracturas
- Escalamiento
- Calidad de Fractura
- Modelamiento de Sistemas Fracturados
  - Análisis Estático de Esfuerzos ("Stress Shadow")
  - Indice de Fracturamiento SubCrítico

Sombra de Esfuerzo (Análisis Estático)

- La reducción del esfuerzo causada por la generación de una fracturas elimina energía disponible para que otras fracturas se formen en un área alrededor de la fractura inicial
- El tamaño de la *sombra de esfuerzo* incrementa con la longitud de la fractura

Cálculo de la Perturbación de los Esfuerzos alrededor de la Fractura

- Modelado numérico en tensión uniaxial
- Desarolla una fractura modo I perpendicular a la tensión aplicada
- Resultados simétricos alrededor de la fractura (mostraré solo una mitad)

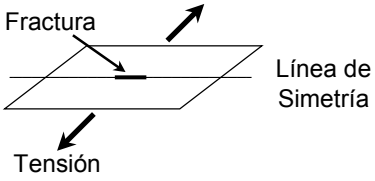

Crecimiento de la *Sombra de Esfuerzo* - L=6

Length =6

Esfuerzos se concentran en la punta de la fractura

Sombra de Esfuerzo

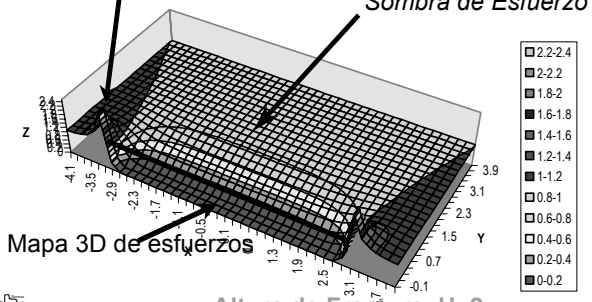

Mapa 3D de esfuerzos

Altura de Fractura, H=2

Sombra de Esfuerzo & Espaciamiento entre Fracturas

Espesor capa = 2

El espaciamiento entre fracturas es proporcional al tamaño de la *sombra de esfuerzo*

Nueva fractura

Espesor capa = 4

Espesor capa = 6

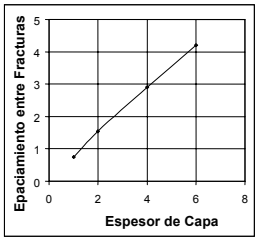

Espaciamiento Vs. Espesor de capa

Qué le falta al Concepto de *sombra de esfuerzo* ?

- No tiene en cuenta propagación dinámica :
  - Fracturas pueden crecen simultáneamente
  - Interacción entre fracturas cambia la distribución espacial y de apertura del sistema de fracturas
  - Fracturas pueden crecer a diferentes velocidades

Ley de Propagación Crítica de Fracturas

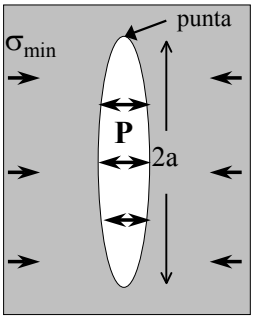

- Esfuerzo se concentra en la punta de la fractura :

  $K_I = (P-\sigma_{min}) (\pi\ a)^{1/2}$
- Propagación crítica (catastrófica o instantánea) ocurre cuando K_I excede K_{Ic} ("fracture toughness")

Porqué Crecimiento Sub-crítico en fracturas naturales en rocas ?

- Indica debilitamiento de la roca debido a :
  - Aplicación de pequeños esfuerzos a largo plazo, similar a procesos geológicos
  - Efecto corrosivo de fluidos en poros (agua)
- Modelamiento produce sistemas de fracturas con geometrías similares a sistemas naturales

Ley de Propagación "Sub-crítica"

- Criterio de la Intensidad del Esfuerzo (modo I)
- Regla de la velocidad de Propagación

  $v \propto (K_I / K_{Ic})^n$

V = velocidad de propagación

n = índice de fracturamiento subcrítico (IFS)

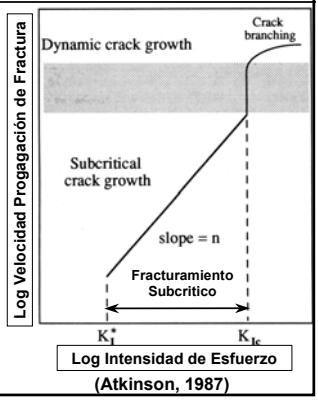

(Atkinson, 1987)

Velocidad de Propagación Vs. Intensidad de Esfuerzo

Bajo n :
- Menor contraste de velocidades
- Mayor propagación a menor intensidad de esfuerzo

Alto n :
- Mayor contraste de velocidades
- Propagación sólo a altos valores de intensidad de esfuerzo

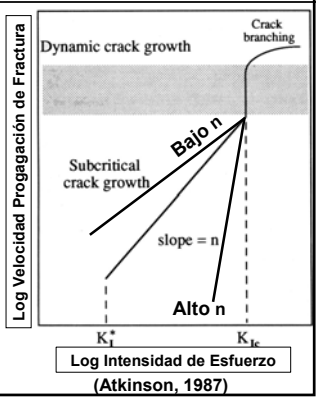

(Atkinson, 1987)

Instrumento para Medir Indice de Fracturamiento Subcrítico

- Resultados repetibles
- n varía con el tipo de roca
- n cambia con material en poros : aceite, agua, aire

Permite obtener valores de n en diferentes horizontes

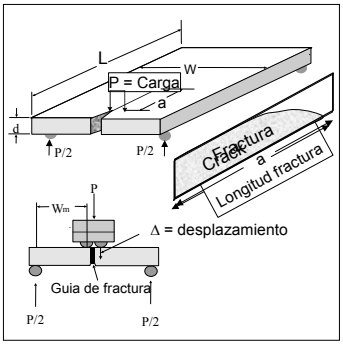

Holder, Olson and Philip, 2000, JGR

Modelo Geomecánico de Fracturamiento Subcrítico

- Tensión uniaxial
- Zero esfuerzo de cizalla ("shear stress")
- Imperfecciones distribuidas al azar, iniciadoras de fracturas
- Todas las fracturas son verticales

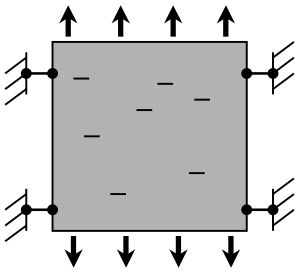

Método Numérico de Fracturamiento Subcrítico

- Tiene en cuenta interacción entre fracturas que se propagan simultáneamente
- Propagación obtenida agregando elementos en la punta de la fractura (criterio de propagación subcrítica)

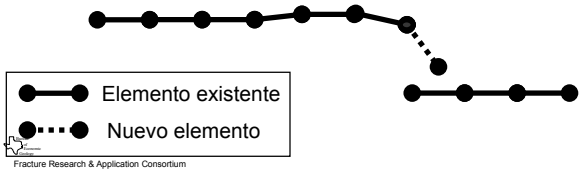

IFS & Espaciamiento entre Fracturas

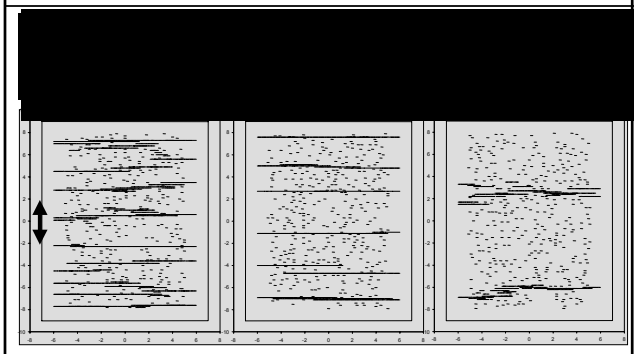

n = 5 n = 20 n = 80

Espaciamiento entre Fracturas

- El tamaño de la *sombra de* esfuerzo ejerce un control básico sobre el espaciamiento entre fracturas pero sólo explica los efectos estáticos
- El IFS, n, controla qué tan agrupada (“ clustering”) y modifica la relación lineal entre espaciamiento y espesor de capa

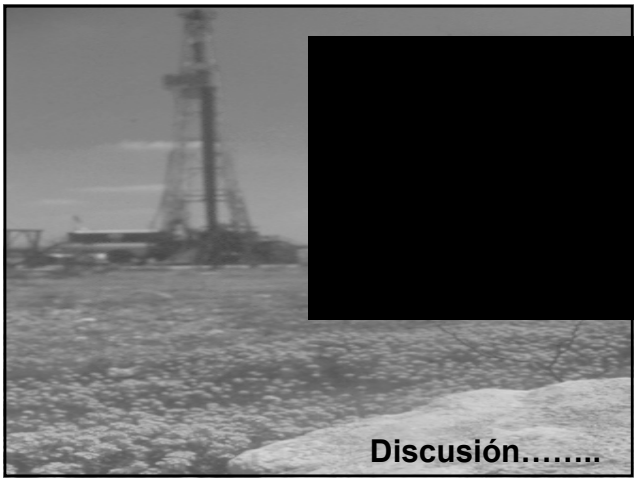

Fracture Research and Application Consortium
Geocosm LLC

Agenda, Saturday June 22, 2002

Application Workshop

Snow King
Jackson, Wyoming

Time	Topic	Presenter
8.30am	**Introduction**	
8.45	**Protocol for fractured sandstone evaluation**	**Laubach**
	Predicting fracture attributes	**Olson**
	Quartz diagenesis and fractures in sandstones	**Lander/Bonnell**
	Measuring microstructural surrogates	**Laubach**
12:00	Lunch at Snow King	
1.00	**Mapping quality using degradation**	**Laubach**
	Assessing fracture intensity using scaling	**Gale**
	Integrating methods to target fractures	**Gale**
	Integrating methods for flow simulation	**Olson**
	Integrating methods to calibrate seismic	**Montoya**[§]
	Deploying the technology	**Laubach/Olson/Lander**
4:45–5:00pm	**Wrap-up discussion**	
Evening	Optional dinner (Dornan's) tbd	

Coffee breaks will occur during morning and afternoon sessions.

[§]*Montoya is unable to attend. Her slides are included and we will discuss the topic.*

Field Trip

Fractured Sandstones of the Rockies
June 21–22, 2002

FRAC

Steve Laubach, E-mail **steve.laubach@beg.utexas.edu**
Jon Olson, E-mail **jolson@mail.utexas.edu**
Eric Potter, E-mail **eric.potter@beg.utexas.edu**
Julia Gale, E-mail **julia.gale@beg.utexas.edu**

GEOCOSM

Rob Lander, E-mail **roblander@geocosm.net**
Linda Bonnell, E-mail **lmbonnell@geocosm.net**

MARATHON

Jiaje (Jeff) Chen, E-mail **JChen@MarathonOil.com**
Pauline Chung, E-mail **pchung@MarathonOil.com**
Gary Benteau, Calgary office
Case Caulfield, Calgary office
Martin Dobson, Cody Office
Daniel Miller, Cody Office

SCHLUMBERGER

Dick Plumb, E-mail **plumb1@houston.oilfield.slb.com**
Bob Young, E-mail **byoung@houston.geoquest.slb.com**
Barbara Luneau, E-mail **bluneau@denver.oilfield.slb.com**

SHELL

Dan Worrall, E-mail **dmworrall@Shell.Com**
Orlando Ortega, E-mail **Orlando.Ortega@shell.com**

TOM BROWN INC.

Steve Parks, Calgary office
Terri Olson, Denver office
Harold (Hal) Harper, Denver office
Rob Pryde, Denver office
Glenn Bixler, Midland office
Dave Thomas, E-mail **dthomas@tombrown.com**

WILLIAMS

Robin Ausbrooks, E-mail **Robin.Ausbrooks@Williams.com**